Department of Applied Geology

Petrogenesis of Granitoid and Greenstone Rocks in the Yalgoo Area, Murchison Domain of the Youanmi Terrane, Yilgarn Craton, Western Australia, with Emphasis on Granitoid-Hosted Gold Mineralization

S. M. Mahbubul Ameen

This thesis is presented for the Degree of
Doctor of Philosophy
of
Curtin University

November 2012

Declaration

To the best of my knowledge and belief this thesis contains no material previously published by any other person except where due acknowledgment has been made.

This thesis contains no material which has been accepted for the award of any other degree or diploma in any university.

Signature: …….

Date: 30-11-2012

Abstract

The present study is focused on the poorly-studied Yalgoo area in the central-west Murchison Domain, Yilgarn Craton, Western Australia. The major objectives of the study were to determine the petrological and geochemical characteristics of the volcanic and granitoid rocks in the area, determine the age of the granitoids and mafic dykes, characterize the nature of the granitoid-hosted-gold mineralization and thereby propose a crustal evolution model for the area.

The mafic volcanic rocks are considered to belong to the oldest (~2.82 Ga) Murrouli Basalt Formation, which is intruded by small granitoid bodies (4 -6 km^2), minor felsic porphyries and mafic dykes. The Yalgoo area also contains a small number of historical gold mining centres and is considered to have potential for further gold mineralization.

Two groups of mafic volcanic rocks were identified. The first group is Low-Ti enriched tholeiite (LET) with low SiO_2 (52.15%), TiO_2 (0.59%) and moderate MgO (7.51%) contents, moderately-enriched LREE $(La/Sm)_{CN}$ = 0.96-1.43) and fractionated HREE [$(Gd/Lu)_{CN}$ = 0.67–0.74)]. These characteristics indicate a boninitic affinity. The second group is Low-Ti depleted tholeiite (LDT), having similar SiO_2 (51.93%), slightly lower TiO_2 (0.51%) and higher MgO (9.72%) contents than LET, moderate depletion in LREE $(La/Sm)_{CN}$ = 0.62-0.79) and unfractionated HREE ($(Gd/Lu)_{CN}$ = 0.85–0.88). An andesite shows strong resemblance in chemical composition to the Archean High-Mg basalt. The Lady Lydia granitoid (LLG), Yalgoo east granitoid (YEG) and Yalgoo north granitoid (YNG) are the three granitoids present in area. They form three suites, i) granodiorites (from both LLG and YEG) with strongly fractionated REE patterns and high LREE contents (average La_{CN} > 100), very low HREE contents, (Yb_{CN} <3) weakly positive Eu anomalies and shows Archean TTG affinity; ii) biotite hornblende monzogranite (from LLG) with the LREE/HREE ratio less [$(La/Yb)_{CN}$ =19] than the granodiorite samples and a weak negative Eu (0.97) anomaly and iii) biotite monzogranites (from YNG)) with high LREE/HREE [$(La/Yb)_{CN}$ =57.5] enrichment and prominent negative Eu (0.40-0.46) anomalies. All the granitoids show strong calc-alkaline characterstics. The biotite hornblende monzogranite hosts gold mineralization (in the Brilliant open pit, LLG), with the highest grade concentrated in quartz-pyrite veins.

Granodiorites (n=6) were dated by SHRIMP U-Pb zircon methods and record ages of 2763-2752 Ma. The biotite monzogranites (n=2) recorded ages of 2636-2634 Ma. No zircons were found in the biotite monzogranite. A porphyritic microgranodiorite, geochemically similar to the granodiorite, gave an age of 2762 Ma. A dolerite dyke, geochemically similar to the LDT recorded an age of 1.85 Ga, which is the youngest Proterozoic event documented in the Murchison Domain of the Yilgarn Craton.

The geochemical characteristics of the LET samples suggest that the parental melt for these rocks formed from a metasomatized mantle, depleted by a previous melt extraction event in an intraoceanic fore-arc setting. The LDT rocks were derived from a deeper source as evidenced by their high Mg#, Ni and Cr contents. These lavas probably would have erupted through fissures present in an early fore-arc. The high-Mg andesite with relatively high silica (62.1%), high Mg # (068), Cr and Ni (244, 134 ppm, respectively) implies the parental melt was generated from high-silica adakites (from slab melting) by interaction with the mantle and an enriched source. Abundant (3.00 – 2.94 Ga) xenocrystic zircons and the Lu-Hf isotopic characteristics of the granitoid samples imply a long history of crustal recycling in the Yalgoo area, including an isotopic signature suggesting the presence of Hadean (~4.13 Ga) crust [strongly –ve εHf(t) values] in the source of the granodiorites. The mafic volcanic package with distinct uncontaminated boninitic character favours the accretion of the mafic volcanics onto the

continental block (present base of the greenstone) analogous to accretion of an (incomplete) ophiolite, as documented in the 3.8 Ga Isua supracrustal belt in Greenland. Therefore, an intraoceanic supra-subduction model is proposed for the formation of the mafic volcanics. After accretion, the prevalent ~2.76 Ga granodiorites were formed from melts generated from mainly two sources, at ~3.6 Ga and ~3.3 Ga, in the subcontinental lithospheric mantle, which interacted with an early (3.00 Ga to 2.94 Ga) lower crust. Increased crustal thickening due to the convergence (after cessation of subduction) caused melting in the upper/mid-crustal level, which generated parental melt for the ~2635 Ga biotite monzogranites. Immediately after that the Noongal Shear Zone (NSZ) formed due to continued east-west regional compression at ~2.63 Ga. Given the foliation-parallel mineralized sigmoidal quartz-pyrite veins and similar trend of the NSZ and mineralized veins, ~2.63 Ga is also suggested to be the age of the granitoid-hosted gold mineralization in the Yalgoo area, which is in agreement with the age bracket of 2.65 -2.62 Ga of the craton-wide major pulse of gold mineralization. Emplacement of a dolerite dyke at 1.85 Ga could represent a previously unrecognized Proterozoic event in the Yilgarn Craton, which warrants further study.

The absence of komatiite/komatiitic basalt, the presence of supra-subduction zone boninitic rocks and calc-alkaline granitoids, high-Mg andesite and a long history of crustal recycling does not favour plume-related magmatism, as recently proposed for the crustal development of the Murchison Domain. However, given the small area covered in the present study, further work is required to understand the crustal development of the central-west Murchison Domain.

Acknowledgements

At first I offer my sincere indebtedness to the Almighty Allah who has got me through this long (May 2004 to November 2012) ordeal. I also offer thanks to the Government of Australia for awarding me an Endeavour International Postgraduate Research Scholarship (EIPRS). I gratefully acknowledge the financial assistance provided by Mr. Richard Dawson, former Director, Prosperity Resources Limited (PRL). I am thankful to the authority of Jahangirnagar University, Bangladesh for granting me leave of absence from my lectureship position that allowed me to pursue the higher studies. My sincere appreciation goes to the Geological Survey of Western Australia for providing me a part-time employment opportunity in the Geological Mapping Division.

My heartfelt gratitude goes to my supervisor Professor Simon A. Wilde for the way he assisted me to get the EIPRS, for his patient and meticulous guidance particularly in proof reading and showing scientific inconsistencies in the draft. I really enjoyed and benefitted from the long discussions in the late hours in my Curtin days. His supervision in the laboratory protocols and field trip are also gratefully acknowledged. Discussions with co-supervisor Professor Peter Kinny have also been of great help.

Mr. Lyle Thorne, former Project Geologist (PRL), provided access to varied published and unpublished mining materials. Mr. Dave Holden and Ms. Georgina Harvey (PRL) helped me in core sample collection. Warm hospitality provided by the authority of the Carlaminda Homestead made the two field trips in the Yalgoo area pleasant.

Discussion with Drs. Jeff Vaughan, Peter Collins and Nick Timms of the Department of Applied Geology, Curtin University assisted me in clarifying many issues on ore petrography, fluid inclusion studies and deformation processes. Discussions with Drs. Nicolas Thébaud and Kate Evans also contributed greatly with fluid inclusion and EMPA data reduction.

I benefited from the classes by Associate Professor Ron Watkins, Dr. Mehrooz Aspandiar, and Professor Ian Fitzsimons of the same department. Elaine Miller and Stuart Dunn provided help in the SEM study. Assistance provided by Dr. Janet Muhling at the Centre for Microscopy, Characterisation and Analysis, University of Western Australia during EMPA analysis is gratefully appreciated. Exchange of ideas with Drs. Allen Kennedy, Matthew Grant, Simon Bodorkos and Michael Wingate has contributed in understanding the SHRIMP analytical techniques, data processing and interpretation. Assistance from Messrs Adam Frew and Eric Thern during SHRIMP data collection sessions is highly appreciated. Here I recall with great pleasure the encouraging words and a photo taken with Dr. Lance Black during a SHRIMP analytical session. Dr. Stephen Wyche of the Geological Survey of Western Australia kindly allowed me to use unpublished geochemical data. My thanks are also due to Drs. Bataa Ali, Kamal Ali, Hisham Herbi, Srinibash Sharma and Santanu Bhowmik (visiting fellows) for many stimulating discussions. I also thank Ms Lynda Frewer and Mr. Warwick, for allowing me to work casually at the Diatech Laboratory, Perth.

Bob Crossley and Peter Glover made all the thin-, polished- and fluid inclusion-sections. Geochemical analyses were carried out at the State Key Laboratory of Continental Dynamics, Northwestern University, Xi'an, China, and at Genalysis Laboratory Services, Perth, Australia. U-Pb ages were obtained by SHRIMP II in the John de Laeter Centre for Isotope Research at Curtin University. Zircon Hf isotopic analyses were conducted at the Institute of Geology and Geophysics, Chinese Academy of Sciences in Beijing, China.

After I returned to Bangladesh, help and support provided by my senior colleagues in the Department of Geological Sciences, namely Professor Delwar Hossain, Professor Md. Sharif Hossain Khan and Mr. Emdadul Haque (Chairman) has been of enormous value. Among the junior colleagues, Messrs. Zahidul Bari, Md. Sakawat Hossain, Rashed Abdullah, Rumana Yeasmin, Hossain Md. Sayem, Mazeda Islam, Abu Sadat Md. Sayem, and Mizanur Rahman shared workloads in many instances to allow me free time to finish the write up. Candid help provided by my former student Shireen Akter, project students Md. Sakawat Hossain, Sudeb Das and Al-Tamini Tapu, in particular, is greatly appreciated. I am also grateful to Mrs. Annette Labrooy in Applied Geology at the Curtin University and to all the staff members (Atahar Ali and Yousuf Ali, in particular) at the Department of Geological Sciences, Jahangirnagar University for continuous encouragement to finish the thesis.

This thesis would not have been completed without the sincere co-operation and prolonged sacrifices of my extended family. Continuous monitoring of the progress of thesis, inspiration, and prayers provided my parents, father Md. Anwarul Ameen in particular, has been a strong driving force for completing the thesis. Co-operation and support provided by my mother Mrs. Jahanara Begum and sister Saadia Afreen has also been invaluable. My wife Naznin Akter endured a lot for allowing me free time for the thesis. I hardly recall that I spent a full stress-free day with our only son Raif. It put me in tears to recall how many times I refused to embrace my son Raif during the gruelling time at the last (long last one and half years) stage of my write up. It is amazing that except for the gold mineralization and granitoid chapters, all the final interpretations (of course with close and thorough online supervision by my supervisor) of remaining chapters have been constructed here in Bangladesh. Numerous discussions with my wife assisted me a lot in finalizing those chapters.

I am indebted to my fellow PhD students Rami Al Rashwadi, Avijit Das, Stuart Dunn, John, Wen Jen and MSc student Zaed Iqbal for their warm company and assistance. My heartfelt gratitude also goes to friends Khalid, Adnan, Askar Ali, Shudha, Nazmul, Moazzem, and Aunt Amira for providng me with a happy Perth life.

CONTENTS

LIST OF TABLES

LIST OF FIGURES

Chapter 1 Introduction

The Yalgoo area falls within the west central portion in the Murchison Domain of the Yilgarn Craton, Western Australia (Fig. 1.1a). The area is dominated by layered mafic rocks with minor banded iron formation (BIF) of the Luke Creek and Mount Farmer groups that constitute the Yalgoo greenstone sequence, and are intruded by granite and local felsic porphyries (Fig. 1.1b). The whole package of rocks has been affected by a north-northeast trending Neoarchean shear zone known as the Noongal shear zone (NSZ). A few northwest-trending mafic dykes cut across the Archean stratigraphy. The area was mined locally in the past and has been considered to have potential for Archean shear-hosted gold mineralization. However, the presence of only sub-economic gold in the area has acted as a deterrent to conducting further detailed geological studies by mining companies. The area formed part of the regional mapping programme of the Geological Survey of Western Australia during the 1970s and 1990s.

A systematic geological study encompassing petrology, geochemistry, geochronology and isotope geology of the greenstone and granitoid rocks was conducted in the Yalgoo area in order to understand its development and relationship to other parts of the Murchison Domain. The present study is thus aimed at constraining the genesis of the major lithologies, along with interpretation of granitoid-hosted gold mineralization in the North Yalgoo area, thereby adding to the understanding of the geological evolution and gold mineralization of this part of the Murchison Domain.

1.1 Location and Access

Yalgoo is an old gold mining centre located about 459 km NNE from Perth in Western Australia, between Geraldton to the west and Mt. Magnet to the east. The study area lies north of Yalgoo and extends from latitudes 28º07'00"S to 28º12'51"S and longitudes 116º42'17"E to 116º44'15"E. Access to most parts of the study area is via a graded road that runs about 20 km northeast from the Yalgoo-Mt Magnet road up to Noongal, and then continues to the north past the City of Melbourne mine for about 15 km until it meets an east-west trending track beyond the study area. The mine sites are accessible via tracks branching off the graded road. The area is characterized by wide valleys and salt lakes between areas of higher ground containing outcrop or Cenozoic sandplain that falls within the physiographic division of Salinaland by Jutson (1950). The drainages are internal into salt lakes or calcrete areas. The topography is mostly flat and monotonous with elevation rising gradually from 280 to 391m above mean sea level (Muhling and Low, 1977). Semi-

arid climate prevails for most of the year with an average annual rainfall of about 350mm. Gum trees are locally present, particularly over greenstone rocks, whereas saltbush is abundant around the salt lakes and in the major creeks of the area (Baxter, 1982; Beard, 1976; Groves, 1981).

Yalgoo is a small township with a population of less than 200. A number of historical mine workings, namely: Brilliant, Melville, City of Melbourne and Noongal are testimony to the area's past production of gold, with potential for further discoveries. In recent years, many of these workings have been re-investigated by different mining companies.

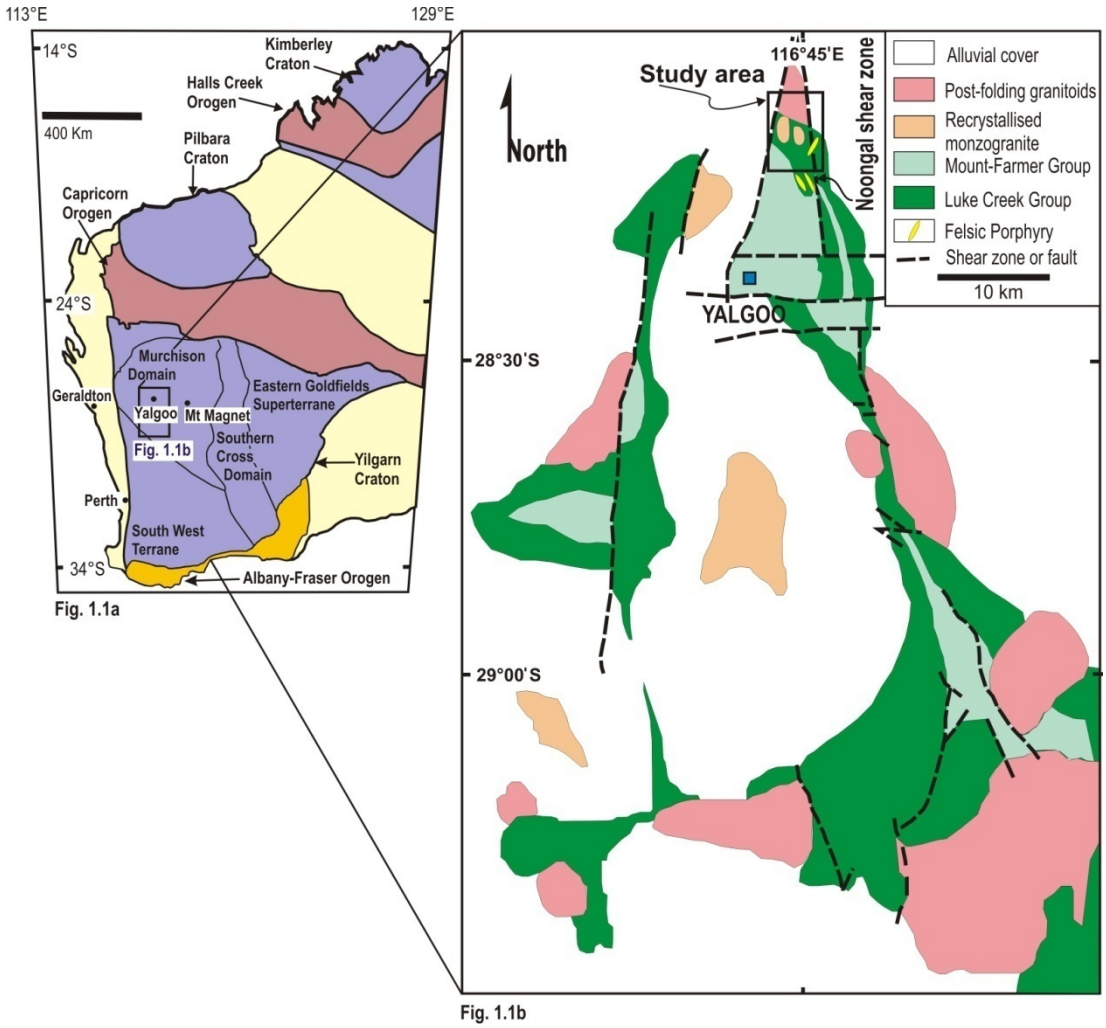

Fig. 1.1(a) Outline of the geology of Western Australia, showing three cratons and three major orogens. Modified after Cawood and Tyler (2004) and Watkins and Hickman (1990). Outlines of the subdivisions of the Yilgarn Craton are after Cassidy et al. (2006). 1.1(b) Simplified geology of the Yalgoo area, after Watkins and Hickman (1990).

1.2 Objectives

The primary aim of this research was to provide an improved understanding of the origin of the granite-greenstone rocks, to characterize the gold mineralization and thereby

construct a crustal evolution model for the Yalgoo area. These objectives have been achieved through the following stages:

1. Study of the major phases of the supracrustal and granitoid rocks with the aid of field investigations, petrography and comprehensive geochemical studies to decipher their genesis and to infer tectonic settings. Minor felsic volcanics, constituting an important member of the greenstones, were studied for the first time to infer their genesis and establish their relationship with the other rock types.

2. Determination of the ages of the granitoid and felsic volcanic rocks, which along with geochemical analysis and isotopic studies will help to provide a meaningful comparison with granitoids and felsic volcanics across the Murchison Domain and other parts of the Yilgarn Craton.

3. A comprehensive study of the cross-cutting mafic dykes and determination of their ages to obtain a better insight into their genesis and their relationships with the other mafic phases.

4. Study of older crustal components and the age of the source reservoirs of the granitoids, volcanics and mafic dykes using combined U-Pb and Lu-Hf isotopic studies.

5. Characterization of the granitoid-hosted gold mineralization was undertaken by studying the host granitoid and ore minerals hosted within quartz-pyrite veins that dissect the granitoid which, along with fluid inclusion study of the vein quartz, was used to establish a genetic model of gold mineralization.

6. A crustal evolution model for the Yalgoo area is proposed using the combined results of the study.

1.3 Research Methodology

Two essential techniques were adopted for achieving the research objectives. They were-1) fieldwork and 2) analytical techniques.

1.3.1 Fieldwork

Two fieldtrips were conducted to study the selected mine sites and surrounding areas in the Yalgoo area and to undertake sample collection from carefully selected portions of granitoid (Lydia granite), vein systems and major lithologies of the area. Forty samples were obtained for various analyses, namely petrology, geochemistry, geochronology, vein relationships, ore petrography and fluid inclusion studies. Five diamond drill core samples, including three felsic volcanic/sediment and two mafic dyke samples, were collected

Table 1.1: Sample catalogue showing the analyses carried out.

Sl no	Sample no	Rock type (based on field observ.)	MGA Positions		Analytical studies carried out							
			Northing	Easting	Petro.	Geochem.	SHRIMP	Lu-Hf	Fl. Incl.	Ore Mic.	SEM/ QEMScan	EMPA
1	MA 03	Granitoid	6890363	474449	X	X	X	X				
2	MA 04	Granitoid	6890337	473685	X	X	X	X				
3	MA 06	Granitoid	6887624	471340	X	X	X	X				
4	MA 09	Granitoid	6887603	471350	X	X	X	X				
5	MA 10	Felsic porphyry	6887595	471347	X	X	X	X				
6	MA 13a,b,c,d,e	5 vein samples	Samples from pit floor		X				X	X	X	
7	MA 14a,b,c,d,e,f	6 vein samples			X				X	X	X	X
8	MA 15	Felsic porphyry	6885251	472368	X	X	X	X				
9	MA 16	Felsic porphyry	6885201	472400	X	X	X	X				
10	MA 18	Mafic	6884553	475604	X	X						
11	MA 19	Mafic	6884553	475604	X	X						
12	MA 20	Mafic	6884664	475587	X	X						
13	MA 21	Mafic	6884707	475606	X	X						
14	MA 22	Mafic	6884301	475575	X	X						
15	MA 23	Felsic volcanic	6884295	475580	X	X						
16	MA 24	Mafic	6883743	475388	X	X						
17	MA 25	Mafic	6883347	475503	X	X						
18	MA 26	Mafic	6882867	474124	X	X	X	X				
19	MA 27	Felsic porphyry	6882481	474995	X	X	X	X				
20	MA 28	Granitoid	6887626	471316	X	X					X	X
21	MA 33	Mafic	6887077	475706	X	X						
22	MA 34	Mafic	6887216	475702	X	X						
23	MA 37	Mafic	6884229	475235	X	X						
24	MA 38	Granitoid	6886212	474569	X	X	X	X				
25	MA 40	Granitoid	6886367	474620	X							
26	MA 41	Mafic	6884899	475281	X	X						
27	MA 42	Dolerite dyke	6884664	475199	X	X						
28	MA 43	Dolerite dyke	6884585	475219	X	X						
29	MA 44	Mafic	6883858	475508	X	X						
30	MA 45	Mafic	6882879	475472	X	X						
31	MA 46	Dolerite dyke	6882730	475306	X	X						
32	MA 47	Mafic	6882570	475432	X	X						
33	MA 49	Granitoid	6887660	471302	X	X						
34	MA 50	Granitoid	6886901	471744	X	X	X	X				
35	MA 51	Granitoid	6885237	472394	X							
36	MA 52	Granitoid	6885237	472394	X	X		X				
37	MA 53	Granitoid	6885237	472394	X			X				
38	MA 54	Granitoid	6885195	472394	X							
39	MA 55	Granitoid	6885195	472394	X	X						
40	MA 56	Granitoid	6885195	472394	X	X						
41	PRCD 108/1 (83.40-83.75)	Porphyry	6882100	475955	X	X						
42	PRCD 108/2 (114.65-115.00)	Felsic volcanic	"	"	X							
43	PRCD 108/3 (140.18-140.3)	Felsic sediment	"	"	X	X						
44	PD 001/1 (28.90-29.00)	Dolerite dyke	6887208	475679	X	X						
45	PD 001/2 (44.00-44.15)	Dolerite dyke (chilled margin)	"	"	X							

from the City of Melbourne area to deduce petrological characteristics and infer petrogenesis and to compare the results with those obtained from the field samples. Sample locations were recorded with a hand held Garmin GPS 12 using the WGS 1984

datum with a nominal accuracy of 15 meters. A list of all samples on which further work was undertaken and the analytical techniques applied to each is shown in Table 1.1.

1.3.2 Analytical Techniques

Five sets of techniques were applied: namely petrology, geochemistry, geochronology, fluid inclusion studies and electron microprobe analysis.

1.3.2.1 Petrology

Thin section Petrography: Petrological study was conducted both on hand specimens and using a transmitted light microscope. A total of 103 petrographic thin sections (25 x 75x 0.03 mm slide) were made from 45 samples. Among these, 87 were prepared from three orthogonally cut sections from 29 coarse-grained samples. Single thin sections were made from the remaining 16 (mostly fine-grained and core) samples. Mineral identification and textural studies were carried out using a Nikon petrographic microscope. In coarse-grained rocks, modal analyses were conducted on 87 thin sections, using a mechanical stage in combination with a twelve-channel digital point counter attached to the microscope. A x10 objective lens was used to obtain the point counting data over an area ranging from ~260 mm^2 to 510 mm^2, contained 1600 to 2600 points within each thin section. The results of the three sections are reported in volume percent (vol %) normalized to 100 and to two decimal places. Minerals that were observed in thin-section, but either not counted during this procedure, or making up less than 0.1%, are reported as trace amounts (tr). Modal compositions were also obtained for single thin sections which were prepared mostly from core samples. For porphyritic samples, first the groundmass and phenocrysts were determined visually from thin sections and then modes of the phenocrysts and groundmass were estimated using x10 and x20 magnification, respectively, and combined to arrive at the modal composition. Modal compositions of very fine-grained rocks (grain size $\leq$ 0.1mm) were deduced from visual estimation.

Ore Petrography: Eight polished thin sections were prepared from the mineralized zone at the Brilliant open pit to determine the mode of occurrence of gold-bearing minerals and decipher the paragenetic sequence.

QEMSCAN Petrography: QEMSCAN (based on the QEM*SEM, Quantitative Evaluation of Minerals by Scanning Electron Microscope) is a sophisticated technique and one of most powerful **mineralogical instruments** currently available. The QEMSCAN is capable of conducting an automated, rapid and accurate mineralogical analysis that enables rapid discrimination of most ore- and rock-forming minerals in 10 milliseconds

(Pirrie et al., 2004). Selected thin sections and thick sections (rock slabs remaining after making thin sections) were studied by QEMSCAN and also provided a measure of the modal mineralogy of the fine-grained rocks. This was done by BSE (Back-Scatter Electron) Imaging and Energy Dispersive X-ray analysis from 5x5 to 40x40 micron pixels over a total area of ~ 400 mm^2. The QEMSCAN study was conducted under the guidance of Dr. Chi Ly, at the Minerals Division of CSIRO, Curtin Campus.

The operational protocol of the QEMSCAN is outlined by Gottileb et al. (2000). Subsequent work by Butcher et al. (2000) (gold analysis), Camm et al. (2003, 2004) (environmental characterization), Lui et al. 2004 (coal characterization), Pirrie et al. 2004, Pascoe et al. (2007) (forensic geoscience), and Goodall et al. (2005a,b, 2007) (mineral liberation) provided improved understanding of the application of QEMSCAN in various fields. The system is based on a Zeiss Evo 50 scanning electron microscope fitted with up to four light element Silicon Drift X-ray detectors (SDD) and pulse processor technology. It runs in a PC windows-based environment, which allows for both online and offline interpretation of data. BSE Intensity and Energy Dispersive (EDS) X-ray spectra are used to create digital mineral images (Goodall and Scales, 2007). The EDS x-ray is generated under 25kV operating voltage which then interacts with 1 µm to 2 µm of the specimen and extends across a similar distance beneath the surface of the specimen. These rays are rapidly collected by the four SDD. The data obtained for each point analysis are compared with a mineral database, developed by analysis of known standard mineral samples, which contains a list of essential and accessory elements for different minerals. Minerals with similar x-ray spectra and Back Scattered Intensity (BEI), such as chalcopyrite and cubanite, are differentiated by element peak ratios. Species with similar spectra, but distinct BEI, such as magnetite and hematite, are differentiated by BEI (Gottileb et al., 2000).

Several analysis modes are available on the QEMSCAN system that allow examination of anything from bulk mineralogy to the identification of any trace minerals present within the sample under study (Gottileb et al., 2000; Goodall and Scales 2007). They are: i) Bulk mineralogical analysis (BMA), ii) Particle mineralogical analysis (PMA), iii) Specific mineral search (SMS), iv) Trace mineral search (TMS), and v) Field Scan. For the purpose of the present study, Bulk mineralogical analysis (BMA), and Field Scan were employed.

All the samples were carbon coated prior to running on the QEMSCAN to prevent the sample becoming charged while being exposed to the electron beam. The carbon coating

was obtained using an EMITECH carbon coater using carbon rod evaporation, over a duration of 2500 ms.

Bulk mineralogical analysis (BMA) was performed on selected samples using a line scan analysis to identify the number and length of intercepts with mineral species at a pixel spacing between 5μm and 40μm over an area of about 320 to 400 square mm. The data obtained were used to determine modal abundance.

1.3.2.2 Geochemistry

After careful petrographic study, a total of 36 fresh rock samples were selected for whole-rock geochemical analyses. In the first batch, 17 samples were selected for 10 major and 31 selected trace element (including 14 rare earth elements) analyses followed by a further 19 samples in the second batch for the same 10 major elements and 31 trace elements (again including 14 rare earth elements). The complete geochemical analyses are presented in the relevant chapters. Major element analyses of the first and second batch samples were conducted by X-ray fluorescence (XRF) at the State Key Laboratory of Continental Dynamics, Northwestern University, Xi'an, China, and at Genalysis Laboratory Services, Perth, respectively.

The trace and rare earth elements of both the first and second batch samples were carried out in the same laboratory, using Laser ablation-inductively coupled plasma-mass spectrometry at the State Key Laboratory of Continental Dynamics, Northwestern University, Xi'an, China, according to the method described in Gao et al. (2002) with analytical uncertainties ranging from 1 to 3%.

For geochemical analyses, rock samples were first trimmed of weathered and stained material with a rock saw. About 200 to 400g samples were then crushed in an hydraulic press to an aggregate of ~ 1cm^3 pieces. About 10-15g were then placed into a tema mill and run over a period 45 seconds for self-contamination. The tema mill was thoroughly cleaned with a stiff sample brush to eliminate any chance of contamination from the previous sample run. Then about 20 g fragments were placed into the tema and run for about 2 minutes. The fine rock powder is then transferred onto a coning station on the work bench. The milling was continued until all remaining rock fragments were powdered. Rock powder at the coning station was then quartered and coned ten times in order to thoroughly homogenize. Portions of this rock powder were then transferred into two pre-labeled sterilized plastic bottles with up to 100 to 120 grams in each bottle.

Table 1.2: Measured (Mean), reference values (Ref. value), standard deviation (stdev) and relative standard deviation (RSD %) of the trace element concentrations for USGS standards AGV-1, BHVO-1 and BHVO-2 for (a) first batch and (b) second batch of sample analyses.

(a)	AGV-1				BHVO-1				(b)	AGV-1				BHVO-2			
	Mean	Ref. Value	Stdev	RSD %	Mean	Ref. value	Stdev	RSD %		Mean	Ref. Value	Stdev	RSD %	Mean	Ref. Value	Stdev	RSD %
Li	10.87	12.00	1.25	11.5	5.03	4.60	5.06	8.2		10.77	12	0.15	1.4	4.97	4.60	0.16	3.3
Be	2.27	2.10	0.19	8.2	1.00	1.10	0.38	10.7		2.12	2.1	0.02	0.9	1.08	1.10	0.02	2.1
Sc	12.37	12.20	1.32	10.7	32.12	31.80	0.25	3.8		12.34	12.2	0.13	1.1	31.42	31.80	0.81	2.6
V	120.00	121.00	12.43	10.4	320.53	317.00	4.73	3.4		119.98	121	0.93	0.8	320.71	317.00	3.41	1.1
Cr	9.68	10.10	1.41	14.5	302.03	289.00	1.33	2.7		9.23	10.1	0.79	8.6	280.45	0.00	2.71	1.0
Co	15.35	15.30	1.66	10.8	43.22	45.00	0.54	2.3		15.21	15.3	0.11	0.7	44.85	45.00	0.61	1.4
Ni	16.29	16.00	1.45	8.9	119.00	121.00	1.48	3.0		15.87	16	0.16	1.0	119.81	121.00	1.34	1.1
Cu	57.38	60.00	5.63	9.8	134.35	136.00	1.32	4.2		56.79	60	1.19	2.1	127.59	136.00	0.74	0.6
Zn	86.54	88.00	9.12	10.5	104.37	105.00	10.59	4.5		87.57	88	0.67	0.8	107.59	105.00	7.58	7.0
Ga	20.80	20.00	2.24	10.8	20.08	21.00	2.58	4.1		20.25	20	0.22	1.1	21.46	21.00	0.27	1.3
Ge	1.24	1.25	0.12	10.0	1.59	1.64	0.09	3.6		1.21	1.25	0.03	2.5	1.65	1.64	0.04	2.7
Rb	71.40	67.30	4.56	6.4	10.21	11.00	11.35	6.5		67.66	67.3	0.97	1.4	9.72	11.00	0.07	0.7
Sr	662.62	662.00	29.06	4.4	389.63	403.00	19.85	2.1		660.36	662	1.13	0.2	393.74	403.00	4.12	1.0
Y	20.04	20.00	0.93	4.7	26.88	27.60	0.76	1.7		19.84	20	0.15	0.7	26.38	27.60	0.34	1.3
Zr	235.70	227.00	9.51	4.0	173.17	179.00	11.15	2.2		224.73	227	1.97	0.9	167.62	179.00	3.81	2.3
Nb	14.66	15.00	0.52	3.5	18.98	19.00	0.63	2.2		14.31	15	0.25	1.8	18.26	19.00	0.15	0.8
Cs	1.48	1.28	0.03	2.0	0.11	0.13	0.15	1.2		1.27	1.28	0.01	0.6	0.10	0.13	0.00	0.8
Ba	1225.34	1226.00	23.71	1.9	136.83	139.00	103.62	0.8		1207.13	1226	6.37	0.5	131.60	139.00	1.40	1.1
Hf	4.97	5.10	0.25	5.1	4.44	4.38	0.58	2.5		4.97	5.1	0.12	2.4	4.20	4.38	0.08	2.0
Ta	0.86	0.90	0.04	4.3	1.25	1.23	0.06	2.3		0.88	0.9	0.01	1.5	1.17	1.23	0.03	2.5
Pb	40.38	36.00	2.79	6.9	2.27	2.60	3.29	2.1		36.24	36	0.69	1.9	2.08	2.60	0.45	21.7
Th	5.94	6.50	0.36	6.1	1.16	1.08	2.28	1.8		6.38	6.5	0.10	1.6	1.18	1.08	0.02	1.3
U	1.86	1.92	0.11	5.8	0.41	0.42	0.18	1.5		1.90	1.92	0.02	1.2	0.42	0.42	0.00	1.1
La	38.32	38.00	0.85	2.2	15.60	15.80	5.32	1.1		38.35	38	0.13	0.3	15.21	15.80	0.20	1.3
Ce	67.42	67.00	2.21	3.3	37.72	39.00	6.56	1.9		68.17	67	0.51	0.8	37.48	39.00	0.52	1.4
Pr	8.25	7.60	0.18	2.2	5.26	5.70	1.30	1.7		7.96	7.6	0.14	1.8	5.20	5.70	0.07	1.4
Nd	32.09	33.00	0.64	2.0	24.84	25.20	2.73	1.9		32.05	33	0.38	1.2	24.87	25.20	0.26	1.0
Sm	5.85	5.90	0.10	1.7	6.18	6.20	0.29	1.9		5.80	5.9	0.07	1.2	6.15	6.20	0.05	0.8
Eu	1.65	1.64	0.05	2.8	1.98	2.06	0.10	1.8		1.63	1.64	0.05	2.9	2.02	2.06	0.04	2.0
Gd	5.26	5.00	0.15	2.9	6.04	6.40	0.98	2.2		4.93	5	0.20	4.0	6.16	6.40	0.12	2.0
Tb	0.69	0.70	0.03	4.5	0.94	0.96	0.06	3.0		0.68	0.7	0.02	3.3	0.92	0.96	0.02	2.1
Dy	3.67	3.60	0.10	2.7	5.28	5.20	0.14	2.1		3.61	3.6	0.06	1.6	5.29	5.20	0.05	1.0
Ho	0.67	0.67	0.03	4.1	0.98	0.99	0.04	2.5		0.70	0.67	0.01	1.7	1.03	0.99	0.01	1.1
Er	1.74	1.70	0.05	2.6	2.37	2.40	0.05	2.3		1.83	1.7	0.02	0.8	2.53	2.40	0.01	0.4
Tm	0.25	0.25	0.01	3.7	0.33	0.33	0.04	2.1		0.27	0.25	0.01	4.6	0.33	0.33	0.00	0.6
Yb	1.67	1.72	0.05	3.1	2.06	2.02	0.06	1.5		1.66	1.72	0.03	1.6	2.01	2.02	0.02	0.9
Lu	0.26	0.27	0.01	5.0	0.31	0.29	0.01	2.6		0.25	0.27	0.00	1.8	0.28	0.29	0.00	0.3

The sample preparation stages used in determining the full suite of selected trace elements and full set of REE by ICP-MS at Northwestern University, Xi'an, China, were as follows: (1) 40 mg of sample is mixed with 1.5 ml HF/HNO3 (2:1 mixture) in a screw top Teflon beaker and ultrasonically vibrated for 10-15 min, followed by evaporation to dryness at a temperature of 150°C. (2) Re-dissolved using 2.0 ml HF/HNO_3 (3:1) mixture and heated for 7-10 days at a temperature of 170°C, followed by evaporation to dryness. (3) Dissolved using 2 ml HNO_3 for 2-5 hours, followed by evaporation to dryness. (4) Dissolved and

heated using 3 ml $HNO_{3,}$ (5) After adding an internal standard solution of 10 ppb Rh, the trace element concentrations are measured using a Finnigan MAT High Resolution ICP-MS. The United States Geological Survey (USGS) rock standard AGV-1 was used for felsic rocks and BHVO-1 for mafic rocks in analyzing the first batch of samples. For the second batch samples, the USGS standards AGV-2 and BHVO-2 were used for felsic rocks and mafic rocks, respectively (Table 1.2). Analytical precisions are estimated as follows: 2– 7% for REE, Y, Hf, Ta, Cs, Zr, Nb, Ta, Rb, Sr and Ba; 10-15% for Ni, and Th; and 20–30% for Be, Sc, V, Cr, Ni, Cu, Zn, Ga and Ge for the granitoid samples of the first batch. For the second batch of granitoid samples, the precisions are estimated as: 1–5% for all the trace elements including the REEs. The analytical precisions in the analyses of mafic samples from the first batch are estimated as 1– 5% for all the trace elements including the REEs, except for Li, Be and Rb which are between 7-11%, whereas for the second batch of mafic samples it ranges from 1– 3% for all the trace elements including the REEs, except for Pb at 22% (Table 1.2).

1.3.2.3 Geochronology

U-Pb Geochronology: Samples were prepared from about 500 gm of rock from each representative sample and these were crushed in a hydraulic press and then ground in a tungsten–carbide tema mill for 12 seconds. The powder was then sieved to pass through a −100 mesh nylon sieve.

The rock powder was then transferred into a glass beaker filled with water and stirred with a glass rod to settle the heavier fraction at the bottom. The suspended portion was poured off. This process was repeated a couple of times until the water on top became clear. The concentrate of the coarser material was transferred into a small beaker and bathed with acetone, stirred again and the acetone-water fraction then drained off. This acetone washed coarser fraction was then dried in a fume cupboard for 4/5 hours and under an infra-red heat lamp overnight. The dried powder was then separated in heavy liquids (Methylene Iodide MI; density = 3.3g/ml). The heavy fraction was dried and highly magnetic particles were removed using a hand magnet.

The remaining fraction was passed though a Franz isodynamic separator with the magnetic current of 0.5 A at 10° of side tilt, then with the magnetic current at 1.5A and at progressively lower angles of side tilt (6° and 2°). All zircons analyzed were extracted from the non-magnetic fractions and were hand-picked under a binocular microscope. Crystals were mounted onto double-sided adhesive tape and set in Epirez™ resin, along with several grains of the Curtin University Sri Lankan gem zircon standard (CZ3) which

has a measured $^{206}Pb/^{238}U$ value of 0.0914 and $^{206}Pb/^{238}U$ age of 564 Ma (Nelson, 1997). When dry, the mount was polished to expose the zircons' interior structure, by removing approximately 50% of the grains. Transmitted and reflected light photographs of the mount were taken, and the mount was then gold coated.

Cathodoluminescence (CL) imaging: To identify the growth pattern, degree of homogeneity and internal structure of the zircon crystals, cathodoluminescence (CL) images were obtained for all the mounts using a Philips PW6886 CL detector on a Philips XL30 Scanning Electron Microscope under an accelerating voltage of 12kV, with spot sizes 5 and 6. Generally, zones with high-U or high Pb contents have a very low CL response, appearing dark in greyscale images. In contrast, zones with a low-U content appear light. In many crystals, areas having small differences in U-content produced images with poor contrast, and it was not possible to resolve various zones. On most images, including ones with poor zonal contrasts, post- imaging manipulation was performed using Microsoft Office Picture Manager and CorelDraw X4 software to remove noise and increase contrast at greyscale.

SHRIMP analytical techniques: The Th-U-Pb studies of the zircon grains were conducted on the Western Australian consortium SHRIMP II at Curtin University of Technology. The analytical and data reduction techniques were similar to those described by Nelson (1997) and Williams (1998), utilizing seven-cycle runs through the mass stations.

A 10kV primary beam of oxygen ions (O_2-) focused to a spot diameter of ca. 25-30 μm was used. A total of 11 samples were run over 8 analytical sessions. Eight secondary ion species namely: Zr_2O+, $^{204}Pb+$, $^{206}Pb+$, $^{207}Pb+$, $^{208}Pb+$, $^{238}U+$, ThO+ and UO+, along with background (baseline) near $^{204}Pb+$, were measured during each run. One standard (CZ3) analysis was carried out after four (often 3) unknown analyses during each analytical session. The raw data reduction was carried out using SQUID V1.02 (Ludwig, 2001) that calibrates the Pb/U ratio of unknown analyses by comparing the weighted mean (Pb^+/U^+) / (UO^+/U^+) ratio of the CZ3 standard zircon analyses with the known $^{206}Pb/^{238}U$ ratio of the CZ3 standard. The exponent 2 was the empirically derived slope of ln(Pb+/U+) versus ln(UO+/U+) from standard zircon analyses. During CZ3 standard analyses in 7 of the 8 analytical sessions, this slope varied between 1.82 and 2.20 (mean slope = 1.98). For one analytical session the slope was 1.34. The 2s error of the weighted mean (Pb+/U+)/(UO+/U+)2 of the standard ranged from 0.59 to 1.33% and is quoted as an indication of the uncertainty in the calibration constant for each analytical session. Pb/U

ratios in the unknown analyses were corrected using the $\ln(Pb^+/U^+)$ / ln(UO+/U+) relationship as measured in the standard zircon CZ3. During the analytical sessions sensitivity ranged from 16.2 to 24.3 cps/(nA ppm), and the primary current was typically between 3 and 4 nA. The radiogenic Pb composition was determined using the ^{204}Pb correction (Compston et al., 1984). The common Pb as measured in the standard analyses was considered to have originated from surface contamination (Kinny, 1986) in the gold coating (Nelson, 1997). The ^{204}Pb-correction method has been applied assuming the isotopic composition of Broken Hill lead (Cumming and Richards, 1975).

Weighted mean values, concordia diagrams, concordia ages and upper intercept ages were calculated using Isoplot/Ex 2.49 (Ludwig, 2001). Analytical errors for individual analyses are quoted at the 1-sigma level whereas uncertainties in calculated group ages are quoted at 95% confidence limits (2σ).

Lu-Hf Isotopes: To constrain the source of the major rock types, Lu-Hf isotopic studies were carried out on 11 samples whose ages had been determined by SHRIMP U-Pb geochronology. Hf data were collected for almost every SHRIMP spot in the 11 samples. In a few instances, where smaller zircons had two analyses (core/rim), Hf data were collected from a single spot. Zircon Hf isotopic analyses were conducted using a Geolas-193 laser-ablation microprobe, attached to a Neptune multi-collector ICP-MS at the Institute of Geology and Geophysics, Chinese Academy of Sciences in Beijing, China. Data were collected over a period of ~200 cycles for each measurement with typical ablation times of 30s, 10Hz repetition rate, and a laser power of 100 mJ/pulse. A spot size of 40μm was used for most of the analyses, with the exception of samples MA 26 and MA 06, where a beam diameter of 60 and 50 μm were used, respectively. Raw count rates for ^{172}Yb, ^{173}Yb, ^{175}Lu, ^{176}(Hf + Yb + Lu), ^{177}Hf, ^{178}Hf, ^{179}Hf and ^{180}Hf were collected.

The isobaric interference of ^{176}Lu on ^{176}Hf was corrected assuming ^{176}Lu/^{175}Lu = 0.02655 (Machado and Simonetti, 2001), and the mean mass bias value of Yb obtained during analysis on the same spot was applied for the interference correction of ^{176}Yb on ^{176}Hf (Iizuka and Hirata, 2005), assuming a value of 0.5886 for ^{176}Yb/^{172}Yb. During analysis, the ^{176}Hf/^{177}Hf and ^{176}Lu/^{177}Hf ratios of the standard zircon (91500) were 0.282294±15 (2σ, n = 20) and 0.00031, similar to the commonly accepted ^{176}Hf/^{177}Hf ratios measured using the solution method (Wu et al., 2006).

During analyses, the ^{176}Hf/^{177}Hf ratio of the standard zircon CZ3 was close to the recommended value of 0.281732±7 (2s) obtained by Wu et al. (2006). This study used

SHRIMP spot ages to calculate εHf(t) and Hf model ages which enables comparison of Hf isotopes with variable ages due to zircon inherence. A decay constant of 1.865×10−11yr-1 was used (Scherer et al., 2001) and the chondritic ratios of 0.282772 for $^{176}Hf/^{177}Hf$ and 0.0332 for $^{176}Lu/^{177}Hf$, as recommended by Blichert-Toft and Albarède (1997), were adopted to calculate εHf values. Single stage model ages relative to depleted mantle (T_{DM1}) were calculated using a present-day $^{176}Hf/^{177}Hf$ of 0.28325 and $^{176}Lu/\ ^{177}Hf$ of 0.0384 (Griffin et al., 2000). Two-stage model ages (T_{DM2}) were calculated using the same assumption as Keto and Jacobsen (1987) for Nd isotopes: $T_{DM2} = T_{DM1}-(T_{DM1}-t)((f_{lc}-f_s)/(f_{lc}-f_{DM}))$ where f_{lc}, f_s, f_{DM} = fLu/Hf values of the lower crustal source, the sample and the depleted mantle, respectively. In our calculation, f_{lc} =−0.34 ($^{176}Lu/^{177}Hf$ = 0.022, average lower crust; Blichert-Toft and Albarade (2008) and f_{DM} =0.157 ($^{176}Lu/^{177}Hf$ = 0.0384; Griffin et al., 2000), and t = the crystallization age of zircon. In the present study a two-stage depleted mantle model age, T_{DM2}, is adopted assuming that the parental magma of the zircon was produced from a lower crust that originally was derived from the depleted mantle.

1.3.2.4 Fluid Inclusion Study

Fluid inclusion work was conducted on samples from the granitoid-hosted mineralization to determine the nature (temperature, salinity and chemical composition) of the ore-bearing fluid.

Six quartz veins from granitoid-hosted mineralized zones from the Brilliant open pit were initially selected for fluid inclusion study. Thin section study was carried out to investigate the number and quality of the fluid inclusions present (if any). Three veins were finally found to be suitable and samples sent to Minerex Laboratory at Kalgoorlie for fluid inclusion sections to be made. In most of the fluid inclusion sections, various inclusion types enabled a sound classification to be determined (based on criteria as stated in Roedder, 1984; Shepherd et al., 1985). However, every caution was taken to study only those inclusions whose origin could be determined with a high degree of confidence. Microthermometric measurements were conducted mostly on primary fluid inclusions. A LEITZ Laborlux D microscope fitted with a FLUID INC. adapted USGS gas-flow heating-freezing system was used in the study at the Department of Applied Geology, Curtin University of Technology.

Freezing runs were carried out using liquid nitrogen connected to the stage while heating runs were performed by a thermal resistor with a TM-93 control unit. The lower and upper temperature limits of the stage are -190 and + 700°C, respectively. The stage was

calibrated using H_2O and CO_2-bearing synthetic calibration standards supplied by SYN FLINC with known melting and homogenization temperatures. The microthermometric measurements were accurate within ± 0.2℃ for the temperature range up to 22 ℃ and within ± 5℃ from 22° to 400 ℃.

Samples were first cooled rapidly to temperatures below -100 ℃ and then heated slowly at a rate of 3 to 4 degrees C/min to temperatures below 31 ℃. Heating rate was increased to 5 to 10℃/min until total homogenization occurred. In this study, four phase transition temperatures were measured during heating runs: (i) final melting temperature of CO_2; (ii) final melting temperature of ice; (iii) melting temperature of clathrate ($T_m$clathrate); (iv) homogenization temperature of CO_2. The final homogenization of the CO_2-H_2O–NaCl and H_2O–NaCl inclusions was observed only in a few inclusions, as most of the inclusions were ruptured due to internal over-pressure during the heating run, before reaching total homogenization.

1.3.2.5. Electron Probe Micro Analysis (EPMA)

To determine mineral chemistry and carry out hornblende-plagioclase geothermobarometry on the mineralized host granitoid sample (MA 28), gold-bearing quartz vein 14A was studied on the Electron MicroProbe Analyser. First, a suitable fresh assemblage of plagioclase, hornblende and biotite was marked on two polished thin sections. The sections were then carbon coated. Caution was taken to identify the minerals which were in contact with each other to ensure only minerals that are in textural equilibrium were studied. Hornblende, biotite, plagioclase were circled using a luminous permanent marker pen, which contains ink showing up under electron imaging. They were analyzed for major element compositions (SiO_2, TiO_2, Al_2O_3, FeO, MnO, MgO, CaO, Na_2O, K_2O) using a JEOL JSM-6400 Scanning Electron Microscope equipped with a Wavelength-dispersive X-ray Detector (WDS) and MORAN SCIENTIFIC WDS SOFTWARE at the Center for Microscopy, Characterization & Analysis at the University of Western Australia. To standardize all silicate standards, 15 kV of accelerating voltage and 20 nA of beam current were set. The counting times for upper background, peak and lower background were set at 10, 40 and 10 seconds, respectively (suggested values). The elements Na, Mg, Al, Si, Mn, Fe, K, Ca, and Ti were standardized using standard minerals including albite, olivine, garnet, pyroxene, apatite, orthoclase, wollastonite and rutile. Then the selected minerals (hornblende, plagioclase, and biotite) were analyzed.

1.4 Organization of the Thesis

The thesis is organized into eight chapters.

Chapter 1 presents an introduction, the objectives and the methodology employed in the study.

Chapter 2 outlines the regional geological setting and metamorphism of the Murchison Domain in the Yilgarn Craton, with reference to the classification schemes and ages for the major lithologic units. The chapter also describes the geological setting of the study area. A short account gold mineralization is also presented.

Chapter 3 presents details based on the field investigations, petrography and geochemistry of the mafic volcanic rocks within the Yalgoo greenstone belt.

Chapter 4 describes the field, petrographic, geochemical data for the felsic volcanic rocks and their geochronology and origin applying SHRIMP U-Pb and Lu-Hf isotopic data, respectively.

Chapter 5 discusses the granitoid rocks of the area. It presents the field, petrographic, and geochemical data. This chapter also presents the geochronology using SHRIMP U-Pb and Lu-Hf isotopic study of the granitoids and discusses the genesis of these rocks.

Chapter 6 describes the field, petrographic, and geochemical data of the mafic dykes. A SHRIMP U-Pb and Lu-Hf isotopic study was also conducted to determine the ages and genesis, respectively.

Chapter 7 provides a detailed account on the only notable granitoid-hosted gold mineralization in the area, in terms of characterization of the metallic phases, ore fluids and host rocks. A genetic model for the gold is proposed.

Chapter 8 reviews the existing models of crustal development in the Murchison Domain. Integrating the findings of the present study, this chapter presents a crustal evolution model for the study area.

Chapter 2 Geological Setting

2.1 Yilgarn Craton

The Yilgarn Craton is located in south-central Western Australia and is the largest of the two cratons, occupying an area of over 657,000 km^2 (Trendall, 1990). It is separated from the Pilbara Craton to the north by Proterozoic fold and thrust belts of the Capricorn Orogen and by a series of sedimentary basins. To the south, it is bounded by the Proterozoic Albany-Fraser Orogen, to the west by the Pinjarra Orogen and the sedimentary rocks of the Perth Basin and to the east by Phanerozoic sediments of the Gunbarrel and Eucla basins (Fig. 2.1). The Yilgarn Craton consists mainly of low-grade granite-greenstone terranes characterized by arcuate belts of deformed and metamorphosed volcano-sedimentary rocks. Higher grade terrains occur in the west and north.

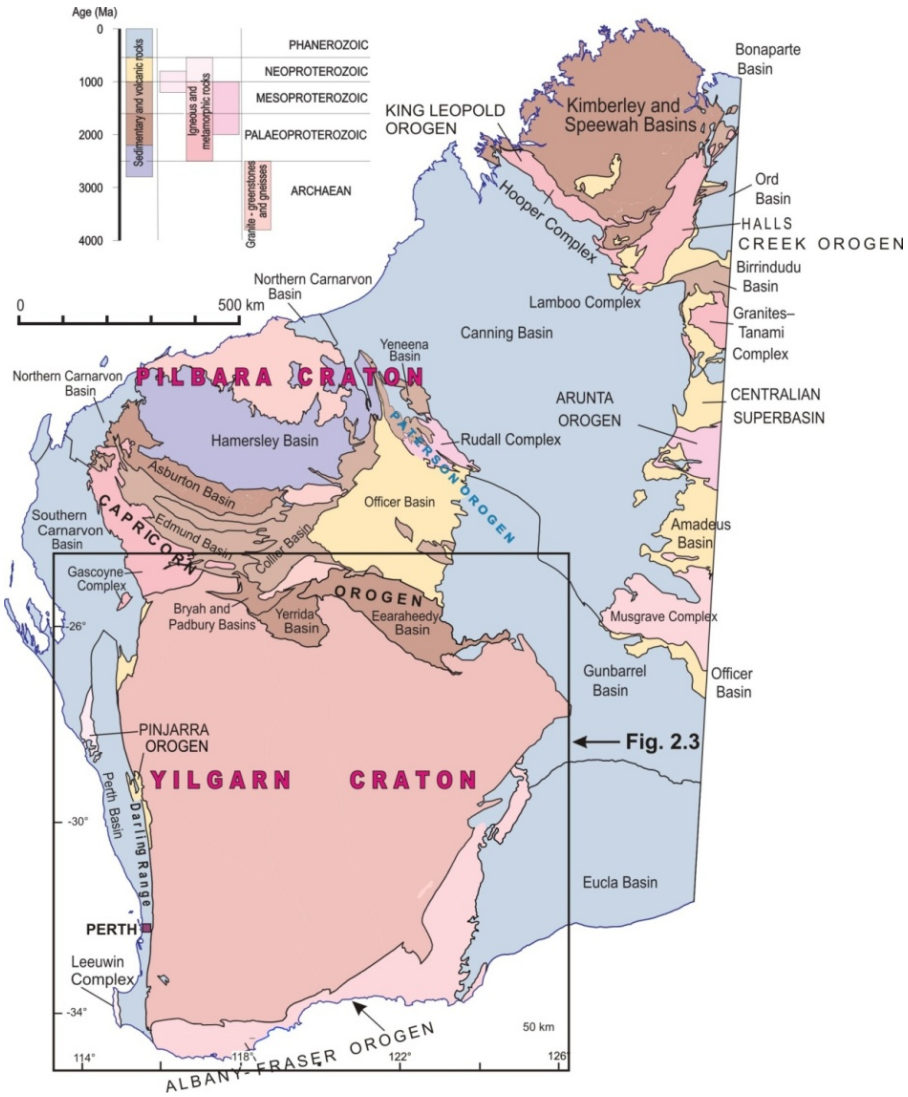

Fig. 2.1. Tectonic subdivision of Western Australia modified from the (Geological Survey of Western Australia, 2002). The outline of the Yilgarn Craton is after Cassidy et al. (2006).

The craton was formed mostly between ca. 3.05 and 2.62 Ga (Cassidy et al., 2006), and has remained integral and free of significant disturbance since emplacement of the Widgiemooltha dyke suite at 2420 Ma (Nemchin and Pidgeon, 1998). The craton is characterized by greenschist facies metamorphism, although in the southwest and northwest, granite gneiss and greenstones were recrystallized to granulite facies at 2640 Ma (Nemchin et al., 1994). The oldest components of craton are ca. 3700-3300 Ma rocks of the Narryer Terrane in the northwest that were recrystallized in granulite facies at ca. 2700 Ma (Myers, 1990b).

2.1.1 Subdivisions of the Yilgarn Craton

In the first attempt by the Geological Survey of Western Australia to subdivide the craton, three provinces were identified, namely: the Eastern Goldfields Province, the Murchison Province and the South-western Province (Williams, 1974). This was later modified by Gee (1975, 1979a) followed by a major rationalization by Gee et al. (1981) into four tectono-stratigraphic provinces, namely: the Murchison, the Eastern Goldfields, and the Southern Cross Provinces and the Western Gneiss Terrain. Distribution of gneiss and greenstone, metamorphic and deformation patterns, granitoid emplacement and available geochronology served as the basis of the Gee et al. (1981) classification. Later, Myers (1995) interpreted the Yilgarn Craton as a remnant continental block formed by the assembly of fault-bounded multiple rafts of sialic crust, each having different geological histories. Myers (1993, 1995), Wilde et al. (1996), Myers and Swager (1997) and Witt et al. (1998) re-evaluated the geological relationships of the juxtaposed crustal units and introduced the terrane accretion model based on studies of the tectono-stratigraphic units between large fault systems, the shape and trend of greenstone belts and new geophysical and geochronological data. The classification scheme proposed by Myers (1997) was widely accepted for more than a decade. From west to east the terranes are i) West Yilgarn Superterrane consisting of the Narryer terrane, Murchison terrane and Southwest composite terranes, ii) Southern Cross Superterrane and iii) Eastern Goldfields Superterrane (Fig. 2.2). A further subdivision of the southeastern Yilgarn Craton into a number of terranes, and the terranes into domains, was proposed by Swager et al. (1992) and Swager (1995, 1997), while Wilde et al. (1996) came up with similar divisions in the Southwestern Yilgarn Craton. Despite being formed at different times, each terrane recorded widespread tectonic, thermal and metamorphic episodes from 2780 to 2630Ma (Myers, 1995). All these activities were interpreted by (Myers, 1990c) as a direct result of Archean plate tectonic movements joining up diverse crustal blocks to form the craton.

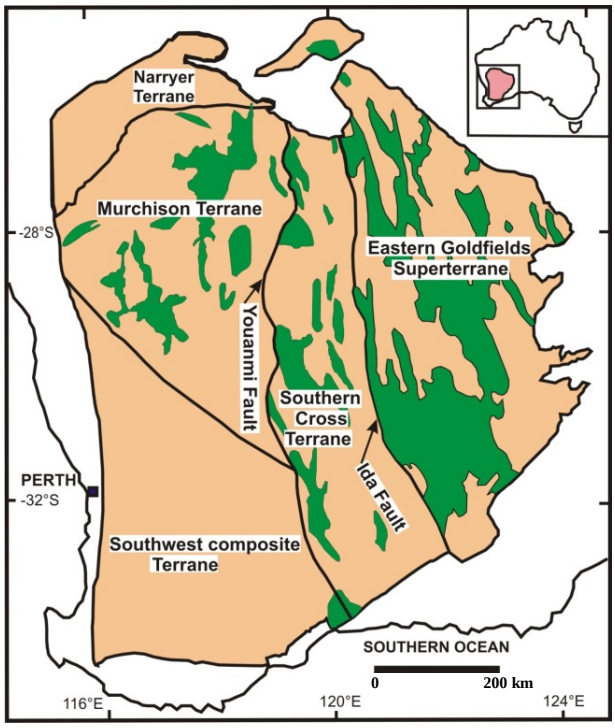

Fig. 2.2. Main tectono-stratigraphic units of the Yilgarn Craton showing major granite and greenstone components and faults after Myers (1997). Greenstones are coloured green and granitoids light brown.

Recently, regional mapping and new geological data acquired over the past ten years has resulted in a revised tectonic scheme for the Yilgarn Craton (Cassidy et al., 2006). A wide range of new geophysical, geochemical and geochronological data have been collected during a series of AMIRA (Australasian Minerals Industry Research Association), and Minerals and Energy Research Institute of Western Australia (MERIWA) projects undertaken by Geoscience Australia (GA), the University of Western Australia (UWA) and Monash University, Victoria, in collaboration with the Geological Survey of Western Australia (GSWA). The proposed classification has a four-fold tectonic unit hierarchy that consists of Craton > Superterrane > Terrane > Domain. Domains are defined as fault-bounded, geologically contiguous blocks within terranes. Terranes are defined by Neuendorf et al. (2005) as fault-bounded bodies of rock of regional extent, characterized by a geological history different from those of adjacent terranes. A group of related, adjacent terranes make up a superterrane. The assembly of all of these elements forms a craton. Cassidy et al. (2006) modified the boundaries of the earlier proposed terranes and identified new terranes in the eastern part of the Yilgarn Craton. They divided the Yilgarn Craton into six terranes (Fig. 2.3); i) Youanmi, ii) Narryer, iii) Southwestern, iv) Kalgoorlie, v) Kurnalpi, and vi) Burtville. Recent study of Pawly et al. (2012) introduced the newest Yamarna Terrane in the eastern part of the previously undivided Burtville Terrane. The latter four terranes are combined to make the Eastern Goldfields

Superterrane. This classification scheme amalgamated the Murchison and Southern Cross granite-greenstone terranes of Myers and Swager (1997) and Witt et al. (1998) and classifies them as domains within the Youanmi Terrane. The western and northern granite and granitic gneiss-dominated Narryer and South-West terranes were slightly reduced to accommodate newly-drawn northern and southern boundaries of the Murchison Domain.

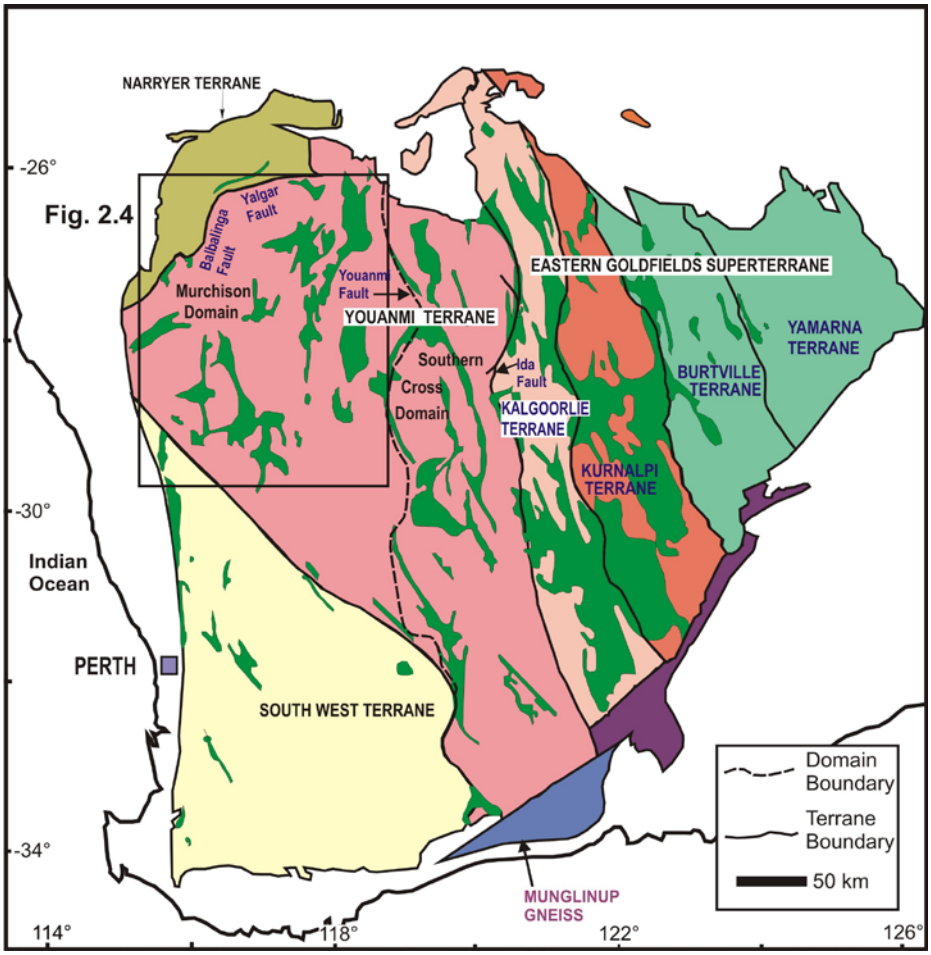

Fig. 2.3. Tectonic subdivisions of the Yilgarn Craton, simplified after Cassidy et al. (2006), showing the greenstones (coloured in dark green). The trend of the Youanmi Fault is taken from Myers (1997). Positions of the Balbalinga and Yalgar faults are taken from Spaggiari et al. (2008), and the boundary between the Burtville and Yamarna Terranes is taken from Pawly et al. (2012).

A brief account of the Youanmi Terrane, where the study area is located, is presented in the following section, to set the context for discussion of the major lithologies and crustal development in the Yalgoo area.

2.1.2 Youanmi Terrane

The term ‘Youanmi Terrane’ was introduced by Cassidy et al. (2006), based on the similarities in the lithostratigraphy and tectonic history of the former Murchison and Southern Cross granite–greenstone provinces (Chen et al., 2003) and Sm–Nd and Hf isotopic data favouring a common pre–3.05 Ga crustal source for both terranes (Barley et

al., 2003; Griffin et al., 2004; Cassidy et al., 2005). The Youanmi Terrane occupies an area of ~300,000 km^2 in the western half of the Yilgarn Craton (Van Kranendonk et al., 2013).

Combining the more recent geochronological studies and mapping (Schiøtte and Campbell, 1996; Wang et al., 1998; Pidgeon and Hallberg, 2000; Van Kranendonk, 2008; Van Kranendonk and Ivanic, 2009), Van Kranendonk et al. (2013) identified four supracrustal associations in the Murchison Domain, at ca. 2960–2935, 2825–2805, 2800–2735 and 2735–2700 Ga. The oldest 2960–2935 Ma volcanic and volcaniclastic rocks have been reported from the Golden Grove area (Fig. 2.4). The 2825–2805 Ma Norie Group has widespread mafic-ultramafic volcanic rocks, which is overlain by the 2800–2735 Ma Polelle Group having a similar succession as the Norie Group. The youngest 2735–2700 Ma Glen Group consists mainly of sedimentary and ultramafic rocks and minor rhyolite. An account of the supracrustal rocks of the Murchison Domain is given in section 2.1.3.1. The eastern margin of the Murchison Province (as defined by Watkins and Hickman, 1990) is characterized by a series of c. 2.81 Ga layered mafic intrusions (the Windimurra and Narndee gabbros), associated with minor 2.81 Ga felsic volcanic rocks (Ahmat, 1990; Geological Survey of Western Australia, 2005). Cassidy et al. (2006) consider the Youanmi Terrane acted as nucleus onto which later terranes (Narryer Terrane, Eastern Goldfields Superterrane) were accreted. The Southwest Composite Terrane is thought to have collided after 2.8 with the Youanmi Terrane Ga (Myers, 1993; Nutman et al., 1993; Qiu and Groves, 1999; Cassidy et al., 2005) which was accompanied by the emplacement of voluminous granites at 2.64 – 2.62 Ga and associated high-grade metamorphism (Wilde et al., 1996; Qiu and Groves, 1999).

In the Southern Cross Domain, previously known as the Southern Cross Terrane (Tyler and Hocking, 2001), is an elongate almost north-south trending granite-greenstone terrane, that is bounded by the Youanmi Fault to the west and the Ida Fault to the east (Fig. 2.3). Chen et al. (2001, 2003) and Morris et al. (2007) provided a detailed description of the lithostratigraphy and deformation events in the Southern Cross Domain. The Late Archean Marda–Diemals greenstone belt comprises a widespread mafic-dominated 3.0 Ga lower succession with a basal quartzite and BIF unconformably overlain by a ca. 2.73 Ga succession of interlayered volcanic, pyroclastic and minor volcaniclastic rocks (Dalstra et al., 1999; Chen et al., 2003) with detrital zircon ages up to 4.35 Ga old (Wyche et al., 2004). The calc-alkaline volcanic succession in the 2.73 Ga upper succession is known as the Marda Complex while the clastic sedimentary rocks are known as the Diemals

Formation. Chen et al, (2001, 2003) recognized three deformation events in the Marda–Diemals greenstone belt: (1) a north–south (D1), low-angle thrusting event that affected the lower greenstone succession prior to the deposition of the upper greenstone succession. (2) during east–west (D2) at ca. 2730–2680 Ma, an early folding event forming upright folds was followed by a progressive inhomogeneous east–west shortening (D3), that resulted in deposition and later deformation of the Diemals Formation. During the D3 event regional scale shear zones and large arcuate structures were also formed by impingement of competent granitoid blocks into less competent greenstone belts during progressive east-west shortening (Evanston–Mount Dimer arcuate structure: see Fig. 2, Chen et al., 2001). Sinistral shear zones developed along northwest-trending margins of the granitoid blocks, whereas dextral shear zones developed along northeast-trending margins. The major episode of felsic volcanism in the Southern Cross Domain occurred at 2.73-2.74 Ga (Pidgeon and Wilde, 1990). The collision between the older Murchison–Southern Cross granite–greenstone nucleus and the Eastern Goldfields Superterrane has been estimated at ca. 2.67 Ga and the Yilgarn Craton was completely amalgamated at ca. 2.63 Ga marked by emplacement of post-kinematic intrusions (Chen et al., 2003).

2.1.3 Murchison Domain

The Murchison Domain of Cassidy et al. (2006) embodies a significantly larger area, especially at the eastern and southwestern margins, than the Murchison Province of Watkins and Hickman (1990), which was mainly based on the classification of Gee et al. (1981). To the east, it includes the layered mafic-ultramafic rocks at Windimurra and Narndee and is delineated by the Youanmi Fault. To the west, it extends into the northern extension of the Western Gneiss Terrain of Gee et al. (1981) and to the south and southeast includes significant parts of the Southern Cross Province of Gee et al. (1981). It is separated from the Narryer Terrane to the north by the Yalgar and Balbalinga faults (Myers, 1990a, 1993, 1997; Myers and Hocking, 1998) and from the Southern Cross domain to the east by the Youanmi Fault (Myers 1993, 1997) (Fig. 2.3). The domain extends over an area of ~100,000 square kilometres. Geological studies in the Murchison Domain began in the mid 1960s by de La Hunty, Baxter and Muhling of the Geological Survey of Western Australia. A series of 1:250,000 scale geological maps were published between 1973 and 1985; these include Cue (de la Hunty, 1973; Watkins et al., 1987), Murgoo (Baxter, 1974), Yalgoo (Muhling and Low, 1977), Belele (Elias, 1982), Ninghan (Lipple et al., 1983), Perenjori (Baxter and Lipple, 1985) and Sandstone (Tingey, 1985) with the latter a contribution from the Bureau of Mineral Resources (BMR). Later the

BMR published aeromagnetic, radiometric and bouguer gravity anomaly maps of these areas. The Murchison Province was later re-mapped by (Watkins and Hickman 1990). Pidgeon and Wilde (1990) dated some felsic rocks in their effort to constrain felsic volcanic episodes across the Yilgarn Craton.

The Murchison Domain as currently defined consists of two greenstone sequences, the lower Luke Creek Group and overlying Mount Farmer Group, both intruded by several suites of granitoids (Watkins and Hickman, 1990; Wiedenbeck and Watkins, 1993). Recently, Van Kranendonk et al. (2013), introduced a new lithostratigraphic scheme for the northeastern Murchison Domain and suggested the model may well be applicable to the rest of the Murchison Domain of the Youanmi Terrane.

The oldest plutonic episode in the domain is recorded by 2.95-2.91 Ga monzogranite and granodiorite, followed by emplacement of extensive monzogranites and porphyries and other felsic rocks over the period 2.75 to 2.64 Ga (Wiedenbeck and Watkins, 1993; Schiøtte and Campbell, 1996; Pidgeon and Hallberg, 2000; Wiedenbeck and Watkins, 1993). The crustal evolution of granitoids from different suites was addressed by Watkins et al. (1991). Wiedenbeck and Watkins (1993) carried out the first U-Pb SHRIMP dating of granitoids from different suites and proposed a time-scale for granitoid emplacement in the domain based on single zircon geochronology. It needs to be mentioned here that the greenstone stratigraphy, geochronology and crustal evolution model proposed by Van Kranendonk (2008) and Van Kranendonk and Ivanic (2009) are based on their study in the northern part of the Murchison Domain, outside the study area; therefore, the following discussions mostly refers to the regional study of Watkins and Hickman (1990) covering the entire Murchison, including the Yalgoo area.

2.1.3.1 Greenstone Stratigraphy

The earliest attempts at elucidating the stratigraphy in the Murchison were carried out by de la Hunty (1973), Baxter (1974) and Muhling and Low (1977) based on mapping in the Cue, Murgoo and Yalgoo areas, respectively. A four-part stratigraphic scheme was later adopted, based on the concept of ‘lithological associations’. This was further developed by later GSWA mapping: Belele by Elias (1982); Ninghan by Lipple et al. (1983); Baxter and Lipple (1985) and by the petrochemical studies of Hallberg (1976). The four lithological associations from base to top were i) lower mafic association, ii) lower felsic-sedimentary association, iii) upper mafic association and iv) upper felsic-sedimentary association. A later review by Baxter and Lipple (1985) revealed major inconsistencies in terms of local occurrences of various lithologies and compositional variations within the same

association over wide areas, all of which eventually made the scheme untenable. Archibald (1982) and Baxter (1982) proposed more detailed stratigraphic schemes based on mapping at Mount Magnet and in part of the Yalgoo-Singleton greenstone belt, but this too failed to address many of the earlier problems. Following detailed remapping of the Cue 1:250,000 sheet, Watkins et al. (1987) proposed a classification of the Murchison Domain is based on lithology, and relative superposition with reference to distinctive marker units.

Watkins and Hickman (1990) divided the greenstone sequences of the Murchison into two groups: the Luke Creek Group and overlying Mount Farmer Group, which together form the Murchison Supergroup. The Murchison Supergroup consists of approximately 70% mafic volcanic and 20% felsic volcanic and felsic volcaniclastic rocks. The generalized stratigraphic column is presented in Table 2.1.

Table 2.1. Simplified stratigraphic column for the Murchison Terrane after Watkins and Hickman (1990). For clarity of presentation, seven broadly contemporaneous felsic, tholeiitic-high Mg volcanic assemblages of the Mount Farmer Group are excluded from the table.

Supergroup	Group/Subgroup		Formation	Lithologic description	Group/ Subgroup	Formation	Lithologic description
Murchison Supergroup	Mount Farmer	Yalgoo Subgroup	Wadingarra Basalt	Interlayered high-Mg and tholeiitic basalt	Porlell Subgroup	Woolgra Formation	Felsic volcaniclastic, dacite, andesite.
						Stockyard Basalt	Tholeiitic basalt interlayered in the upper part with High-Mg basalt.
			Camberathunun Formation	Felsic volcanic rocks,minor basalt		Lordy Basalt	High-Mg basalt interlayered with minor tholeiitic, ultrmafics and volacogenic clastic rocks.
	Group		Formation				Lithologic description
	Luke Creek		Windaning Formation				Felsic volcaniclastic rocks interlayered with gray chert and jaspilitic BIF.
			Gabanintha Formation				Ultrmafic rocks, interlayered high-Mg and tholeiitic basalt, felsic volcanoclastic rocks.
			Golconda Formation				Mafic rocks interlayered with quartz-hematite BIF.
			Murrouli Basalt				Interlayered high-Mg and tholeiitic basalt.

The Luke Creek Group consists of two sequences of submarine tholeiitic and high-Mg basalt lava flows which formed during two separate episodes of lava-plain volcanism, both of them overlain by BIF and felsic volcanic rocks. Felsic volcanic rocks predominate in the upper part of the Luke Creek Group. The four formations of the Luke Creek Group, from bottom to top are i) Murrouli Basalt, ii) Golconda Formation, iii) Gabanintha Formation and iv) Windaning Formation. The formations of the Luke Creek Group are continuous throughout most of the greenstones and form a layer-cake stratigraphy about 10km thick.

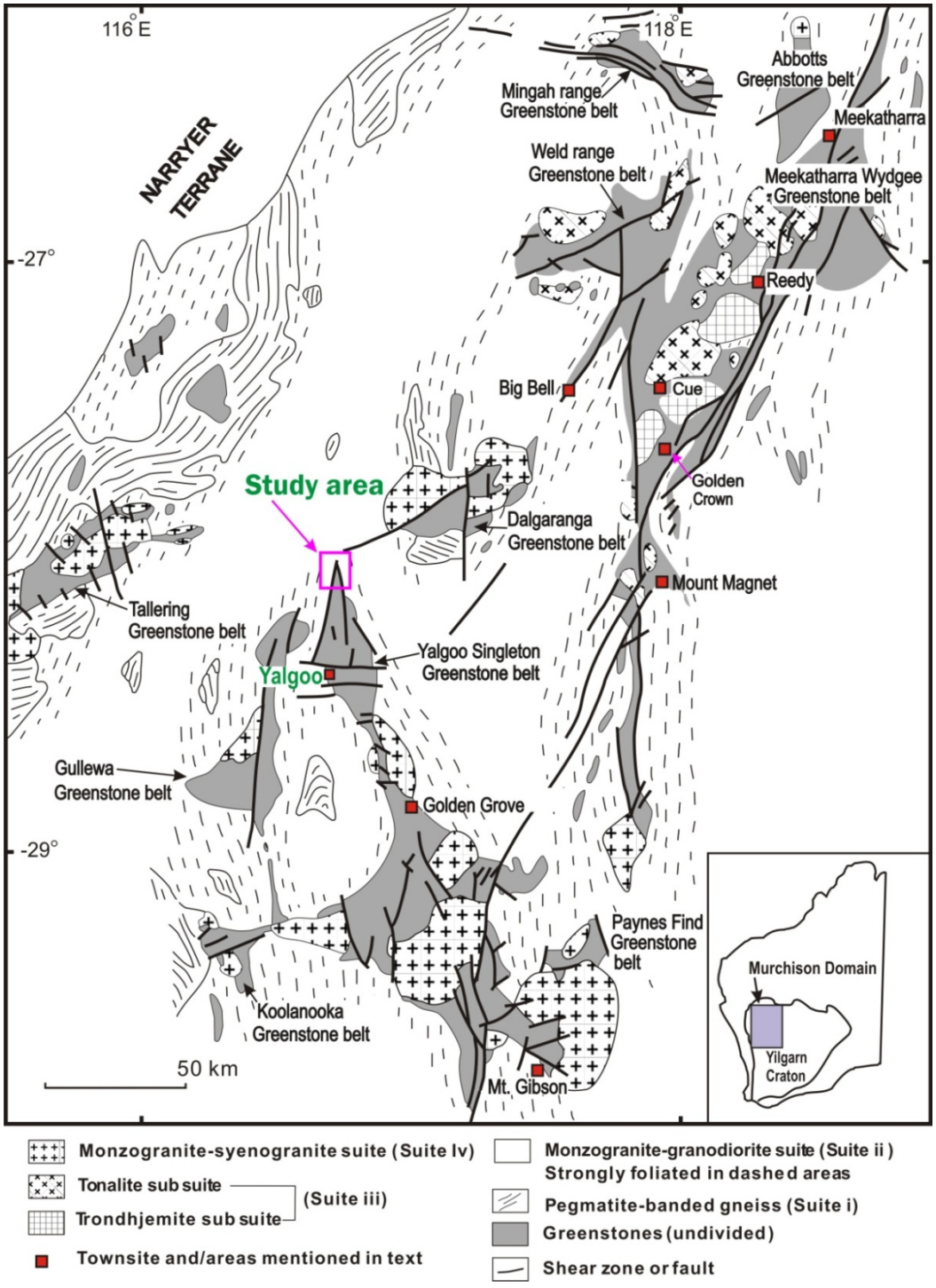

Fig. 2.4. Simplified Archean geology of the Murchison Domain showing major greenstone belts and location of areas mentioned in text. Modified from Watkins and Hickman (1990) and Yeats and Groves (1998).

The Mount Farmer Group consists mainly of felsic volcanics (dacite, andesite tuff), and high-Mg to tholeiitic basalt (Plate 2 in Watkins and Hickman, 1990). The volcanic centres and sedimentary basins are all of local extent. The Mount Farmer Group comprises two subgroups and eight formations. The thickness of the individual Mount Farmer subgroups varies from 1 to 5 km. The basaltic rocks are fairly homogeneous in composition all across

the area and show evidence of crustal contamination due to assimilation of felsic crustal materials. The thickness of the supergroup varies considerably across the area.

Observing the difficulties in correlating different units between isolated greenstone belts, Pidgeon and Hallberg (2000) proposed an informal stratigraphic subdivision. They grouped the greenstones into five assemblages. The lower units (assemblages 1–3) consist of ultramafic, mafic and intermediate volcanic rocks deposited without significant breaks in volcanism. Felsic volcanic packages (assemblage 4) are conformable with underlying units, but are spatially restricted. Discordant units of graphitic sedimentary rocks are developed along major crustal structures (assemblage 5).

The work of Van Kranendonk (2008) and Van Kranendonk and Ivanic (2009) pointed out several inconsistencies that stemmed mainly from ascribing inappropriate ages to particular formations in the classification of Watkins and Hickman (1990) and Pidgeon and Hallberg (2000) in the northeastern Murchison. Based on the above studies, and recent geochronological studies and regional mapping by GSWA, Van Kranendonk et al. (2013) suggested a new lithostratigraphic scheme for the entire Murchison Domain, which is presented in Table 2.2. They divided the greenstones into four groups. From oldest to youngest, they are i) Mount Gibson Group, ii) Norie Group, iii) Polelle Group and iv) Glen Group.

i) Mount Gibson Group: The oldest ca. 2960–2935 Ma Mount Gibson Group was identified in the Golden Grove and Mount Gibson areas in the southern part of the domain. The group is composed of mafic and felsic volcanic and volcaniclastic rocks. However, the ca. 3.01 Ga felsic volcanic rocks from the Weld greenstone belt (Pidgeon and Wilde, 1990) were not included in the oldest group of Van Kranandonk et al. (2013).

ii) Norie Group: The Norie Group is best exposed east of the Murrouli Range, southwest of Meekatharra. The Murrouli Basalt forming the base of the group is comprised of interbedded pillowed and massive, tholeiitic and komatiitic basalt (Watkins and Hickman, 1990). The overlying Yaloginda Formation consists of fine- to medium-grained volcaniclastic rocks and interbedded ferruginous shale and/or BIF.

iii) Polelle Group: Rocks of the ca. 2800–2730 Ma Polelle Group are best exposed in the hinge of the Polelle Syncline. The base of the Polelle Group is marked by the Coodardy Formation, which contains discontinuous and thin units of quartzite and metamorphosed iron-formation. The conformably overlying Meekatharra Formation consists of tholeiitic basalt, komatiitic basalt, komatiite, and minor felsic volcaniclastic rocks. The Greensleeves Formation comprises andesitic to rhyolitic volcanic and volcaniclastic rocks

that overlies the Meekatharra Formation. The Greensleeves Formation is overlain by BIF, felsic volcaniclastic rocks, and shale of the Wilgie Mia Formation.

iv) Glen Group: The ca. 2735–2710 Ma Glen Group is divided into the lower Ryansville Formation of clastic sedimentary rocks (up to 1 km thick), and the conformably overlying Wattagee Formation of komatiitic basalt and rhyolite (up to 3 km thick). Van Kranendonk et al. (2013) correlated these rocks with a conformable sequence of sedimentary rocks and komatiitic basalts that unconformably overlie the ca. 2.93 Ga greenstones near Mt Magnet (Thompson et al., 1990; Watkins and Hickman, 1990).

Table 2.2: Stratigraphic scheme for supracrustal rocks of the northeastern Murchison Domain, from Van Kranendonk et al. (2013).

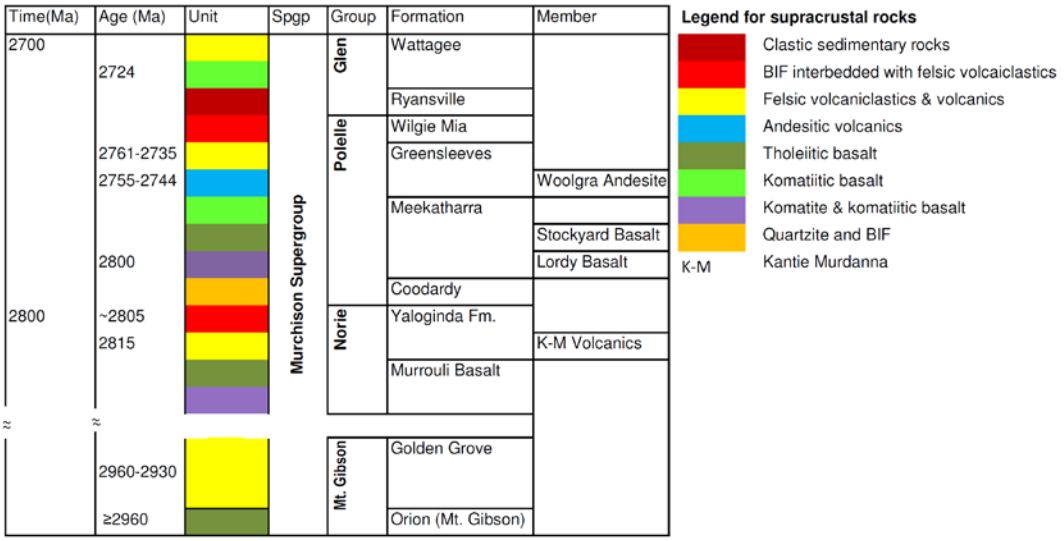

Geochronology of the Greenstones: Despite significant advances, the time span of greenstone belt development in the Murchison is still poorly constrained, as was earlier stated by Watkins and Hickman (1990). Table 2.3a summarizes the results of U-Pb ages on felsic volcanic samples in the Murchison Domain using the classification scheme of Watkins and Hickman (1990). The older Luke Creek Group was dated at ca. 3.0 Ga to 2.93 Ga (Pidgeon and Wilde, 1990; Wang et al., 1998). Pidgeon (1986) obtained U-Pb zircon ages from felsic volcanic rocks at Golden Grove and Twin Peaks of ca. 2952 Ma and 3046 Ma, respectively. Andesite from the Meekatharra-Wydgee greenstone belt formed at ca. 2976 (Pidgeon, 1986). However, Pb-Pb model ages from galena and pyrite from the mineralized zone at Golden Grove, Gossan Hill and Scuddles yielded significantly older dates between 3020-3050 Ma (Fletcher et al., 1984; Browning et al., 1987; Dahl et al., 1987) for the same formation. Hence, an age of ca. 3.0 Ga was suggested as the time of formation of the upper part of the Luke Creek Group (Pidgeon and Wilde, 1990; Schiøtte and Campbell, 1996). Only very limited age data are available for the

Mount Farmer Group. Watkins and Hickman (1990) assigned a 2818 ± 57 Ma Sm-Nd isochron age to the Mount Farmer Group. Later, recognizing a 2703 Ma sheared quartz porphyry associated with the Wattle Creek Basalt of the Mount Farmer Group overlying the 2727 Ma Morning Star felsic volcanic unit, Schiøtte and Campbell (1996) suggested that the Mount Farmer Group is ~ 2.7 Ga old.

Table 2.3a :U-Pb age constraints on supracrustal development in the Murchison Domain.

Events represented	Location	Rock type	Stratigraphic position (Watkins and Hickman 1990)	Age (Ma) and Method	References
Youngest Felsic volcanism	Dalgaranga	Felsic tuff	Dalgaranga Formation	2749-2740	Pidgeon and Hallberg (2000)
				2761±1 (combination	"
				2761±4 of TIMS U-Pb &	"
	Cue	Felsic tuff	Gabanintha Formation ?	2750-2700 SHRIMP II U-Pb)	"
				2716±4	"
2nd Felsic volcanism (proposed!)	Mount Magnet	Chert	Windaning Formation	2798±8 SHRIMP U-Pb	Schiøtte and Campbell (1996)
	"	Chert	Windaning Formation	2801±19 SHRIMP U-Pb	
	Golden Grove	Volcanogenic sandstone	Windaning Formation	2809±5 SHRIMP U-Pb	
Oldest Felsic volcanism	Weld Range	Felsic volcanic rock	"	3010 Convent. U-Pb	Pidgeon and Wilde (1990)
	Golden Grove	Volcaniclastic rock	Gabanintha Formation	2938±10 Convent. U-Pb	
	Golden Grove	Rhyodacite	"	2945±4 SHRIMP U-Pb	Wang et al. (1998)
	"	Rhyolite	"	2960±6 SHRIMP U-Pb	"
	"	Qtz rich lava	"	2953±7 SHRIMP U-Pb	"

Table 2.3b. Selected SHRIMP U-Pb ages of the supracrustal rocks according to the classification of Van Kranendonk and Ivanic (2013) in the northeastern Murchison Domain.

Group	Formation/Location	Rock type	SHRIMP U-Pb Age (Ma)	References
Glen	Dalgaranga greenstone belt	Gabbroic sill	2719±6	Pidgeon and Hallberg (2000)
	Wattagee Formation	Metarhyolite schist	2725±4	Wingate et al. (2009a)
	Ryansville Formation	Quartz sandstone	≤ 2740±4	Van Kranendonk et al. (2012)
Pollele	Wilgie Mia Formation	Felsic crystal tuff	2752±9	Wang et al. (1998)
	Greensleeves Formation	Flow banded felsic rock	2727±6	Schiøtte and Campbell (1996)
	Greensleeves Formation	Fine-grained crystal tuff	2743±4	Pidgeon and Hallberg (2000)
	Greensleeves Formation	Rhyolite tuff	2761±6	Pidgeon and Hallberg (2000)
	Meehkatharra Formation/Woolgra andesite member	Andesite	2755±5	Wingate et al.(2008c)
	Meehkatharra Formation	Volcaniclastic sandstone	2799±2	Wingate et al.(2008b)
Norie	Yaloginda Formation	Flow-banded rhyolite	2806±4	Van Kranendonk et al. (2012)
	Yaloginda Formation	Amygdaloidal basalt	2815±7	Wang et al.(1998)
Mount Gibson	Mount Gibson mine	Orion quartz porphyry	2929±3	Yeats et al. (1996)
	Golden Grove mine	Quartz-phyric rhyodacite	2945±4	Wang et al.(1998)
	Mount Gibson mine	Quartz-rich lava	2953±7	Wang et al.(1998)
	Mount Gibson mine	Quartz-pyhric rhyolite	2960±6	Wang et al.(1998)

Pidgeon and Wilde (1990) revealed an earlier felsic event at the Weld Range at 3.0 Ga, while a felsic volcaniclastic rock from Golden Grove gave a somewhat younger age ca. of 2.94 Ga. Subsequent SHRIMP U-Pb dating of single zircon also gave similar dates at ca. 2.96-2.94 Ga for the felsic event in the same area (Schiøtte and Campbell, 1996; Wang et al., 1998). From the study of Wang et al. (1998), it appeared that the first felsic volcanic event in the Murchison was protracted and spanned about 60 Ma, at least in the Golden Grove area. In the Mount Magnet area, Schiøtte and Campbell (1996) identified ca. 2.74-2.70 Ga felsic volcanism by SHRIMP U-Pb geochronology, which is inferred to bracket

the second felsic magmatic event in the Mount Farmer Group. They also obtained a SHRIMP zircon U-Pb age of 2798 ± 8 Ma for the Galtee Moore Chert of the Windaning Formation, that is similar to ca. 2.81 Ga volcanogenic sandstone at Golden Grove (Wang et al., 1998). Several felsic episodes were detected in the northern Murchison by Pidgeon and Wilde (1990) between 2749-2740 Ma in the Dalgaranga Greenstone Belt, whereas in the Meekatharra–Mount Magnet Greenstone Belt, the felsic volcanism occurred in two cycles at 2761 and 2716 Ma.

Van Kranendonk et al. (2013) compiled the previous geochronology along with a few new dates obtained by the GSWA from different volcanic units of their four suite classification. A selection of SHRIMP ages from Van Kranendonk et al. (2013) is presented in Table 2.3b. The diachronous nature of the supracrustal rocks is clear from the two tables, perhaps reflecting a more complex pattern of supracrustal development in the Murchison than previously thought. This will be addressed in the central-west part of the Murchison Domain in the present study.

2.1.3.2 Granitoid emplacement

The granitoid plutons in the Murchison Domain have been described and classified in detail by Watkins and Hickman (1990) and Watkins et al. (1991). Watkins and Hickman (1990) identified four suites of granitic rocks on the basis of limited geochronology and geochemical characteristics (Fig. 2.4). These are, in order of intrusion, suite i) pegmatite-banded gneiss; suite ii) recrystallized monzogranite; suite iii) post-folding tonalite-trondhjemite suite; and suite iv) post-folding monzogranite-syenogranite suite. The last two suites are broadly contemporaneous. Wang et al. (1993) proposed a tripartite classification of the granitoids based on spatial, temporal and isotope studies. Schiøtte and Campbell (1996), based on the results of SHRIMP U-Pb geochronology, presented a classification of the granitoids in the Mount Magnet area. Both Wang et al. (1993) and Schiøtte and Campbell (1996) essentially retained the classification of Watkins and Hickman (1991) with modified names for the suites. The regional classification scheme of granites based on the geochemical study of the Eastern Goldfields Superterrane by Champion and Sheraton (1997), was later extended to the northern Murchison Domain (Champion and Cassidy, 2002) and entire Yilgarn Craton (Champion and Cassidy, 2007), which is discussed in section 5.6.3. Incorporating the results of recent mapping of the northeastern part of the Murchison Domain by the GSWA, Van Kranendonk (2008) classified the granitoids between Cue and Meekatharra into five suites. Among all these studies, only the studies of Watkins and Hickman (1990) and Watkins et al. (1991)

addressed all the major plutons across the domain. The following overview is based on the framework of Watkins and Hickman (1990) and Watkins et al. (1991), with mention of the other studies where appropriate.

Suite i) Pegmatite-banded gneiss: These are the oldest granitoids. The outcrops of pegmatite-banded gneiss are mostly along a belt in the west of the domain and occur elsewhere as rafts in recrystallized monzogranite. The rocks consist of two monzogranite-granodiorite phases and one pegmatite phase. The monzogranite-granodiorite is composed of medium-grained, finely banded, biotite-rich and quartz-feldspar rich layers. The pegmatite phase is interlayered with the earlier phase and consists of quartz-feldspar bands a few centimetres thick. The second monzogranite-granodiorite phase intruded the earlier two components as veins and dykes during the deformation producing the gneissosity.

Suite ii) Recrystallized monzogranite: Plutons of this suite were intruded as thick subhorizontal sheets of monzogranite into the base of the Murchison Supergroup, and now occupy most areas between the greenstone belts. Recrystallized monzogranites are leucocratic, generally massive, variably foliated, with local occurrences of porphyritic varieties set within massive granitoid. Rocks of both suites i and ii were recrystallized during regional metamorphism. Wang et al. (1993) included recrystallized monzogranite in their monzogranite-granodiorite suite (suite i), whereas Schiøtte and Campbell (1996) referred to this suite as ‘external monzogranite’ as they surround the greenstone belts and form larger plutons.

Suites iii & iv) Post-folding granitoids: The youngest felsic intrusions belong to the post-folding granitoids that were emplaced as steep-sided, cylindrical or inverted tear-drop shaped bodies. Post-folding granitoids intrude only greenstone belt interiors and at the contacts between recrystallized monzogranite and greenstones. The two suites of post-folding granitoids are suite iii) tonalite-trondhjemite and iv) monzogranite-syenogranite. Suite iii consists of tonalite, trondhjemite, granodiorite, and monzogranite plutons, confined mainly to the northern Murchison Domain, whereas suite iv comprises quartz-rich monzogranite and syenogranite plutons, confined mainly to the southern part of the domain. Both these suites are included within type ii “Discrete undeformed granitoids” of Schiøtte and Campbell (1996).

Revising the granites in the northeastern Murchison, and based on new mapping and geochronology and cross-cutting relationships of the granites in the northeastern Murchison, Van Kranendonk et al. (2013) classified granites of the Murchison Domain into three supersuites that include eight suites (Table 2.4). The suites are, the Mount

Kenneth Suite of 2815‑2800 Ma mafic granodiorite, the Cullculli Suite of 2787‑2735 Ma tonalites, granodiorites, the Eelya Suite of 2759‑2747 Ma HFSE granites within the Annean Supersuite; the Big Bell Suite of 2735–2690 Ma tonalitic to monzogranitic rocks, the 2690–2665 Ma Tuckanarra Suite of granodiorites and monzogranites and the

Table 2.4. Supersuites and suites of the granitic rocks for the northeastern Murchison Domain (after Van Kranendonk et al., 2013).

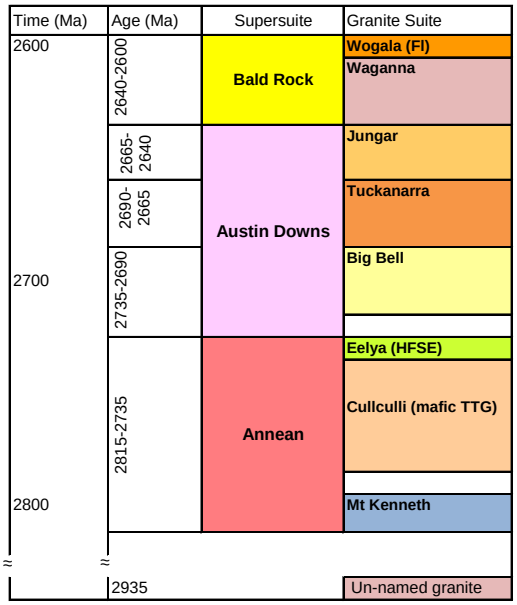

2665–2640 Ma Jungar Suite of dominantly K-feldspar-bearing porphyritic monzogranites within the Austin Downs supersuite; and the two post-tectonic suites: the monzogranitic Walganna Suite and the Wogala Suite of fluorite-bearing alkaline granite included within the 2637–2602 Ma Bald Rock supersuite.

Geochronology of the granitoids: A large number of isotopic ages of the granitoids in the Murchison Domain have been reported by several workers since the early 1990s. However, given the differences in crustal development across the domain and lack of a comprehensive granitoid classification scheme for the entire domain, these ages are often difficult to reconcile. Selected SHRIMP U-Pb ages of the granitoids of the Murchison Domain are presented in Table 2.5.

Wiedenbeck and Watkins (1993) reported a SHRIMP U-Pb zircon age of the pegmatite-banded gneiss of 2919±12 Ma. Yeats et al. (1996) obtained the oldest record at 2935±3 Ma in the domain from a monzogranite sample in the Mount Gibson mine (Fig. 2.4). Pidgeon and Hallberg (2000) suggested the age of zircon rims at ca. 2.7 Ga represented the emplacement age of the granitoid and that the ca 2.9 Ga zircon (cores) were inherited. The recrystallized monzogranites were dated between 2706 and 2640 Ma by SHRIMP U-Pb geochronology (Wiedenbeck and Watkins, 1993; Schiøtte and Campbell,

Table 2.5. Selection of SHRIMP U-Pb zircon ages of the granites in the Murchison Domain.

Area	Rock type	Age (Ma)	References
Mount Gibson mine	Recrystallised monzogranite	2935±3	Yeats et al. (1996)
Badja area 35Km south of Yalgoo	Pegmatite banded gneiss	2912±12	Wiedenbeck and Watkins (1993)
Mount Kenneth bore	Hornblende biotite granodiorite	2813±3	Wingate et al. (2012)
Southwest of Meekatharra	Hornblende tonalite	2787±3	Wingate et al. (2008)
	Reedy trondhjemite	2785±8	Wang et al. (1995)
Mount Mulgine	Syenogranite	2767±10	Oliver (1999)
Norie pluton	Tonalit: massive	2760±8	Wiedenbeck and Watkins (1993)
Queen of May gold mine near Cue	Tonalite: coarse-grained	2759±4	Pidgeon and Hallberg (2000)
	Peter Well granodiorite	2747±6	Wang et al. (1995)
Mount Gibson mine	Porphyry intrusion	2752±5	Schiøtte and Campbell (1996)
	Snake Gully tonalite	2751±6	Wang et al. (1995)
10 km southwest of Glen Homestead	Tonalite with mafic clotty texture	2747±3	Van Kranendonk (2008)
Yalgoo	Monzogranite	2743±4	Oliver (1999)
Airport granite- southwest of Mount Magnet	Granite: massive, coarse-grained	2716±4	Schiøtte and Campbell (1996)
Mount Magnet ,from optical fibre line between Yalgoo and Mount Magnet	Granite with Kf megacrysts	2710±10	Schiøtte and Campbell (1996)
Nalbarra area, ~70km southeast of Yalgoo	Monzogranite	2704±51	Wiedenbeck and Watkins (1993)
The Granites- north of Mount Magnet.	Tonalite	2702±6	Schiøtte and Campbell (1996)
Jumbulyer Granite-southwest of Mount Magnet	Massive granite: coarse-grained	2696±5	Schiøtte and Campbell (1996)
Mount Magnet, west of greenstone belt	Granite	2694±7	Schiøtte and Campbell (1996)
Moyagee area, ~130km northeast of Yalgoo	Monzogranite	2681±6	Wiedenbeck and Watkins (1993)
Mount Magnet, east of greenstone belt	Granite: massive weakly recrystallised	2680±5	Schiøtte and Campbell (1996)
"	Granite: gneissic and strongly recrystallised	2678±5	Schiøtte and Campbell (1996)
"	Granite: moderately recrystallised	2670±6	Schiøtte and Campbell (1996)
"	Leucogranite layer within gneissic granite	2657±9	Schiøtte and Campbell (1996)
Mount Magnet	Massive recrystallised granite	2655±10	Schiøtte and Campbell (1996)
Damperwah pluton	Monzogranite	2641±5	Wiedenbeck and Watkins (1993)
Mount Magnet, from optical fibre line between Yalgoo and Mt Magnet	Granite: massive moderately recrystallised	2640±10	Schiøtte and Campbell (1996)
10 km southwest of Glen Homestead	Biotite monzogranite	2623±9	Wingate et al. (2009b)
Big Bell mine	Monzogranite	2627±8	Mueller et al. (1996)
Koolanooka granite	Syenogranite	2617±14	Wiedenbeck and Watkins (1993)
13.5 km west of Reedy	Foliated biotite monzogranite	2605±10	Wang et al. (1998)

1996; Van Kranendonk, 2008). Oliver (1999) reported older ages for two granitoids (at 2.74 and 2.77 Ga from Yalgoo and Mount Mulgine, respectively) which were mapped originally by Watkins and Hickman (1990) as recrystallized monzogranite. Compositional variation between the tonalite-trondhjemite and monzogranite-syenogranite suites is also reflected in ages of these two suites of post-folding granitoids. Emplacement ages of these granitoids span over 100 Ma across the domain, ranging from 2.6 to 2.72 Ga in the southern part (Wiedenbeck and Watkins, 1993, Pidgeon and Hallberg, 2000; Van Kranendonk, 2008).

2.1.3.3 Metamorphism

Three metamorphic episodes have been identified in the Murchison Domain (Watkins and Hickman, 1990), which are: i) M1, contact metamorphism of greenstones by layered mafic intrusions; ii) M2, contact metamorphism of greenstones by intrusion of the earlier two suites of granitoids; and iii) M3, regional metamorphism of greenstones and granitoids.

The M1 metamorphic episode is of local extent during which the greenstones were subjected to local amphibolite and granulite facies metamorphism by emplacement of the Gabanintha mafic intrusion. A narrow zone (up to 150m) on the northeast of the intrusion reached amphibolite-granulite transition facies in the aureole. A granulite-facies assemblage is found 10km north of Karara Homestead in the Yalgoo-Singleton greenstone belt, and about 3km northeast of the Koolanooka greenstone belt.

M2 metamorphism is essentially the first major metamorphic episode recorded in the domain. Intrusion of protoliths of suite i and suite ii granitoids caused low- to mid-amphibolite facies metamorphism in the basal greenstones. The contact aureoles vary from a few hundred metres to several kilometres. The contact effects on the protolith banded pegmatite granodiorite (suite i) are only recorded from the Tallering and southern Dalgaranga greenstone belts. Most marginal zones of greenstone belts preserve greenschist-amphibolite assemblages and amphibolite facies remnants are preserved within monzogranites.

The M3 metamorphism is a regional event that affected the supracrustal and earlier granitic rocks at greenschist facies over most of the domain. The Abbots and northern Meekatharra-Wydgee greenstone belts preserved upper greenschist facies metamorphism at the marginal zones, with prehnite-pumpellyite facies in the cores. Granulite facies conditions were only reported from a poorly-exposed part of the Koolanooka greenstone belt. In the southwest of the domain, the granitoids of suite i and ii, along with supracrustal rocks, were metamorphosed to amphibolite facies, but to greenschist facies elsewhere in the domain. The exposure of higher-grade rocks in the southwest of the domain was attributed to greater uplift.

Watkins et al. (1991) considered the 2681±6 Ma age of recrystallized monzogranite to represent an older age limit for both the D2 and D3 deformation phases (see section 8.2.1) and their associated greenschist facies regional metamorphism. The crystallization ages of post-folding granitoid (suite iv) (2641±5 and 2617±14 Ma) defines the younger age limit for the termination of both D3 and regional greenschist facies metamorphism.

2.1.3.4 Gold Mineralization in the Murchison Domain

Gold mineralization in the south of the Murchison Domain has been relatively poorly studied, compared to the highly productive districts in the northeastern part of the domain and in the Eastern Goldfields Superterrane. Watkins and Hickman (1990) divided the epigenetic gold deposits in the Murchison Domain into three main types they are: Type 1, basalt-hosted and less commonly, dolerite-hosted quartz vein deposits; Type 2, ultramafic schist-hosted, and less commonly, mafic schist-hosted, shear zone deposits and Type 3, BIF-hosted and chert-hosted deposits. Of these, Type 1 deposits consist of single quartz veins, or simple quartz or quartz-carbonate vein systems, occupying tensional fractures, faults or narrow shears. Limited geological data (e.g. Victoria United, Noongal and Gnows Nest, Messenger Patch) show wall-rock enrichment in K, Ba, Rb, Sr, Pb, and H_2O and depletion in Na, Ca, and Mg. Type 2 deposits are concentrated in wide (0.5-1km), regionally extensive and pervasively sheared zones, with only a minor mafic rock component. Numerous quartz veins and veinlets, generally lenticular and discontinuous, are intruded by quartz-feldspar porphyries, the margins of which localized high gold grades with the development of pyrite, arsenopyrite, fuchsite and sericite. Most of the major ultramafic-hosted deposits are located in the Meekatharra-Reedy area (Fig. 2.4). Along with quartz vein and porphyry contacts, gold mineralization also extends into the ultramafic schist (e.g. at Phar Lap, Meekatharra). Type 3 deposits are further classified into: (a) stratabound sulphide-rich and commonly brecciated ores, and (b) erratic high-grade shoots at intersections with faults and lenses, and quartz veins. Watkins and Hickman (1990) suggested the main period of tectonic development, metamorphism, and plutonism associated with gold mineralization in the Murchison Domain spanned an interval of approximately 60 Ma between about 2680 and 2620 Ma.

Only a few direct ages of gold mineralization are available for the Murchison Domain. Mueller et al. (1996) obtained a U-Pb age (on almandine) of 2662±5 Ma for the main gold-sulphide-scheelite mineralization at Big Bell (Fig. 2.4). There is also a U-Pb titanite age of 2614±2 Ma from a scheelite- and sulphide-bearing andradite-replacement vein southeast to the major orebodies at Big Bell that occurred 80 Ma after peak amphibolite facies metamorphism. The South Emu gold deposit at Reedys was dated at 2637±4 Ma by Wang et al. (1993). A SHRIMP U-Pb age of 2627±13 Ma (on hydrothermal zircon) at the Hornet gold deposit at Mount Gibson represents the youngest episode of mineralization in the Murchison Domain (Yeats et al., 1996).

2.1.4 Geological Setting of the Study Area

The study area is located in the northern part of the north-south striking Yalgoo greenstone belt in the Murchison Domain. The supracrustal succession is dominated by tholeiitic mafic volcanics, high-Mg basalts and gabbro sills. The southern part of the belt contains mostly high-Mg basalts with interbedded BIF horizons. The area is bounded to the north, west and east by granitic rocks. North-northeast trending, locally sheared, felsic porphyry dykes are common in the area. Several broadly east-west trending mafic dykes also cut the Archean stratigraphy (Fig. 2.5). A geological map of the study area with major mine workings is presented as Fig. 2.5.

Mafic volcanic rocks: The thick sequence of mafic rocks, with minor BIF and chert, occupies a significant part of the North Yalgoo area and forms part of the Murrouli Basalt Formation of the older Luke Creek Group greenstone sequence (Watkins and Hickman, 1990). The generalized stratigraphic succession of the Luke Creek Group is given in Fig. 2.6a. The Murrouli Basalt is comprised of laterally extensive interlayered mafic rocks, with minor ultramafic rocks, and associated gabbro and dolerite which are now represented by variably weathered amphibolitic units. In the study area, however the gabbro/dolerite map unit was proved to be Mg-rich tholeiitic basalt (Fig. 2.6b). A linear outcrop of amphibolites and quartz-magnetite BIF of the Golconda Formation is recognized in drillholes, marking the eastern margin of the area (Collins and Stuart, 2000). The BIF is finely laminated and shows small-scale folding. Hallberg et al. (2002) equated the interbedded BIF, dolerite and high-Mg basalt exposed in the area to Assemblage 2 (association of BIFs separated by massive mafic rocks) of Pidgeon and Hallberg (2000). Hallberg et al. (2002) identified three major mafic-ultramafic map units, which are, i) ultramafic rocks, mostly high-Mg basalt with local ultramafic cumulates and schist, ii) mafic rocks, minor basalt and interbedded high-Mg basalt and BIF along the eastern margin of Noongal anticline, and iii) layered sills, ultramafic and mafic cumulate intrusions to the south of the Yalgoo town site. However, the boundaries drawn between different mafic-ultramafic sequences differ considerably from those of Watkins and Hickman (1990).

Felsic porphyries: Several thin NW-trending porphyry intrusions occur parallel to the NW component of Noongal shear zone as mapped by Watkins and Hickman (1990). These porphyries mostly cut through the mafic supracrustals and hence post-date them (Fig. 2.5). Hallberg et al. (2002) reported a well-exposed sequence of quartz-phyric felsic tuffs and felsic volcaniclastic sandstones from the eastern slope of a prominent range of BIF north of Bridge Well lying beyond the eastern boundary of the study area. The felsic rocks are

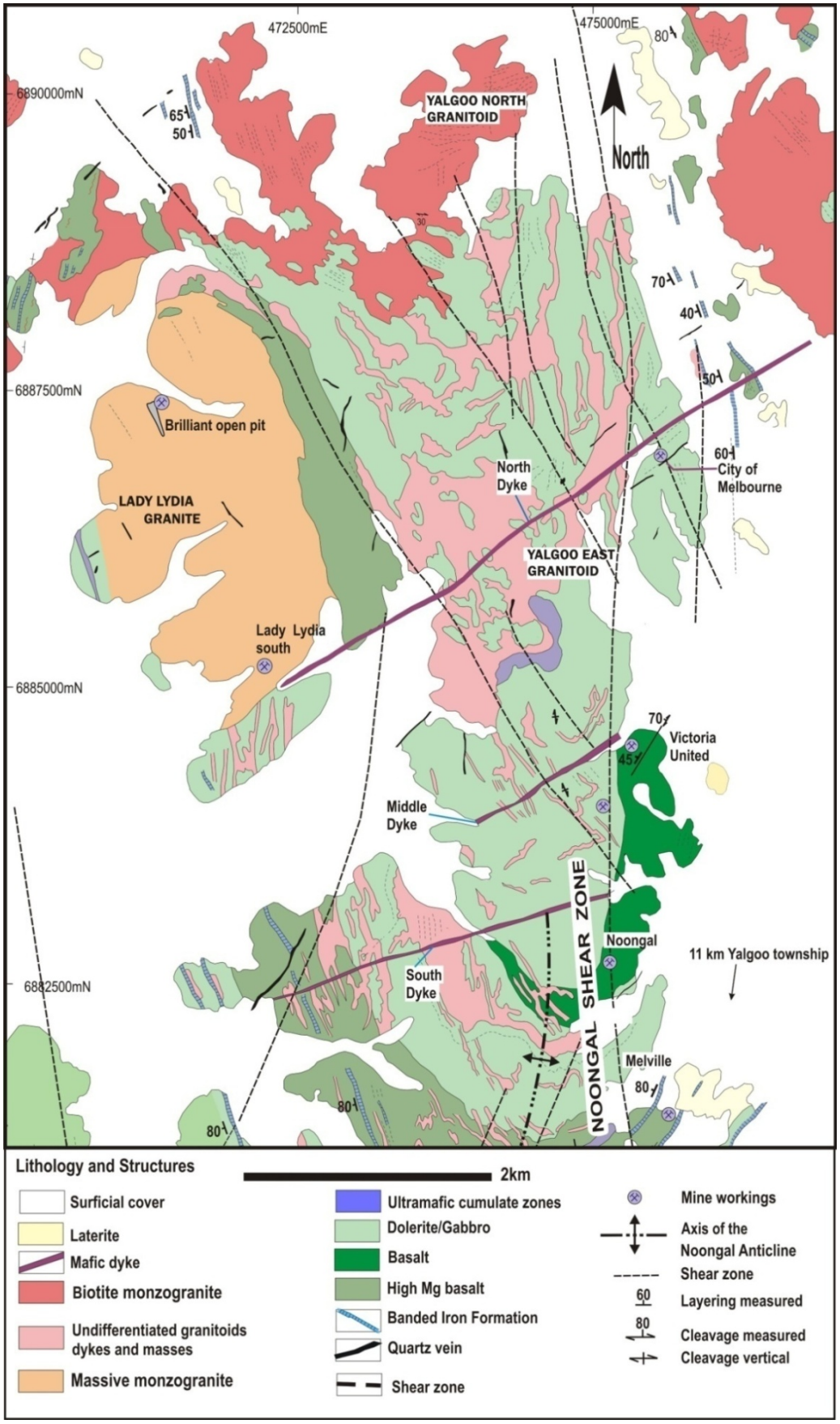

Fig. 2.5. Geological map of the north Yalgoo area showing major mine workings. (From Hallberg et al. 2002, modified after Watkins and Hickman, 1990).

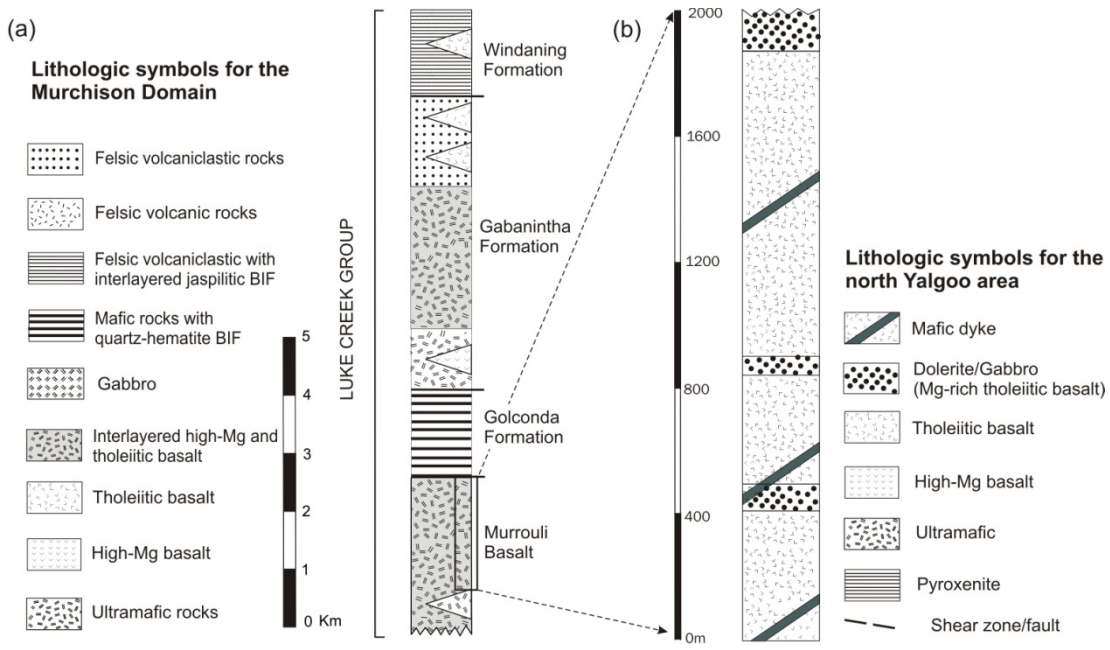

Fig. 2.6. (a) Generalized stratigraphy of the Luke Creek Group after Watkins and Hickman (1990). (b) Lithological units of the Murrouli Basalt in the north Yalgoo area.

interbedded with BIF, the latter being found as 1-2m-wide bands characterized by extensive soft-sediment deformation (Hallberg et al. 2002). Watkins and Hickman (1990) reported an isolated linear outcrop of interbedded grey white chert and felsic volcaniclastic rocks north of the City of Melbourne mine site.

Granitoids : Two distinct types of granitoid intrude the supracrustal rocks in the west and north. There are also patchy granitoid outcrops in the form of small hillocks present in the central-east part of the area.

The granitoids in the Yalgoo area are known by their informal names as found in mine reports and earlier academic research (e.g. Hallberg et al., 2002; Oliver, 1999). Watkins and Hickman (1990) mapped the granitoid in the west and patches of granitoid in the central part of the area as “recrystallized monzogranite” and granitoid in the north as “undivided post-folding granitoid”. Hallberg et al. (2002) divided the granitoids into three units, which are: i) unit 25B- massive monzogranite with large quartz phenocrysts in the west, ii) unit 25A- massive to foliated monzogranite with scattered K-feldspar megacrysts in the north and iii) unit 25- undifferentiated complex masses and dykes of coarse monzogranite with quartz-feldspar porphyry and graphic granite in the eastern part. The unit 25 is foliated coarse-grained granitoid, located to the northern part of the study that is called the “Goolthan Goolthan granitoid” by Oliver (1999).

The granitoid in the west is referred to as the Lady Lydia granite in all previous works. However, there are no distinct names given to the northern and eastern granitoids. The

granitoid in the north is informally known as “older granitoid” to geologists of Prosperity Resources and Comet Resources (Rick Dawson, Personal communication, 2004). Oliver (1999) named the northern and eastern granitoids as the “Goolthan Goolthan granitoid” and “Basin granitoid”, respectively. Failing to find any rationale and uniformity behind these names, a simpler approach is adopted here. The eastern granitoid is referred to as the “Yalgoo east granitoid (YEG)” and the northern is referred to as the “Yalgoo north granitoid” (YNG). Contact between these granitoids could not be seen due to alluvial cover. A description of the three granitoids is presented in chapter 5.

Mafic dykes: Watkins and Hickman (1990) mapped two east-west to north-northeast trending dolerite dykes in the Yalgoo area. The present study identified an additional dyke in the central part of the area, and they will be referred to as the north, middle and south dykes in the subsequent text. These dolerite dykes are thought to be part of the widespread east-west trending Widgiemooltha dyke swarm with an age at 2.41 Ga (Nemchin and Pidgeon, 1998). An account of these dykes is presented in a separate chapter (Chapter 6).

Structure: In the Yalgoo greenstone belt, the north-south trending Noongal Anticline is the major F3 structure and consists of NNW- to NNE- trending upright, tight to isoclinal folds and associated penetrative fabrics formed during the D3 event (Fig. 2.5). The anticline plunges 60-80 degrees to the south and has an overturned (west-dipping) eastern limb and prominent west-dipping axial plane cleavage (Hallberg et al. 2002) (Fig. 2.5). An anastomosing network of NNW- to N-S trending deformation zones and faults cuts the axial part of the anticline. This deformation zone is known as the Noongal shear zone (NSZ), and it postdates the Noongal Anticline and probably formed during the D4 event (Watkins and Hickman, 1990) (Fig. 2.5). The NSZ extends for over 20 km and dips westward at between 40 and 60°, and has a sinistral sense of displacement.

Metamorphism: The rocks in the northern part of the Yalgoo greenstone belt (study area) exposed in the core of the Noongal Anticline are considered to have undergone lower to middle amphibolite facies metamorphism, most likely due to invasion by granitic rocks at shallow depths (Hallberg et al., 2002; Watkins and Hickman, 1990). In contrast, rocks from the southern part of the belt range from virtually unmetamorphosed (some cumulates in the Wadgingarra Complex are thin layered sills- Muhling and Low, 1977) to greenschist facies (Hallberg et al., 2002).

Chapter 3 Nature and Genesis of the Mafic Volcanic Rocks in the Yalgoo Area

3.1 Distribution of the Mafic Volcanic Rocks

The mafic rocks crop out poorly in the North Yalgoo area and are mostly covered by Quaternary reddish-brown colluvium. All the outcrops are situated immediately west of the Noongal shear zone along a ~5km strip between City of Melbourne to the north and Melville to the south. The locations of the samples collected for this study are shown on Figs. 3.1,

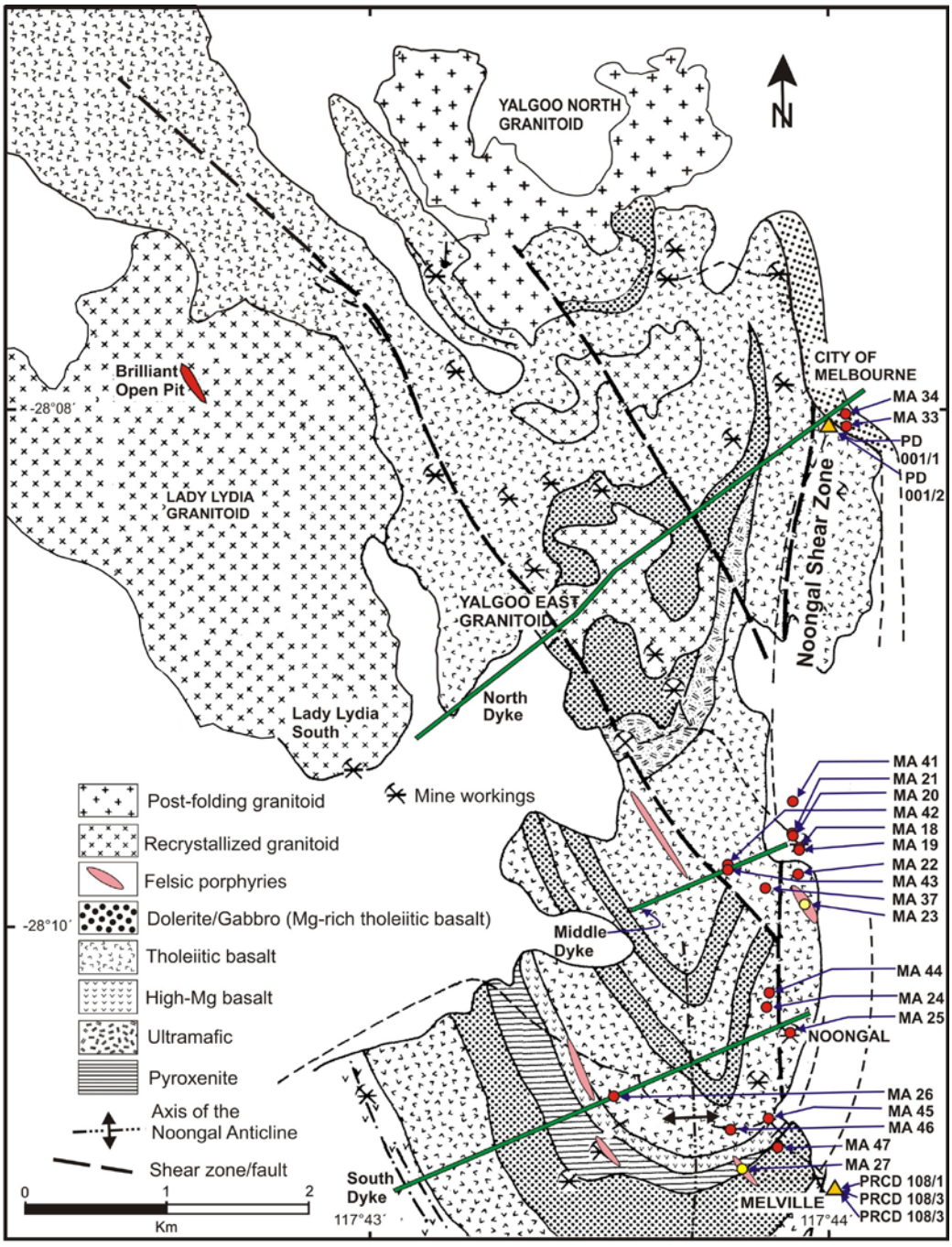

Fig. 3.1. Geological map of the Noongal area after Watkins and Hickman (1990), modified after Hallberg et al. (2002) showing mafic sample locations (red circles represent field samples, orange triangles represent drill samples.

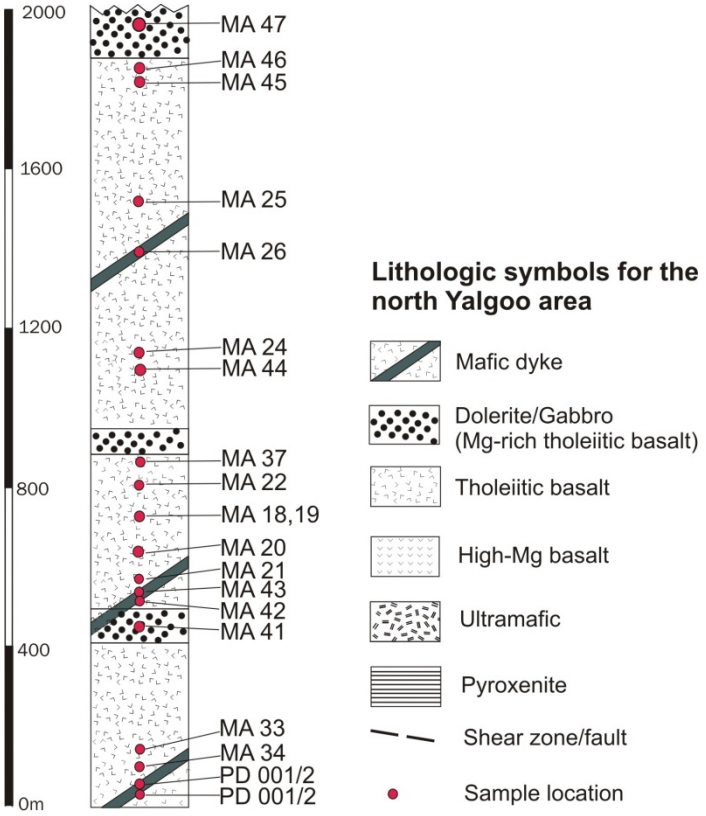

Fig. 3.2. Locations of the samples within different units of basalt stratigraphy in the north Yalgoo area. The stratigraphic positions of the samples are estimated, based on the Noongal traverse map (traverse 52) in Watkins and Hickman (1990).

3.2. Waste dumps around abandoned mine workings provided access to fresh rocks, and a total of twenty mafic rock samples were obtained from these sites. Of these twenty, five samples were obtained from the dykes (see chapter 6). The sample locations are shown on a simplified stratigraphic column of the Murrouli Basalt Formation (Fig. 3.2). Watkins and Hickman (1990) did not include any samples from the Noongal traverse (Fig. 41, Watkins and Hickman, 1990) in their description, as they considered these mafic rocks rocks to be intensely altered. During fieldwork for the present study, a narrow (~2 to 5m wide) strip of sheared and altered mafic rock was noted along the north Yalgoo road which most probably represents a component of the N-S trending Noongal shear zone: no samples were collected from this zone. Geochemical analyses of the fifteen mafic volcanic samples have a maximum of ~1.1% of volatile content (i.e. loss on ignition), and hence are considered to be relatively fresh, so that all samples were studied petrologically and prepared for geochemical study. Relatively coarse-grained samples were crushed to see if they contained any zircons in order to carry out SHRIMP U-Pb geochronological analysis. But zircons were retrieved from only one mafic dyke sample (MA 26) which was subsequently dated by SHRIMP (see section 6.5).

3.2 Petrography of the Mafic Volcanic Rocks

Two different rock types were identified from petrographic and geochemical observations of the fifteen samples from the Murrouli Basalt Formation, these being: i) mafic type I and ii) mafic type II (Table 3.1). All mafic rocks are metamorphosed to amphibolite facies. This section describes the petrographic characteristics of these two rock types, most of which show low to moderate degrees of alteration and metamorphism. Samples MA 18 and 19 were collected from a mafic sequence 2.5m beneath a quartz vein in an abandoned mine adit. The adit intersects a gold-bearing massive quartz vein within the layered mafic sequence. The modal compositions of mafic type I and type II rocks were determined by estimation and are presented in Table 3.2. Mineral abbreviations used in the photomicrographs follow the nomenclature scheme as outlined by Kretz (1983) and Spear (1993).

Table: 3.1 Classification of the mafic samples from the north Yalgoo area.

Rock types	Sample number
i) Mafic type I	MA 18,19,20,21,22,24, 44,45
ii) Mafic type II	MA 33, 34,37,41,46,47

3.2.1 Mafic Type I

Other than samples MA 18 and 19, all mafic type I samples were obtained from discontinuous outcrops within 1km of the Noongal and Melville prospects (Fig. 3.1, 3.2). The abandoned adit (location of samples MA 18 and 19) has a ~70cm wide quartz vein on the northwest wall and thins out to ~10 cm in the southeast wall. Mafic rock immediately above the quartz vein is banded and composed of thin alternating bands of light yellowish brown and green-coloured minerals. Rocks below the quartz vein are greyish-green and similar to most other metabasalt samples (Fig. 3.3). Mafic rocks above and below the quartz vein are strongly foliated (007/45W) and variably altered. The foliation measured in the metabasalt at the location of MA 24 is 354/44W.

In hand specimen, the mafic rocks are dark green to grey coloured, fine-grained and generally have a massive texture. Under the microscope, most show slender plagioclase crystals, randomly oriented within dark green amphibole defining a fine-grained relict igneous texture (Fig. 3.4a). Some rocks show a weak porphyritic texture, as observed in MA 21, where recrystallised plagioclase is enclosed in a bladed aggregate of amphibole and plagioclase (Fig. 3.4b). Sample MA 22 shows a foliated texture composed of weakly-oriented crystals of amphibole and plagioclase (Fig. 3.4c). Accessory minerals are epidote, leucoxene, biotite, chlorite, titanite and quartz. Plagioclase (An_{15-32}) (0.05 to 0.6mm), exhibits traces of primary albite twining and shows local sericitization. Amphibole (0.15 to 0.3 mm) forms subhedral

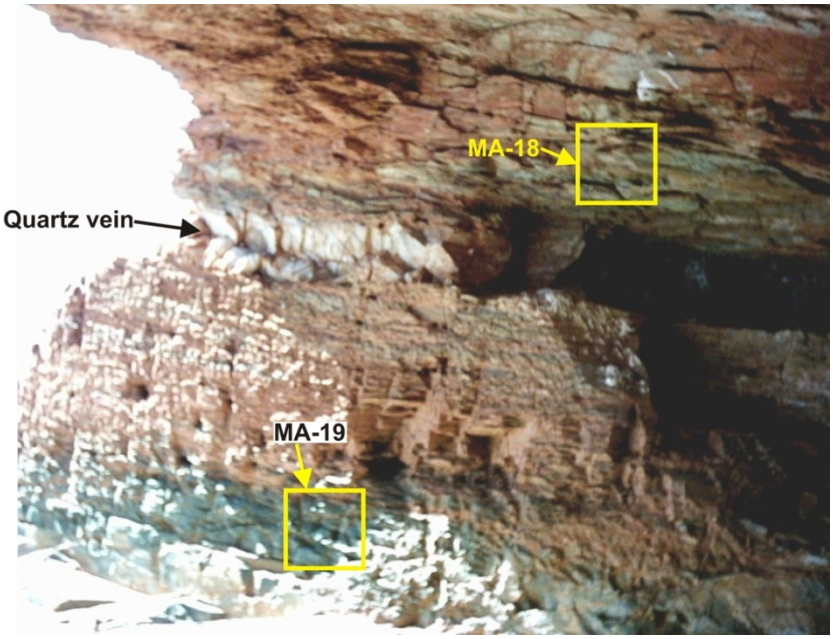

Fig. 3.3. Locations of sample MA 18 and MA 19 within an adit in the Noongal area.

Table 3.2. Modal composition of the mafic rocks (except dykes) of the north Yalgoo area. tr = trace amount.

Minerals	Mafic type I									Mafic type II					
	MA 19	MA 25	MA 45	MA 20	MA 21	MA 22	MA 24	MA 44	MA 18	MA 33	MA 34	MA 37	MA 41	MA 46	MA 47
Quartz	4	3.	5	6	6	8	10	5	2	10	6	5	9	9	12
K-feldspar									3						5
Plagioclase	28	22	23	18	15	3	10	8	2	5	3	tr	2	5	17
Amphibole	67	74	70	76	78	82	75	87	91	79	85	65	66	54	56
Biotite			tr		1	7	5			6	6	7	3	tr	2
Chlorite									tr				2	tr	
Epidote		1	tr			tr	tr	tr	tr	tr	tr	tr	2	tr	7
Clinozoisite	tr									tr	tr	15	11	27	
Leucoxene	0.5	tr	tr	tr	tr	tr	tr		tr			7	tr	tr	
Titanite	0.5		2	tr					tr	tr	tr	2	5	5	1
Opaque/Ilmenite			tr	tr		tr			tr				tr		tr
Fe-oxide/hematite									2	2					
Total	100	100	100	100	100	100	100	100	100	100	100	100	100	100	100

bladed to acicular crystals, and is moderately pleochroic (from pale green to dark green). Locally, amphibole is replaced by biotite and this is subsequently altered to greenish chlorite. Epidote occurs as small (0.4mm), solitary crystals and locally occurs in close association with irregular dark brown iron oxide (Fig. 3.4d). Greyish, cloudy leucoxene-titanite clusters (0.2-0.5 mm) are distributed throughout (Fig. 3.4e). In a few samples (MA 20, 21), thin granitic (quartz-feldspar) veinlets (0.4 to 2.5mm thick) traverse either parallel, or oblique, to the main foliation. Sample MA 18 has a strong fabric resulting from parallel alignment of two slightly different mafic layers.

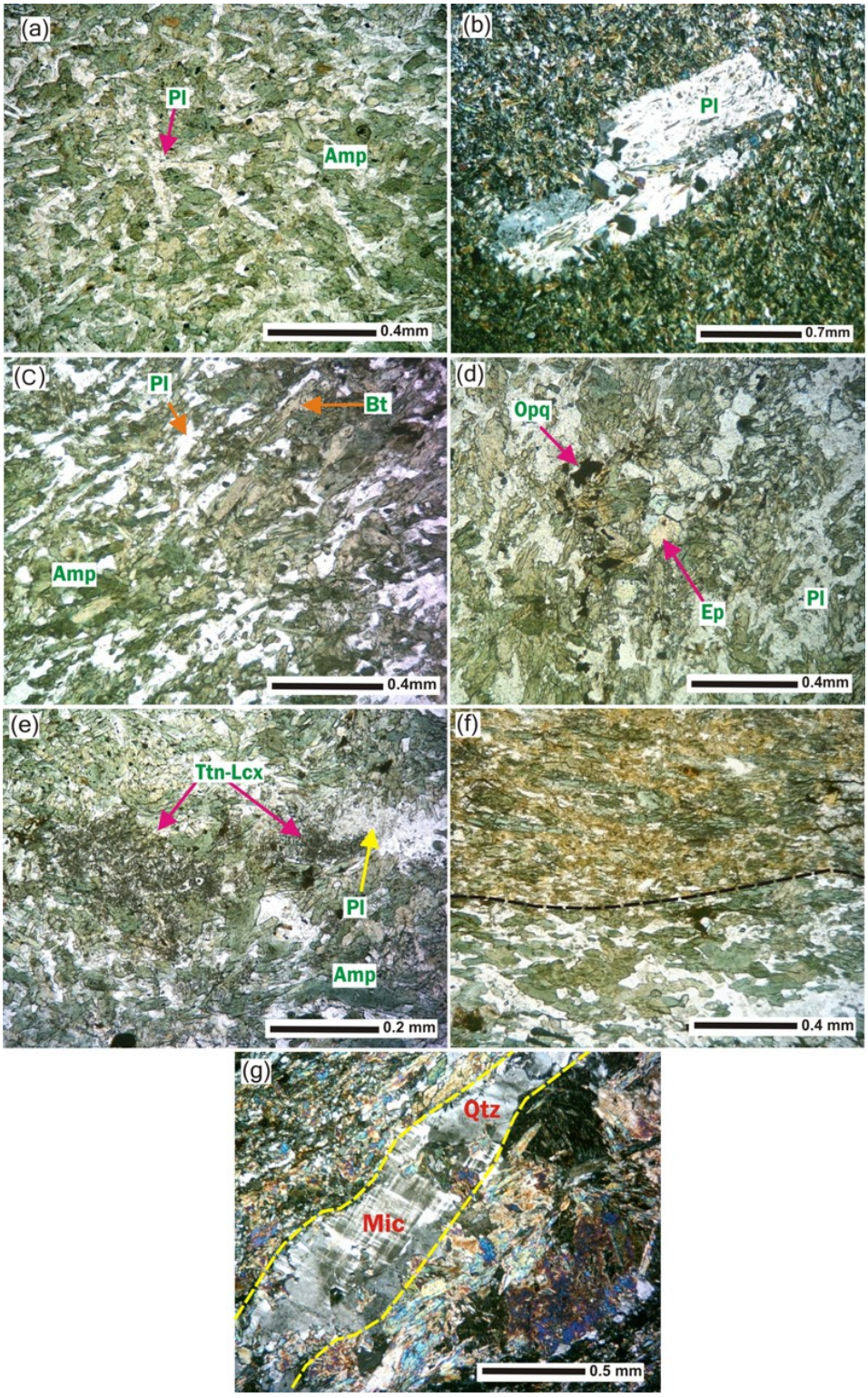

Fig. 3.4. Selected photomicrographs of mafic type I rocks. (a) Fine-grained relict igneous texture formed by slender plagioclase laths (Pl) and dark irregular green amphibole (Amp) grains (MA 19, under plane polarized light-ppl). (b) Large plagioclase crystal mantled by an aggregate of fine bladed amphibole and plagioclase (MA 21, under crossed polarized light-xpl). (c) Foliated texture composed of thin bladed amphibole, biotite (Bt) and plagioclase laths (MA 22, ppl). (d) Granular opaque (Opq) and epidote (Ep) blebs in metabasalt (MA 24, ppl); (e) Fine aggregates of leucoxene (Lcx) and titanite (Ttn) replacing ilmenite. (MA 19, xpl). (f) Sharp contact between fine-grained amphibolite and medium-grained amphibolite. (MA 18, ppl) (g) Late granitic vein (composed of fresh microcline and quartz) cutting through metabasalt (MA 18, xpl).

A thin (8 to 15mm) layer of acicular yellow-brown amphibole alternates with a dark green, largely fresh medium-grained amphibole-rich layer of similar thickness (Fig. 3.4f). Minor amounts of quartz, plagioclase, chlorite, epidote hematite, opaques are present in both layers. Veinlets (~02 to 3mm) of granitic material traverse through the rock parallel to the foliation (Fig. 3.4g).

3.2.2 Mafic Type II

The mafic rocks of type II are similar to mafic type I, with the exception of more locally preserved, slightly coarser-grained intergranular textures. They are primarily composed of amphibole and recrystallised plagioclase, along with minor disseminated opaque oxide granules, and accessory clinozoisite, biotite, quartz, epidote and chlorite.

Sample MA 33 was interleaved with highly-deformed felsic rocks near the City of Melbourne prospect: the foliation was 010/54W. Sample MA 34 was collected from 135m north of sample MA 33 from a waste dump, next to drill hole PD 001 (Fig. 3.1). In thin section, both rocks show a relict intergranular texture, with large subidiomorphic plagioclase partially enclosing bladed to acicular amphibole crystals. Minor granular opaques and accessory quartz, biotite, titanite, and traces of epidote, are disseminated throughout (Fig.3.5a,b). Both samples MA 37 (~360m south of the middle dyke) and MA 41 (from float close to the Victoria United prospect) are dark green, fine- to medium-grained and massive in hand specimen. Sample MA 37 is texturally similar to MA 33 and 34 but contains a significantly higher proportion of clinozoisite and aggregates of granoblastic quartz and plagioclase (Fig. 3.5c,d). Chlorite is a trace mineral in samples MA 33, 34 and 37. Sample 41 has a similar texture and mineralogy to sample MA 37, with slightly higher epidote and leucoxene/titanite contents. Granular brown clusters of leucoxene/titanite most probably formed after primary ilmenite.

Sample MA 46 is medium- to coarse-grained, greyish green with a mottled appearance, which in thin section shows a similar texture and mineral phases to samples MA 37 and 41. Three samples (MA 37, 41 and 46) are clinozoisite rich, with the highest amount occurring in MA 46. Minor chlorite is present both in samples MA 41 and 46. Sample MA 47 (~150m southeast from sample MA 46 next to a quartz vein) is a massive, dark green coarse-grained rock. Thin section study reveals a xenomorphic texture with preservation of original intergranular texture in places (Fig. 3.5f). The rock is comprised of mostly green amphibole, coarse-bladed recrystallised plagioclase, with accessory K-feldspar, quartz, titanite, biotite, epidote and chlorite. Amphibole is acicular and variably altered to actinolite. Epidote forms euhedral rhombic crystals that cut across amphibole crystals (Fig. 3.5e).

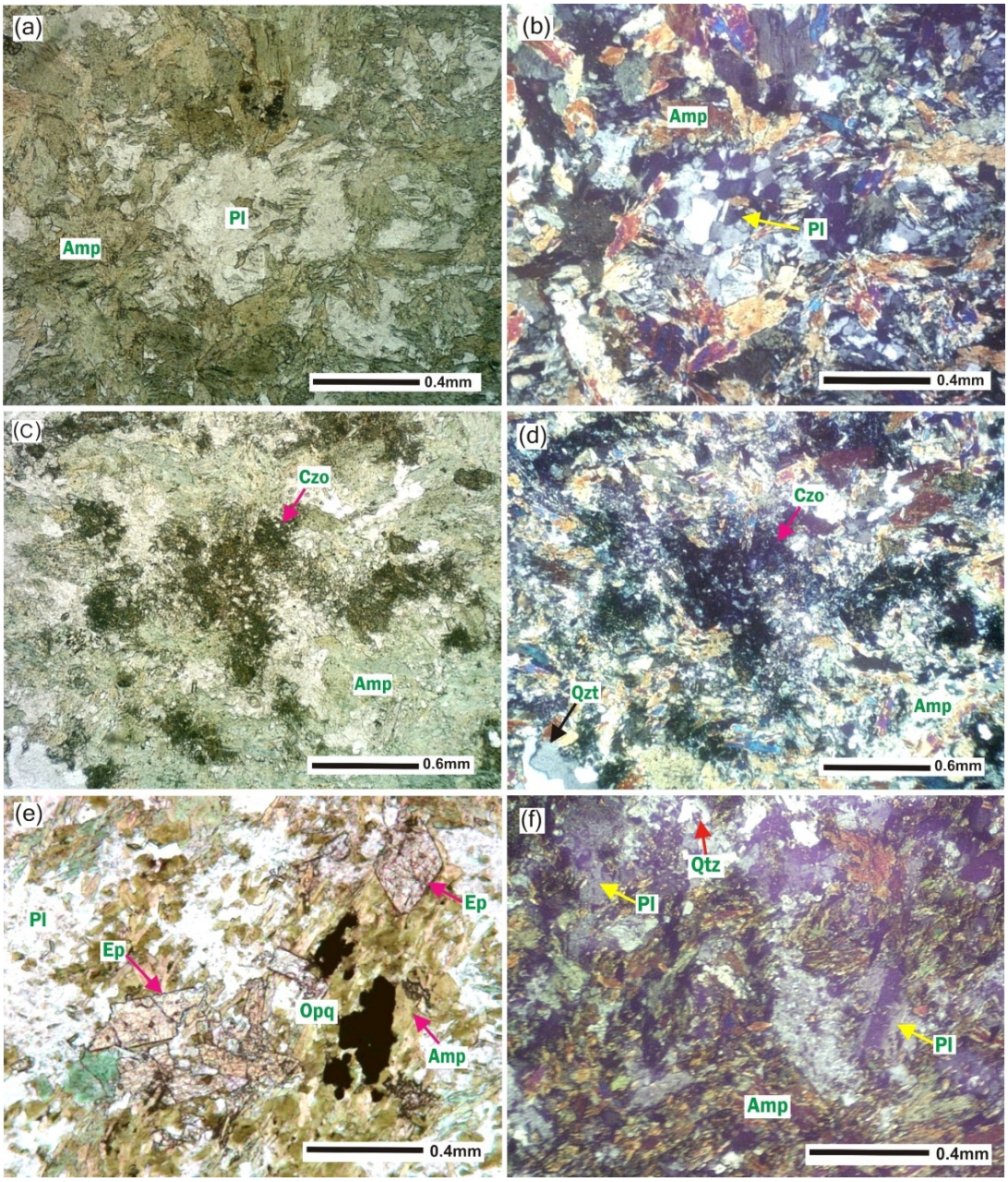

Fig.3.5. Selected photomicrographs of mafic type II rocks. (a) Recrystallised plagioclase (Pl) mantling bladed amphibole (Amp) representing a relict intergranular texture. Plagioclase in the centre is recrystallised into aggregates of granoblastic subgrains (MA 34, ppl). (b) Same field of view as (a) (xpl). (c) Cluster of granular clinozoisite (Czo) within a mesh of recrystallised amphiboles (MA 37, ppl). (d) Same field of view as in (c) (xpl). (e) Idiomorphic crystals of epidote (Ep) cutting across amphibole crystals (MA 47, ppl). (f) Acicular amphibole and moderately sericitized plagioclase define relict intergranular texture. (MA 47, xpl).

3.3 Geochemistry of the Mafic Volcanic Rocks

3.3.1 Magma Series and Subgroups of the Mafic Volcanic Rocks

Table 3.3 presents whole-rock geochemical analyses of mafic rocks from the north Yalgoo area. All the mafic rocks are low in Ti (≤ 0.65%) and relatively high in $Fe_2O_{3(T)}$ (≥ 9.0%) and MgO (≥ 6.9-11%). The rocks have a tholeiitic affinity and form two closely spaced subgroups (with one outlier, sample MA 47) on the AFM (Irvine and Barager, 1971) and the Al,(Fe_{total}+Ti) vs.Mg cation plots of Jensen (1976) (Fig. 3.6a,b). On the Jensen and

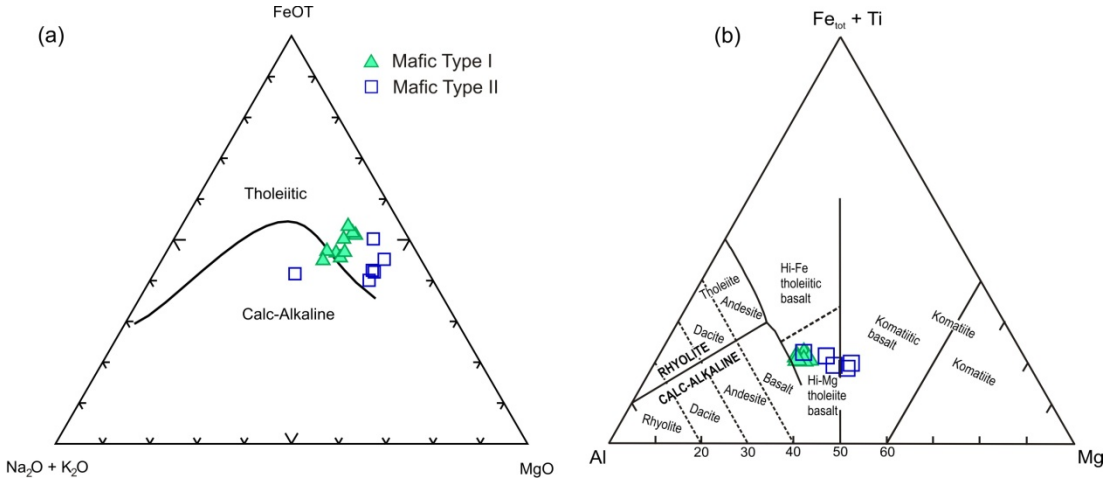

Fig. 3.6 (a) AFM plot (Irvine and Baragar, 1971) and (b) Al-(Fe_{total}+Ti)-Mg cation plot of Jensen and Pyke (1982) showing the mafic rocks from the north Yalgoo area.

Pyke (1982) plot, mafic samples are classified as high-Mg tholeiites with type I samples forming a tight cluster whereas type II samples form an array extending slightly across the boundary into komatiitic basalt. These two geochemical subgroups are also substantiated by incompatible and rare earth element plots and incompatible element ratios in the mafic rocks. Based on Zr (e.g. Zr ≥ 40ppm; Zr < 36 ppm), Nb (Nb ≥ 1.6 ppm; Nb < 1.1 ppm), Y (Y ≥20 ppm; Y<17 ppm), and [$(La/Sm)_{CN}$ ≥ 0.95; $(La/Sm)_{CN}$ < 0.85] and other geochemical parameters, the mafic rocks of the Yalgoo area are divided into two groups: i) LoTi (low titanium) enriched tholeiite (LET), corresponding to mafic type I; ii) LoTi depleted tholeiite (LDT), equating to mafic type II rocks. This classification will be used in the following sections.

3.3.2 Major Element Geochemistry

i) LET: These rocks have a narrow range of SiO_2 (51.08-53.08%), Al_2O_3 (14.30-14.91%), and Fe_2O_3T (9.52-11.23%) contents and low TiO_2 (0.56-0.61%). K_2O is also low (0.23-0.57% for all samples except MA 18, which contains 3.58% K_2O. Sample MA 18 is intruded by thin granitic veins that may account for the higher K_2O content. MgO and CaO contents lie within the range of 6.99-7.93% and 9.6-11.8%, respectively. Na_2O is variable (0.68-3.48%), whereas MnO and P_2O_5 are very low in these rocks.

Table 3.3: Chemical analyses of the mafic volcanic rocks from the north Yalgoo area CN=chondrite normalized, PM = primitive mantle normalized, values from Sun and McDonough (1989). The Eu (Eu/Eu*), Nb (Nb/Nb*), Zr (Zr/Zr*) and Ti (Ti/Ti*) anomalies were calculated with respect to the neighboring immobile elements, following the method of Taylor and McLennan (1985). Normalization was done using chondrite value for determining Eu and primordial mantle values for determining Nb, Zr and Ti anomalies. Mg# =100×mol MgO/(mol.MgO+mol.FeOt).

Rock subgroups	LET									LDT					
Sample no.	**MA 19**	**MA 20**	**MA 21**	**MA 22**	**MA 24**	**MA 25**	**MA 44**	**MA 45**	**MA 18**	**MA 33**	**MA 34**	**MA 37**	**MA 41**	**MA 46**	**MA 47**
Major oxides %															
SiO_2	51.54	51.64	52.76	51.08	52.39	53.08	52.49	52.91	51.47	51.20	52.15	55.34	49.20	50.73	52.95
TiO_2	0.60	0.59	0.58	0.60	0.59	0.59	0.61	0.61	0.56	0.45	0.46	0.55	0.49	0.47	0.65
Al_2O_3	14.90	14.91	14.43	14.92	14.30	14.57	14.42	14.85	14.51	12.51	12.64	12.46	13.67	13.09	14.69
Fe_2O_3T	10.82	11.01	10.42	11.10	11.23	10.01	9.98	9.92	9.52	10.32	10.32	8.99	11.12	9.73	10.97
MnO	0.18	0.17	0.17	0.21	0.17	0.16	0.151	0.15	0.16	0.17	0.169	0.16	0.17	0.17	0.15
MgO	7.78	7.64	7.74	7.69	7.20	6.93	7.93	7.71	6.99	11.02	10.76	9.04	9.07	10.89	7.53
CaO	10.93	10.51	9.60	10.26	10.17	10.74	10.94	11.80	10.26	11.68	11.62	12.92	15.13	11.53	5.83
Na_2O	1.99	2.07	3.29	2.55	2.05	3.48	2.98	2.69	0.68	2.28	2.45	1.28	1.38	1.97	4.17
K_2O	0.23	0.24	0.39	0.41	0.26	0.38	0.57	0.42	3.58	0.42	0.28	0.21	0.24	1.20	2.99
P_2O_5	0.06	0.03	0.06	0.06	0.06	0.06	0.057	0.05	0.06	0.04	0.032	0.04	0.04	0.04	0.06
LOI	0.74	0.87	0.69	0.63	1.11	0.21	0.6	0.58	2.15	0.74	0.63	0.81	1.08	1.37	0.80
Mg#	0.64	0.63	0.64	0.63	0.61	0.63	0.65	0.65	0.64	0.72	0.72	0.71	0.66	0.73	0.62
FeOT	9.74	9.91	9.38	9.99	10.11	9.01	8.98	8.93	8.57	9.29	9.29	8.09	10.01	8.76	9.87
Al_2O_3/TiO_2	24.8	25.3	24.9	24.9	24.2	24.7	23.6	24.3	25.9	27.8	27.5	22.7	27.9	27.9	22.6
CaO/TiO_2	18.22	17.81	16.55	17.10	17.24	18.20	17.93	19.34	18.32	25.96	25.26	23.49	30.88	24.53	8.97
CaO/Al_2O_3	0.73	0.70	0.67	0.69	0.71	0.74	0.76	0.79	0.71	0.93	0.92	1.04	1.11	0.88	0.40
Trace Elements, ppm															
Ba	211	45	138	67	616	127	147	145	1358	54	112	147	241	527	686
Be	0.3	0.3	0.3	0.3	0.3	0.2	0.3	0.2	0.6	0.3	0.3	0.1	0.1	0.1	0.3
Co	51	51	50	48	39	37	35	37	22	51	48	38	43	46	44
Cr	399	393	394	386	256	357	286	298	353	716	629	591	484	559	21
Cs	0.3	0.2	0.6	0.6	0.6	0.2	0.7	0.3	4.5	1.2	1.2	0.1	0.1	5.0	31.1
Cu	88	68	71	51	94	11	3	8	114	71	22	3	4	50	27
Ga	14.7	14.9	14.6	15.1	13.4	13.1	11.9	12.1	12.1	11.2	11.5	12.4	17.3	11.9	13.5
Ge	1.7	1.6	1.7	1.7	1.6	2.2	2.0	2.0	1.4	2.0	1.9	1.9	2.3	2.0	2.1
Hf	1.29	1.24	1.24	1.24	1.14	1.19	1.23	1.22	1.15	0.71	0.74	0.86	0.75	0.80	1.10
Li	9.2	16.1	15.0	9.4	13.7	1.8	3.5	2.9	8.9	13.4	11.5	3.5	2.7	8.6	18.0
Nb	1.72	1.66	1.62	1.55	1.66	1.67	1.69	1.72	1.57	0.53	0.54	1.07	0.74	0.64	0.82
Ni	147	139	147	121	112	119	108	117	97	185	172	144	156	171	59
Pb	19	10	17	25	11	9	5	4	109	13	11	8	11	5	34
Rb	15	12	38	26	6	10	32	17	176	13	8	4	4	68	208
Sc	47.4	48.8	47.8	44.6	45.1	42.6	35.6	36.6	41.2	40.7	37.9	41.2	39.4	37.3	37.3
Sr	113	128	164	140	140	208	161	117	393	107	126	177	128	118	592
Ta	0.12	0.12	0.11	0.11	0.11	0.11	0.15	0.15	0.11	0.04	0.04	0.20	0.12	0.08	0.08
Th	0.59	0.65	0.60	0.58	0.57	0.59	0.66	0.61	0.58	0.17	0.17	0.22	0.18	0.20	0.28
U	0.16	1.39	0.17	0.14	0.16	0.18	0.22	0.20	0.18	0.05	0.05	0.05	0.02	0.06	0.06
V	237	240	238	228	226	211	200	202	211	216	215	227	223	198	231
Y	24.2	23.2	21.1	20.8	21.9	22.0	25.8	24.8	20.2	12.7	12.4	15.3	13.7	15.9	16.4
Zn	88	83	87	112	82	58	60	60	192	63	80	67	71	56	78
Zr	46	44	43	45	44	43	40	41	40	23	24	28	24	25	36
REE, ppm															
La	3.23	4.95	2.92	2.12	3.01	3.45	4.73	5.40	2.43	1.09	1.13	1.19	1.24	1.56	1.24
Ce	7.49	9.88	6.79	5.66	6.11	7.48	9.95	10.39	5.64	2.68	2.69	3.06	2.65	3.85	3.38
Pr	1.11	1.26	1.01	0.87	1.00	1.08	1.32	1.46	0.93	0.40	0.40	0.49	0.44	0.55	0.53
Nd	5.41	5.71	4.97	4.44	4.89	5.18	6.43	6.99	4.68	2.30	2.27	2.81	2.53	3.08	3.12
Sm	1.62	1.68	1.51	1.42	1.50	1.55	1.92	2.03	1.46	0.93	0.93	1.14	1.01	1.21	1.29
Eu	0.55	0.58	0.56	0.49	0.64	0.65	0.68	0.78	0.67	0.40	0.35	0.46	0.45	0.52	0.55
Gd	2.15	2.17	2.01	1.88	1.95	2.06	2.59	2.64	1.91	1.37	1.39	1.70	1.52	1.82	1.89
Tb	0.43	0.43	0.39	0.38	0.39	0.40	0.52	0.54	0.38	0.29	0.29	0.34	0.31	0.37	0.38
Dy	3.19	3.22	2.94	2.86	2.88	2.93	3.79	3.80	2.82	2.01	1.97	2.40	2.17	2.55	2.66
Ho	0.76	0.76	0.69	0.67	0.69	0.69	0.93	0.93	0.66	0.48	0.47	0.56	0.51	0.61	0.63
Er	2.17	2.19	1.99	1.92	1.97	2.00	2.79	2.74	1.95	1.33	1.34	1.58	1.46	1.73	1.78
Tm	0.36	0.36	0.33	0.32	0.32	0.32	0.43	0.42	0.33	0.20	0.20	0.24	0.22	0.26	0.27
Yb	2.59	2.60	2.37	2.31	2.34	2.34	2.95	2.96	2.28	1.34	1.32	1.60	1.46	1.72	1.78
Lu	0.42	0.41	0.39	0.38	0.38	0.38	0.45	0.43	0.37	0.20	0.20	0.24	0.22	0.25	0.28
Total REE	31.5	36.2	28.9	25.7	28.1	30.5	39.5	41.5	26.5	15.0	15.0	17.8	16.2	20.1	19.8
$(La/Yb)_{CN}$	0.89	1.37	0.89	0.66	0.92	1.06	1.15	1.31	0.77	0.58	0.62	0.53	0.61	0.65	0.50
$(La/Sm)_{CN}$	1.29	1.91	1.25	0.96	1.30	1.43	1.59	1.72	1.07	0.76	0.78	0.68	0.79	0.83	0.62
$(Gd/Yb)_{CN}$	0.69	0.69	0.70	0.67	0.69	0.73	0.72	0.74	0.69	0.85	0.87	0.88	0.86	0.88	0.88
$(Ce/Yb)_{CN}$	0.80	1.06	0.80	0.68	0.73	0.89	0.94	0.98	0.69	0.55	0.57	0.53	0.51	0.62	0.53
$(La/Sm)_{PM}$	1.29	1.91	1.25	0.96	1.30	1.44	1.59	1.72	1.07	0.76	0.79	0.68	0.79	0.84	0.62
$(Gd/Yb)_{PM}$	0.69	0.69	0.70	0.67	0.69	0.73	0.72	0.74	0.69	0.85	0.87	0.88	0.86	0.88	0.88
$(La/Yb)_{PM}$	0.89	1.37	0.89	0.66	0.92	1.06	1.15	1.31	0.77	0.58	0.62	0.54	0.61	0.65	0.50
Ba/La	65.2	9.1	47.3	31.6	204.7	36.8	31.0	26.8	558.5	49.5	99.1	123.3	194.0	336.8	552.5
Th/La	0.2	0.1	0.2	0.3	0.2	0.2	0.1	0.1	0.2	0.2	0.2	0.2	0.1	0.1	0.2
Zr/(Zr+Y)	0.7	0.7	0.7	0.7	0.7	0.7	0.6	0.6	0.7	0.6	0.7	0.6	0.6	0.6	0.7
Zr/Sm	28.5	26.1	28.6	31.3	29.1	28.0	20.9	20.3	27.2	24.8	25.5	24.4	23.9	20.4	28.1
Zr/Nb	26.94	26.35	26.67	28.73	26.28	26.03	23.74	23.97	25.34	43.30	43.86	26.00	32.62	38.72	43.91
Zr/Y	1.91	1.88	2.05	2.15	1.99	1.97	1.55	1.66	1.97	1.80	1.92	1.82	1.77	1.56	2.20
Zr/Hf	35.8	35.2	34.7	36.0	38.3	36.5	32.7	33.6	34.7	32.1	32.3	32.2	32.4	31.0	32.8
Ti/Sc	75.8	72.5	72.7	80.6	78.5	83.1	102.7	100.0	81.5	66.4	72.7	80.0	74.6	75.6	104.4
Ti/V	15.2	14.7	14.6	15.7	15.6	16.8	18.3	18.1	15.9	12.5	12.8	14.5	13.2	14.2	16.8
Th/U	3.6	0.5	3.6	4.1	3.6	3.3	3.0	3.0	3.3	3.4	3.3	4.8	8.6	3.2	4.6
Nb/Ta	14.1	14.1	14.2	13.7	14.9	15.1	11.6	11.7	14.6	12.4	12.4	5.3	6.1	8.0	10.0
Y/Ho	31.9	30.6	30.5	31.0	31.7	32.0	27.6	26.6	30.7	26.6	26.1	27.2	26.7	26.0	26.3
P/Nd	48.43	22.92	52.70	58.93	53.55	50.55	38.68	33.11	55.96	66.30	61.50	55.93	70.61	55.18	81.04
Sr/Y	4.7	5.5	7.8	6.7	6.4	9.4	6.2	4.7	19.4	8.4	10.2	11.6	9.3	7.4	36.0
Eu/Eu*	0.89	0.93	0.98	0.92	1.15	1.10	0.93	1.03	1.23	1.08	0.94	1.01	1.11	1.07	1.08
Ti/Ti*	0.74	0.70	0.74	0.82	0.70	0.70	0.62	0.57	0.66	0.82	0.90	0.85	0.81	0.66	0.87
Zr/Zr*	1.08	0.98	1.09	1.23	1.11	1.06	0.79	0.76	1.05	1.09	1.13	1.07	1.05	0.89	1.25
Nb/Nb*	0.59	0.55	0.57	0.57	0.59	0.58	0.55	0.58	0.57	0.60	0.61	0.76	0.69	0.61	0.59

ii) LDT: SiO_2 contents have a wider range (49.20-55.34%), while Al_2O_3 (12.46-14.69%) is overall slightly lower than in LET. TiO_2 (0.45-0.55%) is generally lower than in LET, except for sample MA 47 (0.55%). MgO is generally higher and varies from 7.53 to 11.02%, whereas Fe_2O_3T and K_2O are similar to LET. The highest K_2O (2.99%) is recorded from a hydrothermally altered sample, MA 47. Na_2O, MnO and P_2O_5 values are similar to those of LET.

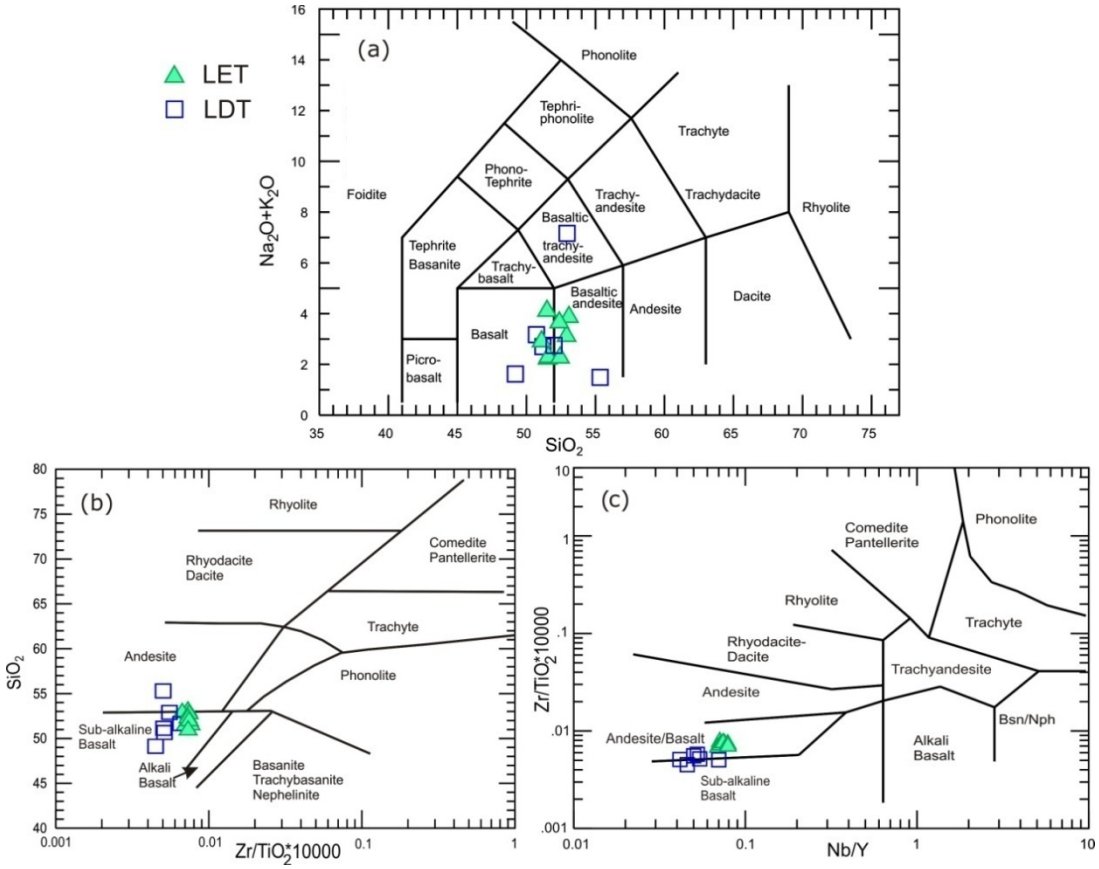

Fig. 3.7. (a) Total alkalis vs. SiO_2 diagram (Le Bas et al., 1986), (b) SiO_2vs. Zr/TiO_2 diagram (Winchester and Floyd, 1977) and (c) Zr/TiO_2 vs. Nb/Y diagram (Winchester and Floyd, 1977).

The mafic rocks straddle the boundary between the basalt and basaltic andesite fields on the total alkalis classification (TAS) scheme of Le Bas et al. (1986) (Fig. 3.7a). This classification can be further tested using the SiO_2 vs. Zr/TiO_2*10000 and Zr/TiO_2*10000 vs. Nb/Y plots (Winchester and Floyd, 1977). On the Zr/TiO_2*10000 vs. SiO_2 and Zr/TiO_2*10000 vs. Nb/Y diagrams, the samples plot in similar fields as in the TAS diagram (Fig. 3.7b,c), which implies low elemental mobility during alteration and metamorphism.

3.3.3 Trace Element Geochemistry

The LILE (Large Ion Lithophile Elements) (Ba, Rb and Sr) in LET and LDT show a wide variation. The highest values for Ba (1358 ppm), Rb (176 ppm) and Sr (393 ppm) are recorded from sample MA 18, an enriched tholeiite cut by granitic veinlets adjacent to a massive quartz vein, (Figs. 3.3, 3.4g). Similarly, the highest Rb (208 ppm) and Sr (592 ppm) values of the

depleted tholeiites are from sample MA 47, which was also collected from near a quartz vein, and therefore affected by hydrothermal fluid.

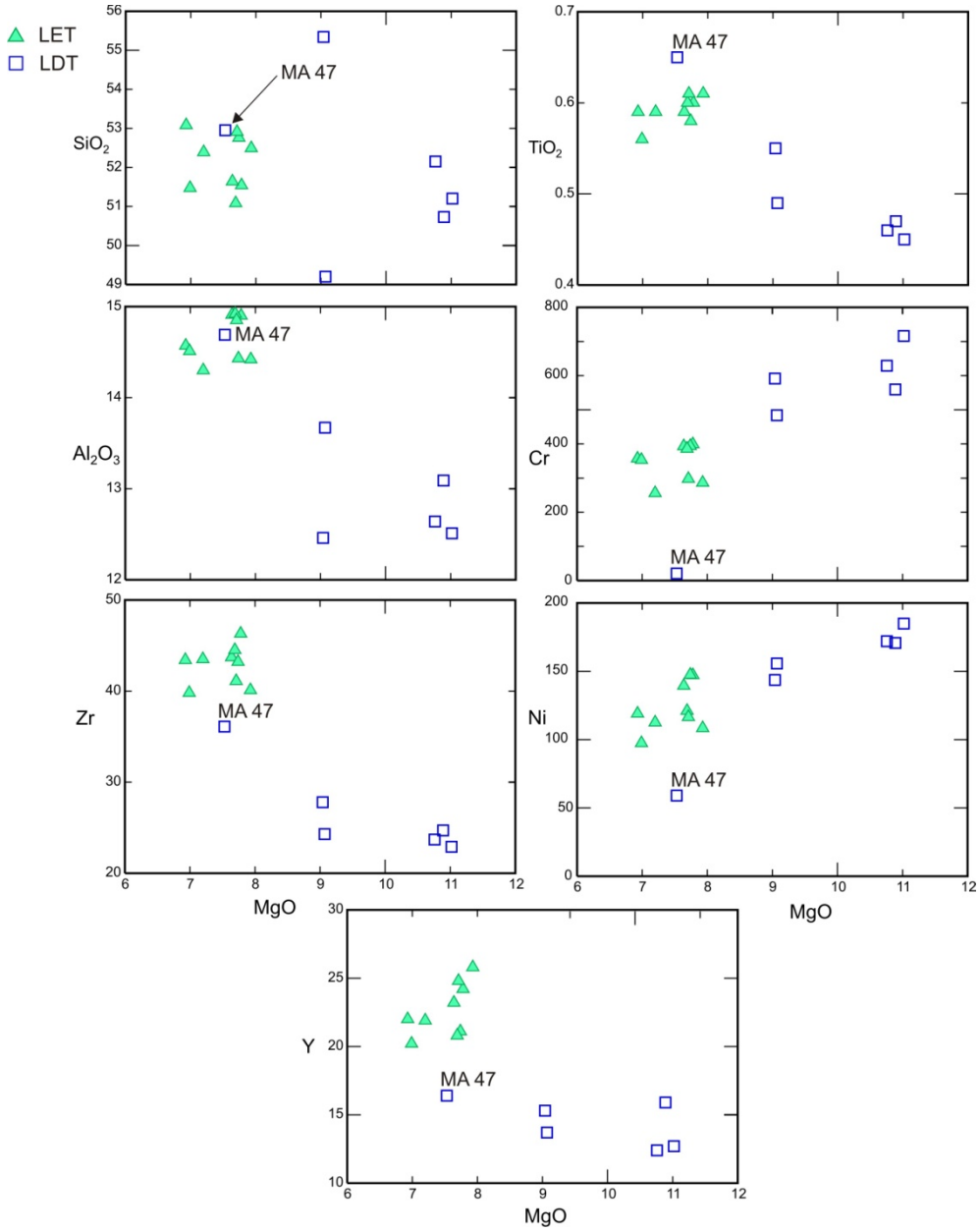

Fig. 3.8. Selected major and trace elements vs. MgO variation diagrams for Yalgoo mafic rocks.

i) LET: These rocks have high contents of HFSE [Zr (40-46 ppm), Nb (1.6-1.7 ppm), Ta (0.11-0.15 ppm) and Hf (0.14 – 1.29 ppm)]. Ni (97-147 ppm) and Cr (256-399 ppm) are generally low.

ii) LDT: Among the HFSE, Zr (23-36 ppm) and Nb (0.53-1.07 ppm) contents are lower, whereas Ta (0.04-0.20 ppm) and Hf (0.71 – 1.10 ppm) overlap with those of LET. Except for anomalously low Ni (59 ppm) and Cr (21 ppm) values for sample MA 47, Ni (144-185 ppm), and Cr (484-716 ppm) values are higher than in LET.

The plots of selected major and trace elements against MgO successfully separate out the two tholeiite subgroups (Fig. 3.8), with the exception of sample MA 47, which in six plots overlaps with the the field of the LET samples. On the Y vs. MgO plot, however, MA 47 falls closer to the LDT rocks. Whether the relatively high SiO_2, TiO_2, Al_2O_3, Zr and low Cr and Ni values at similar MgO content to LET in sample MA 47 represents an inherent genetic attribute or whether these values are the result of mixing or assimilation with a relatively enriched or more evolved magma is examined in the REE and incompatible trace elements plots in sections 3.3.3.1 and 3.3.3.2, respectively. The LET samples are clustered within a small area on most of the elemental plots, except for Ni and Y, which show considerable scatter. The LDT samples (except for MA 47) show similar contents of Ti, Zr, Cr, Ni and Y over a relatively large MgO range (from about 9 to 11 wt%), suggesting a less evolved source for this subgroup.

3.3.3.1 Rare Earth Element (REE) Characteristics

i) LET: Rare earth element patterns normalized to chondritic values (Sun and McDonough 1989) are presented in Fig. 3.9a. The LET rocks have ∑REE contents of 40-47ppm. The LET samples have La at 10–20 times chondrite, show moderate LREE enrichment [$(La/Sm)_{CN}$ =0.96-1.91] and fractionated HREE [$(Gd/Yb)_{CN}$=0.67-0.74], giving rise to slightly concave upward REE patterns (Fig. 3.9a). These samples are characterized by both weakly positive and weakly negative Eu anomalies (Eu*/Eu = 0.89-1.23), of which the highest Eu*/Eu was recorded from sample MA 18 which most likely resulted from late incorporation of Eu during hydrothermal alteration (explained in petrography section).

ii) LDT: These rocks have a significantly lower ∑REE contents (23-36 ppm, at 4-7 times chondrite) than LET. They show depletion in LREE [$(La/Sm)_{CN}$ =0.62-0.79] and HREE are not fractionated [$(Gd/Yb)_{CN}$=0.85-0.88] (Fig. 3.9c). Several of the samples show weak positive Eu anomalies (Eu*/Eu = 1.01-1.08) with only one weakly negative (Eu*/Eu = 0.98) anomaly from sample MA 34. Despite not being included within the main field of the LDT on Fig. 3.8, sample MA 47 follows the patterns for LDT, implying the differences shown by sample MA 47 on the plots in Fig. 3.8 probably resulted from mixing or incorporation with a more evolved magma.

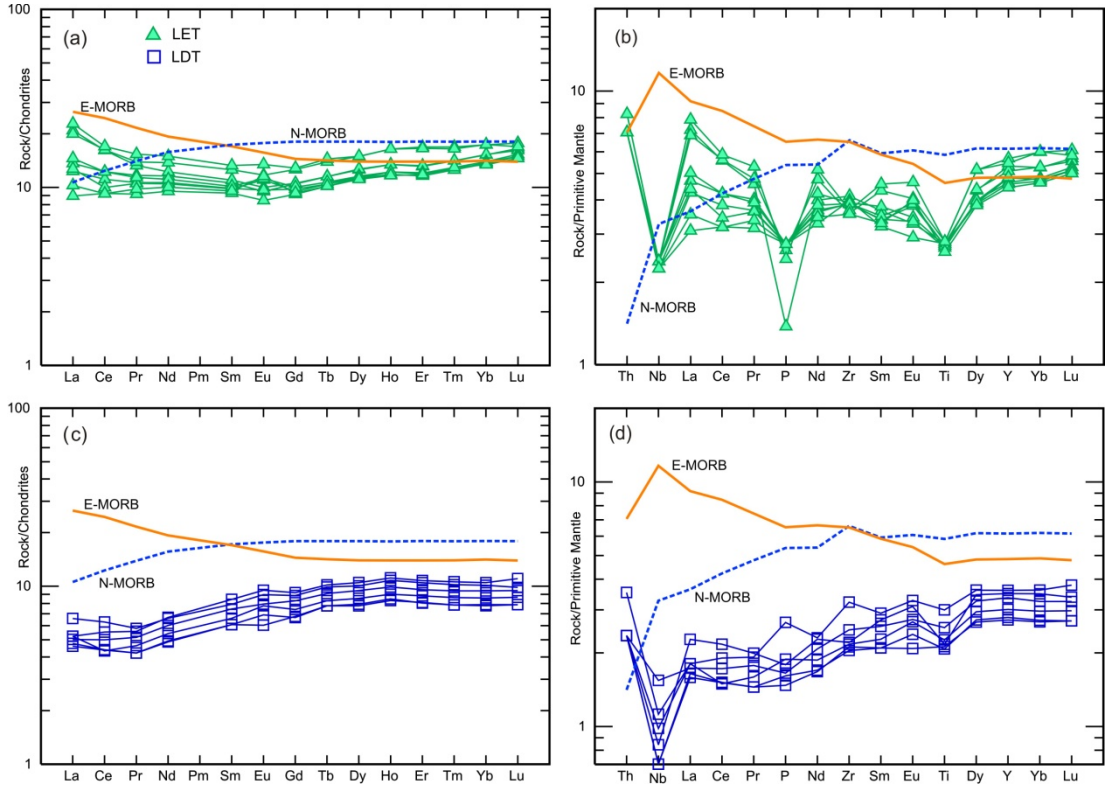

Fig. 3.9. Chondrite-normalised REE and Primitive mantle-normalised incompatible trace element diagrams of the Yalgoo mafic rocks. (a) REE diagram of LET; (b) Incompatible trace element patterns for LET; (c) REE diagram of LDT; (d) Incompatible trace element patterns for LDT. Chondrite and Primitive mantle normalizing values are from Sun and McDonough (1989). Patterns for N-MORB and E-MORB (Sun and McDonough, 1989) are shown for comparison.

3.3.3.2 Incompatible Trace Element Characteristics

i) LET: On the primitive mantle normalized diagram (Sun and McDonough 1989), the samples consistently display moderate to strong negative Nb (Nb/Nb* = 055-059), P and Ti (Ti*/Ti=0.57-0.82) anomalies, but Zr records either negative or positive anomalies (Zr*/Zr=0.76-1.23) (Fig. 3.9b). Nb/Ta (12-15 ppm) and Zr/Hf (33-38 ppm) ratios are close to the primitive mantle values of 17 and 36, respectively. Ti/Zr ratios (52–90), however, are lower than the primitive mantle ratio of 116 for these two elements.

ii) LDT: These rocks also have negative Nb anomalies (Nb*/Nb= 0.59-0.76) and weak negative Ti (Ti*/Ti=0.66-0.87) anomalies. P and Zr are variables with the negative values considerably less than for LET (Zr*/Zr= 0.89-1.25) (Fig. 3.9d). They have variably low Nb/Ta (0.5-12) values and slightly lower Zr/Hf (31-33) ratios than primitive mantle values. Ti/Zr ratios (108-121) are within the primitive mantle range (116).

3.3.4 Petrogenesis of the Mafic Volcanic Rocks

3.3.4.1 Element Mobility During Alteration and Metamorphism

Deciphering petrogenesis of Archean metavolcanic rocks is a difficult task due to element mobility resulting from seafloor hydrothermal alteration and greenschist to amphibolite facies metamorphism (Boily and Dion, 2002). Several studies (Coish, 1977; Winchester and Floyd, 1977; Sun and Nesbitt, 1978; Ludden et al. 1982; Condie, 1994) found that the Large Ion Litholphile Elements (LILE), such as K, Na, Ca, Cs, Ba, Rb and Sr and are typically mobile during alteration, whereas Th, HFSE (Nb, Ta, Zr, Hf, Ti, and Y), transitional metals (Co, Sc, Cr, Ni, V), and REE (except Eu) are considered to be relatively immobile during post-magmatic processes. The variable mobility of elements has also been documented by recent studies of Archean greenstone sequences by Manikyamba et al. (2004, 2008), Arndt (2008), Polat (2009), Said and Kerrich (2009) and Said et al. (2010). All of the samples in this study show minimal secondary alteration, such as hydration and carbonation, except for sample MA 18 (Section 3.1 and 3.2). The loss on ignition (LOI) is generally low, i.e. less than 1.5% (Table 3.3). The major elements MgO, Al_2O_3 and TiO_2, transition metals (Cr, Ni), HFSE (Th, Nb, Ta, Zr, Hf, Y) and REE show consistent trends, with limited scatter on variation diagrams, and hence are considered to have been largely immobile during alteration and reflect the original composition of the rocks. These elements therefore, are considered useful for petrogenetic interpretation.

3.3.4.2 Basement of the Yalgoo Greenstone Belt and Crustal Contamination

In the Murchison Domain, several lines of geological and geochronological evidence suggest the existence of a continental basement underneath the greenstone sequence, especially for the Luke Creek Group (Watkins and Hickman, 1990). The evidence includes: i) epiclastic sandstone units in the Gabanintha Formation indicating the presence of sialic basement during emplacement of the lower greenstone formations; ii) regional gravity surveys, deep seismic refraction, and heat-flow studies (Archibald et al., 1981; Gee et al., 1981) indicate a three-layered stratification of the crust beneath the granite-greenstone terrane of the Yilgarn Craton. Granitoids dominate the upper layer (density = 2.78 g/cm^3), and granulite forms the middle layer (density = 2.94 g/cm^3); iii) the presence of zircon xenocrysts (3.0-2.93 Ga) within the granitoids in the Yalgoo area (present study); and iv) Lu-Hf isotopic studies of the granitoids suggest relicts of crust as old as 4.2-4.1Ga (present study).

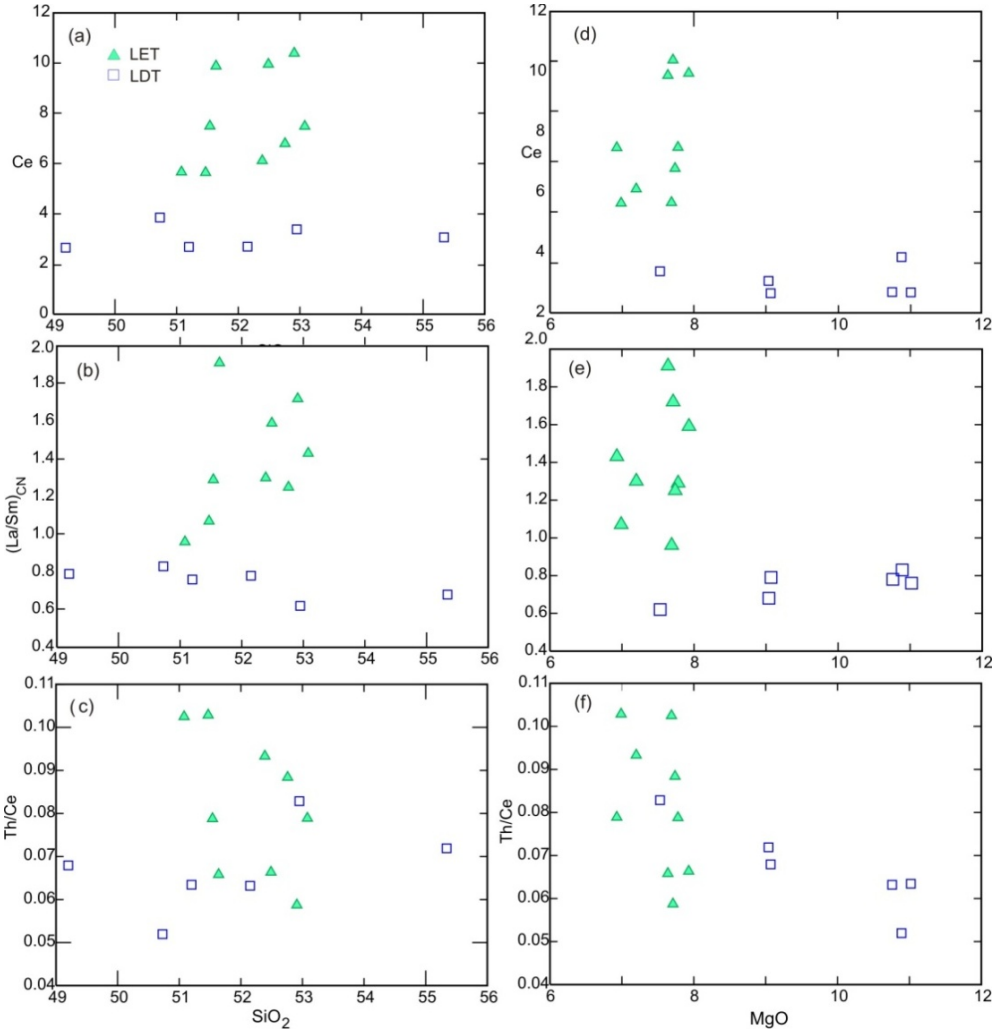

Fig. 3.10. Plots of (a) Ce vs. SiO_2; (b) $(La/Sm)_{CN}$ vs. SiO_2; (c) Th/Ce vs. SiO_2; (d) Ce vs. MgO; (e) $(La/Sm)_{CN}$ vs. MgO; and (f) Th/Ce vs. MgO.

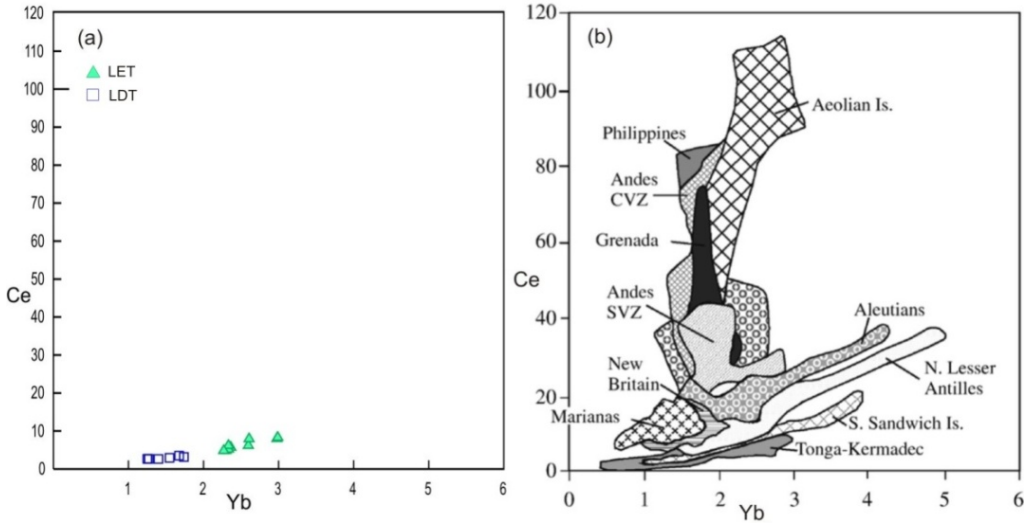

Fig. 3.11 (a) Ce vs.Yb plot of the Yalgoo LET and LDT rocks and (b) Ce vs.Yb plot of different arc basalt suites A comparison between 3.11 (a) and (b) shows that the Yalgoo tholeiites overlap with the fields of the South Sandwich Island and Tonga-Kermedac intraoceanic arc. Modified from Hawkesworth et al. (1993).

Covariations of Ce, Th/Ce, or $(La/Sm)_{CN}$ (indices of assimilation) with SiO_2 or MgO are considered to result from interaction of mafic rocks with felsic crust (Hollings and Kerrich,

2004). Except for minor covariation on the $(La/Sm)_{CN}$ vs. SiO_2 plot of the LET (Fig. 3.10b), no distinct covariation is evident for Yalgoo tholeiites (Fig. 3.10a,c,d,e,f). Therefore, the mafic rocks do not appear to have interacted with felsic arc crust by assimilation-fractional crystallization. Basalts with similar trace element characteristics have been reported by Hollings and Kerrich (2004, 2006) from the 2.8-2.7 Ga tholeiitic LKS (low-K series basalt) of the St. Joseph assemblage in the Uchi Subprovince and 2.86 Ga Pickle Crow assemblage of northwestern Ontario, Canada. On the Ce–Yb plot of Hawkesworth et al. (1993) (Fig. 3.11a), the tholeiites of the present study form two clusters and these plot within the field of the South Sandwich Islands and Tonga–Kermadec arcs, indicating that the tholeiites have erupted through oceanic lithosphere (Fig. 3.11b). Given that the tholeiites of the Yalgoo area formed in an intraoceanic setting, the current position over an older crust must represent post-eruption accretion; similar occurrences of intraoceanic assemblages are reported from the 2.86 Ga Pickle Crow rocks (Hollings and Kerrich, 2004).

Studies by Pearce and Peate (1995) and Rudnick and Gao (2004; and references therein) show that both the continental crust and arc basalts are characterized by distinct negative anomalies of Nb, P, and Ti relative to neighbouring REEs. Tholeiites of the Yalgoo area are characterized by variable HFSE anomalies, details of which are discussed in section 3.3.4.4.

3.3.4.3 Mantle Wedge Characteristics

Niobium content in N-MORB averages 2.33 ppm, and in recent oceanic primitive arc tholeiites is generally <2 ppm (Hollings and Kerrich, 2004). Ratios of Zr/Nb range from 11–39 for MORB (average 32), and 9–87 for recent primitive arc tholeiites, signifying mantle wedges depleted or enriched relative to MORB (Sun and McDonough, 1989; Pearce and Peate, 1995; Davidson, 1996). For Archean intra-oceanic primitive arc tholeiitic basalts (PAT), Nb is mostly <2 ppm and Zr/Nb spans 15–28, within the MORB range (Polat et al., 1998; Wyman et al., 1999; Hollings and Kerrich, 2004, and references therein). Primitive mantle and MORB have almost comparable Ti/Zr ratios of 103 and 116, respectively (Sun and McDonough, 1989) endorsing the conservative nature of these two elements in different subcrustal environments.

Archean basalts associated with komatiites, were likely erupted from mantle plumes and are geochemically comparable to Phanerozoic ocean plateau basalts, such as Ontong Java basalts, Recent plume-related basalts on Iceland, and in ocean basins as oceanic plateaus (Hemend et al., 1993; Mahoney et al., 1995; Puchtel et al., 1998, 1999; Kerrich et al., 1999). These possess Nb mostly ~2 to 7 ppm, and Zr/Nb of 12–20, overlapping with, but extending to lower (less depleted) values than LKS arc basalts (Polat et al., 1998; Kerrich et al., 1999b; Kerrich and

Xie, 2002). Nb contents of both LET and LDT in the Yalgoo area are very low (0.55 to 1.55 ppm), within the range of Archean primitive arc tholeiitic basalts. Zr/Nb values of LET fall within the lower end of the PAT in the Pickle Crow assemblage in the Uchi Subprovince, and the Schreiber-Hemlo and White River-Dayohessarah greenstone belts, Superior Province (Polat et al., 1998; Wyman et al., 1999; Hollings and Kerrich, 2004). Zr/Nb ratios of 24-28 of the LET are within the upper end of N-MORB values; Ti/Zr ratios of 78-91 are also within the range of N-MORB. The higher Zr/Nb ratios of 26-44 for LDT were generated from a Nb depleted source, instead of from an enriched zone with elevated Zr contents (see Table, 3.3; Fig. 3.9b,d). A source similar to depleted N-MORB and/or Primitive Mantle for LDT can also be postulated from the Nb values (average 0.7) compared to Primitive mantle (av 0.713; Sun and McDonough, 1989), in conjunction with lower Zr and Y (higher than the primitive mantle yet lower than N-MORB values).

3.3.4.4 HFSE Anomalies

LET rocks of the Yalgoo area have moderate to strong negative Nb, P and Ti anomalies and weak positive to negative Zr (Hf) anomalies with the neighbouring trace elements. LDT samples however, have similar negative Nb anomalies and slightly weaker Ti anomalies than LET. LDT, in contrast to LET, is characterized by either weak positive or negative P and Zr (Hf) anomalies. Despite having similar positive and negative anomalies of Nb, P, Ti and Zr (Hf), a plot of these anomalies against $(La/Sm)_{CN}$ confirms two different sources of melt for the north Yalgoo tholeiite suites despite showing minor linear trends (in the P/Nd vs. La/Sm_{CN}, P/Nd vs. La/Sm_{CN} plots) of the LET samples (Fig. 3.12). The positive Zr (Hf) and P anomalies in both LET and LDT occur at $(La/Sm)_{CN}$ <1, confirming they are not related to the late enrichment of LREE by a fluid; rather they represents source characteristics (cf. Sun and McDonough, 1989). Hollings and Kerrich (2004, 2006) discussed how positive to negative anomalies of Nb, P, and Zr (Hf) could arise from: (1) a Nb-enriched basalt component, (2) positive anomalies resulting from the influence of an ocean island basalt (OIB), or (3) multistage melting processes in the mantle wedge. Yalgoo tholeiites, however, do not show any positive Nb anomalies; therefore the presence of a Nb-enriched and/or a HIMU-type OIB component (1,2) can be ruled out. Hollings and Kerrich (2004) explained the co-existence of both positive and negative Nb and Zr (Hf) anomalies through a multistage extraction process, where basalts with negative anomalies represent first-stage melts leaving a mantle residue featuring LREE depletion and high Nb/LREE, Hf/MREE, whereas second-stage melts inherit the positive anomalies (Fig. 6, Hollings and Kerrich, 2004). With significant depletion of LREE/MREE [$(La/Sm)_{CN}$ =0.62-0.79] and MREE/HREE [$(Gd/Lu)_{CN}$ =0.85-0.88], the LDT does not show any positive Nb anomaly, which would have been expected had Hollings

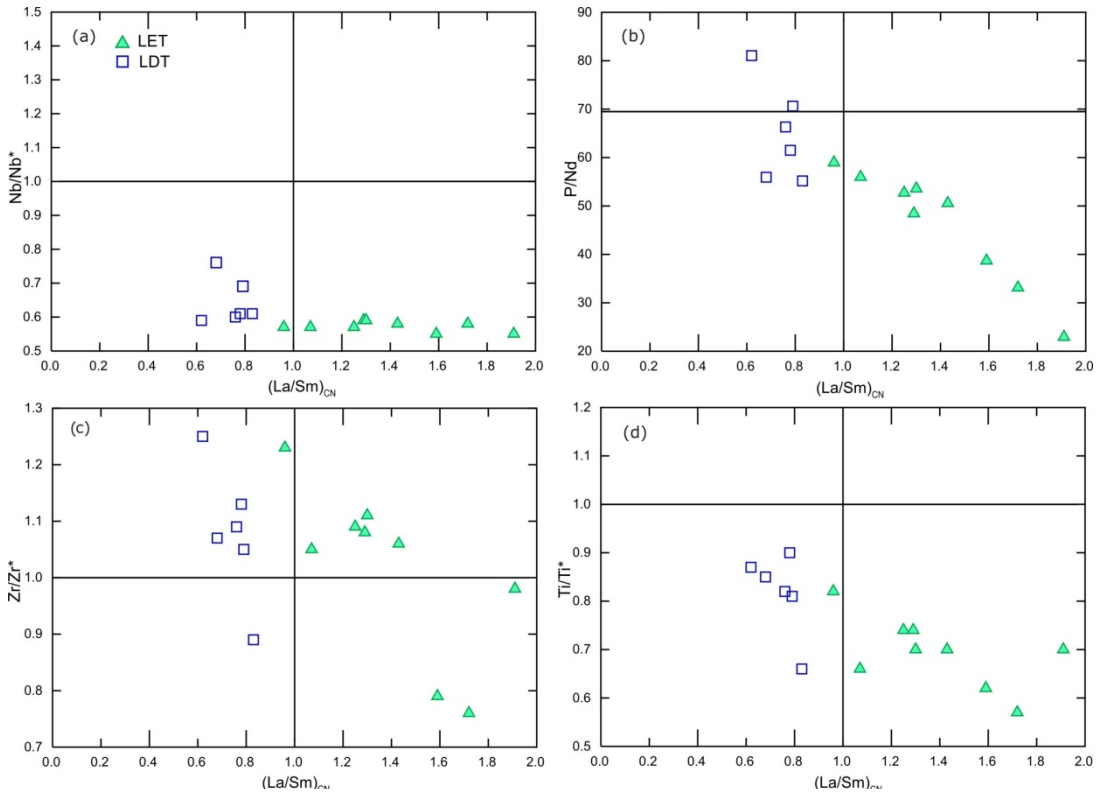

Fig. 3.12. Plots of (a) Nb/Nb*, (b) P/Nd, (c) Zr/Zr*, and (d) Ti/Ti* vs. $(La//Sm)_{CN}$. The values of Nb/Nb*, P/Nd, Zr/Zr* and Ti/Ti* were taken from Table 3.3.

and Kerrich's (2004) explanation been appropriate for the Yalgoo mafic rocks. No positive Nb anomalies are displayed by LET either. Therefore, a two-stage melting process of low-Nb LREE depleted mantle domains may account for the variable negative anomalies observed in both subgroups. The weakly positive Zr anomalies indicate the source magmas for both LDT and LET erupted without any significant fractionation, as often observed in a supra-subduction zone setting. The presence of mostly weak positive to no P anomalies are also reported from Archean high-Mg tholeiites from slightly LREE depleted tholeiite from the Norseman area, Western Australia, and depleted tholeiite from the Ujarassuit and Ivisaatoq greenstone belts, Greenland (McCuaig et al., 1994; Ordóñez-Calderon et al., 2009). Weak positive P anomalies most probably formed as a result of retaining a P-bearing phase (apatite) in the less evolved source melt.

The Ti/Ti* is more pronounced in LET than LDT, signifying fractionation of Ti-bearing phases, such as titanite and ilmenite. Mineralogical studies have revealed that titanite and hornblende accounts for large amounts of the LREE, Ti, Th, Nb, and Ta in amphibolites (Mulrooney and Rivers, 2005; Storkey et al., 2005). Therefore, the pronounced negative Ti anomalies could also indicate residual amphibole in the mantle source of the basaltic protoliths. Relatively weaker negative Ti/Ti* anomalies in the LDT would have resulted from tapping of a less depleted source. Given the distinct differences in the $(Gd/Yb)_{CN}$ ratios in the

LET (0.70) and LDT (0.87), a model involving melting at different stages above the level of the garnet stability field is likely to be responsible for the observed anomalies.

Therefore, from the above discussion, including the distinct differences in the $(Gd/Yb)_{CN}$ ratios, it is apparent that the observed HFSE anomalies are inherent properties of LET and LDT sources.

3.3.4.5 Source Enrichment: Sediments or Fluids?

Pearce (2008) proposed that the Th/Yb-Nb/Yb plot could identify the presence of a crustal signature in mafic volcanic rocks. He suggested that the addition of a crustal component to mantle melts would raise the Th/Yb ratio relative to Nb/Yb, where the latter is taken to indicate the relative depletion of a spinel-peridotite mantle source (high Nb/Yb = less depleted; low Nb/Yb = more depleted). All of the data for LET and LDT plot above the mantle array (Fig. 3.13a) following almost a single trend parallel to the MORB-OIB array. Basalts contaminated by crustal input will plot with a steeper gradient to the MORB-OIB array. Pearce (2008) suggested two mechanisms for increasing Th/Yb ratios. First, Th can be released from subducted sediments and added into the mantle source of the arc melts that yield primitive magmas with Th/Yb that lies above, but parallel, to the MORB-OIB array; second, direct interaction of mantle-derived magmas with continental crust will increase Th/Yb, shifting sample compositions to a steeper gradient from the MORB-OIB array approaching the composition of continental crust (Fig. 3.13b).

Deflection of the LDT to lower Nb/Yb and Th/Yb (excepting Sample MA 37 which has a higher Nb/Yb value) suggests a strongly depleted source for these samples, whereas the LET samples with slightly higher values of Nb/Yb and Th/Yb are suggestive of derivation from a less depleted source. Fairly high Nb/Yb values of Th/Yb=1.4 for sample MA 37 might be the result of tapping of a relatively less depleted section of the mantle. Given the parallel trend to the MORB-OIB trend and an intraoceanic setting (Fig 3.13a) for both LET and LDT samples, it is evident that none of the tholeiite suites have interacted directly with continental crust. Basalts of similar Nb/Yb and Th/Yb ratios were also reported from the tholeiites interstrataified with boninitic rocks in the Archean Fortret Evans greenstone belt, Quebec (Boily and Dion, 2002) and c. 3 Ga greenstones of the Regal Formation in W. Pilbara (Sun and Hickman, 1999) (Fig 3.13a). Pickle Crow IAT also plot with a similar trend, deflecting slightly towards a less depleted mantle composition (Fig 3.13a). Despite showing negative Nb and Ti anomalies, the LDT and LET rocks exhibit significant differences in P and in the magnitude of the Ti anomalies. Typical signatures of arc tholeiitic basalts, i.e. strongnegative Nb, Ti and P anomalies are lacking in the LDT. They show moderate negative Nb,

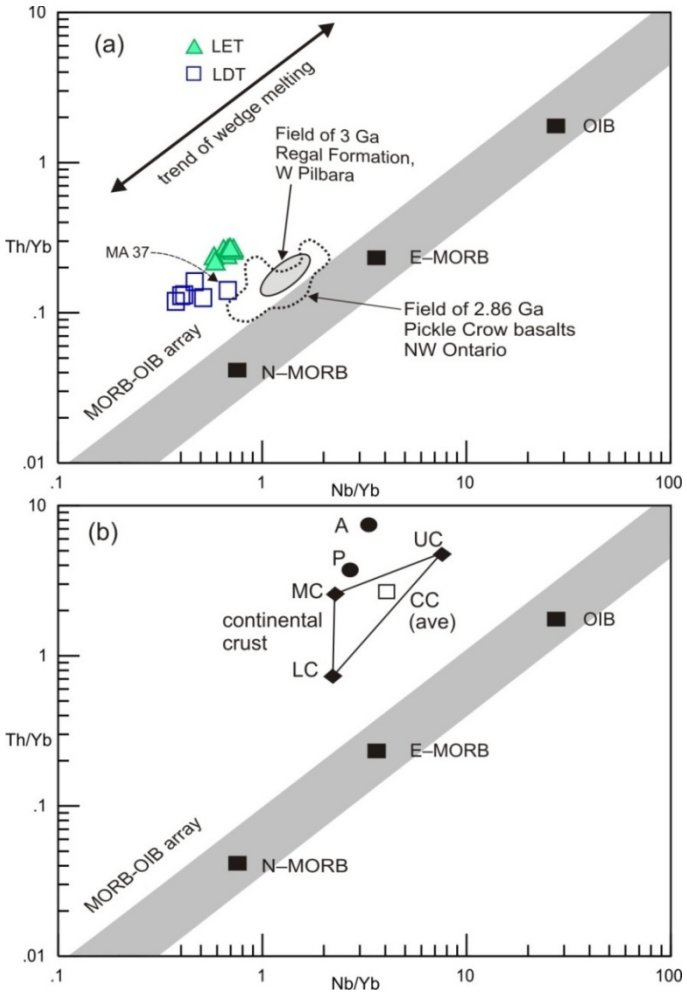

Fig. 3.13. (a) Th/Yb vs.Nb/Yb plot (Pearce, 2008) for the Yalgoo mafic samples showing the fields of c. 3 Ga Regal Formation at Clearville, W Pilbara (Sun and Hickman, 1999) and the 2.86 Ga Pickle Crow assemblage of NW Onatario (Hollings and Kerrich, 2004); (b) Th/Yb vs.Nb/Yb plot of Pearce (2008) showing the role of the different types of crustal input and recycling , causing a shift to compositions above the MORB–OIB array. N-MORB, E-MORB , OIB and Primordial Mantle (PM) are from Sun and McDonough (1989); average lower crust (LC), upper crust (UC), total continental crust (CC) and felsic Phanerozoic (P) and Archean (A) crust are from Rudnick and Fountain (1995).

weak Ti and both weak positive and negative P anomalies. Weak positive to no P anomalies are also reported from Archean high-Mg tholeiites showing near flat to slightly depleted LREE patterns from Norseman, Western Australia (McCuaig et al., 1994) and depleted tholeiite from the Ujarassuit and Ivisaartoq greenstone belts, Greenland (Ordóñez-Calderón et al., 2009).

Chemical characteristics as discussed in the above sections reveal that significant differences exist in the extent of MgO (Mg #), Cr, Nb, Zr, Y, Yb, Th, Ce, and HFSE anomalies, and $(La/Sm)_{CN}$, and $(Gd/Yb)_{CN}$ ratios (Figs. 3.9-3.13) between LET and LDT. Therefore, a LREE-enriched to MREE-depleted mantle, subsequently metasomatised by melts from slab dehydration, is considered to be the source of LET, whereas a depleted mantle domain was the source of LDT.

3.3.4.6 Fractionated Low $(Gd/Yb)_{CN}$ Yalgoo LET: Archean Boninitic Rocks in the Yalgoo Area?

Whether enriched and depleted sources existed in two separate mantle domains (different levels in the mantle) or whether they were the products of continually evolving sub-arc mantle processes needs to be constrained to understand the formation of two contrasting mafic volcanic types in the Yalgoo area. The low-titanium, relatively siliceous, LREE-enriched, HREE fractionated character of LET, prompts a comparison with rocks of similar geochemical character, namely boninite. This section compares LET from Yalgoo to boninites and focuses on the origin and the mantle processes likely to be responsible for the formation of LET.

The first widely-accepted definition of boninite was given by Crawford et al. (1989), as mafic lava representing a significant but rare component of subduction zone magmatism associated with some intra-oceanic island arcs and having SiO_2 >53 wt.% and Mg # > 60. However, this definition has evolved to accommodate boninite/boninite-like rocks, discovered in subsequent studies over the last two decades. Le Maitre (2002) defined boninite as a subtype of high-Mg basalt containing SiO_2 >52 wt.%, MgO >8%, TiO_2 < 0.5% and Mg # > 60. With the exception of having marginally higher TiO_2 (average 0.59%) and less MgO (average 7.51%), the average SiO_2 of 52.15%, and Mg # 63 of the Yalgoo LET conforms with the definition of boninite given by Le Maitre (2002).

Several recent studies have revealed the presence of boninite/boninitic rocks and other mafic rocks with a boninitic affinity in the greenstone belts of several Archean blocks/cratons (Boily and Dion, 2002; Polat et al., 2002; Smithies 2002; Srivastava, 2006; Manikyamba et al., 2008; Ordóñez-Calderón et al., 2009; Dilek and Thy, 2009). In the Yilgarn Craton, most recently Wyman and Kerrich (2012) and Angerer et al. (2013) reported the occurrance of boninites from the Murchison Domain and Southern Cross Domain, respectively. Average values for the major geochemical characteristics of the Yalgoo LET, together with those of both Phanerozoic and selected Archean boninites, are included in Table 3.4.

Wyman and Kerrich (2012) described boninites and associated mafic and ultramafic rocks from the ~2.80-2.76 Ga Polelle Group (Van Kranendonk and Ivanic, 2009) from the Cue and Meekatharra areas in the northern Murchison Domain. These boninites however, have a wider compositional spectrum compared to most Phanerozic boninites and Archean boninitic rocks including the LET from Yalgoo (Table 3.4), with TiO_2 ranging from 0.46 to 1.44%, MgO from 5.5 to 14% and $(Gd/Yb)_{cn}$ from 0.74 to 1.36. One sample ME-4, considered the most primitive of these, has SiO_2 >52%, MgO >8%, TiO_2 <0.5 % and shows a concave REE pattern [$(Gd/Yb)_{cn}$ 0.9] (Wyman and Kerrich, 2012), satisfying the satisfies chemical criteria for boninite

Table. 3.4. Average of the main geochemical paarmeters of Phanerozic boninites, selected Archean boninitc rocks and the LET rocks of the Yalgoo area. Data for the Phanerozoic LEG 125 boninite from Pearce et al. (1992). Data for the Archean boninitic rocks in the Fortret-Evans greenstone belt (FEGB) from Boily and Dion (2002), the Mallina Basin from Smithies (2002), the Ujarassuit and Ivisaartoq greenstone belts from Ordóñez-Calderón et al. (2009), the Koolyanobbing greenstone belt (KGB) from Angerer et al. (2013), and the Cue and Mekkatharra from Wyman and Kerrich (2012).

Chemical composition	**Phanerozoic**	**Archean**					
	LEG 125 (Bonin-Mariana forearc)	FEGB, Opatica subprovince Quebec	Mallina Basin Pilbara	Ujarassuit and Ivisaartoq greenstone belts, Greenland	KGB Southern Cross Domain	Cue and Meekatharra Murchison Domain	Yalgoo LET Murchison Domain
SiO_2, wt.%	55.18	52.72	53.24	52.48	50.05	51.25	52.15
TiO_2	0.22	0.45	0.26	0.31	0.38	0.77	0.59
Al_2O_3	12.12	14.65	17.22	16.07	12.42	13.72	14.65
Fe_2O_3T	7.41	9.61	8.99	9.67	11.17	10.56	10.45
MgO	10.44	8.89	8.15	11.38	14.61	8.28	7.51
Mg#	75	66	64	70	71	60	63
Al_2O_3/TiO_2	56.18	32.91	66.35	52.58	34.81	20.86	24.65
Ni, ppm	222	125	86	149	294	173	123
Cr	750	543	253	425	1092	478	345
Zr	40	41	37	23	26	63	43
Nb	0.6	1.5	1.34	0.54	1.04	2.72	1.65
$(Gd/Yb)_{CN}$	0.98	0.84	0.58	0.72	0.77	0.94	0.70

outlined by Le Maitre (2002). Angerer et al. (2013) discussed boninite series rocks from a mafic-ultramafic-BIF association in the ~3.0 Ga Koolyanobbing greenstone belt (KGB) of the Southern Cross Domain. Except for the slightly lower average SiO_2 content (<51.25%), the geochemical characteristics of these rocks match those outlined for boninite by Le Maitre (2002). Among nine boninite samples from the KGB, three samples (KDM-12,KM-2 and KM-4) have low SiO_2 (46.73 to 49.52%) and Al_2O_3 (7.64 to 9.68%) and high MgO (17.5 to 21.1%) contents. Except for these samples, the range of SiO_2 (49.8-52.76%), Al_2O_3 (13.80 to 14.73%) and TiO_2 (0.33 to 0.50%) contents and $(Gd/Yb)_{cn}$ (0.61 to 0.96) ratios of the rest of the boninite samples from the KGB lie close to those of the LET from Yalgoo. The MgO contents of KGB boninite, however, are higher than the LET samples.

With the exception of a slightly greater TiO_2 range (up to ~0.6 wt%) and low Al_2O_3/TiO_2 (average ~25), the Mg# (61-65), SiO_2 (~51.5-53.4%) values, moderately-enriched LREE $(La/Sm)_{CN}$ = 0.96-1.43) and unfractionated HREE ($(Gd/Lu)_{CN}$ = 0.67–0.74) patterns of the Yalgoo LET fit within spectrum of both Phanerozoic and Archean boninites (Table 3.4). Based on CaO/Al_2O_3 ratios (CaO/Al_2O_3 >0.75 and <0.75 equate with high- and low-Ca boninites, respectively) as proposed by Crawford et al. (1989), most of the LET samples correspond to low-Ca boninite.

Phanerozoic boninites are most likely formed in the forearc, owing to forearc extension during the early stages of subduction (Crawford et al., 1989; Stern and Bloomer, 1992; Kim and Jacobi, 2002; Reagan et al., 2008). Phanerozoic boninites may also be erupted in the back-arc, as a back-arc spreading centre propagates into a volcanic arc and interacts with slab-derived fluids (Deschamps and Lallemand, 2003). The Polelle Group boninitic rocks in the Murchison Domain were interpreted to have erupted into a back arc setting (Wyman and Kerrich, 2012).

Archean boninitic rocks are also interpreted as forming in intraoceanic arcs given the association with primitive island arc tholeiitic basalts (Kerrich and Polat, 2006; Angerer et al., 2013).

Given the variable mantle processes, heterogeneously depleted mantle reservoirs and different crustal dynamics operating within Archean blocks, the present study favors inclusion of "boninites/boninitic rocks/mafic rocks with a boninitic affinity" within the term "Archean boninitic rocks", mainly based on the broad geochemical similarities among these rock suites.

Boninitic Rocks associated with Komatiite: Several high-Mg boninite samples (KDM-12, KDM-26, KDM-29, KM-2 and KM-4) in the KGB, Southern Cross Domain, are intercalated with voluminous basalts and komatitiic basalt (Angerer et al., 2013). In the Abitibi greenstone belt, the evolved depleted tholeiites (DT) (in the Malartic Block) and low-titanium tholeiites (LoTi) overlie and/or are intercalated with Al-undepleted or Al-depleted komatiite flows (Wyman et al., 1999). The DT in the Maraltic Block have SiO_2 (~50.4-55.8%), TiO_2, (0.77-0.99%), MgO (4.7-6.3), Al_2O_3/TiO_2 (14-15) values, and moderately enriched LREE $(La/Sm)_{CN}$= 0.86-1.05), which is similar to many of the geochemical characteristics of boninites (Table 3.4). The lack of interstratified komatiitic flows with the Yalgoo LET precluded any direct comparison between the DT in the Abitibi greenstone belt and the LET at Yalgoo.

Analogue of the Yalgoo LET: The key geochemical characteristics of the Yalgoo LET and LDT are compared with the Archean Fortret-Evans greenstone belt (FEGB); Opatica sub-province, Canada; Pilbara Craton; Cue and Meekatharra; KGB (in the Yilgarn Craton), Proterozoic Amisk Lake (in the Trans-Hudson Orogen) boninites; and associated LREE-depleted rocks, along with Phanerozic boninites, in Fig. 3.14.

Boninite-like rocks and associated melanogabbro from the Pilbara Craton, boninites from both Cue and Meekatharra and the KGB show significant scatter on the SiO_2 vs. Mg# and Al_2O_3/TiO_2 vs. TiO_2 plots, whereas the Yalgoo LET and LDT form a tight cluster and overlie the field of FEGB boninite and LREE-depleted tholeiites (Fig. 3.14a,b). Being high in Al_2O_3 and low in TiO_2, the Pilbara bonitites conform more with the wider field of Phanerozoic boninites on the Al_2O_3/TiO_2 vs. TiO_2 plot (Fig. 3.14b). Yalgoo LET samples lie within the field of FEGB boninite on the TiO_2 vs. Zr plot (Fig. 3.14c). Yalgoo LDT and Cue and Meekatharra boninite (apart from two high Zr and TiO_2 samples) on the other hand, fall mostly on the boundary of/or proximal to the FEGB LREE-depleted tholeiites. KGB bonitite samples on the TiO_2 vs. Zr plot display a slightly wider dstribution, spanning across the field of both Phanerozic and FEGB boninites (Fig. 3.14c), whereas samples from the Pilbara Craton lie

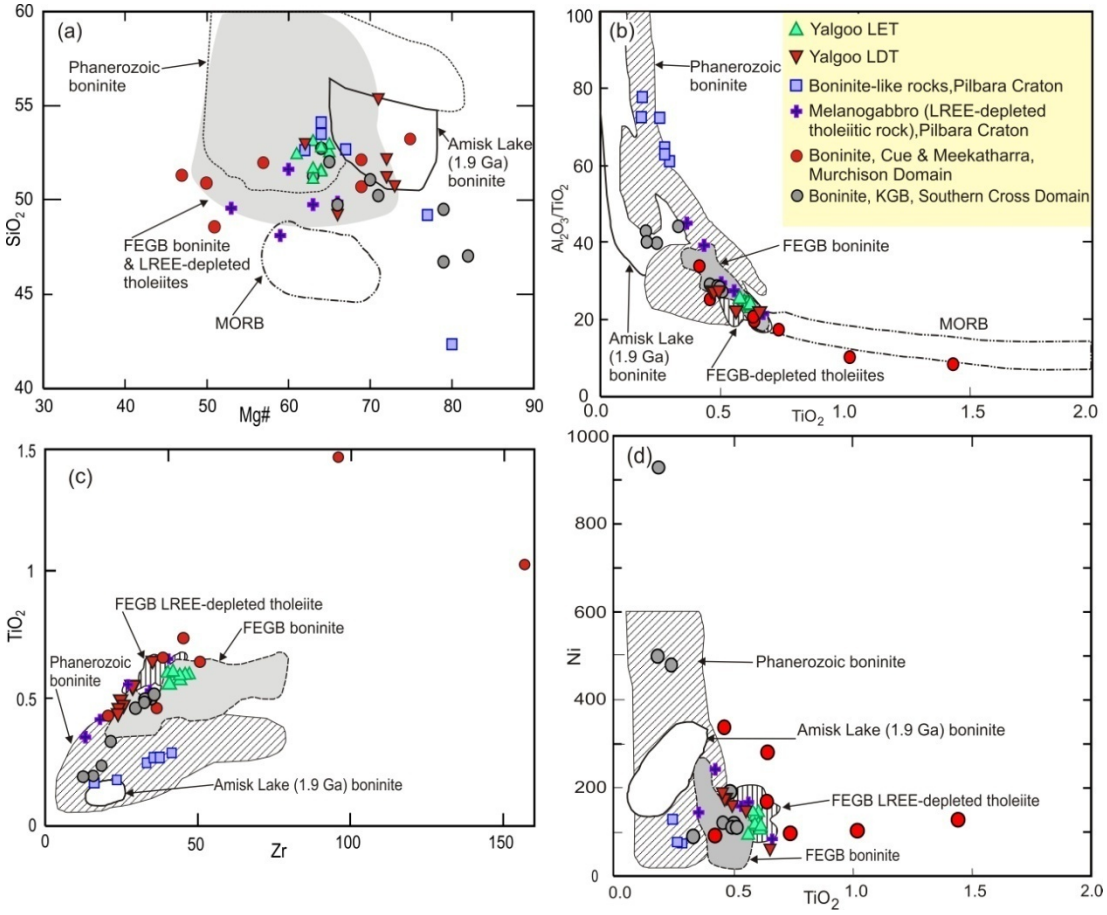

Fig. 3.14. Binary plots for comparison between Phanerozoic and Archean boninitic rocks and depleted tholeiites with Yalgoo LET and LDT: (a) SiO_2 vs. Mg#; (b) Al_2O_3/TiO_2 vs. TiO_2; (c) TiO_2 vs. Z; (d) Ni vs. TiO_2. Fields of FEGB boninites and LREE depleted rocks, Phanerozoic boninite, Amisk Lake boninite and MORB are from Boily and Dion (2002). Data for Pilbara boninite and melanogabbro are taken from Smithies (2002), boninities from the Cue and Meektharra area from Wyman and Kerrich (2012), and boninities from the KGB from Angerer et al. (2013).

within the field of Phanerozoic boninite. Boninites from both Cue and Meekatharra and the KGB demonstrate significant scatter on the Ni vs. TiO_2 plot (Fig. 3.14d), whereas the LET and LDT samples concentrate in the field of LREE- depleted tholeiites along the margin of the FEGB boninite field. On the whole, Yalgoo LET shows a remarkable similarity with Archean boninites of the FEGB, Opatica sub-province, Canada. Among the Yilgarn Craton boninites, a number of the KGB samples fall close to the Yalgoo LET and LDT samples in these binary plots (Fig. 3.14a,b,c,d), especially when compared to the other Murchison Domain boninites.

The REE and incompatible trace element patterns of the above-mentioned Archean boninitic rocks, along with island arc tholeiites of the Pickle Crow assemblage, are further compared with the mafic volcanic rocks from Yalgoo (Fig. 3.15). Boninites from the Pilbara show much stronger enrichment of LREE/MREE and depletion of MREE/HREE and strong negative Nb anomalies compared to the Yalgoo LET (Fig. 3.15a,b,c,d). LREE-depleted melanogabbros from the Pilbara Craton also differ from the Yalgoo LDT by having stronger depletion of MREE/HREE and strong negative Nb anomalies and moderate positive P anomalies (Fig.

3.15a,b,e,f). The REE and incompatible trace element patterns of tholeiites from the Pickle Crow assemblage differ considerably from the LET, which essentially attests to generation from different mantle source regions (Fig. 3.16e,f). As seen in the binary plots (Fig. 3.15a,b,c,d), the REE and incompatible trace element profiles of the LET samples show the closest similarity with boninites of the FEGB from the Opatica sub-province of Canada (3.15c,d,e,f).

Owing to the large variation in the REEs and the incompatible trace elements, the Cue and Meekatharra boninite form broad fields, and overlap the REE profiles of the LET samples (Fig. 3.15g,h). The incompatible trace element profiles of the Yalgoo LET samples differ from those of the Cue and Meekatharra boninite samples in having strong negative P and Ti anomalies, implying a difference in the source region. The REE and incompatible trace element profiles of the most primitive boninite sample ((ME-4) from the Cue and Meekatharra area, however, show a relatively close macth to those of the Yalgoo LET, with the exception of having moderate Nd depletion, strong negative Tm and strong positive P anomalies (Fig. 3.15g,h).

The KGB boninite samples show a similar parallel but much lower normalised element values, on the REE plot (Fig. 3.15g). On the incompatible trace element plot, the Yalgoo LET samples lie in the field of KGB boninite samples, with the exception of P anomalies, with the former showing strong negative and the latter showing strong positive anomalies, (Fig. 3.15h).

Source Characteristics: Formation of boninite lava requires an N-MORB source later mixed with a variably-enriched LREE and LILE source. The Yalgoo LET shows a REE pattern akin to the modern N-MORB with moderate LREE enrichment (Fig. 3.9a). The elevated LREE, Ba, Th, Sr and mostly weak positive Zr (Hf) anomalies are considered to represent the addition of enriched components derived from dehydration of a subducted slab to a moderately-depleted mantle wedge similar to N-MORB (Fig. 3.9c, 3.12).

Boninites in modern arc settings are considered the products of a second-stage melting of refractory harzburgitic asthenospheric mantle, induced by the upwelling of a hot peridotite mantle diapir (Crawford et al., 1981). Alternatively, given the LREE enrichment relative to MREE and negative Nb anomalies, boninites could have formed from decompression melting via fluxing of a refractory sub-arc asthenospheric wedge by fluids from a subducted slab (Sun and Nesbitt, 1978; Hickey and Frey, 1982; Hickey-Vargas and Reagen, 1987; Crawford et al., 1989). An intracratonic setting for boninite-like rocks and associated high-Mg diorite (sanukitoid) suite in the Pilbara Craton was suggested by Smithies (2002). Boily and Dion (2002) suggested moderate Th/La (0.13–0.29), along with high Ba/La ratios (>25;

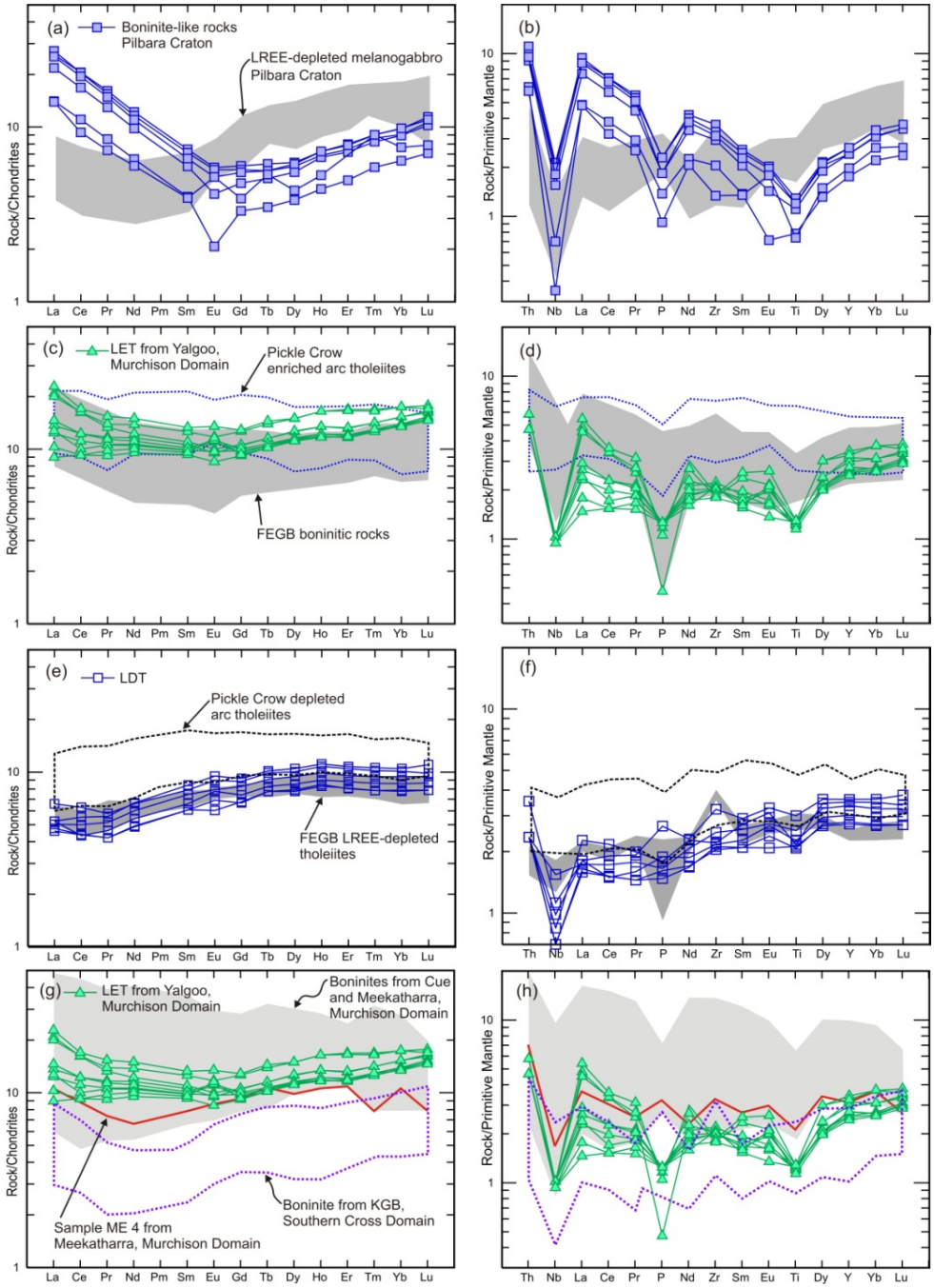

Fig. 3.15. Comparison of the REE (normalised after chondritie values of Sun and McDonough, 1989) and incompatible element characteristics (normalised after Primitive Mantle values of Sun and McDonough, 1989) of selected Archean boninitic and associated LREE-depleted tholeiites and Yalgoo mafic rocks. (a) REE and (b) incompatible trace element plots of the boninitic-like rocks with the field of associated melanogabbro from the Pilbara Craton (Smithies, 2002). (c) REE plot of the LET, along with the fields of FEGB boninitic rocks and Pickle Crow enriched tholeiites (Hollings and Kerrich, 2004). Note, the LET samples have a REE trend parallel to the FEGB boninitic rocks, producing a slightly enriched pattern. (d) Incompatible trace element plot of LET along with the fields of FEGB boninitic rocks and Pickle Crow enriched tholeiites (Hollings and Kerrich, 2004). As in the previous figure, the incompatible trace element plot of the LET samples lies completely in the field of the FEGB boninitic rocks. (e) REE plot of the LDT, along with the REE fields of LREE-depleted tholeiites of the FEGB (Boily and Dion, 2002) and depleted tholeiites of the Pickle Crow assemblage. The LDT samples shows an almost identical REE pattern to the LREE depleted tholeiites of the FEGB. (f) Incompatible trace element plot of the LDT along with the fields of LREE depleted tholeiites of the FEGB boninitic rocks (Boily and Dion, 2002) and depleted tholeiite of the Pickle Crow enriched tholeiites. (g) REE plot of the LET, along with the REE fields of boninites from Cue and Meekatharra, Murchison Domain (Wyman and Kerrich, 2012) and the Koolyanobbing greenstone belt (KGB), Southern Cross Domain (Angerer et al., 2013). (h) Incompatible trace element plot of LET along with the fields of boninites from Cue and Meekatharra, and the KGB, Yilgarn Craton.

Yalgoo LET range 27-206, except for sample MA 18), reflects restricted mantle metasomatism of a depleted mantle source by hydrous fluids from a subducting slab prior to extraction of the boninite. Therefore, it is apparent a depleted mantle source left after a partial melting, possibly associated with Archean sea floor spreading (cf. Ohta et al., 1996; Furnes et al., 2007) was subjected to limited metasomatism by LREE and LILE from a subducting slab, resulting in the source of boninitic lava for the Yalgoo LET.

Source of Heat to Generate Boninite Lava: High temperatures in the sub-arc mantle are required for eruption of boninitic lavas and may be generated from subduction of young, hot oceanic lithosphere, spreading-ridge subduction, subduction initiation across fracture zones, and in the supra-subduction zone (e.g., Stern and Bloomer, 1992; Kim and Jacobi, 2002; Hall et al. 2003; Deschamps and Lallemand, 2003; Schuth et al., 2004; Ishizuka et al., 2006; Dilek et al., 2007). The heat required to generate melting of a metasomatised harzburgite/lherzolite could have been provided by the ascent of MORB diapirs or by upwelling of asthenospheric hot mantle impinging under an arc during extension (Crawford et al., 1989). A supra-subduction zone proto arc-ridge (as inferred from the immature arc setting on the Yb-Ce plot) is probably the most likely candidate for the higher heat flow required to initiate melting of the source of boninitic-like rocks in the Yalgoo area.

3.3.4.7 Yalgoo LDT: Low-Titanium Tholeiite Associated with Plume or Low-Titanium Tholeiite (LoTi) Associated with Boninites?

The Mg#, Cr and Ni contents necessitates a strongly depleted mantle source for the LDT in the Yalgoo area (Fig. 3.10b,d). Whether the depleted mantle source was related to upwelling of a plume into the zone of melting or whether it was a depleted derivative of the same magma forming the LET is discussed here.

A ‘depleted mantle plume’ as defined by Campbell (2001) at the site of melting, after extraction of boninitic magma, has the potential to mimic the unique geochemical characteristics shown by the LDT. Hergt et al. (1989), showed that a small amount of sediments in a plume can produce Nb, Ti, P anomalies, as in the case of the Karoo and Parana basalts. Tholeiitic rocks with similar characteristics were also reported from Norseman (high-Mg tholeiite-HMT), where they are associated with enriched high-Mg tholeiites (EHMT) and interpreted to have originated from a mantle plume.

Campbell (2001) suggested several geochemical criteria (MgO, Ni and Cr contents) and a particular stratigraphic association to distinguish plume-derived basalts from IAB and MORB. An MgO content well above 14%, high Ni (~200-500 ppm at 10-12% MgO) and high Cr (2300 ppm in high-Mg basalt and/or komatiite) contents are considered to be the main

geochemical signatures of basalts derived from plume activity. MgO, Ni and Cr contents of the LDT fall well short to qualify for a plume-derived basalt. Apart from these, a close stratigraphic association of plume-related high-Mg basalt/komatiite/basaltic komatiite also should be taken into consideration when classifying a high-Mg basalt as plume-derived. In the north Yalgoo area, the LDT occurs within the more voluminous LET and shows no distinct contact or interbedding with high-Mg basalt units. However, thin layers of rocks similar to LDT outcroping within high-Mg basalt units were mapped to the south of the study area (Hallberg et al., 2002). These high-Mg basalt units (mostly have MgO ~6 to 16 %, Ni ~100 to 300 ppm, Cr ~300 to 1200 ppm), have low MgO, Ni and Cr compared to a plume-orginated komatiite. Given the lower MgO, Ni, and Cr contents and stratigraphic association in the north Yalgoo area, a plume origin for the LDT and the high- Mg basalt is unlikely.

Tholeiites with variable degrees of LREE enrichment are commonly associated with boninites. Any genetic link (if it existed) between these two lithologies should be apparent in bivariant plots showing the data/fields of the boninite-associated tholeiites. Yalgoo LDT falls within or very close to the LREE-depleted tholeiitic rocks associated with FEGB boninites (Boily and Dion, 2002). (Fig. 3.14). The REE and incompatible element profiles of several LREE-depleted tholeiites associated with Archean boninites and island arc tholeiites of the Pickle Crow assemblage are also compared with the LDT from Yalgoo to test this link. The LDT samples almost completely overlie the field of boninites from the FEGB (Boily and Dion, 2002). With the exception of weak negative Nb and strong negative P anomalies, remaining elements in the LREE-depleted tholeiites in the FEGB match the pattern of the Yalgoo LDT (Fig. 3.15e,f). Therefore, major, HFSE and REE characteristics favour the existence of a depleted mantle left after the extraction of LREE-enriched boninite as the source of the Yalgoo LDT.

3.3.4.8 Partial Melting Model

From their study in the Fortret Evans Greenstone Belt, Boily and Dion (2002) suggested (10–15%) partial melting of a slightly fertile cpx-poor harzburgite residual melt as the source for FEGB boninites. It is suggested in the previous section that the LET and LDT at north Yalgoo have formed from two different depleted mantle domains. The chondrite normalised REE element modelling suggests that the LET rocks can be reproduced by ~ 2% to 6% non-modal partial melting of a modified (source mineralogy) depleted MORB mantle (DMM) source (Workman and Hart, 2005) (Fig. 3.16a). On the other hand, the more depleted LDT rocks require a higher degree (~18%-24%) of non-modal partial melting of a modified DMM source (Fig. 3.16b).

Pearce and Parkinson (1993) devised a Nb-Yb plot for volcanic arc basalts to effectively separate out effects of source depletion from degree of melting. This plot requires Nb and Yb values to be normalised to a given MgO content (9.0 wt%). Pearce and Parkinson (1993), however, excluded boninitic samples, considering they can have slab-related Nb enrichment. During subduction of oceanic lithosphere Th, U, and LREE are preferentially lost from the slab in fluids and/or melts to enrich the sub-arc mantle or enrich the sub-arc crust, whereas Nb and Ti, being more refractory, are retained in the subducting slab, leaving a depleted residual slab with elevated Nb and Ti (Kerrich and Xie, 2002). This residual slab is recycled back into the mantle, often being entrained later into a rising mantle plume. Thus the resulting basalts formed from a mantle plume, as in an ocean plateau, would show positive Nb and Ti anomalies. No such presence of an OIB or enriched HIMU component in the

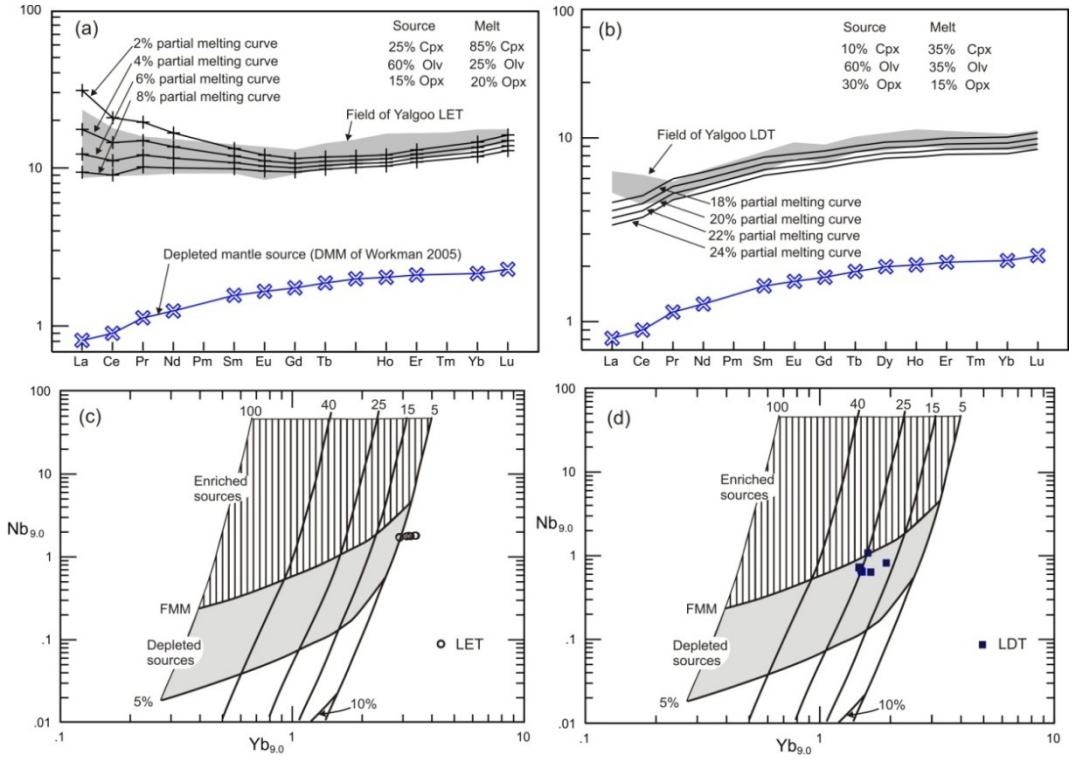

Fig. 3.16. REE modelling of the Yalgoo mafic volcanic rocks. (a) The Yalgoo LET can be produced by 2 to 7% non-modal partial melting of a depleted MORB mantle slightly modified (with source composition 25% clinopyroxene/Cpx, 60% olivine/Olv and 15% orthopyroxene/Opx) from Workman and Hart (2005) producing melt of Cpx 85% Olv 25% and Opx 20%, considered to be the source for the LET. (b) The source for the Yalgoo LDT would have resulted by 18 to 25% non-modal partial melting of a depleted MORB mantle with source composition 10% Cpx, 60% Olv and 30% Opx, slightly modified from Workman and Hart (2005) with the production of melt composed of Cpx 35%, Ol 35% and Opx 15%. Melting models are drawn with the help of Igpet software (Carr, 2006) using partition coefficients for mantle REE of Gill (1981). (c) $Nb_{9.0}$-$Yb_{9.0}$ covariation diagram for Yalgoo LET and (d) LDT samples, after Pearce and Parkinson (1993).

source region is found in either LET and LDT (see sections 3.3.4.4, and 3.3.4.5). Therefore, it is assumed that no slab-related Nb is added to the source of LET and LDT, which rationalises the use of the $Nb_{9\cdot0}$ vs.$Yb_{9\cdot0}$ plot (Pearce and Parkinson, 1993) to constrain the source characteristics.

A low degree of partial melting between ~3-7% from a 2% depleted MORB mantle source has been estimated from the $Nb_{9\cdot0}$ vs.$Yb_{9\cdot0}$ plot of the LET, which is fairly consistent with that of the REE modelling (Fig. 3.16a,c). The $Nb_{9\cdot0}$ vs.$Yb_{9\cdot0}$ plot of the LDT samples suggests the parental melt originated from ~15%-25% partial melting from a slightly depleted MORB mantle source, which is also comparable to the results of REE modelling of the LDT (Fig. 3.16b,d). The elevated LREE contents compared to the modelled melting curves for the LDT samples most probably have resulted from small-scale metasomatism of DMM. The moderately low degree of partial melting supports the view that boninitic lava erupted from a shallow depth under low pressure and substantiates the evaluation made in previous sections about the condition under which the LET rocks formed: it suggests initiation in a subduction zone. However, the mantle domain contributing the melt for the LDT was under considerably higher pressure in a deeper part of the mantle and may have resulted from some reorganisation of the tectonic setting which will be discussed in chapter eight, section 8.4.

3.3.5 Comparison of the Mafic Volcanic Rocks from Yalgoo with the Mafic Rocks from the Murrouli Basalt Formation

As the present work represents the first geochemical data for the mafic rocks belonging to the Murrouli Basalt from the Yalgoo area, it is important to compare the results of this study with the Murrouli Basalt from other locations of the Murchison Domain. Using samples from the Murrouli Range and Mount Magnet traverses, Watkins and Hickman (1990) classified the Murrouli Basalt into four chemically distinct groups. These are: lower, middle, and upper tholeiites, and high-Mg basalt. Three units were recognised in the Mount Magnet traverse - lower and upper tholeiites and high-Mg basalt. Van Kraendonk et al. (2013) retained the Murrouli Basalt as the oldest formation and included it in the ~ 2.82-2.80 Ga Norie Group (oldest) of the Murchison Supergroup in their classification scheme suggested for the Murchison Domain (see section 2.1.3.1).

In a recent study, Wyman and Kerrich (2012) included the boninites from the Cue and Meekatharra area within the Polelle Group that overlies the Norie Group. Wyman and Kerrich (2012) also discussed mafic rocks from the Norie Group, however, they did not assign these rocks to any of the formations of the Norie Group. Table 3.5 shows the average composition of the Murrouli Basalt units from the Murrouli Range and Mount Magnet traverses, and unassigned Norie Group mafic rocks, along with LET and LDT from the Yalgoo. As the Yalgoo LET shows strong boninitic character, therefore, the average composition of the boninite from the Cue and Meekatharra is also included in Table 3.5.

Table 3.5 Comparison of the average of the key geochemical paarmeters of the Murrouli Basalt samples from the Mount Magnet traverse and Murrouli traverse (Watkins and Hickman 1990), Norie Group mafic rocks from Meekatharra (Wyman and Kerrich, 2012), bonitites from Cue and Meekatharra (Wyman and Kerrich, 2012), along with the LET and LDT from the present study area. *LT= lower tholeiite, MT= middle tholeiite, UT= upper tholeiite, HM= high-Mg, Alt.= altered, undif.= undifferentiated.*

	Mount Magnet traverse			Murrouli Range traverse				Meekathrra	Cue and Meekatharra	Yalgoo	
	Murchison Domain			Murchison Domain				Murchison Domain	Murchison Domain	Murchison Domain	
Major	LT	UT	HM- basalt	LT	MT	UT	HM- basalt	Norie Group mafic rocks (undif.)	Boninite, Polelle Group	LET	LDT
oxides	n= 10 (Alt.	n= 10	n=9	n=7	n=4	n=12	n= 2	n= 10	n= 7	n= 9	n= 6
SiO_2	56.4	50.4	50.7	50.1	51.4	50.9	49.4	48.69	51.25	52.15	51.93
TiO_2	0.64	1.45	0.56	1.4	0.76	0.76	0.4	0.70	0.77	0.59	0.51
Al_2O_3	14.4	12.9	10.2	13.5	14.1	14.2	10.7	7.19	13.72	14.65	13.18
FeOT	6.47	12.55	9.69	10.43	9.57	9.38	8.92	11.21	10.56	9.4	9.22
Fe_2O_3	0.99	2.61	1.61	2.31	1.7	1.95	1.25	2.20	2.27	3.64	3.54
FeO	5.58	10.2	8.25	8.35	8.05	7.64	7.77	5.03	8.42	6.81	6.7
MnO	0.2	0.21	0.18	0.19	0.19	0.18	0.2	0.17	0.20	0.17	0.16
MgO	6.63	6.48	12.55	6.92	6.96	7.37	14.35	22.98	8.28	7.51	9.72
CaO	11.45	10.25	11.05	11.97	11.85	11.73	10	6.59	11.68	10.58	11.45
Na_2O	1.34	2.21	1.08	2.24	2.12	1.74	1.15	0.95	2.10	2.42	2.26
K_2O	0.07	0.19	0.1	0.24	0.25	0.15	0.06	0.07	0.20	0.72	0.89
P_2O_5	0.1	0.21	0.09	0.17	0.11	0.1	0.08	0.06	0.08	0.06	0.04
LOI	1.42	2.1	2.94	1.97	2.04	2.74	3.9	5.63	2.30	0.84	0.91
Mg#	68	52	73	60	61	63	77	68	60	63	69
Trace Elements, ppm											
Ba	163	114	51	85	68	43	39	79	96	317	295
Cr	365	114	1166	395	144	266	1304	2031	478	347	500
Co	80	65	67	58	59	56	64	91	55	41	45
Cu	100	82	65	90	95	204	158			56	30
Ni	137	82	278	127	112	116	365	1037	173	123	148
Nb	6	6	3	6	6	4	3	3.48	2.72	1.65	0.72
Rb	1	4	2	9	10	4	2	9	4	37	51
Sr	131	100	70	122	98	82	57	59	97	174	208
V	196	334	227	359	281	281	222	173	314	222	218
Y	25	33	15	30	19	20	15	16	25	23	14
Zn	93	105	77	100	70	97	114			91	69
Zr	87	93	35	87	50	47	32	66	63	43	27
Cr/V	1.87	0.38	5.23	1.14	1	0.94	5.86	11.75	1.52	1.56	2.29
Zr/(Zr+Y)	0.78	0.74	0.7	0.74	0.72	0.70	0.68	0.80	0.71	0.65	0.65

In terms of Ni and Cr contents, the lower tholeiite of the Murrouli Range traverse shows close similarity with the LET. Considering the most conservative elements (excluding Ni, Cr), such as Al_2O_3, TiO_2, MgO, FeOT, Ni, V, Zr and Mg# , the upper tholeiite unit of the Murrouli Range traverse also has a close match with those of the LET (Table 3.5 and Fig. 3.17a).

However, the Yalgoo LET samples have higher Cr (347 ppm) than the upper tholeiite unit of the Murrouli Range traverse (266 ppm). In spite of being nearer to Yalgoo, none of the units from the Mount Magnet (~150km east of Yalgoo) traverse are similar to the north Yalgoo rocks (Table 3.5 and Fig. 3.17b). The LDT samples have higher MgO, Cr, Ni and lower Al_2O_3 than the tholeiite units from both the Murrouli Range and Mount Gibson traverses. Compared with the high-Mg units in both the traverses, the LDT samples have significantly lower MgO, Cr, and Ni, but higher Al_2O_3 and slightly higher TiO_2 (Fig. 3.17a,b).

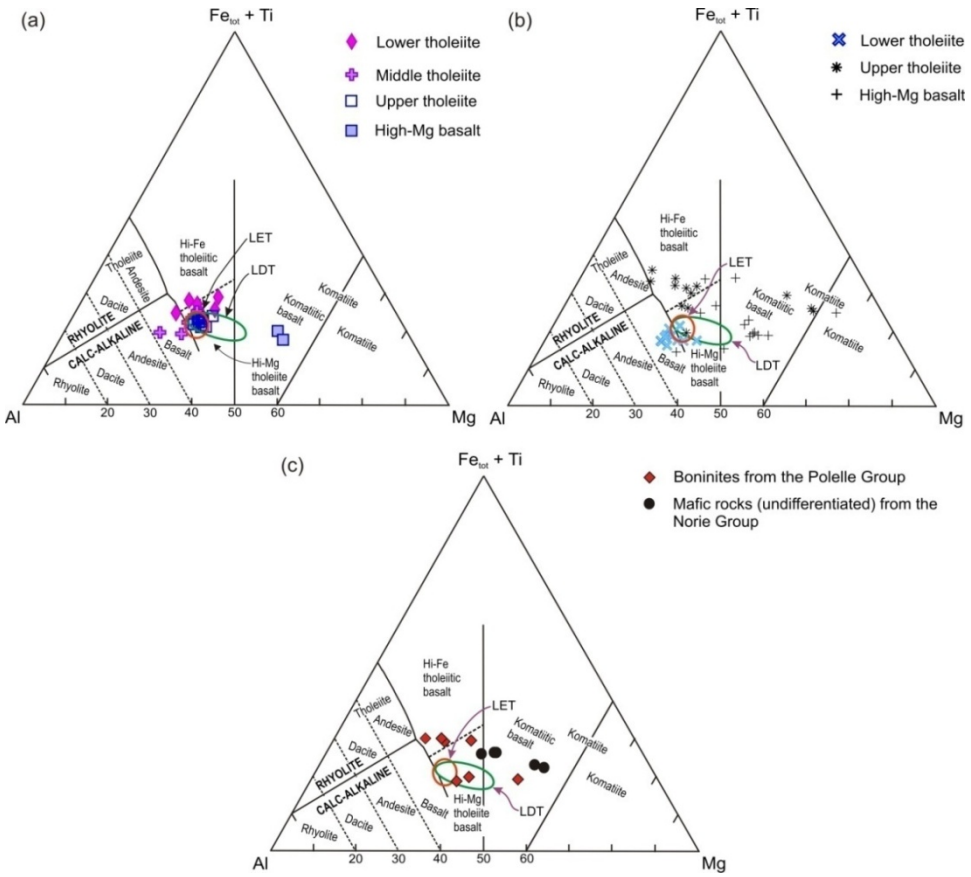

Fig. 3.17. Murrouli Basalt and mafic rock analyses from Cue and Meekathrra, Murchison Domain plotted on a Jensen diagram (Jensen and Pyke, 1982) for (a) the Murrouli Range traverse, (b) the Mount Magnet traverse and (c) Cue and Meekatharra. Also shown are the fields of LET and LDT rocks from the Yalgoo area.

In terms of major elements, both the lower and upper tholeiites of the Murrouli Range traverse have compositions almost identical to boninite from Cue and Meekatharra. When considering collectively, the average TiO_2, MgO, Ni, V, Y, Nb and Zr contents of the upper tholeiite unit of the Murrouli Range traverse produce a very good match to the boninite from Cue and Meekatharra (Table 3.5). Cr and FeOT contents of the upper tholeiite unit of the Murrouli Range traverse however, are lower than the boninite from Cue and Meekatharra. The high-Mg basalt units of both the Mount Magnet and Murrouli traverses differ from the Norie Group mafic (undifferentiated) rocks from Meekatharra in having significantly higher MgO (22.98%), Cr (2031 ppm) and Ni (1037 ppm) contents.

While most elements are similar, the Yalgoo LET has a slightly lower average FeOT, CaO, V and higher Al_2O_3 contents compared to the boninite from Cue and Meekatharra (Table 3.5 and Fig. 3.17c). The Yalgoo LDT also shows a similar composition to the boninite from Cue and Meekatharra. The LDT samples, however, have slightly elevated average MgO and lower FeOT, Y and Zr contents than the boninite from Cue and Meekatharra (Table 3.5 and Fig. 3.17c).

3.3.6 Tectonic Setting

A number of recent studies (Hoffman, 1989; Smithies, 2004; Boily and Dion, 2002; Polat et al., 2002; Condie 2005; Martin, 1986; Martin et al., 2005; Smithies et al, 2007 and references therein) have presented evidence that plate tectonic processes were in operation in the Archean. Among these works in the East Pilbara Craton, modern-style oceanic arc processes are documented at 3.12 Ga by Smithies et al. (2007). Polat et al. (2002) presented geochemical evidence of boninite-like volcanic rocks in the Isua greenstone belt, West Greenland, favouring the existence of Phanerozoic-like plate tectonic processes as early as 3.7–3.8 Ga. Although, the application of tectonomagmatic discrimination diagrams, developed for young basalts to the Archean rocks is yet to have gained unequivocal acceptance, they are capable of distinguishing Archean-OIB and MORB-like rocks from contemporaneous subduction-related rocks, even if subduction processes differered from Phanerozoic ones in some details. Therefore, selected tectono-magmatic discrimination diagrams to infer tectonic setting can be applied to the Archean basalts of the Yalgoo area.

On the Ti vs. Zr (Pearce and Cann, 1973) and Zr/Y vs. Zr (Pearce and Norry, 1979) plots, all the mafic rocks fall within the volcanic arc setting (Fig. 3.18a,b). A similar arc setting (including N-MORB) is indicated in the Hf/3-Nb/16-Th (Wood, 1980) and Nb*2 Y-Zr/4 plots (Meschede, 1986) for the LET and LDT samples (Fig. 3.18c,d). The relationship between paired arc and back-arc basalts is explored using selected HFSE plots from Gamble et al. (1995). On the Ti/Zr, Ti/Sc and Ti/V vs. Zr plots (Fig. 3.18e,f,g), both the LET and LDT samples fall within a (fore) arc setting, outside of the back-arc basalt field, which is consistent with the eruption of the basalts during an early stage of arc formation as revealed on the Ce vs.Yb plot (Fig. 3.11).

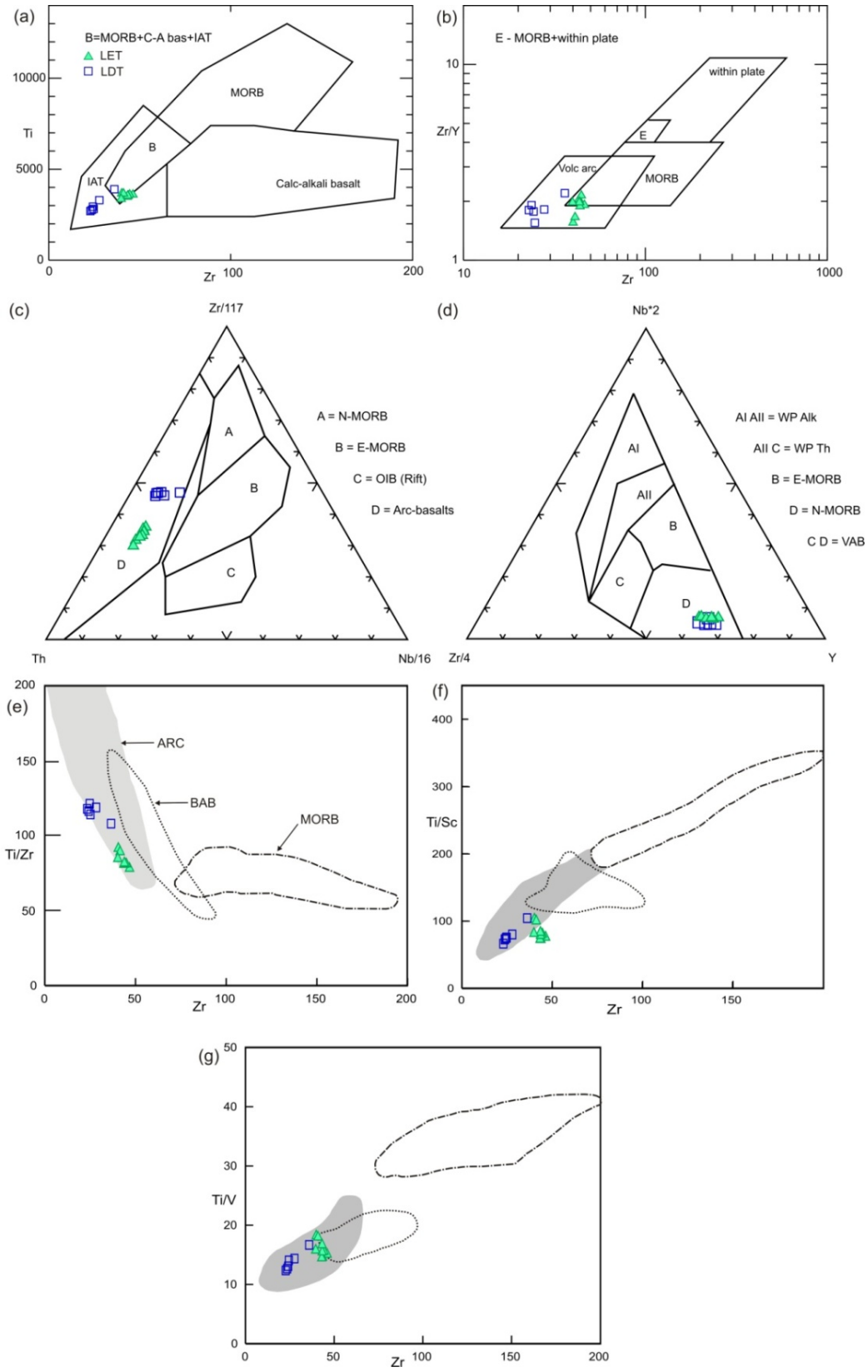

Fig. 3.18. Tectonic discrimination plots for LET and LDT, Yalgoo area. (a) Ti-Zr (Pearce and Cann, 1973). (b) Zr/Y vs.Zr (Pearce and Cann, 1979). (c) Th-Zr-Nb (Wood, 1980). (d) Nb-Zr-Y (Meschede, 1986). Plots (e)-(g) compare Yalgoo mafic volcanics with recent arc-back arc basalt and MORB from recent studies. (e) Ti/Zr vs. Zr. (f) Ti/Sc vs. Zr and (g) Ti/V vs. Zr plots. Arc field is the Kermadec arc (Gamble et al., 1993), Back arc basin (BAB) field from the offshore Taupo Volcanic Zone (Gamble et al., 1995) and MORB field from the South East India Ridge (Klein et al., 1991).

Chapter 4 Nature and Genesis of the Felsic Porphyries in the Yalgoo Area

4.1 Distribution of Felsic Porphyries

In the study area, a number of small NNW-trending lenses of felsic porphyry were mapped by Watkins and Hickman (1990). These porphyries run subparallel to the NNW component of the Noongal shear zone and locally cut across the greenstone stratigraphy (Fig.160, Watkins and Hickman 1990). Hallberg et al. (2002) mentioned quartz-phyric felsic tuffs and felsic volcanoclastic sandstones from south of the study area.

The term "felsic porphyry" in the present context includes small-scale sub-volcanic intrusives both fine-grained (<0. 2mm) and porphyritic in nature, with phenocrysts set in a fine-grained groundmass composed mostly (>65-95%) of felsic minerals. Four samples, including field specimens (MA 23 and MA 27) and drill core samples (PD 002/2 and PRCD 108/3), were collected to characterize the felsic porphyries in the area (Fig. 4.1). A total of 8 petrographic thin sections (three from each of the two field specimens and single thin sections from each of the two drill core samples) were made, complemented by whole rock geochemistry of the three freshest samples (MA 23, MA 27 and PRCD 108/3). Zircons were only recovered from sample MA 27, hence U-Pb SHRIMP geochronology was restricted to this sample.

4.2 Petrography of the Felsic Porphyries

Modal analyses are presented in Table 4.1. Mineral abbreviations used in the photomicrographs follow the nomenclature scheme outlined by Kretz (1983) and Spear (1993).

Table 4.1. Modal composition of the felsic samples from the north Yalgoo area.

Rock types	Microgranodiorite	Microgranodiorite (porphyritic)		Andesite
Mineral volume %	MA 23	PD 002/2	MA 27	PRCD 108/3
Quartz	37	32	38	15
K-Feldspar	11	8	tr	5
Plagioclase	47	50	56	45
Amphibole		tr		21
Biotite	tr	1	6	3
Chlorite		4		9
Epidote		1		tr
Muscovite	5	tr	tr	2
Titanite		1		
Calcite		tr		
Fe Oxides	tr	1	tr	
Ilmenite		2		
Apatite	tr			tr
Others				
Total	100	100	100	100
Point Counted/ Estimation	Estimation	Estimation	6809	Estimation

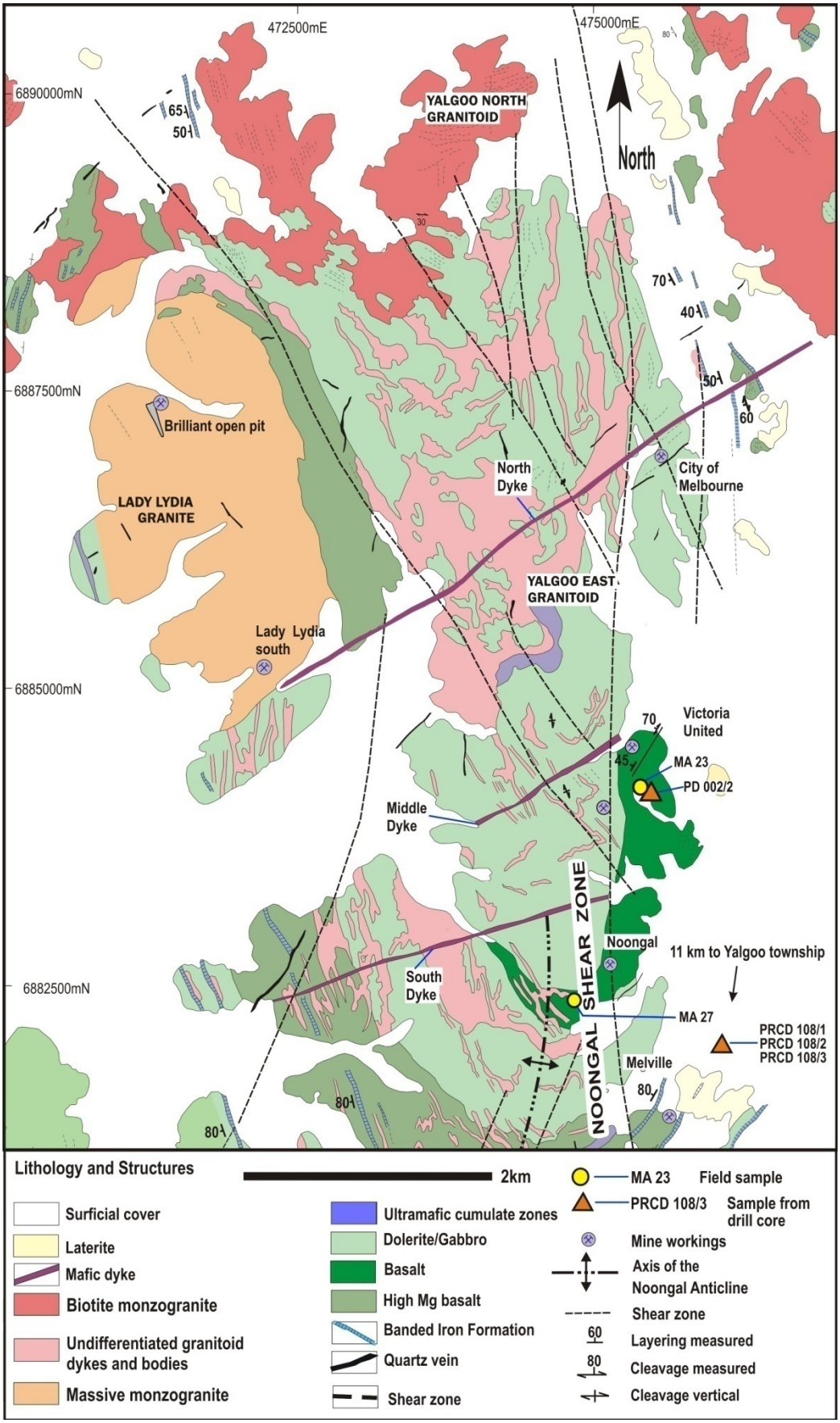

Fig. 4.1. Geological map of the north Yalgoo area showing major locations of felsic porphyry samples (From Hallberg et al., 2002, modified after Watkins and Hickman, 1990).

4.2.1 Microgranodiorite

4.2.2.1 Microgranodiorite (massive)

Sample MA 23 was collected from float of felsic rocks, ~0.4km southeast from the eastern extremity of the middle dyke, around the Victoria United mine site (Fig. 4.1). Sample PD 002/2 was also obtained from the same area from drillhole PD 002 from a depth between 24.30-24.45m (Fig. 4.2). The two samples in hand specimen are massive and aphanitic with MA 23 being cream-brown whereas PD 002/2 is light grey in colour.

Under the microscope, sample MA 23 shows a fine-grained, weakly foliated texture, though fine-grained, massive granular texture is locally observed (Fig. 4.3a,b), whereas, sample PD 002/2 displays a massive granular texture (Fig. 4.3c). Quartz and plagioclase are the predominant phases comprising more than 90% of both the rocks, with minor K-feldspar and small-scale variations in the amount of accessory minerals.

In sample MA 23, subordinate muscovite, biotite and clay minerals make up the accessory phases. Plagioclase (An_{12}) occurs in two forms. The bulk of the grains are fine (0.04-0.06mm) with the presence of local coarser plagioclase, many of which show albite twinning. Plagioclase is moderately altered to sericite and clay minerals and contains minute (0.06-02mm) apatite inclusions. Quartz is anhedral (0.1-0.2mm); K-feldspar is mostly also anhedral microcline (0.1-0.2mm).

In sample PD 002/2, plagioclase, K-feldspar and quartz are of similar size as in sample MA 23, with plagioclase showing stronger alteration. Biotite, pyrite, chlorite, calcite and epidote make up the accessory phases. Pyrite is surrounded by irregular epidote (0.2 to 0.5mm) (Fig. 4.3d). Biotite is retrograded to greenish skeletal chlorite (0.2 to 0.6 mm in length). Greyish brown crystals of granular ilmenite (0.1 to 0.3mm) are rimmed by honey brown titanite, implying the latter is the result of later alteration: they are commonly in close association with chlorite.

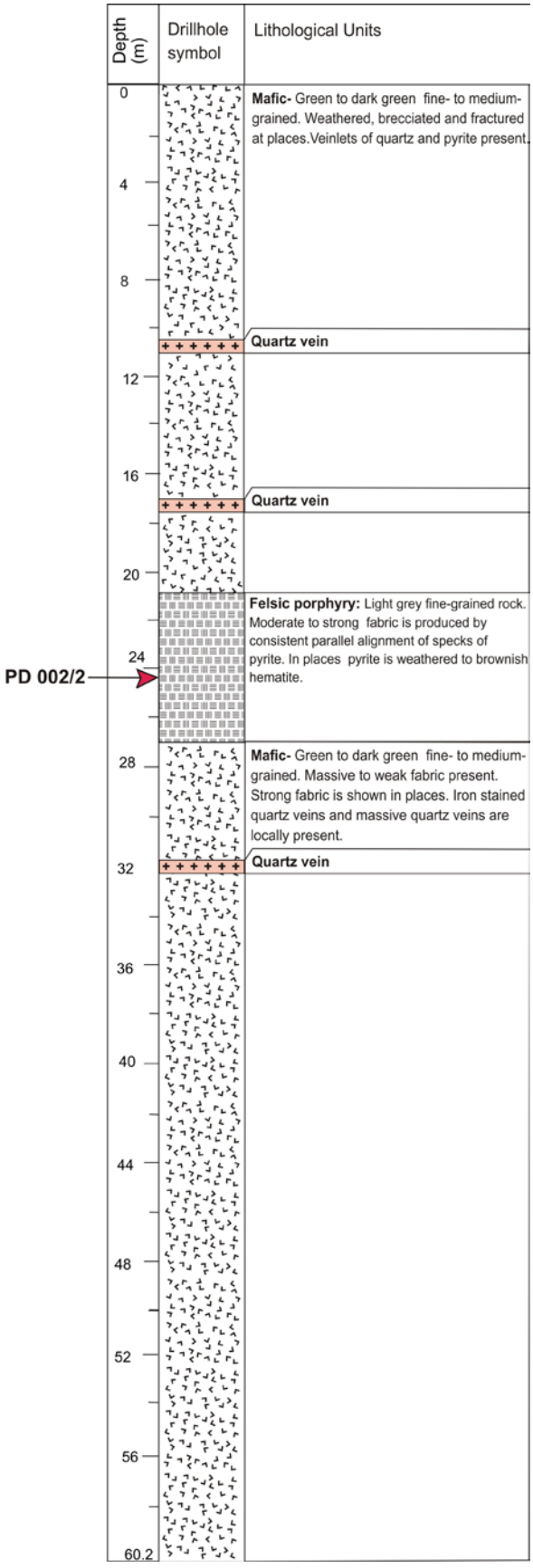

Fig. 4.2. Log of drillhole PD 002 . Red arrow marks the location of sample PD 002/2.

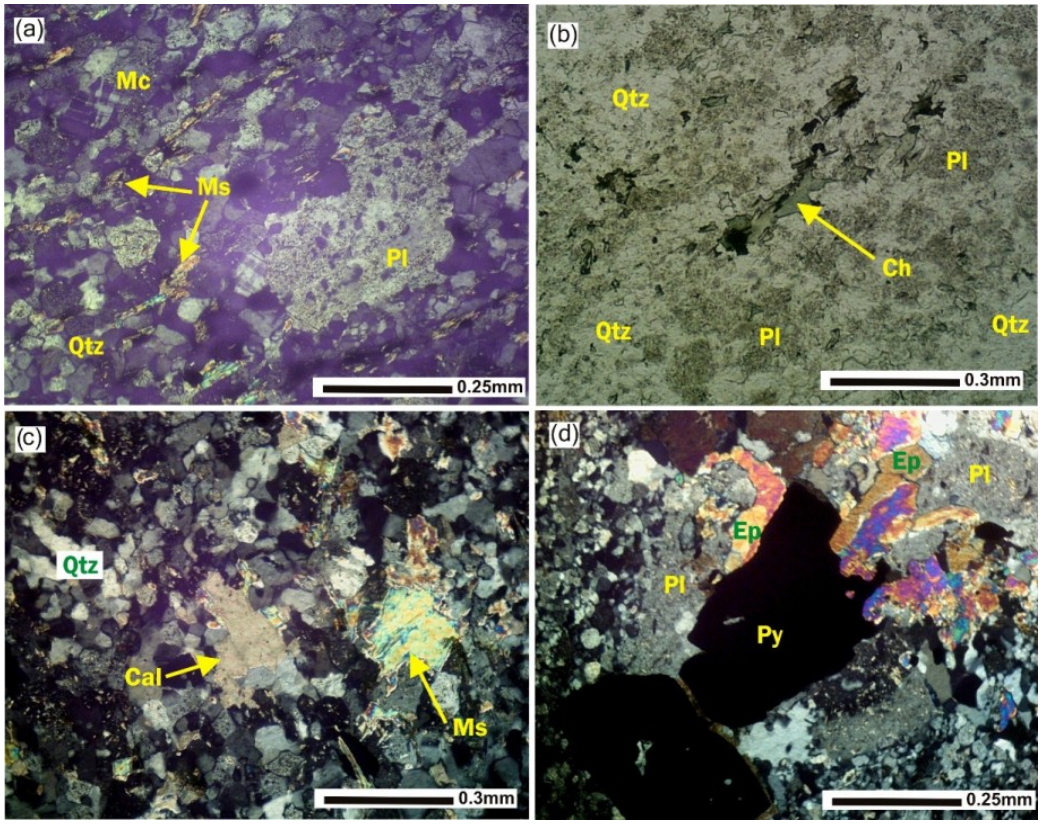

Fig. 4.3. Selected photomicrographs of the felsic porphyries from the north Yalgoo area. (a) Fine-grained foliated texture constituted by granular quartz(Qtz), sericitized plagioclase (Pl), aligned muscovite (Ms) and chlorite (Ch) (MA 23, xpl). (b) Same field of view as (a) (ppl). (c) Granular texture comprising quartz, calcite (Cal) and muscovite (PD002/2, xpl). (d) Pyrite (Py) partially enclosed by epidote (Ep) in sample PD 002/2. Brown prismatic biotite retrogressed to chlorite (PD 002/2, xpl).

4.2.2.2 Microgranodiorite (porphyritic)

Sample MA 27 was collected from ~2.3km south of sample MA 23. It is a pale yellowish-brown coloured, fine- to medium-grained porphyritic rock. White to grey coarse euhedral phenocrysts of quartz and plagioclase are mantled by a microcrystalline groundmass of similar composition (Fig. 4.4a).

Microscopic study reveals plagioclase (An_{18-30}) and quartz are the dominant phenocrysts set in a very fine granular aggregate of quartz and minor K-feldspar. Accessory minerals include distinctive golden brown biotite and flakes of muscovite. Plagioclase is euhedral platy to prismatic, ranging from 0.5-5mm in length (Fig. 4.4a), and is mostly unaltered. Blebs of quartz and sparse golden brown mica form inclusions in the plagioclase (Fig. 4.4a). Quartz occurs as very fine (0.04-0.07mm) granular crystals almost entirely making up the groundmass (Fig. 4.4a,c). The phenocrysts of quartz are ~2 to 6 mm across and form anhedral to polygonal crystals, many showing sub-grain development (Fig. 4.4c). Patches of groundmass locally embay the quartz phenocrysts, whereas some larger quartz phenocrysts are strained. Golden brown mica occurs as small globules (0.2-0.3mm in diameter) in random distribution both in the phenocrysts and the groundmass

(Fig. 4.4a,b,c). This mica also occurs as small cubic crystals (0.2-0.3mm) that could be pseudomorphs after a rectangular mineral (pyroxene!) (Fig. 4.4b,c). However, no fresh isometric minerals could be identified. This golden brown mica appears to form late in response to hydrous reaction. Sericite is present in plagioclase phenocrysts (Fig. 4.4a). Thin linear patches of reddish brown hematite occur within plagioclase crystals. K-feldspar is sparse and occurs as small (0.3-0.8mm) platy microcline crystals. A conspicuous irregular concentration (1.2mm) of diffuse quartz occurs locally within the groundmass (Fig. 4.4d).

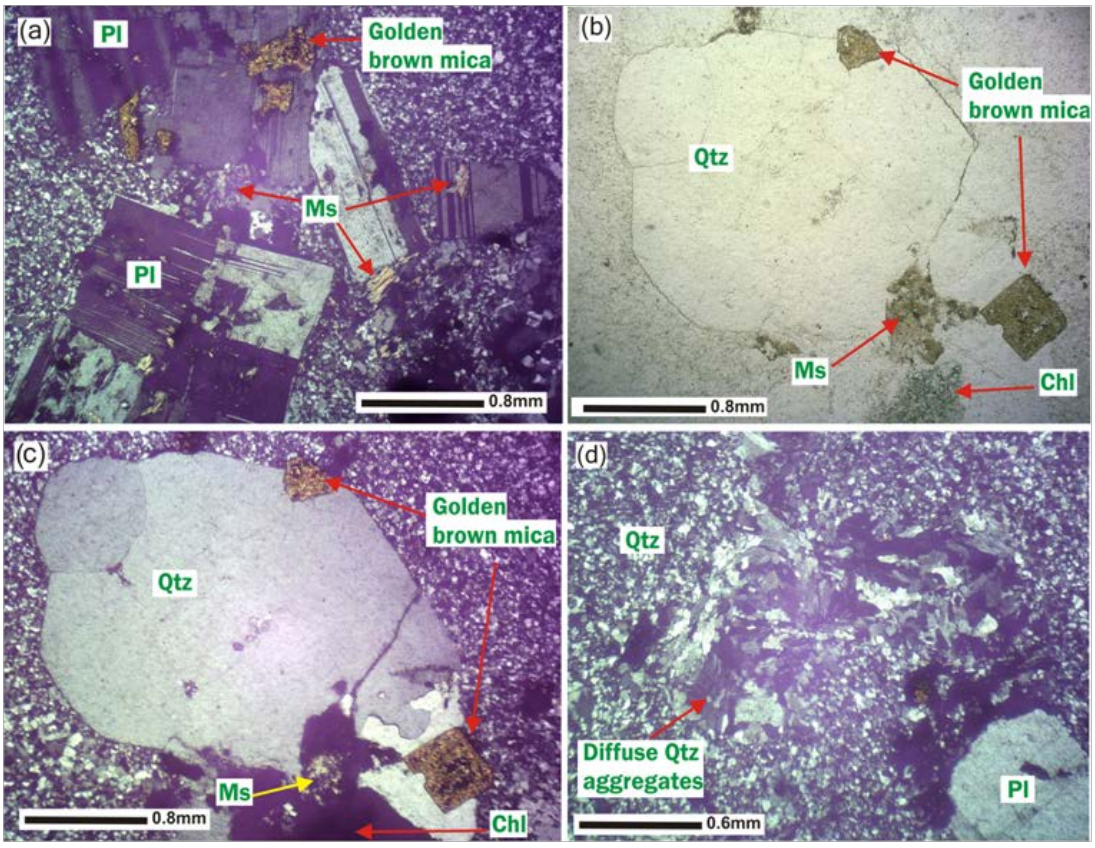

Fig. 4.4 Photomicrographs of the porphyritic microgranodiorite sample MA 27 from the Yalgoo area. (a) Strongly porphyritic texture composed of euhedral relatively fresh plagioclase phenocrysts set in a microcrystalline aggregate of quartz and plagioclase. Golden brown mica and flaky muscovite occur at the margin of plagioclase (xpl). (b) Late golden brown mica pseudomorphs after euhedral (pyroxene!) mineral (ppl). (c) Same field of view as in (b) (xpl). (d) Aggregates of quartz probably growing in a vesicle (xpl).

4.2.2 Andesite

Sample PRCD 108/3 was obtained from drillhole PRCD 108 at a depth from 140.18-140.30m in the Melville area (Fig. 4.1). In hand specimen, it is a light grey coloured fine-grained crystalline rock. The stratigraphy in the drillhole is an alternating sequence of BIF, chert and felsic porphyries with minor massive quartz veins (Fig. 4.5).

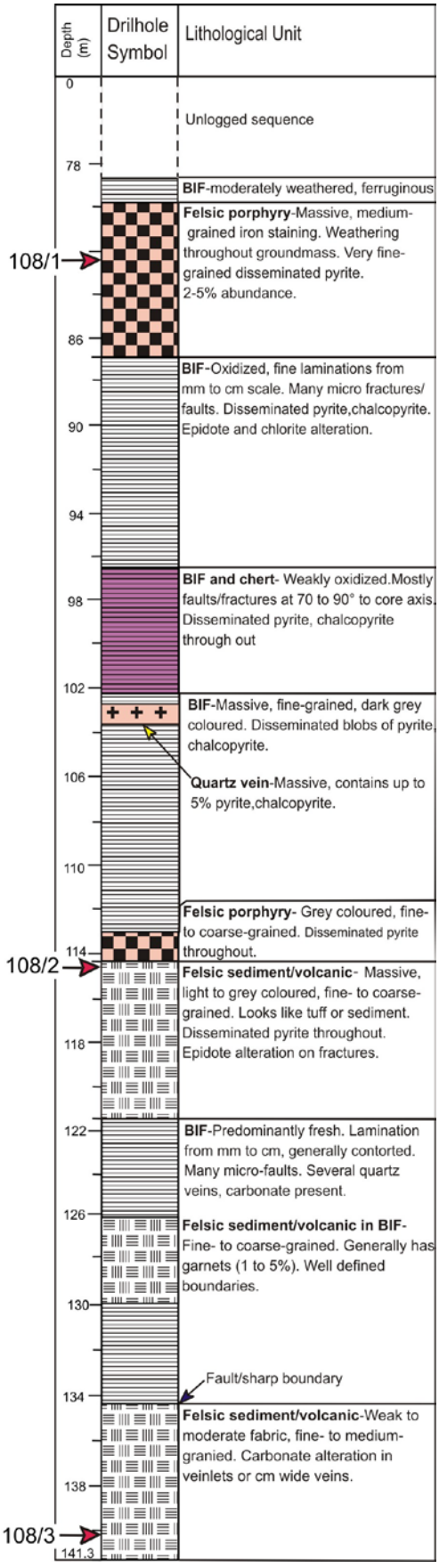

Fig. 4.5. Log of drillhole PRCD 108. Red arrows mark the sample locations.

Under the microscope, the rock is weakly foliated, with a fine-grained microporphyritic texture, with microcrystalline granular aggregates of quartz mantling mostly plagioclase phenocrysts, with amphibole, biotite and chlorite (Fig.4.6a,b). The groundmass is composed of fine-grained (0.05-1mm) recrystallized plagioclase and quartz. A number of quartz/feldspar grains demonstrate 120º intersections attributed to a later thermal metamorphic effect. The plagioclase phenocrysts are subhedral to irregular platy (0.4-1.2mm) in shape, and are moderately sericitized. Minute (0.02-0.04mm) bladed biotite crystals are strongly pleochroic (x= pale brown; z= dark brown) and define a preferred orientation, resulted in a weak planer fabric. Amphibole is actinolite, occurs as radiating curvilinear sheaves (1.2-1.5mm long). Muscovite tends to grow out from quartz and amphibole into early plagioclase and is also seen to cut across biotite crystals, testifying to its secondary origin. Epidote blebs are pleochroic from x=pale yellow, y=reddish yellow, z= dark reddish yellow.

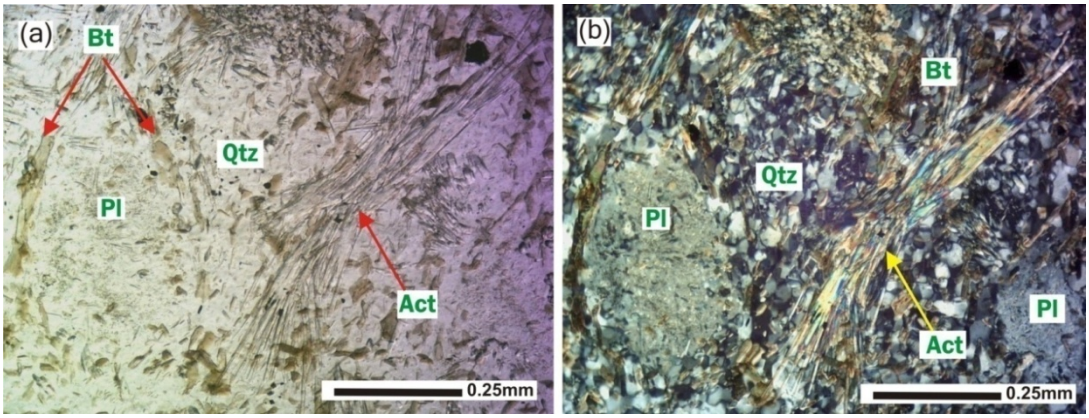

Fig. 4.6. Photomicrographs of andesite sample MA 108/3 from the north Yalgoo area. (a) Fine-grained porphyritic texture composed of recrystallized quartz (Qtz), altered plagioclase (Pl), flaky biotite (Bt) and amphibole needles (Act) (ppl). (b) Same field of view as (a) (xpl).

4.3 Geochemistry of the Felsic Porphyries

Major and trace element data, including rare earth elements, are presented in Table 4.2. Sample PD 002/2 was not analyzed on account of its high degree of alteration.

Table 4.2: Geochemistry of the felsic porphyries.

Major elements %	Microgranodiorite (massive)	Microgranodiorite (porphyritic)	Andesite
	MA 23	MA 27	PRCD 108/3
TiO_2	0.26	0.24	0.45
Al_2O_3	16.08	15.50	15.09
Fe_2O_3T	0.33	0.84	7.2
MnO	<0.01	0.00	0.05
MgO	0.19	0.11	6.96
CaO	0.91	0.37	3.64
Na_2O	5.56	7.95	4.66
K_2O	2.61	0.80	1.03
P_2O_5	0.03	0.03	0.09
LOI	0.92	1.12	0.40
TOTAL	26.89	26.96	39.57
Fe_2O_3*	0.18	0.48	3.17
FeO*	0.15	0.36	4.03
FeO*T	0.297	0.756	6.48
Mg#	0.56	0.22	0.68
A/CNK	1.26	1.09	1.25
K_2O/Na_2O (Mol)	0.31	0.07	0.15
K_2O/Na_2O	0.47	0.10	0.22
FeOT+MgO	0.34	0.47	10.99
FeOT/MgO	0.78	3.28	0.58
CIPW Norms			
Quartz	28.17	22.29	11.01
Orthoclase	15.42	4.73	6.09
Albite	47.05	67.27	39.43
Anorthite	4.32	1.64	17.21
Diopside	0.00	0.00	0.18
Hypersthene	0.47	0.54	22.12
Magnetite	0.00	0.69	4.60
Hematite	0.18	0.00	0.00
Ilmenite	0.32	0.00	0.00
Apatite	0.07	0.07	0.21
Corundum	2.53	0.95	0.00
Total	98.53	98.19	100.84

Trace elements, ppm	MA 23	MA 27	PRCD 108/3
Ba	1766	484	278
Be	2.1	1.9	1.0
Cr	5.2	2.2	244.0
Cs	1.5	0.7	1.5
Cu	3.0	7.9	19.2
Ga	26.1	22.2	15.4
Ge	1.4	1.2	1.4
Hf	3.6	3.9	2.7
Li	10.4	1.2	13.2
Nb	3.6	4.9	3.4
Ni	2.3	2.0	134.3
Pb	18.8	14.9	6.4
Rb	90.8	28.4	46.9
Sc	3.7	2.6	14.1
Sr	541.0	250.6	171.8
Ta	0.2	0.3	0.3
Th	11.3	9.5	3.5
U	2.2	2.4	1.1
V	21.0	17.5	91.2
Y	6.7	8.0	11.4
Zn	14.1	10.4	78.6
Zr	153.7	154.9	98.1
REE, ppm	MA 23	MA 27	PRCD 108/3
La	43.04	34.68	10.48
Ce	70.08	58.38	19.93
Pr	7.00	6.33	2.16
Nd	22.59	22.74	8.81
Sm	2.94	3.36	1.97
Eu	0.83	0.82	0.64
Gd	2.41	2.52	1.96
Tb	0.21	0.25	0.31
Dy	0.97	1.25	1.89
Ho	0.15	0.22	0.40
Er	0.43	0.63	1.15
Tm	0.06	0.09	0.17
Yb	0.41	0.67	1.16
Lu	0.06	0.11	0.18
Total REE	151.17	132.07	51.22
$(La)_{CN}$	181.60	146.33	44.22
$(Yb)_{CN}$	2.43	3.93	6.81
$(La/Yb)_{CN}$	74.87	37.25	6.50
K,ppm	2167	664	855
Nb/Ta	14.62	16.65	11.58
K/Rb	23.86	23.35	18.22
Rb/Sr	0.17	0.11	0.27
Sr/Y	80.75	31.37	15.07
$(Gd)_{CN}$	11.72	12.24	9.56
$(Lu)_{CN}$	2.33	4.20	6.91
$(Gd/Lu)_{CN}$	5.03	2.91	1.38
$(Ce)_{CN}$	114.51	95.40	32.57
$(Yb)_{CN}$	2.43	3.93	6.81
$(Ce/Yb)_{CN}$	47.21	24.28	4.78

4.3.1 Magma Series

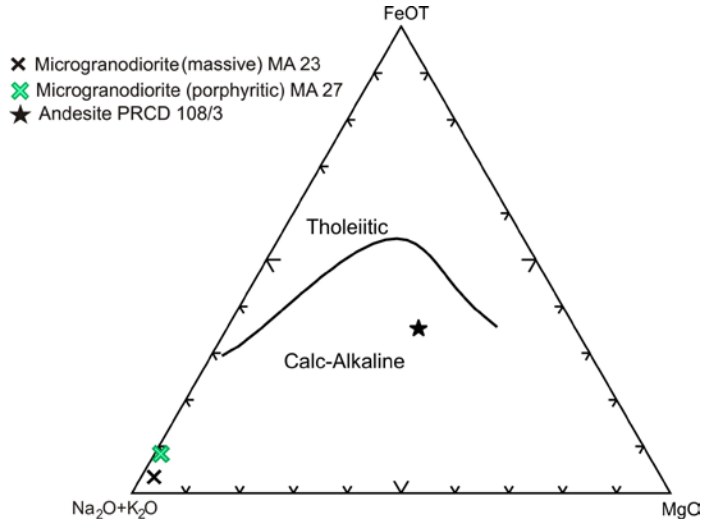

Fig. 4.7. AFM (Irvine and Baragar, 1971) plot for the Yalgoo felsic porphyries.

The felsic porphyries are calc-alkaline, with the two microgranodiorite samples (MA 23, 27) being extremely alkaline, whereas the andesite (PRCD 108/3) falls in the calc-alkaline field (Fig. 4.7).

4.3.1 Major Element Chemistry and Classification of the Felsic Porphyries

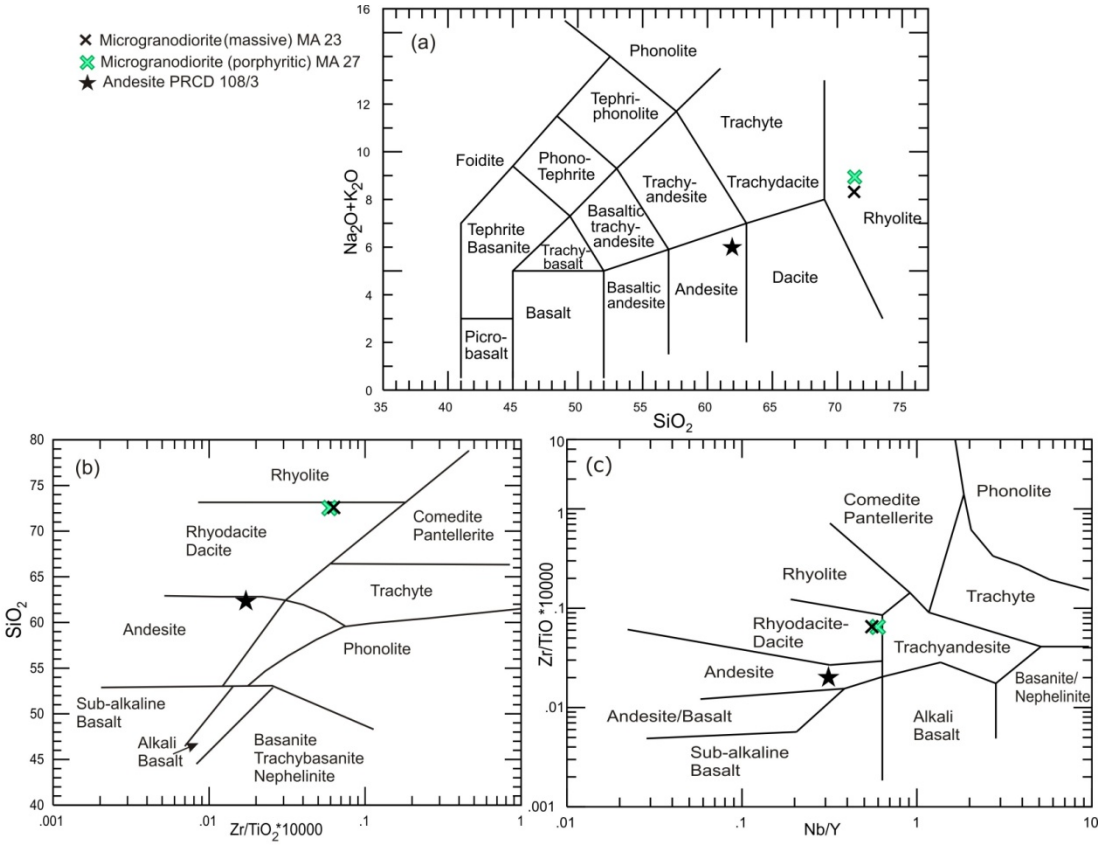

Fig. 4.8. Chemical classification diagrams for the felsic porphyries from north Yalgoo: (a) Total alkalis vs. SiO_2 diagram (Le Bas et al., 1986), (b) SiO_2 vs. Zr/TiO_2 diagram (Winchester and Floyd, 1977) and (c) Zr/TiO_2 vs. Nb/Y diagram (Winchester and Floyd, 1977).

The felsic porphyries were classified using the Na_2O+K_2O vs. SiO_2 (total alkalis silica-TAS) diagram of Le Bas et al, (1986) (Fig. 4.8a) where MA 23 and 27 are classified as rhyolite and sample PDRC 108/3 as andesite. The TAS classification however, contrasts to some extent with the petrographic observations of samples MA 23 and MA 27 where the dominance of plagioclase over K-feldspar indicates a dacitic composition (Table 4.2). Hence, the TAS classification may have been influenced by late addition of silica. To avoid this effect, other classification schemes based on relatively immobile elements, such as SiO_2 vs. Zr/TiO_2 and Zr/TiO_2 vs. Nb/Y (Winchester and Floyd, 1977) were also employed (Fig. 4.8b,c). Samples MA 23 and 27 shifted from the rhyolite to rhyodacite/ dacite fields on both these diagrams (Fig. 4.5b,c) thereby confirming the petrographic observations.

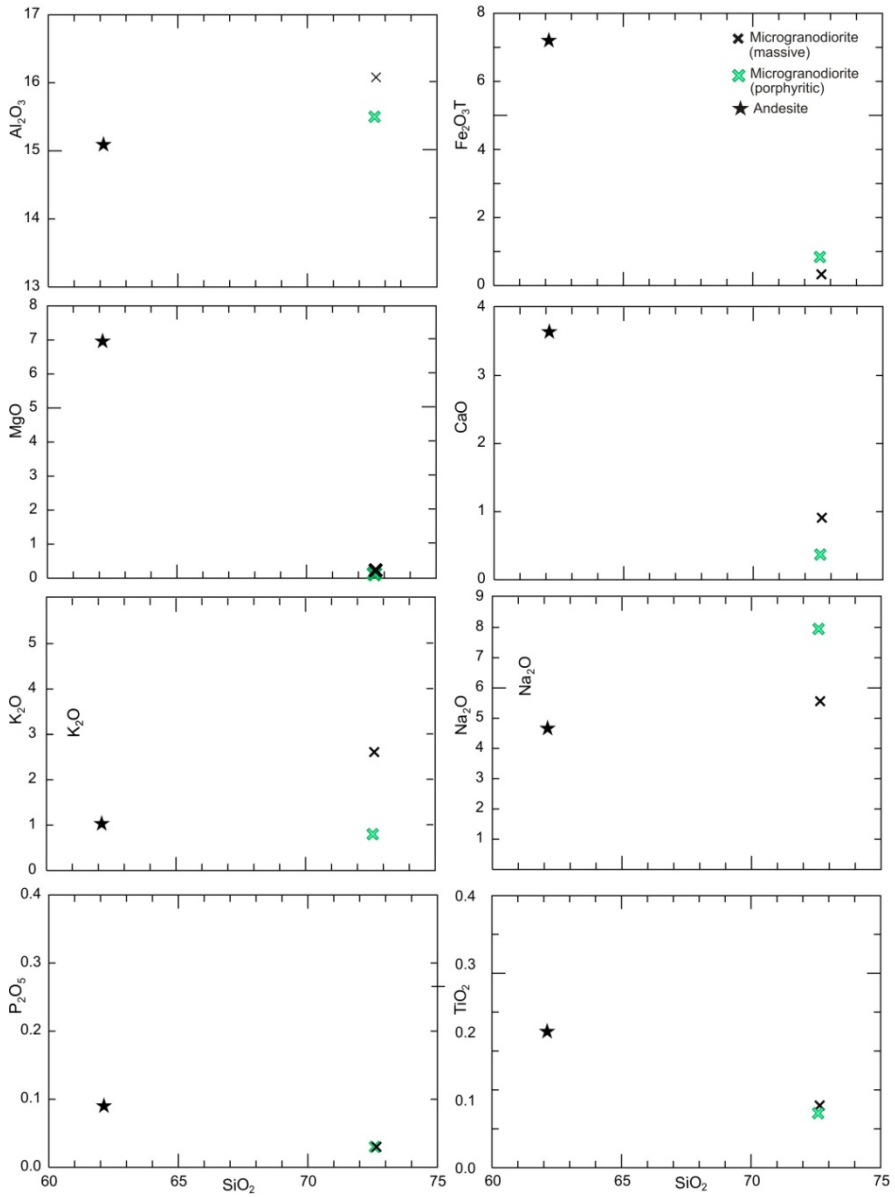

Fig. 4.9 Harker variation plots for major elements in the felsic porphyries.

Both the massive and porphyritic microgranodiorite (samples MA 23 and 27, respectively) have similar SiO_2 (72.65 and 72.59%), TiO_2 (0.26 and 0.24%), Al_2O_3 (16.08 and 15.50%), Fe_2O_3T (0.33 and 0.84%) and CaO (0.91% and 0.37%) contents, with sample MA 27 having slightly higher Na_2O (7.95%) and lower K_2O (0.80%) contents. The MnO, MgO and P_2O_5 contents of these two samples are very low, with no P_2O_5 at the percent level in sample MA 27.

Andesite, on the other hand, has the lowest silica (62.13%) and highest Fe_2O_3T (7.2%) and MgO (6.96%) contents of the three felsic igneous rocks. CaO (3.64%) is also high compared to the microgranodiorites, whereas K_2O, MnO and P_2O_5 are low.

Both samples MA 23 and 27 lie close to each other on most of the Harker variation diagrams (Fig. 4.9) implying a genetic relation. Sample PRCD 108/3 falls far from these two, probably indicating a different origin (see section 4.3.3, 4.3.4).

4.3.3 Trace element Geochemistry

The microgranodiorite samples have higher Ba (1766 and 484 ppm), and Sr (541 and 251ppm) values compared with the andesite (278 and 172 ppm, respectively). Rb content is also variable for the microgranodiorites (91 and 28 ppm), whereas the andesite has 48 ppm which is within the range of the microgranodiorites. The HFSE like Hf, Nb, Ta, Y are generally low (0.2 to 5 ppm) in all the felsic porphyries. The transitional elements Cr (5 and 2 ppm), Ni (2 ppm) and V (21 and 18 ppm) are low in the microgranodiorites; precluding a mantle origin. Andesite on the other hand, recorded the highest values of Cr (244 ppm), Ni (134 ppm) and V (91 ppm) which indicates a less differentiated source.

4.3.3.1 Rare Earth Element Characteristics

The rare earth element (REE) values normalised to chondrite (Sun and McDonough 1989), of the three felsic porphyry samples are shown in Fig. 4.10a. The microgranodiorite samples are strongly fractionated [$(La/Yb)_{CN}$=37-75] with weak negative Eu anomalies. The andesite is less fractionated [$(La/Yb)_{CN}$=6.5] with a concave upward trend and has slightly elevated HREE and shows no Eu anomaly. The pronounced difference in the REE patterns between the microgranodiorites and andesite also suggests two separate magmas.

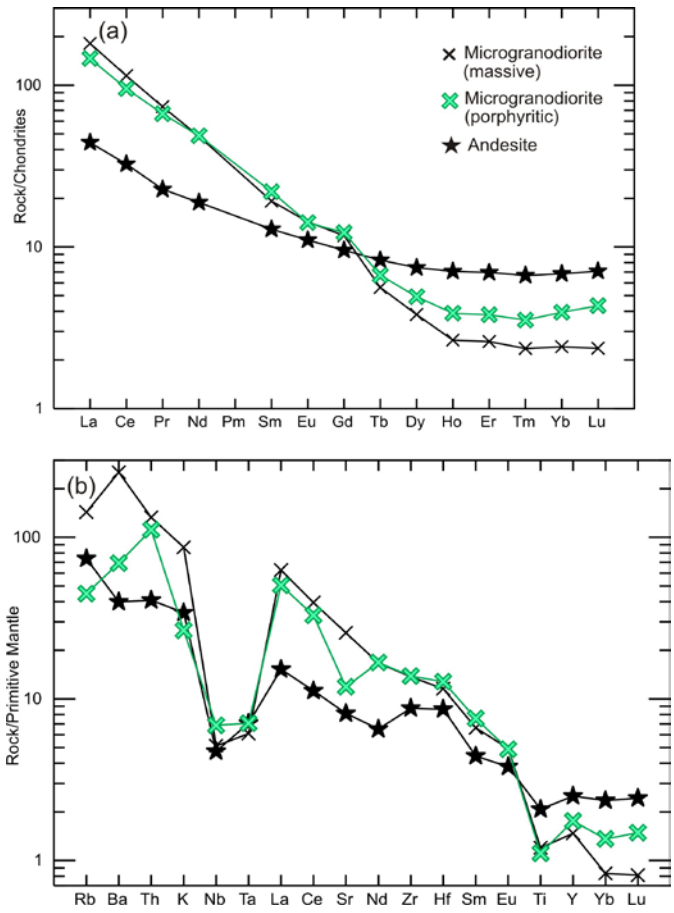

Fig. 4.10. (a) Chondrite-normalized REE patterns; (b) Primitive-mantle (PM) (Sun and McDonough 1989) normalized diagram for the felsic porphyry samples from the Yalgoo area.

4.3.3.2 Incompatible Trace Element Characteristics

The incompatible element values normalised against PM values of the felsic porphyries are presented in Fig. 4.10b. Apart from a negative Sr anomaly displayed by sample MA 27, the microgranodiorite samples show broadly similar patterns with strong negative Nb, Ta, and Ti anomalies and slight differences in incompatible elements. Andesite is characterized by slightly weaker negative Nb, Ta, and Ti anomalies than the microgranodiorites. All the felsic porphyries show enrichment in LILE with slight variations in the degree of enrichment between microgranodiorites and andesite. Microgranodiorites display greater enrichment in Ba and Th than the andesite, whereas Rb and K enrichment of andesite lies between the microgranodiorite samples.

4.3.4 Petrogenesis of the Felsic Porphyries

Microgranodiorite: The microgranodiorite samples have high silica (72.6%), total alkalis (7.17-8.75%) and Al_2O_3 (15.50-16.08%). TiO_2, Fe_2O_3T, MgO, CaO, MnO and P_2O_5 contents are very low, with none > 1%. They have moderate Zr (154-155 ppm), low Y (7-8 ppm), and very low Cr (2-5ppm) and Ni (2 ppm). The low Y and Zr, coupled

with the calc-alkaline trend and LILE enrichment of the microgranodiorite samples, indicate that the they could not have been directly derived by partial melting of primitive mantle, or by crystal fractionation of tholeiitic magma, as interpreted for the Gabanintha Formation felsic volcanic rocks by Watkins and Hickman (1990). In addition, large compositional differences between the mafic and felsic rocks and absence of basaltic andesite in the Yalgoo area imply that the source regions for basalts and microgranodiorites were different. The Sr/Y (31.3 and 80.8) and La/Yb (52 and 105) ratios are moderate to high for the microgranodiorites, necessitating garnet fractionation in the source melt due to deep melting (Moyen 2009). Very low MgO and Ni in microgranodiorites however, negates melt-mantle wedge interaction. Moderate to high Sr/Y ratios in the microgranodiorites might also be the result of a high Sr/Y source component, such as recycled crust, in the subducting slab, as suggested by Moyen (2009).

Andesite: From a single sample in the study area, deciphering the origin of the andesite is difficult as it precludes exploring the trend of important petrogenetic indicators (as discussed above). The andesite is characterized by relatively low SiO_2 (62.13%), high Fe_2O_3T (7.2%), MgO (6.96%), Cr (244 ppm) and Ni (134 ppm). The low LREE/HREE [$(La/Yb)_{CN}$=6.5], Sr/Y (15) and La/Yb (9) ratios suggest an absence of garnet in the source, i.e. melting at relatively low pressure and shallow depth. A detailed overview of similar high-Mg andesite in the Murchison Domain, along with a possible origin for the andesite, is given in section 4.3.5.3.

4.3.5 Comparison with other Felsic Rocks in the Murchison Domain

4.3.5.1 Microgranodiorite

Significant amounts of felsic volcanic and volcaniclastic rocks in the Luke Creek Group are reported from the Upper Gabanintha Formation, the type locality of which is the Gabanintha mining centre, ~250 km northwest of Yalgoo. Here, the formation is composed of intrusive and extrusive ultramafic rocks at the base, overlain successively by interlayered high-Mg and tholeiitic basalt (1100 m thick) and felsic volcanic and volcaniclastic rocks up to 400 m thick. Felsic volcanic rocks are represented mostly by dacite, andesite and minor rhyolite. Since these felsic volcanics are the closest in composition to felsic porphyries in the north Yalgoo area comparison is made in the following paragraphs.

As with the mafic volcanic rocks, chemical analyses of the felsic volcanic rocks of the Gabanintha Formation are also incomplete. It should be mentioned in this regard that none of the analyzed samples were porphyritic/intrusive porphyries. Watkins and Hickman (1990) broadly classified these rocks into low- and high-(Zr+Y) groups. The low-(Zr+Y) group is characterized by ≤207 and 24 ppm Zr and Y, respectively, while the high-(Zr+Y) group has > 212 and 29 ppm Zr and Y, respectively. Both groups show depletion in TiO_2 and Y with increasing SiO_2. The low-(Zr+Y) group samples have variable MgO (0.04-5.18%) and Ni (5-150 ppm), high Cr (65-198 ppm), and Sr (55-504 ppm), and low Nb (5-11 ppm) contents. The high-(Zr+Y) group samples are slightly lower in MgO (0.02-2.56%), Ni (13-80 ppm), Cr (54-61 ppm) and Sr (27-176 ppm), but with similar Nb (6-13 ppm) contents.

Watkins and Hickman (1990) attributed the formation of dacite and rhyolite of the low-(Zr+Y) group to hydrous partial melting of crustal amphibolite, followed by various amounts of crystal fractionation, principally of amphibole. Variations in MgO, Cr, and Ni contents of andesite in the low-(Zr+Y) group were attributed to different degrees of partial melting of the mafic source. Different sub-crustal sources were envisaged for the formation of the high-(Zr+Y) felsic volcanics. Felsic volcanics from the Cuddingwarra traverse (Watkins and Hickman 1990) were considered to have formed from plagioclase-bearing lherzolite. High Cr and Ni contents of the Wydgee high-(Zr+Y) felsic volcanic rocks suggest that they were generated from a more mafic source than the Cuddingwarra rocks (Watkins and Hickman 1990).

The Yalgoo microgranodiorite samples are distinctly different from the Gabanintha Formation felsic rocks, because of their mode of occurrence (as small subvolcanic/porphyry intrusions), their relationships with associated mafic volcanics (intruding and cross-cutting the mafic volcanics) (Figs. 4.1, 4.2) and differences in the Ni, Cr and Nb contents. Felsic volcanic/volcaniclastic rocks interlayered with BIF and cherty BIF are commonly reported from the Golconda Formation (Watkins and Hickman, 1990). In places (Meekatharra-Wydgee greenstone belt), the Gabanintha Formation is also reported to contain thin BIF units interlayered with mafic-ultramafic and felsic rocks (Watkins and Hickman, 1990). The felsic rocks interlayered with the BIF/cherty BIF recorded from drillhole PRCD 108 are similar to the BIF/felsic association (Fig. 4.5) of both the Golconda Formation and the Gabanintha Formation. Therefore, the andesite sample (PRCD 108/3) obtained from drillhole PRCD 108 could be part of either the Golconda Formation or the Gabanintha Formation.

4.3.5.2 Microgranodiorite: Calc-Alkaline High-Level Intrusion

The microgranodiorites of the Yalgoo area most likely represent the same calc-alkaline magma that formed the granodiorites (see chapter 5 for explanation), based on the calc-alkaline trend, the geochemical characteristics, and the occurrence of the felsic rocks as porphyries with cross-cutting relationships,

4.3.5.3 Yalgoo Andesite: Archean High-Mg Andesite in the Murchison Domain?

The silica, alkali, CaO, Ni and Sr contents of the Yalgoo andesite fall within the range of analyses of the andesites from the Wattagee, Wydgee and Reedy traverses by Watkins and Hickman (1990) (Table 4.3). Notwithstanding, the Yalgoo andesite appears unique in the Murchison Domain in having higher MgO, high Cr, and low Nb, V, Y and Zr contents compared to andesites from these three traverses (Table 4.3).

Table 4.3: Comparison of selected chemical compositions of andesites from Watkins and Hickman (1990) with the Yalgoo andesite.

	Wattagee Andesite	Wydgee Andesite	Reedy Andesite	Yalgoo Andesite
	n=6	n=6	n=6	n=1
SiO_2	59.3	60.8	61.4	62.13
TiO_2	1.18	0.71	0.54	0.45
Al_2O_3	16.2	14.2	14.7	15.09
FeO*T	5.60	7.10	5.50	6.48
MnO	0.1	0.09	0.12	0.05
MgO	3.14	4.94	4.73	6.96
CaO	6.7	3.13	5.84	3.64
Na_2O	3.9	5.06	3.43	4.66
K_2O	0.8	0.32	0.94	1.03
P_2O_5	0.28	0.15	0.18	0.09
LOI	2.81	2.67	1.69	0.40
Total	100.01	99.17	99.07	100.98
Fe_2O_3	1.9	2.6	1.1	3.17
FeO	3.87	4.81	4.5	4.03
Ba	299	120	371	278
Co	50	71	47	24.8
Cr	125	189	196	244
Cu	79	45	113	19.2
La	18	nd	19	10.48
Ce	37	nd	32	19.93
Nb	15	8	9	3.4
Ni	82	144	116	134.3
Rb	26	16	47	46.9
Sr	382	78	294	171.8
V	169	120	123	91.2
Y	18	23	16	11.4
Zr	138	171	130	98

Geochemically the Yalgoo andesite has a similar composition to high-Mg andesite (HMA). Kelemen et al. (2003, 2004) defined HMA as andesite having high Mg# (≥0.45)

and SiO_2 (54-64%). Wood and Turner (2009) compiled a list of six primitive HMAs, which are characterized by elevated SiO_2 (54–58 wt %) at high MgO (7–10 wt.%), Mg# =/>0.7 and high total alkalis (3.5–5.2 wt.%). These data are compared with those of the Yalgoo andesite in Table 4.4, which shows the Yalgoo andesite has a good match for most of the elements, except for being slightly enriched in alkalis and low in lime.

Table 4.4: Comparison of the key geochemical characteristics of some primitive HMA (major element oxides in wt.%) and the Yalgoo andesite. Data are taken from Wood and Turner (2009).

Location	White Island, New Zealand	Amphlett Island, Papua New Guinea	Mount Shasta, Cascades	Setouchi belt, Japan	Adak Island, Central Aleutians	Piip volcano, Western Aleutians	Yalgoo greenstone belt, Western Australia
Sample ID	P41600	33629	85-41b	TG1	ADK58	V35-5/5	PRCD 108/3
SiO_2	55.6	54.3	57.9	58.5	56.8	57	62.13
Al_2O_3	13.2	14.8	14.7	13.3	15.5	16	15.09
MgO	10.1	8.7	8.9	9.5	7.4	6.6	6.95
CaO	8.9	7.6	8.1	6.1	8.6	7.7	3.64
Na_2O+K_2O	3.5	5.2	3.9	3.9	4.4	4.8	5.70
Mg#	0.71	0.67	0.74	0.73	0.66	0.72	0.68
Sr/Y	8	32	68	28	33	22	15.00
La/Yb	3.6	–	10.2	9.1	8.8	4.6	9.00

Table 4.5: Compositional ranges of Archean high-Mg/Mg-andesites and the Yalgoo andesite. Data for the high Mg-andesites in the first column are taken from Manya et al. (2007); data for the Mg-andesites in the second column are from Manikymba et al. (2009) and data for the Mg-andesites in the third column are from Polat and Kerrich (2001).

Location	Mousa-Mara greenstone belt, Tanzania	Hutti greenstone belt, India	Wawa greenstone belts, Canada	Yalgoo greenstone belt, (PRCD 108/3) Western Australia
SiO_2 (wt%)	53.8-62.9	58.38-60.44	56.2-63.5	62.13
TiO_2	0.55-0.77	0.82-1.97	0.47-1.81	0.45
Fe_2O_3T	5.35-9.49	9.12-16.56	5.7-9.1	7.2
MgO	2.42-9.47	4.67-6.33	3.4-6.4	6.96
CaO	4.9-8.07	5.14-9.47	5-7.5	3.64
Na_2O	2.68-4.54	2.23-3.03	0.5-2.8	4.66
K_2O	1.21-2.68	0.08-0.15	3-4.8	1.03
Mg#	44-68	38-56	55-64	68
Cr (ppm)	41-387	94-204	110-531	244
Ni	11-108	43-74	21-229	134
Zr	89-157	93-165	81-221	98
Nb	3.75-5.76	4.44-6.42	3.3-12.94	3.4
Ta	0.26-0.43	0.32-0.66	0.16-0.40	0.3
Th	3.5-13.6	1.73-2.42	1.08-6.47	3.5
U	0.85-4.37	0.40-0.64	0.20-1.9	1.1
Y	16.9-25.5	28-45	8.8-21.6	11.4
La	19.8-50.2	5.74-8.53	9.6-61.6	10.5
Ce	42.4-99.5	15.37-22.21	27.8-134.4	19.9
Sm	4.02-7.52	2.30-4.17	2.39-10.8	1.97
Eu	1.12-1.91	0.81-1.53	0.77-2.7	0.64
Yb	1.51-2.23	2.52-4.65	0.78-1.81	1.16
Lu	0.22-0.32	0.38-0.69	0.10-0.24	0.18

Recently, andesites with elevated Mg and Fe contents (referred to as Mg-andesite/high-Mg andesite) have also been reported from several Archean greenstone terranes (see Polat and Kerrich, 2001; Manya et al., 2007; Manikymba et al., 2009). However, the compositional ranges of the Archean HMAs are not so restrictive compared to the primitive HMAs (Table 4.5). The key geochemical features of the single andesite sample

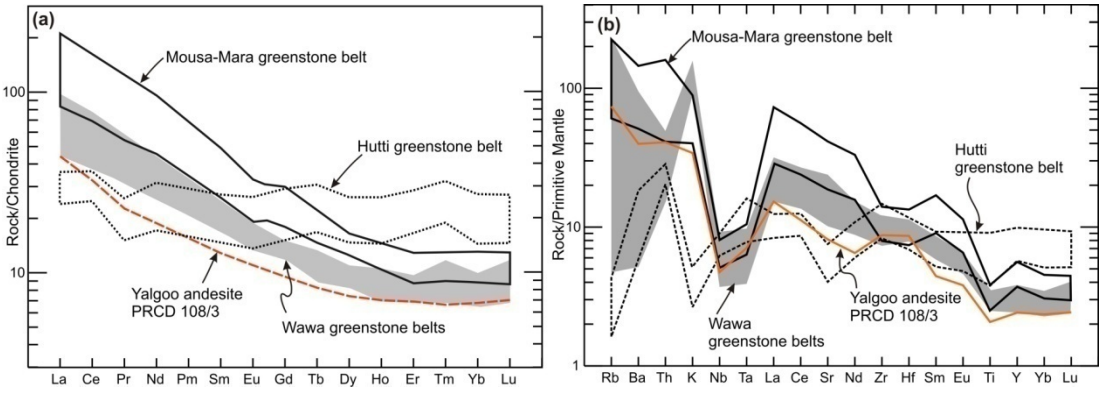

Fig. 4.11. Comparison of (a) Chondrite-normalized REE and (b) Primitive mantle (PM)-normalized incompatible element fields of Archean Mg-/high Mg-andesites and the Yalgoo andesite. Normalizing values are from Sun and McDonough (1989).

(PRCD 108/3) from the Yalgoo area lie within the range of the HMAs from one or more Archean greenstone belts, apart from slight differences in TiO_2, CaO, Na_2O, Sm and Eu contents (Table 4.5). More data are needed on additional samples across the Murchison Domain to get the complete compositional spectrum. The chondrite-normalized REE and PM- normalized incompatible element profiles of the Yalgoo andesite are compared with those of the Archean HMAs from the Mousa-Mara greenstone belt, Tanzania, Hutti greenstone belt, India and Wawa greenstone belt, Canada in Fig. 4.11a,b. Despite showing subtle differences in certain oxides and elements, both the REE and the incompatible trace element profiles of the Yalgoo andesite closely follow those of the HMAs from the Wawa greenstone belt, Canada.

The origin of these HMAs has been a subject of interest for many years (e.g. Kushiro, 1969; Tatsumi, 1981; Hirose, 1997; Grove et al. 2003). Due to their elevated MgO and Mg#, HMA sources are considered near-primary magmas produced in equilibrium with the Earth's mantle, whereas most andesites are derived from basalt magmas via complex and variable processes such as crystal differentiation, crustal contamination, anatexis of pre-existing basaltic crust, and magma mixing (Tatsumi 2006). Experimental work by Kushiro (1969) and Tatsumi (1981) demonstrated that partial melting of peridotite under hydrous conditions can yield melts with HMA compositions. These studies, along with low La/Yb and Sr/Y ratios of the Setouchi HMA, led Tatsumi and Ishizaka (1982) to conclude that hydrous melting of upper mantle peridotite, triggered by direct addition of slab-derived aqueous fluids, can generate HMA magmas in subduction zones. Several experimental studies have indicated that partial melting of peridotite at low pressures and high H_2O content may generate HMA saturated in olivine (e.g. Baker et al. 1994; Wood & Turner 2009). Shellnut and Zellmer (2010) proposed crystal fractionation from a low-H_2O primitive arc basalt in the upper crust as a potential process for the formation

of HMA. Using the reasoning of Zellmer (2009) of 'an elevated surface heat flux resulted from the emplacement of hotter and less hydrous magmas at a shallow level', Shellnut and Zellmer (2010) suggested that under the oxidizing conditions prevalent in arcs, basaltic magmas with relatively low initial H_2O contents will evolve to HMA at lower pressures.

Trace element modelling by Moyen (2009) suggested the low silica adakite/high mg# andesite group can be generated from high-silica adakites (from slab melting) by interaction with the mantle. The REE characteristics of the Yalgoo andesite negate involvement of garnet in its source. The higher SiO_2 and Na_2O contents of 62.13% and 4.66% of the Yalgoo andesite can result from interacting with an enriched crustal component, either by mantle metasomatism or the presence of older crust. The presence of older crust at ~3.0 to 2.94 Ga in the area lends support to an interaction with the latter (see section 4.5).

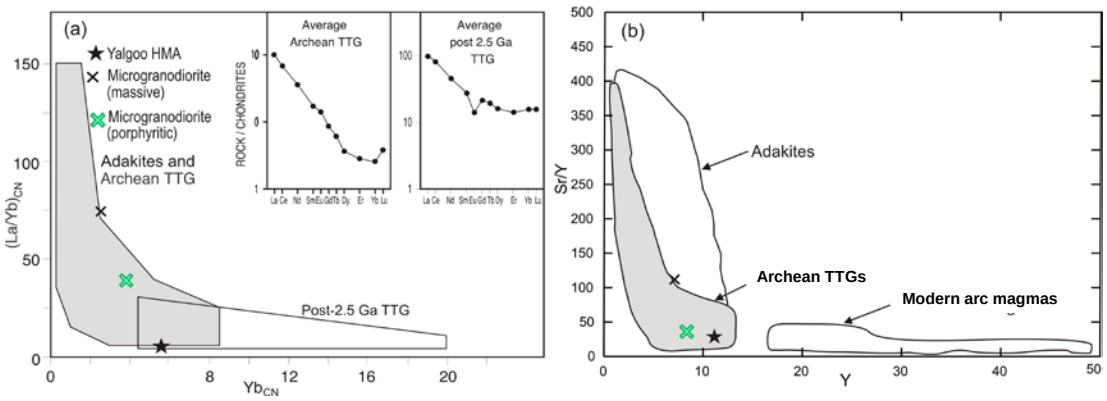

Fig. 4.12. (a) $(La/Yb)_{CN}$ vs. Yb_{CN} plot (Martin, 1986) and (b) Sr/Y vs. Y plot (Drummond and Defant, 1990) of Yalgoo volcanics. "$_{CN}$" denotes chondrite-normalized.

The sample also shows adakitic/Archean TTG signatures in both $(La/Yb)_{CN}$ vs. Yb_{CN} and Sr/Y vs. Y plots (Fig. 4.12a,b), implying the existence of a hot subduction zone allowing the subducted slab to melt rather than dehydrate (cf. Moyen, 2009). Considering the above chemical features, along with high MgO, Ni and Cr, concentrations, it is suggested that the melt of the Yalgoo andesite was derived from a slab within a hot subduction zone followed by interaction with a metasomatized mantle above the stability field of garnet, similar to the models proposed by Moyen (2009), Stern et al. (1996), Beard et al. (1993), Yogodzinski et al. (1995), and Tatsumi and Ishizaka (1982).

Table 4.6: Comparison between chemical composition of the Wydgee andesite and the Yalgoo andesite The composition of andesite sample 83329 was obtained from unpublished GSWA data.

Composition, %	Wydgee Andesite 83329	Yalgoo andesite
SiO_2	62	62.13
TiO_2	0.66	0.45
Al_2O_3	14.4	15.09
FeO*T	6.2	6.48
MnO	0.09	0.05
MgO	4.67	6.96
CaO	3.13	3.64
Na_2O	5.38	4.66
K_2O	0.22	1.03
P_2O_5	0.14	0.09
LOI	2.49	0.40
Total	99.38	100.98
Fe_2O_3	4.04	3.17
FeO	2.4	4.03
ppm		
Ba	107	278
Co	67	24.8
Cr	181	244.0
Ga		15.4
Ge		1.4
Hf		2.7
Li		13.2
Nb	8	3.4
Ni	132	134.3

Composition, ppm	Wydgee Andesite 83329	Yalgoo andesite
Pb		6.4
Rb	14	46.9
Sr	55	171.8
Ta		0.3
Th		3.5
V	113	91.2
Y	22	11.4
Zr	166	98.1
Zn		78.6
La	17.4	10.48
Ce	35.3	19.93
Pr		2.16
Nd	16.5	8.81
Sm	3.55	1.97
Eu	1.14	0.64
Gd		1.96
Tb	0.5	0.31
Dy		1.89
Ho		0.40
Er		1.15
Tm		0.17
Yb	1.59	1.16
Lu	0.24	0.18

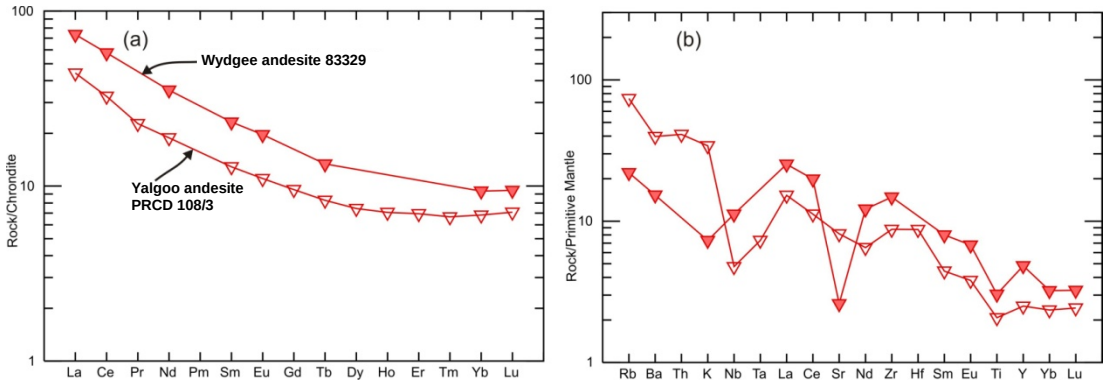

Fig. 4.13. (a) Chondrite-normalized REE patterns and (b) PM-normalized patterns for the Wydgee andesite 83329 and Yalgoo andesite. Both the chondrite and PM values are taken from Sun and McDonough (1989).

Watkins and Hickman (1990) determined Sm-Nd model ages of two andesites (sample 81618 from the Wattagee Hill traverse and sample 83329 from the Wydgee traverse) belonging to the Gabanintha Formation at 2855 and 2886 Ma, respectively. Importantly, the single completely analysed andesite sample obtained from the GSWA unpublished database happens to be the Wydgee andesite 83329. Despite the distance between the Yalgoo andesite and Wydgee andesite, a fair degree of resemblance is noted for SiO_2, FeOT, Na_2O, CaO, Ni, Cr and V (Table 4.6). The REE plot of the Yalgoo andesite also correlates well with that of the Wydgee andesite Yalgoo (Fig. 4.13a). On the incompatible element plot (Fig. 4.13b), the Wydgee andesite shows a similar trend compared to the Yalgoo andesite for the least incompatible elements, but exhibits

enrichment in Rb, Ba, Th and K and is marked by a strongly negative Sr anomaly. The differences were most likely induced by the elevated contents of Th and LILEs, except for the Sr in the Wydgee andesite, which suggests the parental melts for the andesites from these two areas may have been derived from similar sources but underwent different degree of evolution. The MgO content, however, as stated earlier, is notably higher in the Yalgoo Andesite.

4.5 U-Pb Geochronology and Lu-Hf isotopic study of the Porphyritic Microgranodiorite

Zircons from sample MA 27 are prismatic, euhedral in shape and show well-developed magmatic oscillatory zones (Fig. 4.14a,b,c), with some containing light coloured cores bordered by thick zoned rims (Fig. 4.14d). The zircons are from 80 to 150 μm in length, and have an average length to width ratio of >2:1.

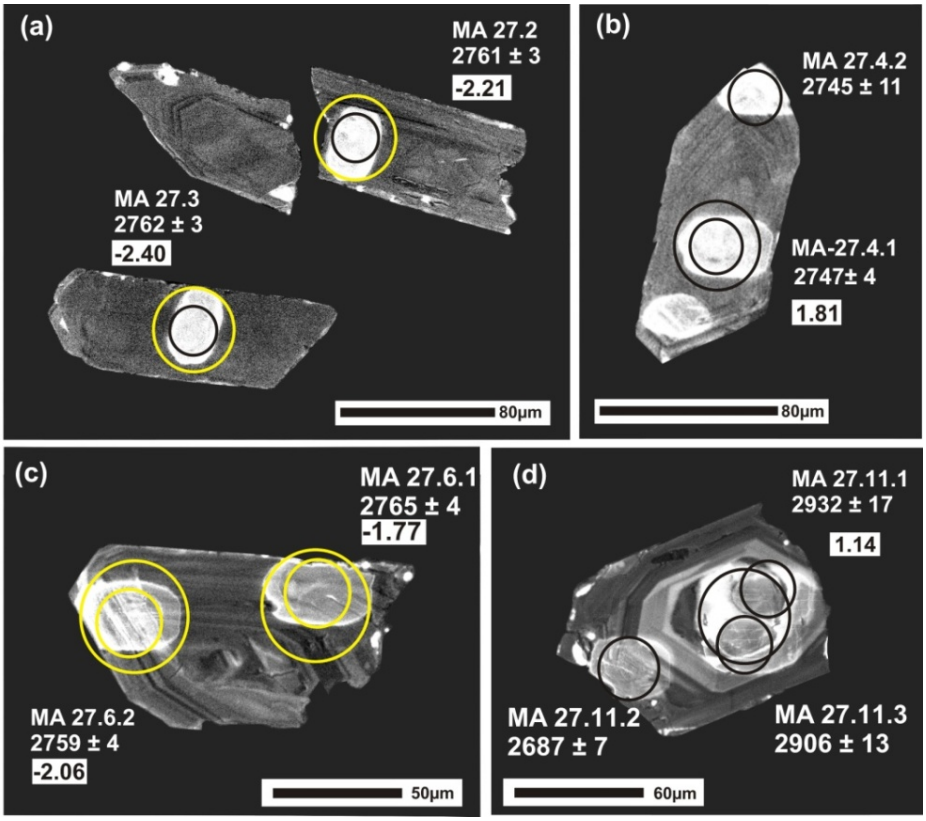

Fig. 4.14 CL images of representative zircons from sample MA 27. Small circles represent sites of SHRIMP analyses, whereas larger circles show sites of Lu-Hf analyses.

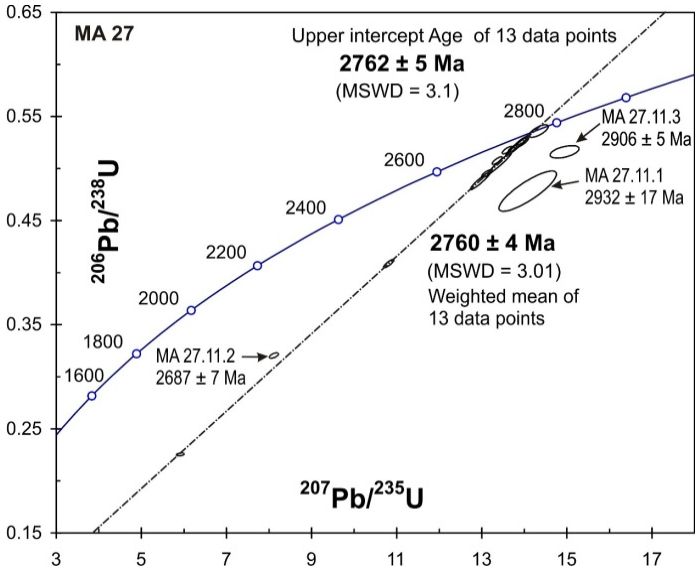

Fig. 4.15. Concordia plot of sample MA 27.

Table. 4.7. U-Pb SHRIMP data for sample MA 27.

Spot	U ppm	Th ppm	Th/U	Rad ^{206}Pb ppm	% comm 206	^{204}Pb /^{206}Pb	^{207}Pb* /^{206}Pb*	% err	^{206}Pb* /^{238}U	±%	^{276}Pb* /^{235}U	±%	^{206}Pb* /^{238}U Age	1σ	^{207}Pb* /^{206}Pb* Age	1σ	% conc
MA 27.1	443	32	0.08	193.3	0.00	0.00000	0.1909	0.2	0.5076	0.3	13.36	0.4	2646	7	2750	3	96
MA 27.2	476	54	0.12	213.6	0.04	0.00003	0.1921	0.2	0.5216	0.7	13.82	0.8	2706	16	2761	3	98
MA 27.3	545	61	0.12	244.4	0.00	0.00000	0.1923	0.2	0.5222	0.8	13.84	0.8	2709	17	2762	3	98
MA 27.4.1	531	63	0.12	236.2	0.07	0.00005	0.1905	0.2	0.5176	0.3	13.60	0.4	2689	6	2747	4	98
MA 27.4.2	1048	3542	3.49	204.6	0.80	0.00059	0.1903	0.6	0.2254	0.2	5.91	0.7	1310	3	2745	11	48
MA 27.5	430	273	0.65	180.7	0.12	0.00009	0.1926	0.2	0.4881	0.7	12.96	0.7	2562	15	2765	4	93
MA 27.6.1	467	141	0.31	210.9	0.04	0.00003	0.1927	0.2	0.5254	0.4	13.96	0.4	2722	8	2765	4	98
MA 27.6.2	427	710	1.72	150.1	0.04	0.00003	0.1919	0.2	0.4087	0.4	10.81	0.5	2209	8	2759	4	80
MA 27.7	330	194	0.61	152.1	0.00	0.00000	0.1940	0.4	0.5360	0.5	14.33	0.6	2767	10	2776	7	100
MA 27.8	425	75	0.18	191.9	0.02	0.00001	0.1921	0.2	0.5249	0.4	13.90	0.5	2720	9	2760	3	99
MA 27.9	484	96	0.21	216.1	0.01	0.00000	0.1918	0.2	0.5196	0.3	13.74	0.4	2697	7	2758	3	98
MA 27.10	451	206	0.47	195.6	0.02	0.00001	0.1927	0.2	0.5048	0.8	13.41	0.9	2634	18	2766	3	95
MA 27.11.1	196	290	1.53	80.7	0.07	0.00005	0.2135	1.1	0.4783	1.7	14.08	2.0	2520	35	2932	17	86
MA 27.11.2	543	1000	1.90	149.7	0.24	0.00018	0.1837	0.4	0.3203	0.3	8.11	0.6	1791	5	2687	7	67
MA 27.11.3	169	110	0.67	75.0	0.04	0.00003	0.2101	0.8	0.5160	0.5	14.95	0.9	2682	10	2906	13	92
MA 27.12	520	398	0.79	221.5	0.03	0.00002	0.1921	0.2	0.4952	0.3	13.12	0.4	2593	6	2760	4	94

% comm 206= amount of common ^{206}Pb in total ^{206}Pb; * = corrected using measured ^{204}Pb; % conc.= [(^{206}Pb/^{238}U age)/(^{207}Pb/^{206}Pb age)] x100

Table 4.8. Hafnium isotopic data for sample MA27. T_{DM2} value is used in the interpretation.

Spot	(t) Ma	^{176}Yb/^{177}Hf	^{176}Lu/^{177}Hf	^{176}Hf/^{177}Hf	2σ	εHf(0)	εHf(t)	T_{DM1}	T_{DM2}	$f_{Lu/Hf}$
MA 27.1	2750	0.027212	0.001049	0.281037	0.000034	-61.37	-1.55	3087	3511	-0.97
MA-27.2	2761	0.031785	0.001168	0.281018	0.000024	-62.05	-2.21	3122	3574	-0.96
MA-27.3	2762	0.044245	0.001427	0.281025	0.000033	-61.77	-2.40	3133	3591	-0.96
MA 27.4.1	2747	0.152362	0.003529	0.281263	0.000045	-53.35	1.81	2971	3219	-0.89
MA 27.5	2765	0.054328	0.001672	0.281005	0.000030	-62.49	-3.52	3181	3690	-0.95
MA 27.6.1	2765	0.029872	0.001102	0.281024	0.000028	-61.83	-1.77	3109	3539	-0.97
MA 27.6.2	2759	0.017822	0.000631	0.280995	0.000023	-62.85	-2.06	3110	3560	-0.98
MA 27.7	2776	0.061558	0.001947	0.280968	0.000053	-63.80	-5.10	3256	3833	-0.94
MA 27.8	2760	0.061004	0.001799	0.281048	0.000047	-60.98	-2.33	3133	3585	-0.95
MA 27.9	2758	0.052395	0.001532	0.281025	0.000026	-61.77	-2.68	3142	3613	-0.95
MA 27.10	2766	0.064850	0.001980	0.281077	0.000032	-59.93	-1.49	3107	3516	-0.94
MA 27.11.1	2932	0.013294	0.000481	0.280965	0.000030	-63.91	1.14	3138	3403	-0.99
MA 27.12	2760	0.076044	0.002113	0.281086	0.000038	-59.64	-1.57	3107	3520	-0.94

Isotopic data were collected during a single analytical session with a total of 16 analyses completed on 12 crystals. The error of the mean Pb/U calibration constant determined from 10 analyses of the CZ3 standard was 0.40% (2σ). Results are listed in Table 4.7.

The U contents vary from 169 to 545 ppm (average 429 ppm), while Th contents have a large range from 32 to 1000 ppm (average 229 ppm). An exception is site MA 27.4.2 with the highest U and Th values of 1048 and 3542 ppm, respectively, probably a metamict grain. Apart from the four most discordant analyses (MA 27.4.2, 27.6.2, 27.11.1, 27.11.2), Th/U ratios are between 0.08 and 0.79.

On a concordia plot (Fig. 4.15), thirteen of the sixteen data points fall on a discordia line, indicating different degrees of recent Pb loss. The oldest age of 2932 ± 17 Ma was obtained from the core (MA 27.11.1) of a single grain (Fig. 4.14d). A second analysis (MA 27.11.2) was also attempted that overlaps with part of the rim, giving a slightly younger age of 2906 ± 13 Ma. The rim (MA 27.11.3) recorded an age of 2687 ± 7 Ma,but is extremely discordant and likely disturbed. The upper intercept of the thirteen data points gives an age of 2762 ± 5 Ma (MSWD = 3.1) (Fig. 4.15). The weighted mean $^{207}Pb/^{206}Pb$ age of the same data points is almost identical at 2759 ± 4 Ma (MSWD = 3.01) within error. Therefore, 2762 ± 5 Ma (MSWD = 3.1) is taken to record the emplacement age of the porphyritic microgranodiorite. The oldest $^{207}Pb/^{206}Pb$ age of 2932 ± 17 Ma is interpreted as the age of crystallization of a xenocryst derived from older felsic crust (see Chapter 8 for discussion).

Lu-Hf data were collected from thirteen analytical sites (Table 4.8). Apart from site MA 27.4, the Lu-Hf data of the remaining zircons are closely clustered. The $^{176}Hf/^{177}Hf$ ratios vary between 0.280965 and 0.281086. The εHf(t) values are mostly moderately –ve to weakly +ve ranging from -5.10 to 1.81 suggesting an enriched crustal reservoir containing some depleted mantle component. Site MA 27.4.1 recorded an anomalously high $^{176}Hf/^{177}Hf$ ratio of 0.281272 along with the highest εHf(t) value of 1.81 and the youngest T_{DM2} age at 3219 Ma, suggesting that the Lu-Hf system of this grain has been disturbed. Site MA 27.13 (2.93 Ga) is the xenocryst has a $^{176}Hf/^{177}Hf$ ratio of 0.280965, records an εHf(t) value of 1.14 and a younger T_{DM2} age at 3403 Ma, indicating derivation from a fairly depleted younger source. The T_{DM2} model ages for most (11 out of 13) of the analyses are between 3511 to 3833 Ma, suggesting the porphyritic microgranodiorite was derived from an evolved source which had been extensively recycled over 300 Ma and has a minimum age of 3.5 Ga.

4.6 Tectonic Setting

The Th–Hf–Nb diagram of Wood (1980), has recently been applied to the Archean volcanic rocks (Manya and Maboko, 2008). This diagram is preferred to infer tectonic setting for felsic as well as intermediate to mafic rocks (Fig. 4.16), since it effectively separates N-MORB from volcanic arc basalts and rocks of tholeiitic affinity from those with calc-alkaline affinities. Both microgranodiorites and andesite plot exclusively in the volcanic arc field with calc-alkaline affinities, with a significant compositional gap to the mafic volcanic rocks.

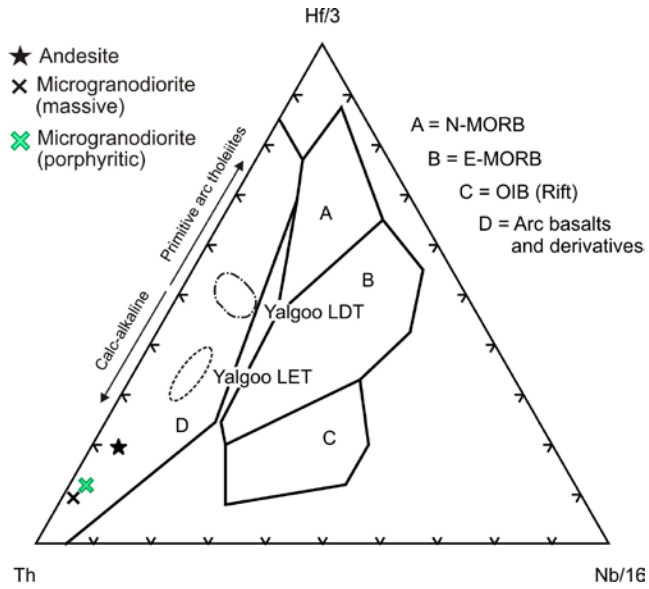

Fig. 4.16. Th–Hf–Nb plot of Wood (1980) for the felsic porphyries of the Yalgoo area.

ratio ≥2:1. Many zircon grains have thin oscillatory zones of magmatic origin, with a few having more homogenous central portions with/without a seam of CL light material forming an internal zone (Fig. 5.15b,d,e,f). This seam may overprint the primary zoning, similar to that described by Pidgeon (1992) and Pidgeon et al. (1998) (Fig. 5.15e). Only one zircon crystal shows core-rim structure (Fig. 5.15f).

Chapter 5 Nature and Genesis of the Granitoid Rocks in the Yalgoo Area

5.1 Nature and distribution of the granitoid rocks

Three granitoids of small dimension (~5 to 6 km^2) in area intruded the volcanic package of the study area, in the west, east and northern parts (Fig. 5.1). The present study attempts to provide a comprehensive account of these granitoids with an integrated approach using petrology, geochemistry, zircon U-Pb SHRIMP geochronology and a Lu-Hf isotopic study. A total of 19 samples, including 18 from surface outcrop and a single sample from drillhole PRCD 108 in the Melville area, were collected (Fig. 5.1). A total of 53 petrographic thin sections were made and 14 samples were selected for whole-rock geochemical studies. Based on the availability of zircons, U-Pb SHRIMP and subsequent Lu-Hf isotopic studies were carried out on 10 samples.

Watkins and Hickman (1990) did not study the Yalgoo granitoids. Oliver (1999) conducted petrographic, geochemical and limited geochronological studies on certain Yalgoo granitoids ("Noongal granitoids" in his study). A comparison with his study is made in section 5.6.

5.1.1 Lady Lydia Granite

The Lady Lydia granite (LLG) is composed of light grey, fine- to medium-grained, massive to weakly foliated leucogranite with local porphyritic phases, especially at Lady Lydia South (Fig. 5.1). A thin veneer of alluvium covers much of the LLG. Samples were collected from two locations, namely: i) Brilliant Open Pit at the northern end and ii) Lady Lydia South (LLS) at the southern end. Brilliant Open Pit is the only location where mutual phase relations can be studied on both walls of the pit. Field observations of the LLG are almost entirely based on studies made in this pit, therefore, a detailed account is provided in subsection 5.1.1.1. Lady Lydia South is poorly exposed, except for remains of historical trenches, many of which are now filled up. Granitoid samples were collected from the float around the trenches.

5.1.1.1 Geology of the Brilliant Open Pit

The Brilliant Open Pit is situated at the northern edge of the LLG. The pit trends 137° and is about 120m long, 20m wide and 15m deep (Fig. 5.2a,b). Three distinct granitic phases were identified in the pit: massive granodiorite (sample MA 9), porphyritic

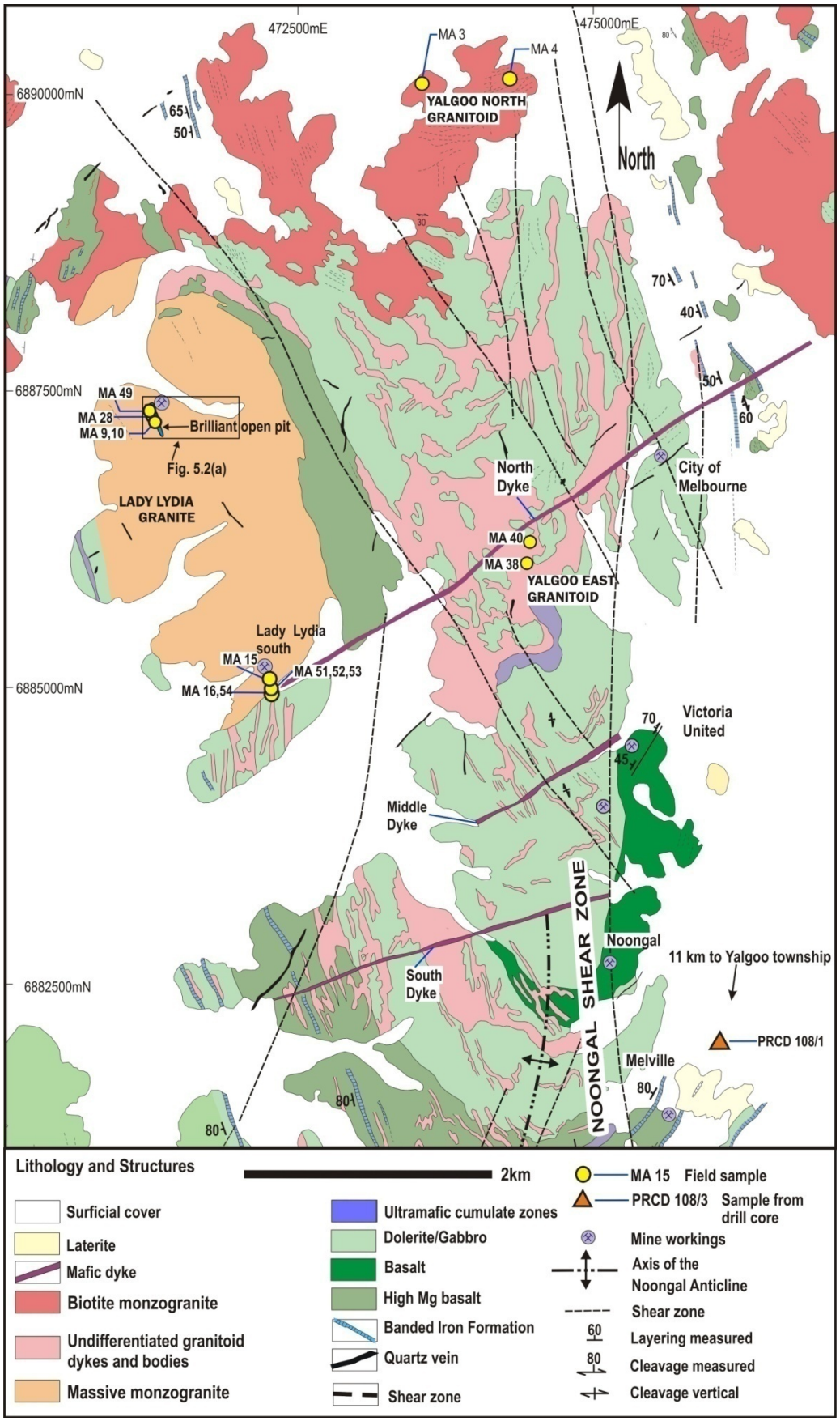

Fig. 5.1. Geological map of the north Yalgoo area showing major locations of granitoid samples (From Hallberg et al., 2002, modified after Watkins and Hickman, 1990).

granodiorite (samples MA 6 and 10), and a fine-grained biotite hornblende monzogranite (sample MA 28). The first two occur in the middle part of the pit, whereas the host rock to mineralization, sample MA 28, occurs at the northern end and extends up to the west wall of the southern end of the pit. Contacts between these three phases are complex and clear only in a few places. A narrow mylonitic contact is observed between samples MA 28 and MA 6 on the east wall (Fig. 5.2c). On the west wall near the northern entry the contact between these two phases is more complex where slivers/enclaves (?) of biotite hornblende monzogranite are included within deformed porphyritic granodiorite (Fig.5.2d,e). From the field relations and occurrence of gold-bearing quartz-pyrite veins, the reported 'mafic granulite' in Holden (2004) appears to be the biotite hornblende monzogranite. Holden (2004) considered the 'mafic granulite' to form large mafic xenoliths, which also suggests it might represent a roof pendant caught up in the granodiorite during ascent (Lyle Thorne-Prosperity Geologist, personal communication 2004). Pegmatite dykes of various dimensions and mineralized quartz veins are common on the west wall. The differences on both sides of the pit have resulted from the removal of part of the mineralized shear zone. Flat-dipping sheet joints are observed in the pit dipping at low angles both to the east and west (Fig. 5.2g). A 090° trending fault transects the pit, with development of slickensides.

Two generations of pegmatites are identified in the pit. An early, thin (2-4 cm wide), locally ptygmatic, pegmatite dyke (146º/86W) is cut by a late massive (099º/64E) pegmatite dyke (Fig. 5.2f). The latter is locally boudinaged, and ranges from 15cm to 2-3m in width and occurs over a distance of ~30 metres. Both generations of pegmatite post-date mineralization, as they dissect mineralized quartz veins (Fig 5.2f). Details of the quartz veins in the pit are presented in section 7.1.2.

From the field relationships, as revealed from the pit walls, the order of emplacement of the granitoid phases is difficult to ascertain. Some equivocal contact relationships have been observed between biotite hornblende monzogranite and porphyritic granodiorite (Fig. 5.2c,d,e). This complex relationship can be interpreted in at least two ways. Observing the exposure on the west wall, biotite hornblende monzogranite appears to represent slivers of an earlier granitoid phase, or xenoliths, within porphyritic granodiorite, as suggested by Holden (2004). Alternatively this may well be interpreted as part of a dyke/plug through the LLG, as proposed by Dale and Goldrick (1994), which has been tilted and developed a complex intrusive contact during subsequent shearing.

Fig. 5.2. Photographs of the Brilliant Open Pit, north Yalgoo area. (a) Aerial view of Brilliant Open Pit (Google Maps, 2012). (b) Brilliant open pit from northern entry. (c) Mylonitized contact between biotite hornblende monzogranite and porphyritic granodiorite (east wall). (d) and (e) Complex intrusive relationship between biotite hornblende monzogranite and porphyritic granodiorite. (f) Massive 099º/64E trending pegmatite dyke cuts across 146º/86W trending thinner ptygmatic pegmatite vein. Note the dilatational displacement at the intersection (west wall). (g) Flat dipping joints and fault plane on the west wall.

The fine-grained texture of the biotite hornblende monzogranite could have resulted from rapid emplacement into the already solidified or near-solidified granodiorite. The mylonitized contact between biotite hornblende monzogranite and porphyritic granodiorite is indicative of ductile deformation, which may be associated with the formation of the NS to NNW trending Noongal shear zone. If the second interpretation is valid, it implies the biotite hornblende monzogranite post-dates the granodiorite and may have been emplaced as a high/mid level intrusion or dyke. Results of SHRIMP U-Pb geochronology and geothermobarometry from EPMA studies might help to resolve this puzzle (this is discussed in sections 5.5.1 and 7.3.1).

5.1.2 Yalgoo East Granitoid

The Yalgoo East granitoid (YEG) crops out to the east of the LLG as a few hillocks protruding through the mafic-ultramafic greenstone sequence in the central-northern part of the study area (Fig. 5.1). The rock is different from the LLG in having an overall pale yellowish brown colour (Fig. 5.3a). The largest hillock extends over ~2 km^2 and forms a whaleback exposure, with discrete small boulders scattered all over it. The granite is weathered, buff-coloured and strongly foliated in the south along the border with the mafic/ultramafic rocks (Fig. 5.1). Sample MA 38 was collected within 30 metres of the contact with basalt. In the central part, the granite is more massive and shows spheroidal weathering (Fig. 5.3a). A small zone of jointed and brecciated quartz, 3-5 metres long and 1.5 metres wide, trends 245° through the outcrop about 30m north east of the location of sample MA 38. Sample MA 40 was obtained from the central part of the outcrop and is a massive to weakly foliated, fine- to medium-grained rock. Field observation revealed the outcrop of YEG is less extensive and more discontinuous than shown on the maps of both Watkins and Hickman (1990) and Hallberg et al. (2002).

5.1.3 Yalgoo North Granitoid

The Yalgoo North granitoid (YNG) is the northernmost granitoid (Fig. 5.1). The outcrop is composed of weathered, dark brown hillocks surrounded by large boulders, cut by pegmatite dykes (Fig. 5.3b,c). Oliver (1999) mentioned an east-west oriented dyke within the granitoid on the northern edge of the YNG. However, no account of the lithology of the dyke was provided. The granitoid consists entirely of coarse-grained, foliated biotite monzogranite, which does not show significant variation. Samples MA 3 and 4 were collected from the central part of this granitoid (Fig. 5.1).

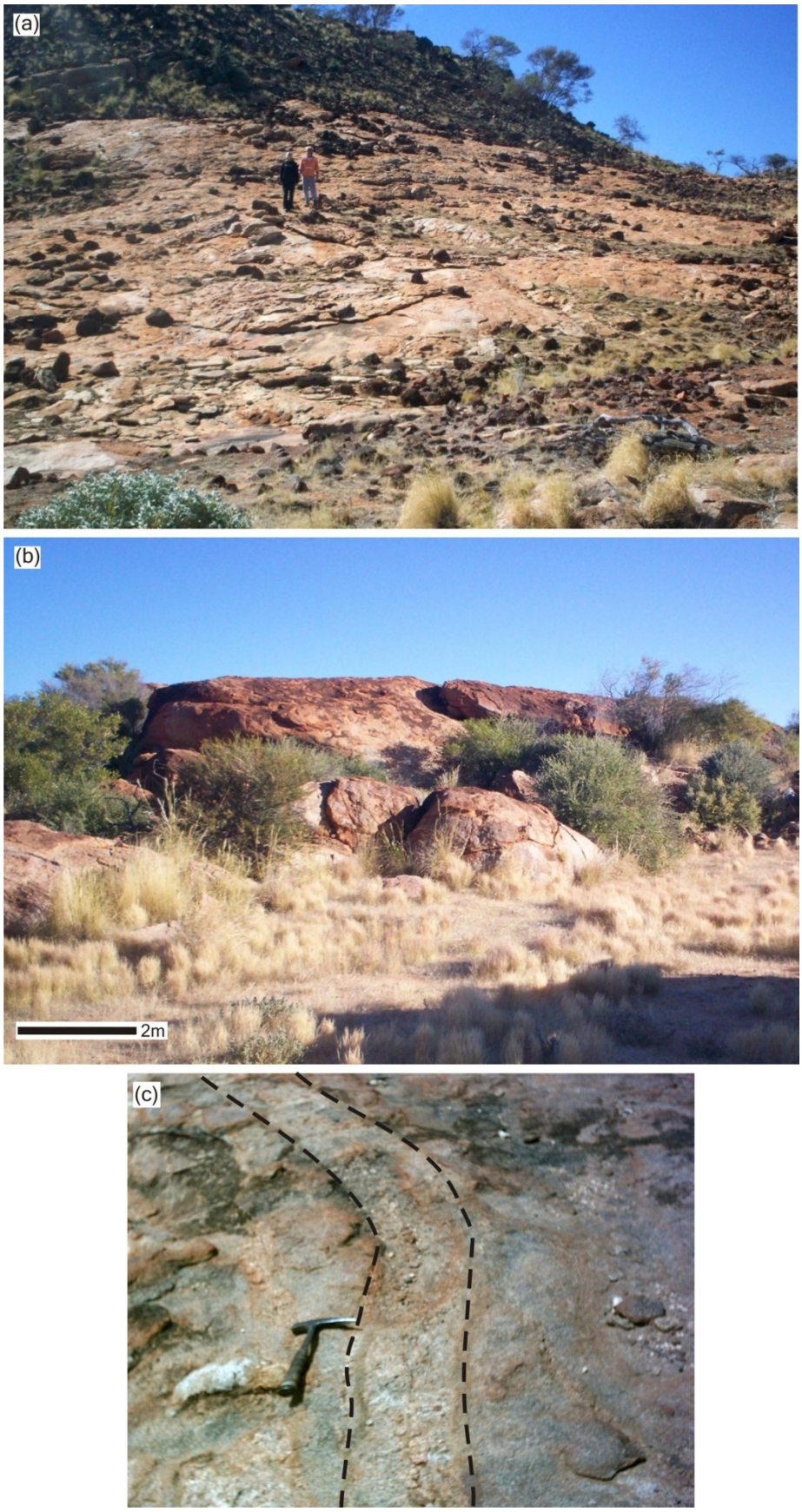

Fig. 5.3. Exposures of (a) Yalgoo east granitoid and (b) Yalgoo north granitoid in the Yalgoo area. (c) Pegmatite dyke, outlined by broken black lines, within the Yalgoo north granitoid. Hammer is 32cm long.

5.2 Petrography and Classification of the Granitoids

Three major granitoid types were distinguished in the area and are listed in Table 5.1, based on the modal quartz, K-feldspar and plagioclase contents of the samples (QAP classification: Streckeisen, 1976). Most of the granitoids are medium- to coarse- grained, therefore modal composition of the rocks was obtained by point counting with a reasonable degree of confidence (Table 5.2). Mineral abbreviations used in the photomicrographs follow the nomenclature scheme as outlined by Kretz (1983) and Spear (1993).

Table 5.1. Granitoid types identified in the north Yalgoo area.

Serial no.	Granite type	Sample no.	Granitoid/area
1)	Massive to microporphyritic granodiorite		
	i) Massive granodiorite	MA 9,52,53	LLG
	ii) Porphyritic granodiorite	MA 6,10,49,51,54,56 MA 38,40	LLG YEG
	iii) Microporphyritic granodiorite	MA 15,16, 55 PRCD 108/1	LLG Melville
2)	Biotite hornblende monzogranite	MA 28	LLG-Brilliant open pit
3)	Biotite monzogranite	MA 3,4	YNG

Petrographic study reveals most of the rocks from the LLG, YEG and Melville areas are granodiorite, with only three samples from LLG and YNG (MA 28, 3 and 4) classified as monzogranite on the modal QAP plot (after Streckeisen, 1976) (Fig. 5.4). Where appropriate, the name of the prominent accessory mafic mineral is used as a prefix. Strong differences in texture, however, and the amount of accessory minerals, necessitate classifying the monzogranites (see section 5.2.2.1, 52.2.2) as two different types: biotite hornblende monzogranite and biotite monzogranite. Therefore the granitoid samples from the Yalgoo area are considered to consist of three rock types, which are: i) granodiorite, ii) biotite monzogranite and iii) biotite hornblende monzogranite. Granodiorite varies from massive through porphyritic to microporphyritic in texture. However, the distinction between the porphyritic and microporphyritic varieties is commonly gradational. In the present study, the rocks with small grains (<.05mm) in a quartz-feldspar groundmass with distinctly coarser phenocrysts are considered to be porphyritic, whereas those with a groundmass showing a seriate range (very fine, ~0.02 to medium 0.5mm) and coarser phenocrysts are termed microporphyritic.

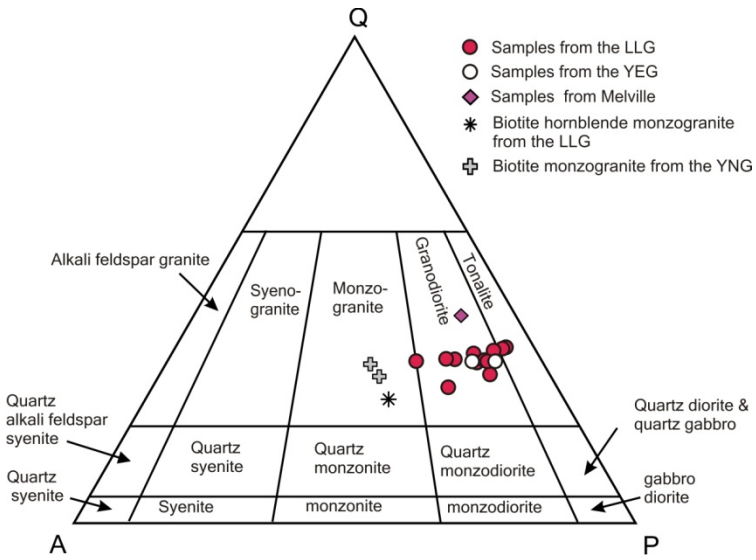

Fig. 5.4. Modal QAP plot of the granitoid samples from the Yalgoo area (after Streckeisen, 1976).

Table 5.2. Modal composition of the granitoid samples from the north Yalgoo area. tr = trace.

Minerals	Massive granodiorite			Porphyritic granodiorite							
	MA 09	MA 52	MA 53	MA 06	MA 10	MA 49	MA 51	MA 54	MA 56	MA 38	MA 40
Quartz	32.3	32.2	28	35.3	29.8	31.6	31.6	33.3	32.8	32.3	35.2
Alkali-feldspar	10.9	15.5	19	7.1	10	7.7	21.1	15.8	10.4	10.7	6
Plagioclase	53.4	46.9	51	56.6	57.3	55.5	41.6	50.3	50.2	51.3	53.8
Amphibole				tr	tr	0.1	0.1			0.4	
Biotite	2.3	3.6	2	0.7	1.9	3.2	1.7	0.8	3.1	3.9	3.8
Chlorite		tr								0.1	
Epidote	1	0.5	tr		0.5	0.8	1.8	0.5	1.9	1.2	1.8
Secondary mica	0.1	0.4				tr	1.3	0.1	0.7		
Titanite		0.5	0	0.4	0.2	1.1	0.5		0.3		0.4
Calcite				tr	0.4				tr		
Opaque and/or Fe oxide		0.5	0		tr	1	0.3	0.2	0.6	0.2	
Apatite	tr			tr		tr	tr		tr		
Zircon	tr	tr	tr	tr	tr	tr	tr		tr		tr
Total	100.0	100.0	100.0	100.0	100.0	100.0	100.0	100.0	100.0	100.0	100.0
Number of points	7547	6353	Estimation	5696	7838	4808	5280	3020	6419	6554	2318

Minerals	Microporphyritic granodiorite				Biotite hornblende monzogranite	Biotite monzogranite	
	MA 15	MA 16	MA 55	PDRC 108/1	MA 28	MA 03	MA 04
Quartz	33.1	42.6	30.8	33	23.4	29.7	26.9
Alkali-feldspar	9.4	9.4	9.4	8	25.5	28.2	26.5
Plagioclase	55.7	47.4	51	51	35.7	33.4	35
Amphibole			0.1		5.4	0.1	0.5
Biotite	1.2	0.6	5.2	3	6.1	8.2	10.7
Chlorite			1.43		tr	tr	tr
Epidote	0.3		0.8	5.5	2.5	0.4	0.5
Secondary mica	tr		1.5				
Titanite	0.2		0.3		1.4		
Calcite					0.3		
Opaque and/or Fe oxide	0.1	0.1	0.5	0.5	1.9		
Apatite	tr	tr		tr	tr		
Zircon	tr	tr	tr		tr	tr	tr
Fluorite						tr	tr
Total	100.0	100.0	100.0	100.0	100.0	100.0	100.0
Number of points	6033	6305	2404	Estimation	4344	7700	7451

5.2.1 Granodiorite

5.2.1.1 Massive Granodiorite

The massive granodiorites were obtained from the LLG and are represented by samples MA 9, 52 and 53. They are leucocratic, grey, massive fine- to medium-grained in hand specimen. They have an allotriomorphic granular texture. Major minerals are quartz, plagioclase and K-feldspar, with minor biotite, titanite and opaque minerals. Chlorite, sericite and epidote are the common secondary minerals. Quartz is generally 0.4-2mm in diameter and crystals are locally strained and show sub-grain development (Fig. 5.5a). Plagioclase (An_{22-30}) forms large (0.4-4mm) subhedral crystals that are variably sericitized, although saussuritized crystals with the development of globules of epidote occur locally. Microcline (0.4-2mm) is free of alteration. Biotite (0.1-1mm) forms small laths and is strongly pleochroic, with local alteration to patchy brownish-green chlorite. Epidote (0.06-0.5mm) forms irregular granules and blebs and is strongly pleochroic (X=pale yellow, Y=yellow green and Z=pale green). Patches of a yellowish-brown fibrous micaceous mineral locally transects biotite, quartz and feldspar. Dark brown titanite (0.04-0.08mm) is sparsely distributed throughout the rock and is also locally found in association with biotite.

5.2.1.2 Porphyritic Granodiorite

These rocks were collected from the LLG and are represented by the samples MA 6, 10, 49, 51, 54 and 56. They show a leucocratic, fine- to medium-grained porphyritic texture. In thin section, they have a massive to weakly foliated texture with quartz, plagioclase and microcline phenocrysts set in a fine-grained groundmass of largely recrystallized quartz and feldspar (Fig. 5.5b,c). These rocks, apart from the porphyritic textures, have identical mineral constituents to the massive granodiorite samples, with the exception of traces of calcite in a few samples (MA 6, 10, 56). Plagioclase is strongly sericitized, whereas quartz occurs both as large anhedral crystals and in the groundmass (Fig. 5.5b). Streaks of biotite-chlorite wrap around recrystallized quartz and coarser plagioclase to form a discontinuous foliation in sample MA 51: this also has the highest amount (~21%) of K-feldspar.

5.2.1.2.1 Porphyritic Granodiorite from the Yalgoo East Granitoid

Two porphyritic granodiorite samples MA 38 and 40 were obtained from the YEG. These rocks differ slightly from the LLG porphyritic granodiorite samples in having a more persistent foliation, higher biotite and epidote contents and the presence of rutile in sample MA 40. Sample MA 38 is slightly more foliated and porphyritic than MA 40, whereas the

latter is fine- to medium- grained allotriomorphic (Fig.5.4d) to locally porphyritic in texture. Conspicuous dark red granular to rectangular rutile occurs in association with epidote and also as isolated crystals.

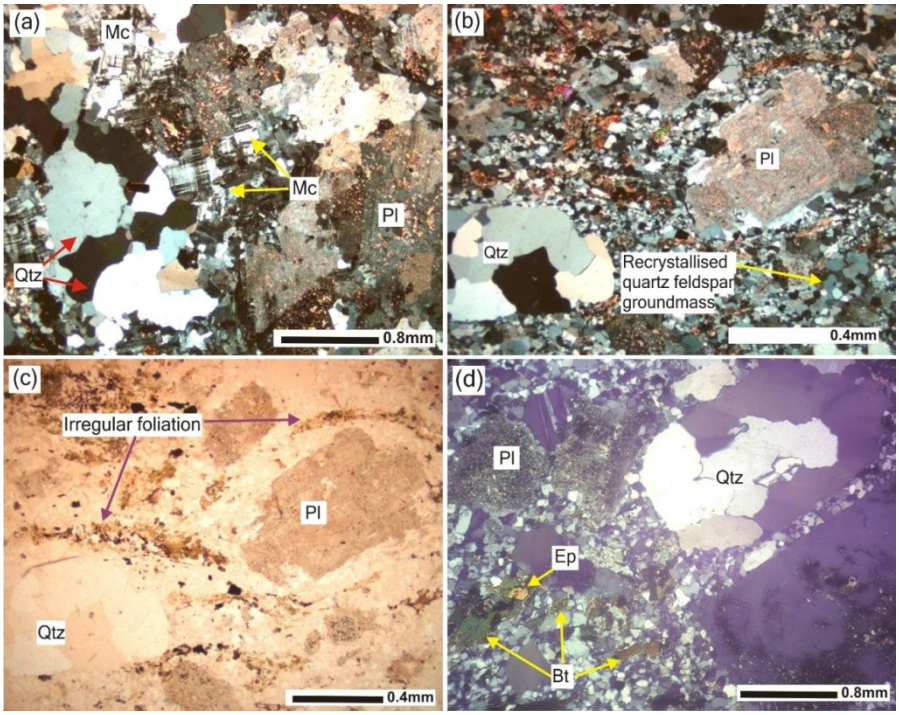

Fig. 5.5. Selected photomicrographs of granodiorites from the Yalgoo area. (a) Allotriomorphic granular texture with moderately sericitized plagioclase (Pl), fresh microcline (mc) and granular and partially recrystallized quartz (Qtz) (MA 52, xpl). (b) Strongly sericitized plagioclase and quartz phenocrysts set in a fine-grained granular groundmass of quartz and feldspar (MA 51, xpl). (c) Fine streaks of biotite wrap around the coarser crystals resulting in a discontinuous foliation. Same area as in (b), under ppl). (d) Microporphyritic texture formed by recrystallized quartz and sericitized plagioclase phenocrysts in a granular quartz-feldspar groundmass. Other minerals shown are biotite (Bt) and epidote (Ep) (MA 38, xpl).

5.2.1.3 Microporphyritic Granodiorite

Three samples (MA15, 16, 55) were collected from around a trench at Lady Lydia South (Fig. 5.6a), whilst a fourth (PRCD 108/1) was obtained from drill core from the Melville area (Fig. 4.5). Samples MA 15 and 55 are leucocratic, fine- to medium-grained and porphyritic, whereas MA 16 is mesocratic and weakly microporphyritic. A distinct cuspate boundary is noted between samples MA 15 and 16 in the field, indicating coeval emplacement of these two phases (Fig. 5.6b). The drill core sample PRCD 108/1, like sample MA 16, is mesocratic and shows a microporphyritic texture. All four samples consist of quartz and plagioclase, with minor K-feldspar, amphibole, biotite, epidote, titanite and opaque minerals. Under the microscope, samples MA 15, 55 and PRCD 108/1 are strongly microporphyritic, containing from ~40% to ~55% phenocrysts compared to the weakly microporphyritic sample MA 16 (~15% phenocrysts). Quartz and plagioclase constitute the phenocrysts in samples MA 15, 55, and PRCD 108/1 and it is mainly plagioclase in sample MA 16.

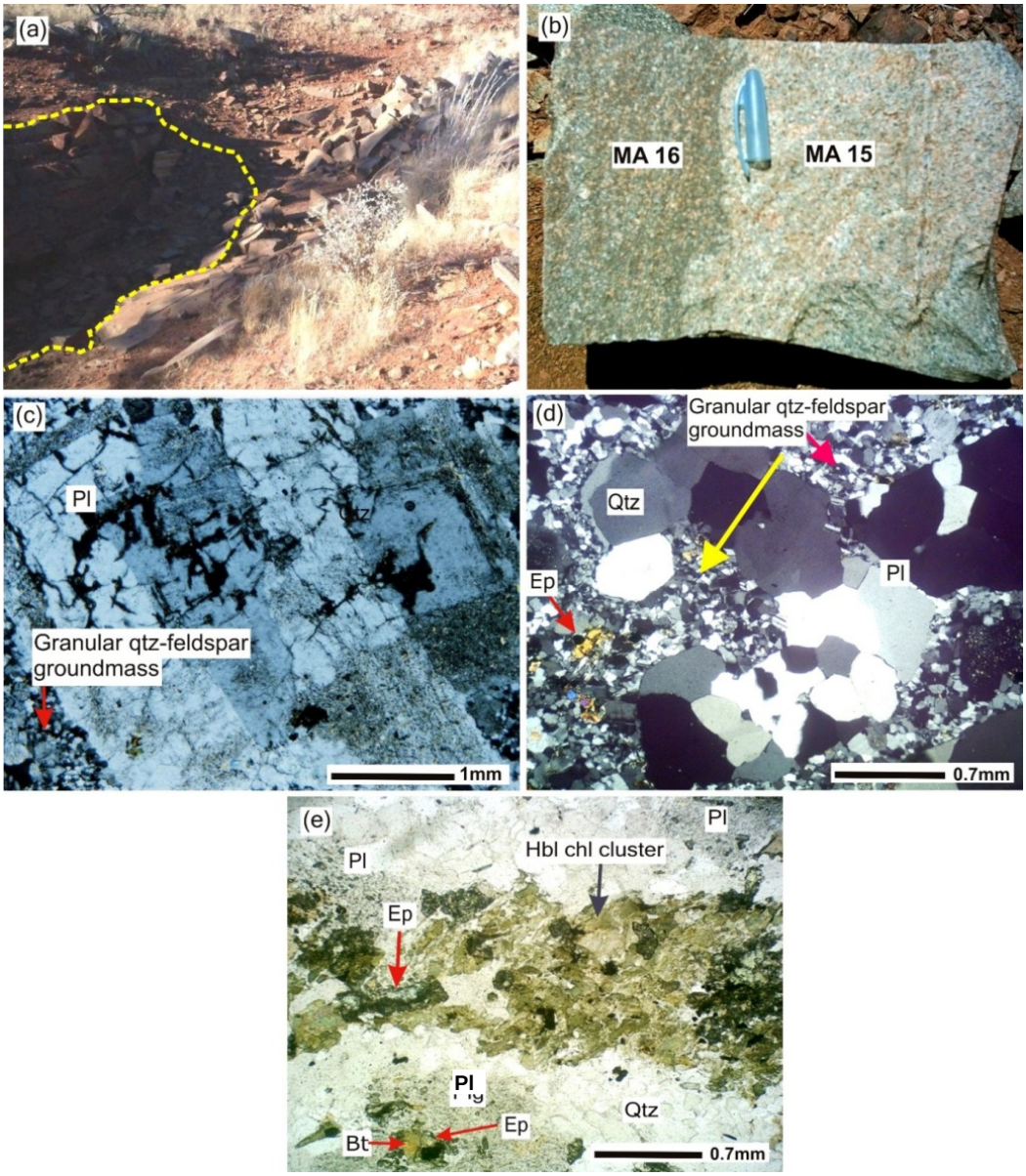

Fig. 5.6. (a) Trench at Lady Lydia South, from which samples MA 15, 16 and 54 were collected. The yellow broken line defines the boundary of the trench. (b) Cuspate contact between dark grey fine-grained microporphyritic granodiorite (MA 16) and medium-grained microporphyritic granodiorite (MA 15). (c) Euhedral large tabular plagioclase (Pl) showing oscillatory zoning and moderate sericitization (MA 16, xpl); (d) Recrystallized quartz (Qtz) phenocrysts and fine- grained epidote (Ep) in microporphyritic granodiorite. (MA 55, xpl); (e) Recrystallized green hornblende/chlorite (hbl chl) cluster, where hornblende is variably altered to patchy chlorite. Also shown are biotite and epidote inclusions in the sericitized plagioclase (MA 55, ppl).

Plagioclase phenocrysts (An_{15}) (2-5mm in most rocks; >5mm across in sample MA 16) are moderate to weakly sericitized (Fig. 5.6c). A few plagioclase crystals, especially in sample MA 16, show oscillatory zoning (Fig. 5.6c). K-feldspar (2-5mm) is microcline and occurs as platy crystals. Quartz constitutes most of the groundmass, but also occurs as phenocrysts (second in abundance to plagioclase) in all rocks and is locally recrystallized (Fig. 5.6d). Biotite forms bladed to flaky (0.25-2mm) crystals and is sporadically distributed throughout the rock. Two different types of biotite can be

identified in samples MA 15 and 16. The unaltered, brown, more prismatic, pleochroic (X=light yellow, Y and Z= dark brown) variety contains small zircon crystals, and local titanite. Altered biotite is found in association with opaques and unaltered biotite and is patchy to fibrous, greenish to greenish brown with weaker pleochroism (X=light yellow, Y and Z =pale greenish brown).

Hornblende (0.05-2mm), biotite, chlorite and epidote are closely associated with each other and locally form mafic clusters (Fig.5.6e). Opaque oxides, titanite, zircon and apatite occur in trace amounts, mostly interstitial to plagioclase and biotite. The opaques appear to originally have been ilmenite, which has altered to magnetite with a granular rim of titanite. Alteration of biotite and hornblende to chlorite is common.

Fine (0.05-0.5mm) granular quartz, K-feldspar and plagioclase are the dominant phases of the groundmass in all samples.

5.2.2 Biotite Hornblende Monzogranite

The biotite hornblende monzogranite sample MA 28 from the LLG is mesocratic, greenish-grey and massive in hand specimen. Under the microscope, it is fine-grained, allotriomorphic granular in texture (Fig. 5.7a). The rock is composed of quartz, plagioclase, biotite, hornblende and opaque minerals (Table 5.3). Minor minerals include titanite, while secondary minerals include epidote and calcite. Considering the fineness of the rock, QEMScan analysis was employed, along with traditional point counting, to obtain the mode of the rock. QEMScan analysis was carried out over an area of 1.8 x 1.8

Table 5.3 Modes of the massive biotite hornblende monzogranite in the Brilliant Open Pit, determined by (a) QEMScan analysis and (b) counting of 4344 points. tr= trace.

(a)

Minerals	Q Scan Mode %
Quartz	20.7
Alkali-feldspar	27.3
Plagioclase	37.9
Biotite	6.3
Hornblende	2.3
Chlorite	0.3
Epidote	0
Titanite	1.5
Calcite	0.7
Apatite	0.5
Magnetite	2.1
Pyrite	0.4
Total	100

(b)

Minerals	Modes %
Quartz	23.4
Alkali-feldspar	24.4
Plagioclase	34.6
Biotite	6.1
Hornblende	5.4
Chlorite	tr
Epidote	2.5
Titanite	1.4
Calcite	0.3
Opaque	1.9
Apatite	tr
Total	100

cm from each of three thin sections (uncovered) at a spacing of 15 microns, which resulted in 4,298,427 points (from three sections). The QEMScan study proved particularly helpful in identifying magnetite and sulphide phases. Quartz forms anhedral

crystals 0.2-0.35mm in diameter that are moderately recrystallized (Fig. 5.7a); a few grains are strained. Microcline (0.3-0.4mm) is relatively fresh (Fig. 5.7a). Plagioclase (An_{25}) has albite twinning and has a similar size, shape, and occurrence to microcline. It is moderately sericitized and also shows the development of fine brownish clay minerals. Biotite is the prominent mafic phase and is greenish-brown in colour, strongly pleochroic (x= pale greenish brown, y and z=greenish brown) and forms platy to elongate crystals ranging from 0.4-0.6mm in length (Fig. 5.7a). Hornblende is green in colour,

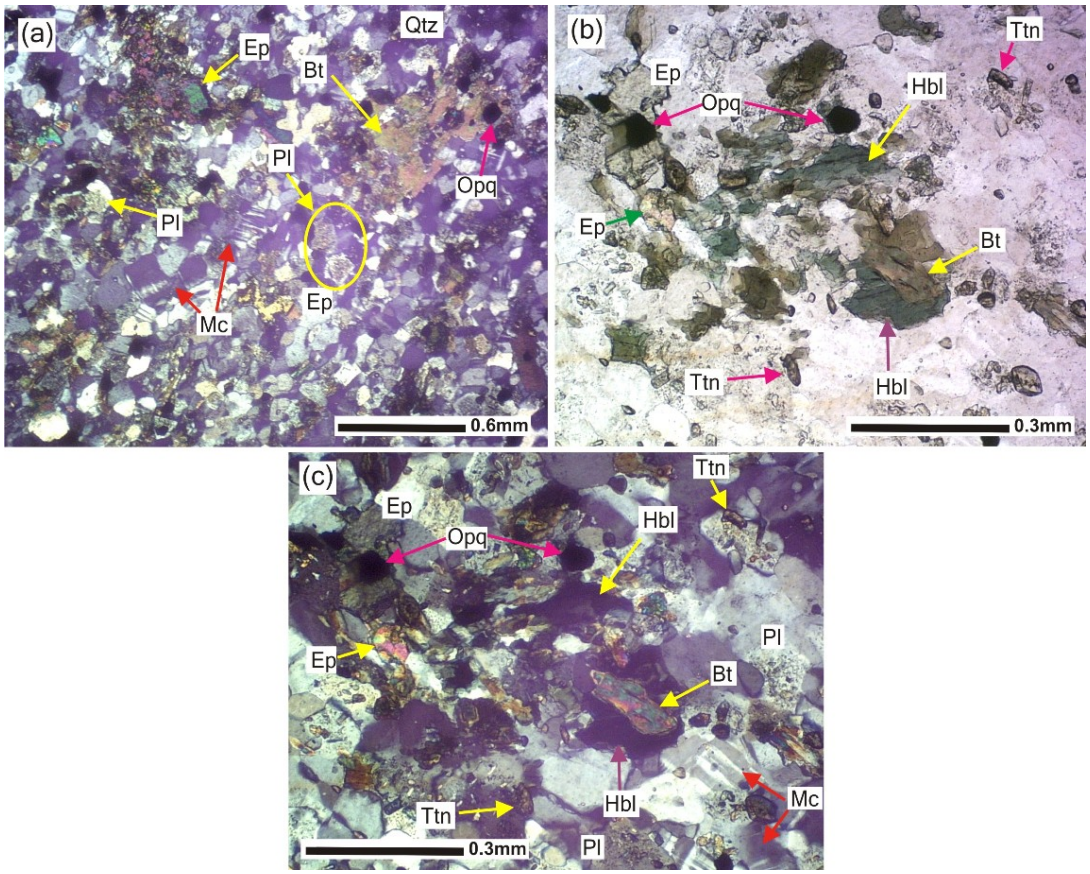

Fig. 5.7. Photomicrographs of biotite hornblende monzogranite (MA 28). (a) Fine-grained allotriomorphic texture of biotite hornblende monzogranite displaying moderately sericitized plagioclase (Pl), partially recrystallized quartz (Qtz), fresh microcline (Mc), biotite (Bt), epidote (Ep) and opaque (Opq) minerals. (under xpl). (b) Hornblende is corroded by biotite. Closely associated minerals are titanite, epidote, and opaque minerals (mostly pyrite by QEMScan analysis) (under ppl). (c) same field of view as (b) under xpl.

moderately pleochroic (x= yellowish green, y= dark yellowish green and z=dark green) and forms subhedral tabular crystals (0.4-0.8mm) (Fig. 5.7b,c). Fibrous sheaf-like chlorite commonly occurs as an alteration of biotite, whereas the latter locally grows around hornblende (Fig. 5.7b,c). Epidote is granular (0.2-0.4mm), and has a distinct pleochroism (x=pale green, y=yellow and z=purple yellow). It is intergrown with opaques (Fig. 5.7a,b). Minor lozenges of brownish titanite, specks of calcite and fine needles of apatite are also present.

5.2.3 Biotite Monzogranite

The biotite monzogranite samples (MA 3 and 4) were collected from the YNG and are leucocratic, grey to brownish grey with an hypidiomorphic texture (Fig. 5.8a,b). They are composed of plagioclase, quartz, K-feldspar and biotite, with minor hornblende, apatite, titanite, zircon, allanite, opaques and fluorite. Plagioclase (An_{15}) is subhedral and ranges from 0.8-3.5mm in length. It is fresher than in all other granitoids, but with local weak sericitization and saussuritization (Fig. 5.8c). Anhedral quartz shows a seriate range from 0.06 to 1.5mm in diameter. K-feldspar is similar to plagioclase in size and is microcline perthite (Fig. 5.8a,b). Local development of myrmekite texture is noted at the boundaries between plagioclase and K-feldspar. Biotite flakes (0.7 to 2mm in in length) locally define a

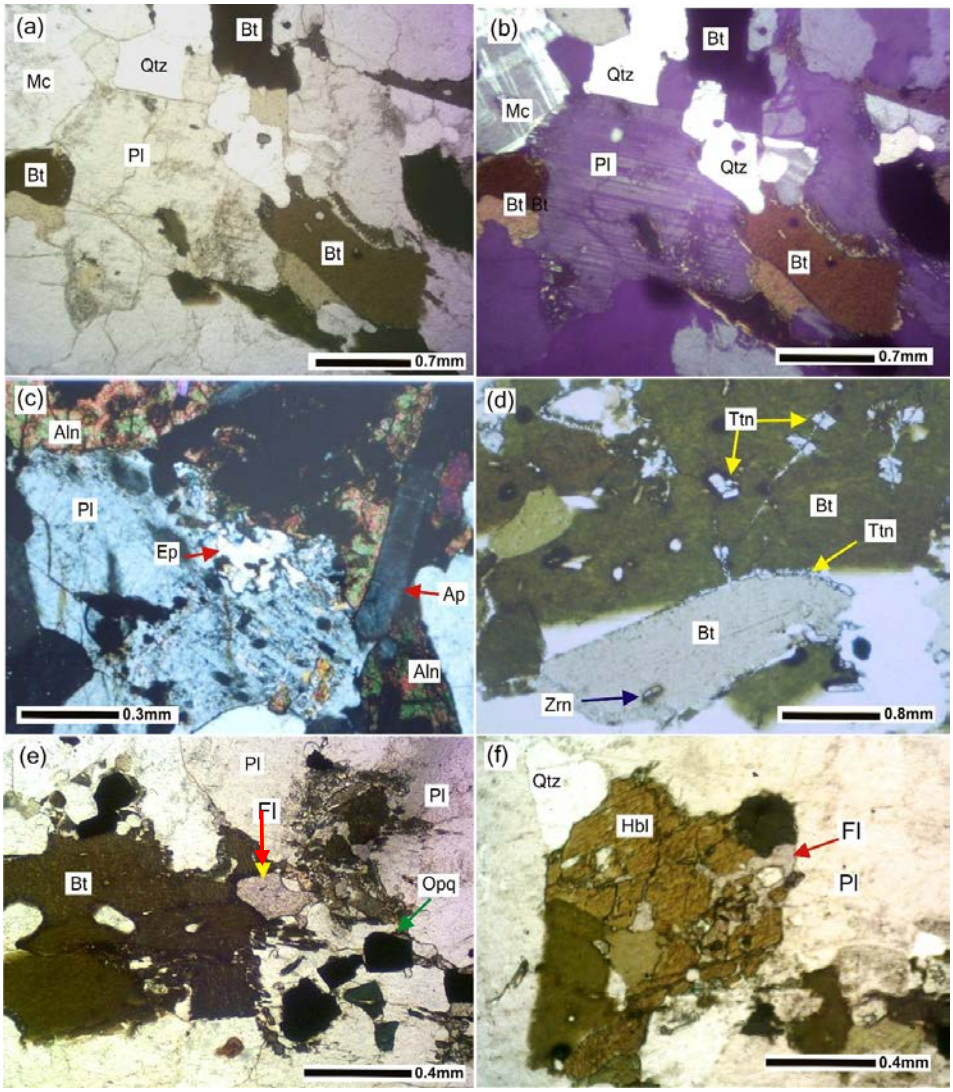

Fig. 5.8. Selected photomicrographs of biotite monzogranite (MA 3, 4). (a) Hypidiomorphic texture consisting of tabular plagioclase (Pl), microcline (Mc), quartz (Qtz) and biotite (Bt) flakes (**under** ppl). (b) Same field of view as (a) under xpl. (c) Saussuritized plagioclase, allanite (Aln) and long apatite crystal **(under** xpl). (d) Dark green, brown platy biotite crystals hosting titanite (Ttn) and zircon (Zrn) inclusions (under xpl). (e) Biotite associated with pale pink fluorite (Fl)(under ppl) and euhedral opaque mineral within plagioclase. (f) Subhedral tabular hornblende(Hbl) crystal partially replaced by biotite and corroded by fluorite along cleavage trace (**under** ppl).

a linear alignment resulting in an irregular foliation. They are highly pleochroic (x=straw yellow, y and z=dark greenish-brown), and intergrown with quartz and plagioclase (Fig. 5.8a,b). Titanite, opaque minerals and zircons are included within biotite (Fig. 5.8d). The other mafic mineral is hornblende (0.06 to 1mm) which is subhedral platy and strongly pleochroic (x=yellow, y=green, z=dark green). Commonly, hornblende is partially altered to greenish chlorite. Apatite forms conspicuous crystals (0.4-0.6mm) (Fig. 5.8c), and fine needles (0.02-0.04mm) within plagioclase. Blebs of epidote are mostly enclosed within plagioclase, biotite and hornblende (Fig. 5.8c). Allanite (0.08 to 0.6mm) forms anhedral to subhedral crystals that are dark brown to honey brown with darker patches and weak pleochroism. Minute (0.2-0.3mm) blebs of fluorite are present in close association with greenish biotite and hornblende (Fig. 5.8e,f). Opaque minerals (0.08-1.4mm) occur as inclusions in biotite, hornblende and allanite.

5.3 Geochemistry of the Granitoids

Major and trace (including the rare earth) elements were determined for 14 representative granite samples, of which 10 were from the LLG, 1 each from the YEG and Melville area and 2 from the YNG. The chemical data are listed in Table 5.4.

5.3.1 Major Element Geochemistry

5.3.1.1 Granodiorite

The SiO_2 content of the granodiorite samples ranges from 69.82–72.69%, with high Na_2O (5.83-5.97%) compared to most Archean granites in the Yilgarn Craton (Table 5.5). Other major oxides show little variability with Al_2O_3 (14.97-15.81%), K_2O (2.16-3.68%), Fe_2O_3T (1.31-2.35%) and MgO (0.42-0.73%) showing consistent values. The MnO (0.01-0.03%) and P_2O_5 (0.04-0.12%) contents are low. Only TiO_2 (0.17-0.29%) and CaO (0.7 to 2.22%) show some variability. These small-scale variations are also reflected on the Harker plots that show no distinct correlation between the major elements and SiO_2 (Fig.5.9).

5.3.1.2 Biotite Hornblende Monzogranite

The biotite monzogranite from the Brilliant Open Pit shows a marked difference in most major oxides when compared with the granodiorite samples. The biotite hornblende monzogranite is significantly lower in SiO_2 (63.85%) and Na_2O (3.76%) and fairly low in Al_2O_3 (14.06%), whereas it is higher in TiO_2 (0.77), K_2O (5.66%), MgO (1.84%), CaO 3.74%), P_2O_5 (0.35%), Fe_2O_3T (6.26%) and MnO (0.09%) compared to the other granitoid samples (Table 5.4).

Table 5.4 Geochemical data for the granitoid samples from the Yalgoo area. Chondrite ($_{CN}$) and Primitive Mantle ($_{PM}$) normalized values are from Sun and McDonough (1989).

Pluton/Area	LLG									YEG	Melville	LLG	YEG	
Rock type	Granodiorite											Biotite hornblende monzogranite	Biotite monzogranite	
	Massive granodiorite		Porphyritic granodiorite				Microporphyritic granodiorite							
Major elements, wt%	MA 09	MA 52	MA 06	MA 10	MA 49	MA 56	MA 15	MA 16	MA 55	MA 38	PRCD 108/1	MA 28	MA 03	MA 04
SiO_2	69.82	72.69	71.25	71.40	71.65	70.68	70.23	70.34	71.22	71.85	71.73	63.85	70.76	69.95
TiO_2	0.24	0.22	0.26	0.17	0.24	0.25	0.23	0.27	0.25	0.24	0.29	0.77	0.46	0.50
Al_2O_3	15.81	15.03	15.77	14.97	15.51	15.53	15.50	15.38	15.33	15.53	15.73	14.11	13.81	14.04
Fe_2O_3T	2.16	1.31	1.96	1.80	2.08	1.87	1.99	2.18	2.2	2.05	2.35	6.26	3.94	4.22
MnO	0.03	0.005	0.01	0.02	0.02	0.01	0.01	0.01	0.009	0.014	0.017	0.09	0.05	0.06
MgO	0.69	0.42	0.60	0.47	0.55	0.68	0.62	0.70	0.71	0.61	0.73	1.84	0.67	0.71
CaO	1.81	0.7	2.31	1.85	1.94	0.81	1.31	1.70	1.39	2.22	1.34	3.74	1.66	2.07
Na_2O	5.48	5.34	5.67	5.57	5.28	5.97	5.81	5.67	5.54	4.87	4.83	3.76	3.23	3.31
K_2O	3.09	3.68	2.16	2.96	2.87	2.96	2.76	2.75	2.73	2.85	3.18	4.66	4.88	4.87
P_2O_5	0.10	0.055	0.09	0.06	0.09	0.04	0.10	0.12	0.064	0.098	0.11	0.35	0.22	0.17
LOI	0.67	1.01	0.38	0.47	0.66	0.91	0.98	0.70	0.98	0.56	1.18	0.78	0.32	0.35
TOTAL	99.90	100.46	100.46	99.74	100.89	99.71	99.54	99.82	100.42	100.89	101.49	100.21	100.00	100.25
Fe_2O_3	1.25	0.55	1.06	1.01	1.14	1.07	1.11	1.20	1.21	1.11	1.27	3.44	2.14	2.28
FeO	0.91	0.76	0.90	0.79	0.94	0.80	0.88	0.98	0.99	0.94	1.08	2.82	1.80	1.94
FeOT	1.944	1.179	1.764	1.62	1.872	1.683	1.791	1.962	1.98	1.845	2.115	5.634	3.546	3.798
Mg#	0.39	0.39	0.38	0.34	0.34	0.42	0.38	0.39	0.39	0.37	0.38	0.37	0.25	0.25
Mg#*100	38.76	38.84	37.75	34.09	34.38	41.87	38.16	38.88	39.00	37.09	38.09	36.80	25.20	25.00
A/CNK	1.01	1.07	0.99	0.95	1.01	1.07	1.04	1.00	1.05	1.03	1.14	0.78	1.01	0.97
K_2O/Na_2O	0.56	0.69	0.38	0.53	0.54	0.50	0.48	0.49	0.49	0.59	0.66	1.24	1.51	1.47
Na_2O/K_2O	1.77	1.45	2.63	1.88	1.84	2.02	2.11	2.06	2.03	1.71	1.52	0.81	0.66	0.68
FeOT+MgO	2.63	1.60	2.36	2.09	2.42	2.36	2.41	2.66	2.69	2.46	2.85	7.47	4.22	4.51
FeOT/MgO	2.82	2.81	2.94	3.45	3.40	2.48	2.89	2.80	2.79	3.02	2.90	3.06	5.29	5.35
CIPW Norms														
Quartz	21.36	25.31	24.25	23.37	25.04	21.90	22.27	22.32	24.50	27.03	27.60	15.63	28.97	26.63
Orthoclase	18.26	21.75	12.76	17.49	16.96	17.49	16.31	16.25	16.13	16.84	18.79	27.54	28.84	28.78
Albite	46.37	45.19	47.98	47.13	44.68	50.52	49.16	47.98	46.88	41.21	40.87	31.82	27.33	28.01
Anorthite	8.33	3.11	10.87	7.10	9.04	3.78	5.85	7.65	6.48	10.37	5.93	7.86	6.80	9.07
Diopside	0.00	0.00	0.00	1.35	0.00	0.00	0.00	0.00	0.00	0.00	0.00	6.71	0.00	0.07
Hypersthene	2.02	1.63	1.86	0.90	1.79	1.88	1.88	2.12	2.19	1.96	2.31	2.61	2.54	2.70
Magnetite	1.81	0.80	1.54	1.46	1.65	1.55	1.61	1.74	1.75	1.61	1.84	4.99	3.10	3.31
Hematite	0.00	0.00	0.00	0.00	0.00	0.00	0.00	0.00	0.00	0.00	0.00	0.00	0.00	0.00
Ilmenite	0.46	0.42	0.49	0.32	0.46	0.47	0.44	0.51	0.47	0.46	0.55	1.46	0.87	0.95
Apatite	0.22	0.12	0.20	0.13	0.20	0.08	0.22	0.26	0.14	0.21	0.24	0.76	0.48	0.37
Corundum	0.40	1.12	0.12		0.41	1.12	0.81	0.27	0.89	0.63	2.17	0.00	0.72	0.00
Total	99.22	99.45	100.07	99.27	100.22	98.79	98.55	99.11	99.44	100.32	100.30	99.38	99.66	99.88
Trace elements, ppm														
Ba	2005	2202	1915	2079	2124	2405	1821	1955	1701	1972	1770	2199	1584	1536
Be	1.6	2.1	1.6	1.8	1.7	2.4	2.1	2.4	1.7	1.6	1.5	3.9	3.3	2.9
Co	4	3	4	3	5	4	4	6	5	5	6	14	5	5
Cr	4	50	1	4	4	6	11	7	6	11	6	8	9	6
Cs	17.3	4.5	17.3	13.7	6.5	3.4	5.1	4.4	7.4	2.6	2.1	10.7	5.3	2.8
Cu	1.8	9.1	1.3	1.3	2.0	3.4	4.0	4.3	5.3	1.8	5.5	6.9	7.5	8.2
Ga	18.6	19.2	19.0	20.1	19.3	19.1	21.1	21.3	18.8	19.2	19.4	19.8	18.9	18.5
Ge	1.0	1.1	0.8	1.1	0.8	1.3	1.2	1.1	1.0	0.9	1.1	1.8	1.6	1.5
Hf	2.8	2.9	3.4	2.6	3.1	3.4	3.1	3.6	3.2	3.2	3.2	5.0	12.6	13.1
Li	51.5	3.1	43.7	22.8	33.2	6.1	9.1	5.9	5.3	68.7	8.0	65.4	28.2	25.8
Nb	3.5	2.7	4.5	2.8	4.3	3.7	3.7	3.6	3.2	4.2	3.4	9.5	32.5	36.1
Ni	3.2	29.5	2.0	2.6	3.3	5.4	4.7	5.5	5.4	7.1	7.3	15.1	5.6	5.2
Pb	25.8	16.0	31.8	31.8	52.0	19.2	38.3	23.8	18.8	26.4	11.2	32.3	52.1	45.1
Rb	170	108	249	75	90	82	110	82	94	71	110	202	312	302
Sc	0.6	2.1	-0.3	0.1	2.3	2.4	1.6	1.0	3.4	2.3	2.6	8.8	3.7	3.5
Sr	706	500	796	798	768	638	682	759	648	733	519	738	124	123
Ta	0.2	0.2	0.3	0.2	0.3	0.3	0.3	0.2	0.3	0.3	0.3	0.6	1.9	2.2
Th	6.9	5.0	7.8	3.7	7.2	9.5	6.6	9.5	7.4	8.6	8.3	10.9	48.1	47.1
U	1.2	1.0	2.5	1.4	1.7	1.1	1.1	1.5	1.3	1.9	2.7	3.2	9.4	7.6
V	21	31	18	17	25	30	37	29	33	23	26	88	26	24
Y	5.2	5.0	4.9	5.1	5.2	9.0	9.4	6.2	6.7	5.3	5.2	23.1	30.7	48.9
Zn	37	32	37	31	44	31	31	29	30	19	25	77	47	43
Zr	120	106	151	105	114	125	115	146	111	115	121	188	596	645

REE, ppm	MA 09	MA 52	MA 06	MA 10	MA 49	MA 56	MA 15	MA 16	MA 55	MA 38	PRCD 108/1	MA 28	MA 03	MA 04
La	22.11	17.69	33.19	17.75	22.91	39.44	26.80	23.96	24.24	26.90	28.01	37.13	124.40	148.89
Ce	40.24	31.55	61.11	30.85	44.67	62.26	40.96	41.11	42.52	48.83	51.14	67.78	243.53	267.42
Pr	4.34	3.52	6.46	3.14	4.26	7.08	4.91	4.57	4.65	5.23	5.35	7.62	21.94	25.66
Nd	15.64	13.30	22.99	11.18	15.77	26.39	17.79	16.02	17.37	19.28	18.85	31.31	69.88	84.35
Sm	2.42	2.21	3.38	1.74	2.63	3.82	2.72	2.38	2.76	3.10	2.84	6.09	9.67	13.09
Eu	0.79	0.79	0.97	0.65	0.88	1.17	0.83	0.79	0.85	0.95	0.87	1.78	1.40	1.67
Gd	1.86	1.65	2.50	1.46	1.94	2.89	2.36	1.91	2.03	2.20	2.05	5.19	9.15	12.39
Tb	0.19	0.18	0.23	0.16	0.20	0.30	0.26	0.20	0.22	0.22	0.21	0.67	1.07	1.54
Dy	0.80	0.89	0.84	0.76	0.90	1.40	1.24	0.88	1.09	0.98	0.96	3.46	5.24	7.71
Ho	0.12	0.16	0.10	0.13	0.15	0.25	0.23	0.14	0.20	0.16	0.16	0.65	0.89	1.38
Er	0.32	0.44	0.27	0.37	0.39	0.67	0.62	0.39	0.55	0.41	0.41	1.64	2.41	3.62
Tm	0.04	0.06	0.03	0.05	0.05	0.09	0.08	0.05	0.08	0.05	0.05	0.23	0.34	0.50
Yb	0.26	0.38	0.20	0.38	0.35	0.53	0.57	0.34	0.50	0.34	0.34	1.40	2.34	3.28
Lu	0.04	0.06	0.03	0.06	0.05	0.08	0.09	0.06	0.07	0.05	0.05	0.20	0.37	0.51
Total REE	89.17	72.90	132.29	68.68	95.14	146.37	99.46	92.81	97.14	108.71	111.28	165.17	492.64	572.00
$(La)_{CN}$	93.31	74.63	140.05	74.88	96.66	166.40	113.10	101.10	102.29	113.51	118.17	156.69	524.90	628.21
$(Sm)_{CN}$	15.81	14.46	22.07	11.35	17.20	24.97	17.78	15.56	18.07	20.29	18.53	39.79	63.17	85.58
$(Yb)_{CN}$	1.55	2.25	1.19	2.21	2.05	3.13	3.36	2.02	2.94	2.01	2.02	8.25	13.75	19.29
$(La/Sm)_{CN}$	5.90	5.16	6.35	6.60	5.62	6.66	6.36	6.50	5.66	5.59	6.38	3.94	8.31	7.34
$(La/Yb)_{CN}$	60.14	33.16	117.20	33.88	47.11	53.12	33.68	50.05	34.76	56.57	58.37	18.99	38.16	32.57
K/Rb	15.1	28.2	7.2	32.6	26.4	30.0	20.8	27.7	24.0	33.5	24.0	19.2	13.0	13.4
Rb/Sr	0.2	0.2	0.3	0.1	0.1	0.1	0.2	0.1	0.1	0.1	0.2	0.3	2.5	2.5
La/Yb	84	46	163	47	66	74	47	70	48	79	81	26	53	45
Sr/Y	134.9	99.6	163.4	156.2	147.9	71.2	72.5	122.4	96.9	138.5	100.8	32.0	4.0	2.5
Nb/Ta	16.22	15.02	17.54	16.54	14.09	14.64	14.60	15.54	11.64	12.06	13.19	17.08	16.81	16.43
$(Gd)_{CN}$	9.0	8.0	12.2	7.1	9.4	14.0	11.5	9.3	9.9	10.7	10.0	25.3	44.5	60.3
$(Lu)_{CN}$	1.70	2.21	1.16	2.52	1.88	2.97	3.54	2.20	2.93	1.89	1.95	8.05	14.76	19.93
$(Gd/Lu)_{CN}$	5.32	3.63	10.51	2.83	5.00	4.73	3.24	4.24	3.38	5.65	5.10	3.14	3.02	3.03
$(Ce)_{CN}$	65.76	51.55	99.85	50.40	72.99	101.73	66.93	67.18	69.47	79.79	83.56	110.76	397.93	436.97
$(Yb)_{CN}$	1.55	2.25	1.19	2.21	2.05	3.13	3.36	2.02	2.94	2.01	2.02	8.25	13.75	19.29
$(Ce/Yb)_{CN}$	42.38	22.91	83.56	22.80	35.58	32.47	19.93	33.25	23.61	39.76	41.27	13.42	28.93	22.65
$(La/Lu)_{CN}$	54.91	33.70	120.80	29.76	51.28	56.05	31.91	46.03	34.95	59.92	60.45	19.46	35.56	31.53

5.3.1.3 Biotite Monzogranite

The biotite monzogranite samples from the YNG have almost identical compositions to the granodiorite samples in terms of most major oxides, except for slightly higher Fe_2O_3T and K_2O and low Na_2O. They have similar values for SiO_2 (69.95-70.76%), TiO_2 (0.46-0.50%), Al_2O_3 (13.81-15.04%), MnO (0.05-0.06%), MgO (0.67-0.71%), CaO (1.66-2.07%), and Na_2O (3.23-3.31%), whereas Fe_2O_3T (3.94-5.22%), K_2O (5.87-5.88%) and P_2O_5 (0.17-0.22%) are slightly higher than those of the granodiorite and biotite hornblende monzogranite samples. The Harker variation diagrams show a weak positive correlation of P_2O_5 with SiO_2, whereas Fe_2O_3T, CaO, MnO, and TiO_2 demonstrate slight negative correlations with increasing SiO_2. Na_2O and K_2O do not show any significant variation (Fig.5.9), but note that because only two samples were analysed it means this cannot be considered definitive.

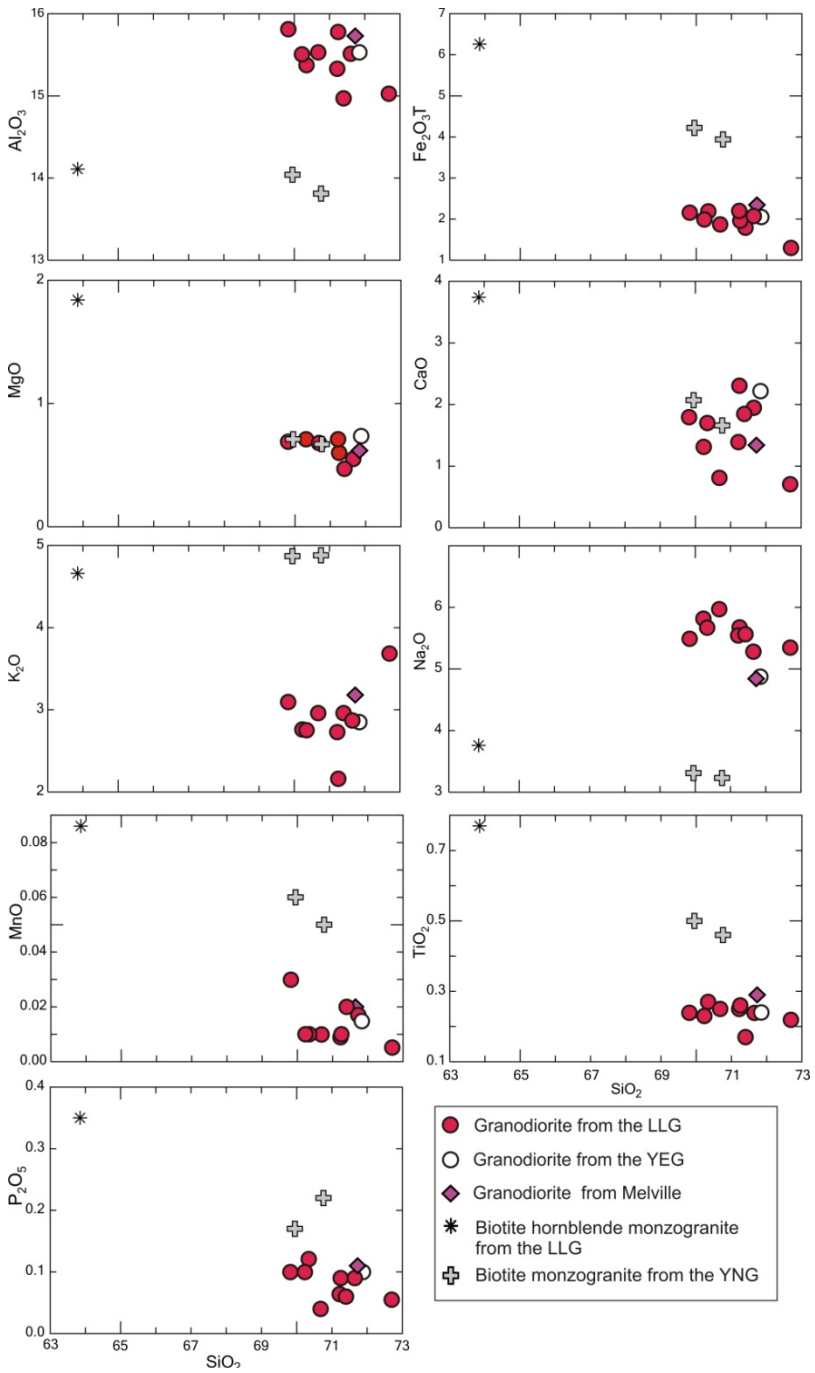

Fig. 5.9 Harker variation plots of major elements for the granitoid samples from the Yalgoo area.

The major oxide compositions have been used to establish a geochemical classification of the granitoids, based on: a) the AFM plot (Irvine and Baragar, 1971), b) the Na_2O+K_2O vs. SiO_2 (total alkalis silica-TAS) diagram (Cox et al., 1979) and c) the Normative An-Ab-Or diagram of Barker (1979). The granitoids are calc-alkaline on the classification scheme of Irvine and Baragar (1971) (Fig 5.10a). On the silica vs. alkali diagram of Cox et al. (1979) (Fig 5.10b), most granitoid samples fall within the alkali granite or granite field extending between alkali and sub-alkali, whereas the biotite hornblende monzogranite lies within the syenodiorite field. The higher Na_2O content of

the granodiorite samples is reflected in the normative Ab-An-Or plot (Barker, 1979) (Fig.5.9c) where the majority of the granodiorite samples fall within the trondhjemite field, whereas both biotite hornblende monzogranite and biotite monzogranite samples fall within the granite field.

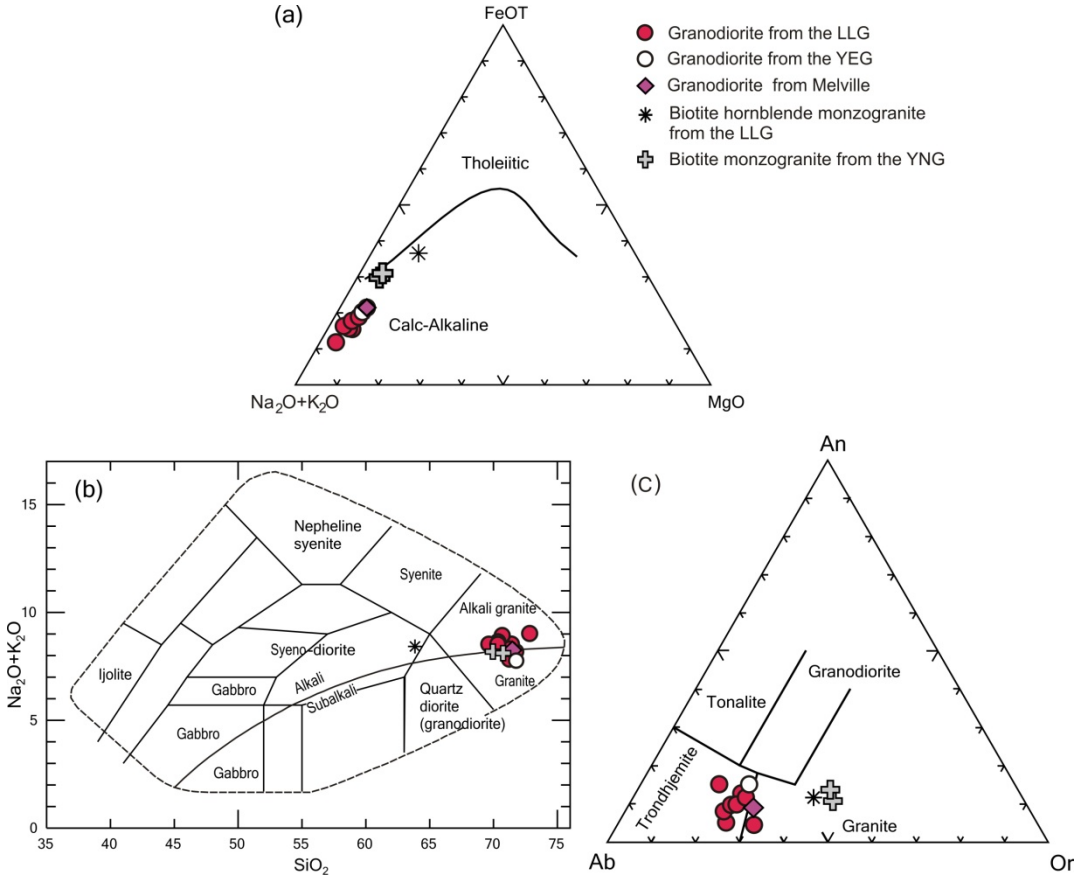

Fig. 5.10. Classification diagrams for the Yalgoo granites. (a) AFM plot (Irvine and Baragar, 1971). (b) Na_2O+K_2O vs.SiO_2 diagram (Cox et al., 1979). (c) Normative An-An-Or diagram of Barker (1979).

The strong similarities of the major element oxides and CIPW norms among the granodiorite samples is suggestive of a possible genetic link between the LLG and YEG and Melville granodiorites, which is discussed in section 5.3.3.

5.3.2 Trace Element Geochemistry

The behavior of selected trace elements is displayed on Harker variation diagrams (Fig. 5.11). In all the plots, biotite hornblende monzogranite plots away from the granodiorite and biotite monzogranite. The Sr, Th, Zr and Y plots clearly differentiate between the granodiorite, biotite hornblende monzogranite and biotite monzogranite. Except for sample MA 52, the Ni and Cr values for the other granodiorite, biotite hornblende monzogranite and biotite monzogranite samples are low, ranging from 2 to 15 ppm (Fig. 5.11). Sample MA 52 has the highest Ni and Cr contents at 30 and 50 ppm, respectively, and relatively low Co (3 ppm).

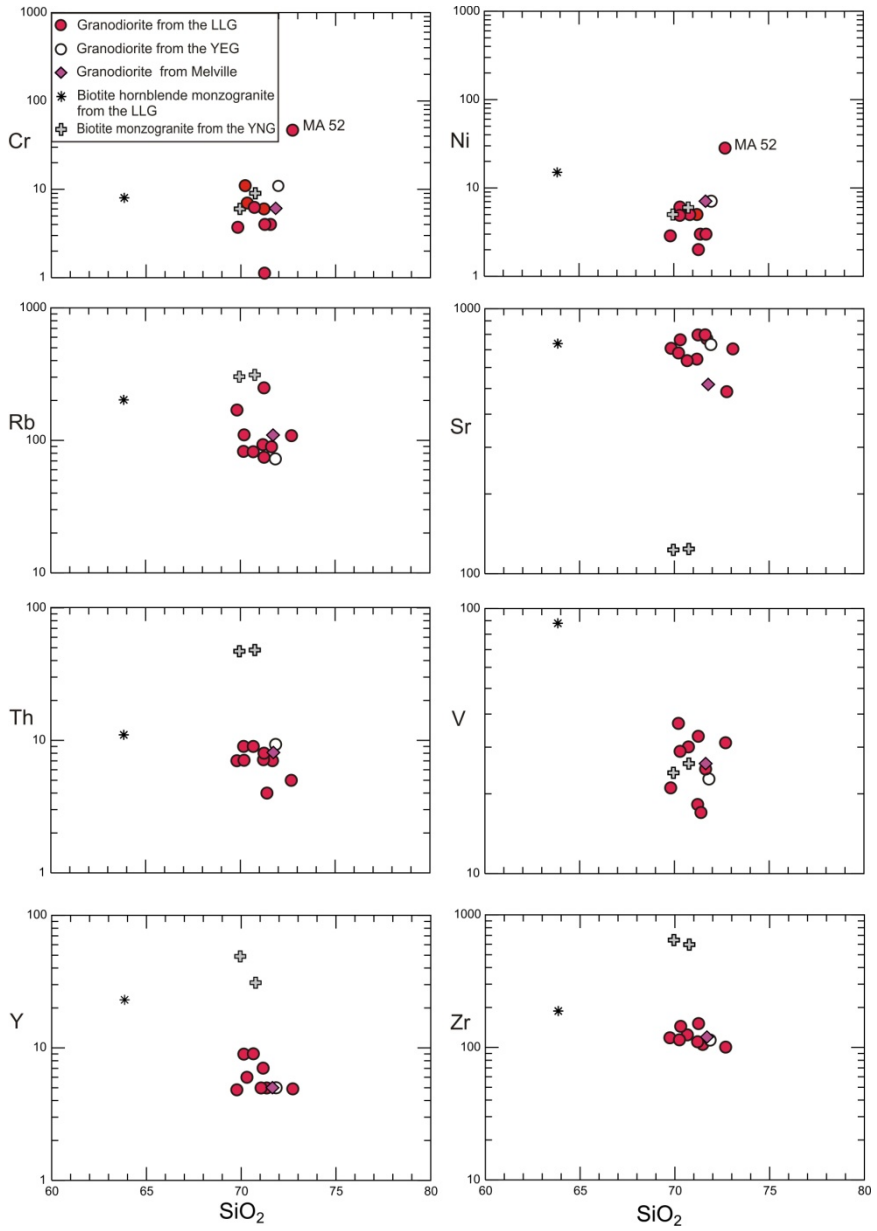

Fig. 5.11 Harker variation plots for selected trace elements for the granitoid samples from the Yalgoo area.

5.3.2.1 Rare Earth Element Characteristics

The rare earth element (REE) data of the all granitoid samples are normalized against the chondrite values of Sun and McDonough (1989). The REE plots show LREE enrichment (Fig. 5.12a). However, the plots also distinguish the granodiorite samples from the biotite hornblende monzogranite and biotite monzogranite. The granodiorite, biotite hornblende monzogranite and biotite monzogranite differ significantly in their total REE contents, patterns and size of the Eu anomaly. The granodiorite samples, therefore, are considered to belong to a single group (group I). The one sample MA 28 of biotite hornblende monzogranite defines group II, whereas the two samples of biotite monzogranite (MA 3, 4) constitute the third group (group III).

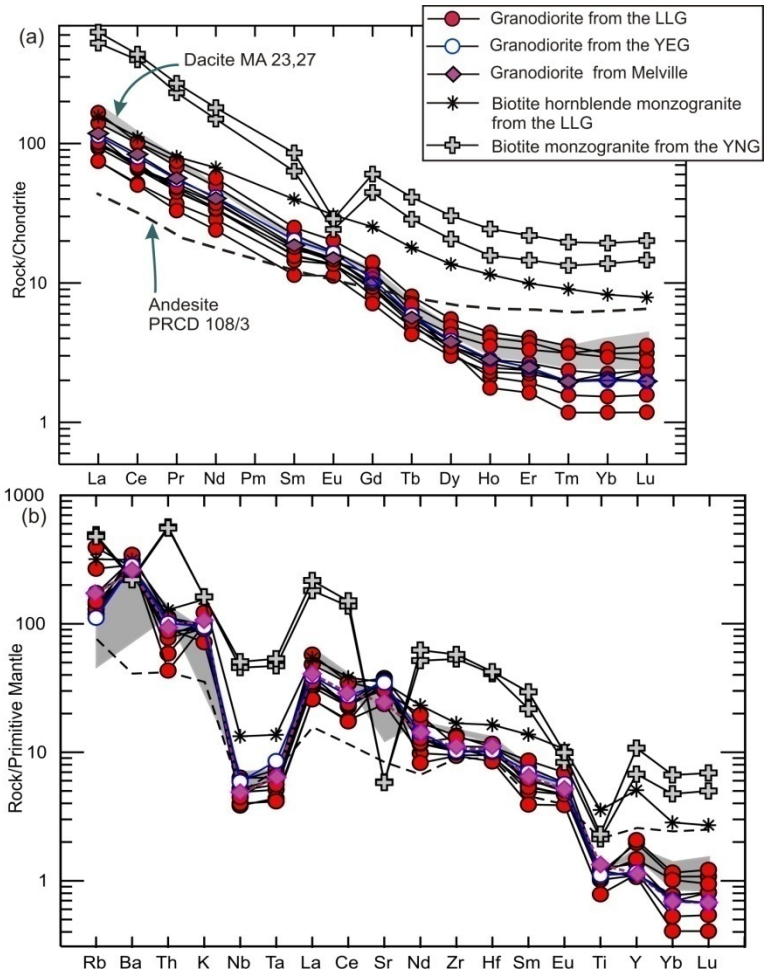

Fig. 5.12. Chondrite-normalized REE and Primitive Mantle-normalized incompatible trace element diagrams of the granitoid samples from the Yalgoo area. (a) REE diagram; (b) Incompatible trace element diagram. Chondrite and Primitive Mantle normalizing values are from Sun and McDonough (1989). The REE and incompatible trace element profiles of the felsic porphyries (MA 23,27 and PRCD 108/3) are also shown for comparison.

The total REE contents of the group I samples range from 68.68 to 146.37 ppm, averaging 101.41 ppm. The group displays strong LREE enrichment relative to HREE (the (La/Yb)CN ranges from 33.16-146.37 averaging (La/Yb)CN = 51.1, 'CN' denotes chondrite-normalized). All the granodiorite samples show moderate to weak positive Eu anomalies (Eu/Eu*= 1.11 to 1.24) (Fig. 5.12a), indicating the parent magma was formed from a relatively undepleted source below the depth of plagioclase stabilization or that it was unfractionated. Despite being collected from three different plutons/areas (LLG, YEG and Melville), all the granodiorite samples follow the same general trend thereby strongly suggesting formation from a single source.

The group II sample MA 28 has a slightly higher total REE (165.17 ppm) content compared to the granodiorite samples. The REE pattern differs from the trend of the granodiorite samples with a slightly flatter gradient and elevated MREE and HREE

contents. The LREE/HREE ratio is less [(La/Yb)CN =19] than the granodiorite samples and the sample has a weak negative Eu (Eu/Eu*=0.97) anomaly.

The group III granites, comprising biotite monzogranite, have REE patterns distinct from the two previous groups in having the highest LREE and HREE contents and prominent negative Eu (Eu/Eu*= 0.40-0.46) anomalies. The LREE/HREE enrichment [(La/Yb)CN =57.5] is slightly higher than the group I samples. The large Eu anomaly suggests plagioclase fractionation during crystallization, which along with strong LREE enrichment implies a more fractionated source for the biotite monzogranite.

5.3.2.2 Incompatible Trace Elements Characteristics

The Th, Nb and Y contents are low (averaging 7.3, 3.6 and 6.1 ppm respectively) for all three granitoid groups. On the PM (primitive mantle)-normalized incompatible element diagram (Fig. 5.12b), granodiorite samples show strong enrichment in Rb, Ba, K and Th and slightly elevated values for Zr, Y and Sr, and large negative Nb and Ta anomalies and weak negative Ti anomalies. The trend of biotite hornblende monzogranite differs from the trend of the granodiorite samples in having slightly weaker negative Nb, Ta and Ti anomalies and higher Zr, Hf, Sm, Y, Yb and Lu values.

The biotite monzogranite differs considerably from the other two granitoids in having higher Zr (620 ppm), Th (47.7 ppm), Nb (35.3 ppm) and Y (39.9 ppm). On the PM-normalized incompatible trace element diagram, the biotite monzogranite samples show pronounced negative Sr and Ti anomalies and weak negative Nb and Ta anomalies. One of the samples shows a strong positive Th anomaly. These samples have the highest Y, Yb and Lu contents (Fig. 5.12b).

5.4 U-Pb SHRIMP Geochronology and Lu-Hf Isotopic Study of the Granitoids

5.4.1 Granodiorites

5.4.1.1 Massive granodiorite

Sample MA 9

Zircons from the massive granodiorite sample MA 9 are tabular and show well developed oscillatory zoning (Fig. 5.13a,b), although a few grains are recrystallized (Fig. 5.13c,d). They range in size from 100 to 280 μm and have an average length:width ratio ≥2:1. Isotopic data were collected during a single analytical session with a total of 13 analyses completed on 9 grains. The error of the mean Pb/U calibration constant determined from 9 analyses of the CZ3 standard was 1.00% (2σ). Results are listed in Table 5.5.

The zircons have low U (7 to 484 ppm, averaging 258 ppm) and Th (0 to 188 ppm, averaging 67 ppm) contents, with low to moderate Th/U ratios (0.12 to 0.80, averaging 0.3), with the lowest U and Th value recorded from analysis MA 9.5.

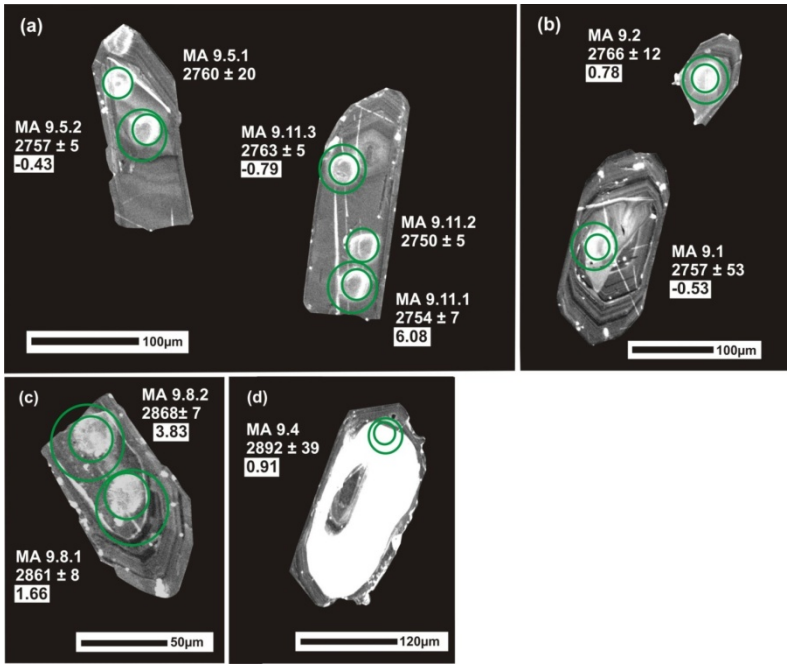

Fig. 5.13. Cathodoluminescence (CL) images of representative zircons from sample MA 9. Small and large circles indicate the locations of SHRIMP U-Pb analyses and LA-ICP-MS Hf analyses, respectively. The U–Pb ages and εHf(t) values are given for each spot.

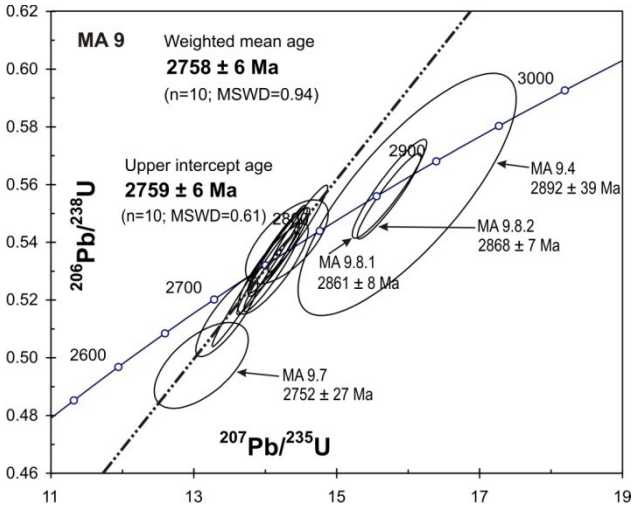

Fig. 5.14. Concordia plot of sample MA 9.

On the concordia diagram (Fig. 5.14), the data forms two distinct populations. The older population consists of three concordant analyses (MA 9.4, 9.8.1 and 9.8.2), although one has a larger error. These ages are interpreted to record the minimum age of zircons inherited either from the source or from the wallrocks. The younger population of ten data points define a weighted mean age of 2758 ± 6 Ma (MSWD = 0.94) and an identical

Isoplot upper intercept $^{207}Pb/^{206}Pb$ age of 2759 ± 6 Ma (MSWD = 0.61). This is interpreted to record the age of emplacement of the massive granodiorite.

Table 5.5. U-Pb SHRIMP geochronological data for sample MA 9.

Spot	U ppm	Th ppm	Th/U	Rad ^{206}Pb ppm	% comm 206	^{204}Pb /^{206}Pb	$^{207}Pb^*$ /$^{206}Pb^*$	% err	$^{206}Pb^*$ /^{238}U	±%	$^{276}Pb^*$ /^{235}U	±%	$^{206}Pb^*$ /^{238}U Age	1σ	$^{207}Pb^*$ /$^{206}Pb^*$ Age	1σ	% conc
MA 9.1	168	50	0.30	78.0	0.14	0.00010	0.1918	0.4	0.5367	1.2	15.19	1.2	2770	26	2757	7	100
MA 9.2	121	15	0.13	55.0	0.05	0.00004	0.1928	0.8	0.5308	1.2	15.11	1.4	2745	27	2766	12	99
MA 9.3	283	70	0.26	126.0	0.86	0.00064	0.1899	0.7	0.5142	1.1	13.46	1.3	2676	25	2741	12	98
MA 9.4	7	0.0	0.00	3.0	0.49	0.00037	0.2083	2.4	0.5566	3.1	15.99	3.9	2853	71	2892	39	99
MA 9.5	322	60	0.19	151.0	1.15	0.00085	0.1920	1.2	0.5401	1.1	15.3	1.7	2785	26	2760	20	101
MA 9.5.2	306	36	0.12	140.0	0.05	0.00004	0.1918	0.3	0.5311	1.2	15.04	1.3	2746	28	2757	5	100
MA 9.7	130	100	0.80	56.0	1.85	0.00137	0.1911	1.6	0.4973	1.2	13.1	2.1	2602	26	2752	27	95
MA 9.8.1	301	133	0.46	145.0	0.64	0.00048	0.2044	0.5	0.5586	1.3	15.74	1.4	2861	29	2861	8	100
MA 9.8.2	327	188	0.59	157.0	0.43	0.00033	0.2053	0.4	0.5560	1.1	15.73	1.2	2850	25	2868	7	99
MA 9.10	484	62	0.13	220.0	0.08	0.00006	0.1928	0.4	0.5297	1.1	15.08	1.1	2740	24	2767	6	99
MA 9.11.1	237	44	0.19	111.0	0.05	0.00004	0.1925	0.3	0.5447	1.1	15.45	1.2	2803	26	2763	5	101
MA 9.11.2	303	53	0.18	138.0	0.07	0.00005	0.1909	0.3	0.5284	1.9	13.91	1.9	2736	42	2750	5	99
MA 9.11.3	370	62	0.17	171.0	0.22	0.00016	0.1913	0.4	0.5372	1.1	15.17	1.2	2772	25	2754	7	101

% comm 206= amount of common ^{206}Pb in total ^{206}Pb; * = radiogenic lead corrected using measured ^{204}Pb; % conc.= [($^{206}Pb/^{238}U$ age)/($^{207}Pb/^{206}Pb$ age)] x100.

Table 5.6. Hafnium isotopic data for sample MA 9. T_{DM2} value is used in the text.

Spot	t (Ma)	$^{176}Yb/^{177}Hf$	$^{176}Lu/^{177}Hf$	$^{176}Hf/^{177}Hf$	2σ	$e_{Hf}(0)$	$e_{Hf}(t)$	T_{DM1}	T_{DM2}	$f_{Lu/Hf}$
MA 9.1	2757	0.032012	0.001084	0.281064	0.000034	-60.41	-0.48	3053	3424	-0.97
MA 9.2	2766	0.007727	0.000272	0.281055	0.000022	-60.72	0.94	3001	3308	-0.99
MA 9.4	2892	0.010666	0.000394	0.280979	0.000024	-63.40	0.91	3111	3395	-0.99
MA 9.5.2	2757	0.016526	0.000576	0.28104	0.000027	-61.25	-0.37	3045	3414	-0.98
MA 9.7	2752	0.014498	0.00043	0.281003	0.000028	-62.57	-1.56	3083	3512	-0.99
MA 9.8.1	2861	0.024072	0.000764	0.281043	0.000028	-61.15	1.74	3056	3303	-0.98
MA 9.8.2	2868	0.042789	0.001284	0.281127	0.000027	-58.19	3.86	2983	3125	-0.96
MA 9.10.1	2767	0.029877	0.001048	0.281245	0.000056	-55.01	6.23	2804	2851	-0.97
MA 9.11.1	2763	0.015515	0.000546	0.281216	0.000073	-55.03	6.08	2807	2862	-0.98
MA 9.11.3	2754	0.011855	0.000436	0.281021	0.000042	-61.92	-0.87	3059	3454	-0.99

Eleven Lu-Hf analyses were obtained from sample MA 9 and are listed in Table 5.6. Most of the young zircon population show a restricted range in $^{176}Hf/^{177}Hf$ ratios (0.281003 to 0.281063), εHf(t) (-1.56 to 0.94) and T_{DM2} model ages (3308 to 3512 Ma) excepting two significantly higher $^{176}Hf/^{177}Hf$ ratios (0.281245 and 0.281216), εHf(t) (6.23 and 6.08) and younger T_{DM2} ages (2851 and 2862 Ma) from sites MA 9.10 and MA 9.11.1, respectively. The higher εHf(t) values can be explained in terms of a depleted mantle component that contributed to magma genesis at ~2760 Ma. The three older analyses display $^{176}Hf/^{177}Hf$ ratios of 0.280979 to 0.281127 and T_{DM2} model ages of 3125 to 3395 Ma, similar to the younger population. The εHf(t) values are slightly more positive, varying from 0.91 to 3.86, which suggests a greater mantle contribution. The εHf(t) values (6.08 and -0.79) from two sites (MA 9.11.1, MA 9.11.3) on a single grain differ considerably despite having similar ages (2754 ± 7 and 2763 ± 5 Ma) within error, indicating irregular incorporation of more and less juvenile materials during zircon growth.

5.4.1.2 Porphyritic granodiorite

Sample MA 6

Most zircon grains in porphyritic granodiorite sample MA 6 are euhedral, elongate and prismatic in shape. They are 90 to 180 µm in length with an average length to width ratio ≥2:1. Many zircon grains have thin oscillatory zones of magmatic origin, with a few having more homogenous central portions with/without a seam of CL light material forming an internal zone (Fig. 5.15b,d,e,f). This seam may overprint the primary zoning, similar to that described by Pidgeon (1992) and Pidgeon et al. (1998) (Fig. 5.15e). Only one zircon crystal shows core-rim structure (Fig. 5.15f).

Fig. 5.15. Cathodoluminescence (CL) images of representative zircons from sample MA 6. Small and large circles indicate the locations of SHRIMP U-Pb analyses and LA-ICP-MS Hf analyses, respectively. The U–Pb ages and εHf(t) values are given for each spot.

U-Pb data were collected from sample MA 6 during a single SHRIMP analytical session with a total of 15 analyses on 13 grains. The error of the mean Pb/U calibration determined from 10 analyses of the CZ3 standard was 0.82% (2σ). Analytical results are presented in Table 5.7.

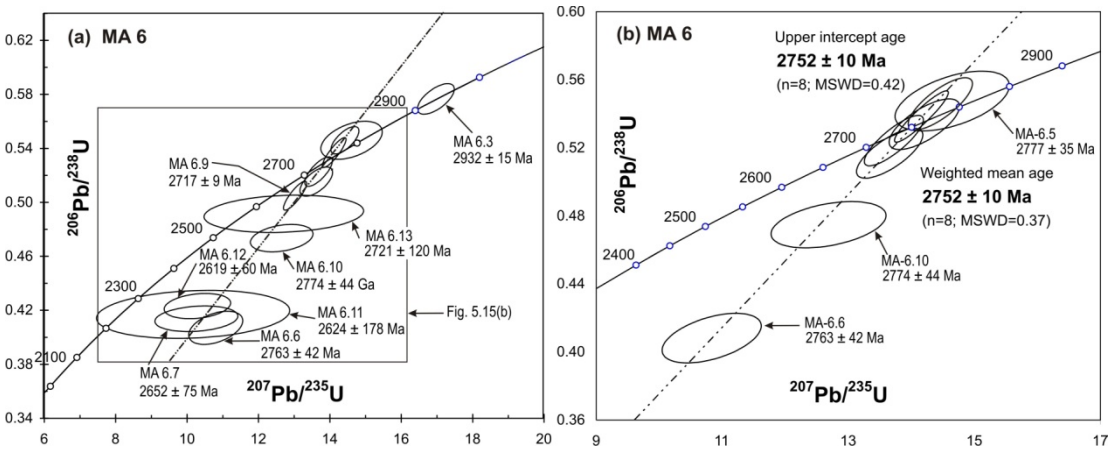

Fig. 5.16 Concordia plot of sample MA 6. (a) Plot of all grains, (b) plot of eight grains considered in the age calculation.

The U varies from 272 to 719 ppm, averaging 429 ppm, whereas the Th content ranges from 32 to 709 ppm, averaging 249 ppm. The Th/U ratio ranges from 0.07 to 1.65, averaging 0.57. A concordia plot of all analyses (Fig. 5.16a) reveals most of the data points lie on a single discordia line. Four analyses (MA 6.7, 6.11, 6.12 and 6.13) with near zero lower intercept age (-86 ± 670 Ma), high common Pb (4 to 14%), and variable discordance with high errors, are considered to have undergone recent lead loss and were rejected from the age calculation. One analysis from a core region (MA 6.3) yielded a significantly older age of 2932 ± 15 Ma indicating inheritance from an older crust. Both the weighted mean $^{207}Pb/^{206}Pb$ and Isoplot upper intercept age of the eight concordant to near concordant data points are identical; 2752 ±10 Ma (MSWD = 0.37 and 0.42 for the weighted mean $^{207}Pb/^{206}Pb$ and Isoplot upper intercept ages, respectively) (Fig. 5.16b).

Table 5.7. U-Pb SHRIMP geochronological data for sample MA 6.

Spot	U ppm	Th ppm	Th/U	Rad ^{206}Pb ppm	% comm 206	^{204}Pb $/^{206}Pb$	$^{207}Pb^*$ $/^{206}Pb^*$	% err	$^{206}Pb^*$ $/^{238}U$	±%	$^{276}Pb^*$ $/^{235}U$	±%	$^{206}Pb^*$ $/^{238}U$ Age	1σ	$^{207}Pb^*$ $/^{206}Pb^*$ Age	1σ	% conc
MA 6.1.1	639	65	0.11	305.2	1.13	0.00084	0.1916	0.8	0.5475	1.1	15.46	1.4	2815	25	2755	13	102
MA 6.1.2	497	32	0.07	231.0	0.45	0.00033	0.1907	0.5	0.5384	1.1	15.16	1.2	2777	26	2749	8	101
MA 6.3	447	300	0.69	225.1	1.41	0.00108	0.2134	1	0.5782	1.1	17.02	1.5	2941	26	2932	15	100
MA 6.4	315	149	0.49	141.9	1.43	0.00106	0.1916	1.1	0.5168	1.2	13.66	1.6	2685	25	2756	18	97
MA 6.5	333	277	0.86	161.1	2.82	0.00210	0.1940	2.2	0.5475	1.3	15.65	2.5	2815	30	2777	35	101
MA 6.6	225	53	0.24	80.8	2.27	0.00168	0.1925	2.6	0.4081	1.5	10.83	3.0	2206	27	2763	42	80
MA 6.7	597	592	1.02	225.7	5.28	0.00384	0.1799	5.5	0.4149	1.2	10.29	5.7	2237	23	2652	75	84
MA 6.8	272	152	0.58	123.7	0.94	0.00069	0.1898	0.8	0.5242	1.2	13.72	1.4	2717	26	2741	13	99
MA 6.9	293	81	0.29	128.0	0.48	0.00035	0.1871	0.5	0.5063	1.2	13.06	1.3	2641	25	2717	9	97
MA 6.10	392	135	0.36	166.5	3.99	0.00296	0.1938	2.7	0.4748	1.2	12.68	2.9	2504	24	2774	44	90
MA 6.11	718	631	0.91	298.9	13.65	0.00988	0.1769	11	0.4181	1.9	10.2	10.9	2252	36	2624	178	86
MA 6.12	494	239	0.50	189.2	5.88	0.00353	0.1764	3.6	0.4243	1.2	10.32	3.8	2280	23	2619	60	87
MA 6.13	443	709	1.65	207.9	9.78	0.00720	0.1876	7.1	0.4928	1.4	12.74	7.2	2583	30	2721	117	95
MA 6.14	345	73	0.22	160.7	1.54	0.00114	0.1930	1.1	0.5338	1.1	15.2	1.6	2758	26	2768	19	100

% comm 206= amount of common ^{206}Pb in total ^{206}Pb; * = radiogenic lead corrected using measured ^{204}Pb; % conc.= [($^{206}Pb/^{238}U$ age)/($^{207}Pb/^{206}Pb$ age)] x100.

Therefore, the age of 2752 ±10 Ma (MSWD = 0.37) is taken to record the age of crystallization of the porphyritic granodiorite.

Table 5.8. Hafnium isotopic data for sample MA 6. T_{DM2} value is used in the text.

Spot	t (Ma)	$^{176}Yb/^{177}Hf$	$^{176}Lu/^{177}Hf$	$^{176}Hf/^{177}Hf$	2σ	$e_{Hf}(0)$	$e_{Hf}(t)$	T_{DM1}	T_{DM2}	$f_{Lu/Hf}$
MA 6.1.1	2755	0.010809	0.000353	0.281037	0.000015	-61.35	-0.11	3031	3389	-0.99
MA 6.1.2	2749	0.01075	0.000297	0.281069	0.000017	-60.23	0.98	2985	3292	-0.99
MA 6.3	2932	0.019792	0.000673	0.281107	0.000016	-58.87	5.82	2962	3001	-0.98
MA 6.4	2756	0.015013	0.000497	0.280961	0.000022	-65.05	-3.07	3144	3645	-0.99
MA 6.5	2777	0.019214	0.000701	0.280952	0.000019	-65.36	-3.29	3172	3678	-0.98
MA 6.7	2652	0.016874	0.000543	0.28081	0.000016	-69.39	-10.9	3349	4247	-0.98
MA 6.8	2741	0.019564	0.000612	0.280983	0.000021	-63.27	-2.84	3124	3615	-0.98
MA 6.9	2717	0.018075	0.000586	0.280992	0.000018	-62.93	-3	3109	3613	-0.98
MA 6.10	2774	0.015612	0.000463	0.281023	0.000019	-61.87	-0.4	3059	3428	-0.99
MA 6.11	2624	0.023851	0.000746	0.280808	0.000016	-69.46	-11.97	3369	4320	-0.98
MA 6.13	2721	0.01857	0.000595	0.281065	0.000016	-60.35	-0.33	3012	3386	-0.98
MA 6.14	2768	0.011942	0.000392	0.281022	0.000017	-61.89	-0.42	3054	3427	-0.99

Twelve Lu-Hf analyses were obtained from the sites analyzed by SHRIMP and results are listed in Table 5.8. The Lu-Hf data of nine analyses, including the eight concordant analyses considered in the age calculation, show some variation in the $^{176}Hf/^{177}Hf$ ratios (0.280952 to 0.281069), εHf(t) values (-3.29 to 0.98), with a range in the T_{DM2} model ages from 3292 to 3678 Ma, implying that the parent magma of the porphyritic granodiorite was sourced from a slightly enriched to chondritic reservoir between ~3.77 and 3.29 Ga.

The oldest xenocrystic core (MA 6.3, 2932 Ma) has a slightly higher $^{176}Hf/^{177}Hf$ ratio (0.281107), with positive εHf(t) (5.82) and slightly younger T_{DM2} model age (3001 Ma) compared to the zircons comprising the main group, indicating some variation between the sources of the xenocryst and the porphyritic granodiorite. Two analyses (MA 6.7 and 6.11), affected by recent Pb loss, show significantly lower $^{176}Hf/^{177}Hf$ ratios (0.280810 and 0.280808), anomalously negative εHf(t) values (-10.9 and -11.97) and much older T_{DM2} ages (4247 and to 4320 Ma) when compared with rest of the analyses..

Sample MA 10

Zircons from porphyritic granodiorite sample MA 10 are dark brown, euhedral, elongate prismatic in shape and most show thin oscillatory zones of magmatic origin (Fig. 5.17c,d,e). A number of grains are broken (Fig. 5.17f,g). The zircons range from 80 to 180 μm in length, and have an average length to width ratio of >2.5:1.

Isotopic data were collected during a single analytical session with a total of 17 analyses completed on 15 zircons. The error of the mean Pb/U calibration constant determined from 10 analyses of the CZ3 standard was 0.40% (2σ). Results are listed in Table 5.9.

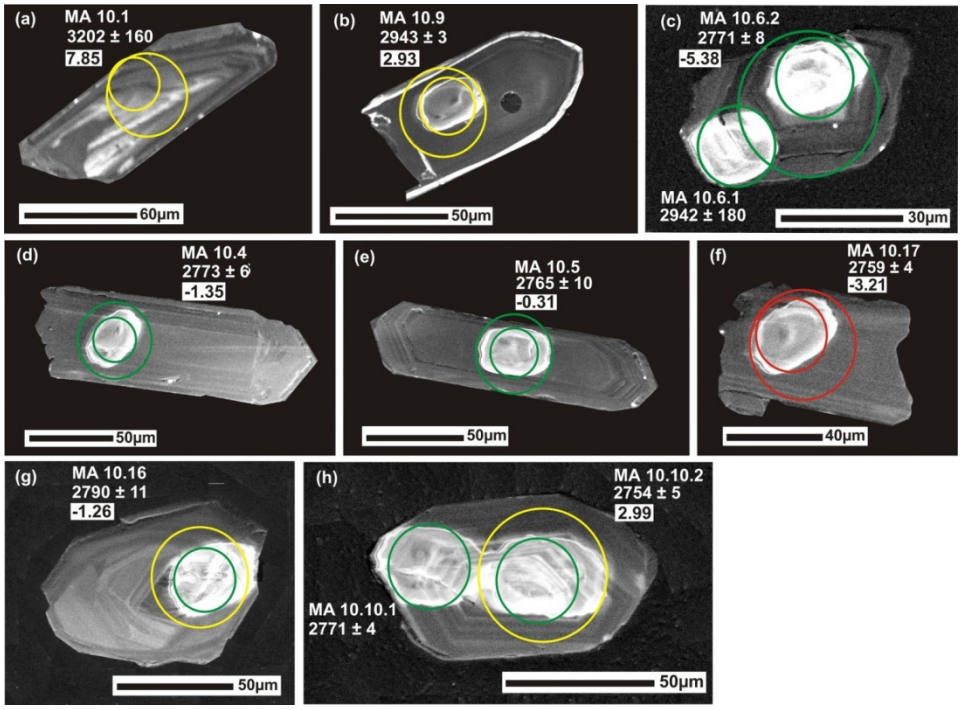

Fig. 5.17. Cathodoluminescence (CL) images of representative zircons from sample MA 10. Small and large circles indicate the locations of SHRIMP U-Pb analyses and LA-ICP-MS Hf analyses, respectively. The U–Pb ages and εHf(t) values are given for each spot.

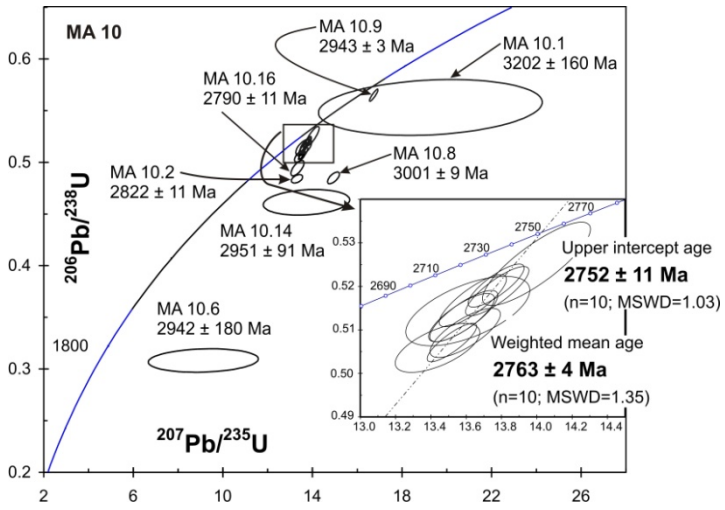

Fig. 5.18. Concordia plot of sample MA 10.

The U contents vary from 40 to 505 ppm (average 294 ppm). The Th content show a range from 12 to 405 ppm, averaging 142 ppm (excluding sites MA 10.1, 10.15 and 10.6 that have higher Th contents of 732, 2024 and 4552 ppm, respectively). The Th/U ratios, except for the three higher values (from MA 10.1, 10.15 and 10.6) range from 0.06 to 0.98 with an average value of 0.58. A concordia plot shows that 10 analyses produces a tight cluster of weakly discordant points giving a weighted mean $^{207}Pb/^{206}Pb$ age of 2763 ± 4 Ma (MSWD = 1.35), whereas an Isoplot upper intercept of the same data points gives an age of 2752 ± 11 Ma (MSWD = 1.03) (Fig. 5.18). The weighted mean

$^{207}Pb/^{206}Pb$ age of 2763 ± 4 Ma is interpreted to mark the minimum age of crystallisation of porphyritic granodiorite sample MA 10.

Three of the seven older analyses (MA 10.1, 10.6.1 and 10.15) show anomalously high Th/U ratios and common Pb contents (Table 5.19) suggesting inclusions may have been intersected during the analyses. The oldest age (3202 ± 160 Ma) was obtained from a small recrystallized patch partially obliterating thin magmatic zoning in grain MA 10. Therefore, the 3202 ± 160 Ma age is considered to be influenced by the isotopic disturbance that occurred during a recrystallization event. The remaining three of the four older ages (3006 ± 9, 2943 ± 3, and 2822± 9 Ma) are interpreted as inherited magmatic grains. Analysis MA 10.16 with slightly older age (2790 ± 11 Ma) compared to the crystallization age (2763 ± 4 Ma) of the granodiorite is interpreted to belong to the older group, having undergone ancient Pb loss during the subsequent magmatic crystallization.

Table 5.9. U-Pb SHRIMP geochronological data for sample MA 10.

Spot	U ppm	Th ppm	Th/U	Rad ^{206}Pb ppm	% comm 206	$^{204}Pb/^{206}Pb$	$^{207}Pb^*/^{206}Pb^*$	% err	$^{206}Pb^*/^{238}U$	±%	$^{276}Pb^*/^{235}U$	±%	$^{206}Pb^*/^{238}U$ Age	1σ	$^{207}Pb^*/^{206}Pb^*$ Age	1σ	% conc
MA 10.1	274	732	2.76	136.0	5.59	0.00369	0.2527	10	0.5530	2	19.3	10.6	2838	46	3202	160	89
MA 10.2	425	405	0.98	178.0	0.83	0.00062	0.1994	0.7	0.4840	0.3	13.31	0.8	2545	7	2822	11	90
MA 10.3	241	46	0.20	106.0	0.21	0.00015	0.1920	0.3	0.5128	0.4	13.57	0.6	2669	10	2759	6	97
MA 10.4	284	236	0.86	124.0	0.00	0.00002	0.1936	0.4	0.5093	0.5	13.59	0.6	2654	10	2773	6	96
MA 10.5	373	61	0.17	162.0	0.04	0.00003	0.1927	0.6	0.5059	0.5	13.44	0.7	2639	10	2765	9	95
MA 10.6.1	748	4552	6.29	236.0	16.04	0.01227	0.2147	11	0.3082	1.5	9.1	11.0	1732	23	2942	180	59
MA 10.6.2	96	76	0.81	43.6	0.17	0.00012	0.1933	0.5	0.5252	0.7	15	0.9	2721	17	2771	8	98
MA 10.8	211	152	0.74	88.3	0.32	0.00025	0.2234	0.6	0.4849	0.5	15.94	0.7	2549	10	3006	9	85
MA 10.9	379	140	0.38	184.0	0.00	0.00001	0.2149	0.2	0.5649	0.4	16.74	0.5	2887	10	2943	3	98
MA 10.10	382	86	0.23	166.0	0.06	0.00005	0.1934	0.2	0.5071	0.4	13.52	0.4	2644	8	2771	4	95
MA 10.11	193	13	0.07	85.7	0.03	0.00003	0.1914	0.3	0.5167	0.5	13.64	0.6	2685	10	2754	5	97
MA 10.12	112	82	0.75	49.7	0.47	0.00035	0.1919	0.8	0.5143	0.6	13.61	1.1	2675	14	2759	14	97
MA 10.13	243	120	0.51	108.0	0.00	0.00001	0.1925	0.3	0.5189	0.4	13.78	0.5	2695	10	2764	5	97
MA 10.14	205	12	0.06	90.3	0.11	0.00008	0.1920	0.3	0.5132	0.5	13.59	0.6	2670	10	2760	6	97
MA 10.15	286	2024	7.32	123.0	7.96	0.00610	0.2159	5.6	0.4613	1.1	13.73	5.7	2445	22	2951	91	83
MA 10.16	171	224	1.35	73.2	0.57	0.00043	0.1956	0.7	0.4944	0.6	13.33	0.9	2589	13	2790	11	93
MA 10.17	371	340	0.95	166.0	0.16	0.00012	0.19198	0.3	0.5202	0.4	13.77	0.50	2700	9	2759	4	98

% comm 206= amount of common ^{206}Pb in total ^{206}Pb; * = radiogenic lead corrected using measured ^{204}Pb; % conc.= [($^{206}Pb/^{238}U$ age)/($^{207}Pb/^{206}Pb$ age)] x100.

Fifteen Lu-Hf analyses were obtained from sample MA 10 and are listed in Table 5.10. Most of the zircons from the main population show $^{176}Hf/^{177}Hf$ ratios ranging from 0.280893 to 0.281062, εHf(t) values from -5.81 to 0.79 and T_{DM2} ages from 3316 to 3853 Ma, excepting a higher $^{176}Hf/^{177}Hf$ ratio of 0.281172, weakly +ve εHf(t) value of 2.99 and the T_{DM2} model age (3123 Ma) from site MA 10.11. The older inherited grains MA 10.8 and MA 10.9 have $^{176}Hf/^{177}Hf$ ratios of 0.281021 and 0.281083, overlapping with those of the main population, similar +ve εHf(t) values of 3.43 and 2.93 and identical T_{DM2} model ages of ~3256 Ma, which are younger than those of the main population. The youngest inherited grain MA.10.2 (2822 ± 11 Ma) has a $^{176}Hf/^{177}Hf$ ratio of 0.280953,

Table 5.10. Hafnium isotopic data from sample MA 10. T_{DM2}(Hf) value is used in the text.

Sample No.	t (Ma)	$^{176}Yb/^{177}Hf$	$^{176}Lu/^{177}Hf$	$^{176}Hf/^{177}Hf$	2sσ	eHf(0)	eHf(t)	TDM_1	TDM_2	fLu/Hf
MA 10.1	3202	0.007255	0.000212	0.280963	0.000023	-63.99	7.85	3119	3011	-0.99
MA 10.2	2822	0.011602	0.000373	0.280953	0.000024	-65.34	-1.62	3145	3565	-0.99
MA 10.3	2759	0.011508	0.000405	0.281062	0.000023	-60.46	0.79	3001	3316	-0.99
MA 10.4	2773	0.022171	0.000709	0.28101	0.000032	-62.32	-1.35	3096	3509	-0.98
MA 10.5	2765	0.022017	0.000739	0.281046	0.000026	-61.05	-0.31	3050	3414	-0.98
MA 10.7	2771	0.003743	0.000118	0.280866	0.00003	-67.39	-5.38	3239	3853	-1.00
MA 10.8	3006	0.034452	0.001156	0.281021	0.000025	-61.93	3.43	3117	3256	-0.97
MA 10.9	2943	0.049776	0.001805	0.281083	0.000028	-59.73	2.93	3085	3256	-0.95
MA 10.11	2754	0.035149	0.001248	0.281172	0.00003	-56.59	2.99	2918	3123	-0.96
MA 10.12	2759	0.005966	0.000173	0.280893	0.000031	-66.45	-5.81	3208	3796	-0.99
MA 10.13	2764	0.007234	0.000236	0.280915	0.000029	-65.66	-5.02	3184	3732	-0.99
MA 10.14	2760	0.04289	0.001393	0.281012	0.000027	-62.24	-2.85	3148	3629	-0.96
MA 10.15	2951	0.039238	0.001217	0.281007	0.000033	-62.43	1.58	3141	3378	-0.96
MA 10.16	2790	0.0146	0.000556	0.280993	0.00003	-62.91	-1.26	3106	3512	-0.98
MA 10.17	2759	0.018733	0.000612	0.280961	0.000033	-65.05	-3.21	3153	3659	-0.98

εHf(t) value of -1.62 and T_{DM2} model age of 3565 Ma, similar to the main population. One of the disturbed (U-Pb isotope) grains (MA 10.1) has a +ve εHf(t) value of 7.85 and T_{DM2} model age of 3011 Ma, which is younger than the crystallisation age (3202 Ma), suggesting that this grain underwent disturbance to the Lu-Hf system. Despite showing a disturbed U-Pb isotopic system, the Lu-Hf isotopic system of grain MA 10.15, however, remained unaffected, as suggested by a comparable $^{176}Hf/^{177}Hf$ ratio, εHf(t) value and T_{DM2} model age to the main population. The dominance of near chondritic to moderately –ve εHf(t) values (0.79 to -5.81) and T_{DM2} ages of 3316 to 3853 Ma indicate that the parental magma of the porphyritic granodiorite was sourced from a slightly enriched to chondritic reservoir between ~3.85 and 3.32 Ga. Nonetheless, the presence of +ve εHf(t) values and slightly younger T_{DM2} ages (3256 to 3123 Ma) from several grains (MA 8, MA 9 and MA 11) suggest that the source area was also modified by a more juvenile component.

Sample MA 38

Only thirteen zircon grains were obtained from sample MA 38. Zircons are brown and form euhedral slender prisms and have distinct oscillatory zoning (Fig. 5.19a,b,c,d,e). A few grains show convolute zoning suggestive of recrystallization (Fig. 5.19f,g). The zircons range in length from 80 to 180μm, and have an average length to width ratio of >3:1.

Isotopic data were collected during a single analytical session with a total of 12 analyses completed on 11 zircons. The error of the mean Pb/U calibration constant determined from 9 analyses of the CZ3 standard was 1.62% (2σ). Results are listed in Table 5.11. The zircons have moderate U contents ranging from 253 to 671 ppm (average 419 ppm) and

low to moderate Th ranging from 44 to 769 ppm (average 219 ppm). Th/U ratios are generally low to moderate (0.16 to 0.81) except for values of 1.18 and 1.56 from analyses MA 38.5 and 38.4, respectively. On a concordia plot (Fig. 5.20), 8 of the 12 data points lie on a discordia line with an Isoplot upper intercept age of 2758 ± 10 Ma (MSWD = 1.6) Ma which is taken to record the crystallization age of the porphyritic granodiorite sample MA 38. Three discordant older analyses, MA 38.8, 38.7 and 38.9 with ages >2.9 Ga are interpreted as inherited grains that were incorporated in the porphyritic granodiorite.

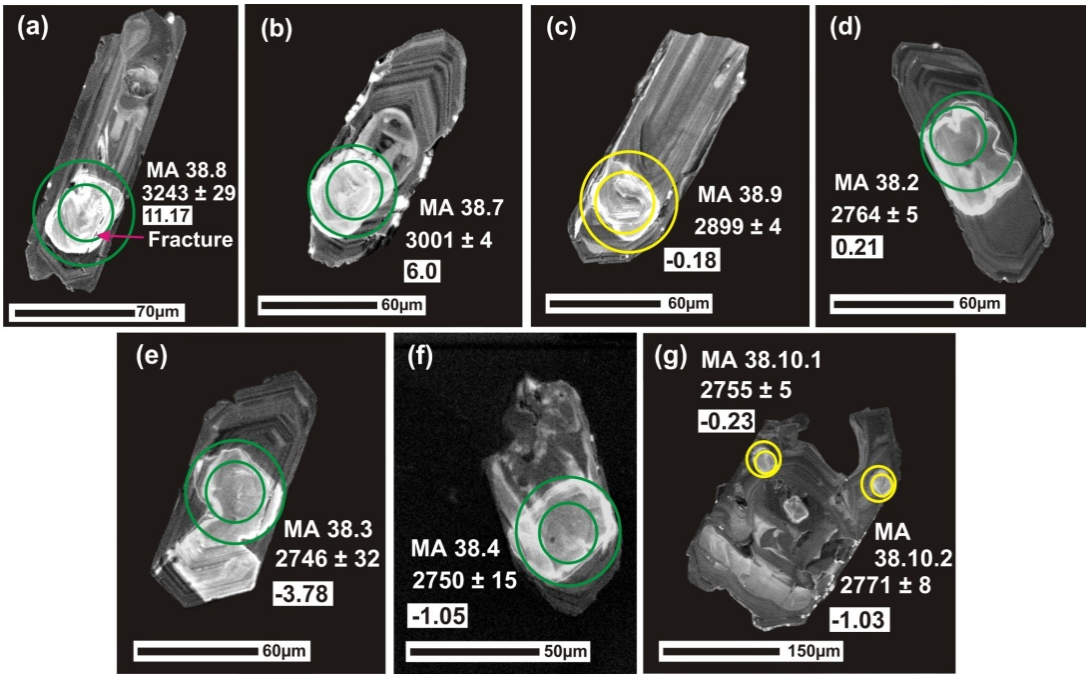

Fig. 5.19. Cathodoluminescence (CL) images of representative zircons from sample MA 38. Small and large circles indicate the locations of SHRIMP U-Pb analyses and LA-ICP-MS Hf analyses, respectively. The U–Pb ages and εHf(t) values are given for each spot.

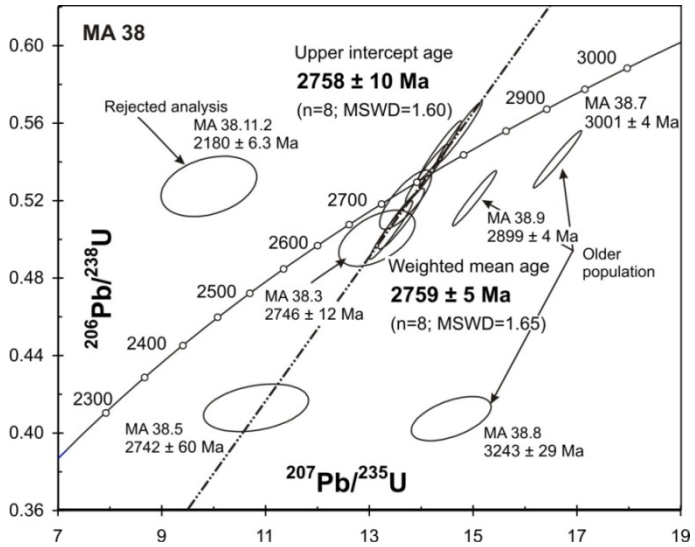

Fig. 5.20. Concordia plot of sample MA 38.

Lu-Hf analyses were obtained from eleven of the twelve spots analysed by SHRIMP, and are listed in Table 5.12. The $^{176}Hf/^{177}Hf$ ratio ranges from 0.280935 to 0.281095, except

for a higher value of 0.281182 from MA 38.5. Seven of the eight analyses of the main group, have a narrow range of εHf(t) from -3.78 to 0.21, with a much more positive value (5.03) from analysis MA 38.5. The εHf(t) values of the three inherited grains (MA 38.8, 38.7 and 38.9) are -0.18, 6.0 and 11.17, respectively. The anomalously higher εHf(t) value of 11.17 from MA 38.8 should be treated with caution as the analytical site was placed over a small fracture (Fig. 5.19a), that may have acted as a channel causing redistribution of REEs that consequently resulted in disturbed Lu-Hf systematics as suggested by Corfu et al. (2003). Apart from the much younger T_{DM2} model ages of 3025 and 3032 Ma recorded from MA38.5 and MA 38.7, respectively, the T_{DM2} model ages of all other spots are distributed within a narrow range from 3369 to 3685 Ma. Analysis MA 38.8, with the oldest age (3243 Ma) has a markedly lower T_{DM2} age of 2755 Ma, which corroborates disturbance of the Lu-Hf isotopic system, as discussed above. Analyses MA 38.5 and MA 38.7 have similar T_{DM2} model ages of 3025 to 3033 Ma and positive +ve εHf(t) values of 5.03 and 6.00, respectively, suggesting the incorporation of a more juvenile component into the source area.

Table 5.11. U-Pb SHRIMP geochronological data for sample MA 38.

Spot	U ppm	Th ppm	Th/U	Rad ^{206}Pb ppm	% comm 206	^{204}Pb/^{206}Pb	^{207}Pb*/^{206}Pb*	% err	^{206}Pb*/^{238}U	±%	^{276}Pb*/^{235}U	±%	^{206}Pb*/^{238}U Age	1σ	^{207}Pb*/^{206}Pb* Age	1σ	% conc
MA 38.1	424	113	0.28	199.0	0.02	0.00001	0.1908	0.3	0.5460	1.1	15.36	1.2	2808	26	2749	5	102
MA 38.2	499	137	0.28	238.0	0.08	0.00006	0.1926	0.3	0.5549	1.2	15.73	1.2	2846	27	2764	5	103
MA 38.3	376	57	0.16	166.0	2.83	0.00209	0.1904	2	0.5006	1.2	13.14	2.3	2616	25	2746	32	95
MA 38.4	253	383	1.56	114.0	0.92	0.00068	0.1909	0.9	0.5205	1.2	13.7	1.5	2701	26	2750	15	98
MA 38.5	671	769	1.18	251.0	5.17	0.00381	0.1900	3.6	0.4130	1.2	10.82	3.8	2229	23	2742	60	81
MA 38.6	485	61	0.13	211.0	0.05	0.00004	0.1928	0.3	0.5048	1.2	13.42	1.3	2634	26	2766	5	95
MA 38.7	604	203	0.35	281.0	0.00	0.00005	0.2227	0.2	0.5413	1.1	16.62	1.1	2789	25	3001	4	93
MA 38.8	443	349	0.81	155.0	0.00	0.00019	0.2595	1.8	0.4074	1.1	15.58	2.2	2203	21	3243	29	68
MA 38.9	526	340	0.67	236.0	0.00	0.00004	0.2091	0.3	0.5212	1.1	15.03	1.2	2704	25	2899	4	93
MA 38.10.2	286	56	0.20	125.0	0.00	0.00006	0.1934	0.5	0.5107	1.3	13.62	1.3	2659	27	2771	8	96
MA 38.10.1	380	115	0.31	174.0	0.02	0.00002	0.1915	0.3	0.5341	1.2	15.1	1.2	2759	26	2755	5	100
MA 38.11.2	214	44	0.21	96.8	0.00	0.00004	0.1363	3.6	0.5274	1.2	9.91	3.8	2730	27	2180	63	125

% comm 206= amount of common ^{206}Pb in total ^{206}Pb; * = radiogenic lead corrected using measured ^{204}Pb; % conc.= [(^{206}Pb/^{238}U age)/(^{207}Pb/^{206}Pb age)] x100.

Table 5.12. Hafnium isotopic data for sample MA 38. T_{DM2} value is used in the text.

Spot no.	t (Ma)	^{176}Yb/^{177}Hf	^{176}Lu/^{177}Hf	^{176}Hf/^{177}Hf	2σ	$e_{Hf}(0)$	$e_{Hf}(t)$	T_{DM1}	T_{DM2}	$f_{Lu/Hf}$
MA 38.1	2749	0.013662	0.000493	0.280994	0.000033	-62.87	-2.03	3099	3551	-1
MA 38.2	2764	0.017618	0.000621	0.281054	0.000027	-60.74	0.21	3029	3369	-1
MA 38.3	2746	0.024383	0.000802	0.280963	0.000026	-63.96	-3.78	3166	3699	-1
MA 38.4	2750	0.011452	0.000399	0.281016	0.000047	-62.09	-1.05	3062	3467	-1
MA 38.5	2742	0.022639	0.000737	0.281182	0.000054	-56.23	5.03	2866	3025	-1
MA 38.6	2766	0.01142	0.000337	0.280935	0.000029	-65.97	-3.46	3166	3685	-1
MA 38.7	3001	0.03182	0.001137	0.281095	0.000065	-59.31	6.00	3015	3032	-1
MA 38.8	3243	0.028483	0.000924	0.281073	0.000042	-60.08	11.17	3027	2755	-1
MA 38.9	2899	0.031255	0.001134	0.280986	0.000027	-63.17	-0.18	3163	3493	-1
MA 38.10.2	2771	0.013379	0.000455	0.281006	0.000022	-62.44	-1.03	3080	3480	-1
MA 38.10.1	2755	0.010928	0.000384	0.281035	0.000022	-61.43	-0.23	3036	3401	-1

5.4.1.3 Microporphyritic granodiorite

Sample MA 15

Two distinct groups of zircons are identified in microporphyritic granodiorite sample MA 15 based on transmitted light (TL) microscopy and cathodoluminescence (CL) studies. Type 1 zircons are transparent to pale brown in colour and form stubby crystals with broken edges. They contain cracks and are almost free of inclusions. The zircons range from 120 to 260 μm in length. CL images reveal well-developed broad oscillatory zoning of magmatic origin (Fig. 5.21a,b). Type 2 zircons are pale brown in colour, elongate, mostly euhedral, with well-developed prism and pyramidal faces. They range in length from 120 to 260 μm, with an average length to width ratio of 2.5:1. Many grains are irregularly fractured and contain elongate, rod-like apatite and/or opaque inclusions. CL images reveal the presence of thin oscillatory zoning in most of the zircons (Fig. 5.21c, grain MA 15.5 and MA 15.10), although some are unzoned. Central domains of a few grains show irregular recrystallized patches (Fig. 5.21c, MA 15.10).

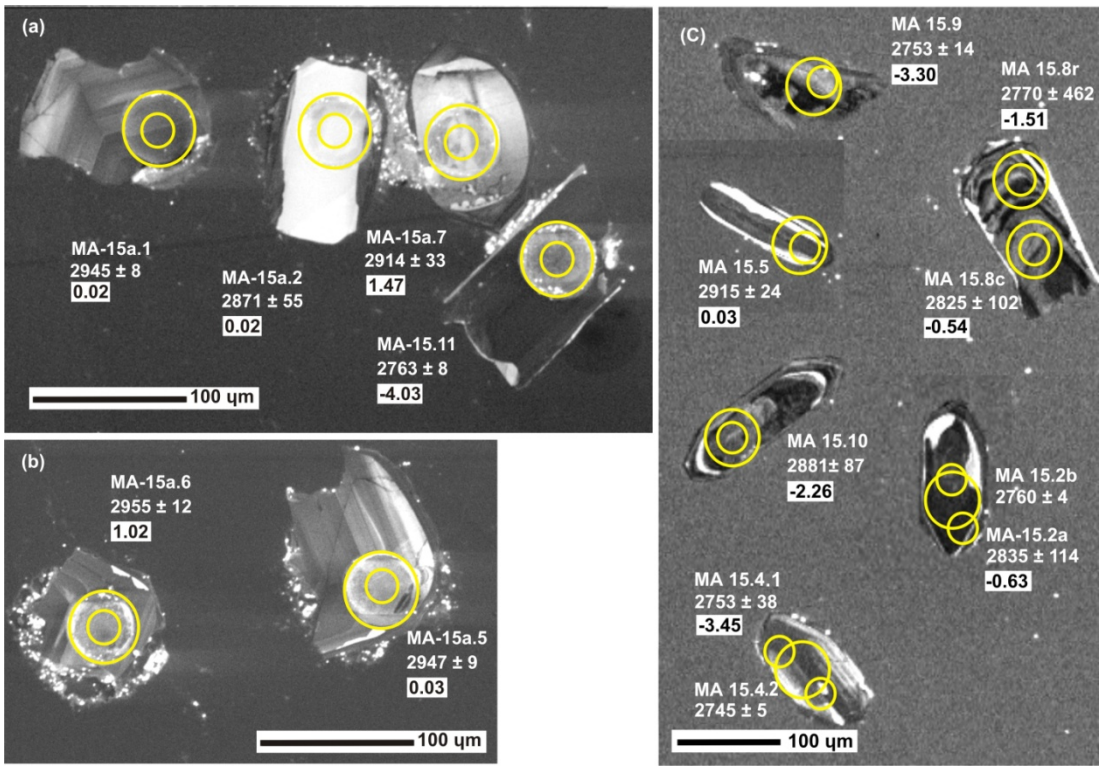

Fig. 5.21. Cathodoluminescence (CL) images of representative zircons from sample MA 15 (a), (b) older grains & (c) younger grains. Small and large circles indicate the locations of SHRIMP U-Pb analyses and LA-ICP-MS Hf analyses, respectively. The U–Pb ages and εHf(t) values are given for each spot. c and r after the spot number refer to core and rim, respectively.

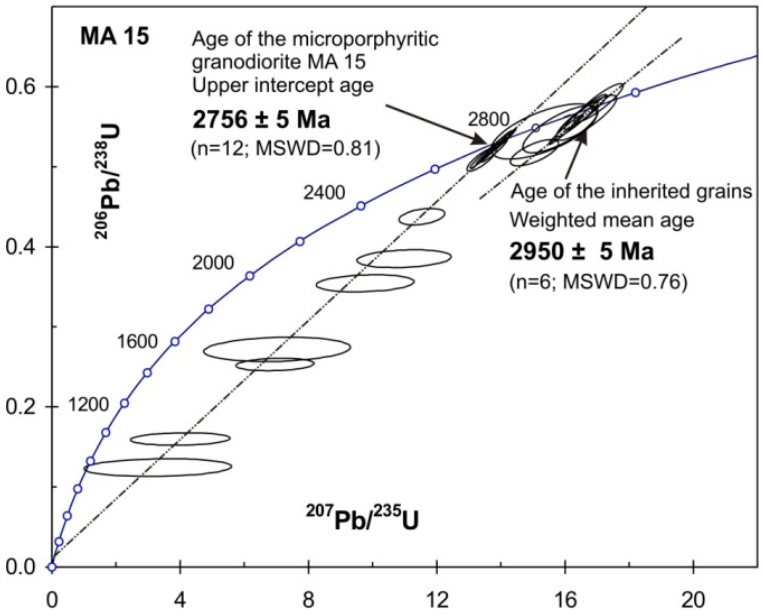

Fig. 5.22. Concordia plot of sample MA 15.

Table 5.13. U-Pb SHRIMP geochronological data for sample MA 15. c and r after the spot number refer to core and rim, respectively.

Spot	U ppm	Th ppm	Th/U	Rad ^{206}Pb ppm	% comm 206	^{204}Pb / ^{206}Pb	^{207}Pb* / ^{206}Pb*	% err	^{206}Pb* / ^{238}U	±%	^{276}Pb* / ^{235}U	±%	^{206}Pb* / ^{238}U Age	1σ	^{207}Pb* / ^{206}Pb* Age	1σ	% conc
Inherited grains																	
MA 15a.1	184	118	0.66	89.6	0.37	0.00028	0.2152	0.5	0.5645	1.4	16.75	1.5	2885	32	2945	8	98
MA 15a.2	16	6	0.39	7.9	3.41	0.00258	0.2055	3.4	0.5417	2.5	15.35	4.2	2790	56	2871	55	97
MA 15a.4	38	10	0.27	18.6	0.56	0.00043	0.2181	1.1	0.5655	1.8	17.01	2.1	2889	42	2967	18	97
MA 15a.5	132	72	0.56	65.2	0.26	0.00020	0.2154	0.5	0.5725	1.4	17.01	1.5	2918	32	2947	9	99
MA 15a.6	78	22	0.29	39.1	0.40	0.00031	0.2165	0.8	0.5821	1.5	17.38	1.7	2957	35	2955	12	100
MA 15a.7	23	7	0.30	10.8	1.43	0.00109	0.2110	2.0	0.5441	2.1	15.83	2.9	2800	48	2914	33	96
MA 15a.8	325	175	0.56	160.2	0.14	0.00011	0.2165	0.3	0.5730	1.2	17.10	1.3	2920	29	2955	4	99
MA 15a.9	427	299	0.72	203.7	0.31	0.00024	0.2153	0.3	0.5532	1.2	16.42	1.3	2839	28	2946	5	96
MA 15.5	476	73	0.16	215.6	2.19	0.00167	0.2112	1.5	0.5162	1.2	15.03	1.9	2683	27	2915	24	92
MA 15.10	709	788	1.15	250.7	7.58	0.00573	0.2069	5.3	0.3804	1.4	10.85	5.5	2078	25	2881	87	72
Microporphyritic granodiorite																	
MA 15.1	369	77	0.22	167.4	0.26	0.00019	0.1912	0.3	0.5264	1.3	13.88	1.3	2726	29	2753	5	99
MA 15.2a	1342	1180	0.91	324.0	10.38	0.00779	0.2011	7.0	0.2519	1.5	6.98	7.1	1448	20	2835	114	51
MA 15.2b	500	113	0.23	227.4	0.13	0.00010	0.1921	0.2	0.5291	1.2	14.01	1.3	2738	28	2760	4	99
MA 15.3	489	225	0.47	190.3	3.54	0.00262	0.1912	2.3	0.4367	1.2	11.51	2.6	2336	24	2753	38	85
MA 15.4.1	368	233	0.65	162.5	0.15	0.00011	0.1913	0.3	0.5125	1.2	13.51	1.3	2667	27	2753	4	97
MA 15.4.2	390	302	0.80	170.4	0.31	0.00023	0.1903	0.3	0.5068	1.2	13.30	1.3	2643	26	2745	5	96
MA 15.6	995	1330	1.38	270.2	12.67	0.00932	0.1874	13.1	0.2760	2.4	7.13	13.3	1571	33	2719	216	58
MA 15.7	1132	1487	1.36	193.6	19.24	0.01404	0.1819	15.7	0.1608	2.1	4.03	15.8	961	19	2671	260	36
MA 15.8r	1121	3302	3.04	170.6	30.74	0.02280	0.1933	28.2	0.1227	3.6	3.27	28.4	746	25	2770	462	27
MA 15.8c	499	103	0.21	166.6	9.29	0.00696	0.2000	6.3	0.3529	1.5	9.73	6.4	1949	25	2826	102	69
MA 15.9	225	82	0.38	98.6	1.13	0.00084	0.1912	0.9	0.5038	1.3	13.28	1.5	2630	27	2753	14	96
MA 15.10	709	788	1.15	250.7	7.58	0.00573	0.2069	5.3	0.3804	1.4	10.85	5.5	2078	25	2881	87	72
MA 15.11	357	70	0.20	158.7	0.08	0.00006	0.1925	0.5	0.5166	1.3	13.71	1.3	2685	28	2763	8	97

% comm 206= amount of common ^{206}Pb in total ^{206}Pb; * = radiogenic lead corrected using measured ^{204}Pb; % conc.= [(^{206}Pb/^{238}U age)/(^{207}Pb/^{206}Pb age)] x100.

Isotopic data were collected during two SHRIMP analytical sessions, where a total of 22 analyses were performed on 19 grains. The error of the mean Pb/U calibration constant determined from 14 analyses of the CZ3 standard from the two sessions was 0.63% (2σ). Results are listed in Table 5.13.

Table 5.14. Hafnium isotopic data for sample MA 15. T_{DM2} value is used in the text.

Spot	t (Ma)	$^{176}Yb/^{177}Hf$	$^{176}Lu/^{177}Hf$	$^{176}Hf/^{177}Hf$	$2s_m$	$e_{Hf}(0)$	$e_{Hf}(t)$	T_{DM1}	T_{DM2}	$f_{Lu/Hf}$
Inherited grains										
MA 15a.1	2945	0.037250	0.001449	0.280980	0.000015	-63.37	0.02	3197	3507	-0.96
MA 15a.2	2871	0.033848	0.001517	0.281030	0.000017	-61.60	0.02	3134	3457	-0.95
MA 15a.4	2967	0.025200	0.000990	0.280968	0.000014	-63.80	1.02	3175	3437	-0.97
MA 15a.5	2947	0.038349	0.001486	0.280981	0.000015	-63.34	0.03	3199	3508	-0.96
MA 15a.6	2955	0.036382	0.001435	0.281001	0.000014	-62.63	1.02	3167	3428	-0.96
MA 15a.7	2914	0.040895	0.001752	0.281057	0.000020	-60.65	1.47	3116	3362	-0.95
MA 15.6	2955	0.056550	0.002083	0.281058	0.000021	-60.61	1.75	3142	3366	-0.94
MA 15.7	2946	0.080667	0.002962	0.281005	0.000020	-62.49	-2.11	3294	3690	-0.91
MA 15.5	2915	0.039710	0.001289	0.280990	0.000034	-63.02	0.03	3170	3486	-0.96
MA 15.10	2881	0.068695	0.002521	0.281015	0.000023	-62.13	-2.26	3240	3660	-0.92
Magmatic grains										
MA 15.1	2753	0.083713	0.002727	0.281025	0.000030	-61.78	-5.04	3244	3812	-0.92
MA 15.2.1	2835	0.052944	0.001884	0.281054	0.000020	-60.76	-0.63	3131	3489	-0.94
MA 15.3	2753	0.066844	0.002268	0.280949	0.000023	-65.47	-6.88	3310	3970	-0.93
MA 15.4.1	2753	0.015203	0.000514	0.280953	0.000022	-65.33	-3.45	3156	3676	-0.98
MA 15.6	2719	0.027538	0.001047	0.281187	0.000073	-56.05	3.11	2882	3088	-0.97
MA 15.7	2671	0.048947	0.001695	0.281045	0.000022	-61.07	-5.19	3128	3685	-0.95
MA 15.8r	2770	0.030216	0.000993	0.281022	0.000018	-61.89	-1.51	3102	3521	-0.97
MA 15.8c	2826	0.029471	0.000960	0.281012	0.000014	-62.24	-0.54	3113	3475	-0.97
MA 15.9	2753	0.064071	0.002197	0.281046	0.000021	-61.04	-3.3	3169	3663	-0.93
MA 15.11	2763	0.021970	0.000847	0.280948	0.000015	-65.50	-5.03	3190	3732	-0.97

Two zircon populations are evident on the concordia plot (Fig. 5.22). Zircons in the older and younger groups correlate with the Type 1 and Type 2 zircons, respectively. The older group comprises six concordant analyses and four analyses with intermediate ages (MA 14a2, MA 15a.7, MA 15a.5 and MA 15a.10) which are interpreted to result from resetting of the isotopic system during the crystallisation of the younger zircons. The U and Th content varies from 16 to 427 ppm (average 153 ppm) and from 6 to 299 ppm (average 88 ppm), respectively. The Th/U ratio ranges from 0.27 to 0.72, averaging 0.51. In the older group, six analyses define an Isoplot upper intercept age of 2957±13 Ma (MSWD = 0.35) and a similar weighted mean $^{207}Pb/^{206}Pb$ age of 2950 ± 5 Ma (MSWD = 0.76). The weighted mean $^{207}Pb/^{206}Pb$ age of 2950 ± 5 Ma (MSWD = 0.76) is preferred as defining the crystallization age of the older, inherited zircons.

The younger group consists of twelve analyses, which fall along a discordia line including a subgroup of five near concordant analyses. Their U and Th contents range from 6 to 299 ppm (average 88 ppm) and 70 to 3296 ppm (average 713 ppm). The Th/U ratio ranges from 0.20 to 3.05, averaging 0.85. All twelve analyses of the younger group define a weighted mean $^{207}Pb/^{206}Pb$ age of 2755 ± 5 Ma (MSWD = 0.81) and an identical Isoplot upper intercept $^{207}Pb/^{206}Pb$ age of 2756 ± 5 Ma (MSWD = 0.81), which is interpreted to record the age of formation of the microporphyritic granodiorite MA 16. The six discordant analyses with very large errors and high common Pb indicate recent lead loss (lower intercept at 95 Ma).

The two age populations are also reflected in the Hf data (Table. 5.14). The εHf(t) values of the two groups are distinct with the younger group having εHf (t) values ranging from -6.88 to -0.63 with one positive value of 3.11, whereas the older group ranges from 0.02 to 1.75, with two negative values of -2.11 and -2.26 (Table 5.19). The average T_{DM2} model ages of the younger and older groups are 3615 and 3471 Ma, respectively, corresponding to average $^{176}Hf/^{177}Hf$ values of 0.2810023 and 0.281009, respectively. The relationship between the younger and older zircons is explained in section 8.4. The positive εHf(t) value of 3.11 from analysis MA 15.6 from the younger group can be explained in terms of a disturbed isotopic system, which is supported by the high common Pb content (12.67 ppm) of the grain. The only negative εHf(t) values of -2.11 and -2.26 from analyses MA 15.7 and 15.10, respectively, from the inherited grains might reflect slight enrichment from a crustal source.

Sample MA 16

Zircon crystals from microporphyritic granodiorite sample MA 16 are mostly euhedral and prismatic, but a few are broken. They are 75 to 310 μm in length. Most zircon crystals are stubby with length:width ratios ≥2:1. They are grey in CL with fairly homogeneous central domains, bordered by thin zoned and/or unzoned domains (Fig. 5.23a,b,f), with the exception of an extensively recrystallized crystal (Fig. 5.23h). A few zircon crystals have a broad pale grey core bordered by a thick oscillatory zoned rim (Fig. 5.23e,g).

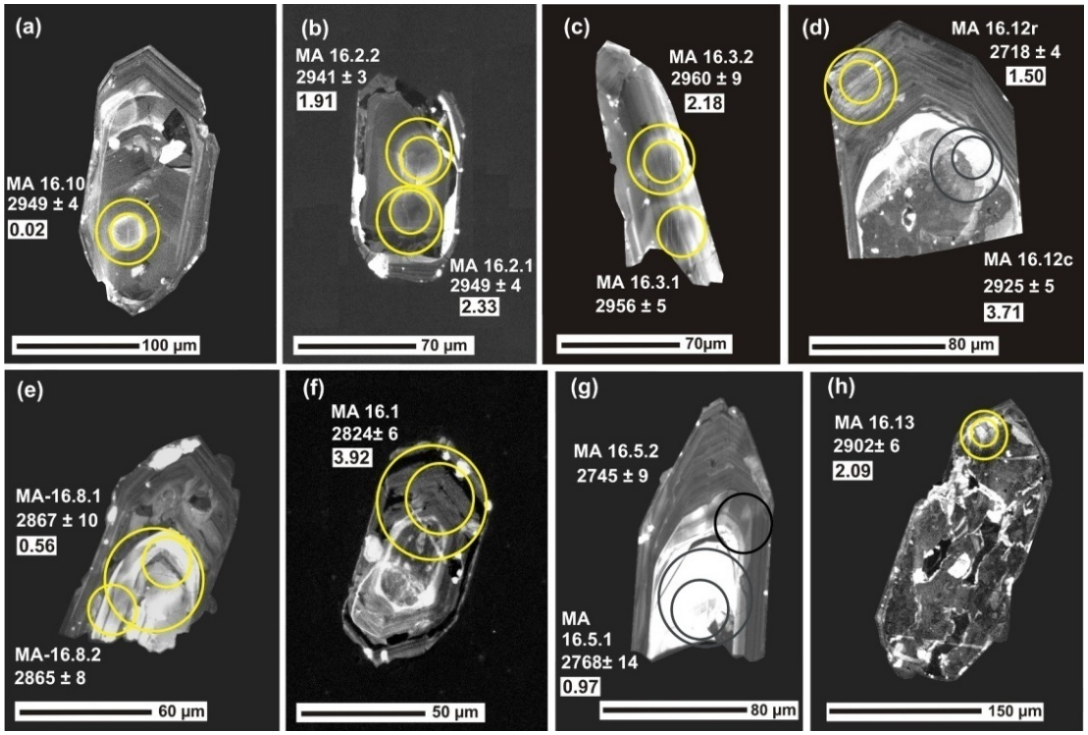

Fig. 5.23. Cathodoluminescence (CL) images of representative zircons from sample MA 16. Small and large circles indicate the locations of SHRIMP U-Pb analyses and LA-ICP-MS Hf analyses, respectively. The U–Pb ages and εHf(t) values are given for each spot. c and r after the spot number refer to core and rim, respectively.

U-Pb isotope data were collected during a single SHRIMP analytical session from 13 crystals. The error of the mean Pb/U calibration constant determined from 8 analyses of the CZ3 standard was 1.00% (2σ). Results are listed in Table 5.15.

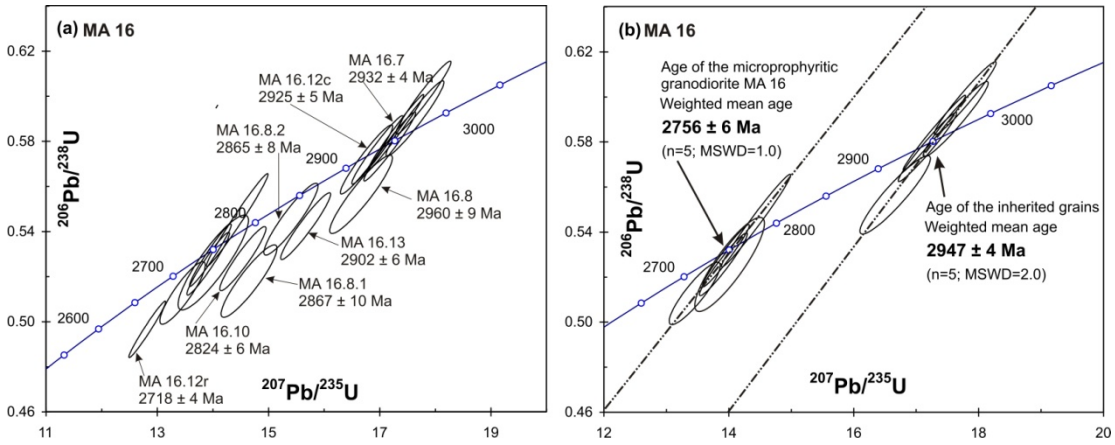

Fig. 5.24. Concordia plot of sample MA 16. (a) Plot of all the grains, (b) plot of the grains considered for the age calculations.

A concordia plot of all analyses highlights two groups with slight reversely discordant trends (Fig.5.24a,b). Some of intermediate ages (MA 16.7, MA 16.12r, MA 16.8.1, MA 16.10, MA 16.13.) plot between the two groups (Fig.5.24a) and are interpreted to result from members of the older group having undergone ancient Pb loss during subsequent magmatic crystallisation. The zircons in the older group have U contents ranging from 101 to 545 ppm (average 157), Th from 25 to 402 ppm (average 161 ppm) and Th/U ratios from 0.03 to 0.76 with an average of 0.53. The older group is represented by five concordant analyses (MA16.1, 16.2.1, 16.2.2, 16.3.1 and 16.3.2) with ages between 2960 and 2941 Ma; (Table 5.15) giving a weighted mean age of 2947 ± 4 Ma (MSWD = 2). The Isoplot upper intercept of these data points produces a similar $^{207}Pb/^{206}Pb$ age of 2951± 10 Ma (MSWD=2) and the weighted mean age is interpreted to be the minimum age of crystallisation of the older group of inherited grains.

The U and Th contents of the five younger concordant grains range from 35 to 915 ppm (average 415 ppm) and from 1 to 319 ppm (average 118 ppm), respectively. Their Th/U ratios vary from 0.03 to 0.38 (average 0.23). They have near concordant ages ranging from 2768 to 2745 Ma, with a weighted mean $^{207}Pb/^{206}Pb$ age of 2756 ± 6 Ma (MSWD =1.0) and an Isoplot upper intercept age of 2757 ± 7 Ma (MSWD = 0.85); the former age is interpreted as the minimum age of crystallisation of the microporphyritic granodiorite sample MA 16.

Table 5.15. U-Pb SHRIMP geochronological data for sample MA 16. c and r after the spot number refer to core and rim, respectively.

Spot	U ppm	Th ppm	Th/U	Rad ^{206}Pb ppm	% comm 206	^{204}Pb /^{206}Pb	^{207}Pb* /^{206}Pb*	% err	^{206}Pb* /^{238}U	±%	^{276}Pb* /^{235}U	±%	^{206}Pb* /^{238}U Age	1σ	^{207}Pb* /^{206}Pb* Age	1σ	% conc
Inherited grains																	
MA 16.1	527	251	0.49	239.9	0.32	0.00024	0.19970	0.4	0.52799	1.1	14.54	1.2	2733	25	2824	6	97
MA 16.2.1	358	227	0.65	177.7	0.03	0.00002	0.21567	0.2	0.57773	1.1	17.18	1.1	2939	26	2949	4	100
MA 16.2.2	545	402	0.76	273.7	0.02	0.00002	0.21470	0.2	0.58410	1.2	17.29	1.2	2965	28	2941	3	101
MA 16.3.1	182	134	0.76	92.3	0.06	0.00005	0.21672	0.3	0.59014	1.2	17.63	1.2	2990	28	2956	5	101
MA 16.3.2	101	64	0.66	48.3	0.06	0.00005	0.21716	0.5	0.55653	1.3	16.66	1.4	2852	29	2960	9	96
MA 16.7	375	245	0.68	186.0	0.14	0.00011	0.21344	0.3	0.57620	1.1	16.96	1.1	2933	25	2932	4	100
MA 16.8.1	169	41	0.25	75.7	0.39	0.00029	0.20509	0.6	0.51801	1.3	14.65	1.4	2691	28	2867	10	94
MA 16.8.2	138	25	0.19	64.7	0.30	0.00023	0.20478	0.5	0.54551	1.2	15.40	1.3	2806	27	2865	8	98
MA 16.10	263	136	0.54	135.7	0.03	0.00002	0.21519	0.3	0.59943	1.1	17.79	1.1	3028	27	2945	4	103
MA 16.12c	297	108	0.37	146.3	0.31	0.00024	0.21253	0.3	0.57196	1.1	16.76	1.1	2916	26	2925	5	100
MA 16.13	280	137	0.51	130.8	0.24	0.00018	0.20949	0.4	0.54239	1.1	15.67	1.2	2793	25	2902	6	96
Magmatic grains																	
MA 16.4	417	80	0.20	189.9	0.09	0.00006	0.19111	0.3	0.52953	1.1	13.95	1.1	2739	24	2752	4	100
MA 16.5.1	35	1	0.03	16.0	0.20	0.00015	0.19301	0.9	0.52628	1.6	14.01	1.8	2726	36	2768	14	98
MA 16.5.2	288	68	0.24	127.1	0.32	0.00024	0.19029	0.6	0.51277	1.1	13.45	1.2	2668	24	2745	9	97
MA 16.9	530	196	0.38	239.6	0.18	0.00013	0.19194	0.3	0.52574	1.1	13.91	1.1	2723	24	2759	5	99
MA 16.11	303	44	0.15	141.9	0.02	0.00002	0.19208	0.3	0.54512	1.5	14.44	1.6	2805	35	2760	5	102
MA 16.12r	915	319	0.36	391.1	0.19	0.00014	0.18721	0.2	0.49660	1.0	12.82	1.1	2599	22	2718	4	96

% comm 206= amount of common ^{206}Pb in total ^{206}Pb; * = radiogenic lead corrected using measured ^{204}Pb; % conc.= [(^{206}Pb/^{238}U age)/(^{207}Pb/^{206}Pb age)] x100.

Table 5.16. Hafnium isotopic data for sample MA 16. T_{DM2} value is used in the text.

Spot	t (Ma)	^{176}Yb/^{177}Hf	^{176}Lu/^{177}Hf	^{176}Hf/^{177}Hf	$2s_m$	$e_{Hf}(0)$	$e_{Hf}(t)$	T_{DM1}	T_{DM2}	$f_{Lu/Hf}$
Inherited grains										
MA 16.1	2824	0.037256	0.001167	0.281150	0.000049	-57.37	3.92	2942	3090	-0.96
MA 16.2.1	2949	0.073199	0.002336	0.281097	0.000026	-59.23	2.33	3109	3307	-0.93
MA 16.2.2	2941	0.056518	0.001845	0.281097	0.000020	-60.91	1.91	3130	3348	-0.95
MA 16.10	2945	0.055721	0.001789	0.281050	0.000027	-60.91	1.82	3130	3353	-0.95
MA 16.3.2	2960	0.067956	0.002243	0.281076	0.000050	-59.97	2.18	3130	3332	-0.93
MA 16.7	2932	0.102257	0.003534	0.281044	0.000088	-61.11	-2.16	3290	3686	-0.89
MA 16.8	2867	0.017062	0.000581	0.280996	0.000025	-62.80	0.56	3104	3408	-0.98
MA 16.12c	2925	0.025467	0.000785	0.281059	0.000023	-60.58	3.71	3036	3177	-0.98
MA 16.13	2902	0.036155	0.001399	0.281062	0.000018	-60.47	2.09	3080	3301	-0.96
Magmatic grains										
MA 16.5.1	2768	0.008851	0.000384	0.281061	0.000022	-60.52	0.97	3002	3306	-0.99
MA 16.11	2760	0.016454	0.000607	0.281175	0.000081	-56.47	5.44	2866	3002	-0.98
MA 16.12r	2718	0.019343	0.000671	0.281123	0.000029	-58.33	1.5	2941	3227	-0.98

Twelve Lu-Hf analyses were obtained from sample MA 16 and are presented in Table 5.17. The Lu-Hf data, however, do not provide any clear distinction between the older and younger groups. The ^{176}Hf/^{177}Hf ratios of the older grains (Table 5.16) range from 0.281044 to 0.281150, whereas the zircons in the younger age group also show a similar range from 0.281061 to 0.281123. The εHf(t) values are also indistinguishable between the two groups; all but one have +ve εHf(t) values; the exception is a –ve value of -2.71 from analysis MA 16.7. Some variation between the two groups is evident in the T_{DM2} model ages. Slightly older T_{DM2} model ages are noted for the older group, ranging from 3090 to 3686 Ma. Three younger analyses have T_{DM2} ages ranging from 3002 to 3306

Ma. The Lu-Hf isotopic data of the granodiorite zircons in sample MA 16 are discussed in section 8.4 in more detail.

5.4.2 Biotite monzogranite

Sample MA 3

Zircons from biotite monzogranite sample MA 3 are euhedral, elongated prismatic and characterized by oscillatory zones (Fig. 5.25a,b,c). A few crystals with banded zones are also present (Fig. 5.25d,e,f). Zircons range in length from ~150 to 400µm, with an average length to width ratio ≥3:1.

Isotopic data were collected during a single SHRIMP analytical session with 15 analyses completed on 15 zircons. The error of the mean Pb/U calibration determined from 7 analyses of the CZ3 standard was 1.71% (2σ). Analytical results are presented in Table 5.17.

The U content ranges from 149 to 1224 ppm (average 512 ppm), whereas the Th content varies from 69 to 208 ppm (average 123 ppm). The Th/U ratio varies from 0.04 to 0.91, averaging 0.41. A concordia plot of the analyses suggests strong recent Pb loss in all the grains as the analyses fall on a single discordia (Fig. 5.26). The Isoplot upper intercept age defined by all 15 analyses is 2636 ±11 Ma (MSWD = 1.12) (Fig. 5.26), with

Fig. 5.25. Cathodoluminescence (CL) images of representative zircons from sample MA 3. Small and large circles indicate the locations of SHRIMP U-Pb analyses and LA-ICP-MS Hf analyses, respectively. The U–Pb ages and εHf(t) values are given for each spot.

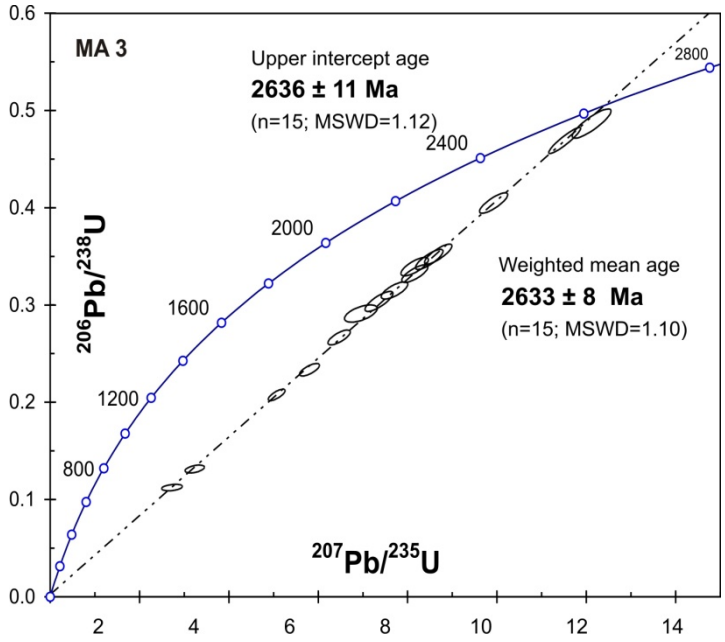

Fig.5.26. Concordia plot of sample MA 3.

a similar weighted mean age of 2633 ±8 Ma (MSWD = 1.1). Therefore, the Isoplot intercept age of 2636 ±11 Ma (MSWD = 1.12) of 15 data points is preferred as recording the crystallisation age of the biotite monzogranite.

Lu-Hf analyses were obtained from 14 of the 15 SHRIMP analytical sites and results are listed in Table 5.18. The $^{176}Hf/^{177}Hf$ ratios for most (twelve) of the zircons range from 0.280812 to 0.281063, corresponding to a more –ve εHf(t) values of -5.24 to -10.82, and significantly older T_{DM2} model ages of 4295 Ma to 3727 Ma. These are the first report of positive evidence of >4 Ga recycled crustal material in this part in the Yilgarn Craton.

Table 5.17. U-Pb SHRIMP geochronological data for sample MA 3.

Spot	U ppm	Th ppm	Th/U	Rad ^{206}Pb ppm	% comm 206	^{204}Pb / ^{206}Pb	$^{207}Pb^*$ / $^{206}Pb^*$	% err	$^{206}Pb^*$ / ^{238}U	±%	$^{276}Pb^*$ / ^{235}U	±%	$^{206}Pb^*$ / ^{238}U Age	1σ	$^{207}Pb^*$ / $^{206}Pb^*$ Age	1σ	% conc
MA 3.1	1224	45	0.04	366.8	1.11	0.00081	0.1774	0.9	0.3448	2	8.43	2.1	1910	32	2629	14	73
MA 3.2	1152	134	0.12	402.4	1.01	0.00073	0.1778	0.8	0.4024	2	9.87	2.0	2180	34	2633	12	83
MA 3.3	390	69	0.18	89.9	1.18	0.00086	0.1759	1.1	0.2650	2	6.43	2.2	1516	25	2615	18	58
MA 3.4	401	150	0.39	101.9	2.12	0.00153	0.1732	1.8	0.2895	2	6.91	2.6	1639	28	2589	29	63
MA 3.5	149	79	0.55	61.9	0.36	0.00026	0.1807	0.7	0.4836	2	12.05	2.1	2543	41	2659	12	96
MA3.6	344	132	0.40	93.6	1.28	0.00093	0.1775	1.1	0.3130	2	7.66	2.2	1755	29	2630	18	67
MA 3.7	615	85	0.14	71.3	3.20	0.00232	0.1786	2.4	0.1306	2	3.22	3.1	791	14	2640	40	30
MA 3.8	259	208	0.83	105.0	0.23	0.00017	0.1780	0.5	0.4662	2	11.45	1.9	2467	38	2635	8	94
MA 3.9	497	103	0.21	89.1	1.16	0.00084	0.1772	1.0	0.2063	2	5.04	2.1	1209	21	2627	17	46
MA 3.10	467	90	0.20	95.2	1.20	0.00088	0.1804	1.1	0.2320	2	5.77	2.1	1345	22	2656	18	51
MA 3.11	213	125	0.61	65.4	0.67	0.00049	0.1788	0.8	0.3502	2	8.63	2.1	1936	32	2642	14	73
MA 3.12	397	98	0.25	105.1	1.16	0.00084	0.1758	1.1	0.3019	2	7.31	2.3	1701	30	2613	17	65
MA 3.13	809	160	0.20	79.9	2.89	0.00209	0.1760	3.3	0.1116	2	2.71	3.8	682	12	2616	55	26
MA 3.15	470	103	0.23	135.3	0.85	0.00061	0.1782	1.0	0.3302	2	8.11	2.1	1840	29	2636	16	70
MA 3.16	290	257	0.91	85.2	1.20	0.00087	0.1743	1.0	0.3374	2	8.11	2.1	1874	30	2599	17	72

% comm 206= amount of common ^{206}Pb in total ^{206}Pb; * = radiogenic lead corrected using measured ^{204}Pb; % conc.= [($^{206}Pb/^{238}U$ age)/($^{207}Pb/^{206}Pb$ age)] x100.

Table 5.18. Hafnium isotopic data for samples analyzed from sample MA 3. T_{DM2} value is used in the text.

Spot	t (Ma)	$^{176}Yb/^{177}Hf$	$^{176}Lu/^{177}Hf$	$^{176}Hf/^{177}Hf$	$2s_m$	$e_{Hf}(0)$	$e_{Hf}(t)$	T_{DM1}	T_{DM2}	$f_{Lu/Hf}$
MA 3.1	2629	0.010549	0.000334	0.280816	0.000020	-69.17	-10.82	3323	4226	-0.99
MA 3.2	2633	0.013049	0.000420	0.280876	0.000021	-67.06	-8.76	3251	4052	-0.99
MA 3.3	2615	0.020213	0.000714	0.280867	0.000029	-67.37	-10.01	3288	4146	-0.98
MA 3.4	2589	0.089674	0.002449	0.281166	0.000032	-56.79	-3.01	3021	3528	-0.93
MA 3.5	2659	0.066411	0.001941	0.280991	0.000032	-62.98	-6.82	3223	3902	-0.94
MA 3.6	2630	0.014350	0.000458	0.280844	0.000023	-68.20	-10.05	3297	4160	-0.99
MA 3.7	2640	0.029623	0.000915	0.280935	0.000025	-65.96	-7.39	3213	3938	-0.97
MA 3.8	2635	0.026040	0.000761	0.280812	0.000023	-69.30	-11.59	3365	4295	-0.98
MA 3.9	2627	0.018784	0.000578	0.280842	0.000023	-68.26	-10.39	3310	4187	-0.98
MA 3.10	2656	0.042718	0.001306	0.280834	0.000029	-68.55	-11.34	3384	4288	-0.96
MA 3.11	2642	0.023209	0.000709	0.280896	0.000024	-66.35	-8.37	3249	4024	-0.98
MA 3.12	2613	0.096009	0.002592	0.281132	0.000032	-58.01	-3.98	3082	3628	-0.92
MA 3.15	2636	0.026424	0.00078	0.280839	0.000027	-68.35	-10.64	3330	4214	-0.98
MA 3.16	2599	0.059651	0.001766	0.281063	0.000026	-60.42	-5.24	3108	3727	-0.95

Analyses MA 3.4 and MA 3.12 have significantly higher $^{176}Hf/^{177}Hf$ ratios of 0.281166 and 0.281132, more –ve εHf(t) values of -3.01 and -3.98 and younger T_{DM2} model ages of 3528 and 3628 Ma, respectively.

Sample MA 4

Zircons are euhedral, elongate to prismatic in shape and, as in biotite monzogranite sample MA 3, most of them are characterized by oscillatory zones (Fig. 5.27a,b,c). In the corner of one grain, the magmatic zoning is transgressed by a local recrystallized patch(Fig. 5.27b). Zircons range in length from ~100 to 200μm, with an average length to width ratio of ~2:1. Isotopic data were collected during a single SHRIMP analytical session, where a total 12 analyses were performed on 12 grains. The error of the mean

Pb/U calibration determined from 7 analyses of the CZ3 standard was 0.37% (2σ). Analytical results are presented in Table 5.19.

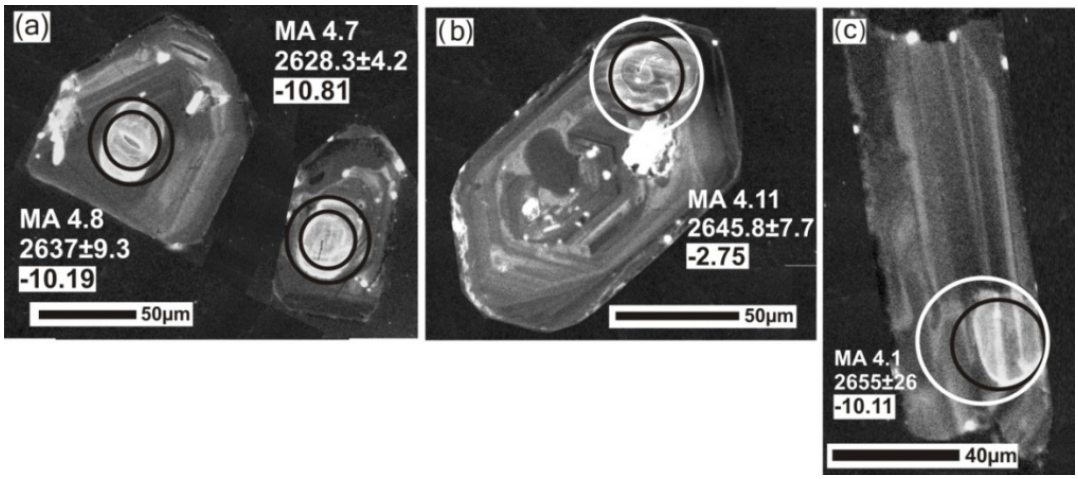

Fig. 5.27. CL images of representative zircons from sample MA 4. Small and large circles indicate the locations of SHRIMP U-Pb analyses and LA-ICP-MS Hf analyses, respectively. The U–Pb ages and εHf(t) values are given for each spot.

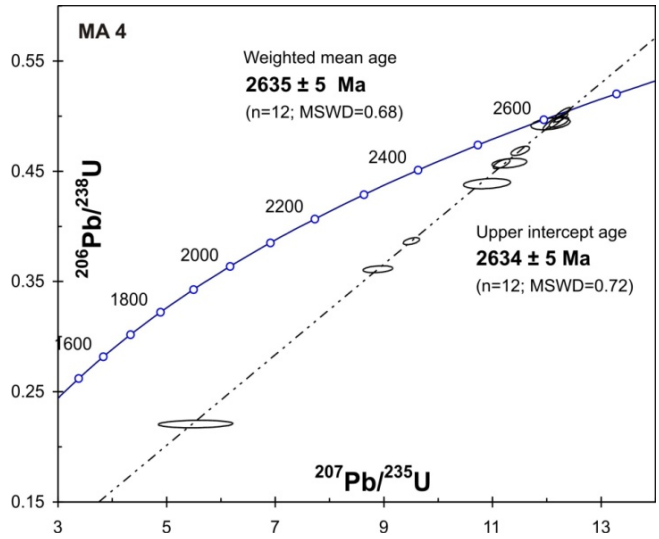

Fig. 5.28. Concordia plot of sample MA 4.

The zircons have a large range in U contents from 284 to 1351 ppm (average 464 ppm). Th content varies from 144 to 356 ppm (average 199 ppm) and the Th/U ratio from 0.12 to 0.73 (average 0.51). The zircons, as in sample MA 3, show strong recent lead loss and lie on a single discordia line (Fig. 5.28). The Isoplot upper intercept age defined by all twelve analyses is 2634 ± 5 Ma (MSWD = 0.72), with an almost identical weighted mean age of 2635 ± 5 Ma (MSWD = 0.68). It is therefore considered that the Isoplot age best records the crystallization age of the biotite monzogranite sample MA 4.

Table. 5.19. U-Pb SHRIMP geochronological data for sample MA 4.

Spot	U ppm	Th ppm	Th/U	Rad ^{206}Pb ppm	% comm 206	^{204}Pb /^{206}Pb	^{207}Pb* /^{206}Pb*	% err	^{206}Pb* /^{238}U	±%	^{206}Pb* /^{235}U	±%	^{206}Pb* /^{238}U Age	1σ	^{207}Pb* /^{206}Pb* Age	1σ	% conc
MA 4.1	346	187	0.56	133.0	2.00	0.00145	0.1802	1.6	0.4388	0	10.90	1.6	2345	8	2655	26	88
MA 4.2	353	154	0.45	142.0	0.26	0.00019	0.1782	0.5	0.4685	0	11.51	0.6	2477	8	2636	8	94
MA 4.3	391	214	0.56	156.0	1.49	0.00108	0.1793	1.1	0.4574	0	11.31	1.2	2428	8	2647	18	92
MA 4.4	1351	153	0.12	275.0	6.76	0.004j93	0.1819	5	0.2207	1	5.54	5.1	1286	7	2670	83	48
MA 4.5	305	152	0.52	129.0	0.00	-0.00002	0.1779	0.3	0.4939	1	12.12	0.6	2588	12	2633	5	98
MA 4.6	284	144	0.52	121.0	0.84	0.00061	0.1775	1.1	0.4931	1	12.07	1.2	2584	10	2629	9	98
MA 4.7	410	183	0.46	177.0	0.00	-0.00002	0.1774	0.3	0.5028	0	12.30	0.5	2626	9	2628	4	100
MA 4.8	499	268	0.55	167.0	0.58	0.00042	0.1784	0.6	0.3866	0	9.51	0.7	2107	6	2638	9	80
MA 4.9	323	155	0.50	127.0	0.32	0.00023	0.1774	0.4	0.4567	0	11.17	0.6	2425	8	2628	7	92
MA 4.10	474	242	0.53	203.0	0.00	-0.00001	0.1784	0.2	0.4987	0	12.27	0.4	2608	7	2638	4	99
MA 4.11	333	186	0.58	142.0	0.36	0.00026	0.1792	0.5	0.4946	0	12.22	0.6	2590	8	2646	8	98
MA 4.12	504	356	0.73	159.0	1.68	0.00122	0.1785	1.2	0.3611	0	8.89	1.3	1988	6	2639	20	75

% comm 206= amount of common ^{206}Pb in total ^{206}Pb; * = radiogenic lead corrected using measured ^{204}Pb; % conc.= [(^{206}Pb/^{238}U age)/(^{207}Pb/^{206}Pb age)] x100.

Twelve Lu-Hf analyses were obtained and results are listed in Table 5.20. Except for analysis MA 4.11, the ^{176}Hf/^{177}Hf ratios are low, ranging from 0.280776 to 0.28859 with large –ve εHf(t) values (-10.11 to -12.31). Ivanic et al. (2012) also obtained highly –ve εHf(t) values of -5.6 to -12.78 and -4.6 to -10.3 corresponding to T_{DM2} model ages of 3.46 to 3.84 Ga and 3.41 to 3.77 Ga from 2.62 Ga Walaganna and 2.61 Ga Wogala suites (see section 2.1.3.1), respectively. The sites with the oldest T_{DM2} model ages (4169 to

4364 Ma) are similar to values recorded from the Jack Hills (Kemp et al., 2010) in the Yilgarn Craton.

Table 5.20. Hafnium isotopic data for sample MA 4. T_{DM2} value is used in the text.

Spot	t (Ma)	$^{176}Yb/^{177}Hf$	$^{176}Lu/^{177}Hf$	$^{176}Hf/^{177}Hf$	$2s_m$	$e_{Hf}(0)$	$e_{Hf}(t)$	T_{DM1}	T_{DM2}	$f_{Lu/Hf}$
MA 4.1	2655	0.038386	0.001118	0.280859	0.00003	-67.64	-10.11	3333	4181	-0.97
MA 4.2	2636	0.015868	0.000528	0.280817	0.000023	-69.14	-10.99	3339	4244	-0.98
MA 4.3	2647	0.018029	0.000585	0.280776	0.000024	-70.60	-12.31	3399	4364	-0.98
MA 4.4	2670	0.018233	0.000549	0.280813	0.000018	-69.28	-10.39	3346	4215	-0.98
MA 4.5	2633	0.027390	0.000871	0.280856	0.000029	-67.75	-10.27	3316	4180	-0.97
MA 4.6	2629	0.023665	0.000763	0.280856	0.000027	-67.75	-10.17	3306	4169	-0.98
MA 4.7	2628	0.013654	0.000444	0.280825	0.000026	-68.87	-10.74	3321	4218	-0.99
MA 4.8	2638	0.025158	0.000791	0.280851	0.000024	-67.95	-10.22	3316	4180	-0.98
MA 4.9	2628	0.020785	0.000657	0.280825	0.000029	-68.86	-11.11	3339	4249	-0.98
MA 4.10	2638	0.016593	0.000538	0.280818	0.000022	-69.12	-10.94	3339	4241	-0.98
MA 4.11	2646	0.013705	0.000521	0.281042	0.000053	-61.19	-2.75	3038	3544	-0.98
MA 4.12	2639	0.034005	0.001057	0.280834	0.000033	-68.54	-11.26	3361	4269	-0.97

Strong –ve εHf(t) values, along with ~4.4 to 4.2 Ga T_{DM2} model ages, implies incorporation of recycled Hadean crust in the source. The fairly high $^{176}Hf/^{177}Hf$ (0.281042), weakly –ve εHf(t) value of -2.75 and young T_{DM2} model age of 3544 Ma obtained from analysis MA 4.11 indicates incorporation of more juvenile material in the source area.

5.5 Petrogenesis of the Granitoids

5.5.1 Genetic classification: I- or S-type?

A classification of granitoids related to their source rocks was proposed by Chappell and White (1974), based on studies in the Berridale–Kosciuszko region of the Lachlan Fold Belt in Australia. They divided the granitoids into I- and S- type; based on whether protoliths were “igneous” or “sedimentary”, respectively. Ishihara (1977) introduced a similar classification of granitoids with two classes (“magnetite” and “ilmenite”) that in many respects correspond to the I- and S- types of Chappell and White (1974). Chappell and White (1974, 2001) and Hine et al. (1978) suggested a combination of mineralogical, chemical, and field characteristics to differentiate between the I- type and S- type granitoids. A (anorogenic) - type granites were introduced by Loiselle and Wones (1979), and these were generally emplaced in an extensional tectonic regime not directly related to convergent margins (i.e.“anorogenic” or “post-tectonic”), although this definition has now been widened (see Collins et al., 1982). They have higher SiO_2, alkali metals, Fe/Mg, halogens (F and Cl), Ga/Al and most high field-strength trace elements (Whalen et al., 1987; Eby, 1990) than the I- and S- types. An M-type granitoid (for direct mantle source) was introduced by White (1979) to include both immature arc

plutons and the oceanic "plagiogranites" found in ophiolite-oceanic crust. However, distinguishing between the I-, A- and S- type granitoids is often difficult, as with progressive crystallisation many of the characteristics (such as ASI index) overlap with one another (Whalen et al., 1987; Chappell and White, 1992, 2001; Chappell, 1999).

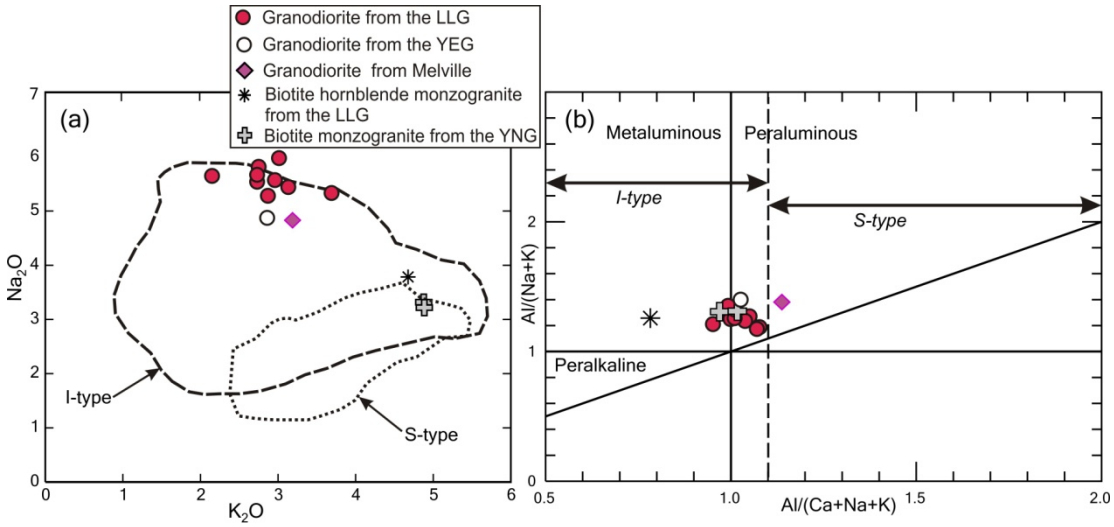

Fig. 5.29 (a) Na_2O vs. K_2O plot for the granitoid samples from the Yalgoo area. The boundaries of the I-type and S-type granites (containing >57% SiO_2) were drawn from the plot of I- and S- type granites of the Lachlan Fold Belt (Chappell and White, 2001). (b) Shand's molar parameters A/NK [$Al_2O_3/(Na_2O+K_2O)$] vs. A/CNK [$Al_2O_3/(CaO + Na_2O+K_2O)$] after Maniar and Piccoli (1989). Dashed line represents boundary between I- and S-type granites (Chappell and White, 1992).

The granodiorite and biotite hornblende monzogranite samples from north Yalgoo are all high in Na_2O (averaging 5.25% and 3.74%, respectively), while the biotite monzogranite samples have slightly lower Na_2O (averaging 3.27%) contents. On the Na_2O vs. K_2O plot, most of the granodiorite samples lie within the field of I-types, with biotite monzogranite samples overlapping with the S-type field (Fig. 5.29a). The single biotite hornblende monzogranite sample also lies within the field of I-type (Fig. 5.29a).The alumina saturation index (ASI) plot confirms the I-type nature of most granitoid samples, with one granodiorite sample (PRCD 108/1) plotting within the field of S-type granite (Fig. 5.29b). The granodiorite samples form a tight group straddling the metaluminous and peraluminous fields (Fig. 5.28b). The biotite hornblende monzogranite and biotite monzogranite are metaluminous (ASI averaging 0.78 and 0.99, respectively). Most of the granitoid samples have <1% normative corundum (Table 5.2). Combining the high Na_2O content, ASI <1.1, the presence of <1% normative corundum, along with the petrographic characteristics such as the presence of primary hornblende, titanite and magnetite and minute apatite crystals in most of the samples, all the granitoid samples in the Yalgoo area appear to belong to the I-type.

5.5.2 Partial Melting and/or Fractional Crystallization

The relatively close scatter of major and trace elements on the Harker diagrams indicates low degrees of fractionation of the granodiorite samples (Fig. 5.9, 5.11). The single biotite hornblende monzogranite sample (MA 28) and two biotite monzogranite samples (MA 3,4) plot far from the granodiorite group in most of the plots, for which a trend of differentiation (if present) is difficult to infer.

On the Ba-Rb-Sr diagram (El Bouseily and El Sokkary, 1975), most of the granodiorite samples plot in the unfractionated granodiorite and quartz diorite field, with few in the 'anomalous' granite field (Fig 5.30a). This is consistent with the absence of plagioclase in the residue as evidenced by positive or no Eu anomalies and elevated Ba and Sr contents in the incompatible trace element plots (Fig. 5.12a,b). The biotite hornblende monzogranite, along with some granodiorite samples, plots within the 'anomalous' granite field on the Ba-Rb-Sr diagram (Fig. 5.30a), whereas the biotite monzogranite samples fall within the fractionated field of normal granites (Fig 5.30a).

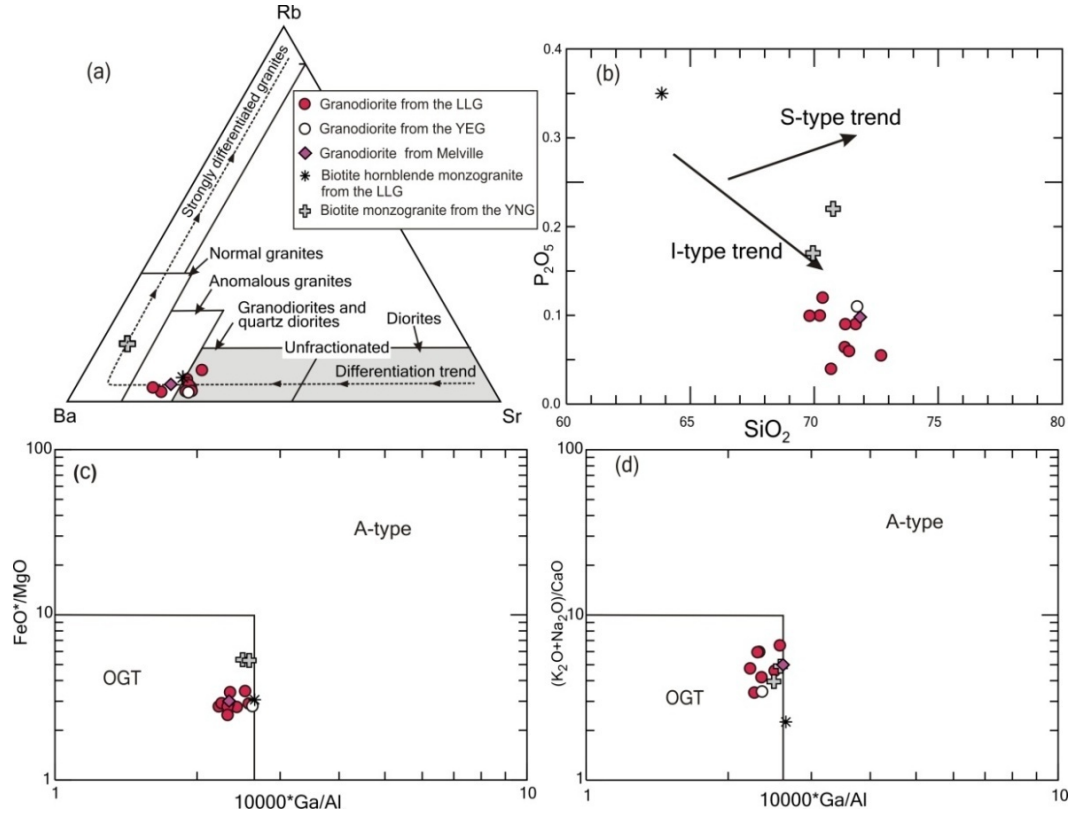

Fig. 5.30. (a) Ba-Rb-Sr plot (El Bouseily and El Sokkary, 1975). (b) P_2O vs. SiO_2 (Chappell and White,1992). (c) FeO*/MgO vs.10000 Ga/Al (Whalen et al., 1987). (d) K_2O+Na_2O /CaO vs. 10000 Ga/Al (Whalen et al., 1987) plots of the granitoid rocks of the north Yalgoo area. Field OGT includes unfractionated M-, I- and S-type granites.

A progressive depletion in P_2O_5 with increasing silica is noted for the granodiorite samples on the P_2O_{5-} vs. SiO_2 plot, which reflects a typical internal fractionation trend of

I-type granites (Fig. 5.30b). The biotite hornblende monzogranite has higher P_2O_5 and plots away from the granodiorites, as do the biotite monzogranite samples (Fig. 5.30b).

The unfractionated nature of the granodiorite samples can be further established using the FeO*/MgO vs. 10000 Ga/Al and K_2O+Na_2O /CaO vs. 10000 Ga/Al plots of Whalen et al. (1987). On these two plots (Fig. 5.30c,d), almost all the samples fall within the field of OGT (orogenic granite) that include unfractionated M-, I- and S- type granites, with two falling close to the field of A- type granite. The biotite hornblende monzogranite sample lies within the OGT field in the FeO*/MgO vs. 10000 Ga/Al plot (Fig. 5.30c) and on the K_2O+Na_2O/CaO vs.10000 Ga/Al plots just in the field of A- type granitoid (Fig. 5.30d). The biotite monzogranite samples plot within the field of OGT (orogenic granite) on both diagrams (Fig. 5.29c,d).

5.5.3 Archean TTG: Source for the Yalgoo Granitoids?

Jahn et al. (1981) introduced the term TTG that stands for tonalite, trondhjemite and granodiorite for a suite of felsic rocks in the Pilbara Craton. Prior to that, Barker and Arth (1976) and Barker (1979) first discussed different aspects of trondhjemite and related rocks. Barker (1979) suggested several distinctive geochemical features for trondhjemite and related rocks, that include: i) SiO_2 >68%, generally <75%; ii) Al_2O_3 typically >15% at 70% SiO_2 (High-Al TTG) and <14% at 75% SiO_2 (Low -Al TTG); iii) (FeOT + MgO) < 3.4%, and FeOT/MgO commonly ranges from 2-3; iv) CaO ranges from 1.5-3, and in calcic trondhjemite from 5.4-5.5%; Na_2O typically ranges from 4-5.5%; v) K_2O is < 2.5%, and typically <2%. Archean TTGs largely belong to the high-Al subgroup that has high Sr and Eu, fractionated REEs, with low HREEs and high Sr/Y ratios (Martin, 1994; Condie, 2005;, Martin et al., 2005). Archean TTG series rocks are the volumetrically dominant component in many Archean terranes, corresponding to as much as 80% to 90% of the preserved Archean continental crust (Martin, 1986,1994; Moyen et al., 2010). Recent studies, however (Moyen, 2008, 2009; Moyen et al., 2010; Smithies et al., 2009), argue against using the term “TTG”, as “TTG” chemical signatures in rocks can be attained from diverse origins—with variably enriched sources melting at different depths.

The major element characteristics of the Yalgoo granodiorite samples comply with those of the “TTG” as defined by Barker (1979). However, when plotting the granodiorite samples on the Na-K-Ca diagram only two samples fall inside the Archean TTG field of Martin (1994), reflecting the slightly higher K and lower Na contents of the granodiorites (Fig. 5.31a). The normative Ab-An-Or plot however includes most of the

samples in the Archean TTG field (Fig. 5.31b), leaving only two outside this field. The elevated K content in the granodiorite samples most probably can be explained in terms of

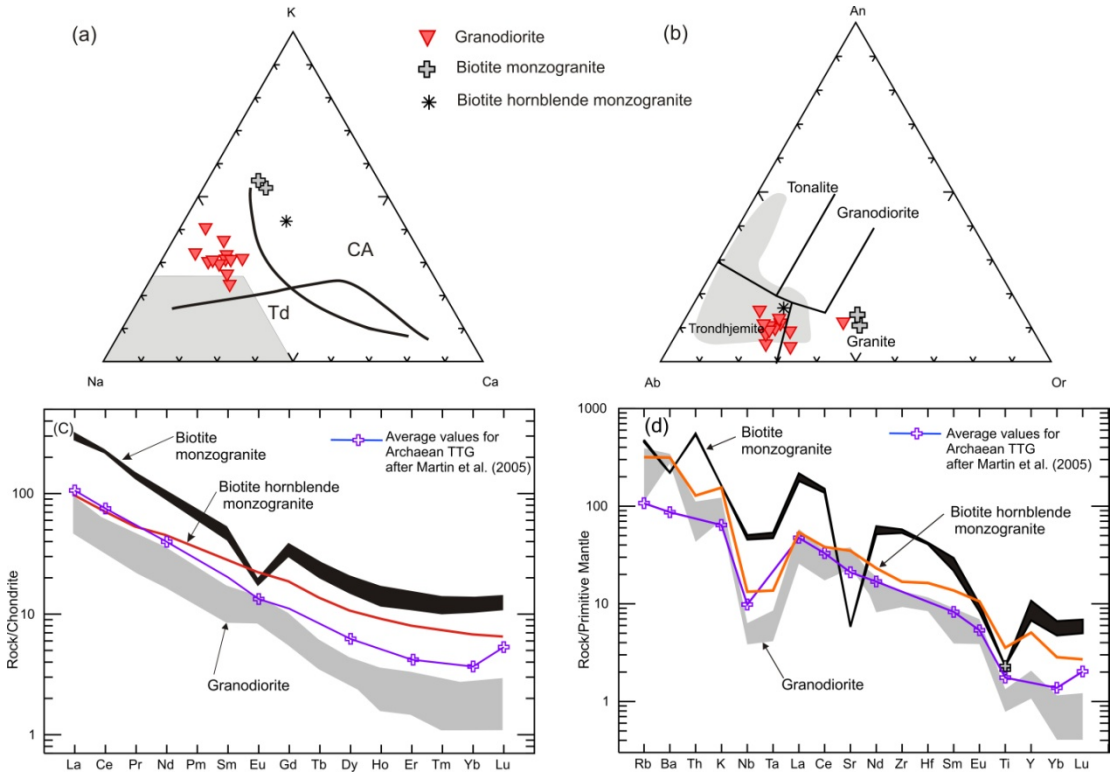

Fig. 5.31. (a) Na-K-Ca plot (Barker and Arth, 1976). Shaded area represents the field of Archean TTG from Martin (1994).Td= Trondhjemitic trend; CA = Classical Calc-alkaline trend. (b) normative Ab-An-Or plot (Barker, 1979). Field of Archean TTG taken from Martin (1994). (c) Chondrite-normalized REE patterns showing the fields of Yalgoo granitoids compared with the average composition of the Archean TTG from Martin et al. (2005). (d) PM-normalized patterns showing the fields of the Yalgoo granitoids compared with the average Archean TTG from Martin et al. (2005).

the K enrichment of some TTG in the Late Archean, referred to as "enriched TTG" (Moyen et al., 2003). Champion and Smithies (2001, 2004) also described similar granitoids as "transitional TTG". They suggested these granitoids are characterized by high LILE contents and show strong K_2O enrichment with increasing differentiation compared to 'true" TTGs, yet possessing a high-Al signature. Champion and Smithies (2007) mentioned that regardless of the ultimate origin of such rocks, their presence in Archean terranes can be used as an indicator of the presence of pre-existing felsic crust and provide temporal constraints on the crustal evolution of a craton (e.g. Champion and Smithies, 2001).

The Yalgoo granodiorite samples have strongly fractionated REE patterns, with high LREE contents (average La_{CN} > 100), very low HREE contents (Yb_{CN} <3) slight concavity at the HREE end, and with weakly positive Eu anomalies (Table 5.4, Fig. 5.12a). All these characteristics are typical of Archean TTG (Martin, 1986, 1987a,b, 1994; Martin et al., 2005). Chondrite-normalized REE patterns (Sun and McDonough,

1989) of the Yalgoo granodiorite samples fall close to the average TTG (from Martin et al., 2005) (Fig. 5.31c). The PM-normalized (Sun and McDonough,1989) incompatible trace element plot of the granodiorite samples also reflects their TTG affinity (Fig. 5.31d). It should be mentioned here that lack of data for several elements from the Archean TTGs barred making a complete comparison in the REE and incompatible element plots, even though this did not appear to have any significant affect on the overall patterns.

5.5.4 Source Characteristics and Melting Model

5.5.4.1 Granodiorite

Moyen (2009) investigated source and pressure effects using high Sr/Y ratios, which are commonly interpreted as reflecting deep melting. In a deep melting environment, with increasing pressure, plagioclase becomes unstable (therefore releasing Sr), whereas garnet becomes stable and traps Y. An "enriched" source (Sr/Y of ca. 15; average continental

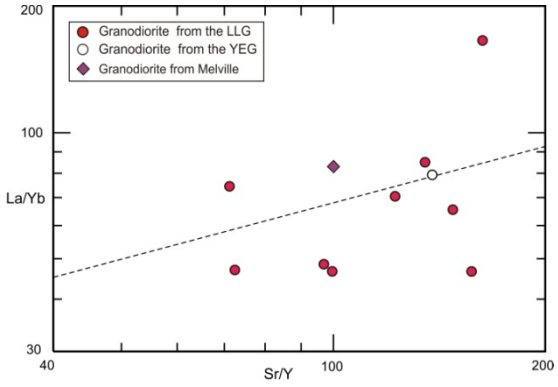

Fig. 5.32. La/Yb vs. Sr/Y plot by the granodiorite samples from the Yalgoo area showing positive correlation.

continental crust, Taylor and McLennan, 1985) can also contribute to high Sr/Y values in the melt, because they have intrinsically higher Sr/Y ratios, but also because they are more aluminous and have more potential for forming garnet at moderate depths. Therefore, high Sr/Y ratios alone cannot be considered an indicator of deep melting. Experimental studies by Muntener and Ulmer (2006), Ulmer (2007), Muntener et al. (2008) and Ulmer et al. (2008) established that high Sr/Y ratios, complemented by high La/Yb ratios, can result from garnet fractionation of calc-alkaline magmas at relatively high pressures (>12 Kbar). The Yalgoo granodiorite samples display a positive correlation between Sr/Y and La/Yb, implying deep source melting at high pressure (Fig. 5.32).

The melting curves on the $(La/Yb)_{CN}$ vs. Yb_{CN} plot for different likely sources suggest that the melt for the Yalgoo granodiorite samples was mostly derived from an eclogite source, with a minor contribution from garnet amphibolite (Fig. 5.33a). This implies that

garnet was stable in the source as a residual mineral during melt extraction. The $(La/Yb)_{CN}$ vs. Yb_{CN} plot further supports an Archean TTG affinity for the Yalgoo granodiorite samples. The Nb/Ta ratio (11.64 to 17.54) of the Yalgoo granodiorite samples spans the critical Nb/Ta ratio of ~ 15, which is considered to be consistent with deep rutile-present melting (Foley et al., 2000, 2002; Schmidt et al., 2004) (Fig. 5.33b). Similar melting patterns, i.e. near the boundary between amphibolite and hornblende-eclogite melting and rutile-eclogite was also suggested for high-Al TTGs (Condie, 2005)

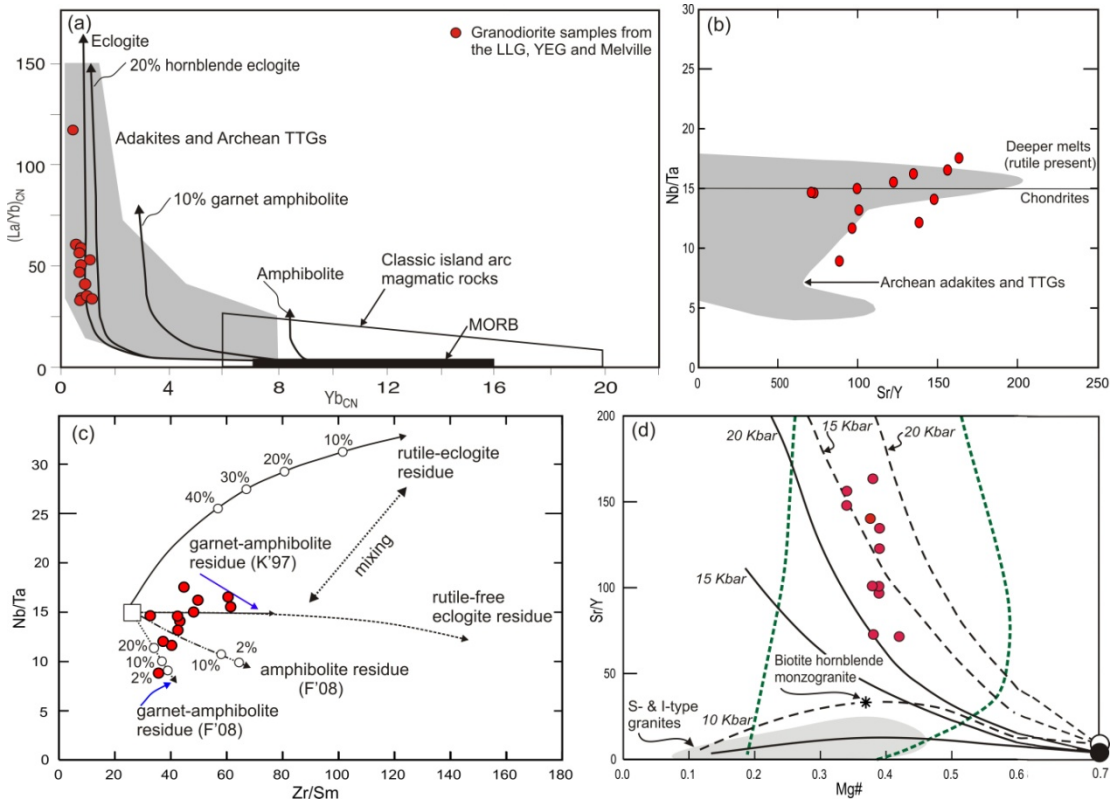

Fig. 5.33. (a) $(La/Yb)_{CN}$ vs. Yb_{CN} plot for the Yalgoo granodiorite samples. Fields for adakites and classical island arc magmatic rocks are from Drummond and Defant (1990) and Martin et al. (2005). Partial melting curves for basalt leaving residues of eclogite, garnet amphibolite and amphibolite are from Drummond and Defant (1990). (b) Nb/Ta vs. Sr/Y plot for the Yalgoo granodiorite samples. Archean adakites, together with the TTGs (grey field), show a bimodal distribution with both low Nb/Ta (typically with relatively low Sr/Y values) and high Nb/Ta (with higher Sr/Y) values. (c) Nb/Ta vs. Zr/Sm plot for the Yalgoo granodiorite samples. Partial melting curves are constructed using a mafic tholeiitic protolith, for different source compositions, including amphibolite, garnet-amphibolite and rutile eclogite (Hoffman et al. 2011). F'08: amphibole/melt partition coefficients taken from the compilation of Foley (2008); K'97: amphibole/melt partition coefficients taken from Klein et al. (1997). (d) Sr/Y vs. Mg# diagram for the Yalgoo granodiorite and biotite hornblende monzogranite sample, showing model for melting of high and low Sr/Y MORB-type sources. Melting curves are calculated by fitting the experimental data for different pressure bands (as presented in Fig. 4 in Moyen, 2009) by curves giving the enrichment in Sr/Y (and in mg#) as a function of F, and by calculating the resulting evolution for two source compositions. Black filled circle represents a low Sr/Y (=3) source, and white circle represents a higher Sr/Y (=10) source. The solid curves are melting curves originating from a low Sr/Y source, and the light dashed curves originate from the higher Sr/Y source. Green dashed curves on both sides limit the field of Archean TTGs.

and the Neoproterozoic I-type granitoids in the Kuluketage area, NW China (Long et al., 2011). Recently, Hoffman et al. (2011) showed that compositional variations in the 3.85–2.8 Ga TTGs and related rock types from southern West Greenland, W-India and

from the Superior Province in Canada can be explained by melting of typical Isua-type tholeiites in both the rutile-bearing eclogite stability field (>15 kbar, high Nb/Ta) and the garnet-amphibolite stability field (10–15 kbar, low Nb/Ta). The same is observed in the formation of the parental melt of the Yalgoo granodiorites. On the Nb/Ta vs. Zr/Sm plot (Hoffman et al., 2011), the linear trend of data points suggests the granodiorites were generated from melt derived from rutile eclogite, garnet amphibolite and amphibolite (Fig. 5.33c). A similar conclusion is arrived at from the Sr/Y vs. Mg# plot (Fig. 5.33d), where the Yalgoo granodiorite samples plot along the trend generated by high pressure (~18–12 kbar), deep melting of a predominantly mafic source, most likely from a high Sr/Y(=10) basalt, as suggested for Archean adakite by Moyen (2009). For a melt to be generated from a lower Sr/Y(=3) source, the pressure required would have to be anomalously high (well above 20 kbar) which is difficult to explain.

Summing up, from the trace element relationships (Fig. 5.33a,b,c,d) and the U-Pb and Lu-Hf isotopic study (see section 5.4.1), it is apparent that the granodiorite melts originated in both the rutile-bearing eclogite and the garnet-amphibolite stability fields, with addition of older felsic crustal components (as evidenced by ~3.02 and 2.94 Ga inherited zircon grains in the granodiorites). The dominance of near chondritic to moderate negative εHf(t) values (-0.92 to -4.54) in most (MA 6, 10, 15 and 38) granodiorite samples points to the existence of an older crustal source. The isotopic characteristics and ages of the parental melts are discussed in more detail in section 8.4.

Due to high heat flow, Archean oceanic crust was possibly thicker (3 times thicker than modern oceanic crust, assuming a 300°C hotter mantle; van Thienen et al., 2004), therefore, a more buoyant oceanic crust would have subducted at a much lower angle than in modern subduction zones (e.g. Abbott and Hoffmann, 1984; Martin, 1986; Abbott et al., 1994). An Archean shallow subduction zone environment is preferred for the origin of the primary melts of the Yalgoo granodiorites. The minimum pressure for rutile stability during partial melting of hydrous mafic rocks is at least 1.5 GPa, which corresponding to a depth >50km (Xiong et al., 2005; Xiong, 2006; Nair and Chacko, 2008). This high-pressure melt would have mixed with melt having a slightly enriched component, produced by the melting of the upper part of an Archean subducting plate, which also incorporated older crustal components (~3.02 and 2.94 Ga inherited grains). Slab melting must have occurred in a rutile-absent environment leaving garnet amphibolite and amphibolite residue at low-pressure (~10 to 12 kbar).

A melt generated from subducting oceanic crust is expected to interact with the mantle peridotite and inherit a signature with high Mg#, Ni and Cr contents. The relatively low

Mg# (34 to 42), low Ni (2 to 7 ppm, except for 30 ppm in sample MA 52), and Cr (1 to 11 ppm, except for 50 ppm from in MA 52) contents of the granodiorite samples therefore, requires explanation, if the slab melt component is to be accommodated in the origin of the granodiorites. The experimental study of Moyen (2009) showed that high melt:rock ratios can be obtained where large magma conduits restrict the contact surface between the melt and the peridotite. In a high melt:rock ratio scenario, only limited portions of the mantle are able to react with the melt, which makes further reactions difficult to impossible. Furthermore, Moyen (2009) also suggested, where the interactions result mostly in the formation of new minerals out of the melt, the resulting melt becomes enriched in incompatible elements, and has high La/Yb and Sr/Y ratios, and generates lower mg# melts, as is observed in most of the Yalgoo granodiorite samples. Mixing of both relatively low-pressure (10 to 12 kbar) and high-pressure (15 to 20 kbar) melts might have occurred within the lower mafic crust and therefore inherited signatures of both rutile-poor and rutile-free melting remain, as was documented by the trace HFSE relationships (Fig. 5.33a,b,c,d).

5.5.4.2 Biotite hornblende monzogranite

Compared to the granodiorite samples, the biotite hornblende monzogranite has higher chondrite-normalized MREE and HREE ratios and weaker negative Nb-Ta and Ti anomalies on the PM-normalized incompatible element plot (Fig. 5.12a,b). The biotite hornblende monzogranite also contains the highest amount of mafic oxides (CaO, Fe_2O_3T and MgO), which is manifested by the presence of mafic minerals (see Table 5.2, 5.4). These characteristics therefore, suggest a mafic source for the biotite hornblende monzogranite. The higher HREE content of the biotite hornblende monzogranite can be explained by the absence of garnet in the source, which implies a source formed within an intermediate to shallow crustal regime, i.e. under moderate to low pressure. High Sr content (738 ppm) is also indicative of low pressure, with early formed plagioclase in the source (Winter, 2001). The high Ni (15 ppm) and Cr (14 ppm) contents of the biotite hornblende monzogranite may have resulted from addition of a mantle component (c.f. Foden et al., 1984; Hallberg and Giles, 1986; Wyborn, 1993; Witt and Swager, 1989; Cassidy et al., 1991; Champion and Sheraton, 1993). Observing the variations in LILE and LREE, Champion and Sheraton (1997) invoked the interaction of mantle and crustal components to generate these magmas. Champion and Sheraton (1997) and Champion and Cassidy (2000, 2002, 2007) suggested partial melting of a mafic (basaltic) source in combination with varying amounts of a LILE-

enriched component (felsic crust?) could generate granite of this type. The absence of garnet however, precludes a deep source, i.e. lower crust/upper mantle mafic component being the main source of the biotite hornblende monzogranite. Summing up the above characteristics, mixing of a mid-crustal source with a mafic component at a shallower level is considered the source for the biotite hornblende monzogranite. A shallow level, low pressure genesis is also supported by the melting diagram, where the biotite hornblende monzogranite falls along the 10 kbar melting curve originating from a high Sr/Y (=10) source (Fig. 5.32d).

5.5.4.3 Biotite monzogranite

Biotite monzogranite samples have relatively high concentrations of HREE with $(La/Yb)_{CN}$ ratios of 32.6-38.2, with moderate to strong negative Eu anomalies (Fig. 5.11a). Moreover, they also show moderate negative Ba, and strong negative Sr anomalies in the PM-normalized incompatible element diagram, implying plagioclase fractionation (Fig. 5.12b). The high Y (averaging 40 ppm), and Yb (averaging 2.8 ppm) contents and K_2O/Na_2O ratio (averaging 1.5) of the biotite monzogranite samples preclude garnet in the residue (Table 5.4). The strongly –ve εHf(t) values (-5.24 to -12.31), along with Hadean T_{DM2} model ages (~4.4 to 4.0 Ga) indicate a significant component of recycled ancient crust was incorporated in the source of the biotite monzogranite samples. The trace element characteristics, as discussed above, indicate that biotite monzogranite samples were derived from partial melting of a fractionated source, within middle/upper crust, at low pressure (<15 kbar) (Patiño Douce and Beard, 1995; Skjerlie and Johnston, 1996; Skjerlie and Patiño Douce, 2002; Litvinovsky et al., 2000; Patiño Douce, 2005).

5.6 Comparison with Archean Granitoids in the Yilgarn Craton

5.6.1 Comparison with Previous Studies in the Yalgoo Area

Oliver (1999) classified granitoid samples from the LLG as ‘altered monzogranites’, YEG (Basin granitoid in his study) as ‘recrystallized monzogranites’ and YNG (Goolthan Goolthan granitoid in his study) as ‘monzogranites’. The classification of the LLG granitoid by Oliver (1999) should be viewed with caution as his samples were mostly altered and collected only from the middle part of the plutons. The results obtained here differ considerably from Oliver (1999), which is evident on the modal QAP diagram where all the granitoid samples of Oliver are placed in the monzogranite field (Fig. 5.34). He considered that the Basin and Lady Lydia granites belong to what he

referred to as the Lady Lydia suite. The present study, however, differs from considering LLG as an altered, recrystallized granitoid as claimed by Oliver (1999). Detail travesrsing

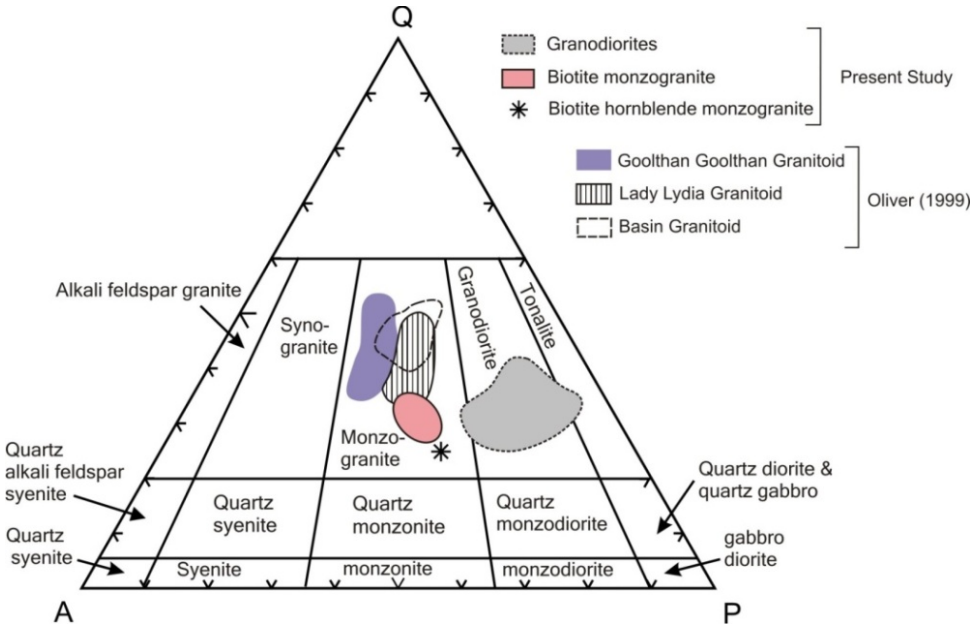

Fig. 5.34. Comparison of the classification used in the present study of the Yalgoo granitoid samples with that of Oliver (1999).

across the granitoid, and the petrographic study, found the LLG is mostly unaltered. The small-scale alteration of plagioclase and recrystallization of the quartz-feldspar groundmass are considered to be late magmatic to deuteric alteration. The LLG is only weakly mineralized, with gold confined mostly within sparsely-occurring quartz veins and disseminated within relatively narrow zones within the wall rock (see chapter 7). Therefore, the chance of introducing large-scale metasomatic changes during hydrothermal activity, as stated by Oliver (1999), appears unlikely.

Oliver (1999) obtained a SHRIMP U-Pb age of emplacement for the Lady Lydia suite of 2743 ± 4 Ma, which appears to be ~15 Ma younger than the ages obtained from the LLG in the present study. He also determined the age of crystallisation of the Mount Mulgine Granite (~150 km south of the LLG) at 2767 ± 10 Ma, which within error, matches the age of the LLG obtained in the present study.

5.6.2 Comparison with Previous Studies in the Murchison Domain

The average compositions of the Murchison granitoids (Watkins and Hickman, 1990; Wang et al., 1993) and granitoids across the Yilgarn Craton (Champion and Sheraton, 1997), along with the granitoids in the present study, are listed in Table 5.21. It should be mentioned that these studies lacked most of the trace elements, which bars a comparison of the present studies using the REEs. Watkins and Hickman (1990) classified the granitic

rocks of the Murchison Domain into four Suites, which in order of intrusion, are Suite I) pegmatite-banded gneiss; Suite II) recrystallized monzogranite; Suite III) Post-folding tonalite-trondhjemite; Suite IV) Post-folding Monzogranite-syenogranite (see section 2.1.3.1). When compared with the available data from Watkins and Hickman (1990), the Yalgoo granodiorite samples match well with Suite II-recrystallized monzogranite, whereas the biotite monzogranite samples fall within Suite IV-post-folding granitoid. Most of the major elements, except for K_2O, of the biotite hornblende monzogranite, equate well with those of the tonalite sub-suite of Suite III post-folding granitoid of Watkins and Hickman (1990). However, most of the trace elements, apart from Sr, Ni and Ce, of the biotite hornblende monzogranite do not correlate with those of

Table 5.21. Average chemical composition of the Archean granitoid suites in the Yilgarn Craton. A comparison with the average composition of Yalgoo granitoids from the present study and other classification schemes is also presented. Data for the granitoid samples from the Murchison Domain were obtained from Watkins and Hickman (1990), Wang et al. (1993); for the Eastern Goldfields Province from Champion and Sheraton (1997). *RM = Recrystallized monzogranite, TTr = Tonalite-Trondhjemite, Grdt =Granodiorite, BHMzgrt =Biotite hornblende monzogranite, BMzgrt =Biotite monzogranite Mzgrt =Monzogranite, Tr =Trondhjemite, SynGrnt =Syenogranite-monzogranite. FeOT=Total iron calculated as FeO.(a), (b), (c) and (d)= Average of 91,4,24 and 16 analyse, respectively. SD =Standard Deviation.*

	Murchison Granitoids after Watkins and Hickman (1990)								Eastern Goldfields Province Granitoids after Champion and Sheraton (1997)		Yalgoo granitoids (present study)				
	Suite II RM subsuite		Suite III: Post-folding granitoid TTr subsuite				Suite IV: Post-folding granitoid Mzgrt-SynGrt subsuite								
Classification schme	Murchison Granitoids after Wang et al. (1993)														
	Suite I Mzgrt subsuite		Suite IIa Tr subsuite		Suite IIb T subsuite		Suite III Mzgrt-SynGrt subsuite		High-Ca Low Y	Low -Ca High Y	Grdt		BHMzgrt	BMzgrt	
Chemical composition, %	n=171	SD	n=52	SD	n=44	SD	n=34	SD			n=11	SD	n=1	n=2	SD
SiO_2	71.19	2.40	72.17	1.58	65.32	1.61	73.74	3.50	71.93	73.10	71.17	0.84	63.85	70.36	0.57
TiO_2	0.20	0.19	0.21	0.06	0.49	0.08	0.26	0.18	0.20	0.20	0.24	0.03	0.77	0.48	0.03
Al_2O_3	14.30	0.73	14.84	0.91	14.68	0.60	12.71	0.89	14.83	13.80	15.46	0.27	14.11	13.93	0.16
FeOT	2.21	0.91	1.76	0.43	4.04	1.22	2.54	1.34	1.67	1.43	1.88	0.29	5.63	3.68	0.18
MnO	0.03	0.02	0.02	0.01	0.05	0.02	0.05	0.03	<0.1	<0.1	0.01	0.01	0.09	0.06	0.01
MgO	0.53	0.39	0.60	0.20	2.82	1.07	0.37	0.52	0.53	0.30	0.62	0.10	1.84	0.69	0.03
CaO	1.74	0.62	1.99	0.33	4.40	0.86	1.35	0.84	1.97	1.00	1.58	0.52	3.74	1.87	0.29
Na_2O	4.32	0.60	5.08	0.41	4.32	0.66	3.12	0.36	4.70	3.80	5.46	0.36	3.76	3.27	0.06
K_2O	3.58	1.11	1.95	0.39	1.29	0.58	4.22	0.40	2.93	5.00	2.91	0.37	4.66	4.88	0.01
P_2O_5	0.12	0.09	0.08	0.04	0.15	0.04	0.14	0.11	0.10	0.10	0.08	0.03	0.35	0.20	0.04
Trace elements, ppm															
Ba	1403	786	650	193	524	232	1076	688	902	968	1995	203	2199	1560	34.1
Rb	177	109	64	25	64	30	227	85	97	241	113	53	202	307	7.51
Sr	352	212	455	185	298	80	143	140	426	193	686	103	738	123	0.91
Zr	186	74	137	22	152	27	257	173	120	191	121	15	188	621	35.0
Nb	11	4	7	3	10	1	20	7	5	13	3.61	0.57	9.5	34	2.52
Y	11	8	8	3	18	5.5	54	26	6	19	6.1	1.62	23.05	40	12.9
Ni	20	8	16	11	81	35	20	13	5	3	6.9	7.7	15.14	5	0.3
Cr	130	83	111	117	185	86	153	77	7	4	10.1	13.5	7.99	7	1.8
F	493	302	330	123	372	174	1051	362							
La	56 (a)		29 (b)		18 (c)		107 (d)		28.3	92.0	25.7	6.4	37.1	136.7	17.3
Ce	99	77	42	15	46	20	197	133	51.3	167.0	45.0	10.3	67.8	255.5	16.9

the tonalite sub-suite of Suite III post-folding granitoid. Suite III post-folding granitoids were suggested to be limited to the northeastern part of the Murchison Domain (Watkins and Hickman, 1990) and so the biotite hornblende monzogranite in the north Yalgoo area may not be correlatable with any of the Watkins and Hickman (1990) types.

5.6.3 Comparison with Granitoids in the Yilgarn Craton

Champion and Sheraton (1997) proposed a detailed classification of granitoids based on petrological and geochemical characteristics of the granites in the Leonora-Laverton region

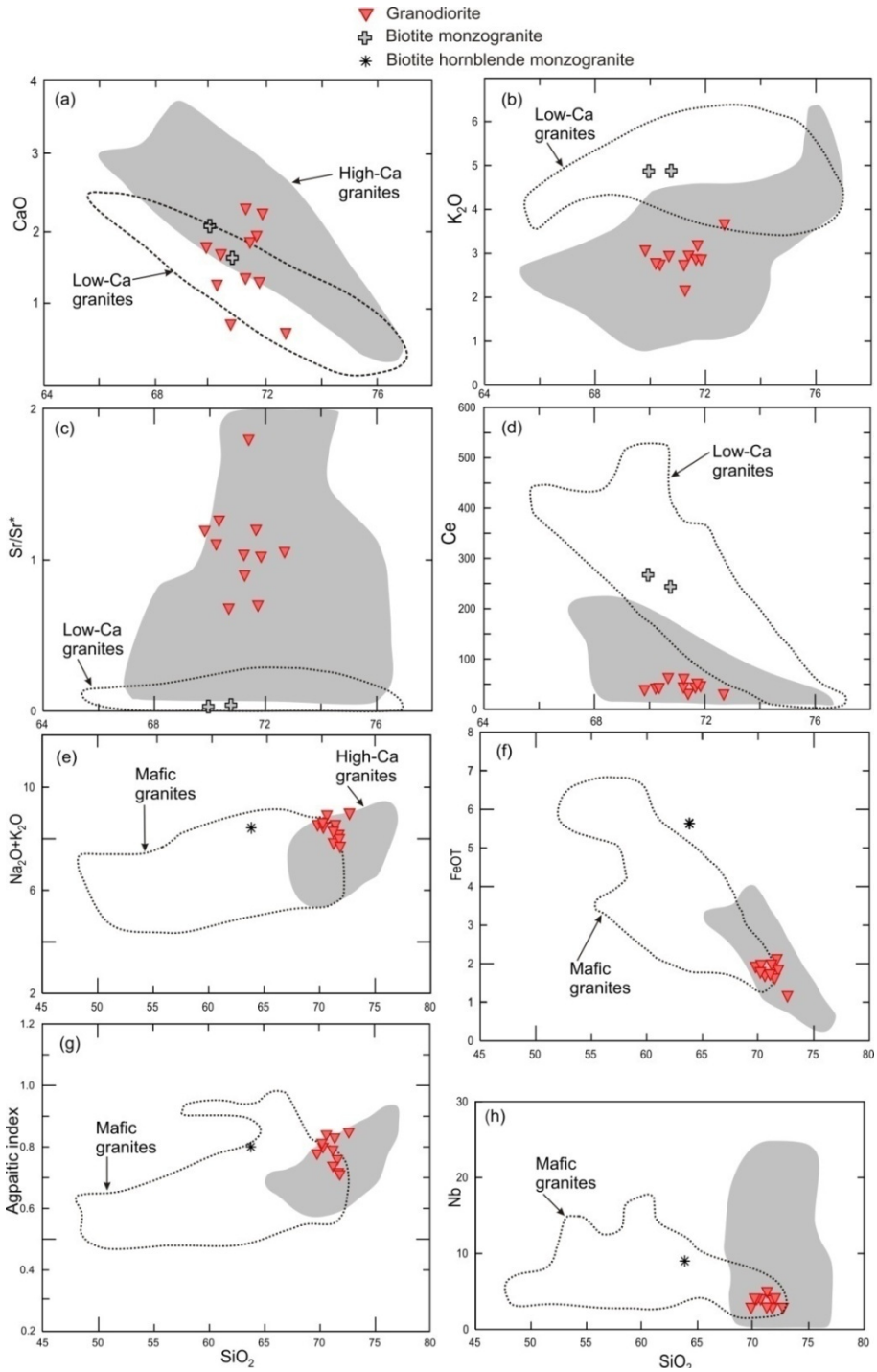

Fig. 5.35. (a) CaO vs. SiO_2, (b) K_2O vs SiO_2, (c) Sr/Sr* vs.SiO_2 and (d) Ce vs. SiO_2 variation diagrams showing the high-Ca, and low-Ca group granitoids from the Eastern Goldfields Province (Champion and Sheraton, 1997). Sr/Sr* is PM-normalized Sr abundance divided by the interpolated value obtained by averaging the normalized Ce and Nd. Biotite hornblende monzogranite is excluded from the above plots, as this sample does not fall in either of the granite classes. (e) Na_2O + K_2O vs. SiO_2, (f) FeOT vs SiO_2, (g) Agpaitic index vs.SiO_2 and (h) Nb vs. SiO_2 variation diagrams. Agpaitic Index is molecular $A1_2O_3/Na_2O$ + K_2O. Biotite monzogranites are excluded from these plots, as the samples do not fall in either of the granite classes.

region of the Eastern Goldfields Superterrane,. Later work by Cassidy et al. (2002) and Champion and Cassidy (2007) extended the classification to the entire Yilgarn Craton. A comparison is attempted in order to assess how the Yalgoo granitoids might fit into the classification of Champion and Sheraton (1997) (Table 5.21). The high-Ca and low-Ca rocks comprise over 60% and 20%, respectively, of the total granites, while the three minor geochemical groups [high-HFSE, syenitic (A-type) and mafic] constitute from ~5-10% each.

The high-Ca group (68-77% SiO2) are characterized by high Al2O3, Na2O and Sr, and low Y, and show many features of typical Archean TTG suites, with the exception of higher K2O, Rb, and Th contents. The low-Ca group (70-76% SiO2) has lower AI2O3, CaO, and Na2O and higher K2O, Rb, Th, Zr and LREE than the high-Ca group. The high-HFSE granites are siliceous (74-77% SiO2) and contain high TiO2, total FeO, MgO, Y, Zr and Ce, but only moderate Rb, Th and Pb contents. The A-type syenites (50-68% SiO2) are distinguished by their high total alkalis and mainly occur along tectonic lineaments. The mafic group (55-70% SiO2) is lithologically diverse and has a wide range of K2O, Rb, Th, La and Ce contents.

Champion and Sheraton (1997) divided the high-Ca group into two subgroups based on Y contents. They are: volumetrically dominant low-Y subgroup (<10 ppm Y) and subordinate high-Y subgroup (10 - >25 ppm Y). They proposed a similar subdivision of the low-Ca group, i.e. Low-Ca high Y (10-30 ppm) and Low-Ca (<10 ppm) low Y subgroups.

The Yalgoo granodiorite samples show strong similarity with the voluminous low-Y subgroup of high-Ca group, with slightly higher Na2O, higher Ba and Sr and similar La, Ce and Lu (Table 5.21). The biotite monzogranite samples have slightly higher K2O, Rb, Zr, and Y and lower Na2O than the granodiorite samples and yet plot within the low-Ca group; more specifically within the high-Y subgroup. The comparison of the Yalgoo granodiorite and biotite monzogranite samples with the classification of Champion and Sheraton (1993) is further tested by specific binary plots (Champion and Sheraton, 1993) (Fig. 5.35). Even though the CaO plot gives overlapping results in discriminating the granodiorite and biotite monzogranite samples, the K2O, Sr/Sr* and Ce plots separate the two groups quite well (Fig. 5.35a,b,c,d). The biotite hornblende monzogranite (MA 28) shows a broadly similar elemental composition to the mafic granitoid plutons, as revealed by the Na2O+ K2O, FeOT, Agpaitic index and Nb vs. SiO2 diagrams (Fig.5.35e,f,g,h).

5.7 Tectonic Setting

Using tectonic discrimination diagrams (cf Pearce et al., 1984, Harris et al., 1986 etc.) for younger granitoids to infer tectonic setting of Archean granitoid rock is still a matter of controversy among researchers. Nonetheless, these diagrams have been applied by several works on Archean granitoids, such as on 3.2-2.8 Ga tonalitic intrusive and migmatitic rocks from the Hearne Province, northern Mudjatik Domain, Canada (Harper, 2004) and on late Archean high K-granites from the Musoma-Mara Greenstone Belt, Tanzania Craton (Mshui and Maboko, 2012). In the present study, the presence of older boninitic rocks in an arc-like setting (see Chapter 3) imply a supra-subduction zone tectonic setting was present in the Archean and therefore provides rationale to apply these diagrams to deduce the tectonic setting of the granitoid samples from the Yalgoo area.

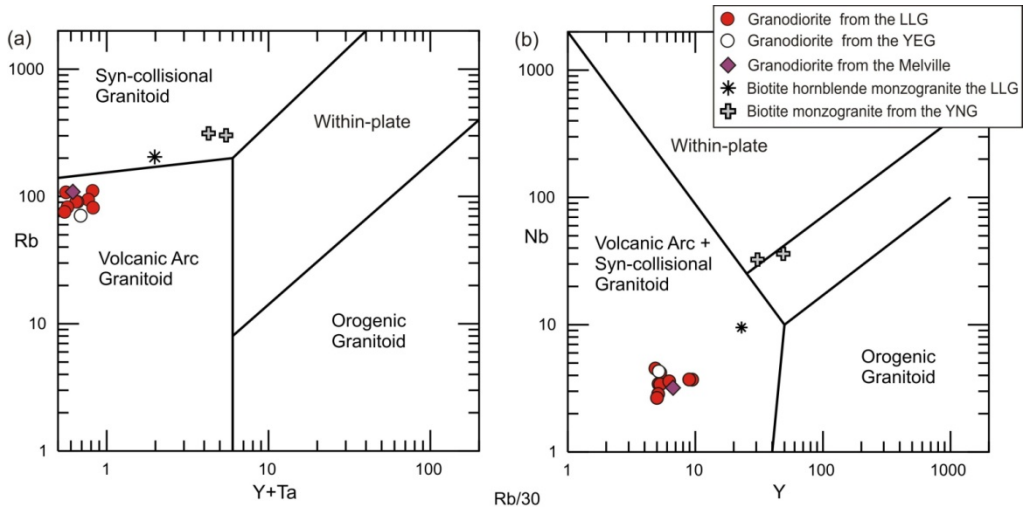

Fig. 5.36. Tectonic discrimination diagrams for the Yalgoo granitoid samples. (**a**) Rb vs. Y+Ta. (b) Nb vs. Y (after Pearce et al., 1984).

Yalgoo granodiorite samples plot within the volcanic arc granitoid field in the Rb vs. Y+Ta and Nb vs. Y plots (Fig. 5.36a,b). On the Rb vs. Y+Ta diagram, the single representative of the biotite hornblende monzogranite falls within the syn-collisional granitoid field proximal to the volcanic arc setting (Fig. 5.36a). Syn-collisional to volcanic arc + syn-collisional settings are inferred for the biotite monzogranite samples on the Rb vs. Y+Ta and Nb vs. Y plots (Fig. 5.36a,b). The volcanic arc signature of the Yalgoo granodiorite samples is also manifested by variably negative Nb–Ta–Ti anomalies on the PM-normalized incompatible element diagram (Fig. 5.12b). The stages of arc development are discussed in the crustal evolution section (8.5).

Chapter 6 Mafic Dykes in the Yalgoo Area

6.1 Distribution of the Mafic Dykes

The north Yalgoo area contains three distinct mafic dykes located between the City of Melbourne in the north and Melville in the south (Figs. 2.6, 3.1 and 6.1). In the present study, these are referred to as the north, middle and south dykes, respectively.

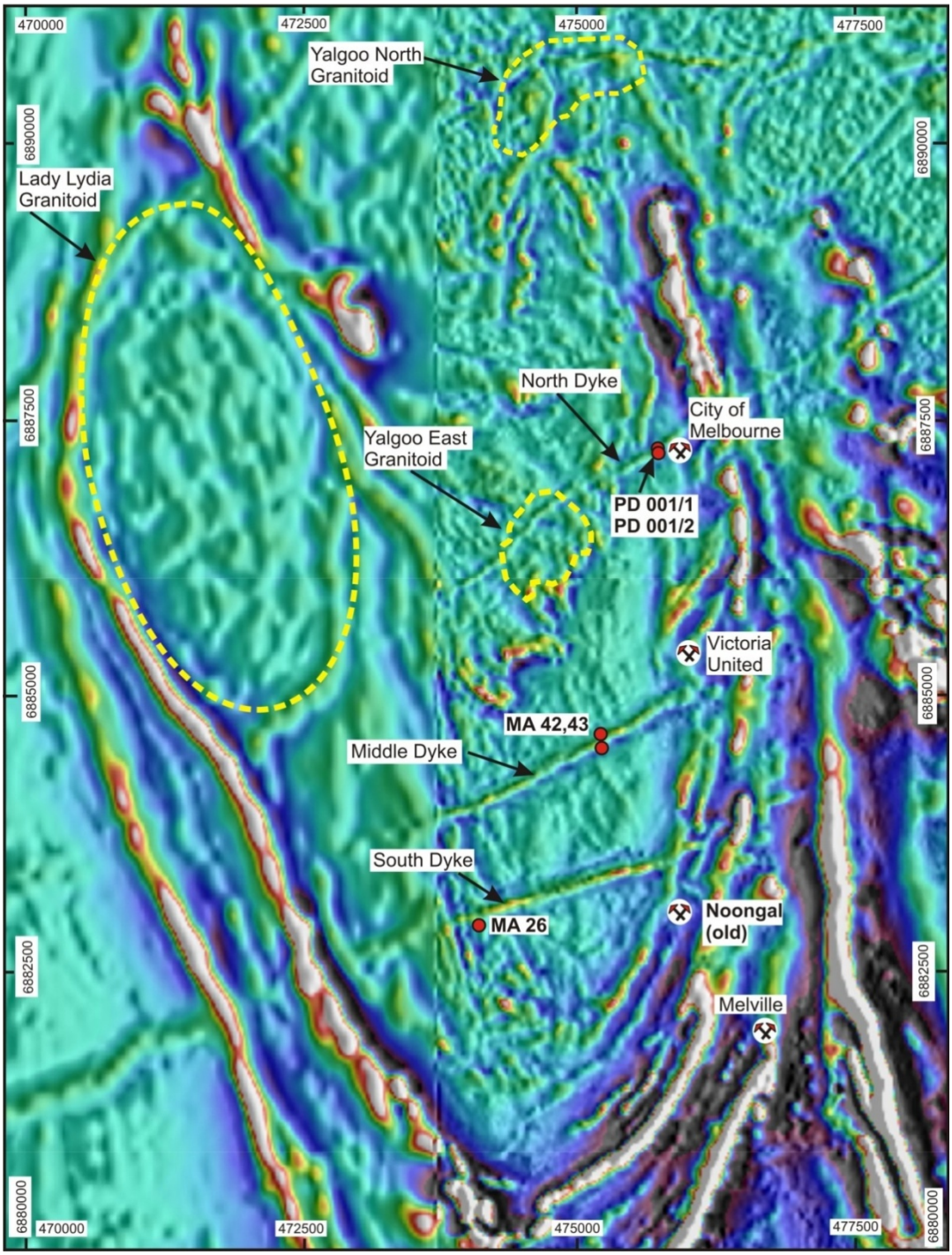

Fig. 6.1. False colour aeromagnetic image of the north Yalgoo area showing the three mafic dykes and major mine workings. (Source: Prosperity Resources Limited, 2004). Sample locations are shown by red circles.

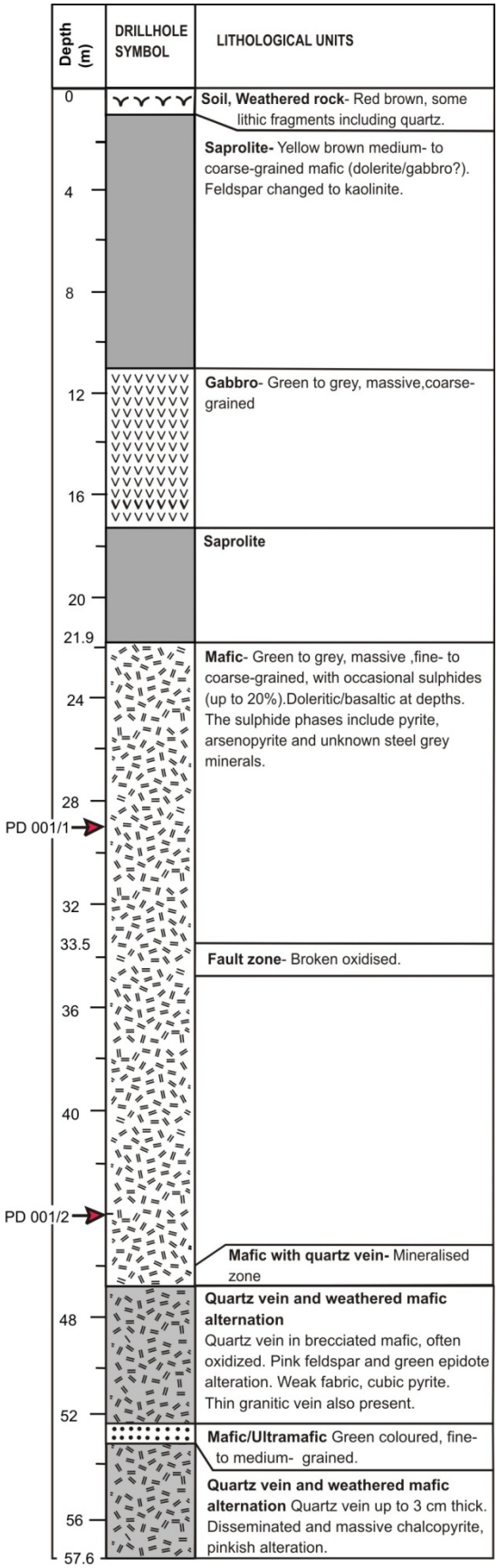

Fig. 6.2. Log of drillhole PD 001 at the City of Melbourne, Yalgoo area. Red arrows mark the locations of the dyke samples.

All the dykes trend ENE and can be distinguished clearly on aeromagnetic images (Fig. 6.1). Outcrop, however, is often discontinuous. Previous work (de la Hunty, 1975; Watkins and Hickman, 1990) referred to the mafic dykes in the Murchison as "dolerite" and correlated them with the 2.42 Ga Widgiemooltha dyke suite (Nemchin and Pidgeon, 1998), since most trend broadly east-west. This study is the first to characterise and date the dykes in the north Yalgoo area.

6.1.1 North Dyke

The northern dyke trends 052^0 just north of the City of Melbourne mine-site, and was intersected in the Prosperity Resources Limited drillhole PD 001. Even though the dyke is shown in Fig. 160 of Watkins and Hickman (1990), no surface outcrop could be found. The dyke intrudes into a mafic sequence (now saprolite) and extends from ~21.9-46.5m in drill hole PD 001. Two samples, PD 001/1 and PD 001/2 were collected from the north dyke. Both the samples were crushed for zircon separation in order to carry out U-Pb SHRIMP analysis. Microscopic study of the heavy fraction, however, failed to identify any zircon grains. Geochemical analysis was carried out on the more representative sample PD 001/1.

6.1.2 Middle Dyke

The Middle dyke is situated about 3 km south of the north dyke and can be traced from ~ 100m west of Victoria United prospect (Fig. 6.1). The dyke is distinguishable in the field by discontinuous (up to 35cm high) dark brown mafic rocks trending 072/85, dissecting the regional north-south trend of the mafic sequence (Fig. 6.3). The dyke is about 40-50m

Fig. 6.3. Almost E-W trending middle dyke in the Yalgoo area. Broken black lines mark the approximate boundaries of the dyke.

wide. Two samples (MA 42 and 43) were collected from the northern and southern margins of the dyke, respectively, to cover any compositional variation that may exist across its width. Thin sections and whole rock geochemical studies were carried out on both the samples. The samples were also crushed for zircon separation. Like sample PD 001/2, none of the samples (MA 42 and 43) contained zircon, precluding U-Pb SHRIMP geochronology.

6.1.3 South Dyke

Sample MA 26 from the southern dyke (~2.2 km southwest of the middle dyke) was collected from a mound of dark brown rubbly rocks, ~50m x 30m across and 2 to 8 m high. The dyke trends 070°. On the eastern end of the mound, the outcrop narrowed (~50 cm wide) with thin (1 to 2 cm) slivers of weathered, dark brown rock protruding through the mafic sequence (Fig. 6.4). As with the other dyke samples, thin section petrography and whole rock geochemical analyses were carried out on sample MA 26. As zircons were found in this dyke, U-Pb SHRIMP geochronology was also conducted.

Fig. 6.4. The ~070° trending south dyke in the Yalgoo area. Broken yellow lines mark approximate boundaries of the dyke.

6.2 Petrography of the Yalgoo Mafic Dykes

6.2.1 North Dyke

In hand specimen, the north dyke is greenish-grey, fine- (PD001/2) to coarse- (PD 001/1) grained and exhibits an interlocking texture, mottled with light grey patches of altered minerals (Fig. 6.5a). Modal analyses of the dyke are presented in Table 6.1. Mineral abbreviations used in the photomicrographs follow the nomenclature scheme of Kretz (1983) and Spear (1993). Microscopic study reveals a fine to coarse-grained, melanocratic sub-ophitic texture (Fig. 6.5b,c), that is more distinct in the finer variety (PD 001/2) where elongated small plagioclase crystals are partially enclosed within large subhedral clinopyroxene (Fig. 6.5b). The dyke consists mainly of plagioclase and clinopyroxene, with minor quartz, K-feldspar, biotite, chlorite and opaques. Plagioclase (An_{40}) ranges from 2-5 mm in length and is moderately to highly altered, with the development of sericite and fibrous clay minerals (Fig. 6.5c,d). A few crystals also show oscillatory zoning.

Table 6.1. Modal composition of the mafic dykes of the north Yalgoo area. tr = trace amount.

Name of the dykes	North Dyke		Middle Dyke		South Dyke
Sample no.	P D 001/2	PD 001/1	MA 4 2	MA 43	MA 26
Quartz	1.0	6.0	4	1	3
K-Feldsper		1.0			
Plagioclase	47.0	58.0	10	9	12
Amphibole	44.0	9.0	69	64	85
Clinopyroxene		8.0	tr		
Biotite	5.0	12.0			
Clilorite			tr	tr	
Epidote		tr		tr	
Clinozoisite			12	24	
Muscovite				1	
Leucoxene			3	1	tr
Titanite			2		tr
Opaque	3.0	6.0			
Total	100.0	100 0	100 0	100 0	100 0

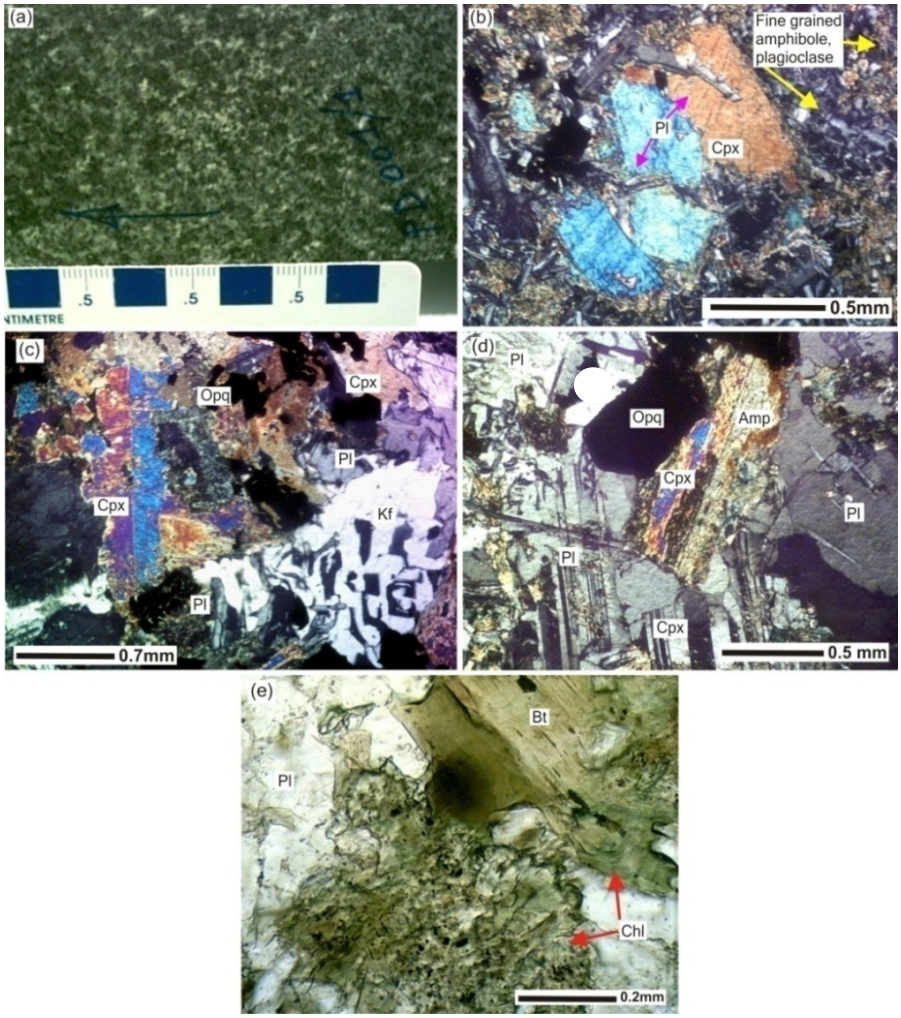

Fig. 6.5. Selected photomicrographs of the north dyke (PD001/1,2) from the City of Melbourne. (a) Drill core specimen of the dyke (PD 001/1, normal photograph). (b) Sub-ophitic texture of the dyke. Ophitic relationship between subhedral clinopyroxene (Cpx) crystals and plagioclase (Pl) (PD 001/1, xpl). (c) Interlocking igneous texture constituted by simple-twinned clinopyroxene (Cpx), plagioclase (Pl), K-feldspar (Kf) and irregular opaques (Opq). Bottom right of the picture shows graphic texture (PD 001/1, xpl). (d) Clinopyroxene (Cpx) partially altered to amphibole (Amp) along twin plane. Rest of the field of view is occupied by plagioclase (Pl) and opaques (Opq) (PD 001/1, xpl). (e) Platy biotite (Bt) retrograded to chlorite (Chl) (PD 001/1, ppl).

K-feldspar is rare and smaller than plagioclase. In a few instances, K-feldspar shows graphic texture (Fig. 6.5c). Clinopyroxene occurs as subhedral platy, simply-twinned crystals (~1.2-4mm), locally altered to amphibole and fine micaceous minerals (Fig. 6.5c,d). Amphibole crystals (0.5-1.3mm) are platy to fibrous and locally retrogressed to chlorite. Short prismatic crystals of brown biotite are also variously altered to chlorite (Fig. 6.5d,e). Cubic opaque minerals (0.05-0.2mm) occur as inclusions within and around amphibole. Thin blades of apatite (0.2-1mm) are scattered throughout the rock.

6.2.2 Middle Dyke

The dyke is massive, medium-grained and dark green in colour and has a mottled appearance with grey specks. Both samples MA 42 and 43 are identical in texture and mineralogy, but with slight differences in the modes (Table 6.1). Optically, they both exhibit a foliated, interlocking texture (Fig. 6.6a,b). Plagioclase, amphibole and clinozoisite are the major minerals in the middle dyke, with minor amounts of quartz, chlorite, epidote, biotite and muscovite.

Both plagioclase and amphibole are aligned in thin parallel lamellae resulting in a moderate foliation, which appears to be syn/post-tectonic. Plagioclase (An_{40-52}) forms subhedral platy crystals (~0.4-1.3 mm), most of which show simple carlsbad twinning (Fig. 6.6c). Plagioclase is weakly to moderately sericitized. Amphibole occurs as thin sheaves of actinolite and less abundant platy hornblende (Fig. 6.6a,b,c). Irregular grey aggregates of clinozoisite replace plagioclase (Fig. 6.6d). In places, clusters of late recrystallized quartz wraps around plagioclase (Fig. 6.6c). Patchy light green chlorite formed after amphibole.

6.2.3 South Dyke

Texturally, the dyke is a dark green, fine- to medium-grained massive to weakly foliated rock. Amphibole and plagioclase constitute more than 95% of the rock, with minor quartz, leucoxene, opaques, apatite, titanite and secondary epidote making up the remainder. Amphibole (0.2 to 0.5 mm), occurs in a dense interlocking network of subhedral platy to minute rhombic crystals (Fig.6.6e). They are strongly pleochroic from yellowish green to dark green. A few grains show simple twins. Locally, part of the amphibole may grade into a patchy dark brown cloudy aggregate of titanite (~01.-0.3mm) (Fig.6.6e,f). Bladed to platy plagioclase (An_{30-34}) crystals (~0.2 to 1 mm in length) occurs with a random orientation. Plagioclase is relatively fresh with some specks of sericite. Apatite (~0.05-0.07mm) needles and smaller hornblende flakes are sparsely distributed within plagioclase. Quartz forms equant crystals (~0.05-0.2 mm) that occupy the interstices between plagioclase and hornblende. Epidote (~0.1-0.3mm) is a secondary mineral after

amphibole and plagioclase. Titanite is found as stringers of small lozenge-shaped crystals partially replacing amphibole (Fig.6.6f).

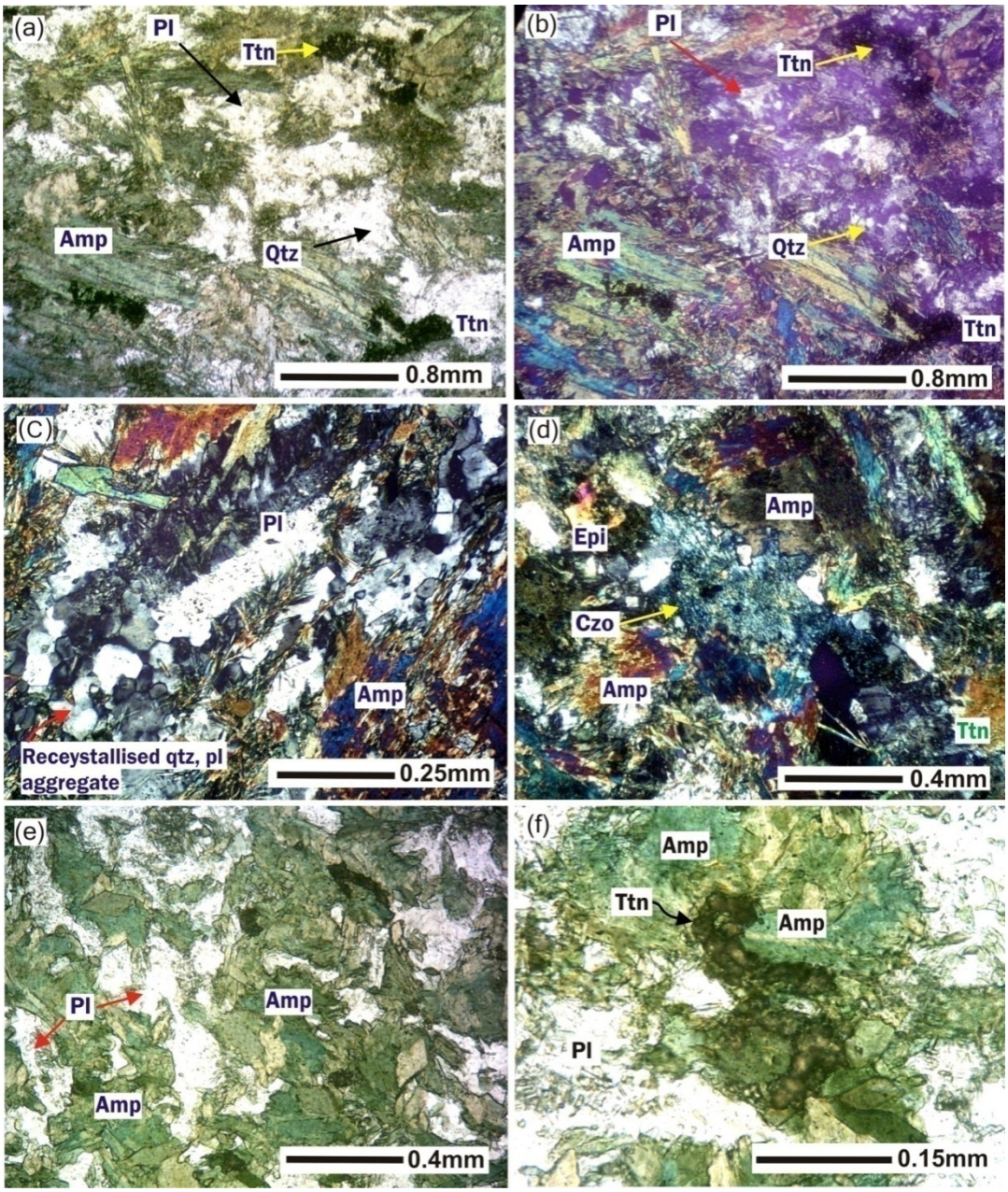

Fig. 6.6. Selected photomicrographs of the middle and south dykes. (a) Moderate foliation produced by the linear array of sheaves of amphibole (Amp) (actinolite). Also shown are weakly altered plagioclase and recrystallized quartz (Qtz) (MA 42, ppl). (b) same field of view as in (a) (xpl). (c) Recrystallized plagioclase (Pl) and quartz in the middle dyke. Bottom right shows a platy amphibole (Amp) crystal (MA 42, xpl). (d) Clinozoisite (Czo) replacing plagioclase (MA 42, xpl). (e) Intergranular texture in the south dyke produced by an interlocking network of relatively fresh plagioclase laths and platy amphiboles (MA 26, ppl). (f) Stringer of titanite (Ttn) formed as a replacement of amphibole (MA 26, ppl).

6.3 Geochemistry of the Mafic dykes

6.3.1 Magma Series and Subgroups of the Mafic Dykes

Geochemical analyses of the mafic dyke samples are presented in Table 6.2. The Yalgoo mafic dykes shows a tholeiitic affinity both on the AFM and Jensen plots (Irvin and Baragar 1971; Jensen 1976) (Fig. 6.7a,b). The north dyke (PD 001/1) has significantly higher Fe_2O_3T and lower MgO and plots in the iron-rich area within the tholeiite field. On the Jensen and Pyke diagram, samples MA 26 and MA 43 plot within the

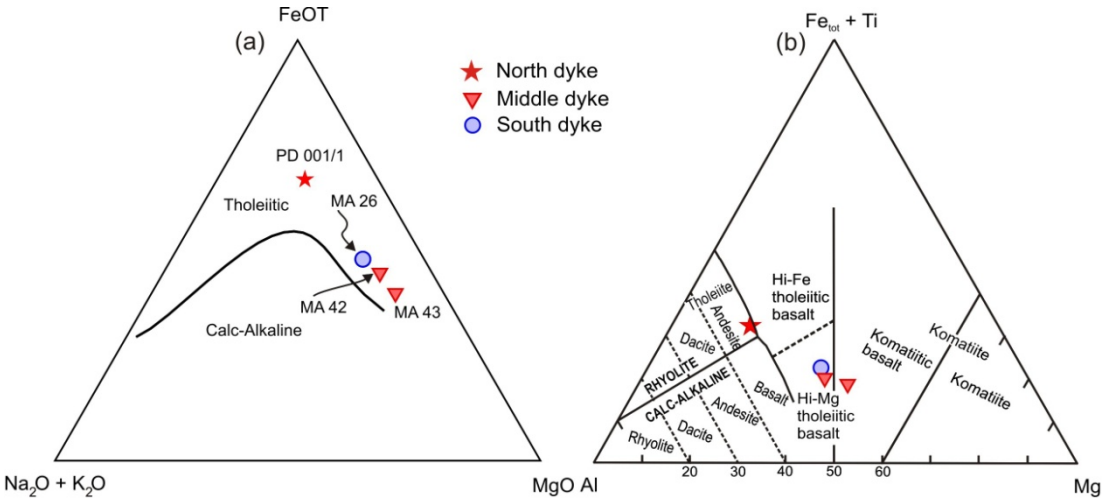

Fig. 6.7. (a) AFM diagram (Irvine and Baragar, 1971) and (b) Discrimination diagram of Jensen and Pyke (1982) of the mafic dyke samples from the north Yalgoo area. *LET= Low Ti enriched tholeiites and LDT= Low Ti depleted tholeiites* from north Yalgoo.

field of Hi-Mg tholeiitic basalt, whereas sample MA 42 plots within the field of komatiitic basalt close to sample MA 42 (Fig. 6.7b). The north dyke (PD 001/1) plots far from these three samples, along the boundary between the Hi-Fe tholeiitic basalt and andesite on the Jensen diagram (Fig. 6.7b). Therefore, combining the textural characteristics (sub-ophitic and interlocking texture; see section 6.2) and plot of the dyke samples on the AFM and Jensen and Pyke diagrams, the mafic dykes from the north Yalgoo area can be divided into two groups, i) dolerite dykes (comprising samples MA 42, 43 and 26) and ii) Fe-rich dolerite dyke (sample PD 001/1).

6.3.2 Major Element Geochemistry

Tholeiite dykes: These rocks show major element contents similar to the LDT, with 51.84-52.62% SiO_2, 12.51-13.6% Al_2O_3, 0.43-0.56% TiO_2, 8.67-1133% MgO and 9.26-10.92% Fe_2O_3T.

Fe-rich tholeiite dyke: The dyke has a SiO_2 content (51.47%) similar to the other dolerite dyke samples, however other major element oxide vary. TiO_2 (2.02%), Al_2O_3 (15.62%), Fe_2O_3T (14.13%) and alkalis (3.07%) are higher and CaO (9.28%) is lower.

Table 6.2: Chemical analyses of the mafic dyke samples from the north Yalgoo area $_{CN}$=chondrite-normalized, $_{PM}$= primitive mantle values of Sun and McDonough (1989). Fe_2O_3T denotes total iron calculated as Fe_2O_3.

Sample no.	North dyke	Middle dyke		South dyke
	PD 001-1	MA 42	MA 43	MA 26
Major oxides %				
SiO_2	51.47	51.77	51.84	52.62
TiO_2	2.07	0.46	0.43	0.56
Al_2O_3	15.62	13.60	12.51	12.64
Fe_2O_3T	14.13	10.27	9.26	10.92
MnO	0.18	0.21	0.19	0.14
MgO	3.80	9.83	11.33	8.67
CaO	9.28	12.05	12.45	10.82
Na_2O	2.68	2.20	1.93	2.38
K_2O	0.39	0.18	0.36	0.32
P_2O_5	0.22	0.05	0.03	0.05
LOI	1.30	0.86	1.33	0.41
Mg#	0.39	0.70	0.75	0.66
FeOT	12.72	9.24	8.33	9.83
Al_2O_3/TiO_2	7.5	29.6	29.1	22.6
CaO/TiO_2	4.48	26.20	28.95	19.32
Trace Elements, ppm				
Ba	79	65	106	561
Be	0.7	0.2	0.1	0.1
Co	39	48	46	43
Cr	37	422	691	479
Cs	2.3	0.3	0.5	1.1
Cu	132	6	2	4
Ga	21.0	12.6	11.2	11.6
Ge	1.5	1.6	1.7	1.9
Hf	3.80	0.81	0.70	0.87
Li	14.8	4.1	4.4	5.5
Nb	9.97	0.75	0.59	0.70
Ni	33.3	149.3	193.6	124.4
Pb	3.6	11.7	3.7	4.2
Rb	18	6	21	12
Sc	28.9	39.3	40.4	37.7
Sr	198	93	99	111
Ta	0.64	0.11	0.08	0.05
Th	1.33	0.21	0.17	0.18
U	0.37	0.06	0.03	0.08
V	278.8	223.6	210.5	202.4
Y	30.4	14.3	12.8	16.8
Zn	123	73	63	38
Zr	152	26	22	32

REE, ppm	North dyke	Middle dyke		South dyke
	PD 001-1	MA 42	MA 43	MA 26
La	10.95	1.25	1.10	2.06
Ce	26.64	3.07	2.53	3.90
Pr	3.78	0.47	0.42	0.63
Nd	18.33	2.69	2.42	3.36
Sm	4.79	1.07	0.96	1.23
Eu	1.63	0.44	0.38	0.51
Gd	5.21	1.58	1.45	1.69
Tb	0.87	0.32	0.29	0.33
Dy	5.32	2.27	2.04	2.38
Ho	1.12	0.53	0.48	0.54
Er	2.95	1.51	1.38	1.44
Tm	0.43	0.23	0.20	0.23
Yb	2.72	1.51	1.35	1.56
Lu	0.40	0.23	0.20	0.24
Total REE	85.1	17.2	15.2	20.1
$(La/Yb)_{CN}$	2.88	0.59	0.59	0.95
$(La/Sm)_{CN}$	1.5	0.8	0.7	1.1
$(Gd/Yb)_{CN}$	1.58	0.87	0.89	0.90
$(Ce/Yb)_{CN}$	2.72	0.57	0.52	0.70
$(La/Sm)_{PM}$	1.5	0.8	0.7	1.1
$(Gd/Yb)_{PM}$	1.6	0.9	0.9	0.9
$(La/Yb)_{PM}$	2.9	0.6	0.6	1.0
Ba/La	7.3	52.1	96.4	271.5
Th/La	0.12	0.17	0.15	0.09
Zr/(Zr+Y)	0.8	0.6	0.6	0.7
Zr/Sm	31.7	24.2	23.1	26.2
Zr/Nb	15.2	34.6	37.5	46.2
Zr/Y	5.00	1.82	1.72	1.93
Zr/Hf	39.9	32.1	31.5	36.9
Ti/Zr	81.7	106.4	116.7	104.0
TiSc	429.8	70.2	63.9	89.1
Ti/V	44.5	12.3	12.2	16.6
Th/U	3.6	3.3	6.4	2.4
Nb/Ta	15.5	7.1	6.9	15.2
Y/Ho	27.3	26.8	26.5	31.3
P/Nd	52.59	74.63	57.76	64.97
Sr/Y	6.5	6.5	7.7	6.6
Eu/Eu*	1.00	1.02	1.00	1.08
Ti/Ti*	1.14	0.75	0.79	0.83
Zr/Zr*	1.12	1.06	1.01	1.10
Nb/Nb*	0.94	0.65	0.65	0.67

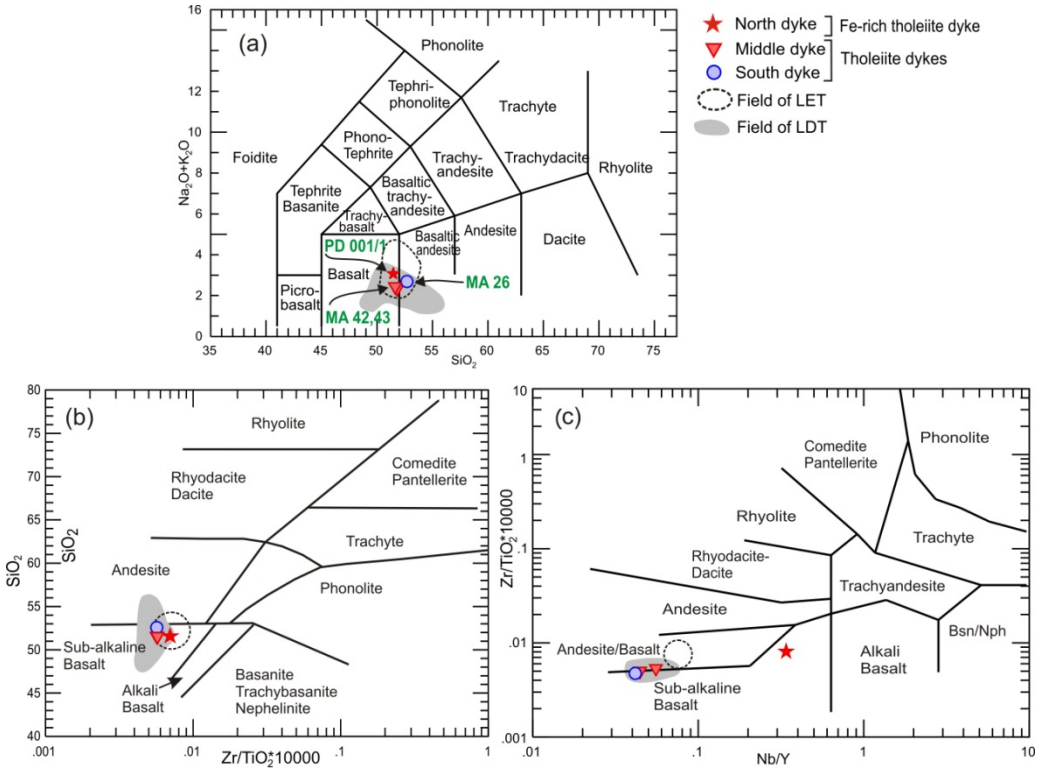

Fig. 6.8. (a) Total alkalis vs. SiO_2 diagram (Le Bas et al., 1986), (b) Zr/TiO_2 vs. SiO_2 diagram (Winchester and Floyd, 1977) and (c) Zr/TiO_2 vs. Nb/Y diagram (Winchester and Floyd, 1977) for the Yalgoo mafic dykes.

All tholeiite dyke samples overlap with the LDT samples on the total alkalis vs. silica (TAS) plot of Le Bas et al. (1986) and are classified as basalt to basaltic andesite (Fig. 6.8a). On the SiO_2 vs. $Zr/TiO_2*10000$ and $Zr/TiO_2*10000$ vs. SiO_2 plots, the samples also overlie the field of LDT (Fig. 6.8b,c). The Fe-rich tholeiite sample lies within the field of LET samples, close to LDT samples on the $Zr/TiO_2*10000$ vs. SiO_2 plot (Fig. 6.8b). On the $Zr/TiO_2*10000$ vs. Nb/Y plot, however, the Fe-rich tholeiite sample plots away from any of the mafic volcanic and dyke samples, within the field of sub-alkaline basalt (Fig. 6.8c).

6.3.3 Trace Element Geochemistry

6.3.3.1 Rare Earth Element Characteristics

The affinity of the tholeiitic dykes to the LDT samples, as seen in the previous section, is also reflected in the trace element compositions. The tholeiite dyke samples overlie or closely follow the trend of LDT on the plots of selected trace elements against MgO (Fig. 6.9). The Fe-rich tholeiite is significantly lower in MgO and plots away from the field of both LET and LDT.

Tholeiite dykes: These are characterized by low ∑REE (15-17 ppm, at 4-7 times chondrite), are depleted to weakly enriched in LREE $(La/Sm)_{CN}$=0.74–1.08) and have unfractionated HREE (Gd/Yb_{CN}=0.89-0.90) patterns (Fig. 6.10a). They follow the REE trend of LDT. In addition, all samples show either no, or weakly positive, Eu anomalies (Eu*/Eu = 1.00-1.08) (Fig. 6.10a).

Fe-rich tholeiite dyke: The Fe-rich tholeiite dyke is significantly higher in ∑REE (85 ppm, at 20-45 times chondrite), shows moderate enrichment both in LREE [$(La/Sm)_{CN}$ =1.47] and HREE [$(Gd/Yb)_{CN}$=1.57] and closely follows the REE pattern of E-MORB (Sun and McDonough, 1989) (Fig. 6.10c), with no Eu anomaly.

6.3.3.2 Incompatible Trace Element Characteristics

Tholeiite dykes: These rocks all display strong negative Nb (Nb*/Nb= 0.65-.67), and moderate negative Ti (Ti*/Ti=0.75-0.83) anomalies, weak positive to negative P and weak positive Zr (Zr*/Zr=1.01-1.10 anomalies on the PM normalized plot (Fig. 6.10b). Apart from the high La (11 ppm) content of sample MA 26, the incompatible trace element pattern of the tholeiite dykes match the trend of the LDT (Fig. 6.10b). However, unlike the LDT samples, the tholeiite dykes have Ti/Zr ratios (104-117) similar to the primitive mantle ratio of 116.

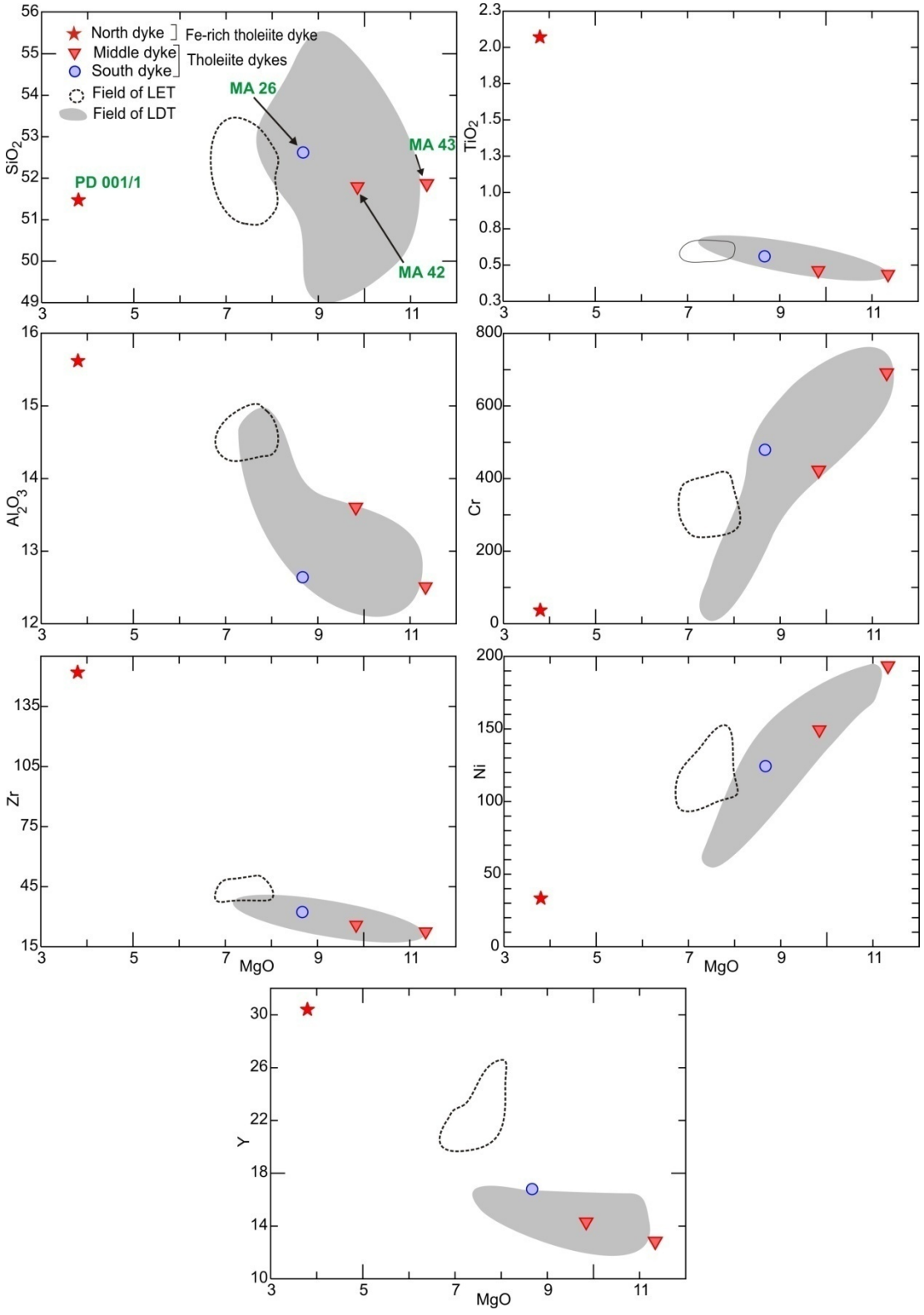

Fig. 6.9. Selected major and trace elements vs. MgO variation diagrams for the Yalgoo mafic dykes. Fields are as shown in Fig. 6.8.

Fe-rich tholeiite dyke: The Fe-rich tholeiite dyke is quite distinct from the other dolerite dykes and exhibits a very weak negative Nb anomaly (Nb*/Nb= 0.94) and has moderately negative P and weakly positive Ti (Ti*/Ti=1.14) and Zr (Zr*/Zr=1.12) anomalies on the PM

normalized plot (Fig. 6.10d). Apart from the distinct positive Nb and weakly negative Ti anomalies, the trend of the incompatible trace elements is subparallel to that of E-

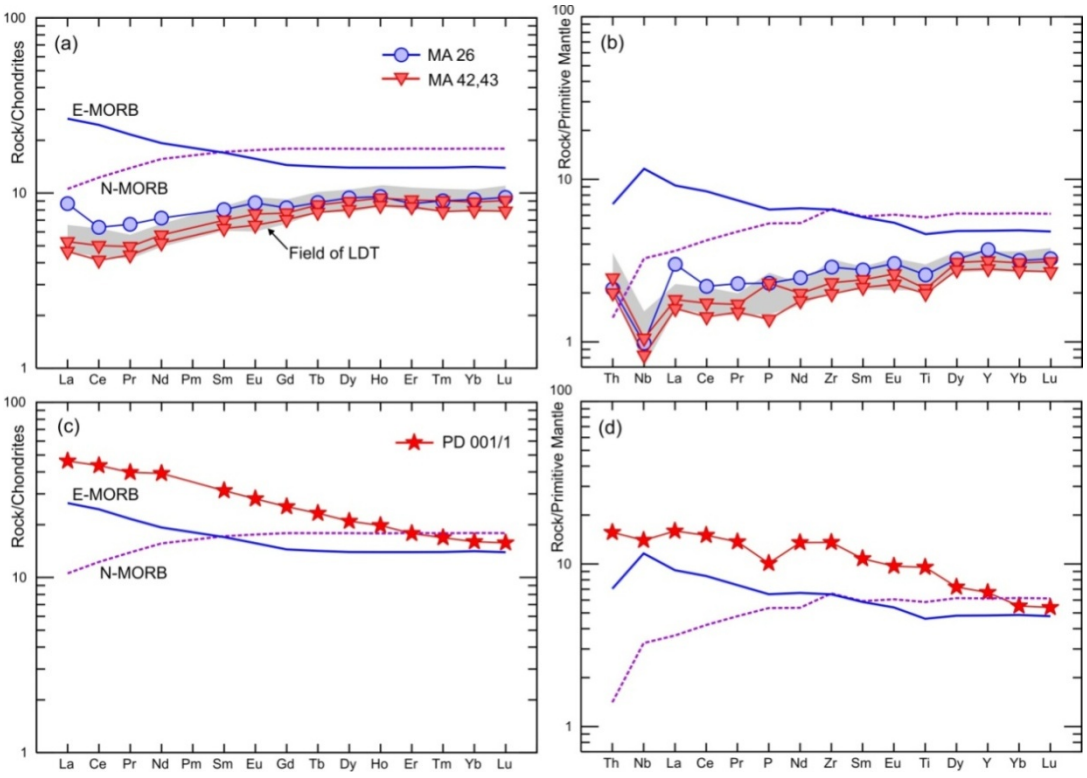

Fig. 6.10. Chondrite-normalized REE and Primitive mantle-normalized trace element diagrams of the mafic dykes. (a) REE and (b) incompatible trace element patterns for dolerite dyke samples. (c) REE and (d) incompatible trace element diagrams for Fe-rich tholeiite dyke. Data for N-MORB and E-MORB are from Sun and McDonough (1989).

MORB, with about 5 to 8 times enrichment in most of the elements. The dyke has Nb/Ta (15.5) and Zr/Hf (40) ratios almost similar to the primitive mantle values of 17 and 36. The Ti/Zr ratio of 81.6, however, confirms the E-MORB (value of 82.2; Sun and McDonough, 1989) affinity.

6.4 U-Pb Geochronology and Lu-Hf Isotopic Study of the South Dyke

Zircon crystals were extracted from sample MA 26 and are light brown in colour, euhedral to subhedral, and elongate with well-formed prismatic faces. They range from 60-130 microns in length and have an average length to width ratio of 2:1. Transmitted light photography reveals patches of irregular opaque inclusions in some crystals. CL images show oscillatory zoning in most crystals (Fig.6.11a,b,c,d).

U-Pb isotope data for sample MA 26 were collected during a single SHRIMP session and 17 analyses were obtained from 17 crystals. The error of the mean Pb/U calibration constant determined from 14 analyses of the CZ3 standard was 0.64% (2σ). Results are presented in Table 6.3.

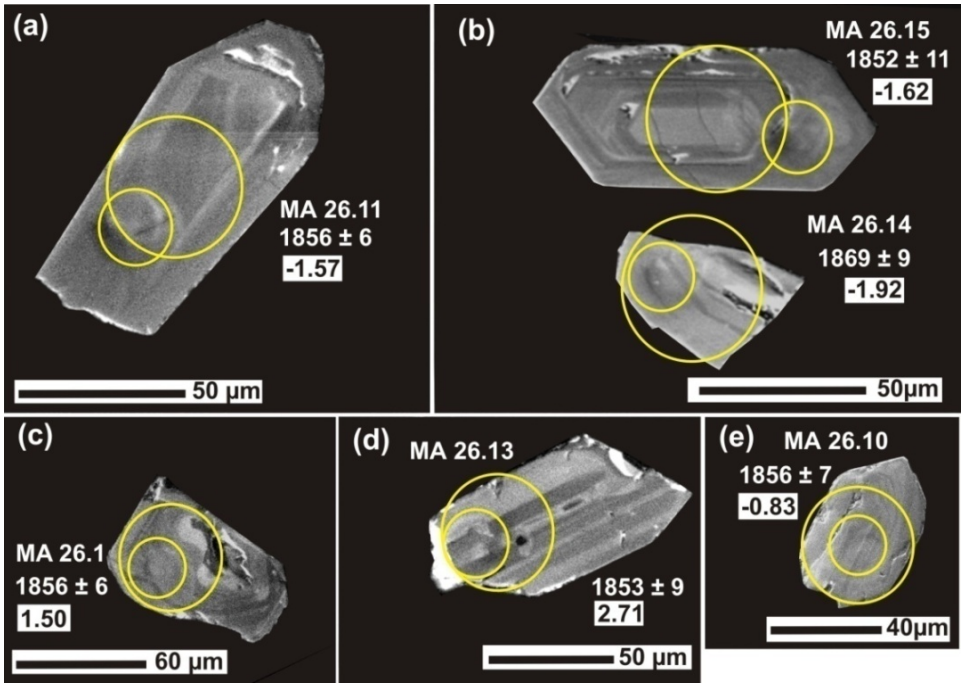

Fig. 6.11 CL images of representative zircons from sample MA 26. Small and large circles indicate the locations of SHRIMP U-Pb analyses and LA-ICP-MS Hf analyses, respectively. The U–Pb ages and εHf(t) values are also given for each spot.

The uranium content of the zircons varies from 187 to 690 ppm (average 366 ppm), and the Th contents range from 60 to 266 ppm (average 114 ppm). The Th/U ratios vary from 0.09 to 0.68 (average 0.36). All these characteristics, along with typical growth zoning as revealed in CL images (Fig. 6.11a,b,c), suggest an homogeneous igneous population.

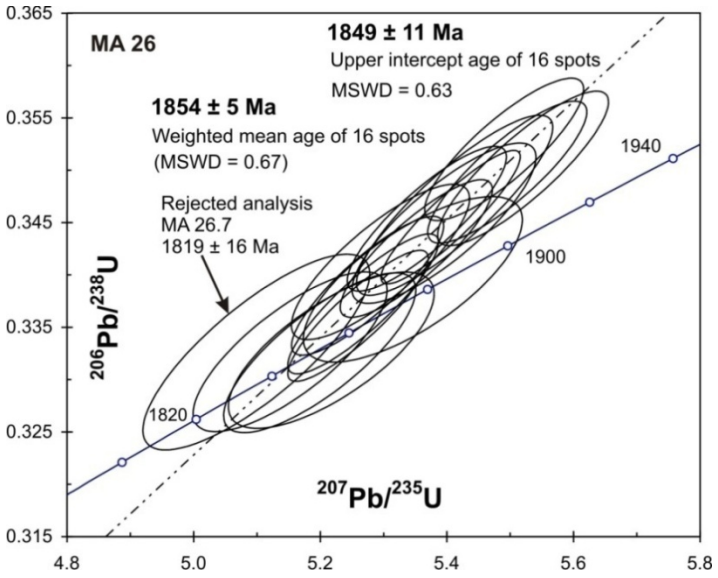

Fig. 6.12. Concordia plot of sample MA 26.

The concordia plot of the seventeen analyses shows strong reverse discordance (Fig. 6.12). The weighted mean $^{207}Pb/^{206}Pb$ age of the seventeen analyses yields an age of 1853 ± 13 Ma (MSWD = 0.92). Analysis MA 26.7 gave a slightly younger age of 1819 ± 16 Ma. If this is excluded, the weighted mean $^{207}Pb/^{206}Pb$ age data is 1854 ± 5 Ma (MSWD = 0.67). Given

Table 6.3. U-Pb SHRIMP geochronological data table for sample MA 26.

Spot	U ppm	Th ppm	Th/U	Rad ^{206}Pb ppm	% comm 206	^{204}Pb /^{206}Pb	^{207}Pb* /^{206}Pb*	% err	^{206}Pb* /^{238}U	±%	^{276}Pb* /^{235}U	±%	^{206}Pb* /^{238}U Age	1σ	^{207}Pb* /^{206}Pb* Age	1σ	% conc
MA 26.1	187	62	0.34	55	0.19	0.00012	0.1142	0.9	0.3394	1.0	5.34	1.3	1884	16	1867	17	101
MA 26.2	445	110	0.25	129	0.06	0.00004	0.1133	0.4	0.3372	0.8	5.27	0.9	1873	13	1853	8	101
MA 26.3	467	108	0.24	136.0	0.04	0.00003	0.1129	0.5	0.3389	0.8	5.27	0.9	1882	13	1846	9	102
MA 26.4	235	102	0.45	67.3	0.24	0.00016	0.1137	0.9	0.3326	0.9	5.22	1.3	1851	15	1859	16	100
MA 26.5	210	139	0.68	60.2	0.14	0.00009	0.1134	0.7	0.3325	0.9	5.20	1.2	1850	15	1854	13	100
MA 26.6	293	138	0.49	86.0	0.12	0.00008	0.1125	0.6	0.3412	0.9	5.29	1.1	1892	15	1841	11	103
MA 26.7	259	104	0.41	74.2	0.24	0.00015	0.1112	0.9	0.3325	1.1	5.10	1.4	1850	18	1819	16	102
MA 26.8	240	97	0.42	68.7	0.18	0.00012	0.1123	0.8	0.3325	0.9	5.15	1.2	1851	15	1837	14	101
MA 26.9	446	133	0.31	134.0	0.01	0.00000	0.1139	0.5	0.3498	0.8	5.50	0.9	1934	13	1863	9	104
MA 26.10	665	60	0.09	192.0	0.11	0.00007	0.1135	0.4	0.3360	0.8	5.26	0.9	1867	12	1856	7	101
MA 26.11	690	167	0.25	205.0	0.08	0.00005	0.1135	0.4	0.3455	0.8	5.41	0.8	1913	12	1856	6	103
MA 26.12	373	78	0.22	111.0	0.11	0.00007	0.1127	0.5	0.3453	0.8	5.37	1.0	1912	14	1844	9	104
MA 26.13	486	266	0.56	143.0	0.14	0.00009	0.1133	0.5	0.3424	0.8	5.35	0.9	1898	13	1853	9	102
MA 26.14	259	117	0.47	77.8	0.00	0.00001	0.1143	0.5	0.3502	0.9	5.52	1.0	1936	14	1869	9	104
MA 26.15	281	80	0.29	83.7	0.13	0.00008	0.1132	0.6	0.3466	1.0	5.41	1.2	1918	17	1852	11	104
MA 26.16	483	95	0.20	146.0	0.16	0.00010	0.1131	0.5	0.3519	0.8	5.49	0.9	1944	13	1850	9	105
MA 26.17	207	94	0.47	61.4	0.05	0.00003	0.1134	0.6	0.3449	0.9	5.40	1.1	1910	15	1855	11	103

% comm 206= amount of common ^{206}Pb in total ^{206}Pb; * = radiogenic lead corrected using measured ^{204}Pb; % conc.= [(^{206}Pb/^{238}U age)/(^{207}Pb/^{206}Pb age)] x100.

Table 6.4. Hafnium isotopic data for sample MA 26. T_{DM1} value is used in the text.

Spot	(t) Ma	^{176}Yb/^{177}Hf	^{176}Lu/^{177}Hf	^{176}Hf/^{177}Hf	2σ	εHf(0)	εHf(t)	T_{DM1}	T_{DM2}	$f_{Lu/Hf}$
MA 26.1	1867	0.044008	0.001390	0.281687	0.000023	-38.37	1.50	2218	2652	-0.96
MA 26.2	1853	0.045699	0.001463	0.281536	0.000021	-43.70	-4.26	2432	3145	-0.96
MA 26.3	1846	0.045631	0.001471	0.281628	0.000023	-40.47	-1.17	2305	2871	-0.96
MA 26.4	1859	0.034231	0.001034	0.281581	0.000021	-42.13	-2.01	2344	2953	-0.97
MA 26.5	1854	0.044523	0.001368	0.281524	0.000022	-44.14	-4.55	2443	3172	-0.96
MA 26.6	1841	0.036439	0.001147	0.281610	0.000023	-41.08	-1.49	2310	2896	-0.97
MA 26.7	1819	0.048275	0.001521	0.281627	0.000024	-40.50	-1.85	2310	2912	-0.95
MA 26.8	1837	0.030387	0.000991	0.281603	0.000028	-41.33	-1.63	2310	2905	-0.97
MA 26.9	1863	0.040298	0.001257	0.281578	0.000025	-42.22	-2.29	2361	2980	-0.96
MA 26.10	1856	0.045298	0.001331	0.281626	0.000025	-40.53	-0.83	2299	2848	-0.96
MA 26.11	1856	0.051194	0.001579	0.281614	0.000021	-40.94	-1.57	2330	2912	-0.95
MA 26.12	1844	0.042513	0.001386	0.281620	0.000021	-40.75	-1.40	2311	2889	-0.96
MA 26.13	1853	0.064570	0.001937	0.281749	0.000027	-36.18	2.71	2163	2536	-0.94
MA 26.14	1869	0.042781	0.001370	0.281588	0.000027	-41.85	-1.92	2353	2952	-0.96
MA 26.15	1852	0.043241	0.001371	0.281608	0.000025	-41.17	-1.62	2327	2914	-0.96
MA 26.16	1850	0.044021	0.001359	0.281593	0.000012	-41.68	-2.16	2346	2960	-0.96
MA 26.17	1855	0.034054	0.001091	0.281597	0.000023	-41.54	-1.58	2324	2913	-0.97

the reverse discordance, the upper intercept age of the sixteen data points is 1849 ± 11 Ma (MSWD = 0.63) and this is considered to be the best estimate of the crystallisation age of the dyke.

Lu-Hf isotopic data (Table 6.4) reveal that all the zircons have uniform ^{177}Hf/^{176}Hf values, averaging 0.281610 ± 0.00005. Fifteen out of seventeen analyses also show a narrow range of –ve εHf(t) values between -4.55 and -0.83, while analyses MA 26.1 and 26.13 have positive εHf(t) values. The T_{DM1} model ages range from 2443 to 2163 Ma. Analyses MA 26.1 and 26.13 yield younger T_{DM1} model ages of 2163 and 2218 Ma, respectively, along with positive εHf(t) values of 1.50 and 2.71, respectively. The dominance of weakly –ve to

near chondritic εHf(t) values indicate the presence of an enriched component in the source of the mafic dyke. This is explained in the context of the combined Lu-Hf isotopic study of all rock units in section 8.4.

6.5 Petrogenesis of the Mafic Dykes

The chemical characteristics of the dolerite dyke samples are remarkably similar to the LDT. Therefore, petrogenetic aspects of the LDT, as discussed in sections 3.4.4.1 to 3.4.4.5, can be applied. However, the single Fe-rich tholeiite dyke, is chemically distinct and its petrogenesis is difficult to infer.

Tholeiite dykes: The tholeiite dyke samples have identical chemical characteristics to the LDT. They do not show covariations of Ce, Th/Ce, $(La/Sm)_{CN}$ with SiO_2 and/or MgO, which negates the possibility of assimilation of crustal material. Therefore, the REE and HFSE of the dykes are considered to be original characteristics of the source magma. Both the tholeiite dykes and LDT samples show almost identical average negative Nb anomalies at 0.65 and 0.66, respectively. Positive and negative P and positive Zr (Zr*/Zr=1.01-1.10) anomalies most probably originated from a near-primitive source retaining the Zr- and P-bearing phases, as explained in section 3.4.4.4, which is also supported by near-primitive mantle Ti/Zr ratios (104-117 vs. 116). The melt for the tholeiite dykes therefore appears to have been extracted from a source similar to the LREE-depleted near-primitive source for the LDT. On the Ce vs. Yb plot of Hawkesworth et al. (1993), tholeiite dyke samples plot with samples of LDT and fall within the field of the South Sandwich Islands and Tonga–Kermadec arcs (Fig. 6.13a). The three tholeiite dyke samples plot within the LDT field on

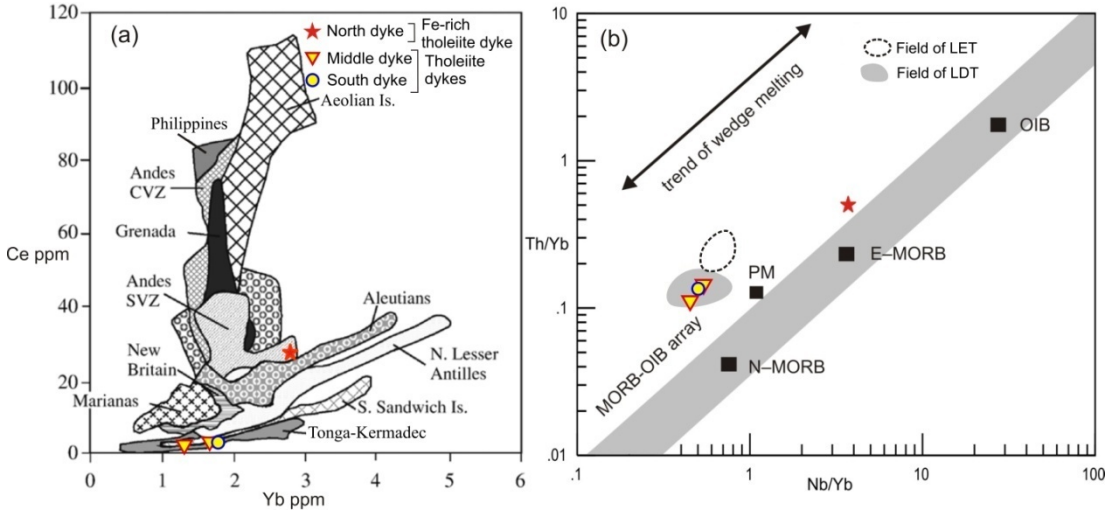

Fig. 6.13. (a) Ce vs. Yb (modified from Hawkesworth et al., 1993) and (b) Th/Yb vs. Nb/Yb diagrams (Pearce, 2008) of the Yalgoo dyke samples.

the Th/Yb vs. Nb/Yb plot following almost a parallel trend to the mantle array, further supporting a depleted mantle source which was not contaminated by subducted sediments (Fig. 6.13b).

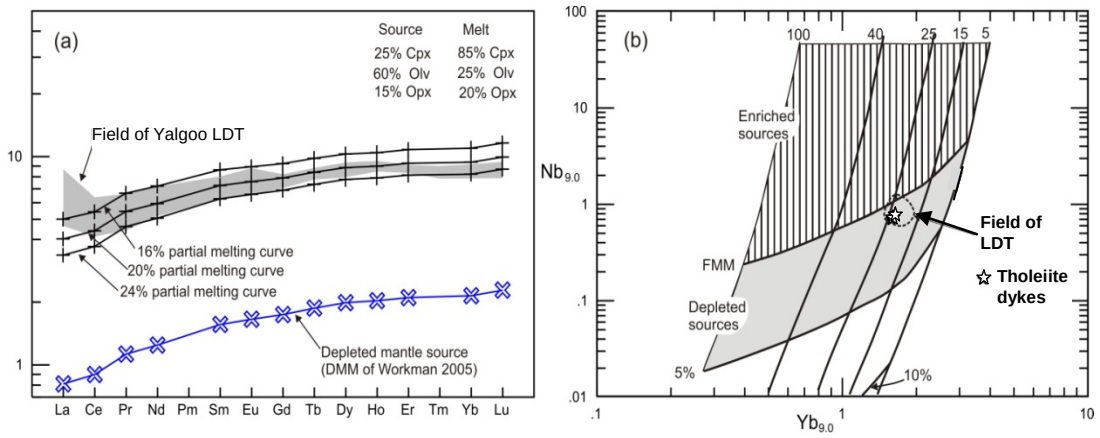

Fig. 6.14 (a) REE modelling for the dolerite dyke samples from a depleted MORB mantle with source composition 25% Cpx, 60% Olv and 15% Opx, slightly modified from Workman and Hart (2005) with the production of melt composed of Cpx 85%, Ol 25% and Opx 20%. Melting models were drawn with the help of Igpet software (Carr, 2006) using partition coefficients for mantle REE of Gill (1981). (b) $Nb_{9.0}$-$Yb_{9.0}$ covariation diagram for the tholeiite dyke samples, after Pearce and Parkinson (1993).

The chondrite-normalized REE modelling suggests a primary melt formed by ~20% - 24% non-modal partial melting of a modified depleted MORB mantle (DMM) source (Workman and Hart 2005) (Fig. 6.14a). The $Nb_{9\cdot0}$–$Yb_{9\cdot0}$ plot also supports this view, where the source melt was derived from ~24% partial melting of a fairly depleted MORB mantle source (Fig. 6.14b). This estimation is strikingly similar to that for the LDT samples, suggesting that these dykes may have been derived from a fossil source related to Archean mafic magmatism that supplied the melt for the LDT.

Fe-rich tholeiite dyke: This dyke is characterized by weak negative Nb (Nb*/Nb=0.94), moderately negative P, and weak positive Ti (Ti*/Ti=1.14) anomalies on the primitive mantle-normalized plot (Fig. 6.10d). The trend of the PM-normalized incompatible trace elements is subparallel to that of E-MORB, with about 5 to 8 times enrichment for most elements. The dyke has Nb/Ta (15.5) and Zr/Hf (40) ratios similar to primitive mantle values of 17 and 36. The Ti/Zr ratio of 81.6, however, closely correspond to the E-MORB value of 82.2 (Sun and McDonough, 1989).

The high ∑REE (85 ppm), moderate enrichment both in LREEs [$(La/Sm)_{CN}$ =1.47] and HREEs [$(Gd/Yb)_{CN}$=1.57], high Th (1.33 ppm), U (0.37 ppm), Zr (152 ppm), and low Mg# (0.39), and Ni (33 ppm), Cr (37 ppm) contents, along with a chondrite-normalized REE trend parallel to E-MORB (6.10c,d), imply an enriched MORB domain as the source for the Fe-rich tholeiite dyke.

The genesis of E-MORB-like magma is attributed to mixing and fractional crystallisation in high-level magma chambers (O'Hara, 1977). Wilson (1989) considered mixing between enriched blobs of hot-spot upwelling from a heterogeneous mantle reservoir and a depleted source region formed E-MORB. Contributions from different mantle domains, melt metasomatism, along with varying mixing models, are proposed to explain the origin of E-MORB components (see Waters et al., 2011 and references therein). Waters et al. (2011) in their work on the East Pacific Rise (EPR) documented enriched geochemical heterogeneities (pyroxenite veins) periodically introduced into the melting regime from different sources and different depths and preferentially melted to produce short episodes of E-MORB magmatism.

The presence of a Fe-rich highly fractionated (as evidenced by late-stage graphic texture; Fig. 6.5c) mafic dyke, such as sample PD 001/1, has not been reported from the Murchison Domain or any other Archean terranes or domains in the Yilgarn Craton. Said and Kerrich (2010) studied three high Mg (MgO 12.79-18.63%) dyke suites from the ~2.7 Ga Kambalda sequence, Kalgoorlie Terrane, which clearly have a different chemistry, source and evolutionary trends from those of both tholeiite and Fe-rich tholeiite dykes from Yalgoo. Of the three dyke suites, Said and Kerrich (2010) suggested that the Butterfly dykes originated from mantle plume melting at the base of the lithosphere; whereas the Norseman and Crown dykes were sourced from a metasomatized mantle lithosphere induced by some combination of rifting and thermal input from the plume.

Given the low MgO (3.8%), very low Ni (33 ppm) and Cr (37 ppm) contents of the Fe-rich tholeiite dyke, it can not be directly attributed to a mantle plume. The Nb/Ta (15.5) and Zr/Hf (40) ratios are similar to the Primitive Mantle values (17 and 40, respectively), and an E-MORB like Ti/Zr ratio (~82), along with the late-stage graphic texture (Fig. 6.5c), are suggestive of late-stage crystallization of quartz, K-feldspar and plagioclase from an Fe-rich mafic magma. The weak positive Ti (Ti*/Ti=1.14) anomaly, along with light REE enrichment, may be the result of late enriched fluid. The Fe-rich tholeiite dyke is high in Ce and lies within the field of theAndes Southern Volcanic Zone (SVZ) on the Ce vs. Yb (Fig. 6.13a) plot and very close to E-MORB composition on the Th/Yb vs. Nb/Yb plot (Fig. 6.13b).

6.6 Regional Implication of the 1.85 Ga Mafic Dyke in the Murchison Domain

6.6.1 Comparison with Dykes of Known Ages in the Yilgarn and Pilbara Cratons

The major Proterozoic dyke swarms in Western Australia, with published ages, are shown in Fig. 6.15. No record of a ~1.85 Ga event (either magmatism or major tectonic activity) has been reported from the Yilgarn Craton. Previously, the abundant W- to SW-trending dykes in the Murchison Domain were correlated with the Widgiemooltha dyke suite (Watkins and Hickman, 1990), dated at 2418±3 Ma (SHRIMP U-Pb baddeleyite age; Nemchin and Pidgeon, 1998). Two previously dated dykes, one 1214 ± 5 Ma in the Darling Range near Perth (Pidgeon and Nemchin, 2001) and another 1204 ± 10 Ma dyke near York, 100 km

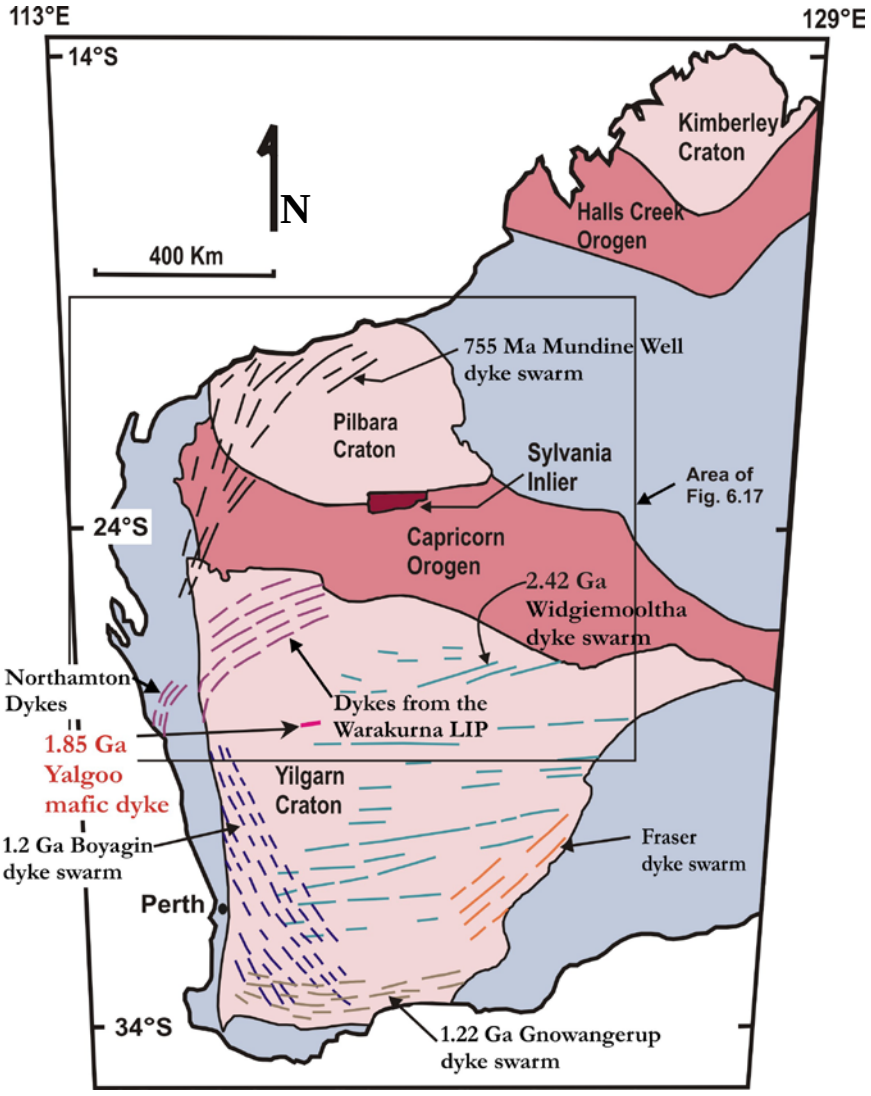

Fig. 6.15. Distribution and trend of major Proterozoic dyke swarms in Western Australia, modified after Nemchin and Pidgeon (1998), Wingate and Giddings (2000) and Wingate (2007).

inland (Pidgeon and Cook, 2003) were grouped together and assigned to the NW trending Boyagin swarm along the western Yilgarn margin by Wingate (2007). The Mundine Well dykes of the Gascoyne and Pilbara regions were dated at 755±3 Ma and palaeomagnetic results suggest that the swarm is equivalent in age to dykes of the Northampton Block(Wingate and Giddings, 2000; Wingate 2007). Several east-northeast trending dykes and small intrusions of medium-grained dolerite (and collectively, but incorrectly, referred to by some as the Muggamurra swarm) are correlated with the Warakurna Large Igneous Province (LIP) based on paleomagnetic data (Wingate, 2002; Wingate et al., 2004), with a SHRIMP baddeleyite and zircon age of 1058 ± 10 Ma (M. Wingate, unpublished data). In the southeast Yilgarn Craton, the northeast-trending Fraser dyke swarm is known only from aeromagnetic images (Isles and Cooke, 1990) and an open-pit mine exposure of a single dyke with a baddeleyite age of 1212 ± 10 Ma (Wingate et al., 2000). The Gnowangerup dyke swarm, considered to be the continuation of the Fraser dyke swarm (Wingate, 2007), runs subparallel to the southern Yilgarn margin, five dykes of which provided precise zircon, baddeleyite and zirconolite $^{207}Pb/^{206}Pb$ ages between 1218 and 1203 Ma (Evans, 1999; Rasmussen and Fletcher, 2004). None of these ages matches the 1.85 Ga dolerite dyke from the Yalgoo area.

6.6.2 Comparison with Mafic Rocks in the Capricorn Orogen

The closest match to the 1.85 Ga dolerite dykes from Yalgoo is a U–Pb SHRIMP date of 1.84 Ga (Rasmussen and Fletcher, 2002) obtained on monazite from a peperite (a rock with clastic, breccia-like texture produced by mixing of lava or shallow intrusions of magma with wet, unconsolidated sediment; Rasmussen and Fletcher, 2002) within the southern part of the Yerrida Basin (Piranjo et al., 2004) (Fig. 6.16). The Yerrida Basin is one of three (Yerrida, Bryah, Padbury-Earaheedy) Paleoproterozoic basins that are part of the Capricorn Orogen along the northern margin of the Yilgarn Craton (Fig. 6.16). The oldest, ca. 2.17 Ga Yerrida Basin, began as an intracontinental sag within which siliciclastics and evaporites accumulated (Pirajno et al. 2004). The ca. 1.83 Ga convergence and collision of the Pilbara and Yilgarn cratons (Capricorn Orogen) resulted in deformation of the Bryah–Padbury Basins and orogenic uplift with coarse clastic sedimentation accompanied by the eruption of flood basalts into the Yerrida Basin (Pirajno et al., 2004).

Rasmussen and Fletcher (2002) considered that monazite crystals were formed in the carbonaceous shale of the Maraloou Formation in the Yerrida Basin from hydrothermal fluid circulation during the intrusion of subvolcanic dolerite sills, related to interlayered basaltic

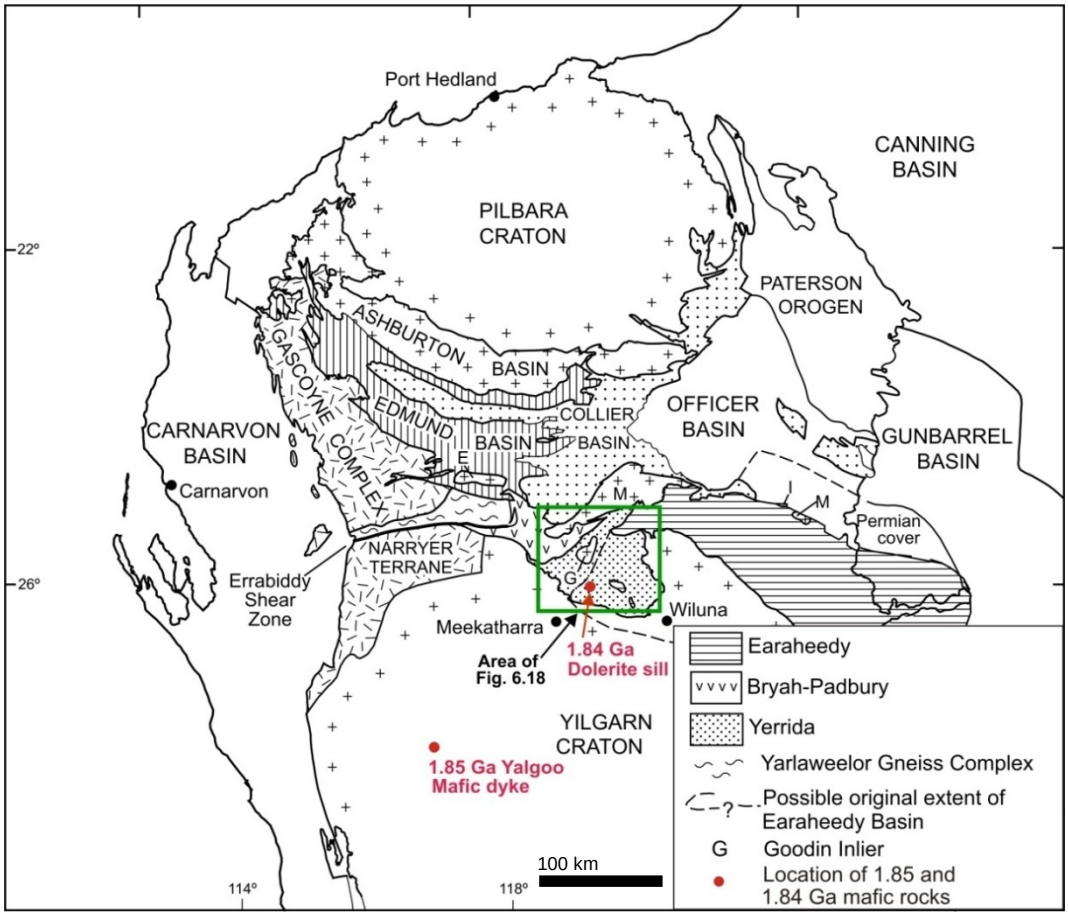

Fig. 6.16. Tectonic units of the Capricorn Orogen and position of the Yerrida, Bryah, Padbury and Earaheedy Basins. E, Egerton Inlier; G, Goodin Inlier; M, Marymia Inlier; S, Sylvania Inlier (from Pirajno et al., 2004).

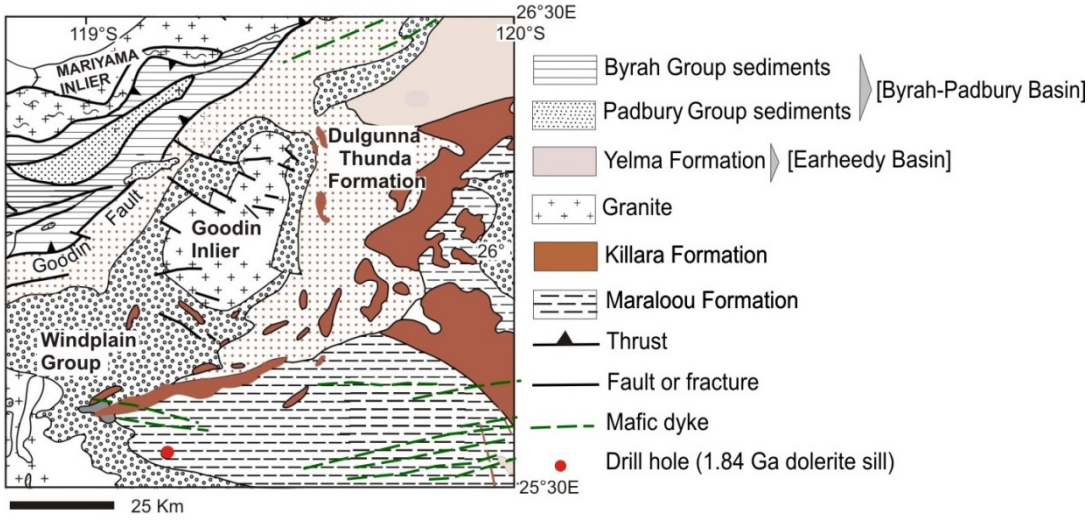

Fig. 6.17. Simplified geological map of the Yerrida Basin (from Pirajno et al., 2004).

Table 6.5. Average chemical analyses of mafic volcanic rocks from the Killara Formation Yerrida Basin (from Pirajno et al., 1998), and the tholeiite dyke and Fe-rich tholeiite dyke samples from the Yalgoo area.

Lthology	Mafic volcanic rocks	Tholeiite dykes	Fe-rich
Location	Killara Formation, Yerrida Basin	Yalgoo	tholeiite dyke
No of samples	n=5	n=3	Yalgoo, n=1
SiO_2	55.79	52.16	51.47
TiO_2	0.91	0.50	2.07
Al_2O_3	14.18	13.05	15.62
Fe_2O_3T	12.76	10.45	14.13
MnO	0.19	0.18	0.18
MgO	5.04	9.48	3.8
CaO	11.95	11.55	9.28
Na_2O	1.60	2.25	2.68
K_2O	0.51	0.26	0.39
P_2O_5	0.08	0.05	0.22
Total	100.00	99.92	1.3
Mg#	0.44	0.69	0.39
Trace Elements, ppm			
Ba	241.4	289.9	79.4
Co	60.6	45.2	39.4
Cr	132.0	477.2	36.9
Cu	123.6	4.4	132.3
Nb	2.78	0.71	9.97
Ni	73.2	143.2	33.3
Pb	5.6	7.5	3.6
Rb	16.6	10.1	18.1
Sc	43.0	38.7	28.9
Sr	172.8	101.4	198
Th	3.36	0.19	1.33
U	0.23	0.07	0.37
V	281.4	212.7	278.8
Y	20.0	15.2	30.4
Zn	99.8	56.3	123.4
Zr	100.8	28.3	152
REE, ppm			
La	11.64	1.47	10.95
Ce	29.70	3.17	26.64
Pr	3.74	0.51	3.78
Nd	14.08	2.82	18.33
Sm	3.34	1.09	4.79
Eu	1.65	0.44	1.63
Gd	4.14	1.57	5.21
Tb	0.71	0.31	0.87
Dy	4.03	2.23	5.32
Ho	0.92	0.52	1.12
Er	2.70	1.44	2.95
Tm	0.44	0.22	0.43
Yb	2.56	1.47	2.72
Lu	0.61	0.22	0.4
Total REE	80.24	17.50	85.14

lavas of the Killara Formation (Fig. 6.17). Therefore, the 1.84 Ga age is suggested to record the minimum depositional age for the Maraloou Formation, and by inference the emplacement of the Killara mafic rocks (Rasmussen and Fletcher, 2002; Pirajno et al., 2004). Numerous tholeiitic sills were emplaced within the sedimentary rocks (Juderina, Thaduna and Doolgunna Formations), and they are distributed along a general east–northeast and northeast trend (Pirajno et al. 1995, 1998, 2004) (Fig. 6.17). Some of the tholeiite lavas and sills were considered to have been fed by east-trending fractures, now filled with dolerite/microgabbroic dykes (Pirajno et al. 1995, 1998). However, no study of these dykes is available to correlate with the tholeiite dykes from the Yalgoo area.

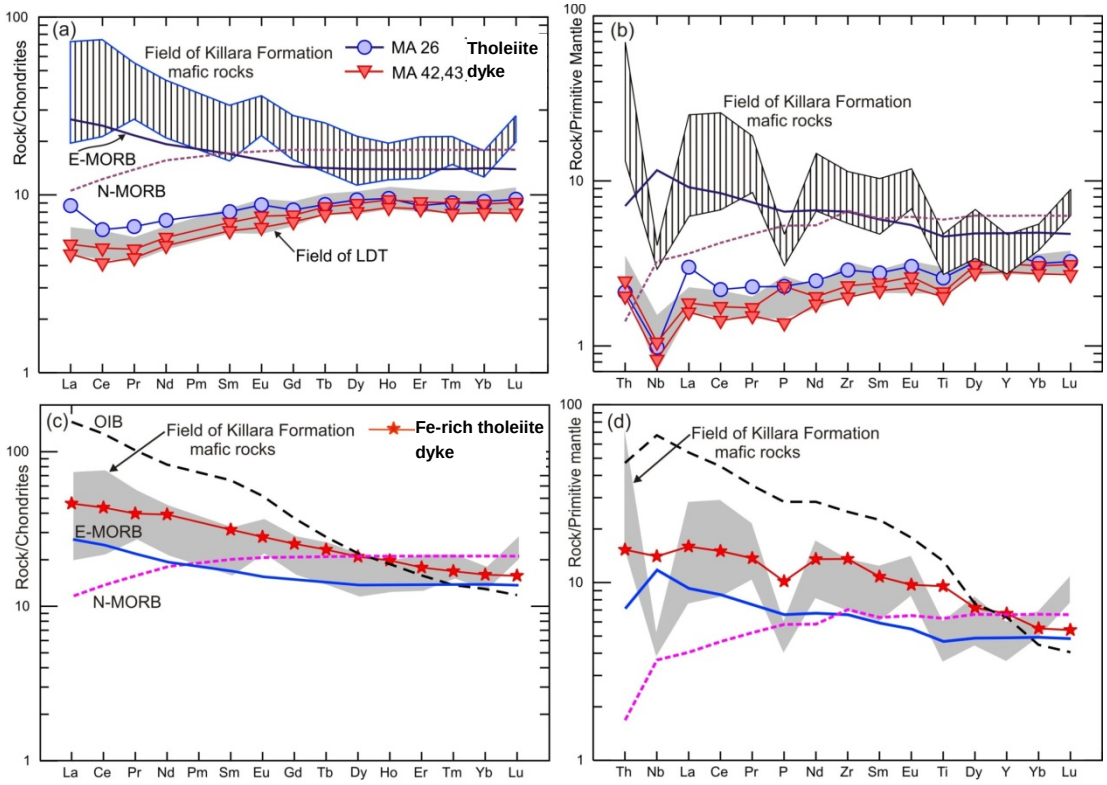

Fig. 6.18. Comparison between the (a) Chondrite-normalized REE patterns and (b) Primitive mantle-normalized incompatible trace element patterns of mafic volcanic rocks from the Killara Formation and dolerite dyke samples from the Yalgoo area. (c) Chondrite-normalized REE patterns and (d) Primitive mantle-normalized incompatible trace element patterns of mafic volcanic rocks from the Killara Formation and single Fe-rich tholeiite sample from the Yalgoo area. Chondrite and Primitive mantle normalizing values are from Sun and McDonough (1989). Patterns for N-MORB, E-MORB, OIB (Ocean Island Basalt) (Sun and McDonough, 1989) and LDT are shown for comparison.

The geochemistry of the Killara Formation is discussed by Pirajno et al. (1998) and Pirajno and Occhipinti (2000). The average chemical compositions of the mafic volcanic rocks from the Killara Formation, tholeiite dyke samples and the Fe-rich tholeiite dyke sample from Yalgoo are presented in Table 6.5. Compared to the tholeiite dyke samples, the major element oxides of the mafic volcanic rocks from the Killara Formation have higher SiO_2, TiO_2 and Fe_2O_3T and lower MgO, Na_2O and K_2O, while the remainder of the major element oxides are similar. The Killara Formation volcanic rocks have lower Ni, and Cr, and variable but high Nb and Zr contents compared to those of the tholeiite dyke samples, implying strong differences in the sources of these two mafic lithologies. The mafic rocks of the Killara Formation show strong enrichment in LREE and strong positive Eu anomalies (average La/Yb_{CN} 2.92 and Eu/Eu*= 1.47; Pirajno et al., 1998a). The PM-normalized incompatible trace element patterns of the mafic rocks of the Killara Formation also differ considerably from those of the tholeiite dyke samples, with the former showing significantly elevated (2 to 30 times PM values) contents in almost all trace elements, and strong –ve Nb and P and moderate –ve Ti anomalies. The lack of a negative Eu anomaly along with variable –ve Nb and P and moderate –ve Ti anomalies is suggestive of little or no plagioclase

fractionation. The enriched LREEs also point toward crustal contamination, or an enriched lithospheric mantle source (Pirajno et al., 1998 and Pirajno and Occhipinti, 2000). An intracontinental rift environment (i.e. continental flood basalt), has been suggested as the most likely setting for the Killara Formation in which fissures were largely responsible for the eruption of lava (Pirajno et al., 1998; Pirajno and Occhipinti, 2000).

The Fe-rich tholeiite dyke has slightly less silica and MgO and higher TiO_2, Fe_2O_3T and Na_2O than the Killara Formation mafic rocks (Table 6.5). The chondrite-normalized REE pattern of the Fe-rich tholeiite dyke however, lies broadly within the field the Killara Formation mafic rocks (Fig. 6.18c). On the PM-normalized incompatible trace element diagram (Fig. 6.18d), the Fe-rich tholeiite dyke differs from the mafic rocks of the Killara Formation by showing weak –ve Nb and weak +ve Ti anomalies, and lower normalized Yb and Lu values. Therefore, despite having similar ages, the large distance (~200 km between Yalgoo and Yerrida Basin, Fig. 6.16) and differences in chemical composition between the 1.85 Ga tholeiite dykes from the Yalgoo area and the 1.84 Ga mafic rocks from the Killara Formation preclude any direct correlation. Further work incorporating more samples between these two areas is needed to establish if any correlation existed between these two Paleoproterozoic events.

Chapter 7 Granitoid-Hosted Gold Mineralization in the Yalgoo Area

7.1 Introduction

The north Yalgoo area contains a number of sites of known gold mineralization, which Watkins and Hickman (1990) included within the Noongal Mining Centre. The mineralization

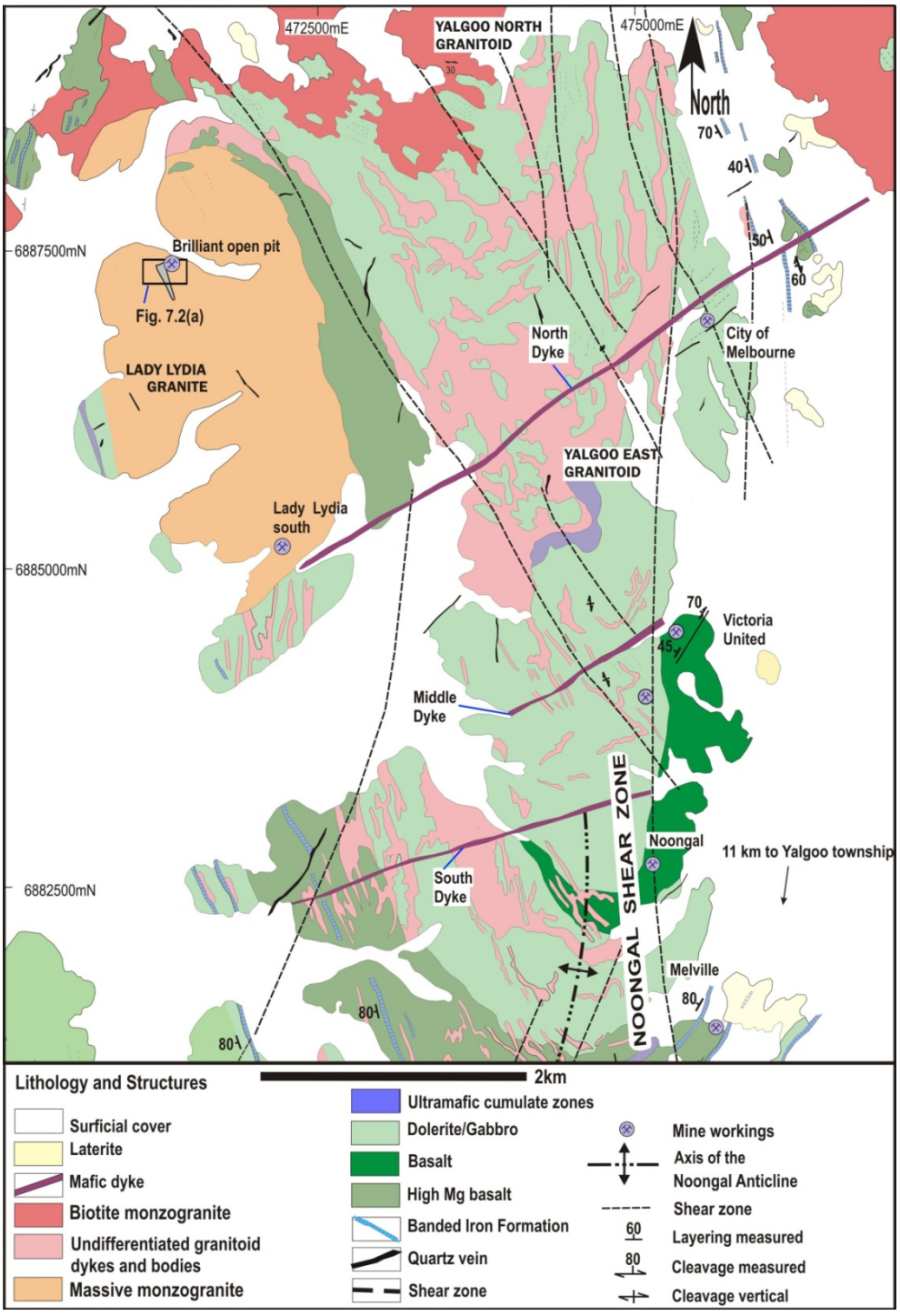

Fig. 7.1 Geological map of part of the north Yalgoo area showing areas of gold mineralization (from Hallberg et al., 2002, modified after Watkins and Hickman, 1990).

in the eastern part of the study area appears to be related to the regional-scale Noongal Shear Zone (NSZ) (Fig. 7.1). The old mine workings that lie along the NSZ extend from Melville in the south through Noongal, Victoria United, to City of Melbourne in the north (Fig. 7.1). A series of north-northwesterly striking faults and fractures transect the area to the west of the NSZ exhibiting negligible displacement and may be tensional and riedel fractures related to the main shear zone (Watkins and Hickman, 1990) (Fig. 7.1).

In the west, the main mine working is Brilliant open pit, located in the Lady Lydia Granite (LLG) (Fig. 7.1). Apart from this, numerous smaller workings occur on faulted and sheared Banded Iron Formation (BIF) with quartz veins. As the area does not contain any large gold deposits, it has not been subjected to a detailed geological and/or metallogenic study, and so the information on the geology from these mine workings is scanty and limited in extent. Only the Brilliant Open pit offers good exposures of both country rocks and mineralized veins, and therefore provides the best opportunity to study the gold mineralization in the area.

7.2 Gold Mineralization in the Quartz Pyrite Veins of the Brilliant Open Pit

Gold mineralization in the Brilliant open pit is confined to early quartz-pyrite veins, bordered by thin zones of hydrothermal alteration. In 2006, Prosperity Resources Limited delineated an ore zone from high ore grades encountered in drill holes in and around the pit (Fig 7.2b,c). Quartz veins in the Brilliant open pit are poorly described in historical reports. At present, it is difficult to match the observed veins with those reported in previous reports, as none of the reports provide a complete description of the vein systems. The pit shows discontinuous remnants of a major mineralized vein, whereas the quartz veins in the pit wall form weak stockworks and may be correlated with the stockwork mentioned by Dale and Goldrick (1994). A suite of eight quartz-pyrite and pyrite vein samples were collected both from the pit floor and the west wall to study gold mineralization and fluid inclusions (Fig. 7.2a). From the position of the ore zone with respect to the floor and west wall of the pit, it is clear that samples represent the main ore zone (Fig 7.2a,b,c) in the Brilliant open pit. Most veins are linear, flat and locally sigmoidal or boudinaged (Fig.7.3 a,b,c); where observed, they appear to follow the foliation in the host rock (Fig.7.3a). They are sub-parallel to the open pit (~137°), and are locally cut by late pegmatite veins (Fig. 7.3b).

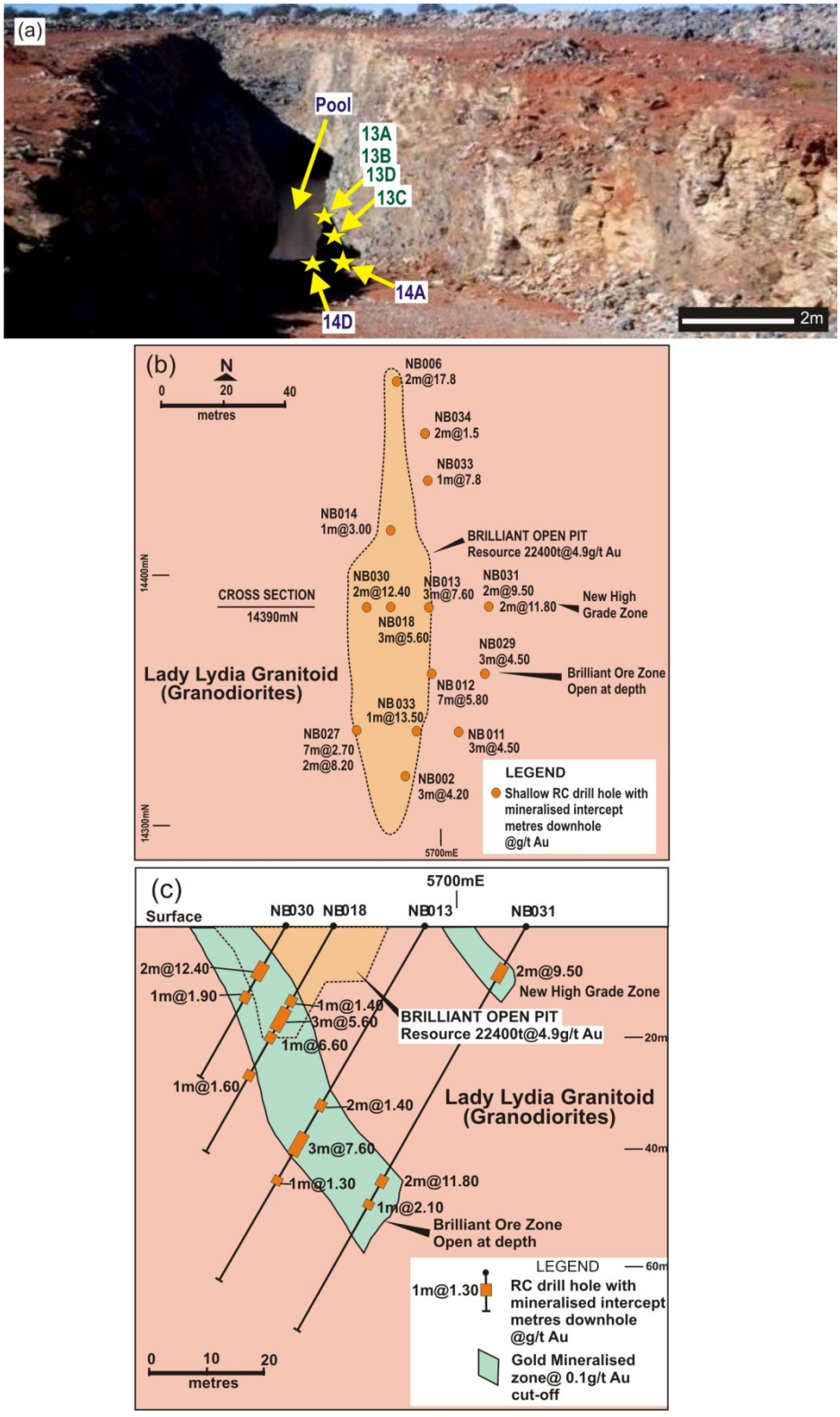

Fig. 7.2. (a) Location of mineralized samples in the Brilliant open pit; view from the northern end (sample locations are marked with solid yellow stars). (b) Plan view of Brilliant open pit showing locations of RC drillholes sunk by Prosperity Resources Limited (2005). Significant intercepts from each drillhole are also shown. (c) Schematic E-W cross-section along 14390mN across the mineralized zone.

After preliminary petrological study, six samples were selected for detailed ore petrographic study (samples 13A-D and 14A, D) since they revealed the presence of ore

minerals in three quartz-pyrite veins (samples 14A, 14D and 13C). These three mineralized veins were later selected for fluid inclusions study. The six vein samples were classified into three types, based on vein mineralogy, degree of deformation, ore and alteration assemblages and sharpness of vein margins. They are:

Type I) Massive to boudinaged quartz-pyrite veins; mineralized : 14A and 13C
Type II) Sigmoidal quartz-pyrite veins; mineralized : 14D
Type III) Thin quartz veins: unmineralized : 13A,13B and 13D

Unmineralized quartz veins are thinner, lack sulphides and are considered to have formed during later brittle deformation. These veins (Type III) are not discussed any further.

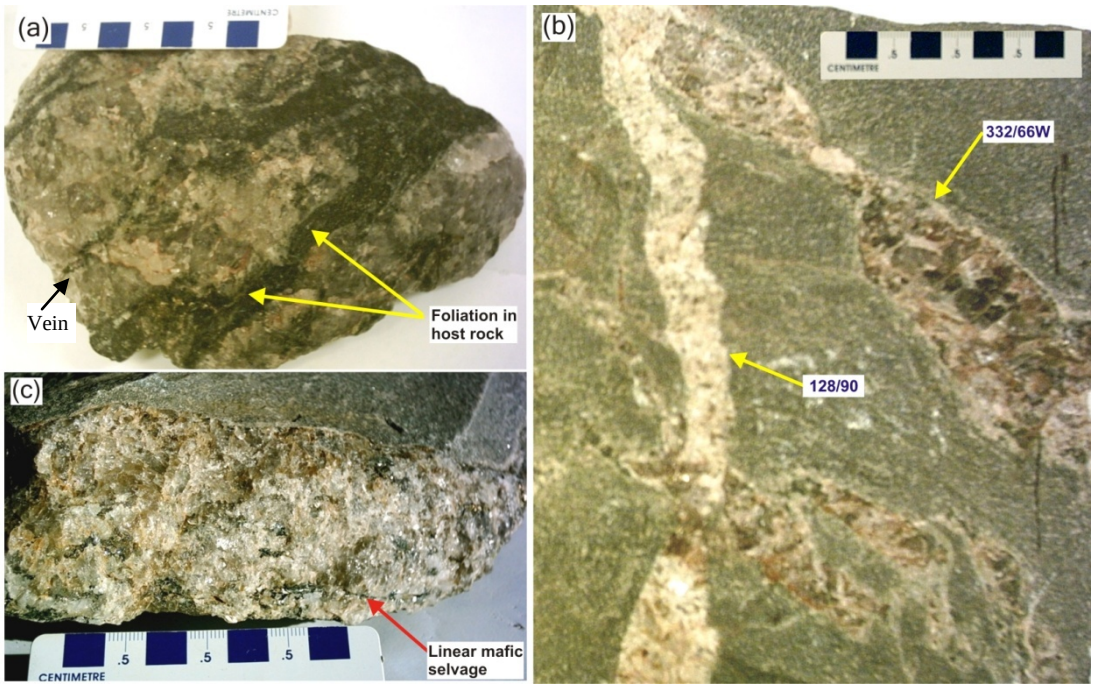

Fig.7.3. Quartz-pyrite veins from the Brilliant open pit, north Yalgoo area. (a) Type II Sigmoidal quartz-pyrite vein (14D) trending parallel to foliation in host rock. (b) Type II Boudinaged quartz-pyrite vein (13C) cut by pegmatite vein. (c) Massive quartz-pyrite vein (14A) Blue divisions on the scale in all photographs represent 10mm.

7.2.1 Petrographic study of quartz-pyrite and quartz veins

Type I veins are massive (sample 14A) to boudinaged (sample 13C) and composed of brown to brown-grey quartz: gold was detected only in vein sample 14A. Considering the medium grade of gold (average ~5gm/tonne; Fig. 7.2c) and the presence of a similar metal association in all mineralized veins (13C and 14D), it is likely that all three veins are part of a single mineralized vein set as suggested by Holden (personal communication, 2006) or part of the main flat-lying quartz vein dipping west (Dale and Goldrick, 1994). Both vein samples14A and 13C have a zone of K-feldspar along the

margins, contain hornblende as a prominent selvedge mineral associated with pyrite, and show a similar alteration mineral assemblage (Table 7.1).

Table: 7.1. Estimation of non-ore minerals in the mineralized quartz-pyrite veins. tr = trace.

Minerals		Veins		
		14A	13C	14D
Vein minerals	Quartz	64	80	93
	Microcline	30	15	3
Selvedge minerals	Plagioclase	1	1	1
	Hornblende	3	1	-
	Biotite	2	2	1
	Titanite	tr	1	2
	Apatite	tr	-	-
	Calcite	tr	tr	tr
	Epidote	tr	tr	tr

In handspecimen, vein sample 14A is part of a massive (~12cm long, ~15cm wide and ~5cm thick) brown quartz vein (Fig. 7.3c). Streaks of mafic selvedge consist of biotite flakes running throughout the vein. Specks of pyrite (1-4mm) are associated with light green epidote and biotite (<1mm) and local staining by reddish brown iron oxide is also present.

Sample 13C represents part of a boudinaged quartz vein trending 332/66ºW, with a thin alteration zone, cut by a 128/90º trending pegmatite vein (Fig. 7.3b). An en echelon array of three thin veins runs parallel to the main boudinaged vein about 3 to 8 cm apart. These en-echelon veins are cut by the same pegmatite and are thus considered coeval with the main boudinaged vein (Fig. 7.3b). The vein has a sharp margin with the country rock. Fluid inclusion and ore petrography studies were carried out on the thicker boudinaged vein of sample 13C (upper right in Fig.7.3b).

Type II veins are represented by sample 14D, which forms part of a sigmoidal vein. It comprises grey brown quartz that anastomoses through the country rock and generally follows the foliation in the host rock (Fig. 7.3a).

Quartz in these veins is anhedral, coarse-grained (3 to 6mm across), and commonly unstrained. Large fresh crystals (2 to 3mm across) of microcline form a thin zone (3 to 5mm) along the margins of samples 14A and 13C (Fig. 7.4a). Large hornblende crystals (12 to 35mm) occur proximal to the vein margin (Fig. 7.4b, 7.5a, b). Local alteration of hornblende to biotite and rarely to chlorite, is also noted in a few crystals (Fig. 7.5a, b). In sample 14A, a large (7 mm) euhedral tabular crystal of apatite is present along the vein margin (Fig.7.4c). In both the veins, plagioclase, biotite and titanite are the major selvedge minerals constituting ~4% of the veins. Epidote is also present.

7.2.2 Alteration Assemblage

Type I veins have a thin (10 to 25mm) alteration halo within the host biotite hornblende monzogranite wall rock. K-feldspar, biotite, sericitized plagioclase, epidote, calcite,

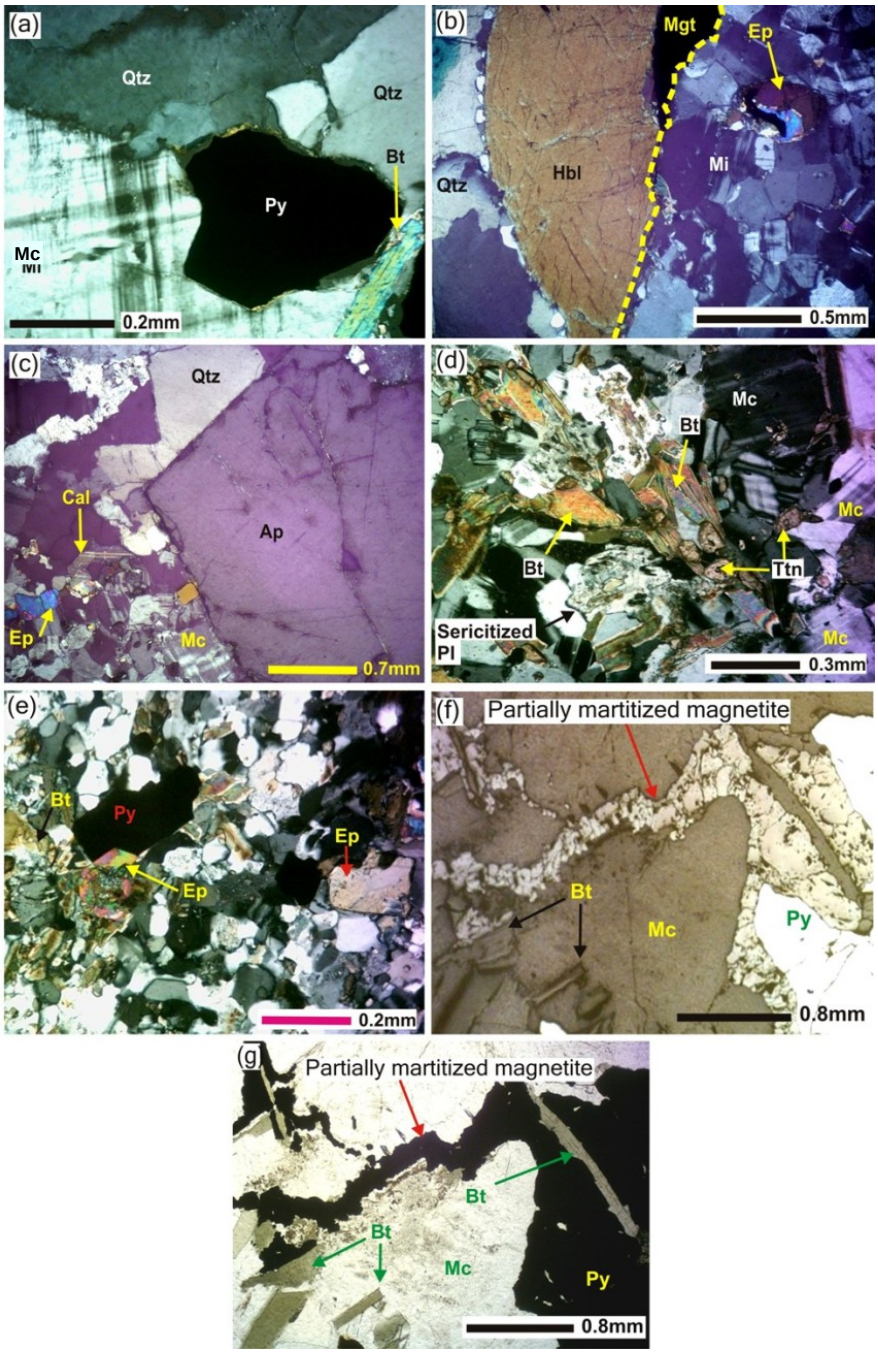

Fig. 7.4. Vein and alteration mineral phases in the Type I veins (sample 14A). (a) Subhedral pyrite (Py) in textural equilibrium with coarse quartz (Qtz) and microcline (Mc) (transmitted xpl). (b) Large hornblende (Hbl) crystal along vein margin. Yellow broken line divides vein (on right) from proximal alteration zone (on the left) (transmitted xpl). (c) Euhedral large tabular apatite (Ap) along the vein margin. Alteration minerals present are calcite (cal), epidote (Ep) and microcline (under transmitted xpl). (d) Proximal alteration mineral phases: microcline (Mc), biotite (Bt), sericitized plagioclase (Pl) and titanite (Ttn) (transmitted xpl). (e) Distal alteration mineral phases: epidote and biotite (transmitted xpl). (f) Weakly martitized magnetite in pyrite that also wrap around microcline (reflected ppl). Also shown is slender greenish brown biotite intergrown with magnetite (reflected ppl). (g) Same field of view as (f) showing intimate association of green-brown biotite, weakly martitized magnetite and pyrite (transmitted ppl).

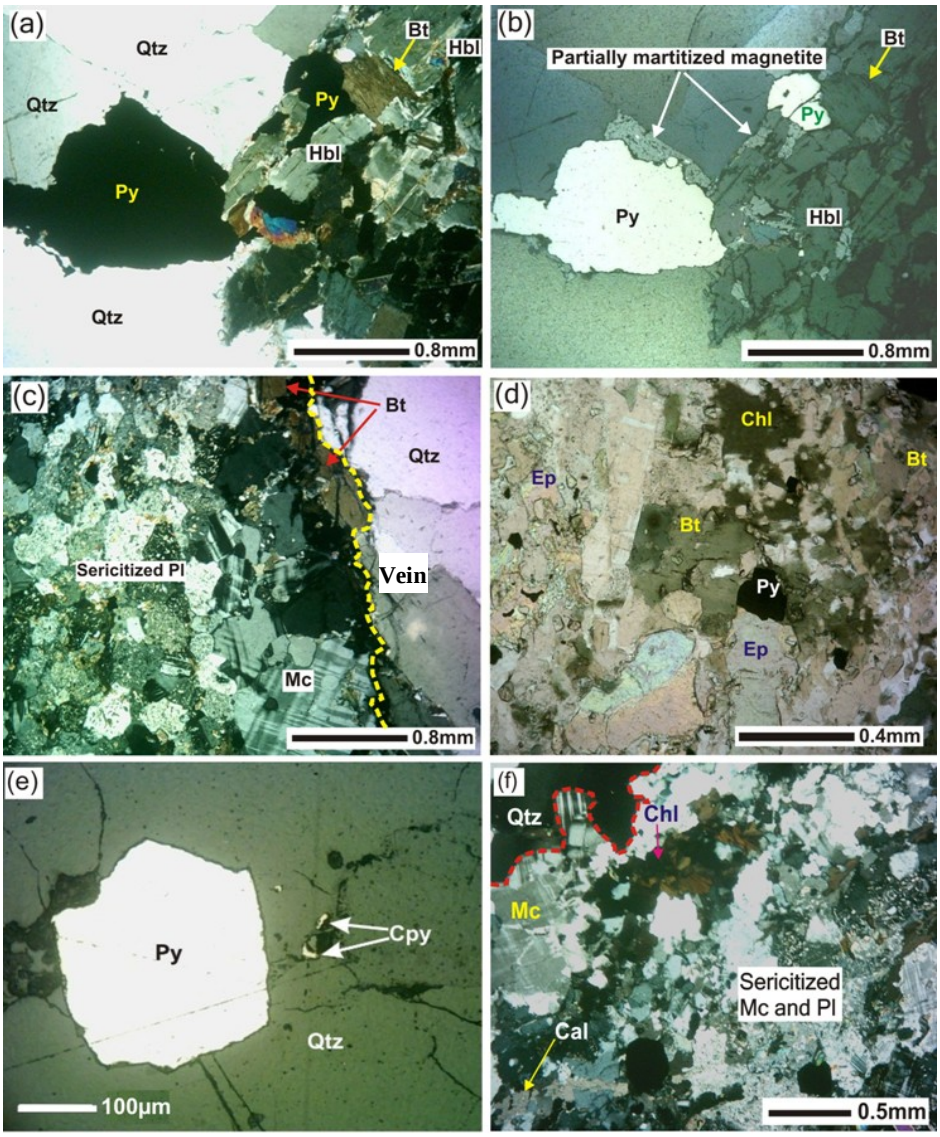

Fig. 7.5. Vein and alteration assemblages in the Type I (sample 13C) and II (sample 14D) veins. (a) Quartz (qtz), pyrite (Py) intergrown with hornblende (Hbl) crystals. Note, hornblende is partially replaced by biotite (Bt) at the top right. (13C, transmitted xpl). (b) Same field of view as (a). Martitized magnetite occurs both as envelope around pyrite and within hornblende. (13C, reflected ppl). (c) Proximal alteration phases in boudinaged vein. Yellow broken line denotes sharp vein margin (13C, transmitted xpl). (d) Distal alteration phases showing epidote (Ep), green brown-biotite and minor chlorite (Chl). (13C, transmitted ppl). (e) Subhedral pyrite and minute chalcopyrite (Cpy) crystals within vein quartz. (14D, reflected ppl). (f) Proximal alteration phases ((chlorite, microcline (Mc), calcite (Cal) and sericitized plagioclase (Pl)) to sigmoidal vein. Red broken line denotes irregular vein margin (14D, transmitted xpl).

chlorite and titanite are the common alteration minerals (Table 7.2a). The exact sequence of the alteration phases could not be ascertained as they largely overlap one another within this narrow zone. In both samples 14A and 13C, a proximal zone of K-feldspar + biotite + sericitized plagioclase + titanite ± epidote ± calcite alteration can be distinguished (Fig. 7.4d & 7.5c). From the vein margin, this zone extends ~8 to 15mm into the wall rock. In the proximal zone, microcline forms small (0.3 to 0.5mm) subhedral crystals (Fig. 7.5c,f). Brown biotite in the proximal zone occurs as small platy crystals (Fig.7.4d), whereas in the vein, biotite forms long, slender green-brown crystals

(~10-25mm across) and is intimately associated with both magnetite and pyrite (Fig. 7.5d). Epidote-biotite-chlorite are more prominent in the distal zones (Fig.7.4d & 7.5d,e). Moderately sericitized plagioclase ($\sim An_{10-18}$) crystals are rare in vein sample 14A, but are present in greater number in samples 13C and 14D (Fig. 7.4c & 7.5c,f). The biotite and titanite in the wallrock are locally aligned parallel to the vein walls. Calcite is associated with pyrite mostly within the vein. Epidote (0.2 to 0.8mm) and pyrite are closely associated with each other and are present both in the vein and the wallrock (Fig. 7.4e & 7.5d).

Type II vein sample 14D has a similar vein mineral assemblage to Type I, with the former having pyrite as the dominant ore mineral, with minor chalcopyrite (Fig. 7.5e). In addition to similar alteration minerals as in Type 1, the Type II veins have an irregular cluster of chlorite along the vein margins (Fig. 7.5f). The proximal K feldspar-chlorite-sericitized plagioclase-calcite zone (15 to 30mm) diffuses out into an epidote, biotite-titanite-alteration zone in the distal part (30-40 mm) (Fig. 7.5f).

Table 7.2. Alteration zones in (a) Type I and (b) Type II veins in the Brilliant open pit.

(a)

14A	10-25mm	15-35mm
Minerals	Proximal	Distal
K-feldspar	———	- - -
Sercitized plagioclase	———	
Biotite	———	———
Chlorite	- - - - - - -	- - - - - - -
Epidote	———	———
Titanite	———	———
Calcite	- - - - - - - - - - - - - - - - - -	

13C	5-15 mm	10-35mm
Minerals	Proximal	Distal
K-feldspar	———	- - -
Sercitized plagioclase	———	- - -
Biotite	- -	———
Chlorite	———	- - - - -
Epidote	- - - - - -	———
Titanite	- -	———
Calcite	- - - - - - - - - - - - - - - -	

(b)

14D	15-30mm	30-40mm
Minerals	Proximal	Distal
K-feldspar	———	- - - - -
Sercitized plagioclase	———	- - - -
Biotite	———	- - - - -
Chlorite	- - - - - - - - - - - -	
Epidote	———	———
Titanite	———	———
Calcite	- - - - - - - - - - - -	

7.2.3 Ore Petrography

A paragenetic sequence of the ores from Type I and II veins is given in Table 7.3. The ore minerals in Type I veins are mainly pyrite (~70%) along with variably martitized magnetite (~30%), with traces of pyrrhotite, bismuth telluride, gold telluride, gold-silver telluride, chalcopyrite, galena and rare native gold. Pyrite occurs in large subhedral to skeletal crystals and smaller euhedral granular forms. The larger pyrite crystals (3 to 10mm) are confined to the vein and occur as solitary subhedral crystals in textural equilibrium with the surrounding quartz and K-feldspar (Fig. 7.4a). Larger pyrite is also intergrown with hornblende in both samples 14A and 13C (Figs. 7.5a,b, 7.6a,b). The

smaller (~0.1 to 0.4mm) pyrite grains occur in hornblende, in both the vein and the wall rock (Fig. 7.5a, b, d).

Hematite intergrowths in primary magnetite are referred to as martitized magnetite (Můcke and Cabra, 2005), and are seen as rims around pyrite in vein samples 14A and 13C (Figs. 7.6a,b & 7.5b). These rims might have been formed during a late oxidation reaction after initial primary magnetite (formed after pyrite). However, a rare subhedral (0.3 mm), almost unaltered, magnetite crystal is enclosed within larger pyrite, suggesting that magnetite in this instance formed prior to the pyrite (Fig 7.6b).

In Type I veins (samples 14A and 13C), the trace assemblages of bismuth-telluride ± sulphide and galena specks (2 to 20 microns) are enclosed mostly in pyrite and within cleavage traces of hornblende (Fig. 7.6d,e). As mentioned earlier, only vein sample 14A has tiny globules (25 μm) within pyrite containing gold-silver, gold-telluride, gold-silver-telluride, chalcopyrite and bismuth-telluride (Fig. 7.6e,f). The planar boundaries between these minerals/mineral associations within a single globule imply they were in equilibrium during formation. The presence of gold-bearing globules in the vein pyrite implies they might be part of a multi-component phase precipitated from the parent gold-bearing sulphide solution. A small native gold speck (~3 microns) is also seen within a weakly martitized magnetite overgrowth on pyrite (Fig. 7.6c). As both the larger pyrite and enveloping martitized magnetite contain small gold specks of similar shapes and sizes, these two phases can be interpreted as forming synchronously.

Pyrite crystals in Type II veins (sample 14D) have similar modes of occurrence as in Type I veins. Minor galena, molydenite and bismuth telluride are enclosed in the larger vein pyrite (Fig. 7.6g,h,i). Unlike Type I veins, magnetite is absent and galena appears to have formed after pyrite (Fig. 7.6i).

Table 7.3 Combined paragenetic sequence of (a) Type I (Samples 14A and 13C) and (b) Type II (Sample 14D) veins in the Brilliant open pit.

(a)

Ore Minerals	Early	Late and/or secondary
Gold	----------	
Gold-Silver	----------	
Gold-Silver Telluride	----------	
Bismuth Telluride	----------	---------?
Galena	----------	
Chalcopyrite	----------	---------?
Pyrrhotite	————	
Pyrite	?————	————
Magnenite	?————	————?
Magnenite-hematite/ Martite	------	————

(b)

Ore Minerals	Early	Late and/or secondary
Bismuth Telluride	————	---?
Silver-Bismuth Telluride	?----	————
Molybdenite	————	---?
Galena	?----	————
Pyrite	————	---?
Chalcopyrite	————	----?

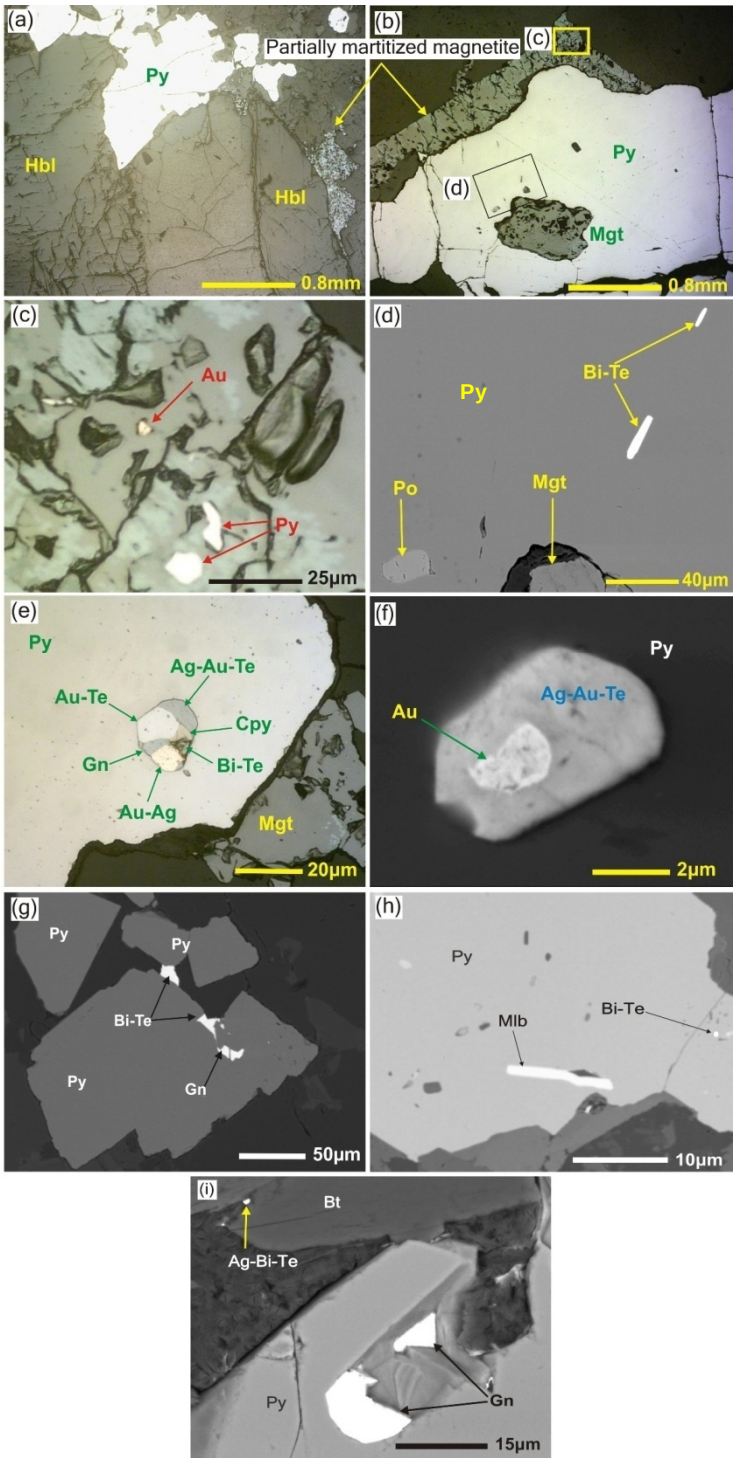

Fig. 7.6. Ore minerals in Type I (14A) and (b) Type II (14D) veins. (a) Pyrite (Py) and hornblende (Hbl) intergrown in the vein. Also shown is martitized magnetite associated with a wedge-shaped hornblende crystal (14A, reflected ppl); (b) Large pyrite encloses early primary magnetite (Mgt) in the centre and then is enveloped by weakly martitized magnetite (14A, reflected ppl); (c) Minute speck of native gold (Au) within the martitized magnetite rim (14A, reflected ppl); (d) Small pyrrhotite (Po) globule and bismuth-telluride lath included within pyrite (14A, reflected ppl); (e) Minute globular inclusion in pyrite containing co-existing gold-silver (Au-Ag), galena (Gn), gold-telluride (Au-Te), silver-telluride-gold (Ag-Te-Au), chalcopyrite (Cpy) and bismuth-telluride (Bi-Te) (14A, reflected ppl); (f) Gold inclusion within a minute Ag-Te-Au crystal enclosed in pyrite (14A, BSE image); (g) Bismuth-telluride and galena inclusions within pyrite. Bi-Te also occurs within wallrock between pyrite, indicating a late origin. (13C, BSE image), (h) Minute molybdenite (Mlb) lath and bismuth-telluride specks in pyrite (14D, BSE image). (i) Galena as fracture filling within pyrite14A. Top left shows tiny silver- bismuth-telluride (Ag-Bi-Te) inclusion within biotite (Bt) (14D, BSE image).

7.3 Hornblende-Plagioclase Thermobarometry of the Host Biotite Hornblende Monzogranite

Electron Probe Micro-Analyses (EPMA) were carried out on a number of mineral phases from vein sample 14A which has the best example of mineralization, containing large hornblende crystals and ore phases, a thin zone of hydrothermal alteration and unaltered wallrock. Minerals analyzed were i) K-feldspar and hornblende from the vein; ii) K-feldspar, plagioclase, titanite, epidote and biotite from the proximal alteration zone; and iii) plagioclase and hornblende from unaltered wallrock, i.e. host biotite hornblende monzogranite. Collective processing of data from all three zones by Thermocalc (Powell and Holland, 2001) failed to construct a P-T path (pesudosection) for the vein and host rock assemblages, which might result from incomplete or disequilibrium reactions among the phases. As a result, only data from plagioclase and hornblende, which were clearly in equilibrium in the unaltered rock and hornblende in the vein, were used to determine a thermobarometric interpretation of this section.

7.3.1 Hornblende-Plagioclase Thermometry

Geothermometry of calc-alkaline rocks is based on two commonly co-existing minerals-amphibole and plagioclase (Blundy and Holland 1990; Holland and Blundy 1994). Using two exchange equilibria, two hornblende-plagioclase geothermometers were proposed (Holland and Blundy 1994). They are:

(A) edenite + 4 quartz = tremolite + albite;

(B) edenite + albite = richterite + anorthite.

Thermometer (A) is applicable to quartz-bearing igneous rocks and thermometer (B) is suitable for both quartz-bearing and quartz-free igneous rocks (Holland and Blundy 1994; Stein and Dietl, 2001). Holland and Blundy (1994) report uncertainties of ±28 °C for thermometer (A) and ±32 °C for thermometer (B). In this study, thermometer (B) was used as this was preferred by Anderson and Smith (1995) based on comparison with other igneous thermometers. However, the temperatures calculated by thermometer (A) are also listed for comparison. Equilibration temperatures for hornblende-plagioclase assemblages were calculated based on the Hb-Plag programme of Holland (2002).

The hornblende and plagioclase crystals selected for analysis were free of any discernible zoning. Analytical points (usually 3 for each crystal) were placed over marginal parts of several pairs of plagioclase, all of which were in contact with quartz or K-feldspar, thereby fulfilling an important requirement for application of aluminum-in-hornblende barometry (Stein and Dietl, 2001; Fig.7.7a,b).

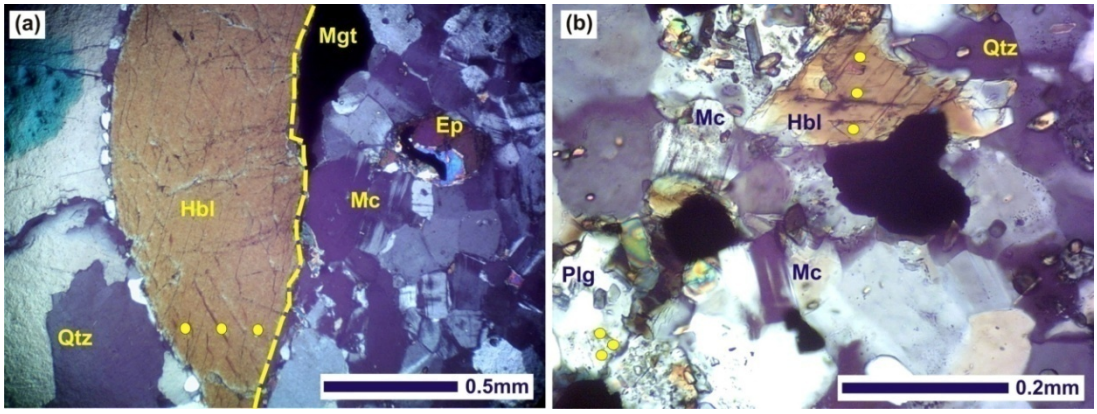

Fig.7.7. (a) Hornblende (Hbl) analyzed from marginal part of vein sample 14A. Left of the yellow broken line marks the margin of the vein. Minerals present in the proximal alteration zone are microcline (Mc), epidote (Ep) and magnetite (Mgt). (b) Hornblende analyzed from unaltered host rock (biotite hornblende monzogranite). Other minerals present are microcline and quartz. Analytical sites are marked with yellow dots.

Hornblende and plagioclase cations were calculated on the basis of 23 and 8 oxygens, respectively, and then recalculated to account for ferric iron using the A-X programme (Holland and Powell, 2003) at 5 kbar and 550°C. Representative plagioclase analyses are given in Table 7.4 and hornblende analyses in Table 7.5. Based on the nomenclature of Leake et al. (1997), the hornblende from the biotite hornblende monzogranite is classified as magnesiohornblende (Fig. 7.8). Although hornblende from the vein has a similar composition to the hornblende from the unaltered wallrock, it is richer in Si and Mg.

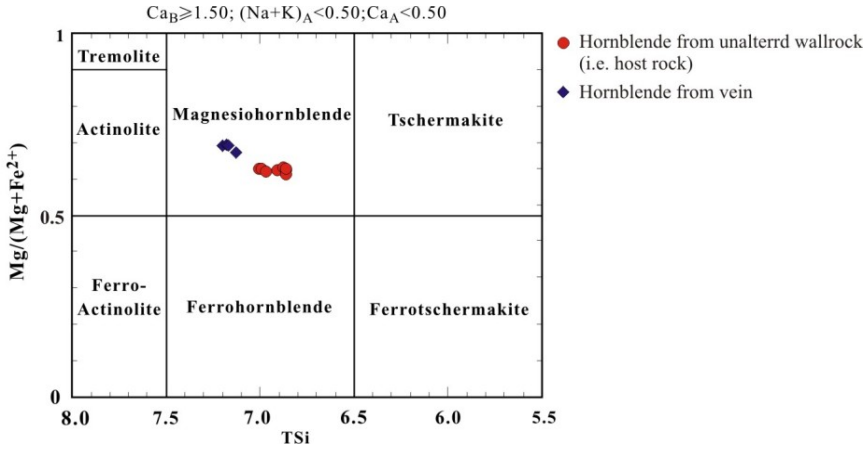

Fig. 7.8. Classification of hornblendes according to the nomenclature of Leake et al. (1997).

The sum of the major element analyses from plagioclase mostly ranged from 96.6 to 97.6% which is slightly lower than the recommended total (~98.5%) for use in the equation of Holland and Blundy (1994). This can be attributed to later alteration. Only analyses 2.1a and 25.1 yielded higher totals of 98.27 and 99.22%, respectively, and therefore are regarded as having retained near primary magmatic compositions. Anorthite (An%) content of plagioclase ranges from 2 to 17% (Table 7.4). Hornblende

data from the unaltered wallrock with xAb (Ab %) values from coexisting plagioclase crystals were processed by the Hb-Plag programme (Holland, 2002) using equations in Holland and Blundy (1994). It should be noted that for xAb >0.9 (i.e. Ab% >90) the Hb-Plag programme cannot calculate the ed-ri (edenite-richterite) equation (B) temperature. Therefore, a reliable calculation of the thermometry was performed using two analyses (Plag 2.1a and Plag 25.1) which have both higher totals and xAb<0.9 (0.86 and 0.83) (Table 7.4). The calculated temperatures (edenite-richterite thermometer) for biotite hornblende monzogranite are 645 (from Plag 2.1a) and 672°C (from Plag 25.1) (±32 °C) (Table 7.4).

7.3.2 Al-in-hornblende barometry

Hammarstrom and Zen (1986) and Hollister et al. (1987) demonstrated that in the presence of an appropriate buffer assemblage, the Al content of calcic amphibole can be used to determine pressure by applying the experimental data of Johnson and Rutherford

Table. 7.4. Representative plagioclase compositions from the biotite hornblende monzogranite.

Analysis name	Plag 1			Plag 2			Plag 25	
Spot no. wt %	Plag 1.1	Plag 1.2a	Plag 1..3	Plag 2.1a	Plag 2.2	Plag 2.3	Plag 25.1	Plag 25.2
SiO_2	62.51	65.44	65.68	64.12	66.77	66.14	64.63	64.9
TiO_2	0.01	0	0.02	0.01	0	0.01	0.04	0.04
Al_2O_3	21.94	19.85	19.950	21.35	19.22	19.2	21.93	20.26
Fe_2O_3	0.04	0.05	0.02	0.21	0.17	0.08	0.56	0.29
FeO	0	0	0	0	0	0	0	0
MnO	0.03	0.03	0.03	0.05	0.02	0.01	0.07	0.04
MgO	0	0.01	0.01	0.01	0.01	0.01	0.01	0
CaO	2.38	1.07	1.07	2.68	0.34	0.31	0.65	1.65
Na_2O	9.15	9.97	10.34	9.64	10.94	10.88	9.07	10.08
K_2O	0.73	0.17	0.09	0.13	0.08	0.11	2.22	0.07
Totals	96.79	96.59	97.21	98.2	97.55	96.75	99.18	97.33
Number of cations on the basis of 8 oxygens								
Si	2.843	2.957	2.952	2.871	2.987	2.983	2.876	2.922
Ti	0	0	0.001	0	0	0	0.002	0.001
Al	1.176	1.057	1.057	1.127	1.014	1.021	1.15	1.076
Fe^{3+}	0.001	0.002	0.001	0.007	0.006	0.003	0.019	0.01
Fe^{2+}	0	0	0	0	0	0	0	0
Mn	0.001	0.001	0.001	0.002	0.001	0	0.003	0.002
Mg	0	0.001	0.001	0.001	0	0.001	0.001	0
Ca	0.116	0.052	0.052	0.129	0.016	0.015	0.031	0.08
Na	0.807	0.873	0.901	0.837	0.949	0.951	0.783	0.88
K	0.042	0.01	0.005	0.007	0.005	0.006	0.126	0.004
Sum	0	4.953	4.971	4.981	4.978	4.98	4.991	4.975
An %	12.0	5.6	5.4	13.3	1.6	1.5	3.3	8.3
Ab%	83.6	93.4	94.1	86.0	97.8	97.8	83.3	91.3
Or %	4.4	1.1	0.5	0.7	0.5	0.6	13.4	0.4
Tehermobarometric results (T in ° C, P in kbar)								
T (ed-tr)	716.0	697.0	701.0	683.0	666.0	680.0	700.0	707.0
T (ed-ri)	662			645			672	

(1989) and Schmidt (1992). Their calibration is: P (kbar) = 4.76Al-3.01-[(T°C-675)/85] X [0.530Al + 0.005294(T°C-675)]. In the present study, only amphibole crystals in the unaltered wallrock, which are either in contact with quartz or K-feldspar, were studied to

determine emplacement pressure of the biotite hornblende monzogranite (Fig.7.7). The temperature-corrected pressures of the biotite hornblende monzogranite, calculated using Al (total) values from sample Amph Unalt (Unalt 2.1 and 3.1) from Table 7.5 using the Anderson and Smith (1995) equation, are 2.28 and 2.59 kbar, respectively.

Table 7.5. Representative hornblende compositions of (a) the mineralized vein sample 14A and (b) the biotite hornblende monzogranite.

Analyses name	(a)	Amph V 1			Amph V 26				(b)	Amph Unalt-1		Amph Unalt-2			Amph Unalt-3	
Spot no.	V 1.1	V 1.2	V 1.3	V 26.1	V 26.1	V 26.3	V 26.4	V 26.5	Unalt 1.1	Unalt 1.2	Unalt 1.3	Unalt 2.1	Unalt 2.2	Unalt 2.3	Unalt 3.1	Unalt 3.2
wt %																
SiO_2	48.4	48.27	48.19	48.62	48.74	48.81	48.42	48.62	45.97	45.62	46.00	46.65	46.26	46.42	45.71	45.51
TiO_2	0.38	0.41	0.42	0.4	0.34	0.39	0.38	0.38	0.47	0.54	0.53	0.48	0.45	0.46	0.55	0.59
Al_2O_3	4.98	5.05	5.12	5.04	4.62	4.85	4.98	4.94	6.77	6.78	6.63	6.1	6.02	6.18	6.58	6.74
Fe_2O_3	3.53	3.66	3.34	3.2	2.91	2.98	3.46	3.33	5.22	4.79	5.03	4.01	4.16	4.09	4.74	4.48
FeO	10.9	10.69	11.51	10.36	10.96	10.75	10.26	10.52	12.57	12.86	12.41	13.02	12.75	13.2	12.63	13.09
MnO	0.66	0.72	0.72	0.86	0.66	0.75	0.69	0.65	0.82	0.7	0.82	0.81	0.73	0.7	0.85	0.77
MgO	14.38	14.2	14.12	14.66	14.76	14.54	14.58	14.77	12.08	11.83	12.12	12.16	12.12	12.23	11.87	11.79
CaO	11.87	11.84	11.96	11.87	12.1	12.3	11.97	11.93	11.69	11.68	11.93	11.58	11.48	11.54	11.36	11.82
Na_2O	1.13	1.04	1.18	1.23	1.11	1.06	1.04	1.16	1.21	1.14	1.1	1.14	1.09	1.35	1.14	1.21
K_2O	0.59	0.65	0.65	0.61	0.54	0.57	0.65	0.63	0.89	0.88	0.8	0.79	0.76	0.8	0.87	0.88
Total	96.49	96.17	97.22	96.85	96.76	97.03	96.47	96.94	97.69	96.82	97.37	96.74	95.82	96.97	96.3	96.88
Number of cations on the basis of 23 oxygens																
Si	7.159	7.16	7.127	7.173	7.205	7.194	7.17	7.168	6.867	6.869	6.881	7.007	7.010	6.973	6.913	6.866
Ti	0.042	0.046	0.047	0.045	0.038	0.043	0.042	0.042	0.052	0.061	0.060	0.055	0.051	0.052	0.062	0.067
Al	0.869	0.884	0.893	0.876	0.805	0.842	0.87	0.859	1.192	1.204	1.170	1.081	1.075	1.094	1.173	1.199
Fe^{3+}	0.394	0.409	0.372	0.356	0.323	0.33	0.385	0.37	0.587	0.543	0.567	0.454	0.475	0.462	0.539	0.509
Fe^{2+}	1.349	1.326	1.424	1.278	1.355	1.325	1.271	1.297	1.570	1.620	1.552	1.635	1.616	1.658	1.598	1.652
Mn	0.083	0.091	0.09	0.108	0.082	0.094	0.086	0.081	0.104	0.089	0.104	0.105	0.093	0.089	0.109	0.099
Mg	3.17	3.139	3.112	3.223	3.253	3.195	3.217	3.246	2.689	2.654	2.702	2.723	2.738	2.737	2.675	2.650
Ca	1.881	1.881	1.895	1.877	1.917	1.943	1.9	1.884	1.872	1.884	1.912	1.864	1.864	1.857	1.840	1.911
Na	0.324	0.299	0.34	0.351	0.319	0.303	0.3	0.332	0.351	0.333	0.318	0.331	0.321	0.393	0.335	0.352
K	0.111	0.123	0.123	0.114	0.102	0.108	0.123	0.118	0.169	0.170	0.152	0.151	0.146	0.153	0.168	0.170
Total	15.382	15.358	15.423	15.401	15.399	15.377	15.364	15.397	15.453	15.427	15.418	15.406	15.389	15.468	15.412	15.475
T-sites																
Si	7.159	7.160	7.127	7.173	7.205	7.194	7.170	7.168	6.867	6.869	6.881	7.007	7.010	6.973	6.913	6.866
Al^{IV}	0.841	0.840	0.873	0.827	0.795	0.806	0.830	0.832	1.133	1.131	1.119	0.993	0.990	1.027	1.087	1.134
Sum -T sites	8.000	8.000	8.000	8.000	8.000	8.000	8.000	8.000	8.000	8.000	8.000	8.000	8.000	8.000	8.000	8.000
M1,2,3 sites																
Al^{VI}	0.028	0.044	0.020	0.049	0.010	0.036	0.040	0.027	0.059	0.073	0.051	0.088	0.085	0.067	0.086	0.065
Ti	0.042	0.046	0.047	0.045	0.038	0.043	0.042	0.042	0.052	0.061	0.060	0.055	0.051	0.052	0.062	0.067
Fe^{3+}	0.394	0.409	0.372	0.356	0.323	0.330	0.385	0.370	0.587	0.543	0.567	0.454	0.475	0.462	0.539	0.509
Mg	0.083	0.091	0.090	0.108	0.082	0.094	0.086	0.081	2.689	2.654	2.702	2.723	2.738	2.737	2.675	2.650
Fe^{2+}	3.124	3.087	3.067	3.181	3.210	3.179	3.188	3.201	1.570	1.620	1.552	1.635	1.616	1.658	1.598	1.652
Mn	1.329	1.323	1.404	1.261	1.337	1.318	1.259	1.279	0.043	0.049	0.068	0.045	0.035	0.024	0.040	0.057
Sum - M1,2,3	5.000	5.000	5.000	5.000	5.000	5.000	5.000	5.000	5.000	5.000	5.000	5.000	5.000	5.000	5.000	5.000
M-4 sites																
Mn	0.020	0.003	0.020	0.017	0.018	0.007	0.012	0.018	0.061	0.040	0.042	0.036	0.060	0.058	0.065	0.069
Fe	0.046	0.052	0.045	0.042	0.043	0.016	0.029	0.045	0.000	0.000	0.000	0.000	0.000	0.000	0.000	0.000
Ca	1.881	1.881	1.895	1.877	1.917	1.943	1.900	1.884	1.872	1.884	1.911	1.912	1.864	1.864	1.857	1.840
Na	0.053	0.064	0.040	0.064	0.022	0.034	0.059	0.053	0.067	0.076	0.047	0.052	0.076	0.078	0.078	0.091
Sum -M4	2.000	2.000	2.000	2.000	2.000	2.000	2.000	2.000	2.000	2.000	2.000	2.000	2.000	2.000	2.000	2.000
A-sites																
Na	0.271	0.235	0.300	0.287	0.297	0.269	0.241	0.279	0.284	0.257	0.266	0.255	0.243	0.315	0.244	0.305
K	0.111	0.123	0.123	0.114	0.102	0.108	0.123	0.118	0.169	0.170	0.152	0.151	0.146	0.153	0.168	0.170
Sum - A	0.382	0.358	0.423	0.401	0.399	0.377	0.364	0.397	0.453	0.427	0.418	0.406	0.389	0.468	0.412	0.475
Al (Total)	0.869	0.884	0.893	0.876	0.805	0.842	0.870	0.859	1.192	1.204	1.170	1.081	1.075	1.094	1.173	1.199
X Mg	0.701	0.703	0.686	0.716	0.706	0.707	0.717	0.715	0.631	0.621	0.635	0.625	0.629	0.623	0.626	0.616
Fe /(Fe+Mg)	0.355	0.356	0.366	0.336	0.340	0.341	0.340	0.339	0.445	0.449	0.440	0.434	0.433	0.436	0.444	0.449

7.3.3 Depth of Emplacement

Pressures were converted to emplacement depth on the assumption that the average crustal density of the Yilgarn Craton was ~3.00 g/cc during the Archean. As the calibration of Anderson and Smith (1995) in pressure determination has an uncertainty of ±0.6 kbar, the corresponding uncertainty in emplacement depth would be ±2 km. Using the two pressure estimates of 2.28 and 2.59 kbar, the biotite hornblende monzogranite yielded palaeodepths of crystallization of 7.75 km and 8.80 km (average 8.3±2 km).

The emplacement depth of the host rock was further examined by plots independent of temperature. Borodina et al. (1999) studied Fe^{3+}, Na, K and Al^{iv} contents of amphibole from granitoids of known depths of emplacement and proposed the Fe^{3+} vs. Na+K and Fe^{3+} vs. Al^{iv} plots broadly differentiate between different levels and igneous versus

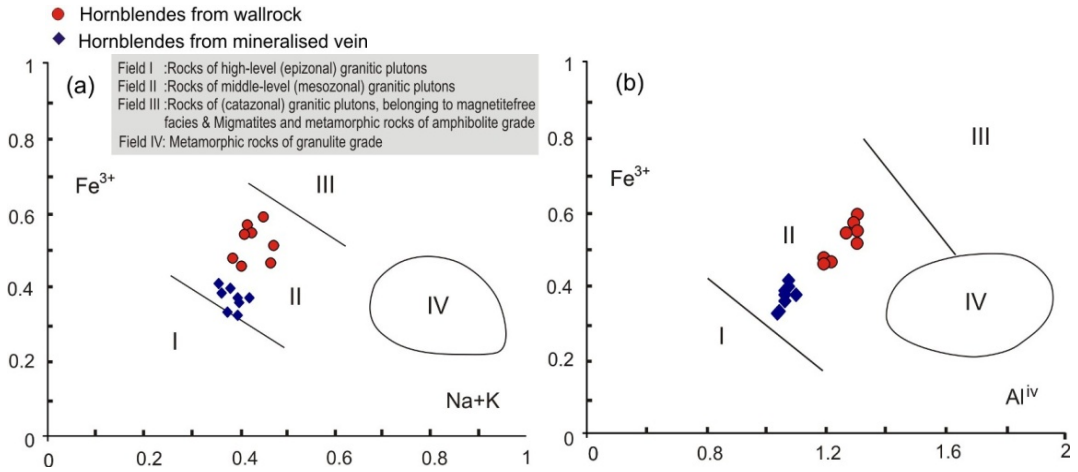

Fig. 7.9 (a) Fe^{3+} vs. Na+K and (b) Fe^{3+} vs. Al^{iv} plots of hornblendes from Brilliant open pit (from Borodina et al., 1999).

high-grade metamorphic rocks (Fig. 7.9a,b). Hornblendes from both vein and host rock plotted within the field of middle-level (mesozonal) granitic plutons (Fig. 7.9a, b), which agrees with the depth of emplacement of ~8.3±2 km determined by Al in hornblende barometry.

7.4 Fluid Inclusions from the Quartz-pyrite Veins

All the studied veins contain fluid inclusions. Mixed aqueous-carbonic and pure carbonic inclusions are abundant only in vein samples 14A and 14D; whereas sample 13C is enriched in aqueous fluid inclusions, with only a few aqueous-carbonic inclusions. Samples 14A and 14D have local zones of high concentration of different kind of inclusions. These fluid inclusions, along with thin cross-cutting trailbound, stretched and splayed fluid inclusions, were excluded from the study to avoid collecting ambiguous data. The classification schemes of Roedder (1984) and Shepherd et al. (1985) were followed to determine the origin of the inclusions in the present study. Primary inclusions are defined as isolated or randomly-occurring inclusions in the centre of quartz crystals or along growth zones in quartz. Pseudosecondary inclusions are formed along discontinuous healed fractures that terminate at the grain boundaries, and secondary inclusions are defined as the inclusions forming long trails, locally cross-cutting each other or crossing grain boundaries.

7.4.1 Relationship of fluid inclusions to gold mineralization in the quartz-pyrite veins

The relationship of the fluid inclusions to the gold mineralization can be established from petrographic observations in sample 14A, where minute gold inclusions occur within large pyrite crystals that are in textural equilibrium with vein quartz and microcline (Fig. 7.4a, 7.5a). This implies that primary fluid inclusions in vein sample 14A were formed from the same fluid precipitating pyrite and gold-silver, gold-telluride, gold-silver-telluride, chalcopyrite and bismuth-telluride globules (Fig. 7.6e.f). Based largely on similar vein morphology, alteration and ore mineralogy, the ore assemblages of vein sample 14D are considered to have been formed from the same fluid that precipitated the ores in vein sample 14A. However, despite having similar (Ag-Bi-Te-galena) ore assemblages, the absence of gold in samples 14D and 13C is attributed more to not finding gold in the sections than to the absence of gold. Based on the above observations, primary aqueous-carbonic and carbonic fluid inclusions in vein samples 14A and 14D are interpreted to be associated with gold mineralization.

7.4.2 Classification of Fluid Inclusions

Based on phase ratios identified from petrographic study at room temperature, three types of inclusions were identified. The ratios of coexisting phases were measured from careful petrographic observation and also following the chart given by Shephard (1985). The three classes are: Type i) CO_2(± H_2O ± NaCl), ii) H_2O-CO_2 (± NaCl), and iii) H_2O ± NaCl. About 1% of all inclusions contain yellowish rectangular, lath-shaped solid phase/s. The melting of these solids was not observed during the heating run up to ~450°C, hence these solids are considered to be small crystals of minerals which were floating in the ore fluid and were eventually trapped within the fluid inclusions.

Type i) CO_2(± H_2O ± NaCl): Fluid inclusions containing >95% CO_2 on visual estimation were classified as Type i inclusions and are almost pure CO_2. These constitute ~1% of all the inclusions in the three veins. They are dark, monophase, and have an occasional thin rim (~5 vol %) of water surrounding the liquid CO_2 (CO_{2L}). These inclusions are sub-spherical and range from 12 to 25μm in diameter and are primary in origin. In many type i inclusions, a CO_2-rich vapour bubble (CO_{2G}) developed during cooling (-4 to -35°C). Type i inclusions are found in association with Type ii inclusions (Fig. 7.10a).

Type ii) H_2O-CO_2(± NaCl): Type ii inclusions are the most abundant (60-75%) in vein samples 14A and 14D, but only minor (~2%) in sample 13C. They are dark, subspherical, elliptical, and also hexagonal to rhombic. The volume percentage of CO_{2L} and H_2O_L, ranges between 30-70% and 70-30%, respectively. They are ~12 to 30 μm in diameter, with some larger inclusions up to 55 μm. These inclusions are primary or pseudosecondary in origin and commonly found in clusters and with Type i clusters and (Fig. 7.10a,b). In a few instances, Type ii inclusions with variable CO_2 ratios occur in

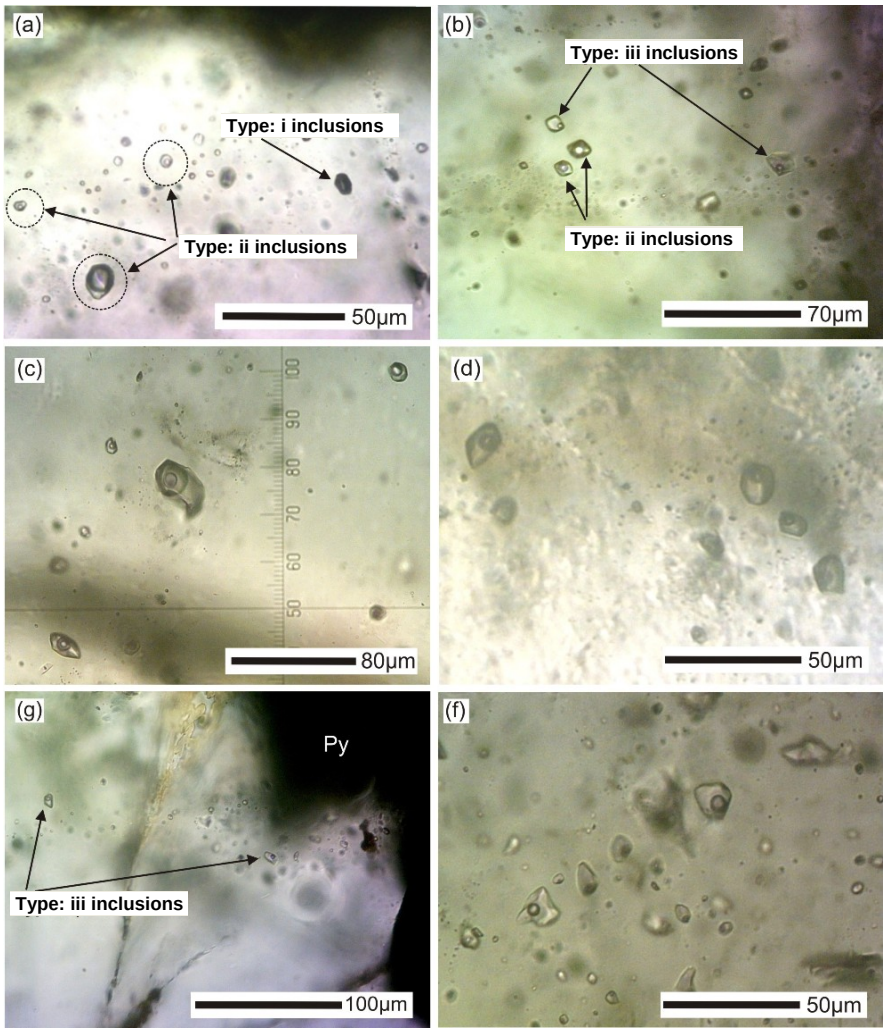

Fig. 7.10. Selected photomicrographs of fluid inclusions from the quartz-pyrite veins at the Brilliant deposit. All photographs were taken under transmitted plane polarised light (a) Cluster of mainly Type ii fluid inclusions associated with rare Type i fluid inclusion (14A). (b) Association of Type ii) and rare Type iii fluid inclusions (14D). (c) Type ii fluid inclusions with variable CO_2 phase ratios (14A). (d) Primary Type iii fluid inclusions (14A). (e) Pseudosecondary fluid inclusions along healed fracture (14D). (f) Trailbound secondary Type iii fluid inclusions (14A).

association of type iii fluid inclusions in a single trail/cluster (Fig. 7.10b,c) that suggests a synchronous formation. Whether it represents a phenomenon of immiscibility or whether they were formed as a result of selective leakage due to later deformation will be examined in the results section.

Type iii) H_2O ± NaCl inclusions: These are light coloured, two phase inclusions that have 5-10% (H_2O_G) vapour surrounded by 90-95% water (H_2O_L), with only a few monophase (H_2O_L) inclusions. These inclusions are elongate, flattened to angular in shape and range from 10 to 25 μm in diameter. They are mostly secondary in origin, with only a few primary inclusions located within the center of quartz crystals (Fig. 7.10d). A few pseudosecondary inclusions are also seen (Fig. 7.10e). Thin trailbound secondary inclusions are common in all veins (Fig. 7.10f).

7.4.3 Microthermometric Observations and Results

Type i) CO_2(± H_2O ± NaCl): Only five of these inclusions were found to contain pure CO_2 which is marked by T_mCO_2 at -56.6°C. All Type i inclusions display homogenisation to a liquid (T_hCO_2L) phase from 8.6 to 29.3°C. The bulk molar volume (V_mBulk) and bulk density (ρBulk) of these five pure CO_2 inclusions range from 50.47 to 68.56 cc/mol and 0.64 to 0.87 gm/cc, respectively. In vein sample 14A, three inclusions with very minor (≤5%) water contents have final ice melting ($T_m$ice) temperatures from -4.5 to -3.6°C, corresponding to salinities from 5.94 to 7.26 % mass NaCl equivalent (eq). The V_mBulk and ρBulk for these three inclusions are within the range of pure CO_2 inclusions (Table 7.6).

Table: 7.6 Summary of the results of the microthermometric calculations from the fluid inclusions studied from the Brilliant deposit.

Vein sample	14A,14D,13C	14A,14D	14A,14D,13C
Inclusion type	**Type ii CO_2 ± (H_2O-± NaCl)**	**Type ii H_2O-CO_2 (± NaCl)**	Type-iii) H_2O-NaCl
Primary Fluid Inclusions			
TmCO2(L) °C	-56.6	-56.6 ± 0.1	
ThCO2(L)°C	24.01 ± 7.2	25.6 ± 3	
TmIce(L) °C	-3.9 ± 0.5	-3.8 ± 0.7	-4.2 ± 0.7
TmClath(L) °C		6.3 ± 1.1	7.4 ± 0.2
Td °C		300.6 ± 49.9	
ThTot(L) °C		310.7 ±3.7	282.8 ± 43.4
VmBulk cc/mol	57.2 ± 7.4	25.7 ± 3.3	22.85 ± 1.8
Density, g/cc	0.7 ± 0	0.9 ± 0	0.8 ± 0.1
xCO2 %	0.7 ± 0.1	0.16 ± 0.1	
xH2O %	0.3 ± 0.1	0.3 ± 0.1	
xNaCl %	0.01 ± 0	0.8± 0.1	
Salinity wt.% NaCl	6.5 ± 0.7	6.7 ± 1.9	6.6± 0.9
Secondary Fluid Inclusions	Not present	Not present	
TmCO2(L) °C			
ThCO2(L)°C			
TmIce(L) °C			-3.7± 1.4
TmClath(L) °C			9
Td °C			
ThTot(L) °C			220.3 ± 50.4
VmBulk cc/mol			21.46 ± 1.7
Density, g/cc			0.9 ± 0.1
xCO2 %			
xH2O %			
xNaCl %			
Salinity wt.% NaCl			6.1 ± 2

Type ii) H_2O-CO_2 (± NaCl): Microthermometric measurements were conducted on a total of fifty three Type ii inclusions. Like Type i, these inclusions have $TmCO_2$ between –56.5° and –56.8°C, with an average of –56.6°C. The $ThCO_2L$ ranges from 17.4 to 28.3°C. The $T_m$ice was observed only in four inclusions between –4.5 to -2.9°C. Clathrate melting ($T_m$clath) was observed between 5.3° to 8.3°C in several inclusions. Both the $T_m$ice and $T_m$clath were used to calculate the salinity, which ranges from 3.33 to 9.59 mass % NaCl eq. The V_mBulk and ϱBulk for these inclusions vary from 22.20 to 32.02 cc/mol and 0.83 to 0.95gm/cc, respectively. T_hTot was determined only for two inclusions at 308.1 and 313.3°C as the rest of the inclusions were decrepitated during heating before final homogenisation. Decrepitation temperatures (T_d) display a wide range between 235 and 375.8°C (Fig. 7.11a).

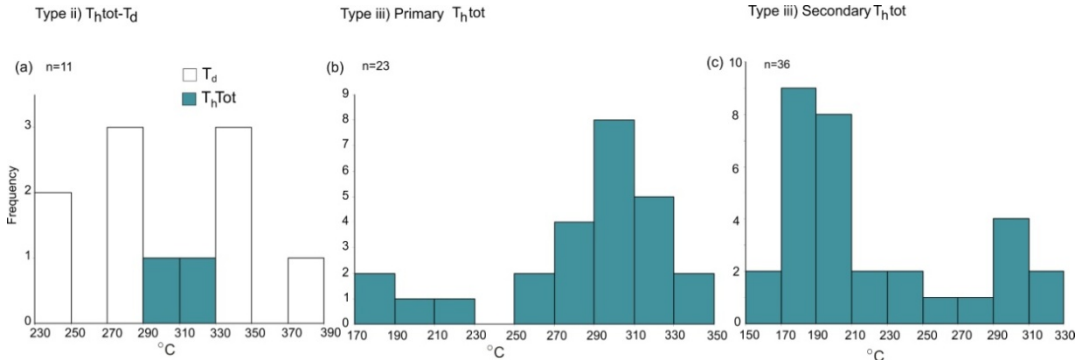

Fig. 7.11. Histograms of microthermometric data for (a) T_d and $T_h$tot of primary Type ii fluid inclusions, (b) $T_h$tot of primary Type iii fluid inclusions and (c) $T_h$tot of secondary Type iii fluid inclusions

Type iii) H_2O-NaCl: Both primary and secondary inclusions have similar $T_m$ice temperatures, ranging from –5.5 to -3.2°C, and from -7.5 to –0.4°C, respectively. Average salinity and V_mBulk are slightly higher for the primary inclusions (22.85 cc/mol and 6.62 mass % NaCl eq) compared to the secondary inclusions (21.46 cc/mol and 6.07 mass % NaCl eq). The ρBulk however, is a little lower for the primary inclusions (0.83 gm/cc) than for the secondary inclusions (0.88 gm/cc). The $T_h$tot temperatures for the primary inclusions display a wide range from 170.5 to 339 °C, with a majority clustering between 270 and 330°C (Fig. 7.11b). The secondary inclusions have a slightly lower $T_h$tot temperature ranging from 159 to 312°C (Fig. 7.11c). A few $T_m$clath temperatures were obtained, varying from 7.2 to 9°C.

7.4.4 Interpretation of Fluid Inclusion Data and P–T Constraints on the Ore Fluid

The primary origin and the abundance of Type ii mixed H_2O-CO_2(± NaCl) fluid inclusions within the Au-Ag bearing veins, together with the spatial association of undeformed quartz and gold–sulphide-tellurides, indicates that these fluid inclusions

represent the ore fluid. The isolated pure CO_2 Type i inclusions most probably represent the earliest phase of an originally homogeneous CO_2-H_2O–NaCl fluid system. The later fractionated end-member of a CO_2-H_2O– NaCl fluid is conceivably represented by aqueous type iii fluid inclusions. A wide range of filling (CO_2L 25 to 65%) in the Type ii inclusions also points to a full spectrum of fluid evolution.

In a few instances, Type ii inclusions with variable CO2 ratios occur in close association with aqueous Type iii inclusions, which visually indicates some degree of fluid unmixing (Fig. 7.10b, c). Ramboz et al. (1982) suggested that homogenisation into opposing phases (one/more inclusions from liquid into vapour and vice versa mode at same temperature) of the inclusions from such associations is one of the diagnostic criteria of fluid immiscibility. Due to decrepitation of almost all studied fluid inclusions before total homogenisation (except for two), this could not be verified, which does not necessarily rule out the presence of fluid immiscibility. In addition, the variable CO2 ratios in Type ii inclusions may be interpreted to have formed from heterogeneous trapping of an initially homogeneous CO2-H2O–NaCl fluid, which is also a very good indication of fluid unmixing (Ramboz et el. 1982, p 44). This characteristic, along with similar salinities of the aqueous–carbonic and aqueous inclusions, as well as comparable CO2 densities in the carbonic (Type i) and aqueous-carbonic inclusions (Type ii), suggests some degree of fluid unmixing of an initially homogeneous CO2-H2O–NaCl fluid that existed during evolution of the ore fluid (e.g. Ramboz et al., 1982; Robert and Kelly 1987; Huizenga and Touret, 1999).

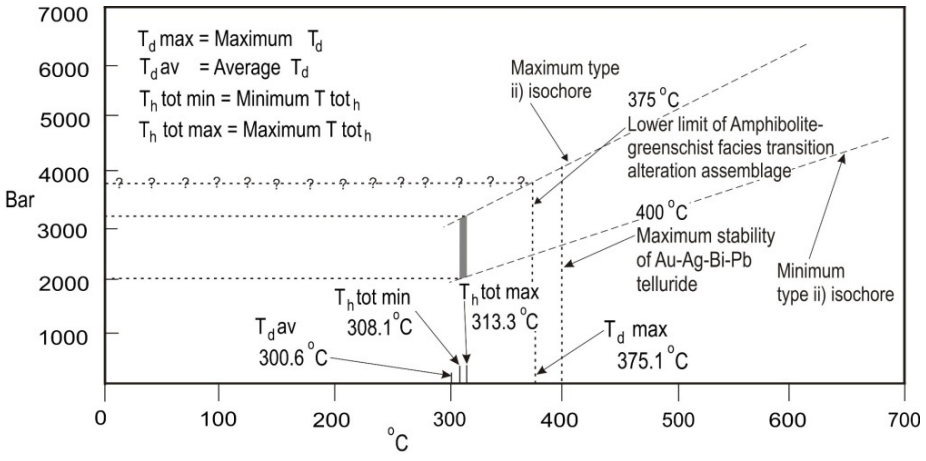

Fig. 7.12.Pressure-temperature diagram showing isochores calculated from Type ii fluid inclusions. Also shown are the lower and upper temperature limit of the hydrothermal alteration assemblage formed during lower amphibolite to upper greenschist facies conditions (McCuaig and Kerrich, 1998). The lower and upper limit of fluid pressure are indicated by the lower and upper horizontal broken lines which are constructed by the intersection of the lowest and highest $T_h$tot with the minimum and maximum isochores. The highest possible fluid pressure is indicated by the horizontal broken line with question marks, which is constrained by the intersection of the highest T_d temperature and maximum isochore. The range of possible P-T trapping conditions is indicated by the narrow shaded field. The upper temperature stability limit for Au-Ag-Bi-Pb telluride mineral assemblages at ~ 400°C (Cabri, 1965) correlates moderately well with the Td max of the present study.

The pressure conditions during gold deposition were estimated by calculating the isochores for Type ii aqueous-carbonic fluid inclusions using the FLINCOR program (Brown, 1989) and the Brown and Lamb (1986) equation of state for the CO_2-H_2O-NaCl system (Fig. 7.12). Paucity of $T_h$tot however, precluded arriving at an accurate range of temperature during deposition of gold. The intersection of the lowest and highest Thtot, (308.1 and 313.3°C) with the minimum and maximum isochores defines a minimum and maximum fluid pressure of 2.0 and 3.2 kbar respectively. In the absence of a sufficient number of $T_h$tot, this pressure range can be regarded as a segment of possibly a larger pressure range of the ore fluid. In Fig. 7.12, a reasonable constraint on the upper limit of fluid pressure is also shown from the intersection of the highest T_d of 375.1°C and the maximum isochore at 3.8 kbar. However, because of the lack of range of $T_h$tot/T_d from Type ii inclusions, this upper limit of fluid pressure (at 3.8 kbar) should be viewed with caution.

Fluid pressures between 2.0 and 3.2 kbars correspond to depths of 6.6 to 9.9 km, assuming lithostatic fluid pressure conditions and a pressure gradient of 3.3 km/1 kbar (Hagemann and Brown, 1996) during fluid entrapment. These pressures and depths are in agreement with the pressure and depth (2-4 kbars and 7-14 km) suggested from the hydrothermal alteration assemblage of Ca-amphibole-biotite-Ca-plagioclase-calcite-K-feldspar-titanite in granitoid-hosted deposits formed at greenschist-amphibolite facies transition by McCuaig and Kerrich (1998). However, the temperature range for this alteration assemblage lies between 375°C and 550°C (McCuaig and Kerrich 1998), which is considerably higher than in the present study, which might be attributed to the unavailability of a wider range of $T_h$tot. The hydrothermal alteration assemblage (amphibole-biotite-plagioclase-K-feldspar-calcite-titanite-epidote-chlorite) in the Brilliant deposits includes minerals species from both upper greenschist facies and greenschist-amphibolite transition facies. This suggests that the Brilliant gold deposit may have formed under upper greenschist facies conditions during retrogression from lower amphibolite facies.

7.5 Comparison with Similar Deposits in the Yilgarn Craton

7.5.1 Comparison with Other Au-Ag-Te-Bi Deposits in the Yilgarn Craton

Several gold deposits spatially associated with granitoid in the Yilgarn Craton have many characteristics in common with the Brilliant deposit (Table 7.11). However, none of the deposits fully matches the Brilliant deposit. Lady Bountiful (Cassidy and Bennett, 1993; Cassidy et al., 1998), Termoola (Nelson, 1996; Duuring et al., 2001, 2004; Fletcher et al., 2001), Jupitar (Duuring et al., 2000; Salier et al., 2005) and Granny Smith (Stage II) deposits (Ojala, 1995; Ojala et al., 1995, 1997; Salier et al., 2005; Cassidy et al., 1998), despite having similar ore minerals, metal associations and several fluid characteristics, have muscovite as a vein phase and are hosted in a brittle structural regime, all of which contrast with the Brilliant deposit. Based on the results of the present study, controls such as composition of host granitoid, crustal depth, type of mineralized vein, vein mineralogy, ore minerals, metal association and ore fluid characteristics of the Great Eastern (stage II) deposit are more closely comparable with the Brilliant deposit than the other deposits (Table 7.7). This implies that the tectono-magmatic setting responsible for the large-scale gold mineralization in the Eastern Goldfields Superterrane was also in operation in some part of the Murchison Domain. Mineralization at Westonia also shows many similar characteristics, however it is hosted by higher metamorphic grade rocks and, therefore, may be viewed as a higher temperature analogue of the Brilliant deposit. However, due to absence of appropriate exposures and samples that precluded inferring detailed relationships of the mineralized veins with the other phases of the LLG, this should be viewed with caution.

Table 7.7. Comparison of the main features of the Archean granitoid-hosted gold deposits in the Yilgarn Craton with the Brilliant gold deposit at Yalgoo in the Murchison Domain (the characteristics of the granitoid-hosted deposits are taken from Duuring, 2007).

	Lady Bountiful	Tarmoola	Jupiter	Granny Smith (Stage II)	Westonia	Great Eastern	Brilliant
Resource (t Au)	11.36	~116	6.08	49.77	27.67	14.74	0.27
Host granitoid composition	Biotite granodiorite	Trondhjemite	Quartz alkali-feldspar syenite	Quartz diorite, granodiorite	Biotite hornblende tonalite gneiss	Bt hb tonalite,granodiorite	Biotite hornblende monzogranite
Fe2O3/FeO			Oxidized (1–2)				3.4
Rb/Sr	~0.08	~0.11	0.18 to 0.28	0.09 to 0.13			0.3
Absolute age of (Ma) of granitoid		2700±11		2665±4	>2640	2666±7	
Crustal depth (km)	Shallow to intermediate (<5–7)	Shallow to intermediate (2-10)	Shallow to intermediate (<5–7)	Shallow to intermediate (<5–8)	Deep (10–15)	Intermediate (7–10)	Intermediate (8)
Metamorphic grade of supracrustal sequence	Lower- mid-greenschist	Greenschist	Greenschist	Upper greenschist	Upper-amphibolite	Upper-greenschist to loweramphibolite	Upper-greenschist Lower-amphibolite
Relative timing of mineralization	Post-peak metamorphism Post-granitoid intrusion	Post-peak metamorphism Post-granitoid intrusion	Post-peak metamorphism Post-granitoid intrusion	Post-contact metamorphism Post-granitoid intrusion	Syn-to post-peak metamorphism,postgranitoid intrusion	Post-peak metamorphism? Postgranitoid intrusion	Syn-to post-peak metamorphism postgranitoid intrusion
Absolute age (Ma) Timing of mineralisation		<2667±8	2657±21	2635; 2653±6	<2640 felsic dikes	2646±25; minor 2592±9	
Structural regime	Brittle to brittle-ductile	Brittle	Brittle	Brittle	Ductile	Brittle-ductile intersection	Ductile-Brittle
Ore shoot control	Intersection of fault zone sets	Along granitoid contact in komatiite and NW-striking veins in granitoid	Syenite and NW-and NE-striking,shallow -dipping shear zones	Along granitoid contact and fault zones within sedimentary rocks	Intersection of shear zone with flexure at footwall contact	of shear zone sets	Intersection of shear zone quartz vein
Mineralized vein type	Brittle en echelon quartz vein sets	Veins oriented subparallel to granitoid margins and foliation in komatiite	Shear zone-hosted, discrete, and ladder veins	Conjugate fractures in granitoid. Veins oriented subparallel to bedding in sedimentary rocks	Foliation parallel veins and quartz reefs	Brittle-ductile shear zone hosted quartz veins;discrete veins±breccia	Flat vein and boudinadged sigmoidal vein
Vein mineralogy	Qz–cc–mu±chl±ru	Qz–ank–mu±ab±chl±cc±fu±ep	Qz–cc–ank–ab±ser	Qz–ank±mu±ru	Stage I: qz–kfbt–cpx±mu±hb±pc±cc Stage II: qz–cpx±hb±bt±kf±pc±tn±cc	Stage I: Qz–bt–cc±kf±tr±mu, Stage II: qz–cc–chl±mu±ab±hm	Qz–kf-bt–pc-bt-tn-ep±cc
Ore minerals	Stage I: py–po–cpy Stage II: py–tell–ga–c-py–sph	Stage I: py Stage II: cpy–sph–ga–tell	Py–cpy–sph–ga–mo tell-(Pb–Au–Bi)–sch	Py–po–cpy–ga-sph–apy–mo–tell	Po–py–ga–cpy–sch–wfr mo±apy±tell	Stage I: py±po±cpy±ga±sch,StageII: py±cpy ga±tell	Py–cpy–ga– tell (Bi±Ag)-mo-(Au±Ag±Bi)-mt
Metal association	Au–Ag–As–Te–Bi-W–Pb	(Pb–Bi–Au)–sch Au–Ag–Cu–Pb–W–Bi–As–Mo–Zn–Te–Sb	Au–Ag–Bi–Te–Cu–Pb–Zn–Mo–W	Au–Ag–As–Sb–Bi–Te–W	Au–Ag–W–Cu–Pb–Mo–Bi–Te	Au–Ag–As–W–Pb–Mo	Au–Ag–Bi–Te–Cu–Pb–Mo
Wallrock alteration	Qz–ab–mu–cc±chl± py±ru±hm	Qz–ank–cc–mu± ab±chl	Qz–cc–ank–ab±ser	Qz–mu–ank–ab–py± ru±chl±kf	Stage I: qz–pc–kf–bt–cpx–po–tn–hb–ilm Stage II: qz-pc-kf-bt-hb-po± mu±cd±sil±ilm	Stage I: qz–bt–pc–cc–py-Kf–mu±chl±chl±tn±±mt±ilm Stage II: qz-chl-ab-cc-mu-py±ep±hm±ru	Kf–hb-bt-pc±chl-ep-ep-tn±cc
Ore fluid characteristics							
Temperature (°C)	Stage I: 300±50 Stage II: 250±50	Stage I: 225 to 400 Stage II: 300±50	200-400	325±50	Stage I: 600±50, Stage II: 600±25	Stage I: 425±50 Stage II: 280 to 415	> 310
Pressure (kbar)	Stage I: ~2 Stage II: 0.5 to 2.0	Stage I:<1–3 Stage II: 0.5 to 3.0	<1–2	0.7 to 2.6	3 to 4	Stage I: 2.0±0.7 Stage II: 0.5 to 2.0	2 to 4
Composition	CO_2–H_2O–NaCl±CH_4	CO_2–H_2O–NaCl±CH_4	CO_2–H_2O–NaCl±CH_4	CO_2–H_2O–NaCl±CH_4	CO_2–H_2O–NaCl±CH_4	CO2–H2O–NaCl	CO_2±H_2O(±NaCl)
XCO_2	0.06 to 0.19	0.01 to 0.44	Moderate	0.21 to 0.59	Variable	Moderate	0.08 to 0.32
Salinity (eq. wt% NaCl)	7 to 10	<5.5			5 to 10	~5	5 to 11
Gold deposition mechanism	Stage II: phase separation	Fluid:wallrock interaction; temperature and pressure decrease	Fluid:wallrock interaction;	Sulfidation±phase separation	Fluid:wallrock interaction	Fluid-wallrock interaction	Sulfidation±phase separation
References	Cassidy and Bennett (1993 Cassidy et al. (1998)	Nelson (1996); Duuring et a (2001,2004); Fletcher et al. (2001)	Duuring et al. (2000); Salier et al. (2005)	Ojala (1995); Ojala et al. (1993 1997); Cassidy et al. (1998); Salier et al. (2005)	Cassidy (1992); Kent et al. (1996);Cassidy et al. (1998); Hagemann and Cassidy (1999)	Cassidy (1992); Cassidy et al. (1998)	Present study Holden (2004)

Abbreviations: ab, albite; am, amphibole; ahd, anhydrite; ank, ankerite; ara, aramayoite; ap, apatite; apy, arsenopyrite; bi, native bismuth; bis, bismuthinite; bt, biotite; cb, carbonate; cc, calcite; cd, cordierite; chl, chlorite; cpy, chalcopyrite;cpx, diopside; cr, chromiumrich; dol, dolomite; ep, epidote; fu, fuchsite; ga, galena; gt, garnet; hb, hornblende; hm, hematite; ilm, ilmenite; inter, intermediate; Kf, alkali-feldspar; mo, molybdenite; mon, monazite; mt, magnetite; mu, muscovite;pc, plagioclase; po, pyrrhotite; py, pyrite; qz, quartz; ru, rutile; sch, scheelite; ser, sericite; sil, sillimanite; sph, sphalerite; tell, tellurides;tn, titanite; to, tourmaline; tr, tremolite; wfr, wolframite; wm, white mica; xe, xenotime; zr, zircon.

Continued on next page

	Lady Bountiful	Tarmoola	Jupiter	Granny Smith (Stage II)	Westonia	Great Eastern	Brilliant
Ore fluid characteristics							
Temperature (°C)	Stage I: 300±50 Stage II: 250±50	Stage I: 225 to 400 Stage II: 300±50	200-400	325±50	Stage I: 600±50, Stage II: 600±25	Stage I: 425±50 Stage II: 280 to 415	> 310
Pressure (kbar)	Stage I: ~2 Stage II: 0.5 to 2.0	Stage I:<1–3 Stage II: 0.5 to 3.0	<1–2	0.7 to 2.6	3 to 4	Stage I: 2.0±0.7 Stage II: 0.5 to 2.0	2 to 4
Composition	CO_2–H_2O–NaCl±CH_4	CO_2–H_2O–NaCl±CH_4	CO_2–H_2O–NaCl±CH_4	CO_2–H_2O–NaCl±CH_4	CO_2–H_2O–NaCl±CH_4	CO2–H2O–NaCl	CO_2±H_2O(±NaCl)
XCO_2	0.06 to 0.19	0.01 to 0.44	Moderate	0.21 to 0.59	Variable	Moderate	0.08 to 0.32
Salinity (eq. wt% NaCl)	7 to 10	<5.5			5 to 10	~5	5 to 11
Gold deposition mechanism	Stage II: phase separation	Fluid:wallrock interaction; temperature and pressure decrease	Fluid:wallrock interaction;	Sulfidation±phase separation	Fluid:wallrock interaction	Fluid-wallrock interaction	Sulfidation±phase separation
References	Cassidy and Bennett (1993); Cassidy et al. (1998)	Nelson (1996); Duuring et al. (2001,2004); Fletcher et al. (2001)	Duuring et al. (2000); Salier et al. (2005)	Ojala (1995); Ojala et al. (1993, 1997); Cassidy et al. (1998); Salier et al. (2005)	Cassidy (1992); Kent et al. (1996);Cassidy et al. (1998); Hagemann and Cassidy (1999)	Cassidy (1992); Cassidy et al. (1998); Fletcher et al. (1998).	Present study Holden (2004)

Abbreviations: ab, albite; am, amphibole; ahd, anhydrite; ank, ankerite; ara, aramayoite; ap, apatite; apy, arsenopyrite; bi, native bismuth; bis, bismuthinite; bt, biotite; cb, carbonate; cc, calcite; cd, cordierite; chl, chlorite; cpy, chalcopyrite;cpx, diopside; cr, chromiumrich; dol, dolomite; ep, epidote; fu, fuchsite; ga, galena; gt, garnet; hb, hornblende; hm, hematite; ilm, ilmenite; inter, intermediate; kf, alkali-feldspar; mo, molybdenite; mon, monazite; mt, magnetite; mu, muscovite;pc, plagioclase; po, pyrrhotite; py, pyrite; qz, quartz; ru, rutile; sch, scheelite; ser, sericite; sil, sillimanite; sph, sphalerite; tell, tellurides;tn, titanite; to, tourmaline; tr, tremolite; wfr, wolframite; wm, white mica; xe, xenotime; zr, zircon.

7.5.2 Classification of the Brilliant Deposit: An Archean Orogenic Granitoid-Hosted Gold Deposit or Archean Intrusion-Related Gold Deposit?

Orogenic gold deposits form along convergent margins during terrane accretion, translation, or collision, which were related to plate subduction and/or lithospheric delamination. They formed typically in the latter part of the deformational-metamorphic-magmatic history of the evolving orogen (Groves et al., 1998, 2000). Orogenic gold deposits hosted in or spatially associated with granitoids in the Yilgarn Craton, as well as other Archean terranes (e.g., Superior, Slave, Zimbabwe), represent a subgroup of the orogenic gold deposit class (Groves, 1993; Cassidy et al., 1998; Groves et al., 1998; Goldfarb et al., 2005). On the other hand, Archean intrusion-related gold deposits are commonly small (<10 t Au), and are spatially and temporally associated with felsic intrusions, hosted mostly in sheeted and lesser in stockwork veins and are characterized by polymetallic metal associations (Au, Bi, W, As, Mo, Te and/or Sb) (see Lang et al., 2000, Lang and Baker, 2001 for details).

The Brilliant deposit exhibits several characteristics in common with both Archean orogenic granitoid-hosted gold deposits and Archean intrusion-related gold deposits (IRGD). These characteristics include : i) the deposits are all granitoid related, ii) are quartz vein hosted and/or show dissemination-style mineralization, iii) show Au + Ag ± As ± Bi ± Sb ± Te ± W metal association, iv) are widely reported from regional greenschist to subgreenschist metamorphic terranes and v) the host granitoid for both types of deposits can include epizonal and mesozonal granitoid (Fig.7.10). Apart from the metamorphic grade, the Brilliant deposit demonstrates all of the above features. These common characteristics, along with the limitation of the present study, has made it difficult to classify the Brilliant deposit. However, the following lines of evidence suggest a closer link to Archean orogenic granitoid-hosted deposits rather than Archean IRGD. The detailed characteristics which the Brilliant deposit shares with orogenic granitoid-hosted gold are as follows:

1) The geochemistry of the host biotite hornblende monzogranite indicates a volcanic arc to syn-collisional setting (Fig. 5.36a,b,c) which is in contrast to widely known continental tectonic settings for the intrusion-related deposits.

2) The large amount of pyrite and magnetite, with small amounts of pyrrhotite, galena, chalcopyrite and telluride,s constitute the ore assemblage in the Brilliant deposit, whereas pyrite typically is absent or constitutes only a small part of the ore assemblage

in the intrusion-related deposits. Magnetite is also present in small amounts or absent in the IRGD.

3) Gold in the Brilliant deposit is sited almost ubiquitously as isolated inclusions and/or as a component of Au +Ag ± Bi ± Te ± Mo ± Pbs aggregates in vein pyrite, with the exception of the presence of minute Ag±BiS grains as inclusions within biotite. This implies the ore assemblages are largely confined within massive quartz-pyrite veins and not in the host rock, which is in contrast to the IRGD, where mineralization occurs in disseminated miarolites, hydrothermal breccias, roof-zone breccias, sheeted veins and within the host rock (Lang and Baker, 2001).

4) The Brilliant deposit is confined entirely within massive, sigmoidal to boudinaged quartz veins parallel to subparallel to the host- rock foliation, which formed relatively early during ductile-brittle deformation. IRGDs are formed generally as thin sheeted veins, cross-cutting the regional foliation of the host rock at late to very late stages during brittle deformation. The second stage of gold mineralization in the Archean Chalice deposit in the Yilgarn Craton, Western Australia is an exception to many of these defining characteristics of typical IRGDs, in that it has disseminated and vein type (conjugate) mineralization formed in a ductile regime, under a higher (amphibolite) metamorphic grade, and is considered to be temporally related to a deeper monzogranite (12 to 14km) dyke (Bucci et al., 2002, 2004).

5) Mineralization occurred in the Brilliant deposit after peak amphibolite facies metamorphism, most probably during retrogression to upper greenschist facies or amphibolite-greenschist transition facies conditions. Intrusion-related gold deposits are usually very late, after the main deformation event and peak regional metamorphism, and commonly under sub-greenschist to greenschist facies conditions

6) Hornblende–plagioclase thermometry of the host rock at Brilliant open pit indicates crustal depths of 8–9 km, whereas the characteristic depth for the majority of the IGRD is between 2 and 6 km, with the exception of Boddington, Chalice stage II and Nevoria, where crustal depths of the host rocks lie between 8 and 14km. The Brilliant deposit differs in most other features from these deposits.

7.6 Towards a Genetic Model of Gold Mineralization in the Brilliant Open Pit

Any genetic model to explain the formation of gold at the Brilliant deposit requires establishment of the relationship between the host biotite hornblende monzogranite and other granodiorite phases of the LLG. The geochronology established that the

granodiorite phases of the LLG were emplaced at ~2.76 Ga (between 276 3± 4 and 2752 ± 10 Ma). Lack of zircon in the biotite hornblende monzogranite precluded determination of an absolute age for this intrusion.

However, foliation-parallel sigmoidal veins in the biotite hornblende monzogranite suggest that it formed under a ductile-brittle structural regime and was syn-kinematic with shear-zone formation. Oliver (1999) obtained a SHRIMP U-Pb age of 2.63 Ga for titanite in the YEG (Yalgoo Eastern Granitoid) and assigned this to the age of formation of the NNW-SSE trending NSZ (Fig.7.1). Watkins and Hickman (1990) also suggested that the NSZ post-dated the ~2.68-2.64 Ga regional amphibolite facies metamorphism in the central and southwest part of the Murchison Domain.

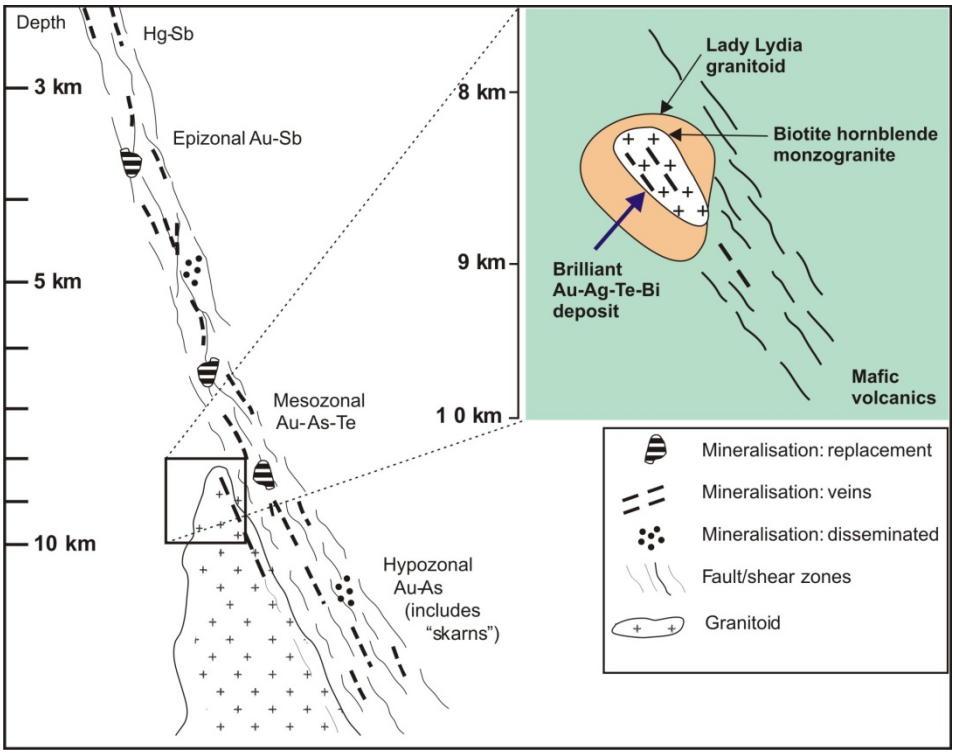

Fig. 7.13. Schematic representation of crustal environment of orogenic gold deposits in terms of depth of formation and structural setting (modified after Groves et al., 2003). Green shaded area depicts a tentative model of the genesis of the granitoid associated orogenic Au-Ag-Bi-Te deposit at Brilliant in the Yalgoo area.

Therefore, considering the presence of amphibolite-greenschist facies mineral assemblages and foliation-parallel sigmoidal, massive veins in the biotite hornblende monzogranite, it appears likely that the biotite hornblende monzogranite post-dated the peak amphibolite facies metamorphism at ~2.68 Ga, and was then subjected to east-west ductile deformation that resulted in the formation of the sigmoidal veins. These veins are considered to be a result of the same cycle of alternating brittle and ductile creep that produced sigmoidal veins as suggested by McCuaig and Kerrich (1998). Results of SHRIMP U-Pb geochronology of the granodiorite phases and geothermometry of the

biotite hornblende monzogranite imply that the biotite hornblende monzogranite post-dated the granodiorite phases of LLG and was emplaced into the LLG at ~ 672-644°C under a lithostatic pressure of ~2.4 kbar and at a depth of ~8.3 km.

A genetic model for the formation of gold at Brilliant in the context of the established model of orogenic granitoid-associated gold deposits (Fig. 7.13) can be summarised as follows:

i) Intrusion of ~2.76 Ga granodiorites of the LLG into the ca. 3 Ga Luke Creek Group greenstone sequence.

ii) Biotite hornblende monzogranite, the host rock to gold mineralization, was emplaced within granodiorites of the LLG as a small mesozonal (~8.3km) plug, post-dating regional amphibolite facies metamorphism at ~2.68-2.64 Ga. Emplacement of the biotite hornblende monzogranite might have been driven by development of NNE and NNW tight isoclinal folding during the continued regional east-west D_3 compression of Watkins and Hickman (1990).

iii) Continued east-west regional compression (D_4 of Watkins and Hickman, 1990) resulted in the formation of a widespread systems of NNW (137°) trending shear zones in the Yalgoo area. Parallel trends of the Brilliant open pit NNW-trending shear zone and gold-bearing massive, sigmoidal to boudinaged quartz veins in the pit all support the formation of these veins during a ductile-brittle structural regime, syn-kinematic with shear zone formation.

iv) Deformation of wall rocks by shearing resulted in fluid pressure fluctuations between suprahydrostatic and supralithostatic in these veins. This reflects alternating episodes of high-strain hydraulic fracturing at high fluid pressure with intervening slow strain and ductile creep at lower fluid pressure during which the veins slowly rotated and widened.

During successive hydraulic fracture events, vein-wall rock systems were broken outside of the veins beyond the zone of wall rock cementation incorporating successive selvedges of wall rock that became rafted into the veins (Cox et al., 1991), including hornblende, plagioclase, biotite and titanite selvedges that occur in vein samples 14A and 13C. Gold- bearing hydrothermal fluid was introduced from a deep source (as evidenced by abundant CO_2-H_2O primary fluid inclusions) and transported along the shear zones into these veins.

v) Numerous studies (Seward 1973, 1991; Shenberger and Barnes, 1989; Mikucki and Groves, 1990) suggest that gold was transported as Au(HS) under greenschist and subgreenschist facies conditions, and as Au $(HS)^0$ under amphibolite facies condition. As

the Brilliant deposit is hosted in greenschist-amphibolite transition facies, the gold in the ore fluid may have been transported as Au (HS)/Au (HS)^0.

vi) The presence of large pyrite crystals as the dominant sulphide phase within marginal parts of the veins suggests that sulphidation was the dominant depositional mechanism for gold responsible for the Brilliant deposit. Sulphidation has been demonstrated as the leading depositional mechanism for many large ore bodies, including Kambalda (Clark et al., 1986, 1989; Neall and Phillips, 1987), Granny Smith stage II (Ojala, 1995; Ojala et al., 1993, 1997; Cassidy et al., 1998 and Salier et al., 2005) and Great Eastern (Cassidy 1992; Cassidy et al., 1998). The loss of sulphur (decrease in ∑s) from the fluid destabilizes the gold-sulphur complexes, causing gold to precipitate by reactions involving Au(HS) + FeOt (silicate, oxides+) = Au + FeS (unbalanced) (McCuaig and Kerrich, 1998). Several authors (Sibson et al., 1988; Kerrich, 1989; Guha et al., 1991; Bouillier and Robert, 1992; McCuaig and Kerrich, 1998) have shown in deposits confined within veins that fluid pressure cycling during quartz vein formation leads to large-scale pressure fluctuation resulting in phase separation of the fluid components, and can also lead to the deposition of gold. A moderate degree of pressure fluctuation (2 to 3.2 kbar) and the presence of CO_2- rich and H_2O inclusions in the same cluster (suggesting at least visually the presence of some degree of immiscibility) in the Brilliant deposit, imply phase separation may also have contributed to some extent in precipitating gold (Figs. 7.10b,c & 7.12).

The source of the ore-bearing fluid at the Brilliant open pit cannot be deduced with certainty at the present level of understanding based only on the fluid inclusion data. However, the presence of abundant CO_2-rich fluid inclusions and a moderate to low salinity (2-9.6% NaCl equivalent mass) is suggestive of a deep source that could be the result of metamorphic devolatization. The presence of Bi-Te-Pb assemblages as minor phases points toward a lesser contribution from magmatic fluids.

Chapter 8 Crustal Evolution in the Yalgoo Area

8.1 Introduction

Modern studies of Archean greenstone belts (Xie et al., 1993; Dostal and Mueller, 1997, 2004; Morris and Witt, 1997; Polat et al., 1998, 2005; Puchtel et al., 1999; Polat and Hofmann, 2003; Boily and Dion, 2002; Dostal et al., 2004; Hollings and Kerrich, 2006; Manikyamba et al., 2004, 2008; Sandeman et al., 2004; Said and Kerrich, 2009; Smithies et al., 2005; Wyman and Kerrich, 2010) have established diverse volcanic rock associations across major cratons, ranging predominantly from komatiite to high-Mg tholeiite and bimodal tholeiitic to calc-alkaline volcanic associations. The komatiite, komatiitic basalt, high-Mg basalt association was erupted from anomalously hot mantle plumes in intra-oceanic basins or at continental margins (Campbell et al., 1989; Hollings et al., 1999; Kerrich et al., 1999a,b; Polat et al., 1999; Kerrich and Xie, 2002; Arndt, 2008; Manikyamba et al., 2008; Wyman and Kerrich, 2012). The second association of bimodal tholeiitic to calc-alkaline volcanic rocks comprises tholeiitic basalt, calc-alkaline basalt, andesite, dacite and rhyolite and is generally considered to be arc-related (Taylor and McLennan, 1985, 1995; Condie, 1994; Sylvester et al., 1997 Polat et al., 1998; Manikyamba et al., 2004, 2005; Wyman and Kerrich, 2009 and references therein).

Apart from these two associations, boninitic to low-Ti basalts (LOTI), variously associated with tholeiitic to calc-alkaline basalt associations in several greenstone belts, are considered to have formed in an intraoceanic subduction environment (Pearce and Peate, 1995; Kerrich et al. 1998; Wyman et al., 1999; Smithies et al., 2004; Boily and Dion, 2002; Manikyamba et al., 2005; Polat and Kerrich, 2006; Wyman and Kerrich, 2009). Smithies (2004) however, argued based on both geological and geochemical evidence, in favour of an intracontinental setting for the high-Mg norite and associated boninite-like rocks in the Mallina Basin of the Pilbara Craton. For calc-alkaline lavas and Nb-enriched basalts in the Schreiber–Hemlo greenstone belt in Canada, an island arc setting on the edge of an oceanic plateau was suggested (Polat et al., 1999; Polat, 2009). Wyman and Kerrich (2010) suggested tholeiitic basalt–komatiite and tholeiite to calc-alkaline basalt successions from the Abitibi and Wawa subprovinces of the Superior Province of Canada were the result of variable degrees of interaction between plume and arc. In the Yilgarn Craton, subsequent research on the Lower Basalt Unit of the Kambalda sequence, Eastern Goldfields Superterrane (Said and Kerrich, 2010), the boninite-Low-Ti basalt association in the northern Murchison Domain (Wyman and Kerrich, 2012), and on the komatiitic, boninitic and tholeiitic association from the

Southern Cross Domain (Angerer et al., 2013), also documented involvement of melting from a mantle plume and proto-arc and/or subduction zone processes.

Greenstone sequences in the central Murchison Domain consist of extensive mafic/ ultramafic lava plains, with minor felsic volcanic rocks (Watkins and Hickman, 1990; Hallberg et al., 2002). South toward the Noongal anticline, large outcrops of high-Mg basalts are present with 6-18% MgO according to Hallberg et al. (2002), although they are virtually absent in the northern part of the central Murchison Domain, i.e. the study area. The greenstone stratigraphy in the study area is dominated by tholeiitic basalts with sub-volcanic gabbro or dolerite sills (Watkins and Hickman, 1990; Hallberg et al., 2002). In the field, however, these two mafic lithologies are difficult to distinguish. Small linear NNW to irregular-trending felsic porphyries intruded this volcanic package in the core of Noongal anticline (Fig. 3.1). The east-northeast trending mafic dykes cross-cut the mafic volcanic sequence. Compared to the two major volcanic successions (i.e. komatiite-high Mg tholeiite and bimodal tholeiitic to calc-alkaline volcanic associations) generally described from Archean cratons, the stratigraphy in the north Yalgoo area does not offer a close match to either. The present study found that LREE-enriched tholeiite (LET), with less prevalent LREE-depleted tholeiite (LDT), dominate the greenstone stratigraphy with very minor lenses of microgranodiorite porphyries and andesite.

8.2 Crustal Evolution Models for the Yilgarn Craton

A wide array of models have been proposed for different terranes and crustal blocks of the Yilgarn Craton over the last three decades. The greenstones of the craton were initially considered to be remnants of primordial simatic crust that was deformed by the diapiric emplacement of steep-sided granite batholiths (Glikson, 1979). During the 1980s, most models interpreted the greenstones and granites as products of intracratonic rifting (Gee et al., 1981; Groves and Batt, 1984; Groves et al., 1985; Hallberg, 1986). Later, (Myers 1993, 1995) interpreted the Yilgarn Craton as a remnant continental block formed by the assembly of fault-bounded multiple rafts of sialic crust (terranes), each having different geological histories. Wilde et al. (1996), Myers and Swager (1997) and Witt et al. (1998) re-evaluated the geological relationships of the juxtaposed crustal units and extended the terrane accretion model based on studies of the tectono-stratigraphic units between large fault systems, the shape and trend of greenstone belts and geophysical and geochronological data.

Post-2000, extensive geophysical and geochemical data, high precision SHRIMP U-Pb zircon ages and Sm-Nd and Lu-Hf isotopic data were collected during a series of AMIRA and MERIWA projects that resulted in a revised tectonic scheme for the Yilgarn Craton

(Cassidy et al., 2006). Cassidy et al. (2006) divided the Yilgarn Craton into different terranes, defined on the basis of distinct sedimentary and magmatic associations, geochemistry and ages of volcanism (see section 2.1.1, Fig. 2.3). The Narryer Terrane in the northwest contains both the oldest detrital zircons yet found on Earth (back to c. 4400 Ma; Wilde et al., 2001) and the oldest rocks in Australia (back to c. 3730 Ma; Kinny et al., 1988). Both the Narryer Terrane and South West terranes are characterised by granite and granitic gneiss, with minor supracrustal greenstone belts, whereas the Youanmi Terrane and the Eastern Goldfields Superterrane comprise substantial greenstone belts with intervening granite and granitic gneiss. Recent revision (Pawley et al., 2012) of the Eastern Goldfields Superterrane has introduced the newest terrane, "Yamarna Terrane", previously referred to as "Yamarna Domain", marking the eastern margin of the craton.

The Sm-Nd (Fig. 2; Champion and Cassidy, 2007) and Lu-Hf (Mole et al., 2010; Wyche et al., 2012) data indicate distinctive crustal histories of the various terranes of the Yilgarn Craton. Recent models for the development of the terranes involve accretion (broadly in an east to west direction) of crustal fragments through a combination of both plume and variable degrees of convergence and extension-related processes (Czarnota et al., 2010; Ivanic et al., 2010, 2012; Wyman and Kerrich, 2012; Wyche et al., 2012; Angerer et al., 2013). The craton was stabilized by 2.62 Ga (Cassidy et al., 2006) and has remained integral and free of significant disturbances since emplacement of the Widgiemooltha dyke suite at 2.42 Ga (Nemchin and Pidgeon, 1998).

The Youanmi Terrane, containing the oldest (c. 3080 Ma) supracrustal rock record in the Yilgarn Craton (Wang et al., 1998; Yeats et al., 1996; Rasmussen et al., 2010; Van Kranendonk et al., 2013) has a varied history, whereas the Eastern Goldfields Superterrane is distinctly more juvenile than the terranes to the west (Wyche et al., 2012). Recent mapping in the northern part of the Murchison Domain of the Youanmi Terrane by the Geological Survey of Western Australia has resulted in a revision of the existing tectonic models for the Youanmi Terrane (Van Kranendonk, 2008; Van Kranendonk and Ivanic, 2009; Van Kranendonk et al., 2013), and a discussion of this, along with the proposed model of crustal evolution for the central-west part of the Murchison Domain, is presented in the following sections.

8.3 Models of Crustal Development in the Murchison Domain

8.3.1 Ensialic Basin Model

The five-stage model of Watkins and Hickman (1990) for the crustal development of the Murchison Domain favours an ensialic basin into which greenstones rocks were erupted,

followed by several stages of plutonism, volcanism and concomitant deformation (Fig. 171 of Watkins and Hickman, 1990). A brief account of the crustal development, as proposed by Watkins and Hickman (1990), is presented below in order to set the background for further discussion.

Table 8.1. Synopsis of the crustal evolution of the Murchison Province after Watkins and Hickman (1990).The major crustal developments are marked in bold font.

Lithological and crustal development	Deformation	Metamorphism	Age
Ensialic basin developed by extension of a pre-existing basement.			>3.0 Ga
Formation of Luke Creek Group formed through rapid eruption of magma on the deep basin floor.			~ 2.99 to 2.94 Ga
Basin development started in the north eastern and central (Yalgoo area) parts with deposition of the **Murrouli Basalt and Golconda Formation**.			
Large mafic intrusion of **Gabanintha Formation**.		M1; Local contact metamorphism of adjacent greenstone belt	
Early granitoid intrusion (**Pegmatite banded gneiss protolith)**.	D1; East-west horizontal compression	M2a; Local contact metamorphism by the intrusion of PBG protolith	~ 2.92 Ga
Epigenetic gold mineralisation resulted from upward migration of fluids derived from partial melting of lower crust.			
Formation of **Mount Farmer Group** volcanism erupted on the infrastructure of the Luke Creek Group.			~ 2.82 Ga
Intrusion of voluminous subhorizontal sheets of **monzogranites** at the base of the Murchison Supergroup.	D2; North-south compression	M2b; Local contact metamorphism by the intrusion of monzogranite protolith	~ 2.69 to 2.68 Ga
Development of NNE and NNW tight isoclinal folds. Strong penetrative fabric formed especially in the Mount Farmer Group volcanics. F3 structure **Noongal anticline** formed.	D3; East-west compression	M3; Regional metamorphism (green schist in the northeast to amphibolite facies metamorphism in the central and southwest parts	~ 2.68 to ~ 2.64 Ga
Monzogranite intrusion continued.			2.68 to ~ 2.64 Ga
Extensive systems of NNE and NNW trending shear zones and strike slip faults formed. **Noongal shear zone** (F4 structure) formed.	D4; Continued east-west regional compression (considered to be different phases of the same overall deformation event)		
Intrusion of **Post-folding granitoids** at the contact of greenstone belts and earlier Pegmatite banded gneiss (PBG).			~ 2.64, 2.62 Ga
Shear zone and fault development in the NW portion of the Province, with mainly east to southeast trend. Foliation formed in the post-folding granitoid in the north Yalgoo area. **Voluminous gold mineralisation** in the north eastern part of the Province	D5		~ 2.65 to ~ 2.60 Ga

i) In the earliest stage, a large ensialic basin formed by thinning and subsidence of a basement composed of older felsic rocks, probably in response to some kind of plate tectonic process. Partial melting of the upper mantle beneath the subsiding basin formed extensive basalt lava plains of the Luke Creek Group (~3.0 Ga). This was followed by the formation of felsic volcanic complexes (not present in the Yalgoo area) via partial melting of the lower crust resulting from the elevation of isotherms, induced by mafic magmatic activity and subsidence of the basin. BIF was deposited during quiescent periods in these two magmatic episodes.

ii) East-west horizontal compression (D1) ensued, accompanied by recumbent folding and thrusting affecting the lowermost greenstone package. This deformation also triggered emplacement of the earliest felsic intrusions (protolith of pegmatite banded gneiss) into the

base of the Luke Creek Group at 2919 Ma (Wiedenbeck and Watkins, 1993). The upper limit of east-west compression is marked by the intrusion of the pegmatite-gneiss protolith.

iii) During the period ca. 2820-2680 Ma, the Mount Farmer Group was deposited around nine volcanic centres and in one epiclastic sedimentary basin in a shallow-water to subaerial environment over the rocks of the Luke Creek Group. Following deposition of the Mount Farmer Group, voluminous monzogranite intruded at ~2690-2681 Ma into the base of the Luke Creek Group which caused amphibolite-facies metamorphism in adjacent greenstones.

iv) The intrusion of monzogranite lasted over 40 million years (ca.2680-2640 Ma). East-west upright folding (D2) deformed the whole sequence and refolded the thrusts and folds of D1. The D2 event produced large-scale dome-and-basin folding and regional metamorphism of the greenstones and early granites. This was followed by intense regional compression with north-northeasterly to north-northwesterly trending tight isoclinal folds (D3), which resulted in major shear zones. Wiedenbeck and Watkins (1993) attributed the age of 2681 ± 6 Ma for a sample of recrystallised monzogranite as defining the older age limit for both the D2 and D3 deformation phases and their associated greenschist facies regional metamorphism across most parts of the Murchison Domain. In the south, amphibolite facies reflects greater post-metamorphic uplift in the area due to the buoyancy of a thicker sialic basement granulite layer in this region. The D3 shear zones and fracture systems acted as passages for the gold-bearing fluids and formed the epigenetic gold deposits at Mount Magnet.

v) Major north-northeasterly to north-northwesterly shear zones developed (D4), which are considered to be a continuation of D3 deformation that lasted some time after intrusion of the post-folding granitoids. Post-folding granitoids (2.60 to 2.64 Ga) post-dated the peak of regional metamorphism. The last event (D5) consisted of shear zones and faults developed in the northwestern part of the domain, with mainly east to southeast trends. East-west trending mafic dykes intruded the greenstones at about 2.42 to 2.41 Ma (Soufoulis, 1966; Turek, 1966; Fletcher et al., 1987, Nemchin and Pidgeon, 1998; French et al., 2002).

8.3.1.1 Problems with the Ensialic Basin Model

Several problems were identified by Van Kranendonk and Ivanic (2009) with the model of Watkins and Hickman, which are: i) ascribing rocks from the same units (with similar ages) to different formations; ii) ascribing two rock units with varied lithology and ages to a single formation; iii) the Luke Creek group rocks are represented by a wide range of ages from ca. 2950 Ma at Mount Magnet, ca. 2815 Ma at Meekatharra, and ca. 2752 Ga in the Weld Range; iv) some formations were shown to include contrasting rock types (e.g. coarse

clastic sedimentary rocks with komatiitic basalt within the Mougooderra Formation); and v) classification of granitic rocks based mainly on structural complexity is inconsistent with new geochronological data. In addition to the above five problems, the present study also detected several more, which are: i) the genesis of the greenstone and granitic rocks in many cases were poorly constrained due to incomplete trace and rare earth element data, as exemplified by identification of Archean boninitic rocks and depleted tholeiite in the Yalgoo area; ii) a crustal reconstruction model for the Murchison Domain excluding samples from the Noongal traverse is proved to be an oversimplification of the complex crustal history of the Murchison Domain; iii) field investigations in the Yalgoo/Noongal area failed to recognise several granitoid (biotite hornblende monzogranite) and volcanic (high-Mg andesite) phases; iv) incomplete geochronology and geochemical data on the granitoids necessitated a re-evaluation of the duration of magmatism and its genesis; and v) Paleoproterozoic activity as young as ca 1.85 Ga affected the domain, which is much younger than the age of 2.42 Ga mentioned by Watkins and Hickman (1990) for dyke intrusion.

8.3.2 Plume-Related Magmatism Model

Van Kranendonk et al. (2013) proposed a lithostratigraphic scheme (Table 8.2) for the Murchison Domain, based on recent mapping and new and previous geochronological results. They suggested crustal development of the Murchison Domain commenced at 2960–2935 Ma, with the formation of the oldest greenstones in the Golden Grove area in the southern part of the Murchison Domain. These ca. 2950 Ma greenstones were tilted by the earliest deformation event (D1), prior to being unconformably overlain by ca. 2810 Ma clastic rocks (Clifford et al., 1990; Wang et al., 1998). The two major periods of crustal formation occurred at ca. 2825 to 2800 Ma (Norie Group) and 2735 to 2710 Ma (Polelle Group), both containing essentially similar lithologies: an older mafic–ultramafic magmatic event followed by a pulse of younger felsic magmatism. Large mafic–ultramafic intrusives accompanied the early stages of each of these cycles, with the latter stages accompanied by voluminous granitic magmatism. In the younger cycle, granitic magmatism continued for at least another 20 Ma, to 2690 Ma, and continued nearly continuously to c. 2600 Ma. The addition of mafic-ultramafic volcanics from both cycles to older (ca. 3.0 Ga) Murchison Domain crust caused widespread partial melting of the older crust as evidenced by the widespread presence of ca. 3.26–2.95 Ga xenocrystic zircons in these rocks (Schiøtte and Campbell, 1996;Yeats et al., 1996; Wang et al., 1998).

Van Kranendonk et al. (2013) invoked a major, deep mantle plume to explain the occurrence of Al-depleted komatiite (Barley et al., 2000) and komatiitic basalt in the northern Murchison Domain, and large-scale layered ultramafic–mafic complexes of the Meeline Suite and Narndee Igneous Complex at 2825–2805 Ma. They suggested mantle melting continued to ca. 2780 Ma and to shallower levels, generating komatiite, komatiitic basalt and tholeiitic basalt of the Meekatharra Formation, gabbroic intrusions (Little Gap Suite), and hornblende tonalites of the Annean Supersuite (Fig. 2 of Van Kranendonk et al., 2013).

At ca. 2750 Ma, widespread intermediate to felsic volcanic rocks (Greensleeves Formation) were accompanied by emplacement of voluminous granitic rocks. Observing the calc-alkaline signatures in some of these post-2.75 Ga felsic rocks, Van Kranendonk et al. (2013) suggested a period of subduction beneath the Murchison Domain may have commenced at ~2.75 Ga.

Older greenstones were uplifted and tilted by D2 >2735 Ma, and were quickly followed by a second stage of mantle plume-induced melting at ca. 2735–2710 Ma and crustal extension with the eruption of Wattagee Formation basalts and emplacement of the Yalgowra Suite of gabbroic sills. Small- to large-scale, east–west trending tight to isoclinal folds (~2.67 Ga D3 structures) affected ca. 2720 Ma greenstones of the Glen Group, south of the Weld Range. The D3 structures were overprinted by a set of north to north-northeast trending folds, north-northeast striking foliations and shear zones of D4 at ~2.63 G. A prolonged spell of (>100 Ma) granite magmatism continued until ~2.60 Ga to complete the crustal development of the Murchison Domain.

8.3.2.1 Problems with the Plume-Related Model

The plume-related magmatism model of Van Kranendonk et al. (2013) has been successful in addressing many of the geochronological inconsistencies in the earlier model of Watkins and Hickman (1990) and providing a rationale for the presence of widespread komatiitic/ultramafic bodies throughout the domain. However, several observations from the present and other relevant studies do not comply with plume-related magmatism as proposed by Van Kranendonk et al. (2013), and are discussed below.

i) Widespread komatiites are present mostly in the northern part of the Murchison Domain. Present and previous studies (Watkins and Hickman, 1990; Collins and Steuart, 2000; Hallberg et al., 2002) in the Yalgoo area confirmed that tholeiitic basalt, minor gabbro/dolerite sills and high-Mg basalt (in the southern Yalgoo area) are the dominant

Table 8.2. Stratigraphic scheme for the Murchison Domain, divided into three main columns for (a) supracrustal rocks, (b) granitic rocks, and (c) mafic-ultramafic intrusive rocks (after Van Kranendonk et al., 2013).

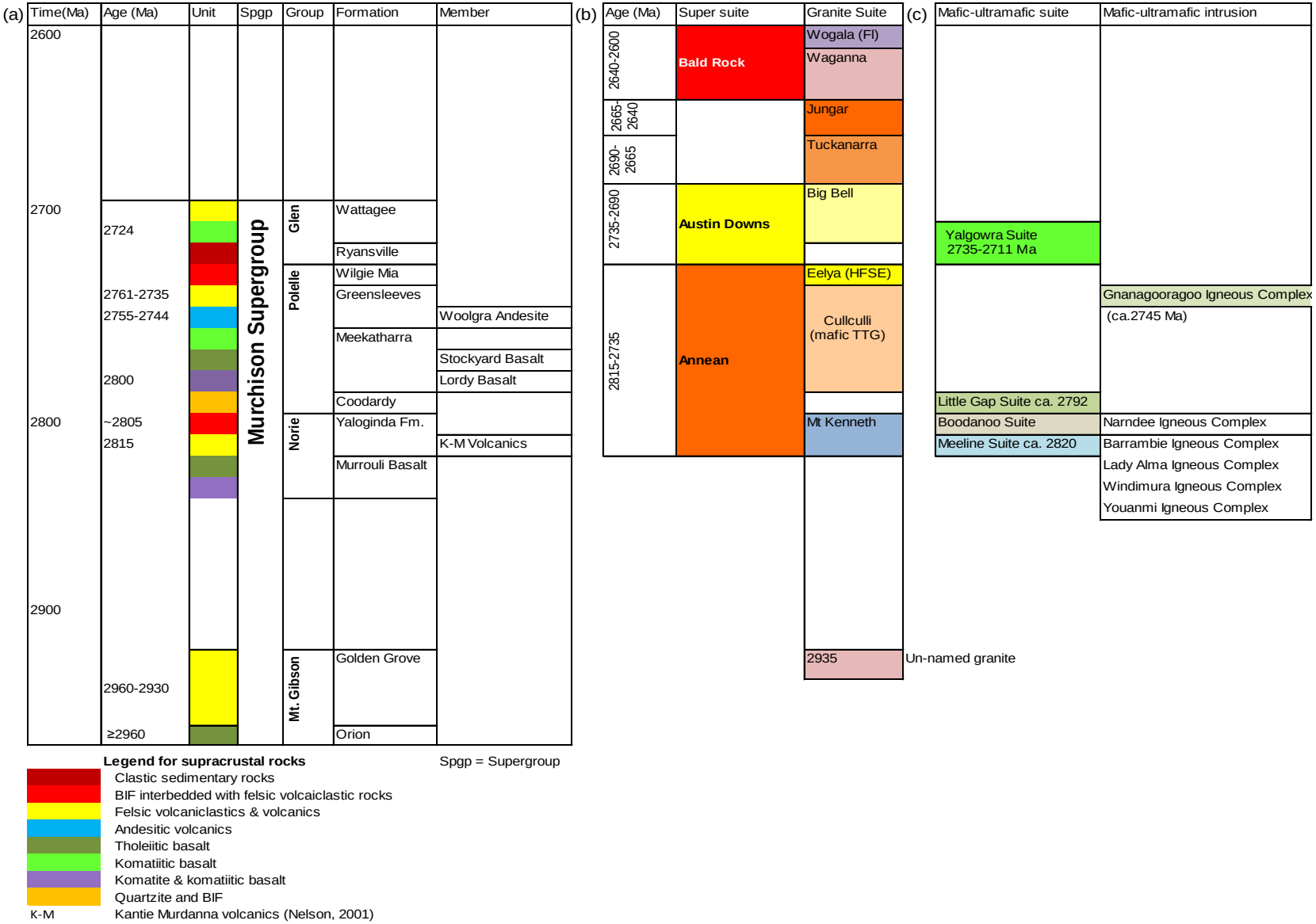

2000; Hallberg et al., 2002) in the Yalgoo area confirmed that tholeiitic basalt, minor gabbro/dolerite sills and high-Mg basalt (in the southern Yalgoo area) are the dominant mafic lithologies. Hallberg et al. (2002) reported one small ultramafic (<1 square kilometer) body from the centre of the study area (Fig. 2.6). Van Kranendonk et al. (2013) however, reported komatiitic basalt formed at 2724 Ma (age assigned from metamict zircon) as being the only mafic/ultramafic lithology (Fig. 27 of Van Kranendonk et al., 2013) in the Yalgoo greenstone belt. It is certainly incorrect for two reasons; firstly present and previous studies showed no komatiitic/komatiitic basalt/significant ultramafic bodies belonging to the Murrouli Basalt of the Norie Group were present in the Yalgoo area and, secondly, no mafic/ultramafic bodies are seen to transect/envelop the granitoids in the Yalgoo area. Therefore, the presence of mantle plume-induced volcanism is unproven, at least in this part of the Murchison Domain (see section 3.4.4.7 for details).

ii) A 2704 ± 50 Ma age is reported from a granite (no details provided), which was considered to record the onset of felsic magmatism in the Yalgoo area (Fig. 27 of Van Kranendonk et al., 2013). Detailed study and SHRIMP U-Pb age data obtained from eight felsic samples from three granitoids and one from a porphyritic microgranodiorite in this study clearly show the beginning of the felsic magmatism is much older at ~2.76 Ga in the Yalgoo area (see section 5.4).

iii) The occurrence of boninitic rocks in the Polelle Group from both the Cue and Meekatharra areas (Wyman and Kerrich, 2012) and from the Murrouli Basalt in the Yalgoo area (see section 3.3.4.6 and 3.3.5) implies the presence of much older and significant supra-subduction zone plate tectonics in the Murchison Domain than suggested (at ca. ~2.75 Ga) by the plume model. Moreover, a long history of crustal recycling has been documented in the Yalgoo area from abundant (>2.87 to 3.00 Ga) xenocrystic zircons within ~2.76 Ga granitoids, which supports the presence of an early convection mechanism in the Archean mantle, i.e. plate tectonics (see section 8.4.2).

iv) Van Kranendonk et al. (2013), citing the work of Barley et al. (2000), attributed a deep mantle plume (>250 km) to the ca. 2820–2790 Ma magmatic events, including the eruption of komatiitic melts. In the Gabanintha area of the Murchison Domain, Barley et al. (2000) classified the porphyritic komatiites and komatiitic volcaniclastic rocks as Ti-rich Al-depleted komatiites. They stated “The distinctive composition of these komatiites is thought to result from magma generation by melting at depths of >250 km in the presence of residual majorite-garnet followed by hydration and enrichment in

incompatible elements through interaction with metasomatized or subduction-modified mantle lithosphere" (last six lines on page 881 of Barley et al., 2000). This statement clearly necessitates the presence of a coeval, if not prior, subduction zone in the path of the mantle plume. Therefore, the study of Barley et al. (2000) allowed the possibility that a subduction zone existed in the northern Murchison Domain.

8.4 Older Crust and Crustal Reservoirs in the Murchison Domain

8.4.1 Ancient Felsic Crust in the Source of the Yalgoo Granodiorites/ Microgranodiorite

A significant number (twenty) of older zircons with ages between ~2.87 to 3.0 Ga were obtained from the granodiorite and porphyritic microgranodiorite samples, strongly suggesting the existence of older felsic crust. Among the twenty, the Gaussian cumulative curve of fourteen analyses yields an age of ~2.94 Ga, while two older zircons yield an age of ~3.0 Ga (Fig. 8.1).

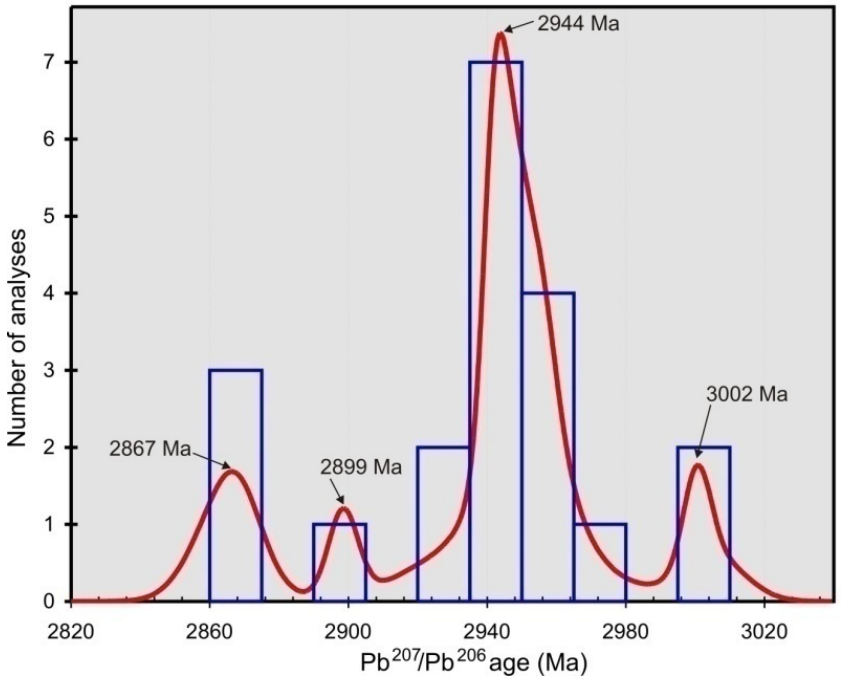

Fig. 8.1 Cumulative probability curve of the older zircons from the granitoids and porphyritic microgranodiorite in the Yalgoo area.

Four other zircon ages, including three of ~ 2.87 Ga and one of ~2.90, Ga together indicate a complex basement with components ranging in age from ~3.0 Ga to ~2.87 Ga.

8.4.1.1 Previous Studies

Xenocrystic zircons >3100 Ma are rare in the Youanmi Terrane (Wyche, 2007), which is consistent with the results of the present study. However, several studies (Pidgeon and

Hallberg, 2000; Cassidy et al., 2002 and Wyche et al., 2004; Wyche, 2007) reported xenocrystic zircons aged between 4350 and 3300 Ma from the Youanmi Terrane.

The study of Griffin et al. (2004) on detrital zircon populations across the Yilgarn Craton suggested the 2.6–2.8 Ga magmatic zircons in the Yeelirrie geophysical domain (after Whitaker 2001), occupying the eastern part of the current outline of the Eastern Goldfields Superterrane, were derived from older (3.6 to 3.7 Ga) continental crust. Based on Sm-Nd

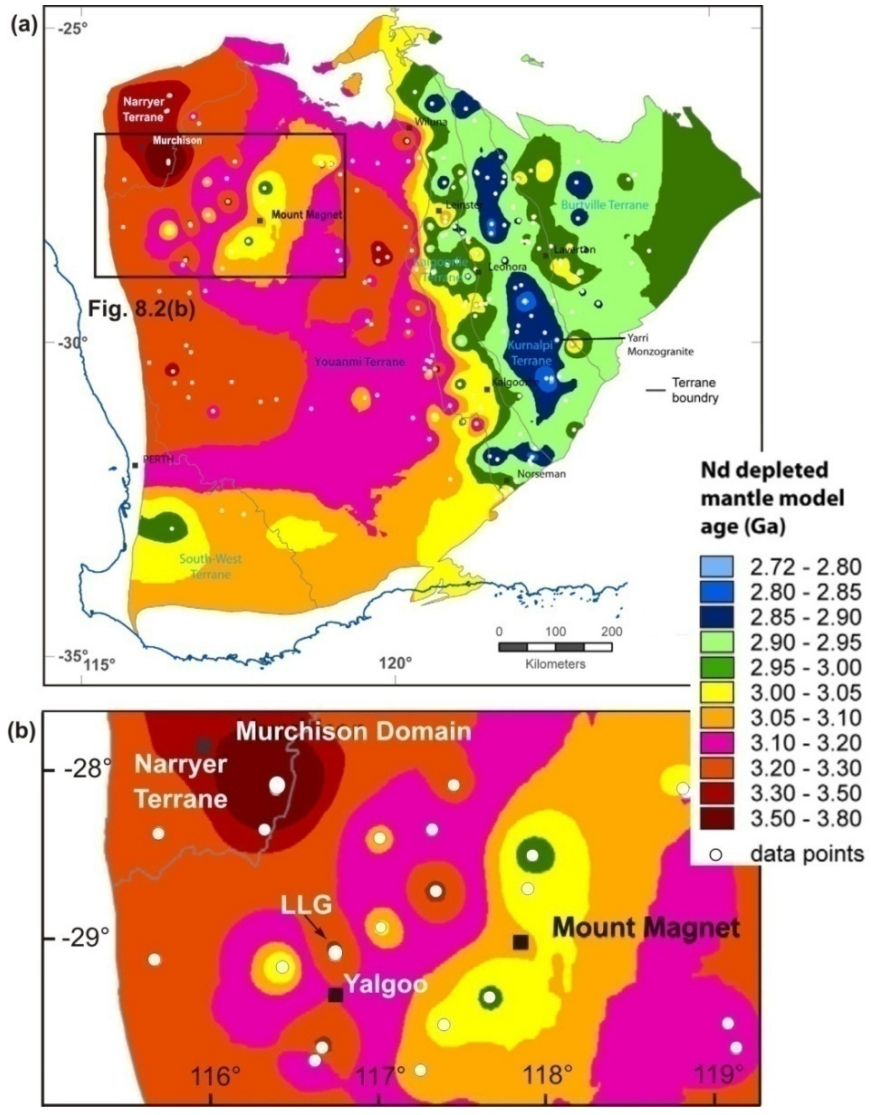

Fig. 8.2 (a) Nd depleted-mantle model age map of the Yilgarn Craton. Image produced by griding Nd depleted-mantle model ages calculated from Sm-Nd point data (after Champion and Cassidy, 2007). (b) Enlargement of Nd depleted mantle age of the study area and its surroundings.

data from granite samples of various ages across the Yilgarn Craton, Champion and Cassidy (2007) prepared a Nd depleted-mantle model age map, which they consider a crude estimate of the bulk (average) age of the crust. In the Yalgoo area, a crustal model age between 3500 to 3300 Ma is inferred from this Nd depleted-mantle model age map, which is within the

hafnium zircon T_{DM2} age range of ~3.6 to 3.3 Ga for the granodiorite samples (Fig. 8.2; Table 8.2).

Nelson (1995) reported a U-Pb zircon age for the Mount Joanna gneissic granodiorite, Eastern Goldfields Superterrane, of 2939±6 Ma which is slightly younger than its Nd depleted mantle model age (T_{DM2} = 3110Ma; Czarnota et al., 2010). The similarity of crystallisation ages and juvenile Nd signatures between the oldest rocks preserved in the Eastern Yilgarn Craton (Kalgoorlie, Kurnalpi and Burtville terranes, according to Czernota et al., 2010) and the granites and greenstones of the Youanmi Terrane, together with the inherited zircon record from granitic rocks, led Czarnota et al. (2010) to propose that the Youanmi Terrane forms the basement to the eastern Yilgarn Craton. Xenocrystic zircons aged between 3.0 and 2.94 Ga (present study) in the Yalgoo area lends further support for the presence of an older crust. Recent geochronology and Lu-Hf isotopic studies of Ivanic et al. (2012) on the granitoids from the northern part of the Murchison Domain demonstrate several periods of juvenile mantle input (at ca. 2980, 2820 to 2640 Ma) and crustal recycling (at ca. 2750 and 2620 Ma) in the sources of these granites.

8.4.2 Crustal Recycling and Mantle Depletion Between >4.13 and 2.94 Ga

Several distinct episodes of juvenile magma generation and recycling and mixing between enriched and depleted source reservoirs have been revealed from the combined study of the U-Pb and Lu-Hf isotopic systematics, and these are summarised in Table 8.3 and Fig. 8.3.

8.4.2.1 Granodiorite

The granodiorite samples (~2.76 Ga) from both the LLG and YEG, along with the porphyritic microgranodiorite, extend down from the depleted mantle evolution line to an εHf value of -6.88 (Fig. 8.3a). An almost identical, but slightly wider, cluster is formed by the xenocrystic cores/inherited grains (~3.0 to 2.94 Ga). The preponderance of near chondritic to weakly negative εHf values suggests contributions from both recycled crust and a juvenile mantle component (Fig. 8.3a). Both the magmatic and xenocrystic zircons plot back to ~3.3 Ga on the depleted mantle line, suggesting the involvement of older continental crust in the genesis of these granitoids. Closer evaluation of the combined U-Pb and Lu-Hf data reveals two distinct episodes (at 3.45 and 3.33 Ga), which are explained below.

Most Granodiorites and Porphyritic Microgranodiorite: Zircons from four (samples MA 15, 6, 10, 38) out of six granodiorite samples and the single porphyritic microgranodiorite sample (MA 27) sample mostly (40 out of 49) have near chondritic to weakly negative εHf values (ranging from 0.21 to -6.88) along with old T_{DM2} ages

(averaging 3.57 Ga) indicating that the sources for these magmas contained an older crustal component. A 3.58 Ga T_{DM2} age is estimated from the evolution trend using the average

Table. 8.3. Summary of the key features of the Pb-U and Lu-Hf isotope studies of the xenocrysts and inherited cores from the granodiorite and microgranodiorite samples from the Yalgoo area. Analyses representing mixed ages and with high U, Th, high degree of discordance and disturbed Lu-Hf isotopic systems are excluded.

SHRIMP spot	t (Ma)	$^{176}Hf/^{177}Hf$	$e_{Hf}(t)$	T_{DM1}	T_{DM2}	$f_{Lu/Hf}$
MA 16.1	2945	0.281050	1.82	3130	3353	-0.95
MA 16.2.1	2949	0.281097	2.33	3109	3307	-0.93
MA 16.2.2	2941	0.281097	1.91	3130	3348	-0.95
MA 16.3.1	2956					
MA 16.8.1	2867	0.280996	0.56	3104	3408	-0.98
MA 16.3.2	2960	0.281076	2.18	3130	3332	-0.93
Average Hf data of MA 16		0.281063	1.76	3120	3350	-0.95
MA 15a.1	2945	0.280980	0.02	3197	3507	-0.96
MA 15a.4	2967	0.280968	1.02	3175	3437	-0.97
MA 15a.5	2947	0.280981	0.03	3199	3508	-0.96
MA 15a.6	2955	0.281001	1.02	3167	3428	-0.96
MA 15.a.8	2955	0.281058	1.75	3142	3366	-0.94
MA 15a.9	2946	0.281005	-2.11	3294	3690	-0.91
Average Hf data of MA 15		0.280999	0.29	3195	3489	-0.95
MA 6.3	2932	0.281107	5.82	2962	3001	-0.98
MA 10.8	3006	0.281021	3.43	3117	3256	-0.97
MA 10.9	2943	0.281083	2.93	3085	3256	-0.95
Average Hf data of MA 10		0.281052	3.18	3101	3256	
MA 27.11.1	2932	0.280965	1.14	3138	3403	-0.99
MA 38.7	3001	0.281095	6.00	3015	3032	-0.97
MA 38.9	2899	0.280986	-0.18	3163	3493	-0.97
Average Hf data of MA 38		0.281040	2.91	3089	3263	-0.97
MA 9.8.1	2861	0.281043	1.74	3056	3303	-0.98
MA 9..8.2	2868	0.281127	3.86	2983	3125	-0.96
Average Hf data of MA 9		0.281085	2.80	3019	3214	-0.97

continental crustal value (Fig. 8.3b). This is, therefore, taken as the average age of the source for the granodiorite and porphyritic microgranodiorite magma. However, the vertical mixing trend in the granodiorite and porphyritic microgranodiorite samples (Fig. 8.3b) implies a contribution from juvenile material. The trace element characteristics of the granodiorite samples also support source heterogeneity (see section 5.5.4 and Fig. 5.32). A deeper high P/T source component, in equilibrium with rutile-bearing eclogite, probably contributed to an enriched to undepleted mantle Lu-Hf isotopic signature. The relatively shallow, low P/T source component, in equilibrium with the garnet-amphibolite field, most likely induced the depleted mantle Lu-Hf isotopic characteristics. The composite histogram of the εHf values of the granodiorites, microgranodiorite and older grains shows the presence of a significant recycled and depleted mantle component, along with a lithospheric mantle component (Fig. 8.4).

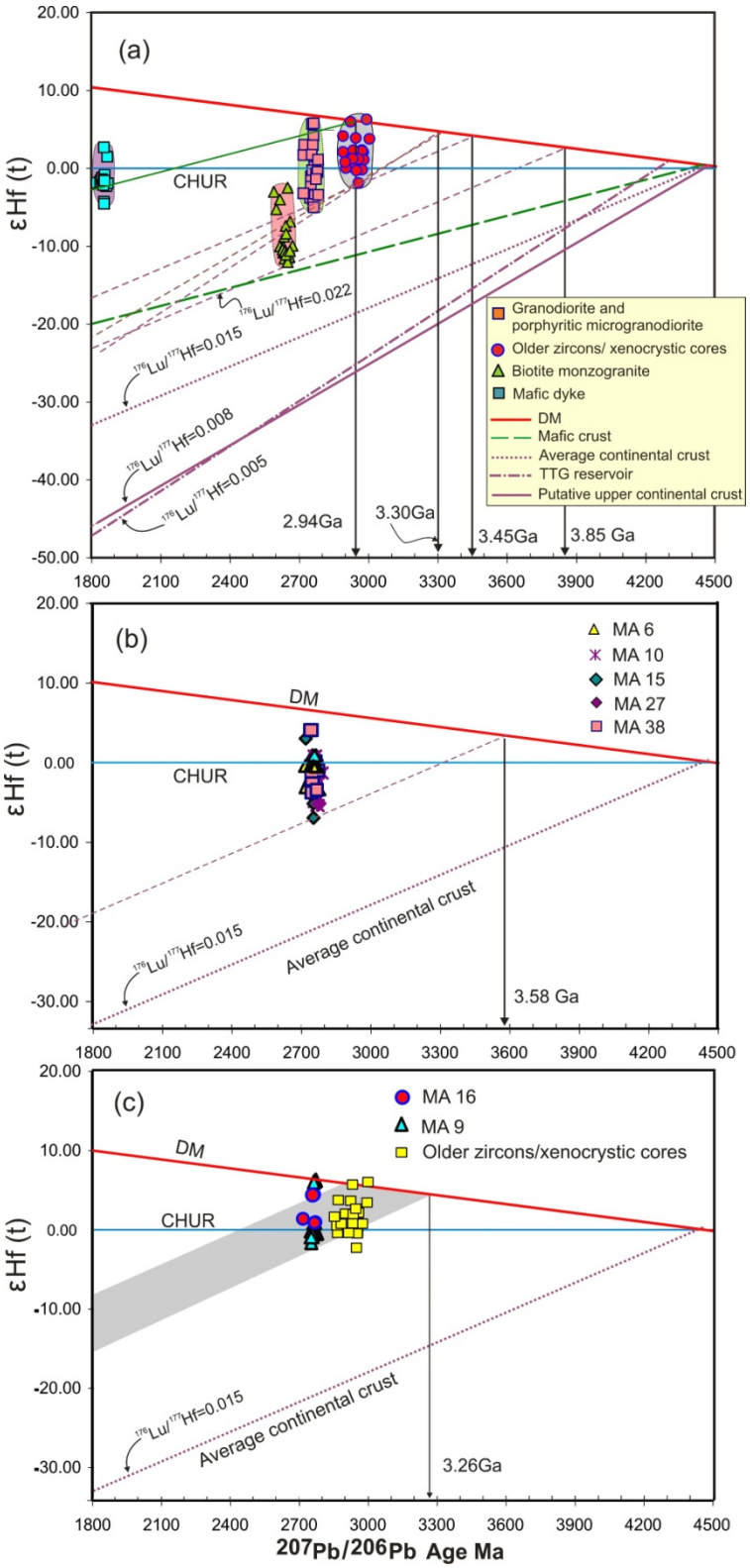

Fig. 8.3. εHf (t) vs.$^{207}Pb/^{206}Pb$ plots for (a) the Yalgoo granitoid and dolerite dyke samples, (b) Selected granodiorite (samples MA 15,6,10, 38) and single porphyritic microgranodiorite sample (MA 27). (c) Older grains in granodiorite samples MA 9 and 16. The isotope evolution line of putative upper continental crust ($^{176}Lu/^{177}Hf$ =0.008; Rudnick and Gao, 2004), mafic crust ($^{176}Lu/^{177}Hf$ =0.022), average continental crust ($^{176}Lu/^{177}Hf$ =0.0015; Griffin et al., 2002) and TTG reservoirs (formed at 4.3 Ga with $^{176}Lu/^{177}Hf$ = 0.005, Blichert-Toft and Albarède, 2008) are shown for reference, assuming silicate Earth differentiation at ~4.5 Ga (Bennett et al., 2007). The model depleted mantle curve (DM), similar to that of Vervoort and Blichert-Toft (1999), was derived by back calculating the isotope composition of mean modern MORB and taking εHf=0 at 4.5 Ga.

Minor Group of Granodiorites and Xenocrystic Zircons: The other two granodiorite samples (MA 16 and 9) contain a few low negative, but mostly moderately positive (-1.57 to6.23) εHf values and considerably lower T_{DM2} model ages (averaging 3.22 Ga), which are in clear contrast to those discussed above. The older zircons have mostly indistinguishable εHf values (-2.11 to 6.00) from samples MA 9 and 16, with the great majority (17 out of 19) of zircons having positive εHf values. The inherited and xenocrystic zircons have younger T_{DM2} model ages (averaging 3.34 Ga) compared to the main population of zircons from

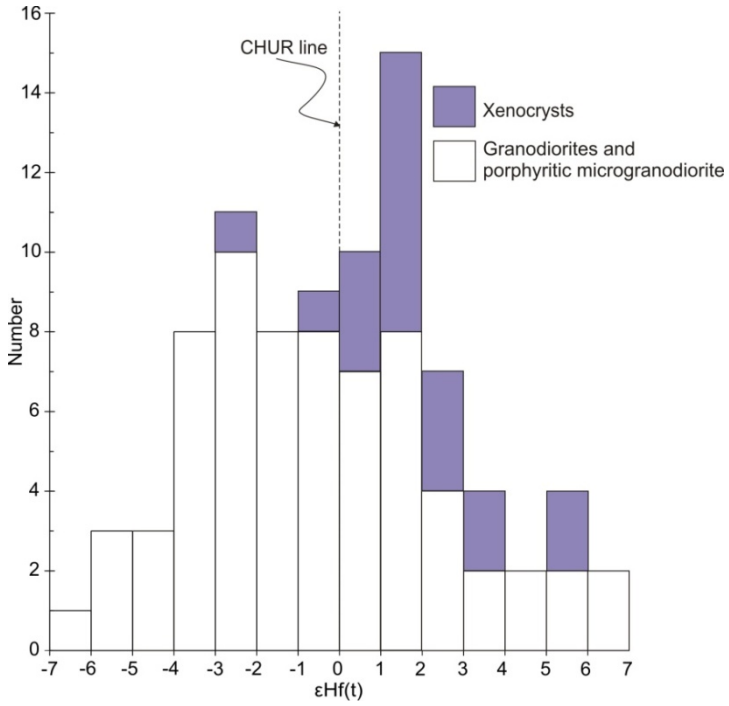

Fig. 8.4. Combined histogram of εHf (t) values for the granodiorites, porphyritic microgranodiorite and xenocrysts from the north Yalgoo area.

samples MA 15, 6, 10, 38 and 27. Apart from slightly older T_{DM2} model ages, the εHf values of the older zircons are comparable to those of samples MA 9 and 16. A T_{DM2} model age of 3.26 Ga is estimated from the evolution trend, using average continental crust (Griffin et al. 2000) for formation of both the parental melts for samples MA 6 and 16 and the inherited grains (Fig. 8.3c).

Older zircons with notably younger T_{DM2} model ages and more positive εHf values than the majority of the granodiorites and microgranodiorite can best be explained by the Hf isotope composition of zircon reflecting mixing of two or more magmas derived from sources with different Hf isotope compositions (e.g. Griffin et al., 2002; Belousova et al., 2006).

The abundant positive εHf values (ranging from 0.02 to 6.00) and younger estimated T_{DM2} model ages (3.26 Ga) of the older grains implies that these zircons were derived mainly from lithospheric mantle (Table 8.2, Fig. 8.3c,8.4). The younger rims (~2.76 Ga) of these older

zircons were sourced from an older recycled crustal component as evidenced by mostly near chondritic to low negative εHf values (ranging from -0.92 to -6.88) and older estimated T_{DM2} model ages (3.58 Ga) (Fig. 8.3b). This explains how the majority of the granodiorite samples formed from an older 3.58 Ga (T_{DM2} model age) source compared to a youger 3.26 Ga source, which produced melt for minor granodiorite zircon samples. Parental melts of samples MA 9 and 16 were most likely derived from the same source that supplied the magma for the older grains.

Two Crustal Reservoirs as the Source of ~2.76 Ga Granodiorites and Porphyritic Microgranodiorite : The Hf data for samples MA 16 and 9 and the older grains cluster between CHUR and the DM evolution line (Fig. 8.3c). This provides strong evidence for the presence of two previously unrecognised isotopic reservoirs in the Central Murchison Domain. The older 3.58 Ga (T_{DM2} model age) material resulted from mixing of largely recycled crustal components with a minor depleted mantle component in the magmas of the ~2.76 Ga rocks (granodiorite samples MA 6,10,15 and 38; and microgranodiorite sample MA 27). The younger 3.26 Ga reservoir was almost entirely made up of moderately depleted components, which supplied parental melts for older grains (at ~3.0 and 2.94 Ga) and two granodiorites (samples MA 9 and 16).

8.4.2.2 Biotite Monzogranite

The ~2.64 Ga biotite monzogranite samples display a wide range of negative εHf values from -2.75 to -12.31 (Fig. 8.3a). Of these (n=26), a majority (n=22) are within the range -6.82 to -12.31. These are by far the most negative εHf values from zircons (both primary and detrital) in the whole of the Yilgarn Craton. The εHf values of samples MA 3 and 4 are almost identical to those of zircons from the Neoarchean monzogranite sample W34 from the Jack Hills with εHf values between − 8.3 and −14.8 (Kemp et al., 2010). High –ve εHf(t) values of -5.6 to -12.78 and -4.6 to -10.3, equating to T_{DM2} model ages of 3.46 to 3.84 Ga and 3.41 to 3.77 Ga respectively, were recently reported from the 2.62 Ga Walaganna and 2.61 Ga Wogala suites (Ivanic et al., 2012).

Considering a crustal source for the biotite monzogranite, projection of the average continental crust (0.015) gives an age of ~3.85 Ga on the depleted mantle evolutionary trend (Fig. 8.3a), which can be considred as the parental source of the biotite monzogranite. The consistently old T_{DM2} model ages (averaging 4.13 Ga) however, also implies that Hadean crust contributed significantly to these Archean magmas, which incorporate weak to moderately radiogenic (higher negative εHf values) Hf through repeated mixing with recycled crust.

8.4.2.3 Mafic Dyke

The mafic dyke sample shows a small range of εHf values (-4.55 to 2.71) with the majority (12 out of 16 analyses) forming a tight cluster of near chondritic values between -2.29 and -0.83, suggesting derivation from an enriched mantle source (Fig. 8.3a). The T_{DM2} model age of ~2.94 Ga obtained from the mafic dyke zircons (Fig. 8.3a) is identical to the age of abundant xenocrysts and inherited grains, implying incorporation of a 2.94 Ga crustal component in the source of the mafic dyke.

8.5 Crustal Evolution Model for the Yalgoo Area

An appropriate model for the voluminous mafic supracrustal rocks and granitoids in the northern Yalgoo area needs to address the key geochemical signatures, geochronology, U-Pb and Lu-Hf isotopic systematics of the individual lithologies, in combination with the field relationships and tectonic and deformation history of the area. A single geodynamic setting to explain the observed diversity among the lithologies with assorted chemical signatures is difficult to formulate. The Lu-Hf isotopic characteristics of the three granitoid types indicate the presence of at least three older felsic components, including one of Hadean age in the protolith source. In addition, one of the dolerite dykes was dated at ~1.85 Ga and identifies a previously unknown Paleoproterozoic event in the area. Thus the supracrustal rocks, granitoids and the mafic dykes span the Neoarchean to Paleoproterozoic. Figure 8.5 summarises a possible sequence for crustal development in the Yalgoo area.

The mafic supracrustal rocks in the Yalgoo area were probably erupted through rifts/fractures developed in an intra-oceanic proto-fore arc setting (Stern and Bloomer, 1992; Stern, 2004, 2010; Ishizuka et al., 2006; Reagan et al., 2008), marginal to an older continent to the northwest and an open ocean to the southeast. Several studies (Champion and Cassidy, 2007; Wyche, 2007; Czarnota et al., 2010) suggest the presence of older (>3.1 Ga) continental crust in the west and northwest part of the Yilgarn Craton. The sub-arc mantle is envisaged of have been depleted in nature owing to the earlier extraction of melt that built the arc (Fig. 8.5a). The parental magma for LET was generated at ca. ~2.95 Ga (considering the age of the oldest greenstones; Watkins and Hickman, 1990; Van Kranendonk et al., 2013) by low pressure decompression melting of the 'refractory' mantle resulting from the introduction of volatiles from the subducting plate into the young hot oceanic lithosphere beneath the rift zone (van der Lann, 1987; Crawford et al., 1989; Tatsumi and Maruyama, 1989; Pearce and Peate, 1995; Bédard, 1999) (Fig. 8.5b). The melting most probably occurred in a supra-subduction environment within a depleted MORB-like mantle (see section 3.4.4.8, Fig 3.17). Slab rollback-induced extension in the

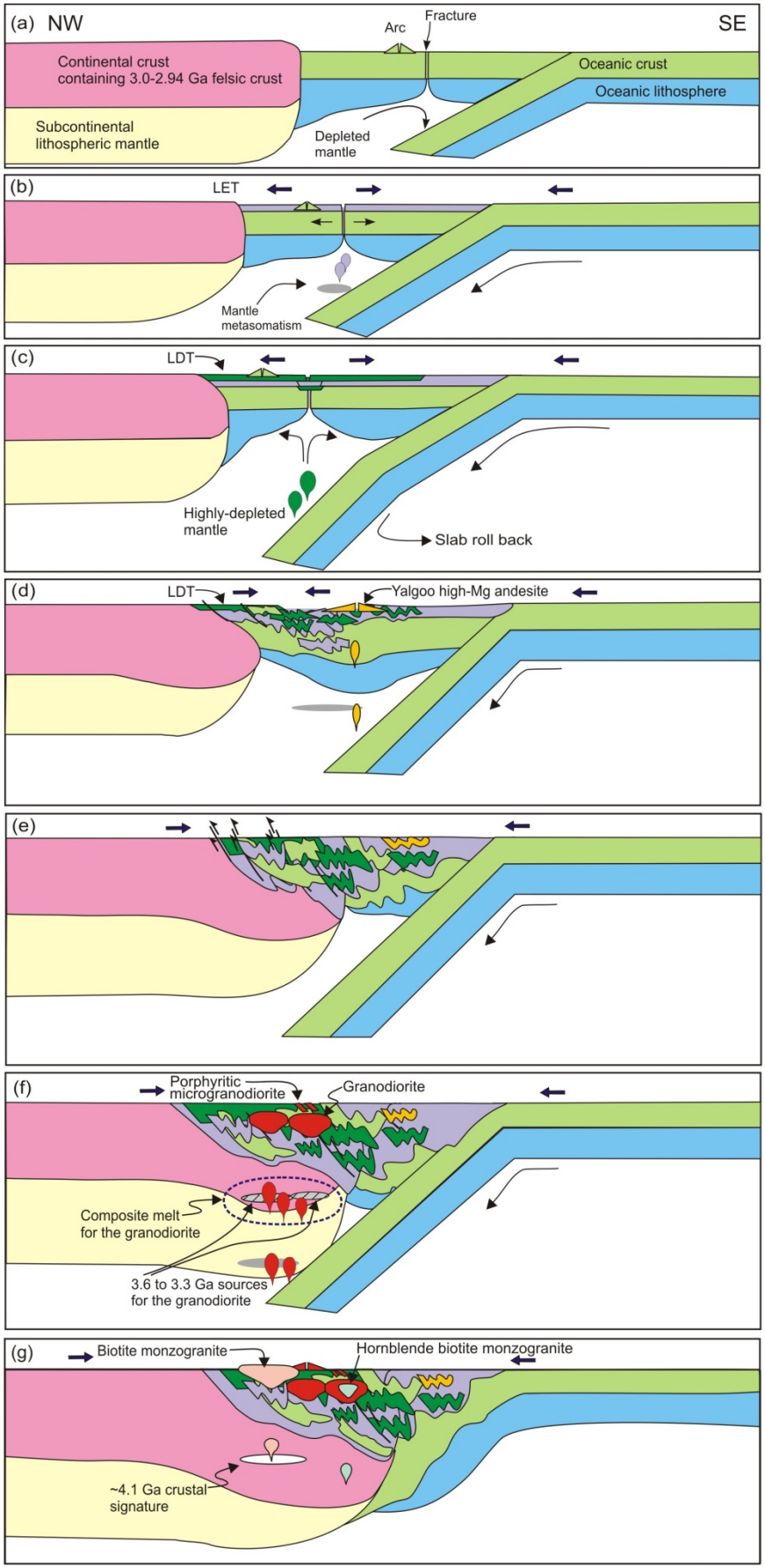

Fig. 8.5. Stages of the crustal development in the Yalgoo area, Murchison Domain. See text for details.

proto-arc–fore arc environment facilitated melting producing the LDT in the deeper part of the mantle above the subducting oceanic slab (Fig.8.5c). The fluid driven off the subducted slab into the wedge, along with decompression melting, caused a high degree of partial melting in the deeper mantle (cf. Pearce and Parkinson, 1993) (Fig. 8.5c). The degree of depletion of this mantle domain was probably slightly less than for the LET melting domain, as suggested by slightly higher MgO, Ni and Cr and slightly lower Y and Zr contents in LDT than LET. About 15% to 25% partial melting is required for the LDT and is therefore in agreement with the values quoted by Pearce and Parkinson (1993).

The Yalgoo high-Mg andesite was also formed from the melt derived from the subducting slab within a hot subduction zone followed by interaction with a metasomatized mantle above the stability field of garnet (Fig. 8.5d). The closure of the ridge-forearc basin was initiated after the eruption of the high-Mg# andesite, due to some reorganization of the tectonic regime. This may have occurred due to shifting of the active zone of melting feeding into the ridge above the subducting slab or increased push from either the oceanic slab to the south or the cratonic block to the north (Fig. 8.5d,e).

Closure of the ridge-forearc basin was quickly followed by progression of continental lithosphere into the collision front, which led to thrusting of the mafic volcanic rocks over the continental crust and eventually resulted in accretion of the LET and LDT, with older felsic crust now serving as basement to the greenstones (Fig. 8.5d,e). This scenario is analogous to accretion of an (incomplete!) ophiolite, as documented in the 3.8 Ga Isua supracrustal belt in Greenland, which represents a suprasubduction-zone fore-arc basin ophiolite, as suggested by Furnes et al. (2009). If this is correct, the minor ultramafic cumulates (Hallberg et al., 2002) in the Yalgoo area may represent the ultramafic component of the ophiolite. Alternatively, the Yalgoo mafic volcanic rocks may represent allochthonous intraoceanic Archean greenstone terranes as reported from the 2.8 Ga Frotet-Evans greenstone belt, Quebec, and the 2.86 Ga Pickle Crow assemblage, Ontario, Canada (Boily and Dion, 2002; Hollings and Kerrich, 2004). Therefore, LET and LDT might represent allochthonous dismembered fragments of Luke Creek Group oceanic crust. The structural and tectonic evidence for accretion would be preserved in the form of NW- SE shear zone or faults. However, identifying the faults and shear zones related to this event is difficult, as the area was later affected by major episodes of deformation.

A heterogeneous mantle domain must have existed around the subduction zone or beneath the continent as exemplified by melt contributions with varying chemical

signatures and ages in the source of the granodiorites (see sections 5.5.4 and 8.4.2). Partial melting ensued within the subcontinental lithospheric mantle and probably in the upper part of the subducting oceanic crust (Fig. 8.5f). Initial melting might have been initiated at relatively high-pressure, leaving garnet amphibolite and amphibolite residue at relatively low-pressure. As subduction progressed, the slab would have descended enough to enter the field of rutile stability under high-pressure and produced a second pulse of melt leaving rutile eclogite residue. Both melts might have interacted with the overlying metasomatized mantle during ascent. The two melt pulses eventually interacted with each other and would have incorporated a Lu-Hf isotopic signature of ~3.6 and 3.3 Ga crust and ~3.0 to 2.94 Ga felsic crust most probably in the lower continental block and became a composite source for the ~2.76 Ga calc-alkaline granodiorites (LLG and YEG), which were emplaced as volcanic arc granitoids through the mafic volcanics in the Yalgoo area. Porphyritic microgranodiorites with a similar chemical signature (calc-alkaline) and age (~2.76 Ga) were extruded as minor volcanics/dykes through older lithologies (Fig. 8.5f).

Biotite monzogranite emplacement post-dated the formation of granodiorites by ~120 Ma. The high thermal pulse generated as a consequence of continued subduction triggered melting in the middle/upper crust. This part of the crust must have contained recycled Hadean (~4.1 Ga) crust as shown by the Lu-Hf signature from the zircons and the melt inherited the Hadean isotopic signature and became the parental melt for the biotite monzogranite as the last stage, or after the cessation, of subduction (Fig. 8.5g). The melt for the biotite hornblende monzogranite would be generated at the same time or just after the generation of melt for the biotite monzogranite by mixing of a mid-crustal source and a mafic component at a shallow level. The heat input required for melting most probably would have originated within the continental crust as a result of crustal thickening (Fig. 8.5g). The parental melt intruded into the ~2.76 Ga granodiorite (LLG) as a small mesozonal pluton (see section 7.3.3).

The Au mineralizing solutions probably were channeled during the development of the NNW-SSE trending Noongal Shear Zone, an indirect age for this event was estimated at ~2.63 Ga (Oliver, 1999). Taking the age of ~2.63 Ga for the development of the NSZ (which might have affected the fabric of the biotite hornblende monzogranite) and the trend (NNW) of the Brilliant open pit, which represents the trend of the biotite hornblende monzogranite, the biotite hornblende monzogranite appears to have been emplaced during D3 or the initial stage of development of the NSZ (D4) (Table 8.1). This gives an indirect estimation of the emplacement age of the biotite hornblende monzogranite as between the

development of the Noongal anticline (D3) at ~2.68 to 2.64 Ga (Watkins and Hickman, 1990) and the deformation of the biotite monzogranite at ~ 2.63 Ga (Oliver, 1999).

The Paleoproterozoic event in the Yalgoo area is marked by the emplacement of a ~1.85 Ga dolerite dyke, having a similar chemical signature to the LDT (Figs. 6. 8 and 6.10). A high degree (~20%-24%) of partial melting of a highly-depleted mantle source is required to supply the melt for this dyke. A Lu-Hf isotopic study of the dated dyke suggests incorporation of a 2.94 Ga component in the source. The emplacement of the 1.85 Ga east-northeast trending dyke so far south of the collision zone between the Yilgarn and Pilbara cratons suggests it was not related to this or to the presence of a late Paleoproterozoic event (compared to the emplacement of ~2.42 Ga Widgiemooltha dyke swarm) in this part of the Yilgarn Craton. The Fe-rich fractionated mafic dyke (sample PD 001/1) is the first report of a fractionated dolerite dyke in the Murchison, the geochemical characteristics of which suggest derivation from mixing of an enriched source (metasomatized lithospheric mantle) and a juvenile mafic magma.

Two critical issues still surround the genesis and tectono-magmatic settings of the mafic dyke. First, the presence of almost similar parental melts for both the LDT and 1.85 Ga mafic dyke implies either that the reservoir for these two lithologies was essentially unchanged for ~1 Ga (considering an indirect minimum age for the Murrouli Basalt of ~2.82 Ga by Van Kranendonk and Ivanic (2009) or that they were similar but not related. Second, the two different crustal domains that supplied melts for the tholeiitic dykes and Fe-rich tholeiitic dyke were only separated by a very small distance (~ 4km between sample MA 26 and PD 001/1). In addressing the first issue, it seems unlikely, but not impossible, to have this unchanged character of the mantle reservoir. It is noteworthy that the Yilgarn Craton had stabilized by ~2.64 Ga. Combined U-Pb SHRIMP/TIMS dating and Lu-Hf /Sm-Nd isotopic study of all three dykes in the north Yalgoo area might substantiate the proposed model or provide an alternative explanation. To address the second issue, it seems unlikely that two separate magmatic events, which produced only three dykes of two types, were restricted to an area of only ~12 km x 7.5 km (Fig. 6.1). The question arises whether the 1.85 Ga tholeiitic dyke and Fe-rich fractionated mafic dykes are more widely distributed across this part of the Murchison Domain. Further work is required to test this.

References

Abbott, D.H., Drury, R. and Smith, W.H.F., 1994. Flat to steep transition in subduction style. Geology, 22: 937-940.

Abbott, D.H. and Hoffman, S.E., 1984. Archaean plate tectonics revised. I. Heat flow, spreading rate, and the age of subducting oceanic lithosphere and their effects on the origin and evolution of continents. Tectonics, 3: 429-448.

Ahmat, A.L., 1990. Windimurra Complex, in Geology and Mineral Resources of Western Australia. Western Australia Geological Survey, Memoir 3: 120-124.

Anderson, J.L. and Smith, D.R., 1995. The effects of temperature and fO2 on the Al-in-hornblende barometer. American Mineralogist, 80: 549–559.

Angerer, T., Kerrich, R. and Hagemanna, S.G., 2013. Geochemistry of a komatiitic, boninitic, and tholeiitic basalt association in the Mesoarchean Koolyanobbing greenstone belt, Southern Cross Domain, Yilgarn craton: Implications for mantle sources and geodynamic setting of banded iron formation. Precambrian Research, 224: 110-124.

Archibald, N.J., 1982. Structure, lithological association units and gold mineralization, Mt. Magnet area. In: J.L. BAXTER (Editor), Archaean geology of the southern Murchison, Excursion guide. Geological Society of Australia (W.A. Division). pp. 15-27.

Archibald, N.J., Bettenay, L.F., Bickle, M.J. and Groves, D.I., 1981. Evolution of Archaean crust in the Eastern Goldfields Province of the Yilgarn Block. In: J.E. Glover and D.I. Groves (Editors), 2nd International Archaean Symposium, 1980 Proceedings. Geological Society of Australia, Perth, pp. 491-504.

Arndt, N.T., 2008. Komatiite. Cambridge University Press, Cambridge.

Baker, M.B., Grove, T.L. and Price, R., 1994. Primitive basalts and andesites from the Mt. Shasta region N. California: products of varying melt fraction and water content, Contributions to Mineralogy and Petrology.

Barker, F., 1979. Trondhjemites, Dacites, and Related Rocks. Developments in Petrology 6. Elsevier Amsterdam, Oxford, New York: 659.

Barker, F. and Arth, J.G., 1976. Generation of trondhjemite-tonalite liquids and Archaean bimodal trondhjemite-basalt suites. Geology, 4: 596-600.

Barley, M.E. et al., 2003. An integrated geological and metallogenic framework for the eastern Yilgarn Craton: developing geodynamic models of highly mineralised Archaean granite-greenstone terranes, Amira International Limited, AMIRA Project no. P624 (unpublished report).

Barley, M.E., Kerrich, R., Reudavy, I. and Xie, Q., 2000. Late Archaean Ti-rich, Al-depleted komatiites and komatiitic volcaniclastic rocks from the Murchison Terrane in Western Australia. Australian Journal of Earth Sciences, 47: 873-883.

Baxter, J.L., 1974. Murgoo, Western Australia: Western Australia Geological Survey, 1:250000 Geological Series Explanatory Notes.

Baxter, J.L., 1982. The regional setting of the southern Murchison. In: J.L. Baxter (Editor), Archaean geology of the southern Murchison. Geological Society of Australia (W.A. Division) Excursion Guide, pp. 1-5.

Baxter, J.L. and Lipple, S.L., 1985. Perenjori, Western Australia: 1:250000 Geological Series Explanatory Notes. Western Australia Geological Survey.

Baxter, J.L., Lpple, S.L. and Marston, R.I., 1983. 1 :250000 Geological Series Explanatory Notes Kirkalocka, Western Australia. Western Australia Geological Survey.

Beard, J.S., 1976. Vegetation survey of Western Australia, Murchison 1:1000000 Vegetation Series, Explanatory Notes on Sheet 6. University of Western Australia Press.

Beard, J.S., Abitz, R.J. and Lofgren, G.E., 1993. Experimental melting of crustal xenoliths from Kilbourne Hole, New Mexico and implications for the contamination and genesis of magmas. Contributions to Mineralogy and Petrology, 115: 88–102.

Bédard, J.H., 1999. Petrogenesis of Boninites from the Betts Cove Ophiolite, Newfoundland, Canada: identification of subducted source components. Journal of Petrology, 40: 1853-1889.

Belousova, E.A., Griffin, W.L. and O'Reilly, S.Y., 2006. Zircon crystal morphology, trace element signatures and Hf isotope composition as a tool for petrogenetic modelling: Examples from eastern Australian granitoids. Journal of Petrology, 47: 329-353.

Bennett, V.C., Brandon, A.D. and Nutman, A.P., 2007. Coupled 142Nd-143Nd Isotopic Evidence for Hadean Mantle Dynamics. Science 318: 1907-1910.

Bennett, V.C., Brandon, A.D. and Nutman, A.P., 2007. Coupled 142Nd-143Nd Isotopic Evidence for Hadean Mantle Dynamics. Science, 318: 1907-1910.

Blichert-Toft, J. and Albarede, F., 1997. The Lu-Hf geochemistry of chondrites and the evolution of the mantle-crust system. Earth and Planetary Science Letters, 148: 243– 258.

Blichert-Toft, J. and Albarede, F., 2008. Hafnium isotopes in Jack Hills zircons and the formation of the Hadean crust. Earth and Planetary Science Letters, 265: 686–702.

Blundy, J.D. and Holland, T.J.B., 1990. Calcic amphibole equilibria and a new amphibole-plagioclase geothermometer. Contributions to Mineralogy and Petrology, 104: 208–224.

Boily, M. and Dion, C., 2002. Geochemistry of boninite-type volcanic rocks in the Frotet-Evans greenstone belt, Opatica subprovince, Quebec: implications for the evolution of Archaean greenstone belts. Precambrian Research, 115: 349–371.

Borodina, N.S., Fershtater, G.B. and Votyakov, S.L., 1999. The oxidation ratio of iron in coexiting biotite and hornblende from granitic and metamorphic rocks: the role of P, T, and $f(O2)$ Canadian Mineralogist, 37: 1423-1429.

Boulllier, A.-M. and Robert, F., 1992. Palaeoseismic events recorded in Abinbi gold-quartz vein networks, Val d'or, Abitibi, Quebec, Canada. Journal of Structural Geology, 14: 161-179.

Browing, P., Groves, D.I., G., B.J. and Rosman, K.J.R., 1987. Lead isotopic constraints on the age and source of gold mineralization in the Archaean Yilgam Block, Western Australia. Economic Geology, 82: 971-986

Brown, P.E., 1989. FLINCOR: a microcomputer program for the reduction and investigation of fluid inclusion data. American Mineralogist, 74: 1390- 1393.

Brown, P.E., 1989. FLINCOR: a microcomputer program for the reduction and investigation of fluid inclusion data. American Mineralogist, 74: 1390- 1393.

Brown, P.E. and Lamb, W.M., 1986. Mixing of H20-CO2 in fluid inclusions; Geometry and Archean gold deposits. Geochimica et Cosmochimica Acta, 50: 474-452.

Browning, P., Groves, D.I., Blockley, J.G. and Rosman, K.J.R., 1987. Lead isotopic constraints on the age and source of gold mineralization in the Archaean Yilgam Block, Western Australia. Economic Geology, 82: 971-986.

Bucci, L.A., Hagemann, S.G., Groves, D.I. and Standing, J.G., 2002. The Archaean Chalice gold deposit: a record of complex, multistage, high-temperature hydrothermal activity and gold mineralisation associated with granitic rocks in the Yilgarn Craton, Western Australia. Ore Geology Reviews, 19: 23-67.

Bucci, L.A. et al., 2004. Timing and Duration of High-Temperature Gold Mineralization and Spatially Associated Granitoid Magmatism at Chalice, Yilgarn Craton, Western Australia. Economic Geology, 99: 1123-1144.

Butcher, A.R. et al., 2000. Advances in the quantification of gold deportment by QEMSCAN, Seventh Mill Operators Conference. AusIMM, Kalgoorlie, pp. 267–272.

Cabri, L.J., 1965. Phase relations in the Au-Ag-Te system and their mineralogical significance. Economic Geology, 60: 1569-1606.

Camm, G.S., Butcher, A.R., Pirrie, D., Hughes, P.K. and Glass, H.J., 2003. Secondary mineral phases associated with a historic arsenic calciner identified using automated scanning electron microscopy; a pilot study from Cornwall, U.K. Minerals Engineering, 16: 1269–1277.

Camm, G.S., Glass, H.J., Bryce, D.W. and Butcher, A.R., 2004. Characterisation of a mining-related arsenic-contaminated site, Cornwall, UK. Journal of Geochemical Exploration, 82: 1–15.

Campbell, I.H., 2001. Identification of ancient mantle plumes. In: R.E. Ernst (Editor), Mantle plumes: their identification through time. Geological Society of America, Special Publication, pp. 5-22.

Carr, M.J., 2006. Igpet for Windows. Terra Softa Inc.

Cassidy, K.F., 1992. Archaean granitoid-hosted gold deposits in greenschist to amphibolite facies terrains: A high P –T to low P –T depositional continuum equivalent to greenstone-hosted deposits. Ph.D. (unpublished) Thesis, University of Western Australia, 296 pp.

Cassidy, K.F., Barley, M.E., Groves, D.I., Perring, C.S. and Hallberg, J.A., 1991. An overview of the nature, distribution and inferred tectonic setting of granitoids of the late- Archaean Norseman-Wiluna Belt. Precambrian Research, 51: 51-83.

Cassidy, K.F. and Bennett, J.M., 1993. Gold mineralization at the Lady Bountiful Mine, Western Australia: an example of a granitoid hosted Archaean lode gold deposit. Mineralium Deposita, 28: 388-408.

Cassidy, K.F. and Bennett, J.M., 1993. Gold mineralization at the Lady Bountiful Mine, Western Australia: and example of a granitoid-hosted Archaean lode gold deposit. Mineralium Deposita, 28: 388-408.

Cassidy, K.F., Champion, D.C. and Huston, D.L., 2005. Crustal evolution constraints on the metallogeny of the Yilgarn Craton, in Mineral Deposit Research. In: J. Mao and F.P. Bierlein

(Editors), Meeting the Global Challenge Proceedings of the Eighth Biennial SGA Meeting. Berlin/Heidelberg, Springer, Beijing, China, 2005, pp. 901–904.

Cassidy, K.F. et al., 2006. A revised geological framework for the Yilgarn Craton, Western Australia. Western Australia Geological Survey, Record 2006/8: 8.

Cassidy, K.F. et al., 2002. Characterisation and metallogenic significance of Archaean granitoids of the Yilgarn Craton, Western Australia. , Minerals and Energy Research Institute of Western Australia (MERIWA).

Cassidy, K.F., Groves, D.I. and Mcnaughton, N.J., 1998. Late-Archaean granitoid-hosted lode-gold deposits, Yilgarn Craton, Western Australia: Deposits charactersistics, crustal architecture and implications for ore genesis. Ore Geology Reviews, 13: 65-102.

Cawood, P.A. and Tyler, I.M., 2004. Assembling and reactivating the Proterozoic Capricorn Orogen: lithotectonic elements, orogenies, and significance. Precambrian Research, 128: 201-218.

Champion, D.C. and Cassidy, K.F., 2000. Granites of the northern Eastern Goldfields: their distribution, age, geochemistry, petrogenesis, relationship with mineralisation, and implications for tectonic environment.

Champion, D.C. and Cassidy, K.F., 2002. Granites in the Leonora-Laverton transect area, north eastern Yilgarn Craton. In: K.F. Cassidy (Editor), Geology, geochronology and geophysics of the north eastern Yilgarn Craton, with an emphasis on the Leonora-Laverton transect area. Geoscience Australia, Record 2002/18, pp. 13-35.

Champion, D.C. and Cassidy, K.F., 2002. Granites in the Leonora-Laverton transect area, north eastern Yilgarn Craton. Record 2002/, Geoscience Australia.

Champion, D.C. and Cassidy, K.F., 2007. An overview of the Yilgarn Craton and it's crustal evolution. Geoscience Australia Record 2007/14: 249.

Champion, D.C. and Sheraton, J.W., 1993. Geochemistry of granitoids in the Leonora-Laverton region, Eastern Goldfields Province. Australian Geological Survey Organisation Record, 54: 39-46.

Champion, D.C. and Sheraton, J.W., 1997. Archaean granitoids of the northern Eastern Goldfields Province, Yilgarn Craton, Australia: Constraints on crustal growth. Precambrian Research, 83: 109-132.

Champion, D.C. and Smithies, R.H., 2001. AGSO-Geoscience Australia, Record 2001. 37: 134-136.

Champion, D.C. and Smithies, R.H., 2004. Archean granites. Geoscience Australia, 2004: 13-17.

Champion D.C. and Smithies, R.H., 2007. Geochemistry of the Paleoarchean granites of the East Pilbara Terrane, Pilbara Craton, Western Australia: Implications for early Archean custal growth. In: M.J. van Kranendonk, R.H. Smithies and V. Bennett (Editors), Earth's Oldest Rocks, Developments in Precambrian Geology Elsevier, Amsterdam.

Chappell, B.W., 1999. Aluminum saturation in I- and S-type granites and the characterization of fractionated haplogranites. Lithos, 46: 535–551.

Chappell, B.W. and White, A.J.R., 1974. Two contrasting granite types. Pacific Geology, 8: 173-174.

Chappell, B.W. and White, A.J.R., 1992. I- and S-type granites in the Lachlan Fold Belt. Transactions of the Royal Society of Edinburgh: Earth Sciences, 83: 1-26.

Chappell, B.W. and White, A.J.R., 2001. Two contrasting granite types: 25 years later. Australian Journal of Earth Science, 48: 489-499.

Chen, S.F., Libby, J.W., Greenfield, J.E., Wyche, S. and Riganti, A., 2001. Geometry and kinematics of large arcuate structures formed by impingement of rigid granitoids into greenstone belts during progressive shortening. Geology, 29: 283–286.

Chen, S.F., Riganti, A., Wyche, S., Greenfield, J.E. and Nelson, D.R., 2003. Lithostratigraphy and tectonic evolution of contrasting greenstone successions in the central Yilgarn Craton, Western Australia. Precambrian Research, 127: 252-266.

Clark, M.E., Archibald, N.J. and Hodgson, C.J. (Editors), 1986. The structural and metamorphic setting of the Victory gold mine at Kambalda, Western Australia Proceedings of Gold'86, An International Symposium on the Geology of Gold. Gold '86, Toronto, 243-254 pp.

Clark, M.E., Hodgson, C.J. and Fu, M., 1989. Wall-Rock alteration, Victory gold mine, Kambalda, western Australia: Processes and P-T-X CO2 conditions of metamorphism In: R.R. Keays, W.R.H. Ramsay and Groves. D.I. 6 (Editors), The Geology of Gold Deposits: The Perspective in 1988. Economic Geology Monograph.

Clifford, B.A., MacMahon, M. and Sheppy, N., 1990. Geological setting of the Scuddles volcanogenic massive sulphide deposits at Golden Grove. In: S. Ho, J. Glover, J.S. Myers and J.R. Muhling (Editors), Third International Archean Symposium Excursion Guidebook. University of Western Australia, Perth, Western Australia, pp. 190-195.

Coish, R.A., 1977. Ocean floor metamorphism in the Betts Cove ophiolite, Newfoundland:

Contributions to Mineralogy and Petrology. Newfoundland: Contributions to Mineralogy and Petrology, 60: 255-270.
Collins, G. and Steuart, P., 2000. Annual report for the period of 1 January to 31 December 2000. E59/642,P59/1397, Anglogold Australasia Limited, Bridgewell.
Collins, W.J., Beams, S.D., White, A.J.R. and Chappell, B.W., 1982. Nature and origin of A-type granites with particular reference to southeastern Australia. Contributions to Mineralogy and Petrology 80: 189-200.
Compston, W., Williams, I.S. and Meyer, C., 1984. U-Pb geochronology of zircon from Lunar breccia 73217 using a sensitive high-mass resolution ion microprobe. Journal of Geophysical Research, 89B: 525-534.
Condie, K.C., 1994. Greenstones through time. In: K.C. Condie (Editor), Archean Crustal Evolution. Elsevier, Amsterdam, pp. 85-120 (Chapter 3).
Condie, K.C., 2005. TTGs and adakites: are they both slab melts? Lithos, 80(1-4): 33-44.
Corfu, F., Hanchar, J.M., Hoskin, P.W.O. and Kinny, P., 2003. Atlas of zircon textures. Zircon. Reviews in Mineralogy and Geochemistry, 53. Mineralogical Society of America, 500-468 pp.
Cox, K.J., Bell, J.D. and Pankhurst, R.J., 1979. The interpretation of igneous rocks. Allen and Unwin, London, 450 pp.
Cox, S.F., Knackstedt, M.A. and Braun, J., 2001. Principles of structural control on permeability and fluid flow in hydrothermal systems. I. In: J. Richards (Editor), Deformation, Fluid Flow and Ore Deposits. Society of Economic Geologists Short Course Proceedings, pp. 1-24.
Crawford, A.J., Beccaluva, L. and Serri, G., 1981. Tectono-magmatic evolution of the West Philippine-Mariana region and the origin of boninites. Earth and Planetary Science Letters, 54: 346-356.
Crawford, A.J., Fallon, T.J. and Green, D.H., 1989. Classification, petrogenesis and tectonic setting of boninites. Boninites and Related Rocks. Unwin Hyman, London: 1–49.
Cumming, G.L. and Richards, J.R., 1975. Ore-lead isotope ratios in a continuously changing earth. Earth and Planetary Science Letters, 28: 155-171.
Czarnota, K., et al., 2010. Geodynamics of the eastern Yilgarn Craton. Precambrian Research 183(2): 175-202.
Dahl, N., McNaughton, N.J. and Groves, D.I., 1987. Trace element and lead isotopic composition of pyrites as guides to gold and base-metal mineralization-a pilot study. Western Australia Mineral and Petroleum Research Institute. Report 22: 57.
Dale, G.R. and Goldrick, S., 1994. Noongal Project Summary Report, Cambrian Resources NL.
Dalstra, H.J., Ridley, J.R., Bloem, E.J.M. and Groves, D.I., 1999. Metamorphic evolution of the central Southern Cross Province, Yilgarn Craton, Western Australia. Australian Journal of Earth Sciences, 46: 765-784.
Davidson, J.P., 1996. Deciphering mantle and crustal signatures in subduction zone magmatism. Subduction Top to Bottom. Geophysical Monograph 96, American Geophysical Union, Washington, DC: 251-262.
de la Hunty, L.E., 1973. Cue, Western Australia: Western Australia Geological Survey, 1:250000 Geological Series Explanatory Notes.
Deschamps, A. and Lallemand, S., 2003. Geodynamic setting of Izu–Bonin–Mariana boninites. In: R.D. Larter and P.T. Leat (Editors), Intra-oceanic subduction systems: Tectonic and magmatic processes. Geological Society of London Special Publications, vol. 219, pp. 163-185.
Dilek, Y., Furnes, H. and Shallo, M., 2007. Suprasubduction zone ophiolite formation along the periphery of Mesozoic Gondwana. Gondwana Research, 11: 453-475.
Dilek, Y. and Thy, P., 2009. Island arc tholeiite to boninitic melt evolution of the Cretaceous Kizildag (Turkey) ophiolite: Model for multi-stage early arc-forearc magmatism in Tethyan subduction factories. Lithos, 113,.044: 68-87.
Dostal, J. and Mueller, W.U., 1997. Komatiite flooding of a rifted Archean rhyolitic arc complex: geochemical signature and tectonic significance of the Stoughton- Roquemaure Group, Abitibi Greenstone Belt, Canada. The Journal of Geology, 105(5): 545-564.
Dostal, J., Mueller, W.U. and Murphy, J.B., 2004. Archean molasse basin evolution and magmatism, Wabigoon Subprovince,. Canada Journal of Geology, 112: 435-454.
Drummond, M.S. and Defant, M.J., 1990. A model for trondhjemite-tonalite-dacite genesis and crustal growth via slab melting - Archean to modern comparisons. Journal of Geophysical Research, 95: 21503-21521.
Duuring, P., Cassidy, K.F. and Hagemann, S.G., 2007. Granitoid-associated orogenic, intrusion-

related, and porphyry style metal deposits in the Archean Yilgarn Craton, Western Australia. Ore Geology Reviews, 32: 157-186.

Duuring, P. and Hagemann, S.G., 2000. A thrust-ramp model for gold mineralisation at the Archaean trondhjemite-hosted Tarmoola deposit, Leonora Camp, Western Australia. Miner Deposita (35): 402-421.

Duuring, P., Hagemann, S.G., Cassidy, K.F. and Johnson, C.A., 2004. Hydrothermal alteration, ore fluid characteristics, and gold depositional processes along a trondhjemite-komatiite contact at Tarmoola, Western Australia. Economic Geology, 99: 423–451.

Duuring, P., Hagemann, S.G. and Groves, D.I., 2000. Structural setting, hydrothermal alteration, and gold mineralisation at the Archaean syenite-hosted Jupiter deposit, Yilgarn Craton, Western Australia. Mineralium Deposita, 35: 402-421.

Duuring, P., Hagemann, S.G. and Love, R.J., 2001. A thrust ramp model for gold mineralization at the Archean trondhjemite-hosted Tarmoola deposit: the importance of heterogeneous stress distributions around granitoid contacts. Economic Geology, 96: 1379–1396.

Eby, G.N., 1990. The A-type granitoids: A review of their occurrence and chemical characteristics and speculations on their petrogenesis. Lithos., 26: 115-134.

El Bouseily, A.M. and El Sokkary, A.A., 1975. The relation between Rb, Ba, and Sr in granitic rocks. Chemical Geology, 16: 207-219.

Elias, M., 1982. Belele, Western Australia: Western Australia Geological Survey, 1:250000 Geological Series Explanatory Notes.

Fletcher, I.R., Dunphy, J.M., Cassidy, K.F. and Champion, D.C., 2001. Compilation of SHRIMP U–Pb geochronology data, Yilgarn Craton, Western Australia, 2000–01, Geoscience Australia, Record 2001/47, pp. 110.

Fletcher, I.R., Libby, W.G. and Rosman, K.J.R., 1987. Sm-Nd dating of the 2411 Ma Jimberlarna dyke, Yilgarn Block, Western Australia. Australian Journal of Earth Sciences, 34: 523-525.

Fletcher, I.R., Rosman, k.J.R., Williams, I.R., Hickman, A.H. and Baxter, J.L., 1984. Sm-Nd geochronology of greenstone belts in the Yilgam Block, Western Australia. Precambrian Research, 26: 333-336.

Foden, J.D., Buick, I.S. and Mortimer, G.E., 1984. The petrology and geochemistry of granitic gneisses from the East Arunta inlier, Central Australia: Implications for Proterozoic crustal development. Precambrian Research, 40/41: 233-259.

Foley, S., 2008. A trace element perspective on Archean crust formation and on the presence or absence of Archean subduction In: K.C. Condie and V. Pease (Editors), When Did Plate Tectonics Begin? Geological society of America Special Paper 440, pp. 31-50.

Foley, S., Tiepolo, M. and Vanucci, R., 2002. Growth of early continental crust controlled by melting of amphibolite in subduction zones. Nature, 417: 837-840.

Foley, S.F., Barth, M.G. and Jenner, G.A., 2000. Rutile/melt partition coefficients for trace elements and an assessment of the influence of rutile on the trace element characteristics of subduction zone magmas. Geochimica et Cosmochimica Acta, 64: 933-938.

French, E.J., Heaman, L.M. and Chacko, T., 2002. Feasibility of chemical U-Th-total Pb baddeleyite dating by electron microprobe Chemical Geology, 188(1-2): 85-104.

Furnes, H., de Wit, M., Staudigel, H., Rosing, M. and Muehlenbachs, K., 2007. A vestige of Earth's oldest ophiolite. Science, 315: 1704–1707.

Furnes, H., Rosing, M., Dilek, Y. and de Wit, M., 2009. Isua supracrustal belt (Greenland)—A vestige of a 3.8 Ga suprasubduction zone ophiolite, and the implications for Archean geology. Lithos, 113: 115-132.

Furnes, H.A.E., Shimron, A.E. and Roberts, D., 1985. Geochemistry of Pan-African volcanic arc sequences in SE Sinai Peninsula and plate tectonic implications. Precambrian Research, 29: 359-382.

Gamble, J., Wright, J. and Baker, J., 1993. Seafloor geology and petrology in the oceanic to continental transition zone of the Kermadec–Havre–Taupo volcanic zone arc system, New Zealand. New Zealand Journal of Geology and Geophysics 36: 417-435.

Gamble, J.A., Wright, I.C., Woodhead, J.D. and McCulloch, M.T., 1995. Arc and back-arc geochemistry in the southern Kermadecarc–Ngatoro Basin and offshore Taupo Volcanic Zone, SW Pacific. In: J.L. Smellie (Editor), Volcanism Associated with Extension at Consuming Plate Margins. Geological Society (special publication), pp. 193-212

Gao, S., 2002. Determination of forty two major and trace elements in USGS and 648 NIST SRM glasses by laser ablation-inductively coupled plasma-mass 649 spectrometry. Geostandards Newsletter, 26(2): 181–196.

Gao, S. et al., 2002 Determination of forty two major and trace elements in USGS and NIST SRM

glasses by laser ablation inductively coupled plasma-mass spectrometry Geostandard Newsletter Journal of Geostandard Geoanalysis 26: 191-196.
Gee, R.D., 1975. Regional Geology of the Archaean nuclei of the Western Shield. In: C.L. Knight (Editor), Economic Geology of Australia and Papua New Guinea. Australasian Institute of Mining and Metallurgy, pp. 43-53.
Gee, R.D., 1979. Structure and tectonic style of the Western Australia shield. Tectonophysics, 58: 327-369.
Gee, R.D., Baxter, J.L., Wilde, S.A. and Williams, I.R., 1981. Crustal development in the Yilgarn Block. In: J.E. Glover and D.I. Groves (Editors), 2nd International Archaean Symposium, Perth, W.A. 1980, Proceedings. Geological Society of Australia, Special Publication No. 7, pp. 43-56.
Geological Survey of Western Australia, 2002. Tectonic Map of Western Australia. Department of Industry and Resources, Western Australia.
Geological Survey of Western Australia, 2005. Compilation of geochronology data, June 2005 update: Western Australia Geological Survey.
Geological Survey of Western Australia, 2008. Compilation of geochronology information 2008 update. Geological Survey of Western Australia.
Gill, J.B., 1981. Orogenic Andesites and Plate Tectonics. Springer-Verlag, Berlin: 358
Glikson, A.Y., 1979. Early Precambrian tonalite–trondhjemite sialic nuclei. Earth Science Review, 15: 1-73.
Glikson, A.Y. and Lambert, I.B., 1976. Vertical zonation and petrogenesis of the early Precambrian crust in Western Australia. Tectonophysics, 30: 55-89.
Goodall, W.R., Leatham, J.D. and Scales, P.J., 2005a. A new method for determination of preg-robbing in gold ores. Minerals Engineering, 18(12): 1135–1141.
Goodall, W.R. and Scales, P.J., 2007. An overview of the advantages and disadvantages of the determination of gold mineralogy by automated mineralogy. Minerals Engineering, 20: 506–517.
Goodall, W.R., Scales, P.J. and Butcher, A.R., 2005b. The use of QEMSCAN and diagnostic leaching in the characterisation of visible gold in complex ores. Minerals Engineering, 18: 877–886.
Google Maps, 2012. Melville, Western Australia, Australia.http://maps.google.com/maps?f= q& source=s_q&hl=en&geocode=&q=300+Summit+.
Gottlieb, P., Wilkie, G., Sutherland, D. and Ho Tun, E., 2000. Using quantitative electron microscopy for process mineralogy applications. Journal of Minerals and Materials Characterisation and Engineering, 52 (4): 24–27.
Griffin, W.L., Belousova, E.A., Shee, S.R., Person, N.J. and O'Reilly, S.Y., 2004. Archaean crustal evolution in the northern Yilgarn Craton: U-Pb and Hf-isotope from detrital zircon. Precambrian Research, 131: 231-282.
Griffin, W.L. et al., 2000. The Hf isotope composition of cratonic mantle: LAM-MC-ICPMS analysis of zircon megacrysts in kimberlites. Geochimica et Cosmochimica Acta, 64: 133–147.
Griffin, W.L. et al., 2002. Zircon chemistry and magma mixing, SE China: in situ analysis of Hf isotopes, Tonglu and Pingtan igneous complexes. Lithos, 61(3-4): 237-269.
Grove, T.L. et al., 2003. Fractional crystallization and mantle melting controls on calc-alkaline differentiation trends. Contributions to Mineralogy and Petrology, 145: 515-533.
Groves, D.I. and Batt, W.D., 1984. Spatial and temporal variations of Archean metallogenic associations in terms of evolution of granitoid–greenstone terranes with particular emphasis on Western Australia. In: A. Kroner, G.N. Hanson and A.M. Goodwin (Editors), Archean Geochemistry. Springer-Verlag, Berlin, pp. 73-98.
Groves, D.I., Goldfarb, R.J., Robert, F. and Hart, C.J.R., 2003. Gold deposits in metamorphic belts: overview of current understanding, outstanding problems, future research, and exploration significance Economic Geology 98: 1-30.
Groves, D.I., Phillips, G.N., Ho, S.E. and Houston, S.M., 1985. The nature, genesis and regional controls of gold mineralization in Archaean greenstone belts of the Western Australian shield -a brief review. Geological Society of South Africa, Transactions, 88: 135-148.
Groves, R.H., 1981. Australian Vegetation. In: R.H. Groves (Editor). Cambridge University Press.
Guha, J., Lu, H., Dub, B., Robert, F. and Gagnon, M., 1991. Fluid characteristics of vein and altered wall rock in Archean mesothermal gold deposits. Economic Geology 86: 667-684.
Hagemann, S.G. and Brown, P.E., 1996. Geobarometry in Archean lode gold deposits. European Journal of Mineralogy, 8: 937-960.
Hagemann, S.G. and Cassidy, K.F., 1999. Archean high P-T, granitoid-hosted gold mineralisation at Westonia, Western Australia: II. P-T-X constraints on a gold-bearing paleohydrothermal

system in a high-grade terrain. In: C. Stanley et.al. (Editor), Mineral Deposits: Processes to Processing. A.A. Balkema, Rotterdam, pp. 1021-1024.

Hall, C., Gurnis, M., Sdrolias, M., Lavier, L.L. and Müller, R.D., 2003. Catastrophic initiation of subduction following forced convergence across fracture zones. Earth and Planetary Science Letters, 212: 15-30.

Harper, C.T. 2004. Overview of the geochemistry of Archean and Proterozoic rocks of the Phelps Lake region, Mudjatik Domain, Hearne Province. In: Summary of Investigations 2004, vol.2, Saskatchewan Geological Survey, Saskatchewan Industry Resources, Misc. Rep. 2004-4.2, CD-ROM, Paper A-7, 24p.

Hallberg, J., 1976. A petrochemical study of a portion of the western Yilgarn Block. FP13: 38.

Hallberg, J.A. and Giles, C.W., 1986. Archaean felsic volcanism in the northeastern Yilgarn Block, Western Australia. Australian Journal of Earth Science, 33: 413-427.

Hallberg, J.A., Hallberg, J. and Associates, 2002. Yalgoo greenstone belt mapping project. Unpublished report.

Hammarstrom, J.M. and Zen, E., 1986. Aluminum in hornblende: An empirical igneous geobarometer. American Mineralogist, 71: 1297-1313.

Hawkesworth, C.J., Gallagher, K., Hergt, J.M. and McDermott, F., 1993. Mantle and slab contributions in arc magmas Annual Reviews in the Earth and Planetary Sciences 21: 175-204.

Hemend, C. et al., 1993. The Heterogeneous Iceland plume: Nd–Sr–O isotope and trace element constraints. Journal of Geophysical Research, 98: 15833-15850.

Hémond, C. et al., 1993. The heterogeneous Iceland plume; Nd–Sr–O isotopes and trace elements constraints. Journal of Geophysical Research, 98: 15833-15850.

Hergt, J.M., Chappell, B.W., McCulloch, M.T., McDougall, I. and Chivas, A.R., 1989. Geochemical and isotopic constraints on the origin of the Jurassic dolerites of Tasmania Journal of Petrology 30: 841-883.

Hickey, R.L. and Frey, F.A., 1982. Geochemical characteristics of boninite series volcanics: implications for their source. Geochimica et Cosmochimica Acta, 46: 1099–2115.

Hickey-Vargas, R. and Reagan, M.K., 1987. Temporal variation of isotope and rare earth element abundances in volcanic rocks from Guam: implications for the evolution of the Mariana arc. Contributions to Mineralogy and Petrology, 97: 497-508.

Hine, R., Williams, I.S., Chappell, B.W. and White, A.J.R., 1978. Contrasts between I- and S-type granitoids of the Kosciusko Batholith. Journal of Geological Society of Australia, 25: 219-234.

Hirose, K., 1997. Melting experiments on lherzolite KLB-1 under hydrous conditions and generation of high-magnesian andesitic melts. Geology, 25: 42–44.

Hoffman, P.F., 1989. Precambrian geology and tectonic history of North America In: A.W. Bally and A.R. Palmer (Editors), The Geology of North America-an Overview. The Geology of North America. A. Boulder, CO: Geological Society of America, pp. 447-512.

Hoffmann, J.E. et al., 2011. Mechanisms of Archean crust formation inferred from high-precision HFSE systematics in TTGs. Geochimica et Cosmochimica Acta, 75: 4157–4178.

Holden, D., 2004. Resource report on the Melville deposit at the Yalgoo north gold project Yalgoo, Western Australia, Prosperity Resources Limited.

Holland, T. and Blundy, J., 1994. Non-ideal interactions in calcic amphiboles and their bearing on amphibole-plagioclase thermometry. Contributions to Mineralogy and Petrology, 116: 433–447.

Holland, T.B.J., 2002. Hornblende-Plagioclase Thermometry (HB-PLAG) Department of Earth Sciences - Cambridge University: Cambridge, GB.

Holland, T.J.B. and Powell, R., 2003. Activity–composition relations for phases in petrological calculations: an asymmetric multicomponent formulation. Contributions to Mineralogy and Petrology, 145: 492-501.

Hollings, P. and Kerrich, R., 2004. Geochemical systematics of tholeiites from the 2.86 Ga Pickle Crow Assemblage, northwestern Ontario: arc basalts with positive and negative Nb-Hf anomalies. Precambrian Research, 134(1-2): 1-20.

Hollings, P. and Kerrich, R., 2006. Light rare earth element depleted to enriched basaltic flows from 2.8 to 2.7 Ga greenstone belts of the Uchi Subprovince, Ontario, Canada. Chemical Geology, 227(3-4): 133-153.

Hollings, P., Wyman, D. and Kerrich, R., 1999. Komatiite-basalt-rhyolite volcanic associations in Northern Superior Province greenstone belts: significance of plume-arc interaction in the generation of the proto continental Superior Province. Lithos, 46: 137-161.

Hollister, L.S., Grissom, G.C., Peters, E.K., Stowell, H.H. and Sisson, V.B., 1987. Confirmation of the empirical correlation of Al in hornblende with pressure of solidification of calc-alkaline plutons. American Mineralogist, 72: 231-239.

Huizenga, J.M. and Touret, J.L.R., 1999. Fluid inclusions in shear zones, the case of the Umwindsi shear zone in the Harare–Shamva–Bindura greenstone belt, NE Zimbabwe. European Journal of Mineralogy 11: 1079-1090.

Iizuka, T. and Hirata, T., 2005. Improvements of precision and accuracy in in situ Hf isotope microanalysis of zircon using the laser ablation-MC-ICPMS technique. Chemical Geology, 220: 121-137.

Irvine, T.N., and Baragar, W.R.A., 1971. A guide to the chemical classification of the common volcanic rocks. Canadian Journal of Earth Sciences 8: 523-548.

Ishihara, S., 1977. The magnetite-series and ilmenite-series granitic rocks. Mining Geology, 27: 293-305.

Ishizuka, O. et al., 2006. Early stages in the evolution of Izu-Bonin arc volcanism: new age, chemical, and isotopic constraints. Earth and Planetary Science Letters, 250: 385-401.

Ivanic, T.J. et al., 2012. Zircon Lu–Hf isotopes and granite geochemistry of the Murchison Domain of the Yilgarn Craton: Evidence for reworking of Eoarchean crust during Meso-Neoarchean plume-driven magmatism. Lithos, 148: 112-127.

Ivanic, T.J., Wingate, M.T.D., Kirkland, C.L., Van Kranendonk, M.J. and Wyche, S., 2010. Age and significance of voluminous mafic- ultramafic magmatic events in the Murchison Domain, Yilgarn Craton. Australian Journal of Earth Sciences 57: 597-614.

Jahn, B.M., Glikson, A.Y., Peucat, J.J. and Hickman, A.H., 1981. REE geochemistry and isotopic data of Archaean silicic volcanics and granitoids from the Pilbara Block, Western Australia: implications for early crustal evolution. . Geochimica et Cosmochimica Acta, 45 1633-1652.

Jensen, L.S. and Pyke, D.R., 1982. Komatiites in the Ontario portion of the Abitibi Belt. In: N.T. Arndt and E.G. Nisbet (Editors), Komatiites, pp. 147-157.

Johnson, M.C. and Rutherford, M.J., 1989. Experimentally determined conditions in the Fish Canyon Tuff, Colorado, Magma Chamber. Journal of Petrology, 30: 711-737.

Jutson, J.T., 1950. The Physiography of Western Australia. Western Australia Geological Survey, Bulletin 95: 140-149.

Kelemen, P.B., Hanghoj, K. and Greene, A.R., 2004. One view of the geochemistry of subduction-related magmatic arcs, with emphasis on primitive andesite and lower crust. In: R.L. Rudnick (Editor), The Crust, Treatise on Geochemistry, vol. 3. Elsevier, pp. 593-659.

Kelemen, P.B., Yogodzinski, G.M. and Scholl, D.W., 2003. Along-strike variation in lavas of the Aleutian island arc: implications for the genesis of high-Mg# andesite and the continental crust. In: E. J. (Editor), Inside the subduction factory. American Geophysical Union. Geophysical Monograph, 138, pp. 223-274.

Kemp, A.I.S. et al., 2010. Hadean crustal evolution revisited: new constraints from Pb-Hf isotope systematics of the Jack Hills zircons. Earth and Planetary Science Letters, 296: 45-56.

Kent, A.J.R., Cassidy, K.F. and Fanning, C.M., 1996. Gold mineralisation synchronous with the final stages of cratonization, Yilgarn Craton, Western Australia: evidence from Sm–Nd and U–Pb ages of crosscutting (post-gold) dikes. Geology, 24: 879-882.

Kerrich, R., 1989. Geodynamic setting and hydraulic regimes: Shear zone hosted mesothermal gold deposits, . In: J.T. Bursnall (Editor), Mineralization and Shear Zones: Geological Association of Canada Short Course Notes pp. 89-128.

Kerrich, R. and Polat, A., 2006. Archean greenstone-tonalite duality: Thermochemical mantle convection models or plate tectonics in the early Earth global dynamics. Tectonophysics, 415: 141–165.

Kerrich, R., Polat, A., Wyman, D. and Hollings, P., 1999a. Trace element systematics of Mg-, to Fe-tholeiitic basalt suites of the Superior Province: implications for Archean mantle reservoirs and greenstone belt genesis. Lithos, 46: 163–187.

Kerrich, R., Wyman, D., Hollings, P. and Polat, A., 1999b. Variability of Nb/U and Th/La in 3.0 to 2.7 Ga Superior Province ocean plateau basalts: implications for the timing of continental growth and lithosphere recycling Earth and Planetary Science Letters, 168: 101-115.

Kerrich, R., Wyman, D., Fan, J. and Bleeker, W., 1998. Boninite series: Low Ti-tholeiite associations from the 2.7 Ga Abitibi greenstone belt. Earth and Planetary Science Letters, 164: 303-316.

Kerrich, R. and Xie, Q., 2002. Compositional recycling structure of an Archean superplume: Nb-Th-U-LREE systematics of Archean komatiites and basalts revisited. Contributions to Mineralogy and Petrology, 142: 476-484.

Keto, L.S. and Jacobsen, S.B., 1987. Nd and Sr isotopic variations of Early Paleozoic oceans. Earth

and Planetary Science Letters, 84: 27–41.
Kim, J. and Jacobi, R.D., 2002. Boninites: Characteristics and tectonic constraints, northeastern Appalachians. Physics and Chemistry of the Earth 27: 109-147.
Kinny, P.D., 1986. 3820 Ma zircons from a tonalitic Amîtsoq gneiss in the Godthåb district of southern West Greenland. Earth and Planetary Science Letters, 79: 337–347.
Kinny, P.D., Williams, I.S., Froude, D.O., Ireland, T.R. and Compston, W., 1988. Early Archaean zircon ages from orthogneisses and anorthosites at Mount Narryer, Western Australia. Precambrian Research, 38: 325-341.
Klein, E., Langmuir, C. and Staudigel, H., 1991. Geochemistry of basalts from the Southeast Indian Ridge, 115 degrees E-138 degrees European Journal of Geophysical Research, 96(2): 2089-2107.
Klein, M., Stosch, H.H. and Seck, H.A., 1997. Partitioning of high field-strength and rare-earth-elements between amphibole and quartz-dioritic melts: an experimental study. Chemical Geology, 138: 257-271.
Knight, J.T., Ridley, J.R. and Groves, D.I., 2000. The Archean Amphibolite Facies Coolgardie Goldfield, Yilgarn Craton,Western Australia: Nature, Controls, and Gold Field-Scale Patterns of Hydrothermal Wall-Rock Alteration. Economic Geology, 95: 49-84.
Kretz, R., 1983. Symbols for rock forming minerals American Mineralogist 68: 277–279
Kushiro, I., 1969. The system forsterite-diopside-silica with and without water at high pressures. American Journal of Science, 267A: 269–294.
Lang, J.R. and Baker, T., 2001. Intrusion-related gold systems: the present level of understanding. Mineralium Deposita, 36: 477-489.
Le Bas, M.J., Le Maitre, R.W., Streckeisen, A. and Zanethin, B., 1986. A chemical classification of volcanic rocks based on total alkalies-silica diagram. Journal of Petrology, 27: 745-750.
Le Maitre, R.W. (Editor), 2002. Igneous Rocks. A Classification and Glossary of Terms. Recommendations of the International Union of Geological Sciences Subcommission on the Systematics of Igneous Rocks. Cambridge University Press.
Leake, B.E. et al., 1997. Nomenclature of amphiboles: Report of the subcommittee on amphiboles of the International Mineralogical Association Commission on New Minerals and Mineral Names. Canadian Mineralogist, 35: 219-246.
Lipple, S.L., Baxter, J.L. and Marston, R.J., 1983. Ninghan, Western Australia: Western Australia Geological Survey, I :250000 Geological Series Explanatory Notes.
Litvinovsky, B.A., Steele, I.M. and Wickham, S.M., 2000. Silicic magma formation in overthickened crust: melting of charnockite and leucogranite at 15, 20 and 25 kbar. Journal of Petrology, 41: 717-737.
Loiselle, M.C. and Wones, D.R., 1979. Characteristics and origin of anorogenic granites. Geological Society of America Program with Abstracts, 11: 468.
Long, X.P. et al., 2011. The discovery of the oldest rocks in the Kuluketage area and its geological implications. China Earth Sciences, 54: 342-348.
Ludden, J.N., Gelinas, L. and Trudel, P., 1982. Archean metavolcanics from the Rouyn-Noranda district Abitibi greenstone belt, Quebec. 2.Mobility of trace elements and petrogenetic constraints Canadian Journal of Earth Sciences, 19: 2276–2287.
Ludwig, K.R., 2001. User manual for Isoplot/Ex rev. 2.49. A geochronological toolkit for Microsoft Exel. 1a, Berkeley Geochronology Centre.
Lui, Y. et al., 2004. Mineral matter–organic matter association characterisation by QEMSCAN and applications in coal utilisation. Fuel.
Machado, N. and Simonetti, A., 2001. U-Pb and Hf isotopic composition of zircon by laser ablation MC-ICP-MS. In: P. Sylvester (Editor), Laser ablation-ICPMS in the Earth Sciences: Principles and Applications. St. John's, Newfoundland, Mineralogical Association of Canada, pp. 121-146.
Mahoney, J.J. et al., 1995. Geochemical characteristics of lavas from Broken Ridge, the Naturaliste Plateau and Southernmost Kerguelen plateau: Cretaceous plateau volcanism in the Southeast Indian Ocean. Chemical Geology, 120: 315-345.
Maniar, P.D. and Piccoli, P.M., 1989. Tectonic discrimination of granitoids. Geological Society of America Bulletin, 101: 635-643.
Manikyamba, C., Kerrich, R., Khanna, T.C., Keshav Krishna, A. and Satyanarayanan, M., 2008. Geochemical systematics of komatiite–tholeiite and adakitic–arc basalt associations: the role of a mantle plume and convergent margin in formation of the Sandur Superterrane, Dharwar craton, India. Lithos, 106(1-2): 155-172.
Manikyamba, C., Kerrich, R., Khanna, T.C., Satyanarayanan, M. and Krishna, A.K., 2009. Enriched

and depleted arc basalts, with Mg-andesites and adakites: A potential paired arc–back-arc of the 2.6 Ga Hutti greenstone terrane, India. Geochimica et Cosmochimica Acta, 73: 1711–1736.

Manikyamba, C., Kerrich, R., Naqvi, S.M. and Mohan, M.R., 2004. Geochemical systematics of tholeiitic basalts from the 2.7 Ga Ramagiri-Hungund composite greenstone belt, Dharwar craton Precambrian Research (134): 21-39.

Manikyamba, C. et al., 2005. Boninites from the Neoarchaean Gadwal Greenstone belt, Eastern Dharwar Craton, India: implications for Archaean subduction processes. Earth and Planetary Science Letters, 230: 65-83.

Manya, S., Makenya, A.H.M. and Nakamurab, E., 2007. The geochemistry of high-Mg andesite and associated adakitic rocks in the Musoma-Mara Greenstone Belt, northern Tanzania: Possible evidence for Neoarchaean ridge subduction? Precambrian Research, 159: 241–259.

Martin, H., 1986. Effect of steeper Archaean geothermal gradient on geochemistry of subduction-zone magmas. Geology, 14: 753-756.

Martin, H., 1987a. Petrogenesis of Archaean trondhjemites, tonalites and granodiorites from eastern Finland: Major and trace element geochemistry. Journal of Petrology, 28: 921-953.

Martin, H., 1987b. Archaean and modern granitoids as indicators of changes in geodynamic processes. Reviews in Brasilian Geoscience, 17: 360-365.

Martin, H., 1994. The Archean grey gneisses and the genesis of the continental crust. In Archean Crustal Evolution K. C.Condie (Editor), Elsevier, Amsterdam: 205-259.

Martin, H., Smithies, R.H., Rapp, R., Moyen, J.F. and Champion, D., 2005. An overview of adakite, tonalite-trondhjemite-granodiorite (TTG), and sanukitoid: relationships and some implications for crustal evolution. Lithos, 79(1-2): 1-24.

McCuaig, T.C. and Kerrich, R., 1998. P–T–t-deformation-fluid characteristics of lode gold deposits; evidence from alteration systematics. Ore Geology Reviews, 12: 381–454.

McCuaig, T.C., Kerrich, R. and Xie, Q., 1994. Phosphorus and high field strength element anomalies in Archean high-magnesian magmas as possible indicators of source mineralogy and depth Earth and Planetary Science Letters, 124: 221-239.

Meschede, M., 1986. A method of discriminating between different types of mid-ocean ridge basalts and continental tholeiites with the Nb-Zr-Y diagram. Chemical Geology, 56: 207-218.

Mikucki, E.J. and Groves, D.I., 1990. Genesis of primary gold deposits: gold transport and depositional models. In: S.E. Ho, D.I. Groves and J.M. Bennett (Editors), Gold deposits of the Archaean Yilgarn Block, Western Australia: Nature, Genesis and Exploration Guides Geology Department and University Extension, The University of Western Australia Publication 20, pp. 212-220.

Mole, D.R. and et al., 2010. Lithospheric controls on the localization of komatiite-hosted nickel-sulfide deposits. In: Tyler I. M. & Knox-Robinson C. M. eds. Fifth International Archean Symposium abstracts. Geological Survey of Western Australia Record 2010: 101-103.

Morris, P.A., Riganti, A. and Chen, S.F., 2007. Evaluating the provenance of Archean sedimentary rocks of the Diemals Formation (central Yilgarn Craton) using whole-rock chemistry and precise U – Pb zircon chronology. Australian Journal of Earth Sciences, 54: 1123 – 1136.

Morris, P.A. and Witt, W.K., 1997. Geochemistry and tectonic setting of two contrasting Archaean felsic volcanic associations in the Eastern Gold fields, Western Australia. Precambrian Research, 83 83-107.

Moyen, J.-F., 2009. High Sr/Y and La/Yb ratios: the meaning of the “adakitic signature”. Lithos, 112: 556–574.

Moyen, J.F., 2008. Is there an Archaean TTG suite? Geochimica et Cosmochimica Acta, 72(12): A657.

Moyen, J.F., Champion, D.C. and Smithies, R.H., 2010. The geochemistry of Archaean plagioclase-rich granites as marker of source enrichment and depth of melting. Earth Sciences.

Moyen, J.F., Martin, H., Jayananda, M. and Auvray, B., 2003. Late Archaean granites: a typology based on the Dharwar Craton (India). Precambrian Research, 127(1–3): 103-123.

Mshiu, E. E., and Maboko, M. E. H., 2012. Geochemistry and petrogenesis of the late Archaean high-K granites in the southern Musoma-Mara Greenstone Belt: Their influence in evolution of Archaean Tanzania Craton. Journal of African Earth Sciences, 66–67: 1–12.

Mucke, A. and Cabra, A.R., 2005. Redox and nonredox reactions of magnetite and hematite in rocks. Chemie der Erde, 65: 271–278.

Mueller, A.G., Campbell, I.H., Schiotte, L., Sevigney, J.H. and Layer, P.W., 1996. Constraints on the age of granitoid emplacement, metamorphism, gold mineralization, and subsequent cooling

of the Archean greenstone terrane at Big Bell, Western Australia. Economic Geology, 91: 896-915.

Muhling, P.C. and Low, G.H., 1977. Yalgoo, Western Australia, Notes1: 250000 Geological Series Explanatory notes. Western Australia Geological Survey.

Mulrooney, D. and Rivers, T., 2005. Redistribution of the rare-earth elements among coexisting minerals in metamafic rocks across the epidote-out isograd: an example from the St. Anthony complex, northern Newfoundland, Canada. The Canadian Mineralogist, 43: 263-294.

Muntener, O. and Ulmer, P., 2006. Experimentally derived high-pressure cumulates from hydrous arc magmas and consequences for the seismic velocity structure of lower arc crust. Geophysical Research Letters, 33(21).

Muntener, O., Ulmer, P. and Perez, R.A., 2008. Role of garnet and amphibole fractionation in the genesis of high Mg# granitoids, Goldschmidt Conference Abstracts 2008 Geochimica et Cosmochimica Acta, pp. A665-A665.

Myers, J.S., 1990a. Precambrian tectonic evolution of part of Gondwana, southwestern Australia. Geology, 18: 537-540.

Myers, J.S., 1990b. Excursion 1: Narryer Gneiss Complex. In: S.E. Ho, J.E. Glover, J.S. Myers and J.R. Muhling (Editors), Third International Archaean Symposium Perth, Western Australia,1990, Excursion Guide Book, pp. 61-95.

Myers, J.S., 1990c. Precambrian tectonic evolution of part of Gondwana, southwestern Australia. Geology, 18: 537-540.

Myers, J.S., 1993. Precambrian history of the West Australian craton and adjacent orogens. Annual Review Earth and Planetary Science, 21: 453-485.

Myers, J.S., 1995. Generation and assembly of an Archaean supercontinent: Evidence from the Yilgarn craton, Western Australia. In: M.P. Coward and A.C. Ries (Editors), Early Precambrian Processes. Geological Society of London, Special publication, pp. 143-154.

Myers, J.S., 1997. Preface: Archaean geology of the Eastern Goldfields of Western Australia — regional overview. Precambrian Research, 83: 1-10.

Myers, J.S. and Hocking, R., 1998. Geological map of Western Australia 1:250000. Geological Survey of Western Australia, Perth.

Myers, J.S. and Swager, C.P., 1997. The Yilgarn Craton. In: M.J. De Wit and L.D. Ashwal (Editors), Greenstone belts. Clarendon Press, Oxford, U.K., pp. 640–656.

Nair, R. and Chacko, T., 2008. Role of oceanic plateaus in the initiation of subduction and origin of continental crust. Geology, 36: 583-586.

Neall, F.B. and Phillips, G.N., 1987. Fluid-wall rock interaction in an Archean hydrothermal gold deposit: A thermodynamic model for the Hunt Mine, Kambalda. Economic Geology 82: 1679-1694.

Nelson, D.R., 1995. Compilation of SHRIMP U-Pb zircon geochronology data 1994. Geological Survey of Western Australia Record, 1995/3.

Nelson, D.R., 1996. Report on the SHRIMP U–Pb zircon dating of an altered granodiorite at Tarmoola for Mt Eden Gold Mines (Australia) Limited. Research Memorandum, Geological Survey of Western Australia, Perth. 2 pp.

Nelson, D.R., 1997. Compilation of SHRIMP U-Pb zircon geochronological data, 1996. Geological Survey of Weatern Australia, Record: 1997/2.

Nelson, D.R., 2001. 169003: vesicular rhyolite, Carron Hill. Compilation of geochronology data, 2000, Western Australia Geological Survey, .

Nemchin, A.A. and Pidgeon, R.T., 1998. Precise conventional and SHRIMP baddeleyite U-Pb age for the Binneringie Dyke, near Narrogin, Western Australia. Australian Journal of Earth Sciences, 45: 673- 675.

Nemchin, A.A., Pidgeon, R.T. and Wilde, S.A., 1994. Timing of late Archaean granulite facies metamorphism in the southwest Yilgarn Craton of Western Australia: evidence from U-Pb ages of zircons from mafic granulites. Precambrian Research, 68: 307-321.

Neuendorf, K.K.E., Mehl, J.P.J. and Jackson, J.A., 2005. Glossary of Geology. American Geological Institute, 779 pp.

Nutman, A.P., Bennett, V.C., Kinny, P.D. and Price, R., 1993. Large-scale crustal structure of the northwestern Yilgarn Craton, Western Australia: evidence from Nd isotope data and zircon geochronology. Tectonics, 12: 971–981.

O'Hara, M.J., 1977. Geochemical evolution during fractional crystallization of a periodically filled magma chamber. Nature 265: 503-507.

Ojala, V.J., 1995. Structural and depositional controls on gold mineralisation at the Granny Smith Mine, Laverton, Western Australia. Unpublished Ph.D. Thesis, University of Western

Australia, Perth.
Ojala, V.J., Groves, D.I. and Ridley, J.R., 1995. Hydrogen isotope fractionation factors between hydrous minerals and ore fluids at low temperatures: evidence from the Granny Smith gold deposit, Western Australia. Mineralium Deposita 30: 328-331.
Ojala, V.J., McNaughton, N.J., Ridley, J.R., Groves, D.I. and Fanning, C.M., 1997. The Archaean Granny Smith gold deposit, Western Australia: age and Pb-isotope tracer studies. Chronique de la Recherche Minière, 529: 75-89.
Ojala, V.J., Ridley, J.R., Groves, D.I. and Hall, G.C., 1993. The Granny Smith gold deposit: the role of heterogeneous stress distribution at an irregular granitoid contact in a greenschist facies terrane. Mineralium Deposita, 28: 409–419.
Oliver, B., 1999. Granitoids of the Mount Mulgine and Noongal Areas, Murchison Province, Western Australia: Origin and relationship with granitophile and gold mineralisation. Unpublished B.Sc. Honours Thesis, University of Western Australia, Perth: 98.
Ordóñez-Calderón et al., 2009. Geochemistry and geodynamic origin of Mesoarchean oceanic crust in the Ujarassuit and Ivisaartoq greenstone belts, SW Greenland. Lithos, 113: 133–157.
Pascoe, R.D., Power, M.R. and Simpson, B., 2007. QEMSCAN analysis as a tool for improved understanding of gravity separator performance. Minerals Engineering, 20: 487–495.
Patinõ Douce, A.E., 2005. Vapor-absent melting of tonalite at 15- 32 kbar. Journal of Petrology, 46: 275-290.
Patinõ Douce, A.E. and Beard, J.S., 1995. Dehydration melting of biotite gneiss and quartz amphibolite from 3 to 15 kbar. Journal of Petrology, 36: 707-738.
Pawley, M.J. et al., 2012. Adding pieces to the puzzle: episodic crustal growth and a new terrane in the northeast Yilgarn Craton, Western Australia. Australian Journal of Earth Sciences, 59: 603-623.
Pearce, J.A., Harris, B.W., and Tindle, A.G., 1984. Trace element discrimination diagrams for the tectonic interpretation of granitic rocks. Journal of Petrology 25: 956-983.
Pearce, J.A., 2008. Geochemical fingerprinting of oceanic basalts with applications to ophiolite classification and the search for Archean oceanic crust. Lithos, 100(1-4): 14–48.
Pearce, J.A. and Cann, J.R., 1973. Tectonic setting of basic volcanic rocks determined using trace element analyses. Earth and Planetary Science Letters, 19: 290-300.
Pearce, J.A. and Norry, M.L., 1979. Petrogenetic implications of Ti, Zr, Y, and Nb variations in volcanic rocks. Contributions to Mineralogy and Petrolgy, 69: 33-47.
Pearce, J.A. and Parkinson, I.J., 1993. Trace element models for mantle melting: application to volcanica rc petrogenesis. Geological Society of London, Special Publication, 76: 373-403.
Pearce, J.A. and Peate, D.W., 1995. Tectonic implications of the composition of volcanic arc magmas. Annual review of Earth and Planetary Sciences, 23: 251-85.
Pearce, J.A. et al., 1992. Boninite and Harzburgite from Leg 125 (Bonin– Mariana Fore-arc): a case study of magma genesis during the initial stage of subduction. In: P. Fryer, J.A. Pearce and L.B. Stokking (Editors), Proceedings for the ocean drilling program Scientific Results, pp. 623-659.
Pidgeon, R.T., 1986. The correlation of acid volcanics in the Archaean of Western Australia. 27, Western Australia Mineral and Petroleum Research Institute.
Pidgeon, R.T., 1986. The correlation of acid volcanics in the Archaean of Western Australia, Western Australia Mineral and Petroleum Research Institute. Report 27.
Pidgeon, R.T., 1992. Recrystallization of oscillatory zoned zircon: some geochronological and petrological implications. Contributions to Mineralogy and Petrology 110: 463-472.
Pidgeon, R.T. and Cook, T.J.F., 2003. 1214 ± 5 Ma dyke from the Darling Range, southwestern Yilgarn Craton, Western Australia. Australian Journal of Earth Sciences, 50: 769–773.
Pidgeon, R.T. and Hallberg, J.A., 2000. Age relationships in supracrustal sequences in the northern part of the Murchison Terrane, Archaean Yilgarn Craton, Western Australia: a combined field and zircon U-Pb study. Australian Journal of Earth Sciences, 47: 153-165.
Pidgeon, R.T. and Nemchin, A.A., 2001. 1.2 Ga mafic dyke near York, southwestern Yilgarn Craton, Western Australia. Australian Journal of Earth Sciences, 48: 751-755.
Pidgeon, R.T., Nemchin, A.A. and Hitchen, G.J., 1998. Internal structures of zircons from Archaean granites from the Darling Range batholith: implications for zircon stability and the interpretation of zircon U-Pb ages. Contributions to Mineralogy and Petrology, 132: 288-299.
Pidgeon, R.T. and Wilde, S.A., 1990. The distribution of 30 and 2.7 Ga volacanic episodes in the Yilgarn Craton of Western Australia. Precambrian Research, 48: 309-325.
Pirajno, F., Jones, J.A., Hocking, R.M. and Halilovic, J., 2004. Geology and tectonic evolution of Palaeoproterozoic basins of the eastern Capricorn Orogen, Western Australia. Precambrian

Research, 128: 315–342.
Pirajno, F. and Occhipinti, S.A., 2000. Three Palaeoproterozoic basins-Yerrida, Bryah and Padbury-Capricorn Orogen Western Australia. Australian Journal of Earth Science, 47: 675-688.
Pirajno, F., Occhipinti, S.A. and Swager, C.P., 1998. Geology and tectonic evolution of the Palaeoproterozoic Bryah, Padbury and Yerrida Basins (formerly Glengarry Basin), Western Australia: implications for the history of the south-central Capricorn Orogen. Precambrian Research, 90: 119-140.
Pirrie, D., Butcher, A.R., Power, M.R., Gottlieb, P. and Miller, G.L., 2004. Rapid quantitative mineral and phase analysis using automated scanning electron microscopy (QEMSCAN): potential applications in forensic geosciences. Forensic geosciences: Principles, techniques and applications, 232: 123–136.
Polat, A., 2009. The geochemistry of Neoarchean (ca. 2700 Ma) tholeiitic basalts, transitional to alkaline basalts, and gabbros, Wawa Subprovince, Canada: implications for petrogenetic and geodynamic processes. Precambrian Research, 168: 83-105.
Polat, A. and Hofmann, A.W., 2003. Alteration and geochemical patterns in the 3.7-3.8 Ga Isua greenstone belt, west Greenland. Precambrian Research, 126: 197-218.
Polat, A., Hofmann, A.W. and Rosing, M.T., 2002. Boninite-like volcanic rocks in the 3.7–3.8 Ga Isua greenstone belt, West Greenland: geochemical evidence for intra-oceanic subduction zone processes in the early Earth. Chemical Geology, 184: 231–254.
Polat, A. and Kerrich, R., 2001. Magnesian andesites, Nb-enriched basalt-andesites, and adakites from late-Archean 2.7 Ga Wawa greenstone belts, Superior Province, Canada: implication for late Archean subduction zone petrogenetic processes. Contributions to Mineralogy and Petrology, 141: 36-52.
Polat, A. and Kerrich, R., 2006. Reading the geochemical fingerprints of Archean hot subduction volcanic rocks: evidence for accretion and crustal recycling in a mobile tectonic regime. AGU Geophysical Monograph Series, 164: 189-213.
Polat, A., Kerrich, R. and Wyman, D.A., 1998. The late Archean Schreiber–Hemlo and White River–Dayohessarah greenstone belts, Superior Province: collages of oceanic plateaus, oceanic arcs, and subduction–accretion complexes. Tectonophysics, 289: 295–326.
Polat, A., Kerrich, R. and Wyman, D.A., 1999. Geochemical diversity in oceanic komatiites and basalts from the late Archean Wawa greenstone belts, Superior Province, Canada: trace element and Nd isotope evidence for a heterogeneous mantle. Precambrian Research 94: 139-173.
Powell, R. and Holland, T.J.B., 2001. Course notes for THERMOCALC workshop 2001: Calculating Metamorphic Phase Equilibria (on CD-ROM).
Prosperity Resources Limited, 2004. False colour aeromagnetic image of the north Yalgoo area
Prosperity Resources Limited, 2005. Plan view of the locations of RC drillholes, significant intercepts from each drillhole and schematic E-W cross section along 14390mN across the mineralized zone in the Brilliant open pit Prosperity Resources Limited.
Puchtel, I.S. et al., 1999. Combined mantle plume-island arc model for the formation of the 2.9 Ga sumozero-kenozero greenstone belt, se baltic shield: isotope and trace element constraints. Geochimica et Cosmochimica Acta, 63(21): 3579-3595.
Puchtel, I.S. et al., 1998. Oceanic plateau model for continental crustal growth in the Archean: a case study from the Kostomuksha greenstone belt, NW Baltic Shield Earth and Planetary Science Letters, 155: 57-74.
Qui, Y. and Groves, D.I., 1999. Late Archaean collision and delamination in the southwest Yilgarn: The driving force for Archaean orogenic lode gold mineralization? Economic Geology, 94: 115-122.
Ramboz, C., Pichavant, M. and Weisbrod, A., 1982. Fluid immiscibility in natural processes: Use and misuse of fluid inclusion data. II. Interpretation of fluid inclusion data in terms of immiscibility. Chemical Geology, 37: 29-48.
Rasmussen, B. and Fletcher, I.R., 2004. Zirconolite: A new U-Pb chronometer for mafic igneous rocks. Geology, 39: 785-788.
Rasmussen, B., Fletcher, I.R., Muhling, J.R. and Wilde, S.A., 2010. In situ U-Th-Pb geochronology of monazite and xenotime from the Jack Hills belt: implications for the age of deposition and metamorphism of Hadean zircons. Precambrian Research, 180: 26-46.
Reagan, M.K., Hanan, B.B., Heizler, M.T., Hartman, B.S. and Hickey-Vargas, R., 2008. Petrogenesis of volcanic rocks from Saipan and Rota, Mariana Islands, and implications for the evolution of nascent island arcs. Journal of Petrology, 49: 441-464.
Robert, F. and Kelly, W.C., 1987. Ore-forming fluids in Archaean gold bearing quartz veins at the

Sigma Mine, Abitibi greenstone belt, Quebec, Canada. Economic Geology, 82: 1464-1482.
Roedder, E., 1984. Fluid inclusions. Reviews in Mineralogy, 12. Mineralogical Society of America, 644 pp.
Rudnick, R.L. and Fountain, D.M., 1995. Nature and composition of the continental crust—a lower crustal perspective. Review in Geophysics, 33: 267-309.
Rudnick, R.L. and Gao, S., 2004. Composition of the continental crust. In: H.D. Holland and K.K. Turekian (Editors), Treatise of Geochemistry. Elsevier, Amsterdam.
Said, N. and Kerrich, R., 2009. Geochemistry of coexisting depleted and enriched Paringa Basalts, in the 2.7 Ga Kalgoorlie Terrane, Yilgarn Craton, Western Australia: evidence for a heterogeneous mantle plume event. Precambrian Research, 174(3-4): 287-309.
Said, N., Kerrich, R. and Groves, D., 2010. Geochemical systematics of basalts of the Lower Basalt Unit, 2.7 Ga Kambalda Sequence, Yilgarn Craton, Australia; plume impingement at a rifted craton margin Lithos, 115: 82-100.
Salier, B.P., Groves, D.I., McNaughton, N.J. and Fletcher, I.R., 2005. Geochronological and Stable Isotope Evidence for Widespread Orogenic Gold Mineralization from a Deep-Seated Fluid Source at ca 2.65 Ga in the Laverton Gold Province, Western Australia. Economic Geology, 100: 1363-1388.
Sandeman, H.A., Hanmer, S., Davis, W.J., Ryan, J.J. and Peterson, T.D., 2004. Neoarchaean volcanic rocks, Central Hearne supracrustal belt, Western Churchill Province, Canada: geochemical and isotopic evidence supporting intra-oceanic, suprasubduction zone extension. Precambrian Research 134: 113-141.
Scherer, E., Munker, C. and Mezger, K., 2001. Calibration of the lutetium–hafnium clock. Science, 293: 683–687.
Schiøtte, L. and Campbell, I.H., 1996. Chronology of the Mount Magnet granite-greenstone terrain, Yilgarn Craton, Western Australia: implications for field based predictions of the relative timing of granitoid emplacement. Precambrian Research, 78: 237-260.
Schmidt, M.W., Dardon, A., Chazot, G. and Vanucci, R., 2004. The dependence of Nb and Ta rutile-melt composition and Nb/Ta fractionation during subduction processes. Earth and Planetary Science Letters 226: 415-432.
Schuth, S. et al., 2004. Geochemical constraints on the petrogenesis of arc picrites and basalts, New Georgia Group, Solomon Islands. Contributions to Mineralogy and Petrology, 148: 288–304.
Seward, T.M., 1973. Thio complexes of gold and the transport of gold in hydrothermal ore solutions. Geochimica et Cosmochimica Acta, 37: 379-399.
Seward, T.M., 1991. The hydrothermal geochemistry of gold. In: R.P. Foster (Editor), Gold metallogeny and exploration. Glasgow, Blackies, pp. 165-209.
Shellnutt, J.G. and Zellmer, G.F., 2010. High-Mg andesite genesis by upper crustal differentiation. Journal of the Geological Society of London, 167: 1081-1088.
Shenberger, D.M. and Barnes, H.L., 1989. Solubility of gold in aqueous sulfide solutions from 150 to 350 C. Geochimica et Cosmochimica Acta, 53: 269-278.
Shepherd, T.J., Rankin, A.H. and Alderton, D.H.M., 1985. A practical guide to fluid inclusion studies. Blackie and Son, Glasgow, 239 pp.
Sibson, R.H., Robert, F. and Poulsen, K.H., 1988. High-angle reverse faults, fluid-pressure cycling and mesothermal gold–quartz deposits. Geology 16: 551-555.
Skjerlie, K.P. and Johnston, A.D., 1996. Vapour-absent melting from 10 to 20 kbar of crustal rocks that Contain multiple hydrous phases: implications for anatexis in the deep to very deep continental crust and active continental margins. Journal of Petrology, 37: 661-691.
Skjerlie, K.P. and Pati ˜no Douce, A.E., 2002. The fluid-absent partial melting of a zoisite bearing quartz eclogite from1.0 to 3.2 Gpa: implications for melting in thickened continental crust and for subduction-zone processes. Journal of Petrology, 43: 291-314.
Smithes, R.H., Champion, D.C., Van Kranendonk, M.J., Howard, H.M. and Hickman, A.H., 2005. Modern-style subduction processes in the Mesoarchaean: Geochemical evidence from the 3.12 Ga Whundo intra-oceanic arc. Earth and Planetary Science Letters, 231: 221-237.
Smithies, R.H., 2002. Archaean boninite-like rocks in an intracratonic setting. Earth and Planetary Science Letters, 197 (1–2): 19–34.
Smithies, R.H., Champion, D.C. and Sun, S.-S., 2004. The case for Archaean boninites. Contributions to Mineralogy and Petrology, 147: 705-721.
Smithies, R.H., Champion, D.C. and Van Kranendonk, M.J., 2009. Formation of Paleoarchean continental crust through infracrustal melting of enriched basalt. Earth and Planetary Science Letters, 281: 298-306.
Smithies, R.H., van Kranendonk, M.J. and Champion, D.C., 2007. The Mesoarchean emergence of

modern-style subduction. Gondwana Research, 11: 50–68.
Soufoulis, J., 1966. Widgiemooltha, Western Australia: Western Australia Geological Survey,1 :250000 Geological Series Explanatory Notes.
Spaggiari, C.V., Wartho, J.A. and Wilde, S.A., 2008. Proterozoic deformation in the northwest of the Archean Yilgarn Craton, Western Australia. Precambrian Research, 162: 354–384.
Spear, F.S., 1993. Metamorphic Phase Equilibria and Pressure – Temperature – Time Paths. Mineralogical Society of America, Washington, D.C.
Srivastava, R.K., 2006. Geochemistry and petrogenesis of Neoarchaean high-Mg low- Ti mafic igneous rocks in an intracratonic setting, Central India craton: evidence for boninite magmatism. Geochemical Journal, 40: 15–31.
Stein, E. and Dietl, C., 2001. Hornblende thermobarometry of granitoids from the Central Odenwald (Germany) and their implications for the geotectonic development of the Odenwald Mineralogy and Petrology, 72: 185-207.
Stern, R.J., 2004. Subduction initiation; spontaneous and induced. Earth and Planetary Science Letters, 226: 275-292.
Stern, R.J., 2010. The anatomy and ontogeny of modern intra-oceanic arc systems. In: T.M. Kusky, M.-G. Zhai and W. Xiao (Editors), The Evolving Continents: Understanding Processes of Continental Growth. Geological Society, London, Special Publications, 338, pp. 7-34.
Stern, R.J. and Bloomer, S.H., 1992. Subduction zone infancy: examples from the Eocene Izu–Bonin–Mariana and Jurassic California arcs. Bulletin of the Geological Society of America. Bulletin of the Geological Society of America, 104: 1621–1636.
Stern, R.J., Bloomer, S.H., Martinez, F., Yamazaki, T. and Harrison, T.M., 1996. The composition of back-arc basin lower crust and upper mantle in the Mariana Trough: A first report. Island Arc, 5: 354–372.
Storkey, A.C., Hermann, J., Hand, M. and Buick, I.S., 2005. Using in situ trace-element determinations to monitor partial-melting processes in metabasites. Journal of Petrology 46: 1283-1308.
Streckeisen, A., 1976. To each plutonic rock its proper name. Earth Science Review, 12: 1-33.
Sun, S.-s. and Nesbitt, R.W., 1978. Geochemical regularities and genetic significance of ophiolitic basalts. Geology, 6: 689–693.
Sun, S.-s. and Hickman, A.H., 1999. Geochemical characteristics of ca 3.0-Ga Cleaverille greenstones and later mafic dykes, west Pilbara: implication for Archean crustal accretion. AGSO Newsletter, 31: 25-29.
Sun, S.-s. and McDonough, W.F., 1989. Chemical and isotopic systematics of ocean basalts: implications for mantle composition and processes. In: A.D. Saunders and M.J. Norry (Editors), Magmatism in the Ocean Basin Geological Society Special Publications, pp. 313–345.
Swager, C.P., 1995. Geology of the late Archaean Kurnalpi-Edjudina greenstone terranes, southeastern Yilgarn Craton. Western Australia Geological Survey, Report 47, 31 pp.
Swager, C.P., 1997. Tectono-stratigraphy of a late Archaean greenstone terranes in the Southern Eastern Goldfields, Western Australia. Precambrian Research, 83: 11-42.
Swager, C.P. et al., 1992. Late Archaean granite-greenstones of the Kalgoorlie Terrane, Yilgarn Craton, Western Australia. In: J.E. Glover and S.E. Ho (Editors), The Archaean: terrains, processes and metallogeny. The University of Western Australia, Geology Department and University Extension, Publication no. 22, pp. 107-122.
Sylvester, P.J., 1989. Post-collisional alkaline granites. Journal of Geology, 97: 261-280.
Sylvester, P.J., Campbell, I.H. and Bowyer, D.A., 1997. Niobium/Uranium evidence for early formation of the continental crust. Science, 275: 521-523.
Tatsumi, Y., 1981. Melting experiments on a high-magnesian andesite. Earth and Planetary Science Letters, 54: 357–365.
Tatsumi, Y., 2006. High-Mg andesites in the Setouchi Volcanic Belt, southwestern Japan: Analogy to Archean magmatism and continental crust formation? Annual review of Earth and Planetary Sciences 34: 467–499.
Tatsumi, Y. and Ishizaka, K., 1982. High magnesian andesite and basalt from Shodo-shima island, southwest Japan, and their bearing on the genesis of cal-alkaline andesites. Lithos, 15: 161-172.
Tatsumi, Y. and Maruyama, S., 1989. Boninites and high-Mg andesites: tectonics and petrogenesis. In: A.J. Crawford (Editor), Boninites and Related Rocks. London (Unwin Hyman), pp. 112-147.
Taylor, S.R. and McLennan, S.M., 1985. The continental crust: its composition and evolution. Blackwell, Oxford, 312 pp.

Taylor, S.R. and McLennan, S.M., 1995. The geochemical evolution of the continental crust. Reviews of Geophysics, 33: 241-265.

Thompson, M.J. et al., 1990. Gold deposits of Hill 50 Gold Mine NL at Mount magnet. In: F.E. Hughes (Editor), Geology of the Mineral Deposits of Australia and Papua New Guinea. Australian Institute of Mining and Metallurgy, Melbourne, pp. 221-241.

Tingey, R.J., 1985. Sandstone, Western Australia: Western Australia Geological Survey, 1:250000 Geological Series Explanatory Notes.

Trendall, A.F., 1990. Yilgarn Craton, introduction. Geology and Mineral Resources of Western Australia. Geological Survey of Western Australia, Memoir 3, pp. 11-13.

Turek, A., 1966. Rubidium-strontium isotopic studies in the Kalgoorlie-Norseman area, Western Australia, PhD Thesis (unpublished), Australian National University.

Tyler, I.M. and Hocking, R.M., 2001. A revision of the tectonic units of Western Australia, Western Australia Geological Survey.

Ulmer, P., 2007. Differentiation of mantle-derived calc-alkaline magmas at mid to lower crustal levels: experimental and petrologic constraints. Periodico di Mineralogia, 76(2-3): 309-325.

Ulmer, P., Muntener, O. and Perez, R.A., 2008. Differentiation of mantle-derived calc-alkaline magmas at mid to lower crustal levels: experimental and petrologic constraints, Goldschmidt Conference Abstracts 2008. Geochimica et Cosmochimica Acta, pp. A966-A966.

van der Laan, S.R., 1987. An experimental study of boninite genesis. [PhD dissert.], University of Illinois, Chicago, 103 pp.

Van Kranendonk, M.J., 2008. New evidence on the evolution of the Cue–Meekatharra area of the Murchison domain, Yilgarn Craton, Geological Survey of Western Australia Annual Review 2006-07. 39-49.

Van Kranendonk, M.J. and Ivanic, T.J., 2009. A new lithostratigraphic scheme for the northeastern Murchison Domain, Yilgarn Craton. Geological Survey of Western Australia Annual Review 2007–08: 34–53.

Van Kranendonk, M.J., Ivanic, T.J., Wingate, M.T.D. and Kirkland, C.L., 2012. Long-lived, autochthonous development of the Archean Murchison Domain, and implications for Yilgarn Craton tectonics. Precambrian Research, (in press), http://dx.doi.org/10.1016/j.precamres.2012.08.009.

van Thienen, P., Vlaar, N.J. and van den Berg, A.P., 2004. Plate tectonics on the terrestrial planets. Physics of the Earth Planet Inter, 142: 61-74.

Vervoort, J.D. and Blichert-Toft, J., 1999. Evolution of the depleted mantle: Hf isotope evidence from juvenile rocks through time. Geochimica et Cosmochimica Acta, 63(3-4): 533-556.

Walker, J.A., Pippin, C.G., Cameron, B.I. and Patino, L., 2002. Tectonic insights provided by Mesoproterozoic mafic rocks of the St. Francois Mountains, Southeastern Missouri. Precambrian Research, 117: 251-268.

Wang, L.G., McNaughton, N.J. and Groves, D.I., 1993. An overview of the relationship between granitoid intrusions and gold mineralisation in the Archean Murchison Province. Mineralium Deposita, 28: 482–494.

Wang, L.G., McNaughton, N.J. and Groves, D.I., 1995. New geochronological data for granitoid intrusions in the Reedy's Area, Murchison Province, Western Australia: constraints on genesis of gold mineralisation. Workshop Programme and Abstracts, Third Australian Conference on Geochronology and Isotope Geoscience., pp. 37.

Wang, Q., Schiotte, L. and Campbell, I.H., 1998. Geochronology of supracrustal rocks from the Golden Grove area, Murchison Province, Yilgarn Craton, Western Australia. Australian Journal of Earth Sciences, 45: 571-577.

Watkins, K.P., Fletcher, I.R. and de Laeter, J.R., 1991. Crustal evolution of Archaean granitoids in the Murchison Province, Western Australia. Precambrian Research, 50(3-4): 311-336.

Watkins, K.P. and Hickman, A.H., 1990. Geological evolution and mineralisation of the Murchison Province, Western Australia, Bulletin 137. Geological Survey of Western Australia, 267 pp.

Watkins, K.P., Tyler, I.M. and Hickman, A.H., 1987. Cue, Western Australia, (2nd edition) Geological Survey of Western Australia, I :250000 Geological Series Explanatory Notes.

Whalen, J.B., Currie, K.L. and Chappell, B.W., 1987. A-type granites: geochemical characteristics, discrimination and petrogenesis. Contribution to Mineralogy and Petrology, 95: 407-419.

White, A.J.R., 1979. Sources of granite magma. Geological Society of America Program with Abstracts, 11: 539.

Winchester, J.A. and Floyd, P.A., 1976. Geochemical magma type discrimination: application to altered and metamorphosed basic igneous rocks. Earth and Planetary Science Letters, 28: 459-469.

Wiedenbeck, M. and Watkins, K.P., 1993. A time scale for granitoid emplacement in Archean

Murchison Province, Western Australia, by single zircon geochronology. Precambrian Research, 61: 1-26.
Wilde, S.A., Middleton, M.F. and Evans, B.J., 1996. Terrane accretion in the southwestern Yilgarn Craton: Evidence from a deep seismic crustal profile. Precambrian Research, 78: 179-196.
Wilde, S.A. and Pidgeon, R.T., 1986. Geology and geochronology of the Saddleback Greenstone Belt in the Archaean Yilgarn Block, southwestem Australia. Australian Journal of Earth Science, 33: 491-501.
Wilde, S.A. and Pidgeon, R.T., 1990. Part III: Geology of the Jack Hills metasedimentary rocks, Third International Archaean Symposium, Excursion Guide Book. Geological Survey of Western Australia, Perth.
Wilde, S.A., Valley, J.W., Peck, W.H. and Graham, C.M., 2001. Evidence from detrital zircons for the existence of continental crust and oceans on Earth 4.4 Gyr ago. Nature, 409: 175–178.
Williams, I.R., 1974. Structural subdivision of the Eastern Goldfields Province, Yilgarn Block. Annual Report 1973: 53-59.
Williams, I.S., 1998. U–Th–Pb geochronology by ion microprobe. Review in Economic Geology, 7: 1–35.
Wilson, M., 1989. Igneous petrogenesis. Unwin Hyman., London, 457 pp.
Winchester, J.A. and Floyd, P.A., 1977. Geochemical discrimination of different magma series and their differentiation products using immobile elements. Chemical Geology, 20: 325-343.
Wingate, M.T.D., 2002. Age and paleomagnetism of dolerite sills of the Bangemall Supergroup on the EDMUND 1:250,000 map sheet, Western Australia. Geological Survey of Western Australia, 4: 48.
Wingate, M.T.D., 2007. Proterozoic mafic dykes in the Yilgarn craton. Geoscience Australia Record, 14: 249.
Wingate, M.T.D., Bodorkos, S. and Kirkland, C.L., 2008a. 178102: hornblende tonalite, Finger Post Bore; Geochronology Dataset 72, in Compilation of Geochronology Information, 2009 Update Geological Survey of Western Australia.
Wingate, M.T.D., Bodorkos, S. and Kirkland, C.L., 2008b. 183921: felsic volcaniclastic rock, Lordy Bore; Geochronology Dataset 733, in Compilation of Geochronology Information, 2009 Update, Geological Survey of Western Australia
Wingate, M.T.D., Bodorkos, S. and Kirkland, C.L. (Editors), 2008c. 178105: andesite, Woolgra Bore; Geochronology Dataset 730, in Compilation of Geochronology Information, 2009 Update. Geological Survey of Western Australia
Wingate, M.T.D., Bodorkos, S. and Kirkland, C.L., 2009a. 183975: metarhyolite, Wattagee Hill; Geochronology Dataset 785, in Compilation of Geochronology Information, 2009 Update Geological Survey of Western Australia.
Wingate, M.T.D., Bodorkos, S. and Van Kranendonk, M.J., 2009b. 178197: Biotite Monzogranite, Milliewarrie Well; Geochronology Record 790, Geological Survey of Western Australia
Wingate, M.T.D., Campbell, I.H. and Harris, L.B., 2000. SHRIMP baddeleyite age for the Fraser Dyke Swarm, southeast Yilgarn Craton, Western Australia. Australian Journal of Earth Sciences, 47: 309-313.
Wingate, M.T.D., Kirkland, C.L. and Ivanic, T.J., 2012. 193967: Hornblende–biotite Granodiorite, Mount Kenneth Bore; Geochronology Record 1010.
Wingate, M.T.D., Pirajno, F. and Morris, P.A., 2004. The Warakurna large igneous province: a new Mesoproterozoic large igneous province in west-central Australia. Geology, 32: 105-108.
Winter, J.D., 2001. An introduction to igneous and metamorphic petrology. Prentice Hall, 697 pp.
Witt, W.K., Hickman, A.H., Townsend, D. and Preston, W.A., 1998. Mineral potential of the Archaean Pilbara and Yilgarn Cratons, Western Australia. Australian Geological Survey Organisation, Journal of Australian Geology and Geophysics, 17(3): 201-221.
Witt, W.K. and Swager, C.P., 1989. Structural setting and geochemistry of Archaean I-type granites in the Bardoc- Coolgardie area of the Norseman-Wiluna Belt, Western Australia. Precambrian Research, 41: 323-351.
Wood, B.J. and Turner, S.P., 2009. Origin of primitive high-Mg andesite: Constraints from natural examples and experiments. Earth and Planetary Science Letters, 283: 59–66.
Wood, D.A., 1980. The application a Th-Hf-Ta diagram to problems of tectonomagmatic classification and to establishing the nature of crustal contamination of basaltic lavas of the British Tertiary volcanic province. Earth and Planetary Science Letters, 50: 11-30.
Workman, R.K. and Hart, S.R., 2005. Major and trace element composition of the depleted MORB mantle (DMM). Earth and Planetary Science Letters, 231: 53-72.
Wu, F.Y., Yang, Y.H., Xie, L.W., Yang, J.H. and Xu, P., 2006. Hf isotopic compositions of the standard

zircons and baddeleyites used in U–Pb geochronology. Chemical Geology, 206: 105-126.
Wyborn, L.A.I., 1993. Constraints on interpretations of lower crustal structure, tectonic setting and metallogeny of the Eastern Goldfields and Southern Cross Provinces provided by granite geochemistry. Ore Geology Review, 8: 125-140.
Wyche, S., 2007. Evidence of pre-3100 Ma crust in the Youanmi and South West Terranes, and Eastern Goldfields Superterrane, of the Yilgarn Craton. In: M.J. Van Kranendonk, R.H. Smithies and V. Bennett (Editors), Earth's Oldest Rocks, Developments in Precambrian Geology Elsevier, Amsterdam.
Wyche, S. et al., 2012. Isotopic constraints on stratigraphy in the central and eastern Yilgarn Craton, Western Australia. Australian Journal of Earth Sciences: An International Geoscience Journal of the Geological Society of Australia, 59: 657–670.
Wyche, S., Nelson, D.R. and Riganti, A., 2004. 4350-3130 Ma detrital zircons in the Southern Cross Granite-Greenstone Terrane, Western Australia: implications for the early evolution of the Yilgarn Craton. Australian Journal of Earth Sciences, 51(1): 31- 45.
Wyman, D.A., Bleeker, W. and Kerrich, R., 1999. A 2.7 Ga plume, protoarc, to arc transition and the geodynamic setting of the Kidd Creek deposit: evidence from precise ICP MS trace element data. Economic Geology Monograph, 10: 511–528.
Wyman, D.A. and Kerrich, R., 2002. Formation of Archean continental lithospheric roots: the role of mantle plumes. Geology, 306(6): 543-546.
Wyman, D.A. and Kerrich, R., 2009. Plume and arc magmatism in the Abitibi subprovince: Implications for the origin of Archean continental lithospheric mantle. Precambrian Research, 168: 4-22.
Wyman, D.A. and Kerrich, R., 2010. Mantle plume – volcanic arc interaction: consequences for magmatism, metallogeny, and cratonization in the Abitibi and Wawa subprovinces, Canada. Earth Science, 47: 565–589.
Wyman, D.A. and Kerrich, R., 2012. Geochemical and isotopic characteristics of Youanmi terrane volcanism: the role of mantle plumes and subduction tectonics in the western Yilgarn Craton. Australian Journal of Earth Sciences, 59: 671–694.
Xie, Q., Kerrich, R. and Fan, J., 1993. HFSE/REE fractionation recorded in three komatiite- basalt sequences, Archean Abitibi belt: implications for multiple plume sources and depths. Geochimica et Cosmochimica Acta, 57: 4111-4118.
Xiong, X.L., 2006. Trace element evidence for growth of early continental crust by melting of rutile-bearing hydrous eclogite. Geology, 34(11): 945-948.
Xiong, X.L., Adam, J. and T.H., G., 2005. Rutile stability and rutile/melt HFSE partitioning during partial melting of hydrous basalt: implications for TTG genesis. Chemical Geology, 218: 339-359.
Yeats, C.J. and Groves, D.I., 1998. The Archaean Mount Gibson gold deposits, Yilgarn Craton, Western Australia: Products of combined synvolcanic and syntectonic alteration and mineralisation. Ore Geology Reviews, 13: 103-129.
Yeats, C.J., McNaughton, N.J. and Groves, D.I., 1996. SHRIMP U-Pb geochronological constraints on Archaean volcanic-hosted massive sulphide and lode gold mineralization at Mount Gibson, Yilgarn Craton, Western Australia. Economic Geology, 91: 1354-1371.
Yogodzinski, G.M., Kay, R.W., Volynets, O.N., Koloskov, A.V. and Kay, S.M., 1995. Magnesian andesite in the western Aleutian Komandorsky region: implications for slab melting processes in the mantle wedge. Geological Society of America Bulletin, 107: 505–519.
Zellmer, G.F., 2009. Petrogenesis of Sr-rich adakitic rocks at volcanic arcs: insights from global variations of eruptive style with plate convergence rates and surface heat flux. Journal of the Geological Society of London, 166: 725–734.